Universität Bremen

ITP

BCCMS

Dissertation

Many-body instabilities in two-dimensional materials

Vielteilcheninstabilitäten in zweidimensionalen Materialien

vorgelegt von Jan Berges

aus Weener

Erstgutachter Prof. Dr. Tim Wehling
Zweitgutachter Prof. Dr. Ludger Wirtz

7. September 2020

Quotation by Yolanda Bedregal taken from “Bajo el Oscuro Sol.”
Published 1971 by Los Amigos del Libro, La Paz, Cochabamba.
Reproduced with kind permission of Rosángela Conitzer de Echazú.

Scripture quotations taken from The Holy Bible, New International Version,® NIV.®
Copyright © 1973 1978 1984 2011 by Biblica, Inc.™
Used by permission. All rights reserved worldwide.

Parts of Chap. 6 published in J. Phys. Condens. Matter **30** © 2018 IOP Publishing Ltd.
Parts of Chap. 8 published in ACS Nano **13** © 2019 American Chemical Society.
Parts of Chap. 9 published in Phys. Rev. B **101** © 2020 American Physical Society.

Typeset with LaTeX in New TX, Cabin, and `Bera Mono`.

Submitted on July 25, defended on September 7, and last amended on September 14, 2020.

Abstract

Two-dimensional materials constitute a prominent showplace of competing many-body instabilities such as superconductivity, charge-density waves (CDWs), and magnetism. Even though these phenomena populate rich phase diagrams whose regions often elude clear demarcation or yet remain to be fully explored, the underlying physics can always be reduced to the well-defined interactions between electrons and atomic nuclei. Here, we focus on CDWs and the associated periodic lattice distortions in the metallic transition-metal dichalcogenides (TMDCs), whose origin has been controversial for several decades. We approach the problem by *downfolding* the full system onto models with a largely reduced number of degrees of freedom that are complex enough to reproduce the relevant physics but at the same time simple enough to be dealt with efficiently. These models describe the low-energy electrons, phonons—the vibrations of the lattice—, and their interaction. Here, all model parameters are obtained from first principles, using methods such as density-functional theory, constrained density-functional perturbation theory (cDFPT), and the constrained random-phase approximation. In this context, we developed a computational scheme that allows us to calculate how the electrons *renormalize* the phonons (via consistent phonon self-energies) and thus effect the observed instabilities of the lattice. In this work, we apply our method to several distinct materials. In the case of a monolayer of the octahedral TMDC 1T-$NbSe_2$, we find that the presence of a CDW strongly impedes the mobility of the low-energy electrons and thus lays the ground on which electronic correlations eventually drive the system into an insulating phase. Independently, we show that in the family of monolayers of trigonal–prismatic TMDCs 1H-MX_2, the electrons and phonons qualitatively behave very similar but that quantitative differences in energies and interaction strengths finally determine the material specifics, including trends toward spin or charge order. Importantly, our cDFPT results reveal that possible lattice instabilities in these materials can be traced back to interactions of the longitudinal–acoustic phonons with the low-energy electrons alone. On this basis, we calculate the complete phase diagram of lattice instabilities in 1H-TaS_2—including stable regions and well as CDWs of different periodicities—as a function of charge doping and hybridization with substrates and thus explain contradictory findings from scanning–tunneling microscopy. Furthermore, introducing the concept of fluctuation diagnostics to the field of electron–phonon physics, we pinpoint the microscopic origin of these instabilities, for which many different mechanisms have been suggested in the past. We can rule out purely electronic mechanisms and confirm the importance of the momentum dependence of the electron–phonon coupling, which we trace back to the relevant electrons being massive Dirac fermions. Beyond this study, the calculation of *ab initio* phonon self-energies and their fluctuation diagnostics promises to be a useful tool that quite generally helps explain phonon anomalies in real materials.

Zusammenfassung

Zweidimensionale Materialien sind prominenter Schauplatz konkurrierender Vielteilcheninstabilitäten wie Supraleitung, Ladungsdichtewellen (CDWs) und Magnetismus. Obwohl diese Phänomene in vielschichtigen Phasendiagrammen angesiedelt sind, deren Regionen sich oft nicht klar voneinander abgrenzen lassen oder noch gar nicht vollständig erschlossen sind, kann die zugrundeliegende Physik immer auf die wohldefinierte Wechselwirkung von Elektronen und Atomkernen reduziert werden. Unser Fokus liegt auf CDWs und begleitenden periodischen Gitterverzerrungen in den metallischen Übergangsmetall-Dichalkogeniden (TMDCs), deren Ursprung jahrzehntelang kontrovers diskutiert wurde. Wir nähern uns dem Problem, indem wir das vollständige System auf Modelle mit reduzierten Freiheitsgraden *herunterfalten,* die komplex genug sind, um die relevante Physik wiederzugeben, aber gleichzeitig einfach genug, um effizient damit arbeiten zu können. Diese Modelle beschreiben die niederenergetischen Elektronen, Phononen – die Gitterschwingungen – und ihre Wechselwirkung. Hierbei berechnen wir alle Modellparameter *ab initio,* mithilfe von Methoden wie Dichtefunktionaltheorie, eingeschränkter Dichtefunktional-Störungstheorie (cDFPT) und cRPA. In diesem Zusammenhang haben wir ein computergestütztes Verfahren entwickelt, das uns erlaubt zu berechnen, wie die Elektronen die Phononen *renormieren* (über konsistente phononische Selbstenergien) und so die beobachteten Gitterinstabilitäten bewirken. In dieser Arbeit wenden wir unsere Methode auf verschiedene Materialien an. Im Falle einer Monolage des oktaedrischen TMDC 1T-$NbSe_2$ stellen wir fest, dass die Präsenz einer CDW die Mobilität der Elektronen stark einschränkt und so die Grundlage schafft, auf der elektronische Korrelationen das System schließlich in eine nichtleitende Phase treiben. Unabhängig davon zeigen wir, dass in der Familie der Monolagen trigonal-prismatischer TMDCs 1H-MX_2 die Elektronen und Phononen sich qualitativ sehr ähnlich verhalten, quantitative Unterschiede in Energien und Kopplungsstärken aber schließlich die Materialbesonderheiten bestimmen, einschließlich Tendenzen zu Spin- oder Ladungsordnung. Insbesondere aber offenbaren unsere cDFPT-Ergebnisse, dass mögliche Gitterinstabilitäten in diesen Materialien ausschließlich von Wechselwirkungen zwischen den longitudinal-akustischen Phononen und den niederenergetischen Elektronen stammen. Auf dieser Grundlage berechnen wir das vollständige Phasendiagramm der Gitterinstabilitäten in 1H-TaS_2 – einschließlich stabiler Bereiche sowie CDWs unterschiedlicher Periodizität – als Funktionen von Ladungsdotierung und Hybridisierung mit Substraten und erklären so widersprüchliche Ergebnisse aus der Rastertunnelmikroskopie. Indem wir das Konzept der Fluktuationsdiagnostik in den Bereich der Elektron-Phonon-Physik einführen, bestimmen wir darüber hinaus den mikroskopischen Ursprung dieser Instabilitäten, für welchen in der Vergangenheit viele verschiedene Mechanismen vorgeschlagen wurden. Wir können rein elektronische Mechanismen ausschließen und bestätigen die Wichtigkeit der Impulsabhängigkeit der Elektron-Phonon-Kopplung, welche wir darauf zurückführen, dass die relevanten Elektronen massive Dirac-Fermionen sind. Die Berechnung phononischer Selbstenergien und deren Fluktuationsdiagnostik verspricht darüber hinaus ein nützliches Werkzeug zu sein, das ganz allgemein dabei hilft, phononische Anonmalien in realen Materialien zu erklären.

Contents

Abstract . . . iii
List of Figures . . . ix
Tables . . . xi
List of Acronyms . . . xii
List of Symbols . . . xiv
1 Introduction . . . 1
2 *Ab initio* model Hamiltonians . . . 4
2.1 Born–Oppenheimer approximation . . . 6
2.2 Downfolding . . . 7
2.3 Electrons . . . 8
2.3.1 Density-functional theory . . . 8
2.3.1.1 Kohn–Sham equations . . . 9
2.3.1.2 Exchange–correlation functional . . . 10
2.3.1.3 Pseudopotentials . . . 11
2.3.1.4 Spin–orbit coupling . . . 12
2.3.2 Tight binding . . . 13
2.3.2.1 Triangular lattice of p orbitals . . . 14
2.3.2.2 Triangular lattice of d orbitals . . . 16
2.3.2.3 Trigonal–prismatic TMDCs . . . 17
2.3.3 Wannier functions . . . 18
2.4 Phonons . . . 19
2.4.1 Harmonic approximation . . . 19
2.4.2 Density-functional perturbation theory . . . 20
2.4.2.1 Calculations without empty states . . . 24
2.4.2.2 Constrained density-functional perturbation theory . . . 26
2.4.3 Mass–spring models . . . 27
2.4.3.1 Triangular lattice . . . 28
2.4.3.2 Trigonal–prismatic TMDCs . . . 30
2.4.3.3 Graphene . . . 31
2.4.4 Classification of eigenmodes . . . 32
2.4.5 Sum rules . . . 33
2.4.6 Goldstone bosons . . . 34
2.4.7 Nonadiabatic effects . . . 35
2.4.8 Anharmonic effects . . . 36
2.4.8.1 Total displacement . . . 36
2.5 Electron–phonon coupling . . . 37
2.5.1 *Ab initio* . . . 38
2.5.2 Tight binding . . . 38
2.5.3 Wannier representation . . . 41

2.6 Electron–electron interaction . . . 41
2.6.1 Random-phase approximation . . . 42
2.6.1.1 Constrained random-phase approximation . . . 42
2.6.2 Hubbard model . . . 43
2.6.3 Dynamical mean-field theory . . . 43
3 Many-body instabilities . . . 44
3.1 Charge-density waves . . . 45
3.1.1 Peierls instability . . . 45
3.1.2 Chan–Heine criterion . . . 46
3.1.3 Periodic lattice distortion . . . 46
3.2 Superconductivity . . . 49
3.2.1 Eliashberg theory . . . 50
3.2.1.1 Local Eliashberg equations . . . 51
3.2.1.2 McMillan's formula . . . 52
3.2.1.3 Linearized finite-bandwidth Eliashberg equations . . . 53
4 Two-dimensional materials . . . 56
4.1 Properties of selected 2D materials . . . 58
4.1.1 Graphene . . . 58
4.1.2 Transition-metal dichalcogenides . . . 58
4.1.2.1 Polytypes . . . 59
4.1.2.2 Optics . . . 59
4.1.3 Phosphorene . . . 60
4.2 Heterostructures . . . 60
4.3 Mermin–Wagner theorem . . . 61
5 Phonon renormalization . . . 62
5.1 Random–phase approximation . . . 62
5.2 Phononic Dyson equation . . . 64
5.2.1 Combination of bare and screened couplings . . . 65
5.2.2 Off-diagonal phonon self-energy . . . 66
5.2.3 Consistent gauge . . . 66
5.2.4 Smearing functions . . . 67
5.2.5 Removable singularities . . . 67
5.2.6 Cancellation of anti-Hermitian coupling . . . 67
5.3 Renormalization of coupling . . . 68
6 CDW and Mott physics in 1T-$NbSe_2$ . . . 71
6.1 Introduction . . . 71
6.2 Methods . . . 73
6.2.1 Density-functional theory . . . 73
6.2.1.1 Effects of nonlocal exchange . . . 73
6.2.2 Density-functional perturbation theory . . . 73
6.2.3 Estimate of screened Coulomb interaction . . . 74
6.2.4 Dynamical mean-field theory . . . 74
6.3 Electronic structure of the undistorted phase . . . 75
6.3.1 Effects of nonlocal exchange on Se-*p* bands. . . . 75
6.4 Periodic lattice distortion . . . 76
6.5 Electronic properties of the distorted phase . . . 77
6.5.1 Possibility of Mott physics . . . 78
6.6 Conclusions . . . 81

7 Material systematics of metallic transition–metal dichalcogenides . . . 82
7.1 Introduction . . . 82
7.2 Results . . . 84
7.2.1 Lattice parameters . . . 84
7.2.2 Electrons . . . 84
7.2.3 Phonons . . . 84
7.2.4 Coulomb interaction . . . 85
7.2.5 Spin susceptibility . . . 86
7.2.6 Electron–phonon coupling . . . 87
7.3 Computational parameters . . . 88
8 Phase diagram of lattice instabilities in mono- and bilayer 2H-TaS_2 . . . 89
8.1 Methods . . . 91
8.2 Results . . . 91
8.2.1 Monolayer . . . 91
8.2.2 Bilayer . . . 94
8.3 Computational parameters . . . 96
9 Fluctuation diagnostics of lattice instabilities in monolayer 1H-TaS_2 . . . 97
9.1 Introduction . . . 97
9.2 Bare and screened phonons . . . 98
9.3 *Ab initio* phonon self-energies . . . 100
9.4 Fluctuation diagnostics of phonon self-energies . . . 101
9.5 Fluctuation diagnostics of CDW formation in 1H-TaS_2 . . . 102
9.5.1 Pristine 1H-TaS_2 . . . 102
9.5.2 Doping dependence . . . 104
9.5.3 Van Hove scenarios . . . 105
9.6 Model electron–phonon couplings of 1H-TaS_2 . . . 107
9.6.1 Tight binding . . . 107
9.6.2 Massive Dirac fermions . . . 108
9.7 Generalizations of the method . . . 111
9.7.1 Effect of spin–orbit coupling . . . 111
9.7.2 Multiple bands and dimensions . . . 111
9.8 Computational parameters . . . 112
9.9 Conclusions . . . 113
10 Conclusions . . . 114
A Software . . . 116
A.1 Quantum ESPRESSO . . . 116
A.2 Wannier90 . . . 120
A.3 EPW . . . 120
A.4 VASP . . . 121
A.5 TRIQS . . . 121
A.6 elphmod . . . 121
A.7 Eliashberg solvers . . . 122
A.7.1 ebmb . . . 122
A.7.2 ebbw . . . 123
A.8 StoryLines . . . 126
A.9 PlasMoS . . . 126
A.10 Phonon renormalization with QE and elphmod . . . 126
B Algorithms . . . 133
B.1 Band disentanglement . . . 133

B.2 Completion of irreducible data . . . 134
B.3 2D tetrahedron methods . . . 135
B.3.1 Density of states . . . 135
B.3.2 Weighted density of states . . . 136
B.3.3 Double-delta approximation . . . 137
B.4 Interpolation . . . 138
B.4.1 Linear interpolation . . . 138
B.4.1.1 Interpolation of angles . . . 139
B.4.2 Fourier interpolation . . . 139
C Concepts and derivations . . . 140
C.1 Lattices . . . 140
C.1.1 Hexagonal lattice . . . 141
C.2 Density of states . . . 142
C.3 Representations and basis transforms . . . 143
C.4 Perturbation theory . . . 144
C.5 Charge and spin susceptibility . . . 146
C.6 Hellmann–Feynman theorem . . . 147
C.7 Occupation smearing . . . 147
C.7.1 Fermi–Dirac smearing . . . 148
C.7.2 Gaussian smearing . . . 148
C.7.3 Methfessel–Paxton smearing . . . 148
C.7.4 Lorentzian smearing . . . 149
C.8 Estimates of the Coulomb interaction . . . 150
C.8.1 Homogeneous disks . . . 151
C.8.2 Radially inhomogeneous disks . . . 151
D Miscellaneous projects . . . 153
D.1 Graphone . . . 153
D.2 Monolayer beryllium . . . 155
D.2.1 *Ab initio* . . . 155
D.2.2 Model . . . 156
D.3 Molecules . . . 158
D.4 CP_3 . . . 160
D.5 Sr_2RuO_4 . . . 161
D.6 Doped bilayer 2H-$MoSe_2$ . . . 163
Acknowledgments . . . 164
Erklärung . . . 165
Publications and presentations . . . 166
Publications . . . 166
Talks . . . 166
Posters . . . 167
Participations . . . 167
Tutorials . . . 168
Bibliography . . . 169

List of Figures

1.1 Remarkable electron–phonon-coupled systems . . . 2

2.1 Downfolding . . . 7
2.2 Triangular tight binding lattice . . . 14
2.3 Tight binding models of 1H-TaS_2 . . . 17
2.4 d_{z^2}-, $d_{x^2-y^2}$-, and d_{xy}-like Wannier functions . . . 18
2.5 Partially screened phonons of 1H-$NbSe_2$ . . . 25
2.6 Bare phonons of 1H-TaS_2 . . . 26
2.7 Triangular mass–spring lattice . . . 28
2.8 Mass–spring model of 1H-$NbSe_2$ . . . 29
2.9 Mass–spring and tight binding models of graphene . . . 32
2.10 Goldstone modes . . . 35
2.11 Anharmonicity in metallic and semiconducting TMDCs . . . 36
2.12 Pair bubble . . . 42

3.1 Peierls instability . . . 45
3.2 Periodic lattice distortion in 1H-$NbSe_2$ . . . 47
3.3 Electrons and phonons of 1H-$NbSe_2$ (unfolded) . . . 48
3.4 Electrons and phonons of 1H-$NbSe_2$ (folded back) . . . 49
3.5 Feynman diagrams of Eliashberg theory . . . 50
3.6 Critical temperature for steplike density of states . . . 51
3.7 Convergence of finite-bandwidth Eliashberg equations . . . 54
3.8 Comparison of Eliashberg theory and McMillan's formula . . . 55

4.1 Two-dimensional materials . . . 56
4.2 Metallic and semiconducting TMDCs . . . 59
4.3 Buckling of (quasi) 2D materials . . . 61

5.1 Feynman diagrams of the RPA phonon renormalization . . . 64
5.2 Comparison of bare, screened, and combined electron–phonon couplings . . . 66
5.3 Importance of correctly screened electron–phonon couplings . . . 67
5.4 Cancellation of anti-Hermitian components . . . 68
5.5 Renormalization of electron–phonon coupling. . . . 69

6.1 Star of David . . . 72
6.2 PBE results for undistorted 1T-$NbSe_2$ . . . 75
6.3 GW and HSE06 results for undistorted 1T-$NbSe_2$ . . . 75
6.4 Phonons and lattice instabilities of 1T-$NbSe_2$ . . . 76
6.5 PBE and HSE06 results for distorted 1T-$NbSe_2$ . . . 77
6.6 Unfolded bands of distorted 1T-$NbSe_2$ . . . 78
6.7 Charge density of distorted 1T-$NbSe_2$ . . . 78

6.8 Electronic self-energy of distorted 1T-$NbSe_2$ . . . 79
6.9 DMFT results for distorted 1T-$NbSe_2$ . . . 80
6.10 Mott–Hubbard or charge-transfer insulator? . . . 80

7.1 Similar dispersions, different bandwidths I: Electrons . . . 83
7.2 Similar dispersions, different bandwidths II: Phonons . . . 85
7.3 Kanamori parametrization . . . 86
7.4 Spin susceptibilities . . . 86
7.5 Similar dispersions, different bandwidths III: Electron–phonon coupling . . . 87
7.6 Comparison of electron–phonon couplings . . . 87

8.1 STM images of 1H-TaS_2 on different substrates . . . 90
8.2 Kohn anomalies for different temperatures and dopings . . . 90
8.3 Phase diagram of lattice instabilities in monolayer 1H-TaS_2 . . . 92
8.4 Effects of Li adsorption and graphene substrate . . . 93
8.5 Lattice instabilities in bilayer 2H-TaS_2 . . . 94
8.6 Effect of interlayer bias potential . . . 95

9.1 Crystal and electronic structure of 1H-TaS_2 . . . 98
9.2 Bare and screened phonons . . . 99
9.3 Changes in phonon-mode character . . . 101
9.4 $\boldsymbol{k}$-resolved fluctuation diagnostics . . . 103
9.5 $\boldsymbol{q}$-resolved fluctuation diagnostics . . . 104
9.6 $\boldsymbol{k}$- and energy-resolved fluctuation diagnostics . . . 105
9.7 Divergence in the Van Hove scenario . . . 106
9.8 Three different Van Hove scenarios . . . 107
9.9 Electron–phonon coupling of 1H-TaS_2 from tight binding model . . . 108
9.10 Electron–phonon coupling of 1H-TaS_2 from Dirac model . . . 109
9.11 Effect of spin–orbit coupling on fluctuation diagnostics . . . 110
9.12 Fluctuation diagnostics for bilayer 2H-TaS_2 . . . 111

B.1 Band disentanglement . . . 133
B.2 2D tetrahedron methods . . . 135
B.3 Double-delta approximation . . . 137
B.4 2D linear interpolation . . . 138

C.1 Hexagonal Bravais and reciprocal lattice . . . 141
C.2 Comparison of smearing functions . . . 148
C.3 Estimates of Coulomb interaction in Star of David phase . . . 150

D.1 Crystal structure, electrons, and phonons of graphone . . . 154
D.2 Fermi surface of graphone . . . 154
D.3 Stability of monoatomic triangular lattices . . . 155
D.4 Electrons and phonons of monolayer beryllium . . . 156
D.5 Tight binding and mass–spring model of monolayer beryllium . . . 157
D.6 Electron–phonon coupling of monolayer beryllium . . . 157
D.7 Ball–stick models of benzene and nitrogen . . . 158
D.8 Electrons and phonons of nitrogen . . . 158
D.9 Electrons and phonons of benzene . . . 159
D.10 Crystal structure of CP_3 . . . 160
D.11 Electrons and phonons of CP_3 . . . 160

D.12 Crystal structure and resistivity of Sr_2RuO_4 161
D.13 Electrons, phonons, and Eliashberg spectral function of Sr_2RuO_4 162
D.14 Electrons and phonons of doped bilayer 2H-$MoSe_2$ 163

Tables

7.1 Competition between spin- and charge order in metallic TMDCs 83
7.2 Lattice parameters of metallic TMDCs 84

D.1 Lattice parameters and band edges of 2H-$MoSe_2$ 162

List of Acronyms

1D one-dimensional (cf. Fig. 3.1)

2D two-dimensional (Chap. 4)

AIM Anderson impurity model (Sec. 2.6.3)

ARPES angle-resolved photoemission spectroscopy

ASR acoustic sum rule (Eq. 2.114)

BO Born–Oppenheimer (approximation) (Sec. 2.1)

BZ Brillouin zone (cf. Fig. C.1)

cDFPT constrained density-functional perturbation theory (Sec. 2.4.2.2)

CDW charge-density wave (Sec. 3.1)

cRPA constrained random-phase approximation (Sec. 2.6.1.1)

CT-QMC continuous-time quantum Monte Carlo (cf. Sec. 6.2.4)

DFPT density-functional perturbation theory (Sec. 2.4.2)

DFT density-functional theory (Sec. 2.3.1)

DMFT dynamical mean-field theory (Sec. 2.6.3)

DOS density of states (App. C.2)

EPC electron–phonon coupling (Sec. 2.5)

EPW Electron–Phonon Wannier (code) (App. A.3)

FLL fully localized limit (cf. Sec. 6.5.1)

GGA generalized gradient approximation (Sec. 2.3.1.2)

GW *GW* approximation (Green function G, interaction W) (Sec. 6.2.1.1)

HGH Hartwigsen–Goedecker–Hutter (pseudopotential) (cf. Secs. 7.3 and 9.8)

HOMO highest occupied molecular orbital (App. D.3)

HSE06 Heyd–Scuseria–Ernzerhof (hybrid functional) (Sec. 6.2.1.1)

HWHM half-width at half-maximum (cf. Fig. C.2)

IFC interatomic force constant (Sec. 2.4.1)

IR infrared (spectroscopy) (Sec. 2.4.4)

KS Kohn–Sham (equations) (Sec. 2.3.1.1)

LA longitudinal–acoustic (phonon mode) (Sec. 2.4.4)

LDA local-density approximation (Sec. 2.3.1.2)

LO longitudinal–optical (phonon mode) (Sec. 2.4.4)

LUMO lowest unoccupied molecular orbital (App. D.3)

MPI Message Passing Interface (Apps. A.6 and A.10)

PAW projector-augmented wave (method) (cf. App. A.4)

PBE Perdew–Burke–Ernzerhof (functional) (Sec. 2.3.1.2)

PLD periodic lattice distortion (Sec. 3.1.3)

PP pseudopotential (Sec. 2.3.1.3)

QE Quantum ESPRESSO (App. A.1)

RTG QM^3 Research Training Group 2247 “Quantum-Mechanical Materials Modelling”

RPA random-phase approximation (Sec. 2.6.1)

SCF self-consistent field (Sec. 2.3.1.1)

SDW spin-density wave (Sec. 7.2.5)

SOC spin–orbit coupling (Sec. 2.3.1.4)

SoD Star of David (PLD) (Figs. 6.1 and C.3a)

STM scanning–tunneling microscopy (Fig. 8.1)

TA transverse–acoustic (phonon mode) (Sec. 2.4.4)

TB tight binding (Sec. 2.3.2)

TMDC transition-metal dichalcogenide (Sec. 4.1.2)

TO transverse–optical (phonon mode) (Sec. 2.4.4)

TP trigonal–prismatic (TMDCs) (Sec. 4.1.2)

VASP Vienna *Ab initio* Simulation Package (App. A.4)

VHS Van Hove singularity (App. C.2)

WFCE Wannier-function continuum electrostatics (Sec. 2.6.1.1)

WS Wigner–Seitz (unit cell or supercell) (cf. Fig. C.1)

XC exchange–correlation (functional) (Sec. 2.3.1.2)

ZA out-of-plane–acoustic (phonon mode) (Sec. 2.4.4)

ZO out-of-plane–optical (phonon mode) (Sec. 2.4.4)

List of Symbols

E total energy

H Hamiltonian

D dynamical matrix

ε electron energy

ω phonon frequency

ψ, U electronic eigenvector

$\boldsymbol{e}$ phononic eigenvector

$\boldsymbol{u}$ atomic displacement

α, β indices of electronic orbitals

m, n indices of electronic bands

i, j indices of atomic displacements

k, l indices of atoms

x, y indices of Cartesian directions

ν, μ indices of phonon branches

$\hat{c}, \hat{c}^\dagger$ electronic ladder operators

$\hat{b}, \hat{b}^\dagger$ phononic ladder operators

t hopping parameter

C interatomic force constant

M atomic mass

$g, d = 2\omega g$ electron–phonon coupling

v bare Coulomb interaction

U partially screened Coulomb interaction

W fully screened Coulomb interaction

ϵ dielectric function

f Fermi function

T temperature

χ_0 bare electronic susceptibility

$G_{(0)}$ (bare) electronic Green function

$D_{(0)}$ (bare) phononic Green function

Σ electron self-energy

Π phonon self-energy

ω_n fermionic Matsubara frequency

ν_n bosonic Matsubara frequency

τ imaginary time

$\boldsymbol{a}_1, \boldsymbol{a}_2, \boldsymbol{a}_3$ Bravais basis vectors

$\boldsymbol{b}_1, \boldsymbol{b}_2, \boldsymbol{b}_3$ reciprocal basis vectors

$\boldsymbol{R}$ Bravais lattice vector

$\boldsymbol{G}$ reciprocal lattice vector

$\boldsymbol{r}$ position in real space

$\boldsymbol{k}$ fermionic wave vector

$\boldsymbol{q}$ bosonic wave vector

N number of lattice points

$\widetilde{\bullet}$ fully screened quantity

$\hat{\bullet}$ representation-free operator

$\bullet^*$ complex conjugate

$\bullet^\dagger$ adjoint operator or matrix

$\bullet^{\mathrm{T}}$ transposed matrix

$m_{\mathrm{e}} = 1$ electron mass

$e = 1$ elementary charge

$\hbar = 1$ reduced Planck constant

$k_{\mathrm{B}} = 1$ Boltzmann constant

$1/4\pi\epsilon_0 = 1$ Coulomb constant

Chapter 1

Introduction

Whereas, all and everything is naturally related and interconnected. A volume could I write you on this subject.

—Ada Lovelace

It may be hard to believe that the overwhelming complexity of the world we live in emerges solely from a handful of simple physical laws. However, it is universally observed—even beyond the scope of physics—that systems exhibit properties that differ significantly from those of their constituents on their own. This phenomenon is called *emergence* [1]. Examples range from mathematics, where complex fractals emerge from simple operations on numbers [2], to sociology, which is about individuals collaboratively creating a society [3]. In all cases, emergence requires some kind of *interaction* between the parts of the system. If this interaction surpasses a critical strength, the original state of the system may not be *stable* anymore but undergo a transition to a new state with unprecedented properties.

Here we consider the readily formulated problem of massive, charged particles in space that interact through a force proportional to their charges and inversely proportional to the square of their distance. (The particles are electrons and atomic nuclei; the interaction is the Coulomb force.) Together with the laws of quantum mechanics (and special relativity), this is enough to explain almost all properties of the material world and completely defines the field of condensed-matter physics. The thesis at hand only deals with a tiny part of this immense research area, but the applied (and thereby refined) concepts and methods serve a much more general purpose.

To be more precise, this work is largely focused on the class of two-dimensional (2D) materials, especially the metallic transition-metal dichalcogenides (TMDCs). Long-known as bulk materials consisting of multiple layers weakly bond by van der Waals forces [4], they lately sparked renewed interest after the realization of isolated monolayers with unexpected properties [5]. From experiment it is known that in these materials a variety of *many-body instabilities* can *emerge*, often in competition to each other [6]. Prominent examples are superconductivity [7], charge-density waves (CDWs) [8], exciton condensates [9], and magnetism [10]. Moreover, these effects are observed to strongly depend on parameters such as the dielectric environment [11, 12], (pseudo) charge doping [13, 14], or optical excitation [15, 16]. Due to the 2D nature of the materials, these can be conveniently manipulated externally, e.g., by varying the number of layers [17–22], using different substrates [23–25], building heterostructures [26, 27], twisting adjacent layers at *magic* angles [28, 29], applying a gate voltage [19], or depositing adatoms [30].

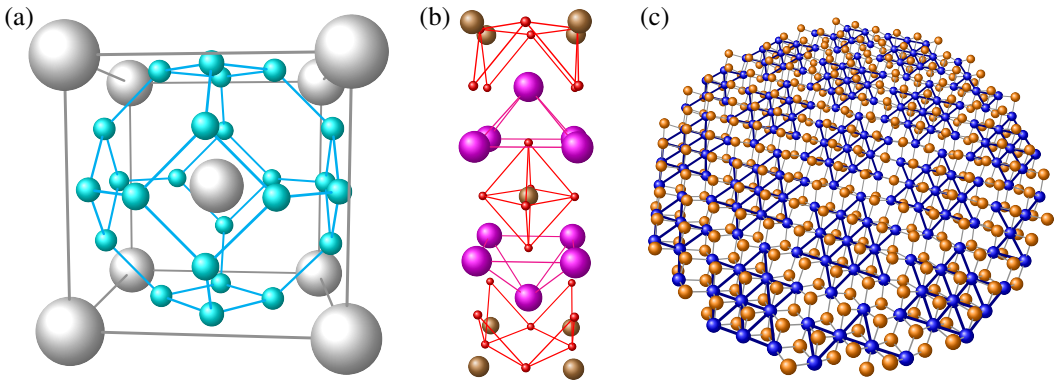

Figure 1.1: Crystal structures of remarkable electron–phonon-coupled systems. (a) Unit cell of CaH_6 *[inspired by Fig. 1c of Ref. 51]*. Hydrides are *conventional* high-T_c superconductors at high pressures. (b) Unit cell of La_2CuO_4 *[inspired by Fig. 3a of Ref. 52]*. Strontium doping generates the "LASCO" high-T_c superconductors $La_{2-x}Sr_xCuO_4$. Cuprates host intertwined superconducting, spin, and charge order. (c) "Star of David" phase of monolayer 1T-TaS_2 (cf. Fig. 2 of Ref. 53). A CDW-induced flat band gives rise to Mott–Hubbard physics.

Experimental control of these competing phases down to the monolayer limit has made significant progress, but yet the range of possibilities remains largely unexplored. Hence, we strive to better understand the underlying physics and investigate ways to engineer specific material properties. The main requirement for such studies is an appropriate atomistic theory.

Ever since the undeniable success of density-functional theory (DFT) [31, 32], it is possible to calculate the relevant material properties—within certain approximations but at an acceptable computational cost—*from first principles* or *ab initio*, i.e., without other free parameters than the atomic composition. Nonetheless, with growing complexity (e.g., system size) this approach still becomes prohibitively time and energy consuming. Also, certain many-body effects such as the Mott transition [33–37] due to strong *correlations* are not properly described. Today, a plethora of *ab initio* codes is publicly available [38–41]. Most of them can be used as a black box, thus providing valuable information with little effort—at the risk of neglecting the critical and in-depth analysis of a particular problem.

A different route is based on the formulation and solution of *lattice models* [33–35, 42–45], whose number of degrees of freedom is reduced to the minimum necessary to still capture the relevant physical processes. This usually requires some intuition but can also open the way to a deeper understanding. Due to their efficiency/lightweightness, models can often help with more challenging problems, both with respect to system size and the required level of approximation. By design, the model parameters are often based on simple guesses or fitted to experiment. As a consequence, results may give a better insight into the physical origin of an experimental observation, but are seldom predictive.

We want to follow a third strategy, namely the combination of *ab initio* and model calculations [46, 47]. All parameters that enter our model, namely the energies on noninteracting (quasi)particles together with their interaction strengths, are derived from first principles. This step of reducing the complexity of the problem is often referred to as *downfolding* [48–50]. The result is a tractable, yet *material-realistic* lattice model. The theoretical foundations of this approach are in principle laid, but a full realization and consistent treatment of all subtleties are missing in many cases.

Especially in the context of lattice vibrations, or *phonons*, and their coupling to electronic degrees of freedom, a lot of work remains to be done—despite the fact that the electron–phonon coupling (EPC) is ubiquitous in condensed-matter physics. Phonons are the driving

force behind several many-body instabilities. For instance, conventional superconductivity arises from a phonon-mediated electron attraction and a CDW can be seen as a (combination of) "frozen" phonon modes. To further illustrate this, in Fig. 1.1, three classes of materials are shown, where the interplay of electrons and phonons gives rise to most interesting phenomena being object of recent studies.

In Fig. 1.1a, the crystal structure of a hydride compound [54] is shown, in this case CaH_6. Already in 1968, Ashcroft envisioned that metallic hydrogen can be a high-temperature superconductor [55]. This has recently been confirmed for H_3S under high pressure by Drozdov *et al.* [56]. The record critical temperature found by these researches today is $T_c \approx -23\,^\circ\mathrm{C}$—almost room temperature—in LaH_{10} under megabar pressures [57]. Notably, the hydrides are really *conventional* superconductors, where phonons mediate the attraction between electrons needed to form Cooper pairs.

This is in contrast to the cuprates [58], a prototypical crystal structure of which is shown in Fig. 1.1b, where the mechanism behind high-T_c superconductivity is still a matter of debate. But also here, lattice degrees of freedom play an important role, since the superconducting order is intertwined with spin- and charge-ordered stripes [59] and any change in the charge density of a system is accompanied by a distortion of the lattice and vice versa. Additionally, cuprates are systems where strong electronic correlations play a role, i.e., where the picture of effectively noninteracting electrons breaks down, which directly leads to the third example.

In Fig. 1.1c, the crystal structure of the correlated CDW system 1T-TaS_2 is shown. Below a temperature of about 200 K, the system forms a CDW, where the tantalum atoms contract in a way that resembles a Star of David (SoD). In the undistorted structure without the CDW, the system is metallic. Upon formation of the CDW, the periodicity of the system changes. An increased lattice constant is accompanied by a reduced dispersion of the electrons resulting in a flat band at the Fermi level. The small bandwidth and a comparatively large Coulomb interaction eventually turn the system into an insulator [60].

These examples make clear that the interplay of electrons and phonons can lead to significant changes in the properties of solids, and in order to understand the latter, a good theoretical handle for the former is needed. In this spirit, the work presented here is very much focused on phonons and the EPC, albeit mostly limited to the context of CDWs in 2D materials in regard to applications. A lot of effort was spent of setting up the appropriate lattice models using constrained density-functional perturbation theory (cDFPT), a downfolding method proposed in 2015 by Nomura and Arita [50], which has only been applied to very few materials to this day [61–63]. On this basis, we were able to consistently calculate renormalized phonon dispersions and, introducing the method of "fluctuation diagnostics" [64, 65] to the field of electron–phonon physics, analyze the controversial origin of CDWs in the metallic TMDCs in detail.

This thesis is organized as follows: We start with the formulation of the general *ab initio* model Hamiltonian and a detailed discussion of its parameters in Chap. 2. Next, in Chap. 3, we introduce selected many-body instabilities as emerge in 2D materials, an overview of which is given in Chap. 4. At the heart of this work, in Chap. 5, we describe our phonon-renormalization scheme. On this basis, we attend to the different projects realized: In Chap. 6, we study the Mott physics in the CDW phase of 1T-$NbSe_2$; in Chap. 7, we systematically classify the metallic TMDCs; in Chap. 8, we present the phase diagram of lattice instabilities of 1H-TaS_2; in Chap. 9, its origins are revealed via fluctuation diagnostics. The conclusions in Chap. 10 are followed by several appendices: Most importantly, in App. A, the software applied and developed for this thesis is documented; in App. B, some of the implemented algorithms are described in detail; in App. C, we collect useful concepts and derivations; finally, in App. D, we summarize miscellaneous side projects.

Chapter 2

Ab initio model Hamiltonians

El hombre ha descubierto las leyes
por las que se rige el núcleo atómico...
pero no las causas polifacéticas
de sus conflictos.[1]

—Yolanda Bedregal

We start at the very beginning. Fortunately, in solid-state physics, we very well know the problem we have to deal with. It is the Hamiltonian of interacting electrons and nuclei,

$$H = -\sum_i \frac{\Delta_i}{2} - \sum_k \frac{\Delta_k}{2M_k} + \sum_{i<j} \frac{1}{|\boldsymbol{r}_i - \boldsymbol{r}_j|} + \sum_{k<l} \frac{Z_k Z_l}{|\boldsymbol{R}_k - \boldsymbol{R}_l|} - \sum_{ik} \frac{Z_k}{|\boldsymbol{r}_i - \boldsymbol{R}_k|}, \tag{2.1}$$

here written in the position representation and atomic units. From left to right, the terms describe the kinetic energy of the electrons, the kinetic energy of the nuclei, the Coulomb repulsion between the electrons, the Coulomb repulsion between the nuclei, and finally the Coulomb attraction between the electrons and the nuclei.

Also fortunately—because there would be no solid-state physics otherwise—, the problem is too difficult to be solved exactly due to the multitude of involved particles that have to be dealt with on a quantum level. Instead, the solution is approximated from various directions and points of views, which all share a common denominator: the complexity of the problem has to be somehow reduced. Often, this process toward the (seldom exact) solution is fruitful in a much broader sense, since it requires the development of general ideas and concepts and finally a deeper understanding of the matter (compared to calculations that act as a *black box*).

The calculation of the kinetics of *noninteracting* electrons and nuclei is a very simple task because it can be carried out for each particle individually. That being said, the complexity of the problem arises from the *interaction* of particles, especially the Coulomb repulsion between the electrons, which have to get along in shared spaces, compared to the nuclei, which are rather confined to the vicinity of their individual equilibrium positions.

The approach that we will take are material-realistic yet tractable quantum lattice models derived from first principles. The idea is to *downfold* the problem to the minimal basis that still captures the relevant physics, so that we only have to deal with a small number of degrees of freedom, namely electronic orbitals and atomic displacements, each *localized* at certain points in space. This way, the solution is usually still challenging but not hopeless. Also,

[1] *Humankind has discovered the laws that reign the atomic nucleus... but not the multifaceted causes of its conflicts.*

whenever we want to describe a certain phase transition, such as the transition to a CDW or a Mott insulator, we adopt the viewpoint of the symmetric phase, where the electronic correlations did not kick in yet and the nuclei are still in their undistorted positions. However, the interactions included in the model are capable of reproducing the transitions of interest.

Lattice models are usually defined in the formalism of second quantization. Here, a very general Hamiltonian describing a system of interacting electrons and phonons (but still excluding anharmonic terms and spin-flip interactions) reads

$$\hat{H} = \sum_{\boldsymbol{k}n\sigma} \varepsilon_{\boldsymbol{k}n\sigma} \hat{c}^\dagger_{\boldsymbol{k}n\sigma} \hat{c}_{\boldsymbol{k}n\sigma} + \sum_{\boldsymbol{q}\nu} \omega_{\boldsymbol{q}\nu} \left[\hat{b}^\dagger_{\boldsymbol{q}\nu} \hat{b}_{\boldsymbol{q}\nu} + \frac{1}{2} \right] + \frac{1}{\sqrt{N}} \sum_{\boldsymbol{q}\nu\boldsymbol{k}mn\sigma} g_{\boldsymbol{q}\nu\boldsymbol{k}mn} \hat{c}^\dagger_{\boldsymbol{k}+\boldsymbol{q}m\sigma} \hat{c}_{\boldsymbol{k}n\sigma} [\hat{b}^\dagger_{-\boldsymbol{q}\nu} + \hat{b}_{\boldsymbol{q}\nu}]$$
$$+ \frac{1}{2N} \sum_{\boldsymbol{q}\boldsymbol{k}mn\sigma\boldsymbol{k}'m'n'\sigma'} U_{\boldsymbol{q}\boldsymbol{k}mn\boldsymbol{k}'m'n'} \hat{c}^\dagger_{\boldsymbol{k}+\boldsymbol{q}m\sigma} \hat{c}^\dagger_{\boldsymbol{k}'n'\sigma'} \hat{c}_{\boldsymbol{k}'+\boldsymbol{q}m'\sigma'} \hat{c}_{\boldsymbol{k}n\sigma}. \quad (2.2)$$

All quantities that enter this Hamiltonian are *bare* by default, since their mutual renormalization is included in the interactions. In practice, however, only a subset of processes is explicitly considered. As a consequence, the model parameters are usually *partially screened* or even fully screened in some cases. In the following, we address the four terms of the Hamiltonian one after the other, with special emphasis on how to obtain them from first principles. Later, in Secs. 2.3 to 2.6, we will discuss them in greater detail.

The first term is the kinetic energy of the (effectively) noninteracting electrons (Sec. 2.3). Often, we obtain it from DFT (Sec. 2.3.1). It can be represented as a tight binding (TB) model (Sec. 2.3.2), a convenient basis for which are Wannier functions (Sec. 2.3.3), which can be constructed using WANNIER90 (App. A.2).

The second term is the phonon energy (Sec. 2.4) in the Born–Oppenheimer (BO) and harmonic approximation (Sec. 2.4.1). We usually obtain it from density-functional perturbation theory (DFPT) (Sec. 2.4.2) or cDFPT (Sec. 2.4.2.2), using QUANTUM ESPRESSO (QE) (App. A.1). In real space, it can be seen as point masses connected by classical springs (Sec. 2.4.3).

The third term is the EPC (Sec. 2.5). It is obtained alongside the phonons from DFPT (Sec. 2.5.1). Alternatively, we can calculate it analytically from any TB model (Sec. 2.5.2). Like electrons and phonons, it is conveniently represented in a localized basis, given by both Wannier functions and atomic displacements (Sec. 2.5.3). This can be accomplished using the Electron–Phonon Wannier (EPW) code (App. A.3). The EPC is the driving force behind many-body instabilities such as CDWs (Sec. 3.1) and conventional superconductivity (Sec. 3.2). A significant part of the work behind this thesis has been spent on understanding its details. We successfully implemented a computational scheme to obtain partially screened EPCs from cDFPT and work with them in a consistent way (Chap. 5 and App. A.6).

The forth term is the Coulomb interaction (Sec. 2.6). It can be obtained from the random-phase approximation (RPA) (Sec. 2.6.1) or the constrained random-phase approximation (cRPA) (Sec. 2.6.1.1), using the Vienna *Ab initio* Simulation Package (VASP) (App. A.4). It is the origin of strong correlations in materials where the single-particle picture breaks down, as described by the Hubbard model (Sec. 2.6.2). A prominent method to tackle such systems is dynamical mean-field theory (DMFT) (Sec. 2.6.3).

To summarize, this chapter is about consistent model Hamiltonians for systems of interacting electrons and phonons, formulated in the localized bases of electronic orbitals and atomic displacements. Before the different model parameters are explained in detail, two basic ideas are introduced, namely the BO approximation (Sec. 2.1) and the concept of downfolding (Sec. 2.2).

2.1 Born–Oppenheimer approximation

The idea behind the BO or *adiabatic* approximation [66] is to decouple electronic and nuclear degrees of freedom and thus greatly simplify the solid-state problem. All results that will be presented in this thesis rely on the BO approximation.

Following the derivation in Ref. 67, we split the full Hamiltonian of the system into the kinetic energy of the nuclei $\hat{T}_\mathrm{n}$ and the rest $\hat{H}_0$,

$$\hat{H} = \hat{H}_0 + \hat{T}_\mathrm{n} \quad \text{with} \quad \hat{T}_\mathrm{n} = \sum_k \frac{\hat{\boldsymbol{P}}_k^2}{2M_k}. \tag{2.3}$$

We suppose that the eigenvalues E_η and -states $|\eta\rangle$ of $\hat{H}_0$ are known,

$$\hat{H}_0|\eta\rangle = E_\eta|\eta\rangle. \tag{2.4}$$

We want to know the eigenvalue $\mathcal{E}$ and -state $|\psi\rangle$ of the full Hamiltonian $\hat{H}$,

$$\hat{H}|\psi\rangle = \mathcal{E}|\psi\rangle. \tag{2.5}$$

Integrating out the electronic degrees of freedom in this equation, we can also write

$$\langle\eta|\hat{H}|\psi\rangle = \langle\eta|(\hat{H}_0 + \hat{T}_\mathrm{n})|\psi\rangle = E_\eta\langle\eta|\psi\rangle + \langle\eta|\hat{T}_\mathrm{n}|\psi\rangle = \mathcal{E}\langle\eta|\psi\rangle. \tag{2.6}$$

Please note that $\langle\eta|\psi\rangle \equiv |\psi_\eta\rangle$ is not a simple number but a state with remaining nuclear degrees of freedom. Using the product rule of the Laplace operator,

$$\Delta(ab) = (\Delta a)b + a(\Delta b) + 2(\boldsymbol{\nabla} a)(\boldsymbol{\nabla} b), \tag{2.7}$$

and a corresponding property for $\hat{T}_\mathrm{n}$, which follows from the position representation of the momentum operator and can be symbolically written as

$$\hat{T}_\mathrm{n} = \sum_\xi \hat{T}_\mathrm{n}|\xi\rangle\langle\xi| = \sum_\xi |\hat{T}_\mathrm{n}\xi\rangle\langle\xi| + |\xi\rangle\langle\hat{T}_\mathrm{n}\xi| + \sum_k \frac{1}{M_k}|\hat{\boldsymbol{P}}_k\xi\rangle\langle\hat{\boldsymbol{P}}_k\xi|, \tag{2.8}$$

it follows that

$$\langle\eta|\hat{T}_\mathrm{n}|\psi\rangle = \hat{T}_\mathrm{n}\langle\eta|\psi\rangle + \sum_\xi \Big[\langle\eta|\hat{T}_\mathrm{n}|\xi\rangle + \sum_k \frac{1}{M_k}\langle\eta|\hat{\boldsymbol{P}}_k|\xi\rangle\hat{\boldsymbol{P}}_k\Big]\langle\xi|\psi\rangle. \tag{2.9}$$

The BO approximation consists in the assumption that the ξ summation can be neglected such that we can write the Schrödinger equation for the nuclei (Eq. 2.6) simply as

$$(E_\eta + \hat{T}_\mathrm{n})\langle\eta|\psi\rangle = \mathcal{E}\langle\eta|\psi\rangle. \tag{2.10}$$

Thus, the nuclei move in an effective potential given by the electrons; for the electrons, the nuclei appear fixed. This is justified by the fact that the electrons are much lighter than the nuclei and move on much shorter time scales.

In the position representation, where $\underline{\boldsymbol{r}} = \{\boldsymbol{r}_1, \boldsymbol{r}_2, \ldots, \boldsymbol{r}_{N_\mathrm{e}}\}$ and $\underline{\boldsymbol{R}} = \{\boldsymbol{R}_1, \boldsymbol{R}_2, \ldots, \boldsymbol{R}_{N_\mathrm{n}}\}$ combine all electronic and nuclear coordinates, the respective Schrödinger equations read

$$[H(\underline{\boldsymbol{r}}, \underline{\boldsymbol{R}}) - T_\mathrm{n}]\psi_\eta^\mathrm{e}(\underline{\boldsymbol{r}}, \underline{\boldsymbol{R}}) = E_\eta(\underline{\boldsymbol{R}})\psi_\eta^\mathrm{e}(\underline{\boldsymbol{r}}, \underline{\boldsymbol{R}}), \tag{2.11a}$$

$$[E_\eta(\underline{\boldsymbol{R}}) + T_\mathrm{n}]\psi_\eta^\mathrm{n}(\underline{\boldsymbol{R}}) = \mathcal{E}\psi_\eta^\mathrm{n}(\underline{\boldsymbol{R}}). \tag{2.11b}$$

The decoupling of electrons and nuclei in the BO approximation does *not* imply that we disregard all EPC. We only neglect electronic transitions driven by the kinetics of the nuclei, namely $\langle\eta|\hat{T}_\mathrm{n}|\xi\rangle$ and $\langle\eta|\hat{\boldsymbol{P}}_k|\xi\rangle$. In this thesis, however, EPC always refers to matrix elements $\langle\boldsymbol{k}'|\partial\hat{H}/\partial\underline{\boldsymbol{R}}|\boldsymbol{k}\rangle$ of electronic *single*-particle states $|\boldsymbol{k}^{(\prime)}\rangle$, where $\hat{H}$ lacks purely nuclear parts. Furthermore, we only consider ground-state energies E_0, i.e., one particular fixed value of η.

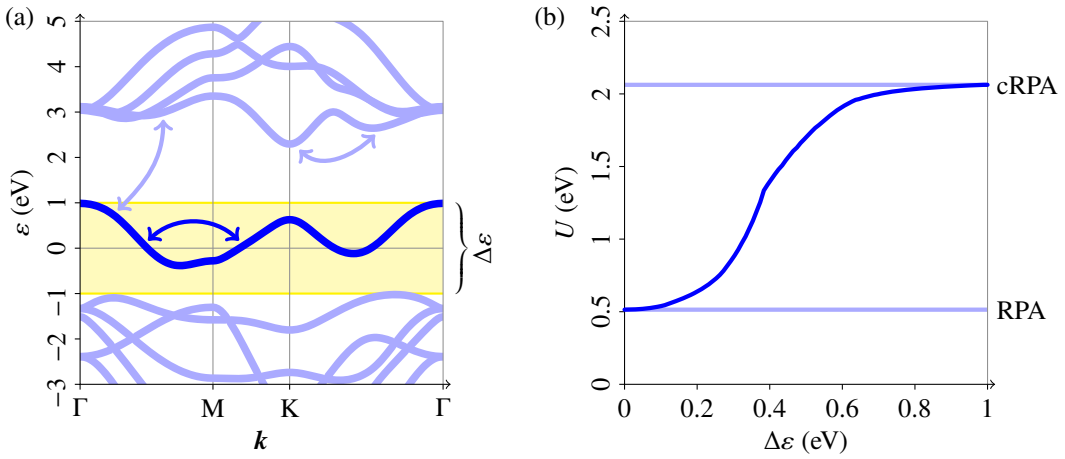

Figure 2.1: Downfolding by the example of 1H-TaS_2. (a) Electronic band structure with the active subspace highlighted in yellow. The arrows indicate possible electronic transitions within, beyond, and across the boundaries of the active subspace. The computational parameters are as in Sec. 9.8. (b) Fully and partially screened local Coulomb interaction of the system. The RPA value includes screening from all bands, the cRPA value excludes screening from processes within the active subspace. Shrinking the energy window $\Delta\varepsilon$ of the active subspace, the cRPA value approaches the RPA value. The cRPA data is from Sec. 7.2.4. The RPA has been realized with a Fermi–Dirac smearing of 5 mRy.

2.2 Downfolding

Downfolding addresses the question of how to obtain effective (i.e., partially screened) parameters for models with an (often significantly) reduced number of degrees of freedom compared to the full system. Several methods to accomplish this downfolding exist, e.g., the cRPA for the Coulomb interaction [48, 49] and the cDFPT for phonon-related properties. The latter was introduced by Nomura and Arita in 2015 [50] and is still not nearly as well established as the former.

Since the reduction of the complexity of the problem by means of downfolding has to be compensated by the partial screening of the model parameters, the latter usually carry complicated dependencies on the involved quantum numbers and are in general also frequency dependent [48], as opposed to the bare parameters prior to renormalization. Often, such dependencies are neglected or simplified. But still, we strive for our models to be *material-realistic*, in the sense that all parameters are derived *ab initio* and that all *relevant* quantum-number dependencies are taken into account. In any case, the active subspace of the model is chosen such that the (usually low-energy) processes that determine the relevant physics, where approximations that are justified for the high-energy processes might fail, are included. In systems that undergo a transition to a phase of reduced symmetry, the parameters of a model describing this phase transition stem from the high-symmetry phase and are thus simpler in this regard.

As an example, Fig. 2.1a shows the electronic band structure of a monolayer 1H-TaS_2. Suppose we want to set up a model with a minimal electronic basis, which only includes the single band around the Fermi level. We call the latter the *active subspace*. Naturally, the model only describes interactions between electrons inside this active subspace. As a consequence, all interactions that involve at least one state outside of the active subspace have to be already effectively included in the model parameters; at the same time, interactions within the active subspace must not be double counted. Therefore, the model interactions are usually larger than the ones before downfolding, as shown for the example of the local Coulomb interaction from RPA and cRPA in Fig. 2.1b.

2.3 Electrons

The electrons are the quantum-mechanical "glue" of the solid state and largely determine its properties. Surprisingly many phenomena can be explained by employing the picture of effectively noninteracting electrons alone (which are, of course, not *bare* electrons but renormalized particles). Thus, we start our discussion of the Hamiltonian with the electrons.

This section is divided into two major parts: First, in Sec. 2.3.1, DFT is introduced, a first-principles method that (despite its weaknesses) has achieved tremendous successes and is likely the most popular tool in condensed-matter theory today. Second, in Sec. 2.3.2, the problem is approached from the model side, precisely via the TB method.

2.3.1 Density-functional theory

DFT [68] has been introduced in 1964 by Hohenberg and Kohn [31] and earned the latter the 1998 Nobel Prize in Chemistry. It is based on the two *Hohenberg–Kohn theorems*,[2] for the proof of which we refer to the original articles [31, 32] or any textbook [67] on the solid state.

We consider an interacting electrons gas in an external potential $V(\boldsymbol{r})$.

1. The external potential $V(\boldsymbol{r})$ (except for a constant), the ground-state wave function $\psi_0(\boldsymbol{r}_1, \boldsymbol{r}_2, \ldots, \boldsymbol{r}_{N_e})$ (except for phase factors), and the ground-state total energy E_0 are unique functionals of the electronic ground-state density $n_0(\boldsymbol{r})$.[3] Without ambiguity,

$$E_0 = E[n_0(\boldsymbol{r})]. \tag{2.12a}$$

2. $n_0(\boldsymbol{r})$ can be found via variation since it minimizes the functional $E[n(\boldsymbol{r})]$,

$$E[n_0(\boldsymbol{r})] \leq E[n(\boldsymbol{r})]. \tag{2.12b}$$

For ground-state calculations it is thus sufficient to consider the ground-state density

$$n_0(\boldsymbol{r}) = \langle\psi_0|\hat{n}(\boldsymbol{r})|\psi_0\rangle \quad \text{with} \quad \hat{n}(\boldsymbol{r}) = \sum_i \delta(\boldsymbol{r} - \hat{\boldsymbol{r}}_i) = \hat{\psi}^\dagger(\boldsymbol{r})\hat{\psi}(\boldsymbol{r}) \tag{2.13}$$

instead of the (much more complicated) ground-state many-body wave function

$$\psi_0(\boldsymbol{r}_1, \boldsymbol{r}_2, \ldots, \boldsymbol{r}_{N_e}) = \langle \boldsymbol{r}_1, \boldsymbol{r}_2, \ldots, \boldsymbol{r}_{N_e}|\psi_0\rangle. \tag{2.14}$$

In principle, this greatly facilitates the calculation of material properties. However, the energy functional $E[n]$ is unfortunately not fully known. More precisely, the only component of the energy, i.e., of the Hamiltonian of interacting electrons

$$\hat{H} = \hat{T} + \hat{U} + \hat{V}, \tag{2.15}$$

that can be written in terms of the density is the one involving the external potential,

$$\hat{V} = \int \mathrm{d}^3 r\, V(\boldsymbol{r})\hat{n}(\boldsymbol{r}). \tag{2.16}$$

In turn, for the kinetic energy $\hat{T}$ and the electron–electron interaction $\hat{U}$, which makes the problem nontrivial, no formulation in terms of the density is known. $\hat{T}$ and $\hat{U}$ are also

[2] A generalization with respect to time-dependent systems is given by the *Runge–Gross theorem* [69].

[3] It is sufficient to formulate the theorem for $V(\boldsymbol{r})$, since $\psi_0(\boldsymbol{r}_1, \boldsymbol{r}_2, \ldots, \boldsymbol{r}_{N_e})$ (except for phase factors) and E_0 are functionals of $V(\boldsymbol{r})$ via the Schrödinger equation.

different from $\hat{V}$ in the sense that the former do not depend on the atomic positions and thus on the specific system considered. Accordingly, they are often combined into the *universal functional* $F[n] = T[n] + U[n]$. In the end, the material properties always result from the external potential, whose functional $V[n]$ of the density is known. That is not to say $F[n]$ is unimportant for the result. The development of DFT is largely about finding useful approximations for $F[n]$.

An early approximation to the unknown $F[n]$ is the *Thomas–Fermi theory* [70, 71], where the Hartree approximation to the Coulomb interaction is applied and the kinetic energy is taken from the special case of the noninteracting homogeneous electrons gas. Then, we can formulate both $\hat{T}$ and $\hat{U}$ as a functional of the density,

$$U[n(\boldsymbol{r})] = \frac{1}{2}\int \mathrm{d}^3r\,\mathrm{d}^3r'\,\frac{n(\boldsymbol{r})n(\boldsymbol{r}')}{|\boldsymbol{r}-\boldsymbol{r}'|}, \tag{2.17a}$$

$$T[n(\boldsymbol{r})] = \frac{3}{10m}(2\pi^2)^{\frac{2}{3}}\int \mathrm{d}^3r\,n^{\frac{5}{3}}(\boldsymbol{r}). \tag{2.17b}$$

However, this approximation often fails, especially for outer regions of atoms and because exchange effects are missing so far [68]. Modern DFT relies on a different approach, namely the Kohn–Sham (KS) ansatz.

2.3.1.1 Kohn–Sham equations

The idea of Kohn and Sham [32], which enabled the breakthrough of DFT in 1965, is to express the electron density as the density of an effective noninteracting auxiliary system. Since we know how to calculate the kinetic energy of a noninteracting system via the Schrödinger equation, we do not need any further assumptions on the kinetic energy as a functional of the density. The Hamiltonian of the noninteracting system reads

$$\hat{H}_0 = \sum_{i=1}^{N_\mathrm{e}} \frac{\hat{\boldsymbol{p}}_i^2}{2} + V_\mathrm{SCF}(\hat{\boldsymbol{r}}_i), \tag{2.18}$$

where the effective external potential V_SCF, where SCF stands for self-consistent field, must be determined such that the ground-state densities of the exact system and the auxiliary one coincide. V_SCF acts on a single electron but is *screened* by all other electrons. For a given V_SCF, the eigenvalues ε_i and -vectors $\psi_i(\boldsymbol{r})$ and the density $n(\boldsymbol{r})$ are given by

$$(H_0 - \varepsilon_i)\psi_i(\boldsymbol{r}) = 0 \quad \text{and} \quad n(\boldsymbol{r}) = \sum_{i=1}^{N_\mathrm{e}} f(\varepsilon_i)|\psi_i(\boldsymbol{r})|^2, \tag{2.19}$$

where f is the electronic occupation. The KS total-energy functional reads

$$E[n(\boldsymbol{r})] = -\frac{1}{2}\sum_{i=1}^{N_\mathrm{e}}\int \mathrm{d}^3r\,\psi_i^*(\boldsymbol{r})\Delta\psi_i(\boldsymbol{r}) + \frac{1}{2}\int \mathrm{d}^3r\,\mathrm{d}^3r'\,\frac{n(\boldsymbol{r})n(\boldsymbol{r}')}{|\boldsymbol{r}-\boldsymbol{r}'|} + \int \mathrm{d}^3r\,V(\boldsymbol{r})n(\boldsymbol{r}) + E_\mathrm{XC}[n(\boldsymbol{r})], \tag{2.20}$$

where the first term is the usual kinetic energy of a noninteracting system. Again, the Hartree approximation to the Coulomb interaction is applied. To account for the missing electronic interaction effects such as the exchange interaction, an additional functional $E_\mathrm{XC}[n]$ is introduced. This unknown exchange–correlation (XC) functional combines all correction terms. It can be considered as the greatest weakness of DFT, since reasonable

assumptions for $E_{\mathrm{XC}}[n]$ are needed to obtain physically sound results. At the same time, introducing a rather empirical correction term, we lose a well-defined starting point, e.g., for diagrammatic extensions of the theory. Finding good functionals $E_{\mathrm{XC}}[n]$ is an important branch of computational chemistry and physics.

The density functional must fulfill the condition $\delta E[n(\boldsymbol{r})] = 0$ for the ground-state density $n(\boldsymbol{r}) = n_0(\boldsymbol{r})$. Thus, variation with respect to $\psi_i^*(\boldsymbol{r})$ under the constraint that $\psi_i(\boldsymbol{r})$ is normalized, i.e., that the particle number is conserved,

$$\delta_{\psi_i^*}\left\{E[n(\boldsymbol{r})] - \sum_{j=1}^{N_\mathrm{e}} \varepsilon_j \left[\int \mathrm{d}^3 r\, |\psi_j(\boldsymbol{r})|^2 - 1\right]\right\} = 0, \tag{2.21}$$

yields the KS equations

$$\left[-\frac{1}{2}\Delta + \overbrace{\underbrace{\frac{1}{2}\int \mathrm{d}^3 r' \frac{n(\boldsymbol{r}')}{|\boldsymbol{r}-\boldsymbol{r}'|}}_{V_{\mathrm{H}}[n](\boldsymbol{r})} + V(\boldsymbol{r}) + \underbrace{\frac{\delta E_{\mathrm{XC}}}{\delta n(\boldsymbol{r})}}_{V_{\mathrm{XC}}[n](\boldsymbol{r})}}^{V_{\mathrm{SCF}}[n](\boldsymbol{r})}\right]\psi_i(\boldsymbol{r}) = \varepsilon_i \psi_i(\boldsymbol{r}), \tag{2.22}$$

which are formally Schrödinger equations, except that the external potential V_{SCF} depends on the solution $\psi_i(\boldsymbol{r})$ via the density occurring in the Hartree potential V_{H} and the *XC potential* V_{XC}, rendering the Hamiltonian nonlinear. Hence, we have a *self-consistency problem*. The KS eigenvalues ε_i and corresponding states $\psi_i(\boldsymbol{r})$ have been introduced as auxiliary quantities without a well-defined physical meaning. (The ε_i can even be considered as mere Lagrange parameters needed to preserve the normalization during the variation.) However, they are most often interpreted as energies of electronic single-particle excitations and wave functions, and they probably constitute the most common "band structures" on the market. Care has to be taken that this interpretation is justified for a particular case.

Please note that the sum of all occupied ε_i does not yield the total energy E of the system. However, we have Janak's theorem $\partial E/\partial n_i = \varepsilon_i$ [72] for the fractional occupation numbers $n_i = f(\varepsilon_i)$. See also Koopmans' theorem [73].

The assumption alone that the interacting density can be represented by a noninteracting auxiliary system does not constitute an approximation. If the XC functional was known, the theory would still be exact. However, no exact XC functional is available, but there are some popular choices that will be discussed in the following.

2.3.1.2 Exchange–correlation functional

The most popular choices for the XC functional are the local-density approximation (LDA) and the generalized gradient approximation (GGA). To define them, it is convenient to represent the XC functional as (cf. Eq. 2.3 of Ref. 32)

$$E_{\mathrm{XC}}[n] = \int \mathrm{d}^3 r\, \varepsilon_{\mathrm{XC}}[n](\boldsymbol{r}) n(\boldsymbol{r}), \tag{2.23}$$

where the XC energy density $\varepsilon_{\mathrm{XC}}$ is in general a functional of the density $n(\boldsymbol{r})$ and a function of the position $\boldsymbol{r}$.

In the LDA, we assume that $\varepsilon_{\mathrm{XC}}$ at a given position $\boldsymbol{r}$ depends only on the density $n(\boldsymbol{r})$ at the same $\boldsymbol{r}$, i.e., $\varepsilon_{\mathrm{XC}} \equiv \varepsilon_{\mathrm{XC}}(n(\boldsymbol{r}))$ is a simple function of $n(\boldsymbol{r})$. More precisely, the exchange part $\varepsilon_{\mathrm{XC}}$ is taken from the homogeneous electron gas, where it is known analytically[4]

$$\varepsilon_{\mathrm{XC}}(n(\boldsymbol{r})) = \varepsilon_{\mathrm{X}}(n(\boldsymbol{r})) + \varepsilon_{\mathrm{C}}(n(\boldsymbol{r})) \quad \text{with} \quad \varepsilon_{\mathrm{X}}(n(\boldsymbol{r})) = -\frac{3}{4}\left[\frac{3n(\boldsymbol{r})}{\pi}\right]^{\frac{1}{3}}. \tag{2.24}$$

[4] By definition, in the context of the homogeneous electrons gas, we would have $n(\boldsymbol{r}) = n_0 = \text{const}$.

As a consequence, also the XC potential $V_{\mathrm{XC}} = \delta E_{\mathrm{XC}}/\delta n = \varepsilon_{\mathrm{XC}}[n](\boldsymbol{r}) + n(\boldsymbol{r})\delta\varepsilon_{\mathrm{XC}}/\delta n$ is a simple function of $n(\boldsymbol{r})$. We find $V_{\mathrm{XC}} = V_{\mathrm{X}} + V_{\mathrm{C}}$ with $V_{\mathrm{X}} = (1 + 1/3)\varepsilon_{\mathrm{X}}$ (cf. Eq. 2.19 of Ref. 32). For the correlation part ε_{X} (absent in the homogeneous electrons gas), there are different approaches. Often, it is approximated as the remainder to some reference value by means of Monte Carlo techniques. A popular parametrization is the one by Perdew and Zunger [74]. By construction, the LDA works best for slowly varying densities.

In the GGA, $\varepsilon_{\mathrm{XC}}$ is still not a complete functional of the density, but now it also depends (in some reasonable way) on the gradient of density,

$$\varepsilon_{\mathrm{XC}} \equiv \varepsilon_{\mathrm{XC}}(n(\boldsymbol{r}), \boldsymbol{\nabla} n(\boldsymbol{r})). \tag{2.25}$$

Here, the Perdew–Burke–Ernzerhof (PBE) parametrization [75, 76] is widely used.

2.3.1.3 Pseudopotentials

As any numerical calculation, solving the KS equations requires a basis in which operators and states can be represented. A mathematically simple and unbiased basis set is given by plane waves $|\boldsymbol{G}\rangle$ with

$$\langle \boldsymbol{r}|\boldsymbol{k}+\boldsymbol{G}\rangle \propto \mathrm{e}^{-\mathrm{i}(\boldsymbol{k}+\boldsymbol{G})\boldsymbol{r}}, \tag{2.26}$$

where $\boldsymbol{G}$ is a reciprocal lattice vector. Since plane waves are completely delocalized in space, they are naturally better suited (in the sense that less basis functions are required) to describe electrons whose wave functions are delocalized too. However, the wave functions of low-energy states are very much localized around the atomic nuclei, and as a consequence the higher-energy wave functions cannot be smooth either, because they have to be orthogonal to the core wave functions.

One way to avoid very large numbers of necessary basis functions (with ever shorter wavelengths) is to use modified plane waves that are by construction orthogonal to the core states. These *orthogonalized plane waves* [77] resemble usual plane waves away from the nuclei, but they also feature the relevant short-range structures around the nuclei. They are obtained by projection onto the complement of the core states,

$$|\widetilde{\boldsymbol{k}+\boldsymbol{G}}\rangle = (1 - \hat{P}_{\boldsymbol{k}})|\boldsymbol{k}+\boldsymbol{G}\rangle \quad \text{with} \quad \hat{P}_{\boldsymbol{k}} = \sum_c |\psi_{\boldsymbol{k}c}\rangle\langle\psi_{\boldsymbol{k}c}|, \tag{2.27}$$

where c labels the bands counted among the core states $|\psi_{\boldsymbol{k}c}\rangle$. Orthogonality, $\langle\psi_{\boldsymbol{k}c}|\widetilde{\boldsymbol{k}+\boldsymbol{G}}\rangle = 0$, is easily verified. The representation of arbitrary valence states in this basis,

$$|\psi_{\boldsymbol{k}n}\rangle = \sum_{\boldsymbol{G}} c_{\boldsymbol{G}\boldsymbol{k}n}|\widetilde{\boldsymbol{k}+\boldsymbol{G}}\rangle, \tag{2.28}$$

usually requires only a few basis states. However, a disadvantage of this approach is that we need a different set of basis functions for each system. It would be more convenient to incorporate the advantages of orthogonalized plane waves into a more transferable solution. This is the idea behind pseudopotentials (PPs) [78]. The electronic states close to the nucleus are combined with the nuclear potential into an effective screened potential. The orbitals belonging to this PP are smooth functions that can be easily represented with plane waves.

We rewrite the valence state as

$$|\psi_{\boldsymbol{k}n}\rangle = (1 - \hat{P}_{\boldsymbol{k}})|\varphi_{\boldsymbol{k}n}\rangle \quad \text{with} \quad |\varphi_{\boldsymbol{k}n}\rangle = \sum_{\boldsymbol{G}} c_{\boldsymbol{G}\boldsymbol{k}n}|\boldsymbol{k}+\boldsymbol{G}\rangle, \tag{2.29}$$

where $|\varphi_{\boldsymbol{k}n}\rangle$ has the same simple representation in the basis of original plane waves as $|\psi_{\boldsymbol{k}n}\rangle$ in the basis of orthogonalized plane waves. The Schrödinger equation reads

$$(\hat{H} - \varepsilon_{\boldsymbol{k}n})|\psi_{\boldsymbol{k}n}\rangle = (\hat{H} - \varepsilon_{\boldsymbol{k}n})(1 - \hat{P}_{\boldsymbol{k}})|\varphi_{\boldsymbol{k}n}\rangle = [\hat{H} + (\varepsilon_{\boldsymbol{k}n} - \hat{H})\hat{P}_{\boldsymbol{k}} - \varepsilon_{\boldsymbol{k}n}]|\varphi_{\boldsymbol{k}n}\rangle = 0. \quad (2.30)$$

For a Hamiltonian $\hat{H} = \hat{H}_0 + \hat{V}$ with the external potential $\hat{V}$, we can rewrite this as

$$[\hat{H}_0 + \hat{V}_{\text{PP}} - \varepsilon_{\boldsymbol{k}n}]|\varphi_{\boldsymbol{k}n}\rangle = 0, \quad (2.31)$$

where we have defined the PP

$$\hat{V}_{\text{PP}} = \hat{V} + (\varepsilon_{\boldsymbol{k}n} - \hat{H})\hat{P}_{\boldsymbol{k}} = \hat{V} + \sum_c (\varepsilon_{\boldsymbol{k}n} - \varepsilon_{\boldsymbol{k}c})|\psi_{\boldsymbol{k}c}\rangle\langle\psi_{\boldsymbol{k}c}|. \quad (2.32)$$

The $\varepsilon_{\boldsymbol{k}c}$ should be approximately $\boldsymbol{k}$-independent, since the core electrons do not disperse. The $|\psi_{\boldsymbol{k}c}\rangle$ are basically Fourier transforms of a lattice of atomic orbitals. The PP is not a simple scalar function of the position, but it is *nonlocal* (i.e., it has off-diagonal elements in the position representation). Also, the eigenenergies $\varepsilon_{\boldsymbol{k}n}$, which we want to determine with the help of the PP, already appear as unknowns in the PP itself.

PPs are not limited to the definition in Eq. 2.32. For practical purposes, it is sufficient to require that the valence electrons are correctly reproduced for a range of environments as large as possible [79].

A popular family of PPs are the normconserving PPs, established in 1979 by Hamann *et al.* [80]. They are defined by the following properties: no energy ($\varepsilon_{\boldsymbol{k}n}$) dependence; real and pseudo energies agree; real and pseudo orbitals agree beyond a certain radius r_c from the nucleus; the $r < r_c$ integral of real and pseudo valence charge densities agree; the logarithmic derivatives of real and pseudo orbitals and their energy derivative agree. Besides the evident advantages of the listed properties, the latter two of them ensure that normconserving PPs are maximally transferable. The PPs by Hamann *et al.* [80] are found by inverting the radial Schrödinger equation and can be written in the form [81]

$$\hat{V}_{\text{PP}} = \hat{V}_{\text{loc}} + \sum_l \sum_{m=-l}^{l} |lm\rangle V_l \langle lm|, \quad (2.33)$$

where the local part $\hat{V}_{\text{loc}}$ can be represented as a simple function of position, as opposed to the second part, which is diagonal in the spherical harmonics $|lm\rangle$.

2.3.1.4 Spin–orbit coupling

For very large orbital angular momenta of the electrons, the relativistic effect of the interaction between the orbital and the spin angular momentum becomes important. This spin–orbit coupling (SOC) leads to changes in the electronic energies and lifts spin degeneracies in many cases. Since the orbital angular momentum is much larger close to the nucleus (and likewise for heavier nuclei), this effect can be conveniently dealt with on the level of the PP.

The idea [82, 83] is to apply the procedure by Hamann *et al.* [80] to the Dirac equation, which yields PPs including SOC, which can finally be used in the Schrödinger equation. These *fully relativistic* PPs can be expressed as in Eq. 2.33 [81], with the replacement

$$V_l \to V_l^{\text{SOC}} \boldsymbol{L} \cdot \boldsymbol{S} + V_l^{\text{ion}}, \quad (2.34a)$$

$$V_l^{\text{SOC}} = \frac{2}{2l+1}\left[V_{l+\frac{1}{2}} - V_{l-\frac{1}{2}}\right], \quad (2.34b)$$

$$V_l^{\text{ion}} = \frac{2}{2l+1}\left[(l+1)V_{l+\frac{1}{2}} + lV_{l-\frac{1}{2}}\right], \quad (2.34c)$$

where $\boldsymbol{L}$ and $\boldsymbol{S}$ are the orbital and spin angular momentum, respectively.

2.3.2 Tight binding

The TB method [84, 85] is an effectively noninteracting theory for the electronic structure of the solid state, where the Hamiltonian has a simple representation in the basis of localized states. Let $|\boldsymbol{R}\alpha\rangle$ be the αth localized state at the lattice site $\boldsymbol{R}$ (cf. App. C.1), e.g., a hydrogen-like orbital localized at an atomic position. In the following, we will use the terms "localized state" and "orbital" interchangeably.

Then, the off-diagonal matrix elements in the basis of such states,

$$t_{\boldsymbol{R}-\boldsymbol{R}'\alpha\beta} = \langle \boldsymbol{R}\alpha|\hat{H}|\boldsymbol{R}'\beta\rangle, \tag{2.35a}$$

are called *hopping parameters*. The diagonal elements

$$\varepsilon_\alpha = t_{0\alpha\alpha} = \langle \boldsymbol{R}\alpha|\hat{H}|\boldsymbol{R}\alpha\rangle \tag{2.35b}$$

are called *on-site energies*. In principle, *any* noninteracting Hamiltonian can be represented in this way, but the representation may not be convenient for systems where the electrons move rather freely. The idea behind TB is that the hopping elements $t_{\boldsymbol{R}-\boldsymbol{R}'\alpha\beta}$ decay rapidly with increasing distance of the orbitals $|\boldsymbol{R}\alpha\rangle$ and $|\boldsymbol{R}'\beta\rangle$. In this case, we describe a system where the electrons are *tightly bond* to the nuclei and can only with difficulty *hop* to sites that are far away. Often, only hopping between orbitals that are nearest or next-nearest neighbors is taken into account.

Using the translational symmetry $\boldsymbol{R} \to \boldsymbol{R}'$, we can partially diagonalize the Hamiltonian by means of a Fourier transform (cf. App. C.3) with respect to $\boldsymbol{R} - \boldsymbol{R}'$.

$$H_{\boldsymbol{k}\alpha\beta} = \sum_{\boldsymbol{R}} t_{\boldsymbol{R}\alpha\beta} \mathrm{e}^{\mathrm{i}\boldsymbol{k}\boldsymbol{R}}. \tag{2.36}$$

In this thesis, we always assume that the basis states $|\boldsymbol{R}\alpha\rangle$ are orthonormal. In this case, the $\boldsymbol{k}$-dependent eigenvalues (or *bands*) $\varepsilon_{\boldsymbol{k}n}$ follow from simple diagonalization of $H_{\boldsymbol{k}\alpha\beta}$. Otherwise, a generalized eigenvalue would have to be solved.

For each combination of lattice vectors representing an interatomic bond, the corresponding hopping is a matrix in the orbital basis. If two bonds in the crystal are equivalent, i.e., can be mapped onto each other via a point symmetry S of the system, also the corresponding hopping matrices t and t' are related via this symmetry operation,

$$t' = S \cdot t \cdot S^{-1}. \tag{2.37a}$$

This equation also holds if a bond is mapped onto itself via a point symmetry. In this case,

$$t = S \cdot t \cdot S^{-1} \tag{2.37b}$$

imposes some constraints on the matrix elements. Usually, many matrix elements must vanish or depend on each other via simple relations because of the point symmetries of the crystal. If the atoms at the ends of the bonds are swapped upon the symmetry transform, the constraint instead reads

$$t^{\mathrm{T}} = S \cdot t \cdot S^{-1}. \tag{2.37c}$$

Analogous constraints hold for the matrices ε of on-site energies.

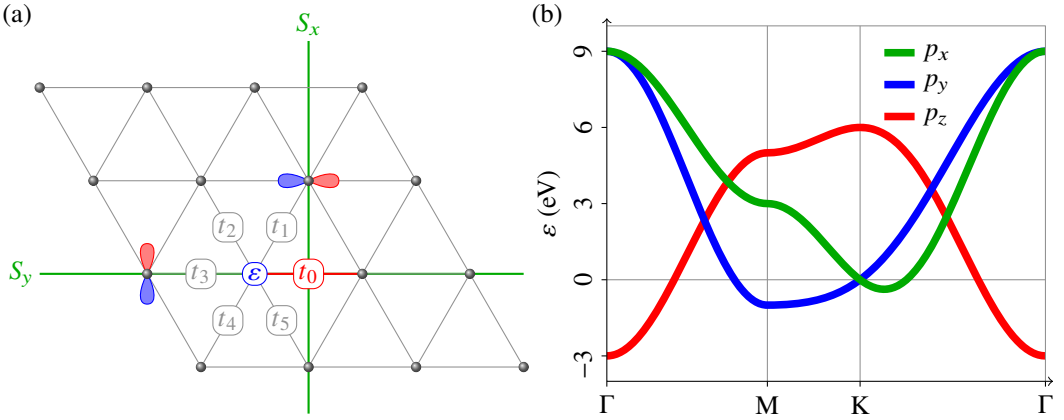

Figure 2.2: Triangular lattice of p orbitals. (a) Lattice with exemplary orbitals, on-site energies, and hoppings. (b) TB dispersion for $\varepsilon_x = \varepsilon_z = 3\,\text{eV}$, $t_x = 1.5\,\text{eV}$, $t_y = 0.5\,\text{eV}$, and $t_z = -1\,\text{eV}$. The path segments Γ–M and M–K–Γ are oriented in the y and x direction, respectively.

2.3.2.1 Triangular lattice of *p* orbitals

As an example, we will now calculate the generic band structure of a triangular lattice of p_x, p_y, and p_z orbitals with nearest-neighbor hopping, as visualized in Fig. 2.2a. The labels x, y, and z indicate that the corresponding orbitals transform exactly as the three orthogonal Cartesian axes. Let the primitive lattice vectors be (cf. App. C.1.1)

$$\boldsymbol{a}_1 = \begin{bmatrix} a \\ 0 \\ 0 \end{bmatrix} \quad \text{and} \quad \boldsymbol{a}_2 = \frac{a}{2} \begin{bmatrix} -1 \\ \sqrt{3} \\ 0 \end{bmatrix}, \tag{2.38}$$

such that all bonds lie in the x–y plane and one of the nearest-neighbor bonds points in the x direction. Then, this bond is invariant with respect to reflections along the y and z axes, and also along the x axis if the atoms at the ends of the bond are swapped. In the Cartesian basis, these three reflections are simply represented as

$$S_x = \text{diag}(-1, 1, 1), \qquad S_y = \text{diag}(1, -1, 1), \qquad S_z = \text{diag}(1, 1, -1). \tag{2.39}$$

We start with the most general matrix for the nearest-neighbor hopping in x direction,

$$t_0 = \begin{bmatrix} t_x & t_{x,y} & t_{x,z} \\ t_{y,x} & t_y & t_{y,z} \\ t_{z,x} & t_{z,y} & t_z \end{bmatrix}. \tag{2.40}$$

The constraints imposed by the different reflection symmetries read

$$t_0 = (S_x \cdot t_0 \cdot S_x^{-1})^\mathrm{T} = \begin{bmatrix} t_x & -t_{y,x} & -t_{z,x} \\ -t_{x,y} & t_y & t_{z,y} \\ -t_{x,z} & t_{y,z} & t_z \end{bmatrix}, \tag{2.41a}$$

$$t_0 = S_y \cdot t_0 \cdot S_y^{-1} = \begin{bmatrix} t_x & -t_{x,y} & t_{x,z} \\ -t_{y,x} & t_y & -t_{y,z} \\ t_{z,x} & -t_{z,y} & t_z \end{bmatrix} = \begin{bmatrix} t_x & 0 & t_{x,z} \\ 0 & t_y & 0 \\ t_{z,x} & 0 & t_z \end{bmatrix}, \tag{2.41b}$$

$$t_0 = S_z \cdot t_0 \cdot S_z^{-1} = \begin{bmatrix} t_x & t_{x,y} & -t_{x,z} \\ t_{y,x} & t_y & -t_{y,z} \\ -t_{z,x} & -t_{z,y} & t_z \end{bmatrix} = \begin{bmatrix} t_x & t_{x,y} & 0 \\ t_{y,x} & t_y & 0 \\ 0 & 0 & t_z \end{bmatrix}. \tag{2.41c}$$

To fulfill all three constraints (the first one being redundant), the hopping must be diagonal.

The hopping matrices for the nearest-neighbor bonds at different angles φ can be generated by repeated rotations R_φ by $\varphi = \pi/3$ about the z axis. In the orbital basis,

$$R_\varphi = \begin{bmatrix} \cos(\varphi) & -\sin(\varphi) & 0 \\ \sin(\varphi) & \cos(\varphi) & 0 \\ 0 & 0 & 1 \end{bmatrix} \overset{\varphi=\frac{\pi}{3}}{=} \begin{bmatrix} \frac{1}{2} & -\frac{\sqrt{3}}{2} & 0 \\ \frac{\sqrt{3}}{2} & \frac{1}{2} & 0 \\ 0 & 0 & 1 \end{bmatrix}. \tag{2.42}$$

We label the hoppings to the six nearest neighbors anticlockwise with $t_0, t_1, \ldots, t_5$ (cf. Fig. 2.2). We find $t_3 = t_0$, $t_4 = t_1$, and $t_5 = t_2$, where

$$t_0 = \operatorname{diag}(t_x, t_y, t_z), \tag{2.43a}$$

$$t_{1,2} = R_{\pm\frac{\pi}{3}} \cdot t_0 \cdot R^{-1}_{\pm\frac{\pi}{3}} = \begin{bmatrix} \frac{1}{4}(t_x + 3t_y) & \pm\frac{\sqrt{3}}{4}(t_x - t_y) & 0 \\ \pm\frac{\sqrt{3}}{4}(t_x - t_y) & \frac{1}{4}(3t_x + t_y) & 0 \\ 0 & 0 & t_z \end{bmatrix}. \tag{2.43b}$$

The constrains following from reflection symmetries equally hold for the on-site energy matrix ε. However, ε must also be invariant with respect to the rotational symmetries, thus

$$\varepsilon = \operatorname{diag}(\varepsilon_x, \varepsilon_x, \varepsilon_z). \tag{2.44}$$

The $\boldsymbol{k}$-dependent Hamiltonian can now be calculated as

$$H_{\boldsymbol{k}} = \varepsilon + t_0 e^{i\boldsymbol{k}\boldsymbol{a}_1} + t_1 e^{i\boldsymbol{k}(\boldsymbol{a}_1+\boldsymbol{a}_2)} + t_2 e^{i\boldsymbol{k}\boldsymbol{a}_2} + t_3 e^{-i\boldsymbol{k}\boldsymbol{a}_1} + t_4 e^{-i\boldsymbol{k}(\boldsymbol{a}_1+\boldsymbol{a}_2)} + t_5 e^{-i\boldsymbol{k}\boldsymbol{a}_2} \tag{2.45a}$$

$$= \varepsilon + t_0 e^{ik_1} + t_1 e^{i(k_1+k_2)} + t_2 e^{ik_2} + t_3 e^{-ik_1} + t_4 e^{-i(k_1+k_2)} + t_5 e^{-ik_2}, \tag{2.45b}$$

where we have defined *crystal coordinates* $k_i = \boldsymbol{k}\boldsymbol{a}_i$.

The x and y directions are decoupled from the z direction. For the latter, the Hamiltonian is already diagonal. The dispersion relation reads

$$\varepsilon_{\boldsymbol{k}3} = \varepsilon_z + 2t_z[\cos(k_1) + \cos(k_2) + \cos(k_1 + k_2)]. \tag{2.46}$$

The in-plane p orbitals are more complicated,

$$\begin{aligned} H_{\boldsymbol{k}} &= \varepsilon_x + 2\cos(k_1)\operatorname{diag}(t_x, t_y) \\ &+ \begin{bmatrix} \frac{1}{2}(t_x + 3t_y)[\cos(k_2) + \cos(k_1 + k_2)] & \frac{\sqrt{3}}{2}(t_x - t_y)[\cos(k_2) - \cos(k_1 + k_2)] \\ \frac{\sqrt{3}}{2}(t_x - t_y)[\cos(k_2) - \cos(k_1 + k_2)] & \frac{1}{2}(3t_x + t_y)[\cos(k_2) + \cos(k_1 + k_2)] \end{bmatrix}. \end{aligned} \tag{2.47}$$

Diagonalization yields

$$\begin{aligned} \varepsilon_{\boldsymbol{k}1,2} = \varepsilon_x &+ (t_x + t_y)[\cos(k_1) + \cos(k_2) + \cos(k_1 + k_2)] \\ &\pm \frac{t_x - t_y}{\sqrt{2}} \sqrt{\begin{matrix} 3 - \cos(k_1) & - \cos(k_2) & - \cos(k_1 + k_2) \\ + \cos(2k_1) & + \cos(2k_2) & + \cos(2k_1 + 2k_2) \\ - \cos(k_1 - k_2) & - \cos(2k_1 + k_2) & - \cos(k_1 + 2k_2). \end{matrix}} \end{aligned} \tag{2.48}$$

The complete dispersion relation is plotted in Fig. 2.2b for some exemplary values of the model parameters. The p_x and p_y bands are degenerate only at Γ and K. They are completely decoupled from the p_z dispersion. In App. D.2, we will develop a similar TB model for a monolayer of beryllium, where we will also have to include s orbitals in the calculation.

2.3.2.2 Triangular lattice of *d* orbitals

As a second example, where the basis functions do *not* transform as the axes, we will now perform similar calculations for a triangular lattice of d_{z^2}, $d_{x^2-y^2}$, and d_{xy} orbitals with nearest-neighbor hopping.

The labels z^2, x^2-y^2, and xy are functions that transform exactly as the corresponding orbitals. E.g., a rotation of $\pi/4$ about the z axis, will transform x^2-y^2 into xy (more precisely, $2xy$) but leave z^2 invariant. In polar coordinates,

$$\begin{aligned} r^2[\cos^2(\varphi-\tfrac{\pi}{4})-\sin^2(\varphi-\tfrac{\pi}{4})] &= r^2\left[\frac{1+\cos(2\varphi-\frac{\pi}{2})}{2}-\frac{1-\cos(2\varphi-\frac{\pi}{2})}{2}\right] \\ &= r^2\left[\frac{1+\sin(2\varphi)}{2}-\frac{1-\sin(2\varphi)}{2}\right] = 2r^2\sin(2\varphi) = 2r^2\sin(\varphi)\cos(\varphi). \end{aligned} \tag{2.49}$$

The primitive lattice vectors $\boldsymbol{a}_1$ and $\boldsymbol{a}_2$ are as in the first example. However, in the basis of the d_{z^2}, $d_{x^2-y^2}$, and d_{xy} orbitals, the three reflections have a different representation,

$$S_x = S_y = \mathrm{diag}(1,1,-1) \quad \text{and} \quad S_z = 1. \tag{2.50}$$

Again, we start with the most general matrix for the nearest-neighbor hopping in x direction,

$$t_0 = \begin{bmatrix} t_{z^2} & t_{z^2,x^2-y^2} & t_{z^2,xy} \\ t_{x^2-y^2,z^2} & t_{x^2-y^2} & t_{x^2-y^2,xy} \\ t_{xy,z^2} & t_{xy,x^2-y^2} & t_{xy} \end{bmatrix}. \tag{2.51}$$

The constraint imposed by the x-reflection symmetry, $t_0 = (S_x \cdot t_0 \cdot S_x^{-1})^{\mathrm{T}}$, couples the elements of the upper and lower triangle of the matrix,

$$t_0 = \begin{bmatrix} t_{z^2} & t_{z^2,x^2-y^2} & t_{z^2,xy} \\ t_{z^2,x^2-y^2} & t_{x^2-y^2} & t_{x^2-y^2,xy} \\ -t_{z^2,xy} & -t_{x^2-y^2,xy} & t_{xy} \end{bmatrix}. \tag{2.52}$$

Additionally, the y-reflection symmetry, $t_0 = S_y \cdot t_0 \cdot S_y^{-1} = S_x \cdot t_0 \cdot S_x^{-1}$, implies that the hopping is symmetric,

$$t_0 = \begin{bmatrix} t_{z^2} & t_{z^2,x^2-y^2} & 0 \\ t_{z^2,x^2-y^2} & t_{x^2-y^2} & 0 \\ 0 & 0 & t_{xy} \end{bmatrix}. \tag{2.53}$$

The z-reflection symmetry does not impose any constraint.

Also the rotations have a different representation in the d-orbital basis,

$$R_\varphi = \begin{bmatrix} 1 & 0 & 0 \\ 0 & \cos(2\varphi) & -\sin(2\varphi) \\ 0 & \sin(2\varphi) & \cos(2\varphi) \end{bmatrix} \overset{\varphi=\frac{\pi}{3}}{=} \begin{bmatrix} 1 & 0 & 0 \\ 0 & -\frac{1}{2} & -\frac{\sqrt{3}}{2} \\ 0 & \frac{\sqrt{3}}{2} & -\frac{1}{2} \end{bmatrix}. \tag{2.54}$$

Thus, $t_3 = t_0$, $t_4 = t_1$, and $t_5 = t_2$, where

$$t_{1,2} = R_{\mp\frac{\pi}{3}} \cdot t_0 \cdot R_{\mp\frac{\pi}{3}}^{-1} = \begin{bmatrix} t_{z^2} & -\frac{1}{2}t_{z^2,x^2-y^2} & \pm\frac{\sqrt{3}}{2}t_{z^2,x^2-y^2} \\ -\frac{1}{2}t_{z^2,x^2-y^2} & \frac{1}{4}(t_{x^2-y^2}+3t_{xy}) & \mp\frac{\sqrt{3}}{4}(t_{x^2-y^2}-t_{xy}) \\ \pm\frac{\sqrt{3}}{2}t_{z^2,x^2-y^2} & \mp\frac{\sqrt{3}}{4}(t_{x^2-y^2}-t_{xy}) & \frac{1}{4}(3t_{x^2-y^2}+t_{xy}) \end{bmatrix}. \tag{2.55}$$

Again, the on-site energy matrix ε must fulfill the reflection *and* rotational symmetries, thus

$$\varepsilon = \mathrm{diag}(\varepsilon_{z^2}, \varepsilon_{x^2-y^2}, \varepsilon_{x^2-y^2}). \tag{2.56}$$

For this example, there is no simple analytical expression for the dispersion relation.

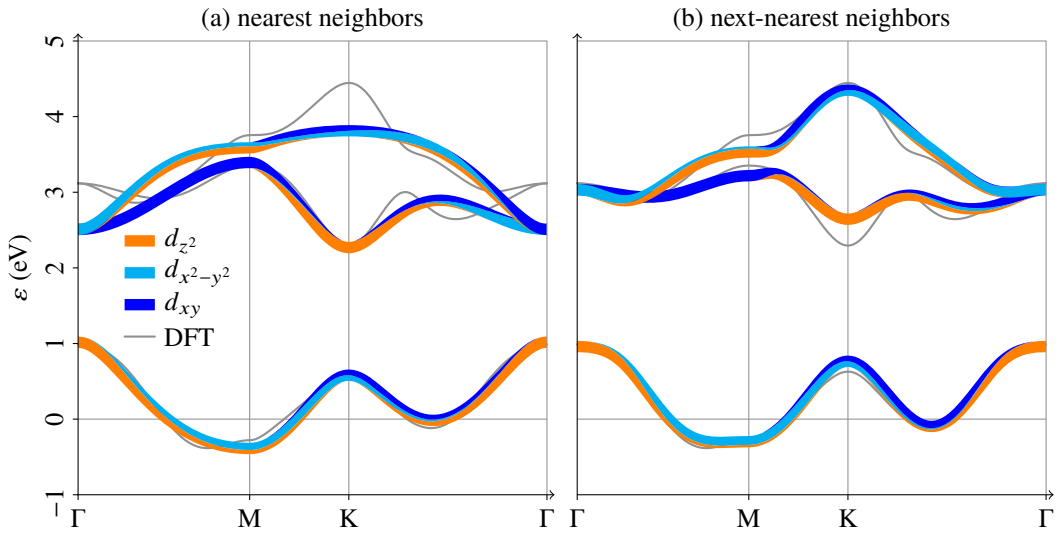

Figure 2.3: TB models of 1H-TaS_2. The path segments Γ–M and M–K–Γ are oriented in the y and x direction, respectively. (a) Only nearest-neighbor hopping is considered. To obtain reasonable results for the lowest band, deviations in the upper bands must be put up with. (b) Additionally, next-nearest-neighbor hopping is taken into account. All three bands are reproduced qualitatively.

2.3.2.3 Trigonal–prismatic TMDCs

Real systems that can be approximately described by the model of a triangular lattice of d orbitals are the trigonal–prismatic (TP) TMDCs. Here, the relevant orbitals are located on the transition-metal atoms only. However, the presence of the chalcogen atoms breaks the S_y symmetry. Thus, we have to settle for Eq. 2.52 and slightly more complicated expressions.

A least-squares fit to DFT data (Sec. 9.8) yields the optimized parameters

$$\varepsilon = \begin{bmatrix} 1851 & 0 & 0 \\ 0 & 2301 & 0 \\ 0 & 0 & 2301 \end{bmatrix} \text{meV}, \qquad t_0 = \begin{bmatrix} -139 & 479 & 383 \\ 479 & -256 & -311 \\ -383 & 311 & 325 \end{bmatrix} \text{meV}. \tag{2.57}$$

The corresponding dispersion relation is plotted in Fig. 2.3a. In order to better reproduce the lowest band, we have allowed larger deviations for the two upper bands (by multiplying the squared errors belonging to the lowest band by a factor of five). We made use of this TB model in Ref. 86 (cf. Sec. 9.6.1). There, however, we formulated it in the basis of complex instead of real harmonics.

It is straightforward to generalize the model with respect to hoppings t' between next-nearest neighbors. We now label the hoppings t and t' with the bond angles $\varphi_n = 2n\pi/3$ and $\varphi'_n = (2n+1)\pi/3$ and define the corresponding bond vectors $\boldsymbol{a}_n = a(\cos\varphi_n, \sin\varphi_n)$ and $\boldsymbol{a}'_n = \sqrt{3}a(\cos\varphi'_n, \sin\varphi'_n)$. This allows us to write the Hamiltonian as

$$H_{\boldsymbol{k}} = \varepsilon + \left[\sum_{n=1}^{3} t_{\varphi_n} \mathrm{e}^{\mathrm{i}\boldsymbol{a}_n \boldsymbol{k}} + \sum_{n=1}^{3} t'_{\varphi'_n} \mathrm{e}^{\mathrm{i}\boldsymbol{a}'_n \boldsymbol{k}} + \text{H.c.} \right], \tag{2.58}$$

where "H.c." is a shorthand for the Hermitian conjugate of preceding terms in brackets. This notation saves us from having to explicitly apply reflections to the hopping matrices.

Including hopping between next-nearest neighbors, the optimized model parameters read

$$\varepsilon = \mathrm{diag}(2280, 2159, 2159)\ \mathrm{meV}, \tag{2.59a}$$

$$t_0 = \begin{bmatrix} -187 & 380 & 365 \\ 380 & -333 & -345 \\ -365 & 345 & 439 \end{bmatrix} \mathrm{meV}, \qquad t_0' = \begin{bmatrix} -33 & -16 & 0 \\ -7 & 141 & 0 \\ 0 & 0 & 45 \end{bmatrix} \mathrm{meV}. \tag{2.59b}$$

The dispersion is plotted in Fig. 2.3b. The presence of more long-range hoppings and the increased number of degrees of freedom allows for a better agreement with the DFT data.

2.3.3 Wannier functions

Wannier functions are localized and orthogonal orbitals [87]. They are often used as basis functions for electronic-structure calculations, e.g., in TB. In contrast to atomic orbitals (at different positions), they are orthogonal to each other, which has the advantage that only a simple instead of a generalized eigenvalue problem has to be solved.

The choice of Wannier functions is not unique and is decisive for whether matrix elements of the Hamiltonian in this basis are short- or long-ranged. Since the electronic Hamiltonian does not couple states without spatial overlap, more localized Wannier functions lead to more short-range TB models. One possible choice of Wannier functions are simple orthogonalized atomic orbitals [88]. A model formulated in this basis can be very insightful because the results have a clear interpretation in terms of well-known objects, especially if all relevant symmetries are preserved. However, such a model might be computationally less convenient because very long-range interactions have to be considered. On the other hand, *maximally localized Wannier functions* [89, 90] often yield very compact models, at the expense that we might have no intuition of the objects we are dealing with.

When setting up a TB model in an orthogonal basis and fitting its parameters to reference band structures, we are effectively choosing a set of Wannier functions without actually having access to their shape in the position representation. An alternative route is to construct Wannier functions starting from a set of Bloch functions $|\boldsymbol{k}n\rangle$, e.g., from a DFT calculation,

$$|\boldsymbol{R}\alpha\rangle = \frac{1}{\sqrt{N}} \sum_{\boldsymbol{k}n} |\boldsymbol{k}n\rangle U^*_{\boldsymbol{k}\alpha n} \mathrm{e}^{\mathrm{i}\boldsymbol{k}\boldsymbol{R}}. \tag{2.60}$$

Here, the unitary matrix $U^*_{\boldsymbol{k}\alpha n}$ mixes the bands at every $\boldsymbol{k}$ point (cf. Eq. C.13) and can be freely chosen (within the constraint of unitarity), resulting in different sets of Wannier functions [90]. If the relevant bands to be described are intertwined with other bands, they have to be isolated using a disentanglement procedure first [91].

A popular tool to obtain Wannier functions in such a way from *ab initio* calculations is Wannier90 [92–94] (cf. App. A.2). Real-space plots of Wannier functions for 1H-TaS_2 that have been constructed starting from atomic d_{z^2}, $d_{x^2-y^2}$, and d_{xy} orbitals without maximal localization are shown in Fig. 2.4. The original shape of the atomic orbitals is largely preserved, however, the symmetry is slightly broken (adapted to the symmetry of the crystal).

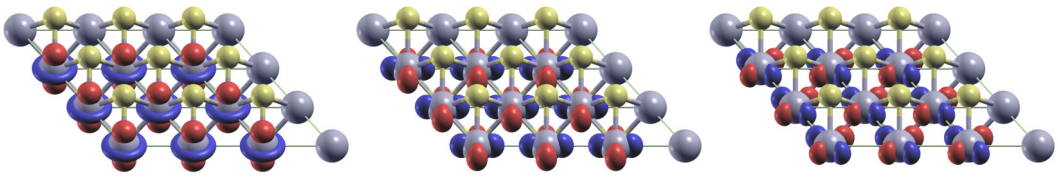

Figure 2.4: d_{z^2}-, $d_{x^2-y^2}$-, and d_{xy}-like Wannier functions.

2.4 Phonons

Now we come to the second part of our Hamiltonian. Phonons are the bosonic quasiparticles or *collective excitations* of lattice vibrations. They play a crucial role for a plethora of effects. For example, they are responsible for $\propto T^3$ and $\propto T^5$ dependencies of the specific heat and the resistivity of materials [67], and they mediate the attraction between electrons at the origin of conventional superconductivity [95]. Also, because they originate from the lattice degrees of freedom, they are tightly linked to phenomena such as periodic lattice distortions (PLDs) or CDWs [96], magnetostriction [97], thermo- [98], and piezoelectrics [99].

Because of the BO approximation, lattice vibrations can be rather well described with a very simple theoretical framework. Within the additional harmonic approximation (on which the usual notion of phonons depends), we only have to consider an assembly of classical coupled harmonic oscillators, as will be explained in the following Sec. 2.4.1. There are several reviews on this topic; we refer to Ref. 100. Afterwards, in Sec. 2.4.2, we will describe how phonons can be calculated in the context of DFT by means of DFPT. The *constrained* variant cDFPT, a downfolding method essential for this work, will be outlined in Sec. 2.4.2.2. Similar to the TB models for the electrons, we can formulate effective mass–spring models for the phonons, to which Sec. 2.4.3 is dedicated. Finally, in Secs. 2.4.7 and 2.4.8, we will briefly discuss nonadiabatic and anharmonic corrections to the presented theory.

2.4.1 Harmonic approximation

Within the BO approximation (cf. Sec. 2.1) the nuclei move in an effective potential mediated by the electrons (which already includes the repulsion between nuclei). This potential, E say, can be expanded as a function of atomic displacements $u_{\boldsymbol{R}i}$ from the equilibrium positions,

$$E = E|_{u=0} + \sum_{\boldsymbol{R}i} \frac{\partial E}{\partial u_{\boldsymbol{R}i}}\bigg|_{u=0} u_{\boldsymbol{R}i} + \frac{1}{2} \sum_{\boldsymbol{R}\boldsymbol{R}'ij} \frac{\partial^2 E}{\partial u_{\boldsymbol{R}i} \partial u_{\boldsymbol{R}'j}}\bigg|_{u=0} u_{\boldsymbol{R}i} u_{\boldsymbol{R}'j} + \dots \tag{2.61}$$

Here, $\boldsymbol{R}$ denotes a Bravais lattice vector and i runs over the Cartesian directions of all basis atoms. The zeroth-order term is only a constant, which can be ignored in the following. The first-order term includes the force, which vanishes because of the assumption that we are at the equilibrium positions. To calculate reasonable phonons, we have to make sure that our atomic positions are *relaxed* in the sense that all interatomic forces (but not necessarily the pressure) are minimized (cf. App. C.6). To second order, we are left with the last term, which includes the interatomic force constants (IFCs)

$$C_{\boldsymbol{R}-\boldsymbol{R}'ij} = \frac{\partial^2 E}{\partial u_{\boldsymbol{R}i} \partial u_{\boldsymbol{R}'j}}. \tag{2.62}$$

Together with the atomic masses M_i,[5] this is all we need to know to describe our phonons. The IFCs tell us how the force acting on one atom in one direction changes upon displacement of another atom in another direction, since $\partial^2 E/\partial x_1 \partial x_2 = -\partial F_1/\partial x_2$. The quantum mechanical problem has been mapped onto an effective classical mass–spring model. (Details on how to set up such models are given in Sec. 2.4.3.) The matrix of IFCs is symmetric and, because of the condition that we are at the minimum of the BO energy landscape, also positive definite.

A Fourier transform (cf. App. C.3) and division by the geometric mean of the atomic masses yields the *dynamical matrix*

$$D_{\boldsymbol{q}ij} = \frac{1}{\sqrt{M_i M_j}} \sum_{\boldsymbol{R}} C_{\boldsymbol{R}ij} \mathrm{e}^{\mathrm{i}\boldsymbol{q}\boldsymbol{R}}, \tag{2.63}$$

[5] The combined index i labels atoms *and* their displacement directions. The mass M_i is of course independent of the directions, but i can still be used to identify the atom.

whose eigenvalues are the squares of the phonon frequencies $\omega_{\boldsymbol{q}\nu}$,

$$(D_{\boldsymbol{q}} - \omega_{\boldsymbol{q}\nu}^2)\boldsymbol{e}_{\boldsymbol{q}\nu} = 0, \tag{2.64}$$

where ν labels the phonon branches. For N_n atoms in the unit cell and d spatial dimensions, there are d acoustic branches and $d(N_\mathrm{n} - 1)$ optical branches. The speed of sound is given by the slope of the acoustic branches, whose frequency goes to zero for small wave vectors.

The phonon eigenvectors $\boldsymbol{e}_{\boldsymbol{q}\nu}$ and a Fourier transform (cf. App. C.3) provide the link between a (collective) phononic eigendisplacement of strength $u_{\boldsymbol{q}\nu}$ and the real Cartesian displacements $u_{\boldsymbol{R}i}$ of the atoms. The complete transform and its inverse read

$$u_{\boldsymbol{q}i} = \frac{1}{N}\sum_{\boldsymbol{R}} u_{\boldsymbol{R}i}\mathrm{e}^{\mathrm{i}\boldsymbol{q}\boldsymbol{R}}, \qquad u_{\boldsymbol{q}\nu} = \sum_i \sqrt{NM_i}\, e^*_{\boldsymbol{q}i\nu} u_{\boldsymbol{q}i}, \tag{2.65a}$$

$$u_{\boldsymbol{R}i} = \sum_{\boldsymbol{q}} u_{\boldsymbol{q}i}\mathrm{e}^{-\mathrm{i}\boldsymbol{q}\boldsymbol{R}}, \qquad u_{\boldsymbol{q}i} = \frac{1}{\sqrt{NM_i}}\sum_{\nu} e_{\boldsymbol{q}i\nu} u_{\boldsymbol{q}\nu}. \tag{2.65b}$$

For each *normal coordinate* $u_{\boldsymbol{q}\nu}$ we can define its *conjugate momentum* $p_{\boldsymbol{q}\nu}$. Going over to operators, $\bullet \to \hat{\bullet}$, we can furthermore express theses canonical coordinates in terms of phononic creation and annihilation operators,

$$\hat{u}_{\boldsymbol{q}\nu} = \frac{1}{\sqrt{2\omega_{\boldsymbol{q}\nu}}}[\hat{b}^\dagger_{-\boldsymbol{q}\nu} + \hat{b}_{\boldsymbol{q}\nu}], \tag{2.66a}$$

$$\hat{p}_{\boldsymbol{q}\nu} = \mathrm{i}\sqrt{\frac{\omega_{\boldsymbol{q}\nu}}{2}}[\hat{b}^\dagger_{-\boldsymbol{q}\nu} - \hat{b}_{\boldsymbol{q}\nu}]. \tag{2.66b}$$

With them, we can write the phononic Hamiltonian, i.e., the combined kinetic and potential vibrational energy according to the virial theorem, in a diagonal form (cf. App. B of Ref. 101),

$$\hat{H}_\mathrm{ph} = \frac{1}{2}\sum_{\boldsymbol{q}\nu}\left[\hat{p}^\dagger_{\boldsymbol{q}\nu}\hat{p}_{\boldsymbol{q}\nu} + \omega^2\hat{u}^\dagger_{\boldsymbol{q}\nu}\hat{u}_{\boldsymbol{q}\nu}\right] = \sum_{\boldsymbol{q}\nu}\omega_{\boldsymbol{q}\nu}\left[\hat{b}^\dagger_{\boldsymbol{q}\nu}\hat{b}_{\boldsymbol{q}\nu} + \frac{1}{2}\right], \tag{2.67}$$

where the $1/2$ term stems from the quantum zero-point motion. $\hat{H}_\mathrm{ph}$ contains, *inter alia,* the harmonic approximations to the terms of the nuclear kinetic energy and the *change* of the nuclear repulsion in the general Hamiltonian (Eq. 2.1).

We can calculate all of this from first principles, using DFPT, as shown in the following.

2.4.2 Density-functional perturbation theory

In the BO approximation, the total energy of a system of interacting electrons and nuclei can be written as a functional E of the ground-state electron density n (cf. Sec. 2.3.1),

$$E_\kappa[n] = F[n] + \int \mathrm{d}^3r\, V_\kappa(\boldsymbol{r})n_\kappa(\boldsymbol{r}) + \Phi_\kappa. \tag{2.68}$$

Here, F is the universal functional composed of the kinetic energy T and the Coulomb repulsion U of the electrons, V is the external potential of an individual electron amid the ensemble of atomic nuclei, and Φ is the electrostatic energy due to the repulsion of the nuclei. Except for F, which is hence called *universal*, all involved quantities depend of the atomic positions, the complete set of which is denoted as κ for brevity.

The derivative with respect to an atomic displacement $u_{\boldsymbol{R}i}$ yields the force

$$-F_{\boldsymbol{R}i} = \frac{\mathrm{d}E_\kappa[n]}{\mathrm{d}u_{\boldsymbol{R}i}} = \frac{\delta E_\kappa[n]}{\delta n_\kappa(\boldsymbol{r})}\frac{\partial n_\kappa(\boldsymbol{r})}{\partial u_{\boldsymbol{R}i}} + \frac{\partial E_\kappa[n]}{\partial u_{\boldsymbol{R}i}}, \tag{2.69}$$

where δ denotes the functional derivative. Since the ground-state density n minimizes E by definition, the functional derivative and thus the first term on the right-hand side vanish [102]. Only the explicit dependence on κ via V and Φ contributes to the derivative.

This equivalently follows from the Hellmann–Feynman theorem $\partial\langle\psi|\hat{H}|\psi\rangle = \langle\psi|\partial\hat{H}|\psi\rangle$, where $|\psi\rangle$ is an eigenstate of the Hamiltonian $\hat{H}$ (cf. App. C.6). The electronic Hamiltonian of the system and its first derivative read

$$\hat{H} = \hat{T} + \hat{U} + \int \mathrm{d}^3 r\, V_\kappa(\boldsymbol{r})\hat{n}(\boldsymbol{r}) + \Phi_\kappa, \tag{2.70}$$

$$\frac{\partial\hat{H}}{\partial u_{\boldsymbol{R}i}} = \int \mathrm{d}^3 r\, \frac{\partial V_\kappa(\boldsymbol{r})}{\partial u_{\boldsymbol{R}i}}\hat{n}(\boldsymbol{r}) + \frac{\partial\Phi_\kappa}{\partial u_{\boldsymbol{R}i}}, \tag{2.71}$$

since the density *operator* (Eq. 2.13) does not depend on atomic positions. Thus, the force is

$$-F_{\boldsymbol{R}i} = \frac{\partial E_\kappa[n]}{\partial u_{\boldsymbol{R}i}} = \frac{\partial\langle\psi|\hat{H}|\psi\rangle}{\partial u_{\boldsymbol{R}i}} = \langle\psi|\frac{\partial\hat{H}}{\partial u_{\boldsymbol{R}i}}|\psi\rangle = \int \mathrm{d}^3 r\, \frac{\partial V_\kappa(\boldsymbol{r})}{\partial u_{\boldsymbol{R}i}} n_\kappa(\boldsymbol{r}) + \frac{\partial\Phi_\kappa}{\partial u_{\boldsymbol{R}i}}. \tag{2.72}$$

The knowledge of the (zeroth derivative of the) density allows us to calculate both the total energy and its first derivative. This is an example of the $2n + 1$ theorem (for $n = 0$) [103]. Hence, the ground-state density allows for the direct calculation of forces and thus molecular dynamics. The second derivative yields the IFCs

$$C_{\boldsymbol{R}-\boldsymbol{R}'ij} = \frac{\partial^2 E_\kappa[n]}{\partial u_{\boldsymbol{R}i}\partial u_{\boldsymbol{R}'j}} = \underbrace{\int \mathrm{d}^3 r\, \frac{\partial V_\kappa(\boldsymbol{r})}{\partial u_{\boldsymbol{R}i}} \frac{\partial n_\kappa(\boldsymbol{r})}{\partial u_{\boldsymbol{R}'j}}}_{\Delta C_{\boldsymbol{R}-\boldsymbol{R}'ij}} + \int \mathrm{d}^3 r\, \frac{\partial^2 V_\kappa(\boldsymbol{r})}{\partial u_{\boldsymbol{R}i}\partial u_{\boldsymbol{R}'j}} n_\kappa(\boldsymbol{r}) + \frac{\partial^2\Phi_\kappa}{\partial u_{\boldsymbol{R}i}\partial u_{\boldsymbol{R}'j}}. \tag{2.73}$$

The first and second term on the right-hand side are sometimes referred to as the linear and quadratic EPC, respectively [50]. If the ground-state density and its first derivative are known, this expression can be readily evaluated. The ground-state density n is accessible in DFT. In turn, its response ∂n can be conveniently evaluated using DFPT [104–106], which combines linear-response theory with DFT. Above, the term that features ∂n is labeled with ΔC. It will be particularly important in the following since it describes how the vibrations of the lattice are *screened* by the surrounding electron density. This *phonon renormalization* will be discussed in detail in Chap. 5.

DFPT is a method that is used to calculate the linear response of the density in general and is thus not limited to a specific application such as the calculation of phonons. For example, it is also possible to calculate Coulomb parameters for extended Hubbard models with the help of DFPT [107].

For the calculation of ∂n, we adopt the KS formalism, where the density is expressed in terms of the wave functions of an effective noninteracting system (cf. Sec. 2.3.1.1). From now on, all dependencies on atomic positions κ are left understood. With KS eigenfunctions $\psi_{\boldsymbol{k}n}(\boldsymbol{r}) = \langle\boldsymbol{r}|\boldsymbol{k}n\rangle$ and using the product rule,

$$n(\boldsymbol{r}) = 2\sum_{\boldsymbol{k}n} f(\varepsilon_{\boldsymbol{k}n})\langle\boldsymbol{k}n|\boldsymbol{r}\rangle\langle\boldsymbol{r}|\boldsymbol{k}n\rangle, \tag{2.74}$$

$$\partial n(\boldsymbol{r}) = 4\,\mathrm{Re}\sum_{\boldsymbol{k}n} f(\varepsilon_{\boldsymbol{k}n})\langle\boldsymbol{k}n|\boldsymbol{r}\rangle\langle\boldsymbol{r}|\partial\boldsymbol{k}n\rangle, \tag{2.75}$$

where f is the Fermi function, the prefactor of 2 accounts for the spin, and $\varepsilon_{\boldsymbol{k}n}$ and $|\boldsymbol{k}n\rangle$ are the eigenvalues and -states of the KS Hamiltonian $\hat{H}_{\mathrm{KS}}$,

$$(\hat{H}_{\mathrm{KS}} - \varepsilon_{\boldsymbol{k}n})|\boldsymbol{k}n\rangle = 0 \quad \text{with} \quad \hat{H}_{\mathrm{KS}} = \frac{\hat{\boldsymbol{p}}^2}{2} + \hat{V}_{\mathrm{SCF}}. \tag{2.76}$$

Upon an atomic displacement $\partial u_{\boldsymbol{R}i}$, these KS equations change as

$$\partial[(\hat{H}_{\mathrm{KS}} - \varepsilon_{\boldsymbol{k}n})|\boldsymbol{k}n\rangle] = (\partial\hat{H}_{\mathrm{KS}} - \partial\varepsilon_{\boldsymbol{k}n})|\boldsymbol{k}n\rangle + (\hat{H}_{\mathrm{KS}} - \varepsilon_{\boldsymbol{k}n})|\partial\boldsymbol{k}n\rangle = 0. \tag{2.77}$$

This is known as the *Sternheimer equation*, albeit originally formulated in another context (cf. Eq. 79 of Ref. 108). Multiplying with $\langle\boldsymbol{k}+\boldsymbol{q}m|$ from the left,

$$\begin{aligned} 0 &= \langle\boldsymbol{k}+\boldsymbol{q}m|(\partial\hat{H}_{\mathrm{KS}} - \partial\varepsilon_{\boldsymbol{k}n})|\boldsymbol{k}n\rangle + \langle\boldsymbol{k}+\boldsymbol{q}m|(\hat{H}_{\mathrm{KS}} - \varepsilon_{\boldsymbol{k}n})|\partial\boldsymbol{k}n\rangle && (2.78a)\\ &= \langle\boldsymbol{k}+\boldsymbol{q}m|\partial\hat{H}_{\mathrm{KS}}|\boldsymbol{k}n\rangle(1 - \delta_{\boldsymbol{q}0}\delta_{mn}) + \langle\boldsymbol{k}+\boldsymbol{q}m|\partial\boldsymbol{k}n\rangle(\varepsilon_{\boldsymbol{k}+\boldsymbol{q}m} - \varepsilon_{\boldsymbol{k}n}) && (2.78b)\\ &= \langle\boldsymbol{k}+\boldsymbol{q}m|\partial\hat{V}_{\mathrm{KS}}|\boldsymbol{k}n\rangle(1 - \delta_{\boldsymbol{q}0}\delta_{mn}) + \langle\boldsymbol{k}+\boldsymbol{q}m|\partial\boldsymbol{k}n\rangle(\varepsilon_{\boldsymbol{k}+\boldsymbol{q}m} - \varepsilon_{\boldsymbol{k}n}). && (2.78c) \end{aligned}$$

Here we used the orthogonality of the KS states $\langle\boldsymbol{k}+\boldsymbol{q}m|\boldsymbol{k}n\rangle = \delta_{\boldsymbol{q}0}\delta_{mn}$, once again the Hellmann–Feynman theorem $\langle\boldsymbol{k}n|\partial H_{\mathrm{KS}}|\boldsymbol{k}n\rangle = \partial\varepsilon_{\boldsymbol{k}n}$, and the fact that H_{KS} depends on the atomic positions only via V_{SCF}. For $\boldsymbol{q} = 0$ and $m = n$, the above equation is trivially true.

We simply ignore this case for a moment and write

$$\langle\boldsymbol{k}+\boldsymbol{q}m|\partial\boldsymbol{k}n\rangle = -\frac{\langle\boldsymbol{k}+\boldsymbol{q}m|\partial\hat{V}_{\mathrm{SCF}}|\boldsymbol{k}n\rangle}{\varepsilon_{\boldsymbol{k}+\boldsymbol{q}m} - \varepsilon_{\boldsymbol{k}n}}. \tag{2.79}$$

Then, using the representation of unity in the basis of the KS states, $1 = \sum_{\boldsymbol{q}m}|\boldsymbol{k}+\boldsymbol{q}m\rangle\langle\boldsymbol{k}+\boldsymbol{q}m|$, the change of the KS states reads

$$|\partial\boldsymbol{k}n\rangle = \sum_{\boldsymbol{q}m}|\boldsymbol{k}+\boldsymbol{q}m\rangle\langle\boldsymbol{k}+\boldsymbol{q}m|\partial\boldsymbol{k}n\rangle = -\sum_{\boldsymbol{q}m}\frac{\langle\boldsymbol{k}+\boldsymbol{q}m|\partial\hat{V}_{\mathrm{SCF}}|\boldsymbol{k}n\rangle}{\varepsilon_{\boldsymbol{k}+\boldsymbol{q}m} - \varepsilon_{\boldsymbol{k}n}}|\boldsymbol{k}+\boldsymbol{q}m\rangle. \tag{2.80}$$

Inserting Eq. 2.80 into Eq. 2.75, we obtain an expression for the density response,

$$\partial n(\boldsymbol{r}) = 4\,\mathrm{Re}\sum_{\boldsymbol{q}\boldsymbol{k}mn}\frac{-f(\varepsilon_{\boldsymbol{k}n})}{\varepsilon_{\boldsymbol{k}+\boldsymbol{q}m} - \varepsilon_{\boldsymbol{k}n}}\langle\boldsymbol{k}n|\boldsymbol{r}\rangle\langle\boldsymbol{r}|\boldsymbol{k}+\boldsymbol{q}m\rangle\langle\boldsymbol{k}+\boldsymbol{q}m|\partial\hat{V}_{\mathrm{SCF}}|\boldsymbol{k}n\rangle. \tag{2.81}$$

A complex conjugation of the sum can be achieved by replacing $-f(\varepsilon_{\boldsymbol{k}n})$ by $f(\varepsilon_{\boldsymbol{k}+\boldsymbol{q}m})$. This can be seen from simply exchanging the names of the dummy variables $\boldsymbol{k}n$ and $\boldsymbol{k}+\boldsymbol{q}m$. Hence, we can rewrite the expression without the use of the Re operator,

$$\partial n(\boldsymbol{r}) = 2\sum_{\boldsymbol{q}\boldsymbol{k}mn}\frac{f(\varepsilon_{\boldsymbol{k}+\boldsymbol{q}m}) - f(\varepsilon_{\boldsymbol{k}n})}{\varepsilon_{\boldsymbol{k}+\boldsymbol{q}m} - \varepsilon_{\boldsymbol{k}n}}\langle\boldsymbol{k}n|\boldsymbol{r}\rangle\langle\boldsymbol{r}|\boldsymbol{k}+\boldsymbol{q}m\rangle\langle\boldsymbol{k}+\boldsymbol{q}m|\partial\hat{V}_{\mathrm{SCF}}|\boldsymbol{k}n\rangle. \tag{2.82}$$

Now, the singularity at $\boldsymbol{q} = 0$ and $m = n$ is removable, since the fraction can be replaced by the derivative of the Fermi function in this case.

Finally, the change in the IFCs $\Delta C_{\boldsymbol{R}-\boldsymbol{R}'ij}$ as defined in Eq. 2.73 can be written as

$$\begin{aligned} \Delta C_{\boldsymbol{R}-\boldsymbol{R}'ij} &= \int \mathrm{d}^3r\,\frac{\partial V(\boldsymbol{r})}{\partial u_{\boldsymbol{R}i}}\frac{\partial n(\boldsymbol{r})}{\partial u_{\boldsymbol{R}'j}} \qquad \langle\boldsymbol{r}|\frac{\partial\hat{V}}{\partial u_{\boldsymbol{R}i}}|\boldsymbol{k}+\boldsymbol{q}m\rangle && (2.83a)\\ &= 2\int \mathrm{d}^3r\sum_{\boldsymbol{q}\boldsymbol{k}mn}\frac{f(\varepsilon_{\boldsymbol{k}+\boldsymbol{q}m}) - f(\varepsilon_{\boldsymbol{k}n})}{\varepsilon_{\boldsymbol{k}+\boldsymbol{q}m} - \varepsilon_{\boldsymbol{k}n}}\langle\boldsymbol{k}n|\boldsymbol{r}\rangle\overbrace{\frac{\partial V(\boldsymbol{r})}{\partial u_{\boldsymbol{R}i}}\langle\boldsymbol{r}|\boldsymbol{k}+\boldsymbol{q}m\rangle}\langle\boldsymbol{k}+\boldsymbol{q}m|\frac{\partial\hat{V}_{\mathrm{SCF}}}{\partial u_{\boldsymbol{R}'j}}|\boldsymbol{k}n\rangle && (2.83b)\\ &= 2\sum_{\boldsymbol{q}\boldsymbol{k}mn}\frac{f(\varepsilon_{\boldsymbol{k}+\boldsymbol{q}m}) - f(\varepsilon_{\boldsymbol{k}n})}{\varepsilon_{\boldsymbol{k}+\boldsymbol{q}m} - \varepsilon_{\boldsymbol{k}n}}\langle\boldsymbol{k}n|\frac{\partial\hat{V}}{\partial u_{\boldsymbol{R}i}}|\boldsymbol{k}+\boldsymbol{q}m\rangle\langle\boldsymbol{k}+\boldsymbol{q}m|\frac{\partial\hat{V}_{\mathrm{SCF}}}{\partial u_{\boldsymbol{R}'j}}|\boldsymbol{k}n\rangle. && (2.83c) \end{aligned}$$

The above expression contains matrix elements formed by a mixture of real- and reciprocal-space objects. For a more insightful representation, we would like to replace the atomic

displacements $u_{\boldsymbol{R}i}$ by their Fourier transforms $u_{\boldsymbol{q}i}$ according to Eq. 2.65. From the product rule, we obtain the corresponding transforms for the derivatives of the potentials,

$$\frac{\partial \hat{V}}{\partial u_{\boldsymbol{q}i}} = \sum_{\boldsymbol{R}} \frac{\partial \hat{V}}{\partial u_{\boldsymbol{R}i}} \frac{\partial u_{\boldsymbol{R}i}}{\partial u_{\boldsymbol{q}i}} = \sum_{\boldsymbol{R}} \frac{\partial \hat{V}}{\partial u_{\boldsymbol{R}i}} \mathrm{e}^{-\mathrm{i}\boldsymbol{q}\boldsymbol{R}}, \tag{2.84a}$$

$$\frac{\partial \hat{V}}{\partial u_{\boldsymbol{R}i}} = \sum_{\boldsymbol{q}} \frac{\partial \hat{V}}{\partial u_{\boldsymbol{q}i}} \frac{\partial u_{\boldsymbol{q}i}}{\partial u_{\boldsymbol{R}i}} = \frac{1}{N} \sum_{\boldsymbol{q}} \frac{\partial \hat{V}}{\partial u_{\boldsymbol{q}i}} \mathrm{e}^{\mathrm{i}\boldsymbol{q}\boldsymbol{R}}. \tag{2.84b}$$

Inserting Eq. 2.84b into Eq. 2.83c yields

$$\Delta C_{\boldsymbol{R}-\boldsymbol{R}'ij} = \frac{2}{N^2} \sum_{\boldsymbol{q}\boldsymbol{k}mn} \frac{f(\varepsilon_{\boldsymbol{k}+\boldsymbol{q}m}) - f(\varepsilon_{\boldsymbol{k}n})}{\varepsilon_{\boldsymbol{k}+\boldsymbol{q}m} - \varepsilon_{\boldsymbol{k}n}} \times \sum_{\boldsymbol{q}'\boldsymbol{q}''} \langle \boldsymbol{k}n | \frac{\partial \hat{V}}{\partial u_{\boldsymbol{q}'i}} | \boldsymbol{k}+\boldsymbol{q}m \rangle \langle \boldsymbol{k}+\boldsymbol{q}m | \frac{\partial \hat{V}_{\mathrm{SCF}}}{\partial u_{\boldsymbol{q}''j}} | \boldsymbol{k}n \rangle \mathrm{e}^{\mathrm{i}(\boldsymbol{q}'\boldsymbol{R}+\boldsymbol{q}''\boldsymbol{R}')}. \tag{2.85}$$

This expression can be further simplified by momentum conservation.

In the position representation, $V(\boldsymbol{r})$ is a sum of contributions from all unit cells,

$$V(\boldsymbol{r}) = \sum_{\boldsymbol{R}} v_{\boldsymbol{R}}(\boldsymbol{r} - \boldsymbol{R}). \tag{2.86}$$

Hence, the derivative with respect to $u_{\boldsymbol{R}i}$ reads

$$\frac{\partial V(\boldsymbol{r})}{\partial u_{\boldsymbol{R}i}} = \frac{\partial v_{\boldsymbol{R}}(\boldsymbol{r} - \boldsymbol{R})}{\partial u_{\boldsymbol{R}i}}. \tag{2.87}$$

Without any lattice distortion, $v_{\boldsymbol{R}} = v_{\boldsymbol{R}'}$ for all $\boldsymbol{R}$ and $\boldsymbol{R}'$. Thus, from Eq. 2.84a,

$$\frac{\partial V(\boldsymbol{r} - \boldsymbol{R})}{\partial u_{\boldsymbol{q}i}} = \sum_{\boldsymbol{R}'} \frac{\partial v_{\boldsymbol{R}'}(\boldsymbol{r} - \boldsymbol{R} - \boldsymbol{R}')}{\partial u_{\boldsymbol{R}'i}} \mathrm{e}^{-\mathrm{i}\boldsymbol{q}\boldsymbol{R}'} = \sum_{\boldsymbol{R}'} \frac{\partial v_{\boldsymbol{R}'-\boldsymbol{R}}(\boldsymbol{r} - \boldsymbol{R}')}{\partial u_{\boldsymbol{R}'-\boldsymbol{R}i}} \mathrm{e}^{-\mathrm{i}\boldsymbol{q}(\boldsymbol{R}'-\boldsymbol{R})} = \sum_{\boldsymbol{R}'} \frac{\partial v_{\boldsymbol{R}'}(\boldsymbol{r} - \boldsymbol{R}')}{\partial u_{\boldsymbol{R}'i}} \mathrm{e}^{-\mathrm{i}\boldsymbol{q}(\boldsymbol{R}'-\boldsymbol{R})} = \frac{\partial V(\boldsymbol{r})}{\partial u_{\boldsymbol{q}i}} \mathrm{e}^{\mathrm{i}\boldsymbol{q}\boldsymbol{R}}. \tag{2.88}$$

Combining the above relation with the Bloch theorem (Eq. C.16),

$$\psi_{\boldsymbol{k}n}(\boldsymbol{r} - \boldsymbol{R}) = \psi_{\boldsymbol{k}n}(\boldsymbol{r}) \mathrm{e}^{\mathrm{i}\boldsymbol{k}\boldsymbol{R}}, \tag{2.89}$$

we can proof that all matrix elements of the deformation potential $\langle \boldsymbol{k}+\boldsymbol{q} | \partial_{\boldsymbol{q}'} \hat{V} | \boldsymbol{k} \rangle$ for $\boldsymbol{q}' \neq \boldsymbol{q}$ vanish, i.e., that momentum conservation holds. We go to the position representation

$$\langle \boldsymbol{k}+\boldsymbol{q}m | \frac{\partial \hat{V}}{\partial u_{\boldsymbol{q}'i}} | \boldsymbol{k}n \rangle = \int \mathrm{d}^3 r \, \langle \boldsymbol{k}+\boldsymbol{q}m | \boldsymbol{r} \rangle \langle \boldsymbol{r} | \frac{\partial \hat{V}}{\partial u_{\boldsymbol{q}'i}} | \boldsymbol{k}n \rangle \tag{2.90a}$$

$$= \int \mathrm{d}^3 r \, \psi^*_{\boldsymbol{k}+\boldsymbol{q}m}(\boldsymbol{r}) \frac{\partial V(\boldsymbol{r})}{\partial u_{\boldsymbol{q}'i}} \psi_{\boldsymbol{k}n}(\boldsymbol{r}). \tag{2.90b}$$

The $\boldsymbol{r}$ integral is over the entire space. It can be split into contributions from the individual unit cells. With Eq. 2.88,

$$\langle \boldsymbol{k}+\boldsymbol{q}m | \frac{\partial \hat{V}}{\partial u_{\boldsymbol{q}'i}} | \boldsymbol{k}n \rangle = \sum_{\boldsymbol{R}} \int_{\mathrm{WS}} \mathrm{d}^3 r \, \psi^*_{\boldsymbol{k}+\boldsymbol{q}m}(\boldsymbol{r} - \boldsymbol{R}) \frac{\partial V(\boldsymbol{r} - \boldsymbol{R})}{\partial u_{\boldsymbol{q}'i}} \psi_{\boldsymbol{k}n}(\boldsymbol{r} - \boldsymbol{R}) \tag{2.90c}$$

$$= \sum_{\boldsymbol{R}} \int_{\mathrm{WS}} \mathrm{d}^3 r \, \psi^*_{\boldsymbol{k}+\boldsymbol{q}m}(\boldsymbol{r}) \frac{\partial V(\boldsymbol{r})}{\partial u_{\boldsymbol{q}'i}} \psi_{\boldsymbol{k}n}(\boldsymbol{r}) \mathrm{e}^{\mathrm{i}(\boldsymbol{q}'-\boldsymbol{q})\boldsymbol{R}} \tag{2.90d}$$

$$= N \int_{\mathrm{WS}} \mathrm{d}^3 r \, \psi^*_{\boldsymbol{k}+\boldsymbol{q}m}(\boldsymbol{r}) \frac{\partial V(\boldsymbol{r})}{\partial u_{\boldsymbol{q}'i}} \psi_{\boldsymbol{k}n}(\boldsymbol{r}) \delta_{\boldsymbol{q}\boldsymbol{q}'}. \tag{2.90e}$$

The $\boldsymbol{R}$ sum together with the corresponding exponential function yields a delta function. Thus, we have the general result of a momentum-conserving deformation potential

$$\langle \boldsymbol{k}+\boldsymbol{q}m|\frac{\partial \hat{V}}{\partial u_{\boldsymbol{q}'i}}|\boldsymbol{k}n\rangle = \langle \boldsymbol{k}+\boldsymbol{q}m|\frac{\partial \hat{V}}{\partial u_{\boldsymbol{q}i}}|\boldsymbol{k}n\rangle\delta_{\boldsymbol{q}\boldsymbol{q}'}. \tag{2.91}$$

With this and Eq. 2.84b, the change in the IFCs from Eq. 2.85 finally becomes

$$\Delta C_{\boldsymbol{R}-\boldsymbol{R}'ij} = \frac{1}{N}\sum_{\boldsymbol{q}} C_{\boldsymbol{q}ij}\mathrm{e}^{-\mathrm{i}\boldsymbol{q}(\boldsymbol{R}-\boldsymbol{R}')}, \tag{2.92a}$$

$$\Delta C_{\boldsymbol{q}ij} = \frac{2}{N}\sum_{\boldsymbol{k}mn}\frac{f(\varepsilon_{\boldsymbol{k}+\boldsymbol{q}m})-f(\varepsilon_{\boldsymbol{k}n})}{\varepsilon_{\boldsymbol{k}+\boldsymbol{q}m}-\varepsilon_{\boldsymbol{k}n}}\langle \boldsymbol{k}n|\frac{\partial \hat{V}}{\partial u_{-\boldsymbol{q}i}}|\boldsymbol{k}+\boldsymbol{q}m\rangle\langle \boldsymbol{k}+\boldsymbol{q}m|\frac{\partial \hat{V}_{\mathrm{SCF}}}{\partial u_{\boldsymbol{q}j}}|\boldsymbol{k}n\rangle. \tag{2.92b}$$

The expression for $\Delta C_{\boldsymbol{q}ij}$ consists of the bare electronic susceptibility and the bare and screened EPC. ($\hat{V}$ and $\hat{V}_{\mathrm{SCF}}$ are the bare and screened external potentials, respectively). The link to the EPC as appears in the Hamiltonian in Eq. 2.2 will be established in Sec. 2.5.1.

2.4.2.1 Calculations without empty states

Only processes between (at least partially) occupied and unoccupied electronic states can contribute to the bare electronic susceptibility and thus to the density response and change of IFCs. This can be used to largely simplify the calculation, as shown by Baroni *et al.* [105] and de Gironcoli [109] for insulators and metals, respectively.

Let v (c) be a shorthand for $\boldsymbol{k}n$ ($\boldsymbol{k}+\boldsymbol{q}m$). Using the property $f(x)+f(-x)=1$ of the Fermi function, we can rewrite Eq. 2.82 as

$$\partial n(\boldsymbol{r}) = 2\sum_{vc}\frac{f(\varepsilon_c)-f(\varepsilon_v)}{\varepsilon_c-\varepsilon_v}[f(\varepsilon_v-\varepsilon_c)+f(\varepsilon_c-\varepsilon_v)]\langle v|\boldsymbol{r}\rangle\langle \boldsymbol{r}|c\rangle\langle c|\partial \hat{V}_{\mathrm{SCF}}|v\rangle \tag{2.93a}$$

$$= 4\,\mathrm{Re}\sum_{vc}\frac{f(\varepsilon_c)-f(\varepsilon_v)}{\varepsilon_c-\varepsilon_v}f(\varepsilon_v-\varepsilon_c)\langle v|\boldsymbol{r}\rangle\langle \boldsymbol{r}|c\rangle\langle c|\partial \hat{V}_{\mathrm{SCF}}|v\rangle \tag{2.93b}$$

$$= 4\,\mathrm{Re}\sum_{v}\langle v|\boldsymbol{r}\rangle\langle \boldsymbol{r}|\underbrace{\sum_{c}\frac{f(\varepsilon_c)-f(\varepsilon_v)}{\varepsilon_c-\varepsilon_v}f(\varepsilon_v-\varepsilon_c)|c\rangle\langle c|\partial \hat{V}_{\mathrm{SCF}}|v\rangle}_{|\partial v\rangle}. \tag{2.93c}$$

Note the reappearance of the prefactor of 4 and the Re operator as in Eq. 2.75[6] Now, due to the Fermi functions, the v (c) summation can be restricted to states that are statistically at least partially occupied (unoccupied)[7] In an insulator, v (c) would label the valence (conduction) states. The denominator $\varepsilon_c-\varepsilon_v$ is positive for most combinations of v and c, but close to the Fermi level it may reach zero or small negative values. To avoid this, we rewrite

$$\frac{f(\varepsilon_c)-f(\varepsilon_v)}{\varepsilon_c-\varepsilon_v} = \frac{(\varepsilon_c-\varepsilon_v+\alpha_c)\frac{f(\varepsilon_c)-f(\varepsilon_v)}{\varepsilon_c-\varepsilon_v}}{\varepsilon_c-\varepsilon_v+\alpha_c} = \frac{f(\varepsilon_c)-f(\varepsilon_v)+\alpha_c\frac{f(\varepsilon_c)-f(\varepsilon_v)}{\varepsilon_c-\varepsilon_v}}{\varepsilon_c-\varepsilon_v+\alpha_c} \tag{2.94}$$

with, e.g., $\alpha_c = \max(0, \max_v \varepsilon_v+\epsilon-\varepsilon_c)$, where ϵ is a small positive number. The operator

$$\hat{\alpha} = \sum_c \alpha_c|c\rangle\langle c| \tag{2.95}$$

[6] In the original derivation in Ref. 109, the Re operator is absent.

[7] Even though the Fermi function will never exactly reach zero, we can very well neglect its value beyond a certain energy. Moreover, in practical calculations, the Fermi function is often replaced by a similar step function such as an integrated Gaussian (cf. App. C.7).

describes a shift of the spectrum of conduction states. Using that ε_c and α_c are the eigenvalues of $\hat{H}_{\mathrm{KS}}$ and $\hat{\alpha}$ belonging to the simultaneous eigenstate $|c\rangle$, we can write

$$|\partial v\rangle = \frac{1}{\hat{H}_{\mathrm{KS}} - \varepsilon_v + \hat{\alpha}} \underbrace{\sum_c \left[f(\varepsilon_c) - f(\varepsilon_v) + \alpha_c \frac{f(\varepsilon_c) - f(\varepsilon_v)}{\varepsilon_c - \varepsilon_v} \right] f(\varepsilon_v - \varepsilon_c) |c\rangle\langle c| \partial \hat{V}_{\mathrm{SCF}} |v\rangle}_{\hat{P}_v - f(\varepsilon_v)} \tag{2.96}$$

since we ensured that $\langle c|(\hat{H}_{\mathrm{KS}} - \varepsilon_v + \hat{\alpha})|c\rangle = \varepsilon_c - \varepsilon_v + \alpha_c > 0$. The projection operator

$$\hat{P}_v = \sum_c \left[f(\varepsilon_c) - f(\varepsilon_v) + \alpha_c \frac{f(\varepsilon_c) - f(\varepsilon_v)}{\varepsilon_c - \varepsilon_v} \right] f(\varepsilon_v - \varepsilon_c) |c\rangle\langle c| + f(\varepsilon_v) \tag{2.97a}$$

$$= \sum_c \Big[f(\varepsilon_c) f(\varepsilon_v - \varepsilon_c) - f(\varepsilon_v) f(\varepsilon_v - \varepsilon_c) + \alpha_c \frac{f(\varepsilon_c) - f(\varepsilon_v)}{\varepsilon_c - \varepsilon_v} f(\varepsilon_v - \varepsilon_c) \Big] |c\rangle\langle c| + f(\varepsilon_v) \tag{2.97b}$$

$$= \sum_c \Big[f(\varepsilon_c) f(\varepsilon_v - \varepsilon_c) + f(\varepsilon_v) f(\varepsilon_c - \varepsilon_v) + \alpha_c \frac{f(\varepsilon_c) - f(\varepsilon_v)}{\varepsilon_c - \varepsilon_v} f(\varepsilon_v - \varepsilon_c) \Big] |c\rangle\langle c| \tag{2.97c}$$

vanishes if $|c\rangle$ is unoccupied since either of the bracketed terms contains any of α_c, $f(\varepsilon_c)$ and $f(\varepsilon_v) f(\varepsilon_c - \varepsilon_v) < f(\varepsilon_c)$, which all vanish on their own. Thus, Eq. 2.96 does not involve any unoccupied states. Rearranged in a linear fashion, it reads (cf. Eq. 2.77)

$$(\hat{H}_{\mathrm{KS}} - \varepsilon_v + \hat{\alpha})|\partial v\rangle = [\hat{P}_v - f(\varepsilon_v)] \partial \hat{V}_{\mathrm{SCF}} |v\rangle. \tag{2.98}$$

Such Sternheimer equations (cf. Eq. 5 of Ref. 108) are also used in different contexts. For example, in Sternheimer GW [110], summations over a very large number of unoccupied states usually required to calculate the RPA polarizability can be avoided.

The Sternheimer approach makes DFPT a relatively efficient method, e.g., compared to the method of frozen phonons. But still, the calculations are quite heavy. For example, calculating the phonons of different monolayer TMDCs with a three-atom unit cell (cf. Fig. 2.5b) has taken between 1000 and 2000 processor hours for a $\boldsymbol{k}$ and $\boldsymbol{q}$ sampling of 36×36 and 12×12 points, respectively.

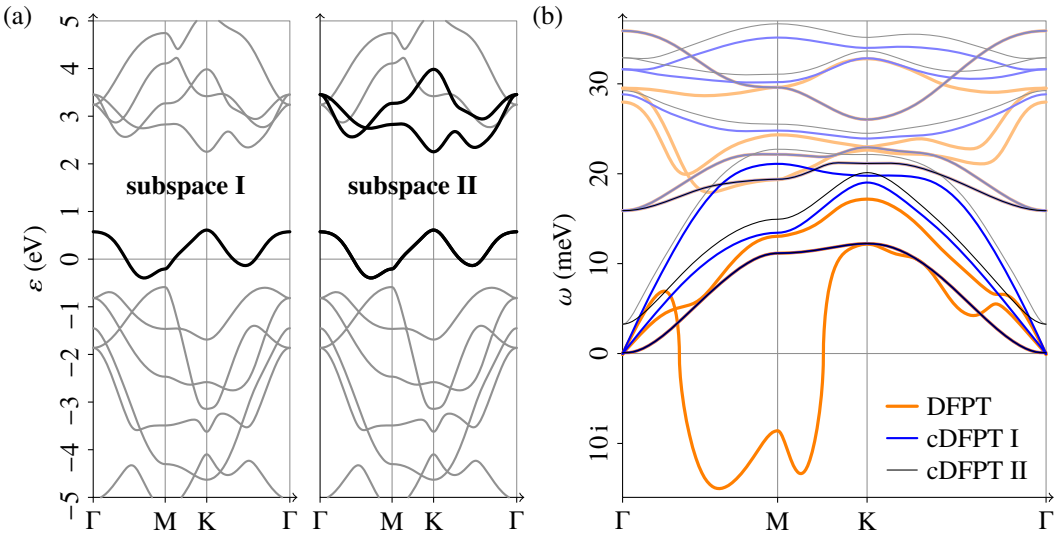

Figure 2.5: Application of DFPT and cDFPT to 1H-$NbSe_2$ for different choices of the active subspace. The computational parameters are as in Sec. 7.3. (a) Possible electronic bands to be excluded from the electronic response to lattice distortions. (b) Resulting phonon dispersions.

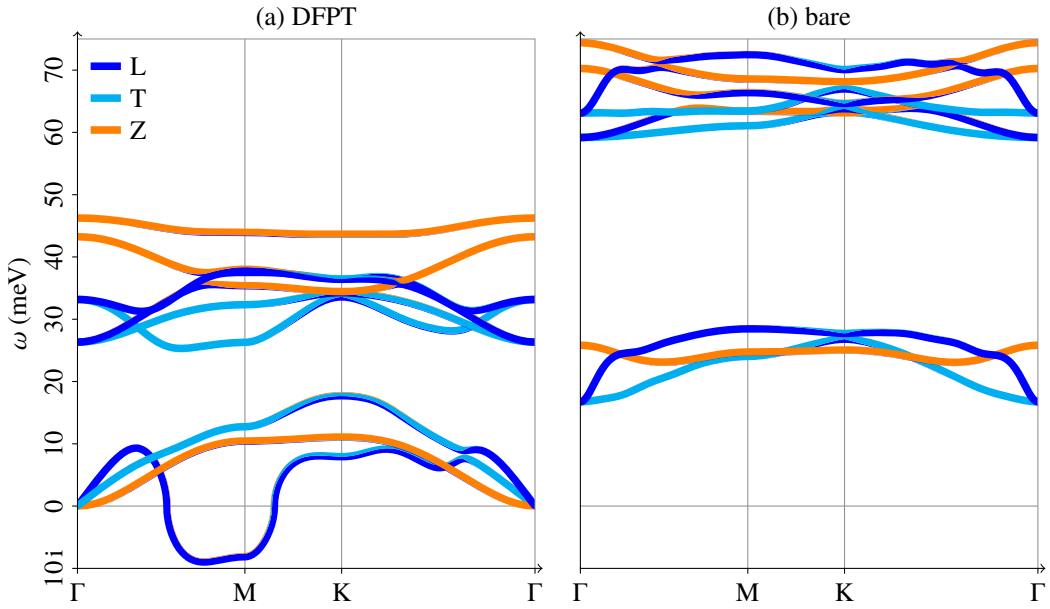

Figure 2.6: (a) DFPT and (b) full-cDFPT phonons of 1H-TaS_2, where *all* bands explicitly considered in DFT are counted among the active subspace. The computational parameters are as in Sec. 9.8.

2.4.2.2 Constrained density-functional perturbation theory

Analogous to the cRPA method used to calculate partially screened Coulomb interaction parameters, which will be presented in Sec. 2.6.1.1, we use cDFPT to obtain partially screened phonon dispersions and EPCs. This promising downfolding method has been introduced in 2015 by Nomura and Arita [50] as a modification of DFPT [106] and has only been applied to very few materials by now [61–63, 86, 111]. Given any code that can do DFPT, such as QE, its implementation is surprisingly simple (cf. App. A.1).

The idea is to exclude contributions from electronic transitions within an active subspace from the response of the electron density, and thus from the resulting phonons and EPCs. The density response is given in Eq. 2.82. To obtain cDFPT results for an active subspace $\mathcal{S}$, we only have to restrict the summation in Eq. 2.82 to states that satisfy the constraint $\{\boldsymbol{k}n, \boldsymbol{k}+\boldsymbol{q}m\} \not\subseteq \mathcal{S}$, i.e., at least one of the two states must *not* belong to the active subspace.

Likewise, in the Sternheimer equation (Eq. 2.98), which is the one actually implemented, we have to modify the projection operator (Eq. 2.97c) as $\hat{P}_v = \sum_c \beta_{vc} |c\rangle\langle c|$ with

$$\beta_{vc} = \begin{cases} f(\varepsilon_v) & \text{if } \{v, c\} \subseteq \mathcal{S}, \\ f(\varepsilon_c) f(\varepsilon_v - \varepsilon_c) + f(\varepsilon_v) f(\varepsilon_c - \varepsilon_v) + \alpha_c \frac{f(\varepsilon_c) - f(\varepsilon_v)}{\varepsilon_c - \varepsilon_v} f(\varepsilon_v - \varepsilon_c) & \text{if not.} \end{cases} \tag{2.99}$$

The single $f(\varepsilon_v)$ in the first case cancels with itself in Eq. 2.82, setting the response to zero.

To illustrate how this constraint to the electronic response affects the phonons, we will show some exemplary results for the metallic TMDCs. Figure 2.5a depicts possible electronic subspaces in the electronic dispersion of 1H-$NbSe_2$, whose exclusion yields the phonon dispersions shown in Fig. 2.5b. In DFPT, there is a *Kohn anomaly* (reduction of phonon frequency) (cf. App. D.2) with an extremum at $\boldsymbol{q} = 2/3\,\mathrm{M}$. There are imaginary frequencies in large parts of the Brillouin zone (BZ), indicating dynamical instability. Excluding the screening from within the metallic band near the Fermi level, all instabilities disappear while four phonon branches remain unchanged. This proofs that lattice instabilities in this class of materials are due to the low-energy electrons alone (cf. Chaps. 7 to 9). Extending the active

subspace by the other two bands also spanned by the d_{z^2}, $d_{x^2-y^2}$, and d_{xy} orbitals, shifts all branches that already changed before by a rather constant value. (This is due to a more uniform bare electronic susceptibility in the interband case, where the energy denominator $\varepsilon_{\boldsymbol{k}+\boldsymbol{q}m} - \varepsilon_{\boldsymbol{k}n}$ in Eqs. 2.82 and 2.92b is always at least as large as the band gap.) Now, the former acoustic branches do not go to zero any longer. cDFPT has broken the acoustic sum rule (ASR) (cf. Sec. 2.4.5).

Conceptually interesting albeit not particularly useful in practice, we can go one step further and exclude *all* DFT bands (all core and valence bands plus a handful of partially occupied conduction bands). Figure 2.6 shows that the ASR is now strikingly broken. We have rather dispersionless branches at significantly enhanced frequencies. These phonons are not *fully* bare because they still include screening from all high-energy bands not explicitly calculated in DFT. In fact, it is basically impossible to calculate fully bare phonons with the Sternheimer approach. However, this could be easily achieved by simply inserting a DFT ground-state density into Eq. 2.73 for $\Delta C = 0$.

In Chap. 5, we will explain how to calculate the exact phonon self-energies through which the phonons from cDFPT and DFPT are related to each other.

2.4.3 Mass–spring models

In Sec. 2.3.2, the method of orthogonal TB has been introduced. We will now show that the description of phonons within the BO and harmonic approximation is largely equivalent. Instead of TB models, we will formulate *mass–spring models*. The basis functions of TB models were localized orbitals or Wannier functions. Here, the basis is given by the Cartesian atomic displacements, "localized" at the atomic positions. The IFCs are the matrix elements of the dynamical matrix, except for scaling factors given by the atomic masses,

$$C_{\boldsymbol{R}-\boldsymbol{R}'kxly} = \sqrt{M_k M_l}\langle \boldsymbol{R}kx|\hat{D}|\boldsymbol{R}'ly\rangle. \tag{2.100a}$$

For the sake of notational simplicity, we use the Dirac notation also here, although the theory is formally fully classical. Besides, we split the combined indices i, j used so far into the atomic indices k, l and the Cartesian displacement directions x, y of the respective atoms. The "on-site" elements

$$C_{0kxky} = M_k\langle \boldsymbol{R}kx|\hat{D}|\boldsymbol{R}ky\rangle, \tag{2.100b}$$

which were free parameters in the TB theory, are a special case here, since they provide the restoring forces that must be exactly the sum of all other forces acting on the atom, see the sum rules in Sec. 2.4.5. Otherwise, a constant displacement of the whole crystal would generate a restoring force, which would be unphysical. Opposed to the Wannier functions in TB, the definition of the $|\boldsymbol{R}kx\rangle$ is rather fixed. We could of course also generate different bases via linear combination, but the interpretation of C as an inter*atomic* force constant would be lost.

The dynamical matrix is exactly as defined in Eq. 2.63. Since the Cartesian displacement directions are orthogonal by definition, we have to solve a simple (as opposed to generalized) eigenvalue problem to diagonalize the dynamical matrix. In the TB case, the single-particle energies are simply the eigenvalues of the Hamiltonian; here, we obtain the *square* of the phonon frequencies $\omega^2_{\boldsymbol{q}\nu}$.

All considerations regarding the point symmetries of the crystal can also be borrowed from the TB formalism. Here, we have the additional simplification that all symmetries are formulated in the Cartesian basis; we do not need different transformation matrices for different sets of orbitals.

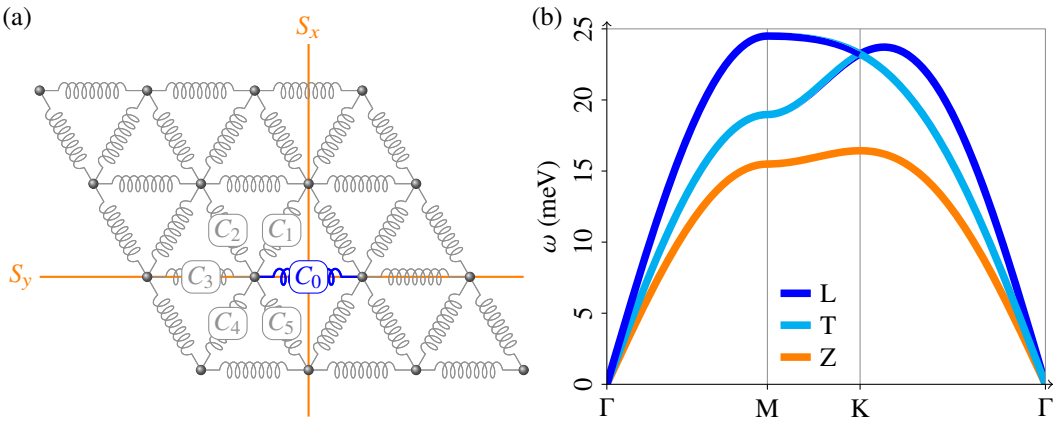

Figure 2.7: Triangular lattice of p orbitals. (a) Mass–spring model. (b) Phonon dispersion for $C_x/M = -90\,\mathrm{meV}^2$ and $C_y/M = C_z/M = -30\,\mathrm{meV}^2$.

2.4.3.1 Triangular lattice

Analogous to the TB section (Sec. 2.3.2.1), we will first apply the theory to a monoatomic triangular lattice with nearest-neighbor coupling, as visualized in Fig. 2.7a.

We start with the most general matrix for the IFCs in x direction (cf. Eq. 2.40),

$$C_0 = \begin{bmatrix} C_x & C_{x,y} & C_{x,z} \\ C_{y,x} & C_y & C_{y,z} \\ C_{z,x} & C_{z,y} & C_z \end{bmatrix}. \tag{2.101}$$

All symmetry constraints and transformations can be applied exactly as in the TB case and yield the IFC matrices $C_0, C_1, \ldots, C_5$ for the six nearest neighbors (cf. Fig. 2.7). Thus, $C_3 = C_0$, $C_4 = C_1$, and $C_5 = C_2$, where (cf. Eq. 2.43)

$$C_0 = \mathrm{diag}(C_x, C_y, C_z), \tag{2.102a}$$

$$C_{1,2} = \begin{bmatrix} \frac{1}{4}(C_x + 3C_y) & \pm\frac{\sqrt{3}}{4}(C_x - C_y) & 0 \\ \pm\frac{\sqrt{3}}{4}(C_x - C_y) & \frac{1}{4}(3C_x + C_y) & 0 \\ 0 & 0 & C_z \end{bmatrix}. \tag{2.102b}$$

However, because of the ASR, the on-site or self force constant must be the negative sum of all other IFCs,

$$C_{\mathrm{self}} = -\sum_{n=0}^{5} C_n = -3\,\mathrm{diag}(C_x + C_y, C_x + C_y, 2C_z). \tag{2.103}$$

Thus, the $\boldsymbol{q}$-dependent dynamical matrix (multiplied by the mass M) reads (cf. Eq. 2.45)

$$\begin{aligned} M D_{\boldsymbol{q}} &= C_{\mathrm{self}} + C_0 e^{+iq_1} + C_1 e^{+i(q_1+q_2)} + C_2 e^{+iq_2} \\ &\quad + C_3 e^{-iq_1} + C_4 e^{-i(q_1+q_2)} + C_5 e^{-iq_2} \qquad (2.104a) \\ &= C_0[e^{+iq_1} - 1] + C_1[e^{+i(q_1+q_2)} - 1] + C_2[e^{+iq_2} - 1] \\ &\quad + C_3[e^{-iq_1} - 1] + C_4[e^{-i(q_1+q_2)} - 1] + C_5[e^{-iq_2} - 1], \qquad (2.104b) \end{aligned}$$

where we have again defined crystal coordinates $q_i = \boldsymbol{q}\boldsymbol{a}_i$.

Also here, the x and y directions are decoupled from the z direction. The dispersion of the out-of-plane–acoustic (ZA) mode reads (cf. Eq. 2.46)

$$M\omega_{\boldsymbol{q}3}^2 = 2C_z[\cos(q_1) + \cos(q_2) + \cos(q_1 + q_2) - 3]. \tag{2.105}$$

The dispersion of the in-plane longitudinal–acoustic (LA) and transverse–acoustic (TA) modes is more complicated (cf. Eq. 2.47),

$$M D_{\boldsymbol{q}} = 2[\cos(q_1) - 1]\,\mathrm{diag}(C_x, C_y) \tag{2.106}$$
$$+ \begin{bmatrix} \frac{1}{2}(C_x + 3C_y)[\cos(q_2) + \cos(q_1 + q_2) - 2] & \frac{\sqrt{3}}{2}(C_x - C_y)[\cos(q_2) - \cos(q_1 + q_2)] \\ \frac{\sqrt{3}}{2}(C_x - C_y)[\cos(q_2) - \cos(q_1 + q_2)] & \frac{1}{2}(3C_x + C_y)[\cos(q_2) + \cos(q_1 + q_2) - 2] \end{bmatrix}.$$

Diagonalization yields (cf. Eq. 2.48)

$$M\omega^2_{\boldsymbol{q}1,2} = (C_x + C_y)[\cos(q_1) + \cos(q_2) + \cos(q_1 + q_2) - 3]$$
$$\pm \frac{C_x - C_y}{\sqrt{2}} \sqrt{\begin{matrix} 3 - \cos(q_1) & - \cos(q_2) & - \cos(q_1 + q_2) \\ + \cos(2q_1) & + \cos(2q_2) & + \cos(2q_1 + 2q_2) \\ - \cos(q_1 - q_2) & - \cos(2q_1 + q_2) & - \cos(q_1 + 2q_2). \end{matrix}} \tag{2.107}$$

The dispersion relation is shown in Fig. 2.7b. The main difference to the corresponding TB dispersion shown in Fig. 2.2 is that all branches go to zero for small $\boldsymbol{q}$. In App. D.2, this mass–spring model will be applied as is to a monolayer of beryllium.

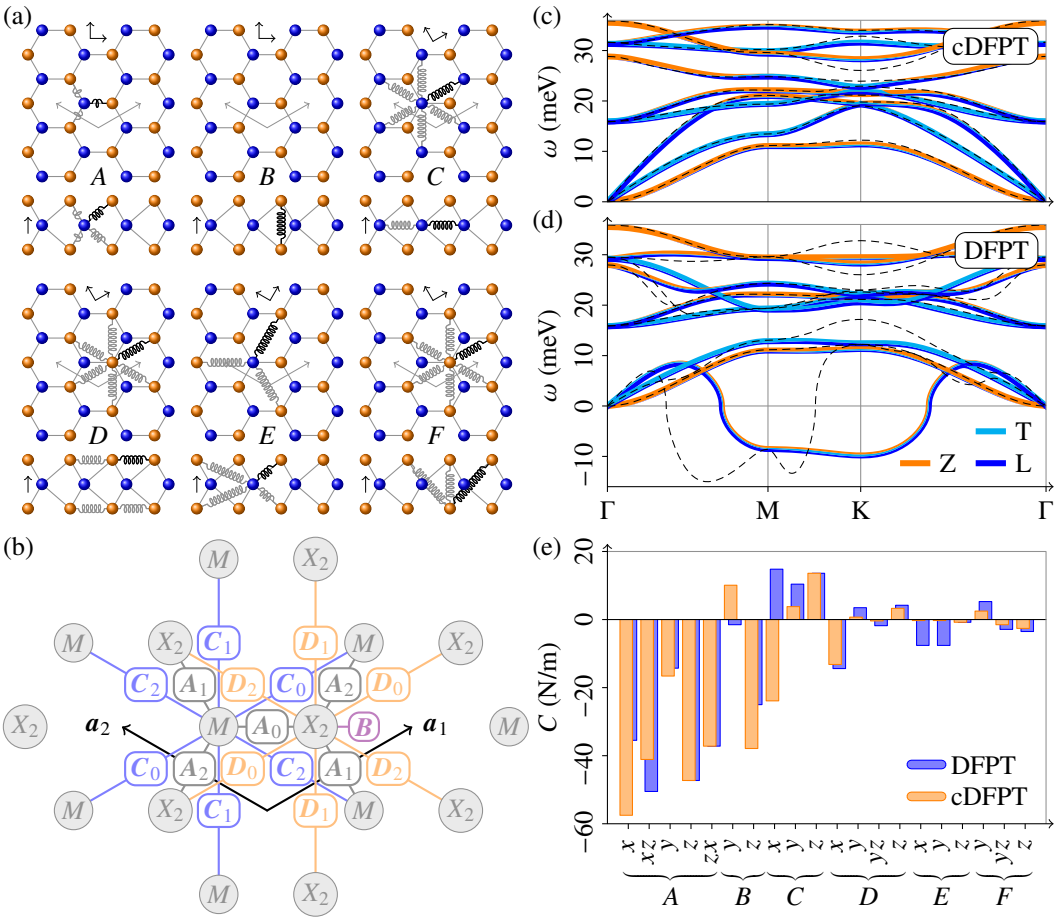

Figure 2.8: Mass–spring model of 1H-$NbSe_2$. (a, b) Visualization of springs. (c, d) Comparison of short- and long-range models. (e) Comparison of short-range IFCs from DFPT and cDFPT.

2.4.3.2 Trigonal–prismatic TMDCs

Now we will set up a more complicated mass–spring model with enough degrees of freedom to satisfactorily fit real phonon dispersions. It describes the class of monolayers of TP TMDCs 1H-MX_2 with a transition metal M and chalcogen X.

We consider the six shortest springs/bonds in the lattice and label them A to F with ascending length, as shown in Figs. 2.8a and 2.8b. Let x, y, and z denote the in-plane projection of the bond direction, the in-plane direction orthogonal to x, and the out-of-plane direction, respectively. Furthermore, we use the attribute "odd" ("even") for transformations that (do not) swap the ends of the spring. Then, the six springs can be classified as follows:

A connects M and X atoms that are nearest neighbors and is invariant under an even reflection along y; B connects X atoms of different layers in the same cell and is invariant under an even reflection along y, an even rotation by 120° about the z axis, and an odd reflection along z; C connects M atoms of neighboring cells and is invariant under an even reflection along z and an odd reflection along x; D connects X atoms of the same layer in neighboring cells and is invariant under an odd reflection along x; E connects M and X atoms that are next-nearest neighbors and is invariant under an even reflection along y; and, finally, F connects X atoms of different layers in neighboring cells and is invariant under an odd rotation by 180° about the y axis. (The listed symmetries can *generate* the complete sets of symmetries of the respective springs.)

After imposing all symmetry constraints, the springs read

$$A = \begin{bmatrix} A_x & 0 & A_{xz} \\ 0 & A_y & 0 \\ A_{zx} & 0 & A_z \end{bmatrix}, \quad B = \begin{bmatrix} B_x & 0 & 0 \\ 0 & B_x & 0 \\ 0 & 0 & B_z \end{bmatrix}, \quad C = \begin{bmatrix} C_x & C_{xy} & 0 \\ -C_{xy} & C_y & 0 \\ 0 & 0 & C_z \end{bmatrix}, \tag{2.108}$$

$$D = \begin{bmatrix} D_x & D_{xy} & D_{xz} \\ -D_{xy} & D_y & D_{yz} \\ -D_{xz} & D_{yz} & D_z \end{bmatrix}, \quad E = \begin{bmatrix} E_x & 0 & E_{xz} \\ 0 & E_y & 0 \\ E_{zx} & 0 & E_z \end{bmatrix}, \quad F = \begin{bmatrix} F_x & F_{xy} & F_{xz} \\ -F_{xy} & F_y & F_{yz} \\ F_{xz} & -F_{yz} & F_z \end{bmatrix}.$$

Due to the point symmetries of the crystal, the number of free parameters is reduced to 28. (The two masses that also have to be chosen could be incorporated directly into the IFCs and thus provide no additional degrees of freedom.)

The rotation sum rule by Wang *et al.* [112], which will be introduced in Sec. 2.4.5, would yield two further constraints,

$$\begin{aligned} 0 &= 2a^2[2A_z + 3C_z + 6D_z + 8E_z + 6F_z] \\ &\quad - ah[\sqrt{3}(A_{xz} + 3A_{zx} + 2E_{xz} + 6E_{zx}) - 12D_{xz} + 24F_{xz}] \\ &\quad + h^2[3A_x + 3A_y + 4B_x + 3E_x + 3E_y + 12F_x + 12F_y], \qquad (2.109a) \\ 0 &= 2A_y + 3C_y + 6D_y + 8E_y + 6F_y, \qquad (2.109b) \end{aligned}$$

where a is the lattice constant and h is the layer thickness, thus reducing the number of free parameters to 26.

We can extract all model parameters from DFPT and cDFPT calculations on a 2×2 supercell, i.e., using a 2×2 $\boldsymbol{q}$-point mesh. The exemplary data has been calculated for 1H-$NbSe_2$ (Sec. 7.3).

Because of the periodic boundary conditions, there are infinitely many images of the same atom. Hence, the IFCs have to be associated with those pairs of (images of) atoms whose distance is minimal (i.e., within the WS supercell). Whenever there are multiple such pairs (i.e., on the edge of the WS supercell), a double-counting has to be compensated by proper weighting (cf. App. B.4.2).

For DFPT, this procedure yields

$$A = \begin{bmatrix} -36 & 0 & -51 \\ 0 & -14 & 0 \\ -37 & 0 & -47 \end{bmatrix} \frac{\mathrm{N}}{\mathrm{m}}, \quad B = \begin{bmatrix} -2 & 0 & 0 \\ 0 & -2 & 0 \\ 0 & 0 & -25 \end{bmatrix} \frac{\mathrm{N}}{\mathrm{m}}, \quad C = \begin{bmatrix} 15 & 0 & 0 \\ 0 & 10 & \\ 0 & 0 & 14 \end{bmatrix} \frac{\mathrm{N}}{\mathrm{m}},$$
$$D = \begin{bmatrix} -14 & 0 & 0 \\ 0 & 4 & -2 \\ 0 & -2 & 4 \end{bmatrix} \frac{\mathrm{N}}{\mathrm{m}}, \quad E = \begin{bmatrix} -8 & 0 & 0 \\ 0 & -8 & 0 \\ 0 & 0 & -1 \end{bmatrix} \frac{\mathrm{N}}{\mathrm{m}}, \quad F = \begin{bmatrix} -1 & 0 & 0 \\ 0 & 5 & -3 \\ 0 & 3 & -4 \end{bmatrix} \frac{\mathrm{N}}{\mathrm{m}}. \tag{2.110}$$

The corresponding values from cDFPT read

$$A = \begin{bmatrix} -58 & 0 & -41 \\ 0 & -17 & 0 \\ -37 & 0 & -47 \end{bmatrix} \frac{\mathrm{N}}{\mathrm{m}}, \quad B = \begin{bmatrix} 10 & 0 & 0 \\ 0 & 10 & 0 \\ 0 & 0 & -38 \end{bmatrix} \frac{\mathrm{N}}{\mathrm{m}}, \quad C = \begin{bmatrix} -24 & 0 & 0 \\ 0 & 4 & 0 \\ 0 & 0 & 14 \end{bmatrix} \frac{\mathrm{N}}{\mathrm{m}},$$
$$D = \begin{bmatrix} -13 & 0 & 0 \\ 0 & 1 & 0 \\ 0 & 0 & 3 \end{bmatrix} \frac{\mathrm{N}}{\mathrm{m}}, \quad E = \begin{bmatrix} 0 & 0 & 0 \\ 0 & 0 & 0 \\ 0 & 0 & -1 \end{bmatrix} \frac{\mathrm{N}}{\mathrm{m}}, \quad F = \begin{bmatrix} 0 & 0 & 0 \\ 0 & 3 & -2 \\ 0 & 2 & -3 \end{bmatrix} \frac{\mathrm{N}}{\mathrm{m}}. \tag{2.111}$$

The resulting phonon dispersions are shown in Figs. 2.7c and 2.7d. The dashed lines show the reference DFPT and cDFPT data from a much larger 12×12 supercell. The smooth cDFPT dispersion is almost perfectly described by the short-range model. However, the instability region of the DFPT data cannot be reproduced. As expected from Fourier analysis, only smooth dispersions are well described by short-range models.

The short-range IFCs are also visualized in the bar diagram in Fig. 2.7e. When going from cDFPT to DFPT, some IFCs increase considerably, especially C_x connecting neighboring Nb atoms in bond direction, which even changes sign. (Positive IFCs go along with negative self force constants, which in turn indicate instability.) This suggests that the PLD in the CDW phase of the TP TMDCs predominantly affects the transition-metal sublattice.

2.4.3.3 Graphene

As a last example, the phonon dispersion of graphene according to a next-nearest-neighbor mass–spring model is shown in Fig. 2.9a. In Cartesian coordinates, where x and z are again the bond and out-of-plane direction, the nearest-neighbor and next-nearest neighbor IFCs, which are equivalent to the (in-plane projections of) springs A and C in Fig. 2.8a, read

$$C^1 = \begin{bmatrix} C_x^1 & 0 & 0 \\ 0 & C_y^1 & 0 \\ 0 & 0 & C_z^1 \end{bmatrix}, \qquad C^2 = \begin{bmatrix} C_x^2 & C_{x,y}^2 & 0 \\ -C_{x,y}^2 & -C_y^1/6 & 0 \\ 0 & 0 & -C_z^1/6 \end{bmatrix}. \tag{2.112}$$

As expected in 2D materials, the ZA dispersion around Γ is not linear but quadratic, as seen in Fig. 2.9b. In the IFCs, this is reflected in constraints that link elements of C^1 to elements of C^2. They have been derived from the rotation sum rule by Wang *et al.* [112] (cf. Sec. 2.4.5). Further constraints that relate or nullify the elements of the same IFC matrix follow from the point symmetries. We choose $C_x^1 = -365\,\mathrm{N/m}$, $C_y^1 = -245\,\mathrm{N/m}$, and $C_z^1 = -98.2\,\mathrm{N/m}$ from Ref. 113 as used in Ref. 114 and $C_x^2 = C_{x,y}^2 = 0$. These values fit well to experimental data from Raman spectroscopy. The authors of Ref. 114 claim that the quadratic ZA dispersion is only obtained after including forth-nearest-neighbor interactions. However, in fact it can already be reproduced in a model including next-nearest neighbors only if we set $C_z^2 = -C_z^1/6$. For a more comprehensive review on the IFCs of graphene and graphite, we refer to Ref. 115.

Interestingly, the shape of the ZA phonon dispersion is identical to the low-energy electron dispersion as results from a nearest-neighbor TB model with a scalar hopping parameter t (for the p_z orbitals). This electron dispersion is shown in Fig. 2.9b for $t = -2.6\,\mathrm{eV}$ [30].

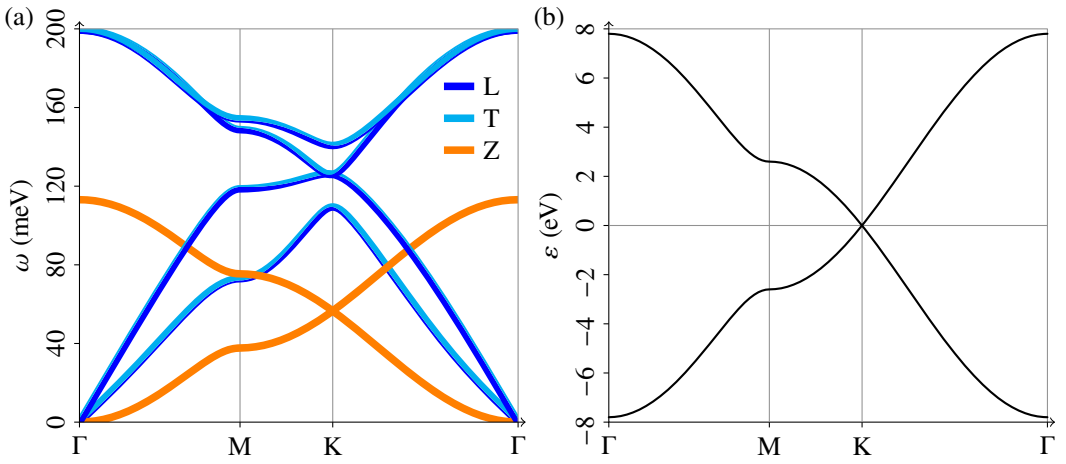

Figure 2.9: Dispersions of graphene. (a) Phonons from next-nearest-neighbor mass–spring model. The in-plane IFCs are restricted to nearest neighbors. (b) Electrons from nearest-neighbor TB model.

2.4.4 Classification of eigenmodes

In many plots of phonons dispersions in this work (e.g., Fig. 2.9a), the branches are classified into longitudinal (L), transverse (T), and out-of-plane (Z) modes. This classification is more convenient than a classification in terms of Cartesian coordinates, since it does not depend on, e.g., rotations of the reference system. To the contrary, L, T, and Z are always defined with respect to the current $\boldsymbol{q}$ vector. L and T are in-plane directions parallel and orthogonal to the projection of $\boldsymbol{q}$ onto the plane, respectively. Z is always the out-of-plane direction.

Let $e_{\boldsymbol{q}\nu i} = e_{\boldsymbol{q}\nu kx}$ be the phonon eigenvector of mode ν at wave vector $\boldsymbol{q}$. Again, we split the combined index i into an atomic index k and the Cartesian displacement direction x of the corresponding atom. Then we can define

$$\mathrm{L} = \sum_k \frac{|e_{\boldsymbol{q}\nu kx} q_x + e_{\boldsymbol{q}\nu ky} q_y|^2}{q_x^2 + q_y^2}, \tag{2.113a}$$

$$\mathrm{T} = \sum_k \frac{|e_{\boldsymbol{q}\nu kx} q_y - e_{\boldsymbol{q}\nu ky} q_x|^2}{q_x^2 + q_y^2}, \tag{2.113b}$$

$$\mathrm{Z} = \sum_k |e_{\boldsymbol{q}\nu kz}|^2, \tag{2.113c}$$

which gives the average displacement direction of all atoms. Since the $e_{\boldsymbol{q}\nu i}$ are normalized, the squares ensure that L + T + Z = 1. For $\boldsymbol{q} = 0$, we cannot distinguish L and T because there is no $\boldsymbol{q}$ direction. Moreover, the modes of the acoustic branches are arbitrarily mixed because of their degeneracy. One way around this is to shift $\boldsymbol{q}$ infinitesimally away from Γ.

Alternatively, phonon modes are often classified group-theoretically according to their irreducible representations and the resultant optical selection rules that tell whether a mode is active in infrared (IR) or Raman spectroscopy [116]. Irreducible representations are often labeled using Mulliken symbols [117] such as A_{1g}, A_{2u}, E', and E'', where uppercase letters denote the dimension of the representation and lowercase letters, primes, and numbers indicate (anti)symmetry with respect to inversion centers, vertical, and horizontal mirror planes, respectively. IR-active modes transform as one of the Cartesian axes x_i, induce dipole moments, and can absorb light; Raman-active modes transform as a product of two axes $x_i x_j$, change the polarizability, and can scatter light. In systems with inversion center, the rule of mutual exclusion states that a mode cannot be IR- and Raman-active at the same time [118].

2.4.5 Sum rules

We have seen that the three acoustic phonons branches approach zero frequency for $\boldsymbol{q} \to 0$ or, equivalently, large wavelengths. Another observation that can be made is that the ZA mode of (quasi) 2D materials features a quadratic dispersion for small $\boldsymbol{q}$, in contrast to the linear dispersion usually expected for acoustic phonons. Both effects result from constraints imposed by invariances of the total energy.

The vanishing frequencies at Γ are a direct consequence of the fact that a translation of the crystal as a whole must not change the total energy of the system or, analogously, induce a restoring force. An acoustic phonon at Γ (infinite spatial wavelength) whose frequency is nonzero would correspond to a rigid body that periodically moves back and forth in absence of any external forces. The constraint imposed by the translational invariance is the ASR [119],

$$\sum_{\boldsymbol{R}l} C_{\boldsymbol{R}kxly} = 0 \tag{2.114a}$$

for all basis atoms k and directions x, y (cf. Eq. 6 of Ref. 120 or Eq. 13 or Ref. 121). Equivalently, we can formulate the ASR as the definition of the self force constant,

$$C_{0kxky} = -\sum_{\boldsymbol{R}\neq 0 \vee l \neq k} C_{\boldsymbol{R}kxly}. \tag{2.114b}$$

The quadratic dispersion in the 2D materials in turn is a direct consequence of the fact that a rotation of the crystal as a whole must not change the total energy. Consider a ZA phonon at very long spatial wavelengths. It is nothing but a very smooth modulation of the vertical positions of the atoms of the layer. Locally, only the zeroth and first derivative of this modulation are observable, i.e., we only find a different vertical position and/or slope of the surface (cf. Fig. 4.3), which can be seen as a rigid translation and/or rotation of the layer [122]. Such a displacement must not induce large restoring forces and thus the ZA frequency is very small even slightly away from Γ, resulting in a quadratic dispersion. The additional constraints imposed by the rotational invariance are given by the *rotation sum rule*. Different sum rules have been proposed. The original rule by Born and Huang [119] reads

$$\sum_{\boldsymbol{R}l} C_{\boldsymbol{R}kxly}(R_{y'} + \tau_{ly'}) - C_{\boldsymbol{R}kxly'}(R_y + \tau_{ly}) = 0 \tag{2.115}$$

for all basis atoms k and directions x, y, y', where $\boldsymbol{R}$ are Bravais lattice vectors as usual and $\boldsymbol{R} + \boldsymbol{\tau}_k$ is the position of the kth basis atom in the respective unit cell (cf. Eq. 11 of Ref. 120 or Eq. 14 or Ref. 121).

However, some authors including Gazis and Wallis [120] and Wang *et al.* [112] have claimed that the conditions by Born and Huang are not complete (trivial for simple Bravais lattices) and that additional constraints hold. For example, the much more complicated sum rule by Wang *et al.* can be written as

$$\begin{aligned}\psi_{mn} = \sum_{\boldsymbol{R}klxx'yy'} \epsilon_{mxx'}\epsilon_{nyy'} \Big[&(C_{\boldsymbol{R}kxly} - C_{\boldsymbol{R}kylx})(R_{x'} + \tau_{kx'})\tau_{ky'} \\ &- \frac{1}{2}(C_{\boldsymbol{R}kxly} + C_{\boldsymbol{R}kylx})(R_{x'} + \tau_{kx'} - \tau_{lx'})(R_{y'} + \tau_{ky'} - \tau_{ly'}) \Big] = -\psi_{nm}.\end{aligned} \tag{2.116}$$

In turn, some authors discount these additional sum rules because their derivations disregard the equilibrium condition (linear term in the Taylor expansion of the BO potential) [123] or fail to recognize that rotational invariance can only be demanded for finite crystals [121]. After all, the question of the ultimate rotation sum rule seems to be still a matter of debate.

Whether justified or not, all constraints can be formulated as orthogonality relations,

$$\sum_{\boldsymbol{R}kxly} \gamma_{\boldsymbol{R}kxly} C_{\boldsymbol{R}kxly} = \boldsymbol{\gamma} \cdot \boldsymbol{C} = 0. \tag{2.117}$$

For example, for the ASR we have $\gamma_{\boldsymbol{R}kxly} = \delta_{kk'}\delta_{xx'}\delta_{yy'}$ for each k', x', y'. This formulation implies that we can impose the constraints via the Gram–Schmidt method (§3 or Ref. 124),

$$\widetilde{\boldsymbol{c}}_i = \boldsymbol{c}_i - \sum_{j=1}^{i-1} \frac{\widetilde{\boldsymbol{c}}_j \cdot \boldsymbol{c}_i}{\widetilde{\boldsymbol{c}}_j \cdot \widetilde{\boldsymbol{c}}_j} \widetilde{\boldsymbol{c}}_j, \tag{2.118}$$

where the vector of vectors $\underline{\boldsymbol{c}} = (\boldsymbol{\gamma}_1, \boldsymbol{\gamma}_2, \ldots, \boldsymbol{\gamma}_N, \boldsymbol{C})$ combines N constraints $\boldsymbol{\gamma}_i$ and the IFCs $\boldsymbol{C}$ as its last element. Because of the best-approximation theorem for orthogonal projections, the fixed parameters $\widetilde{\boldsymbol{C}}$ are closest to the original ones $\boldsymbol{C}$ in the sense of least squares.

A different approach to impose invariance constraints is via internal coordinates [125], i.e., coordinates such as bond length and angles, which do not depend on the reference system and are thus invariant under translations and rotations of the crystal as a whole. The $3N_\mathrm{n}$ Cartesian coordinates, where N_n is the number of atoms, can be mapped onto $3N_\mathrm{n} - 6$ internal coordinates, where 3 translational and 3 rotational degrees of freedom have been subtracted, e.g., via a least-squares fit. The back-transformed Cartesian coordinates will then fulfill all sum rules by construction. The difficulty of this method consists in the choice of internal coordinates. Many different choices are possible, but care has to be taken that all original degrees of freedom are covered.

2.4.6 Goldstone bosons

The acoustic phonon modes with zero frequency are examples of *Goldstone bosons*. According to the Goldstone theorem [126, 127], whenever a continuous symmetry is spontaneously broken, a massless boson appears. In the nonrelativistic mechanics, this corresponds to modes with zero frequency, i.e., without a restoring force. We will illustrate the theorem using two simple examples. A similar example can be found in App. C of Ref. 128.

We consider a rod inside a tube, both of infinite length and pointing in the x direction, as shown in Fig. 2.10a. We further assume that the rod is subject to a gravitational force in y direction. Then, if we nudge the rod in z direction, it will start to oscillate inside the tube at a nonzero frequency. The only continuous spatial symmetry of the system is the translation in x direction. (The symmetry with respect to a rotation around the x axis is broken by the field in y direction.) We can break this symmetry by replacing the rod with a ball. This ball will be able to oscillate in the same way as the rod, but additionally it can freely move along the tube. This translational mode is the Goldstone boson of the broken translation symmetry.

Another typical example is the "Mexican hat" potential displayed in Fig. 2.10b. As soon as the ball, initially located at the maximum of the crown, rolls down to the minimum of the brim, the rotational symmetry is spontaneously broken. At the same time, the ball is allowed to freely move around the circular minimum of the brim. Just like the ball in the rod, it can additionally oscillate at a nonzero frequency in the perpendicular (here radial) direction.

To summarize, whenever the presence of an object breaks a continuous symmetry, the object will feel no restoring force for the degree of freedom belonging to the symmetry.

For atomic systems this translates as follows: Placing a crystal into the empty space breaks all three translational symmetries, but we can still translate the crystal as a whole without changing its energy. This leads to three Goldstone modes. Here, we assume that the rotational symmetry has already been broken by periodic boundary conditions. If we instead consider a freestanding molecule (without periodic boundary conditions), its presence

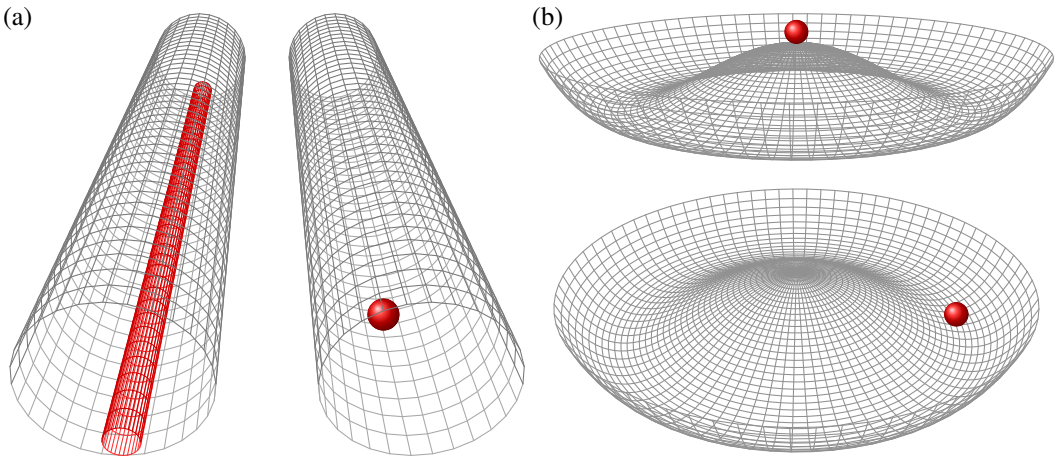

Figure 2.10: Goldstone modes from broken (a) translation and (b) rotation symmetry.

also breaks the three rotational symmetries of the empty space. This leads to another three Goldstone modes (cf. App. D.3).

In Sec. 2.4.2.2, we have seen that the ASR is not necessarily fulfilled in cDFPT, i.e., the translation symmetry is broken. In App. D.3, we will find that the same holds for the rotation sum rule or, more precisely, for the invariance of the total energy under rotations of molecules as a whole. In other words, Goldstone modes may be absent in cDFPT.

2.4.7 Nonadiabatic effects

Since the derivation of DFPT (Sec. 2.4.2) depends on the BO approximation, the IFCs in Eq. 2.82 are static, i.e., do not carry a time dependence or, equivalently, a dependence on the frequency ω in Fourier space. However, the frequency dependence is important to obtain, e.g., proper phononic lifetimes or linewidths. Correct calculations would be based on a time-dependent self-consistent linear response theory [129]. In this case, the term of Eq. 2.73 that depends on the density response would read (cf. Eq. 12 of Ref. 129)

$$\Delta C_{\boldsymbol{R}-\boldsymbol{R}'ij}(\omega) = \int \mathrm{d}^3 r \, \frac{\partial V_\kappa(\boldsymbol{r})}{\partial u_{\boldsymbol{R}i}} \frac{\partial n_\kappa(\boldsymbol{r},\omega)}{\partial u_{\boldsymbol{R}'j}} \tag{2.119}$$

with a frequency-dependent density $n_\kappa(\boldsymbol{r},\omega)$.

Likewise, Eq. 2.92b would become (cf. Eq. 16 of Ref. 129)

$$\Delta C_{\boldsymbol{q}ij}(\omega) = \frac{2}{N} \sum_{\boldsymbol{k}n} \frac{f(\varepsilon_{\boldsymbol{k}n}) - f(\varepsilon_{\boldsymbol{k}+\boldsymbol{q}m})}{\omega + \mathrm{i}0^+ + \varepsilon_{\boldsymbol{k}n} - \varepsilon_{\boldsymbol{k}+\boldsymbol{q}m}} \times \langle \boldsymbol{k}n | \frac{\partial \hat{V}}{\partial u_{-\boldsymbol{q}i}} | \boldsymbol{k}+\boldsymbol{q}m \rangle \langle \boldsymbol{k}+\boldsymbol{q}m | \frac{\partial \hat{V}_{\mathrm{SCF}}(\omega)}{\partial u_{\boldsymbol{q}j}} | \boldsymbol{k}n \rangle, \tag{2.120}$$

see also App. C.4. Since such calculations are prohibitively expensive, Calandra *et al.* have proposed a method [129] where self-consistent albeit static phonons from DFPT are corrected *a posteriori* by adding a non-self-consistent correction term of the form $\Delta C(\omega) - \Delta C$ (cf. Eqs. 22 to 24 of Ref. 129). Here, a Fourier interpolation allows them to calculate $\Delta C(\omega)$ at a much lower electronic temperature than the corresponding ΔC from DFPT. In this context, a phonon-renormalization scheme as given in Chap. 5 can be very helpful.

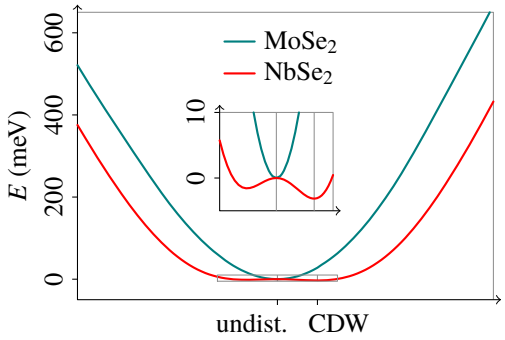

Figure 2.11: *[Calculations by Arne Schobert.]* Presence and absence of anharmonicity in the metallic and semiconducting TMDCs 1H-$NbSe_2$ and 1H-$MoSe_2$, respectively. We show the energy as a function of the amplitude of the displacement visualized in Fig. 3.2. The computational parameters are as in Sec. 7.3.

2.4.8 Anharmonic effects

The presence of an energetically favored CDW phase below a certain temperature, where the atoms are slightly displaced from their symmetric positions, suggests that the potential-energy landscape is a nontrivial function of these displacements. To further investigate this, we calculate the total energy of the semiconductor 1H-$MoSe_2$ and the metal 1H-$NbSe_2$ for the symmetric phase, for the CDW displacement pattern of 1H-$NbSe_2$ as shown in Fig. 3.2, and for any intermediate state obtained via linear interpolation of the atomic positions. The results are shown in Fig. 2.11.

For 1H-$MoSe_2$, which is not known to host a CDW, we find an almost perfectly parabolic potential-energy landscape with a minimum at the symmetric positions. In turn, for 1H-$NbSe_2$, we find the expected global minimum at the CDW displacement as well as another local minimum for a configuration where all atoms are located on the respective other side of the symmetric positions. The symmetric positions are actually associated with a local energy maximum. Such a double-well potential is inherently different from a parabolic potential and thus very anharmonic already at small length scales.

As we have learned from cDFPT results for the metallic TMDCs, the CDW is driven by metallic screening alone (cf. Fig. 2.5), which is naturally absent in the semiconductor 1H-$MoSe_2$. As a consequence, also the anharmonicity in these materials is due to metallic screening. Correspondingly, in App. D.6 we will find a reduction of the phonon frequencies of (bilayer) 2H-MoS_2 upon electron doping, which activates some metallic screening.

2.4.8.1 Total displacement

To quantify the degree of anharmonicity, we need a measure for the atomic displacements. One possible choice is the total displacement defined as the Euclidean norm of the ensemble of atomic displacements,

$$|u| = \sqrt{\frac{1}{NN_\mathrm{n}} \sum_{\boldsymbol{R}i} |u_{\boldsymbol{R}i}|^2}. \tag{2.121}$$

Here, the normalization by the number N of unit cells and the number N_n of atoms per unit cell yields an intensive property. In the following, we will evaluate its time dependence.

We consider a phononic excitation of the form $u_{\boldsymbol{q}\nu} = \sqrt{NM_0}u_0 \mathrm{e}^{\mathrm{i}\omega_{\boldsymbol{q}\nu}t}$, where u_0 and M_0 have the dimensions of a length and mass, respectively. The time t only enters via a phase factor. We calculate the displacement of an individual atom according to Eq. 2.65. Since the physical atomic displacements must not be complex, we take twice the real part, which corresponds to a superposition of opposed complex waves,

$$u_{\boldsymbol{R}i}^{(\boldsymbol{q}\nu)} = u_0 \sqrt{\frac{M_0}{M_i}}\, 2\,\mathrm{Re}\left[e_{\boldsymbol{q}i\nu} \mathrm{e}^{-\mathrm{i}(\boldsymbol{q}\boldsymbol{R}-\omega_{\boldsymbol{q}\nu}t)}\right]. \tag{2.122}$$

The total displacement squared reads

$$|u^{(\boldsymbol{q}\nu)}|^2 = \frac{u_0^2}{NN_\mathrm{n}} \sum_{\boldsymbol{R}i} \frac{M_0}{M_i} 4\,\mathrm{Re}^2\left[e_{\boldsymbol{q}i\nu} \mathrm{e}^{-\mathrm{i}(\boldsymbol{q}\boldsymbol{R}-\omega_{\boldsymbol{q}\nu}t)}\right] \tag{2.123a}$$

$$= \frac{u_0^2}{NN_\mathrm{n}} \sum_{\boldsymbol{R}i} \frac{M_0}{M_i} \left[e_{\boldsymbol{q}i\nu}^2 \mathrm{e}^{-2\mathrm{i}(\boldsymbol{q}\boldsymbol{R}-\omega_{\boldsymbol{q}\nu}t)} + 2e_{\boldsymbol{q}i\nu}e_{\boldsymbol{q}\nu i}^* + (e_{\boldsymbol{q}i\nu}^*)^2 \mathrm{e}^{2\mathrm{i}(\boldsymbol{q}\boldsymbol{R}-\omega_{\boldsymbol{q}\nu}t)}\right]. \tag{2.123b}$$

Using Eq. C.5 with $2\boldsymbol{q}$ instead of $\boldsymbol{k}$ and the fact that $e_{\boldsymbol{q}\nu i} \in \mathbb{R}$ if $2\boldsymbol{q}$ is a reciprocal lattice vector $\boldsymbol{G}$ or, equivalently, a Γ point,

$$|u^{(\boldsymbol{q}\nu)}|^2 = \frac{u_0^2}{N_\mathrm{n}} \sum_i \frac{M_0}{M_i} |e_{\boldsymbol{q}i\nu}|^2 \begin{cases} 4\cos^2(\omega_{\boldsymbol{q}\nu}t) & \text{if } \boldsymbol{q} \in \{\Gamma, \mathrm{M}\}, \\ 2 & \text{otherwise.} \end{cases} \tag{2.124}$$

Hence, considering an infinite crystal or a supercell that is commensurate to the phonon wavelength, the total displacement is a constant in time in most of the cases. The only exceptions are $\boldsymbol{q} = \Gamma$ and $\boldsymbol{q} = \mathrm{M}$ (halfway between two Γ points). Please note however that $\langle 4\cos^2(\omega t)\rangle_t = 2$ for $\omega \neq 0$.

2.5 Electron–phonon coupling

After separate discussions of electrons and phonons, this section is about the interaction between the two. We consider an electronic Hamiltonian $\hat{H}$ that depends parametrically on the atomic positions, e.g., via the external potential. To see how the electrons are influenced by changes in the lattice degrees of freedom, we can linearize this Hamiltonian as a function of atomic displacements,

$$\hat{H} \approx \hat{H}\big|_{u=0} + \sum_{\boldsymbol{R}i} \frac{\partial \hat{H}}{\partial u_{\boldsymbol{R}i}}\bigg|_{u=0} u_{\boldsymbol{R}i} \equiv \hat{H}_\mathrm{el} + \hat{H}_\mathrm{el\text{–}ph}, \tag{2.125}$$

where we have defined the electron–phonon interaction Hamiltonian $\hat{H}_\mathrm{el\text{–}ph}$. It will be more convenient to evaluate the derivatives in Fourier space (cf. Eq. 2.65),

$$\hat{H}_\mathrm{el\text{–}ph} = \sum_{\boldsymbol{R}i} \frac{\partial \hat{H}}{\partial u_{\boldsymbol{R}i}} u_{\boldsymbol{R}i} = \sum_{\boldsymbol{q}i} \frac{\partial \hat{H}}{\partial u_{\boldsymbol{q}i}} u_{\boldsymbol{q}i}. \tag{2.126}$$

Going to the representation of electronic eigenstates and omitting spin indices, we have

$$\hat{H}_\mathrm{el\text{–}ph} = \sum_{\boldsymbol{k}\boldsymbol{k}'mn} \langle \boldsymbol{k}'m|\hat{H}_\mathrm{el\text{–}ph}|\boldsymbol{k}n\rangle \hat{c}_{\boldsymbol{k}'m}^\dagger \hat{c}_{\boldsymbol{k}n} = \sum_{\boldsymbol{q}i\boldsymbol{k}mn} \langle \boldsymbol{k}+\boldsymbol{q}m|\frac{\partial \hat{H}}{\partial u_{\boldsymbol{q}i}}|\boldsymbol{k}n\rangle u_{\boldsymbol{q}i} \hat{c}_{\boldsymbol{k}+\boldsymbol{q}m}^\dagger \hat{c}_{\boldsymbol{k}n}, \tag{2.127}$$

where we used the momentum conservation from Eq. 2.91. Next, expressing the transformed displacement with normal coordinates (Eqs. 2.65 and 2.66a),

$$u_{\boldsymbol{q}i} \to \hat{u}_{\boldsymbol{q}i} = \frac{1}{\sqrt{NM_i}} \sum_\nu e_{\boldsymbol{q}i\nu} \hat{u}_{\boldsymbol{q}\nu} = \frac{1}{\sqrt{2\omega_{\boldsymbol{q}\nu}}} \frac{1}{\sqrt{NM_i}} \sum_\nu e_{\boldsymbol{q}i\nu} [\hat{b}_{-\boldsymbol{q}\nu}^\dagger + \hat{b}_{\boldsymbol{q}\nu}], \tag{2.128}$$

we obtain the usual expression for the Hamiltonian,

$$\hat{H}_\mathrm{el\text{–}ph} = \frac{1}{\sqrt{N}} \sum_{\boldsymbol{q}\nu\boldsymbol{k}mn} g_{\boldsymbol{q}\nu\boldsymbol{k}mn} [\hat{b}_{-\boldsymbol{q}\nu}^\dagger + \hat{b}_{\boldsymbol{q}\nu}] \hat{c}_{\boldsymbol{k}+\boldsymbol{q}m}^\dagger \hat{c}_{\boldsymbol{k}n} \tag{2.129}$$

with the EPC

$$g_{\boldsymbol{q}\nu\boldsymbol{k}mn} = \frac{1}{\sqrt{2\omega_{\boldsymbol{q}\nu}}} \sum_i e_{\boldsymbol{q}i\nu} \frac{1}{\sqrt{M_i}} \langle \boldsymbol{k}+\boldsymbol{q}m | \frac{\partial \hat{H}}{\partial u_{\boldsymbol{q}i}} | \boldsymbol{k}n \rangle. \tag{2.130}$$

The next two section address the question of how the EPC can be calculated in practice; first, by means of DFPT and, second, from a TB model.

2.5.1 *Ab initio*

Knowing how to calculate phonons from DFPT, the *ab initio* calculation of the EPC is straightforward. In fact, it is anyway calculated as a byproduct in the self-consistent solution of Eq. 2.82 or equivalently Eq. 2.98 for the change of the SCF potential ∂V_{SCF}.

We can rewrite Eq. 2.92b as a change of the dynamical matrix

$$\Delta D_{\boldsymbol{q}\mu\nu} = \sum_{ij} e^*_{\boldsymbol{q}i\mu} \frac{\Delta C_{\boldsymbol{q}ij}}{\sqrt{M_i M_j}} e_{\boldsymbol{q}j\nu} \tag{2.131a}$$

$$= 2\sqrt{\omega_{\boldsymbol{q}\mu}\omega_{\boldsymbol{q}\nu}} \frac{2}{N} \sum_{\boldsymbol{k}n} g^*_{\boldsymbol{q}\mu\boldsymbol{k}mn} \frac{f(\varepsilon_{\boldsymbol{k}+\boldsymbol{q}m}) - f(\varepsilon_{\boldsymbol{k}n})}{\varepsilon_{\boldsymbol{k}+\boldsymbol{q}m} - \varepsilon_{\boldsymbol{k}n}} g^{\text{SCF}}_{\boldsymbol{q}\nu\boldsymbol{k}mn} \tag{2.131b}$$

with the bare and screened *ab initio* EPCs analogous to Eq. 2.130 (as appear in a Hamiltonian),

$$g^{(\text{SCF})}_{\boldsymbol{q}\nu\boldsymbol{k}mn} = \frac{1}{\sqrt{2\omega_{\boldsymbol{q}\nu}}} \sum_i e_{\boldsymbol{q}i\nu} \frac{1}{\sqrt{M_i}} \langle \boldsymbol{k}+\boldsymbol{q}m | \frac{\partial \hat{V}_{(\text{SCF})}}{\partial u_{\boldsymbol{q}i}} | \boldsymbol{k}n \rangle. \tag{2.132}$$

The bare *"matrix element $g^{\text{b}}_{mn\nu}(\boldsymbol{k},\boldsymbol{q})$ is obtained from* [the screened] *$g_{mn\nu}(\boldsymbol{k},\boldsymbol{q})$ by replacing the variation of the Kohn–Sham potential by the corresponding variation of the ionic (pseudo)potentials"* [101]. Equivalently, g^{SCF} as obtained from cDFPT calculations is the partially screened coupling to be used in the model Hamiltonian.

Please note that the phonon frequency ω and eigenvector e in the above equation do not depend on the screening level. The former ensures that the EPC has the dimension of an energy and cancels in the above equations. The latter transforms the coupling into the basis of the Hamiltonian. We only have to take care of a consistent choice of these quantities.

Sometimes it is more convenient to work with a quantity that is independent of the phonon frequency (cf. Eqs. 3.10 and 5.12). Thus, we alternatively define the EPC (with the dimension of an energy to the power of one and a half) as

$$d^{(\text{SCF})}_{\boldsymbol{q}\nu\boldsymbol{k}mn} \equiv \sqrt{2\omega_{\boldsymbol{q}\nu}} g^{(\text{SCF})}_{\boldsymbol{q}\nu\boldsymbol{k}mn} = \sum_i e_{\boldsymbol{q}i\nu} \frac{1}{\sqrt{M_i}} \langle \boldsymbol{k}+\boldsymbol{q}m | \frac{\partial \hat{V}_{(\text{SCF})}}{\partial u_{\boldsymbol{q}i}} | \boldsymbol{k}n \rangle. \tag{2.133}$$

2.5.2 Tight binding

We can use Eq. 2.126 to calculate the EPC for a TB model. Here, we follow the derivation by Varma *et al.* [130]. For simplicity, we consider a Hamiltonian with one atom per unit cell,

$$\hat{H}_0 = \sum_{\boldsymbol{R}\boldsymbol{R}'} t_{\boldsymbol{R}'-\boldsymbol{R}} \hat{c}^\dagger_{\boldsymbol{R}'} \hat{c}_{\boldsymbol{R}}. \tag{2.134}$$

The corresponding Hamiltonian of the EPC according to Eq. 2.126 reads

$$\hat{H}_{\text{el–ph}} = \sum_{\boldsymbol{R}''} \frac{\partial \hat{H}_0}{\partial \boldsymbol{R}''} \boldsymbol{u}_{\boldsymbol{R}''} = \sum_{\boldsymbol{R}\boldsymbol{R}'\boldsymbol{R}''} \frac{\partial t_{\boldsymbol{R}'-\boldsymbol{R}}}{\partial \boldsymbol{R}''} \boldsymbol{u}_{\boldsymbol{R}''} \hat{c}^\dagger_{\boldsymbol{R}'} \hat{c}_{\boldsymbol{R}} = \sum_{\boldsymbol{R}\boldsymbol{R}'} \left[\frac{\partial t_{\boldsymbol{R}'-\boldsymbol{R}}}{\partial \boldsymbol{R}'} \boldsymbol{u}_{\boldsymbol{R}'} + \frac{\partial t_{\boldsymbol{R}'-\boldsymbol{R}}}{\partial \boldsymbol{R}} \boldsymbol{u}_{\boldsymbol{R}} \right] \hat{c}^\dagger_{\boldsymbol{R}'} \hat{c}_{\boldsymbol{R}}$$

$$= \sum_{\boldsymbol{R}\boldsymbol{R}'} \frac{\partial t_{\boldsymbol{R}'-\boldsymbol{R}}}{\partial (\boldsymbol{R}'-\boldsymbol{R})} (\boldsymbol{u}_{\boldsymbol{R}'} - \boldsymbol{u}_{\boldsymbol{R}}) \hat{c}^\dagger_{\boldsymbol{R}'} \hat{c}_{\boldsymbol{R}}. \tag{2.135}$$

A transform to the $\boldsymbol{q}$- and $\boldsymbol{k}$-space bases via Eqs. 2.65 and C.14 or, more precisely,

$$\hat{c}_{\boldsymbol{R}} = \frac{1}{\sqrt{N}} \sum_{\boldsymbol{k}} \hat{c}_{\boldsymbol{k}} \mathrm{e}^{-\mathrm{i}\boldsymbol{k}\boldsymbol{R}}, \tag{2.136a}$$

where we used the symmetric transform to preserve the anticommutation relations, yields

$$\hat{H}_{\text{el-ph}} = \frac{1}{N} \sum_{\boldsymbol{q}\boldsymbol{k}\boldsymbol{k}'} \sum_{\boldsymbol{R}\boldsymbol{R}'} \frac{\partial t_{\boldsymbol{R}'-\boldsymbol{R}}}{\partial(\boldsymbol{R}'-\boldsymbol{R})} (\mathrm{e}^{-\mathrm{i}\boldsymbol{q}\boldsymbol{R}'} - \mathrm{e}^{-\mathrm{i}\boldsymbol{q}\boldsymbol{R}}) \mathrm{e}^{\mathrm{i}\boldsymbol{k}'\boldsymbol{R}'-\mathrm{i}\boldsymbol{k}\boldsymbol{R}} \boldsymbol{u}_{\boldsymbol{q}} \hat{c}^{\dagger}_{\boldsymbol{k}'} \hat{c}_{\boldsymbol{k}} \tag{2.137a}$$

$$= \frac{1}{N} \sum_{\boldsymbol{q}\boldsymbol{k}\boldsymbol{k}'} \sum_{\boldsymbol{R}\boldsymbol{R}'} \frac{\partial t_{\boldsymbol{R}}}{\partial \boldsymbol{R}} (\mathrm{e}^{-\mathrm{i}\boldsymbol{q}\boldsymbol{R}'} - \mathrm{e}^{-\mathrm{i}\boldsymbol{q}(\boldsymbol{R}'-\boldsymbol{R})}) \mathrm{e}^{\mathrm{i}\boldsymbol{k}'\boldsymbol{R}'-\mathrm{i}\boldsymbol{k}(\boldsymbol{R}'-\boldsymbol{R})} \boldsymbol{u}_{\boldsymbol{q}} \hat{c}^{\dagger}_{\boldsymbol{k}'} \hat{c}_{\boldsymbol{k}} \tag{2.137b}$$

$$= \frac{1}{N} \sum_{\boldsymbol{q}\boldsymbol{k}\boldsymbol{k}'} \sum_{\boldsymbol{R}\boldsymbol{R}'} \frac{\partial t_{\boldsymbol{R}}}{\partial \boldsymbol{R}} (\mathrm{e}^{\mathrm{i}\boldsymbol{k}\boldsymbol{R}} - \mathrm{e}^{\mathrm{i}(\boldsymbol{k}+\boldsymbol{q})\boldsymbol{R}}) \mathrm{e}^{\mathrm{i}(\boldsymbol{k}'-\boldsymbol{k}-\boldsymbol{q})\boldsymbol{R}'} \boldsymbol{u}_{\boldsymbol{q}} \hat{c}^{\dagger}_{\boldsymbol{k}'} \hat{c}_{\boldsymbol{k}} \tag{2.137c}$$

$$= \sum_{\boldsymbol{q}\boldsymbol{k}} \sum_{\boldsymbol{R}} \frac{\partial t_{\boldsymbol{R}}}{\partial \boldsymbol{R}} (\mathrm{e}^{\mathrm{i}\boldsymbol{k}\boldsymbol{R}} - \mathrm{e}^{\mathrm{i}(\boldsymbol{k}+\boldsymbol{q})\boldsymbol{R}}) \boldsymbol{u}_{\boldsymbol{q}} \hat{c}^{\dagger}_{\boldsymbol{k}+\boldsymbol{q}} \hat{c}_{\boldsymbol{k}}. \tag{2.137d}$$

Finally, with the expression for the displacements in Eq. 2.128, we have

$$\hat{H}_{\text{el-ph}} = \frac{1}{\sqrt{N}} \sum_{\boldsymbol{q}\nu\boldsymbol{k}} g_{\boldsymbol{q}\nu\boldsymbol{k}} [\hat{b}^{\dagger}_{-\boldsymbol{q}\nu} + \hat{b}_{\boldsymbol{q}\nu}] \hat{c}^{\dagger}_{\boldsymbol{k}+\boldsymbol{q}} \hat{c}_{\boldsymbol{k}} \tag{2.138}$$

with the TB EPC (cf. Eq. 2.29 of Ref. 130)

$$g_{\boldsymbol{q}\nu\boldsymbol{k}} = \frac{1}{\sqrt{2\omega_{\boldsymbol{q}\nu}}} \frac{1}{\sqrt{M}} \boldsymbol{e}_{\boldsymbol{q}\nu} \sum_{\boldsymbol{R}} \frac{\partial t_{\boldsymbol{R}}}{\partial \boldsymbol{R}} (\mathrm{e}^{\mathrm{i}\boldsymbol{k}\boldsymbol{R}} - \mathrm{e}^{\mathrm{i}(\boldsymbol{k}+\boldsymbol{q})\boldsymbol{R}}). \tag{2.139}$$

In the case of multiple electronic bands, we only have to assume that t is a matrix in orbital space. Further below in Eq. 2.147a, we will show how to perform the transform into the band basis. On the other hand, since the orbitals are assumed to be located at the same atom, the above equation is limited to the acoustic phonon modes.

The only question that remains to be answered is how the derivative of the hopping is calculated. (We will not discuss changes of the on-site energies.) It is most convenient to approach this problem in spherical or, assuming that we can choose an out-of-plane direction, polar coordinates r and φ, which are the bond length and angle, respectively. This is because, *"The dependence on bond lengths is modeled by scaling* [...]*, which is a generalization of Harrison's* d^{-2} *rule.* [...] *The change in bond angles* [...] *is naturally included through the Slater–Koster tables* [...]*"* [131]. In other words, since a rotation is a unitary transform (preserves all lengths), the φ dependence can be calculated analytically from the transformation properties of the hoppings. For the r dependence, however, we have to make additional assumptions on the scaling behavior.

We start with the angular dependence of the hopping associated to a selected bond of the system. We can write is as (cf. Eq. 2.37a)

$$t = R_{\varphi} \cdot t_0 \cdot R_{-\varphi}, \tag{2.140}$$

where R is a rotation and t_0 the hopping at a reference angle. Using product and chain rule,

$$\frac{\partial t}{\partial \varphi} = R'_{\varphi} \cdot t_0 \cdot R_{-\varphi} - R_{\varphi} \cdot t_0 \cdot R'_{-\varphi} = R'_{\varphi} \cdot R_{-\varphi} \cdot t - t \cdot R_{\varphi} \cdot R'_{-\varphi}, \tag{2.141}$$

where the prime marks a derivative.

For the radial dependence, we usually assume that the logarithmic derivative of the hopping with respect to the bond length is a constant β (cf. Eq. 1 of Ref. 132),

$$\frac{\mathrm{d}\log(t)}{\mathrm{d}\log(r)} = \beta \quad \text{or} \quad t = \left(\frac{r}{r_0}\right)^{\beta} t_0 \quad \text{or} \quad \frac{\partial t}{\partial r} = \frac{\beta}{r} t, \tag{2.142}$$

where r (r_0) is the (equilibrium) bond length. Harrison's traditional d^{-2} rule [85, 133] is given for $\beta = -2$. The best choice for β depends on the system; an educated guess would be $\beta = -5$, -4, and -3 for d–d, p–d, and p–p bonds [85, 134].

Combining Eqs. 2.141 and 2.142, the derivative with respect to $\boldsymbol{a} = r(\cos\varphi, \sin\varphi)$ reads

$$\frac{\partial t}{\partial \boldsymbol{a}} = \frac{\partial t}{\partial r}\frac{\partial r}{\partial \boldsymbol{a}} + \frac{\partial t}{\partial \varphi}\frac{\partial \varphi}{\partial \boldsymbol{a}} = \frac{\beta t}{r}\frac{\boldsymbol{a}_{r\varphi}}{r} + \left[\frac{\partial R_\varphi}{\partial \varphi} \cdot R_{-\varphi} \cdot t + t \cdot R_\varphi \cdot \frac{\partial R_{-\varphi}}{\partial \varphi}\right] \frac{\boldsymbol{a}_{r\varphi+\frac{\pi}{2}}}{r^2}. \tag{2.143}$$

Often, the angular dependence is neglected. If we additionally restrict the hopping to nearest neighbors, we can write Eq. 2.139 using the preceding equation as (cf. Eq. A.4 of Ref. 130)

$$g_{\boldsymbol{q}\nu\boldsymbol{k}} = \frac{1}{\sqrt{2\omega_{\boldsymbol{q}\nu}}}\frac{1}{\sqrt{M}} \boldsymbol{e}_{\boldsymbol{q}\nu} \sum_{\boldsymbol{R}} \frac{\partial t_{\boldsymbol{R}}}{\partial \boldsymbol{R}} (\mathrm{e}^{\mathrm{i}\boldsymbol{k}\boldsymbol{R}} - \mathrm{e}^{\mathrm{i}(\boldsymbol{k}+\boldsymbol{q})\boldsymbol{R}}) \tag{2.144a}$$

$$= \frac{\beta}{a^2}\frac{1}{\sqrt{2\omega_{\boldsymbol{q}\nu}}}\frac{1}{\sqrt{M}} \boldsymbol{e}_{\boldsymbol{q}\nu} \sum_{\boldsymbol{R}} \boldsymbol{R} t_{\boldsymbol{R}} (\mathrm{e}^{\mathrm{i}\boldsymbol{k}\boldsymbol{R}} - \mathrm{e}^{\mathrm{i}(\boldsymbol{k}+\boldsymbol{q})\boldsymbol{R}}), \tag{2.144b}$$

where a is the lattice constant. Using that the group-velocity reads (cf. Eq. A.1 of Ref. 130)

$$\boldsymbol{v}_{\boldsymbol{k}} = \frac{\partial}{\partial \boldsymbol{k}} \langle \boldsymbol{k} | \hat{H}_0 | \boldsymbol{k} \rangle = \frac{\partial}{\partial \boldsymbol{k}} \sum_{\boldsymbol{R}} t_{\boldsymbol{R}} \mathrm{e}^{\mathrm{i}\boldsymbol{k}\boldsymbol{R}} = \mathrm{i} \sum_{\boldsymbol{R}} \boldsymbol{R} t_{\boldsymbol{R}} \mathrm{e}^{\mathrm{i}\boldsymbol{k}\boldsymbol{R}}, \tag{2.145}$$

we can further write (cf. Eq. A.8 of Ref. 130)

$$g_{\boldsymbol{q}\nu\boldsymbol{k}} = -\mathrm{i}\frac{\beta}{a^2}\frac{1}{\sqrt{2\omega_{\boldsymbol{q}\nu}}}\frac{1}{\sqrt{M}} \boldsymbol{e}_{\boldsymbol{q}\nu} (\boldsymbol{v}_{\boldsymbol{k}} - \boldsymbol{v}_{\boldsymbol{k}+\boldsymbol{q}}). \tag{2.146}$$

Both g and $\boldsymbol{v}$ are matrices in the space of electronic orbitals. We can transform them into the electronic band basis via the matrices $U_{\boldsymbol{k}}$ of right eigenvectors of the Hamiltonian $H_{\boldsymbol{k}}$. However, the way they are defined, g and $\boldsymbol{v}$ must be transformed differently,

$$\boldsymbol{v}^{\mathrm{band}}_{\boldsymbol{k}} = U^{\dagger}_{\boldsymbol{k}} \boldsymbol{v}_{\boldsymbol{k}} U_{\boldsymbol{k}}, \tag{2.147a}$$

$$g^{\mathrm{band}}_{\boldsymbol{q}\nu\boldsymbol{k}} = U^{\dagger}_{\boldsymbol{k}+\boldsymbol{q}} g_{\boldsymbol{q}\nu\boldsymbol{k}} U_{\boldsymbol{k}}. \tag{2.147b}$$

Thus, with $A_{\boldsymbol{q}\boldsymbol{k}} = U^{\dagger}_{\boldsymbol{k}+\boldsymbol{q}} U_{\boldsymbol{k}}$ and $U_{\boldsymbol{k}} U^{\dagger}_{\boldsymbol{k}} = 1$ (cf. A.12 of Ref. 130),

$$g^{\mathrm{band}}_{\boldsymbol{q}\nu\boldsymbol{k}} = -\mathrm{i}\frac{\beta}{a^2}\frac{1}{\sqrt{2\omega_{\boldsymbol{q}\nu}}}\frac{1}{\sqrt{M}} \boldsymbol{e}_{\boldsymbol{q}\nu} (A_{\boldsymbol{q}\boldsymbol{k}} \boldsymbol{v}^{\mathrm{band}}_{\boldsymbol{k}} - \boldsymbol{v}^{\mathrm{band}}_{\boldsymbol{k}+\boldsymbol{q}} A_{\boldsymbol{q}\boldsymbol{k}}). \tag{2.148}$$

In the original paper by Varma *et al.* [130] and elsewhere [135, 136], the group velocity is considered to be diagonal in the band basis, i.e., $v^{\mathrm{band}}_{\boldsymbol{k}mn} = v^{\mathrm{band}}_{\boldsymbol{k}nn}\delta_{mn}$. However, for the case of 1H-TaS_2, we noted [86] that these off-diagonal elements play a crucial role (cf. Fig. 9.9).

EPCs from TB are useful for several reasons. They are insightful because they help interpreting corresponding *ab initio* results. Compared to the latter, their calculation is very fast once the TB model is set up. Also, we have full control of the gauge freedom, i.e., of the complex phases attached to the electronic eigenstates, which is not always the case when using ready-made simulation software. Finally, since our TB models are set up to describe

the relevant physics, also the resulting EPCs depend on all relevant quantum numbers, as opposed to simpler model EPCs as proposed by Fröhlich [137] and Holstein [44].

Whether EPCs from TB are accurate enough for qualitative calculations (linewidths, screened phonons, etc.), has to be carefully analyzed for the specific case. Especially the assumptions on the distance dependence of the hopping have to be considered with caution. Furthermore, if the relevant EPC is generated from the potential rather than from the hopping, the presented method is not applicable. Independently, it might be fruitful to connect the theory with other methods such as force fields or DFT-based TB (DFTB).

2.5.3 Wannier representation

Electrons and phonons can be represented in the localized bases of Wannier functions and atomic displacements. This allows for the calculation of the Hamiltonian and the dynamical matrix for arbitrary $\boldsymbol{k}$ and $\boldsymbol{q}$ points via Fourier transforms (cf. App. B.4.2). Often, for converged calculations of properties resulting from the interaction of electrons and phonons, very high $\boldsymbol{k}$ and $\boldsymbol{q}$ resolutions are necessary. Thus, for a complete theory of systems of coupled electrons and phonons, we also need a localized representation of the EPC, i.e., a representation using both Wannier functions and atomic displacements. This has been put forward by Giustino *et al.* in 2007 [138]. Today, a popular tool to obtain the EPC in the localized basis from first principles (and optionally back-transform, i.e., perform a Fourier interpolation) is the EPW code [138–140].

The complete transform between localized and delocalized bases as used in EPW reads

$$g_{\boldsymbol{q}\nu\boldsymbol{k}mn} = \sum_{\boldsymbol{R}i\boldsymbol{R}'\alpha\beta} e_{\boldsymbol{q}i\nu} U^*_{\boldsymbol{k}+\boldsymbol{q}\alpha m} g_{\boldsymbol{R}i\boldsymbol{R}'\alpha\beta} U_{\boldsymbol{k}\beta n} \mathrm{e}^{\mathrm{i}(\boldsymbol{q}\boldsymbol{R}+\boldsymbol{k}\boldsymbol{R}')}, \tag{2.149a}$$

$$g_{\boldsymbol{R}i\boldsymbol{R}'\alpha\beta} = \frac{1}{NN'} \sum_{\boldsymbol{q}\nu\boldsymbol{k}mn} e^*_{\boldsymbol{q}i\nu} U_{\boldsymbol{k}+\boldsymbol{q}\alpha m} g_{\boldsymbol{q}\nu\boldsymbol{k}mn} U^*_{\boldsymbol{k}\beta n} \mathrm{e}^{-\mathrm{i}(\boldsymbol{q}\boldsymbol{R}+\boldsymbol{k}\boldsymbol{R}')}. \tag{2.149b}$$

Here, $\boldsymbol{R}$ and $\boldsymbol{R}'$ are lattice vectors of the WS supercell including its edge, i.e., the number of lattice vectors $\boldsymbol{R}$ and $\boldsymbol{R}'$ exceeds the number of points N and N' of a uniform mesh sampling the supercell. As a consequence, to avoid a double counting of the edge, some elements of $g_{\boldsymbol{R}i\boldsymbol{R}'}$ have a reduced weight. Also, for the lattice degrees of freedom, shifted WS supercells are used (cf. App. B.4.2), i.e., the $\boldsymbol{R}$ summation is in principle over different sets of lattice vectors for each basis atom (encoded in i). However, to keep the formulas simple, we sum over the union of all sets of lattice vectors and in turn set some elements of $g_{\boldsymbol{R}i}$ are to zero.

Besides the possibility to perform a Fourier interpolation (cf. App. B.4.2), the advantage of the Wannier basis as opposed to the basis of electronic eigenstates is that the former have a well-defined complex phase (or are even real). This is important if EPCs from different calculations, e.g., DFPT and cDFPT, are used in the same calculation. If no consistent gauge is applied, the results will be meaningless. For the same reason, the transformation coefficients $U_{\boldsymbol{k}}$ and $U_{\boldsymbol{k}+\boldsymbol{q}}$ have to be elements of the *same* object for most purposes.

2.6 Electron–electron interaction

Since this thesis deals with the interplay of electrons and phonons, the electron–electron or Coulomb interaction plays only a secondary role. However, we effectively take it into account by using model parameters from DFT and DFPT and, e.g., diagrammatic extensions of our theory are possible. In any case, the Coulomb interaction is an indispensable part of the theory of the solid state, and a correct treatment of the latter requires the consideration of the former. Hence, in this section, we will give a short overview of the topic.

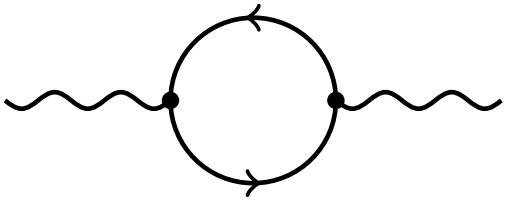

Figure 2.12: Pair bubble.

2.6.1 Random-phase approximation

As in the case of phonons and the EPCs, where we dealt with bare, partially screened, and fully screened quantities, also for the Coulomb interaction different levels of screening must be considered. A very common approximation to the screened Coulomb interaction is the RPA [141–146], which neglects the part of the electronic response that *"tends to average out"* because of random phase factors [141]. Here, we have a Dyson equation,

$$W = v + v\chi_0 W \quad \text{or} \quad W^{-1} = v^{-1} - \chi_0, \tag{2.150}$$

which relates the screened Coulomb interaction W to the bare Coulomb interaction v via the bare electronic susceptibility χ_0 (Eq. 3.1) for each momentum $\boldsymbol{q}$ *individually*. The Feynman diagram for χ_0 is the *pair bubble* shown in Fig. 2.12 (cf. Sec. 5.1). χ_0 is also known as the Lindhard function [147], polarizability, or even polarization. It is not to be confused with the (screened) electronic susceptibility $\chi = \chi_0(1 - v\chi_0)^{-1}$ (cf. Eq. 14.66 of Ref. 148). The ratio of the bare to the screened interaction is given by the dielectric function

$$\epsilon = W^{-1}v = 1 - \chi_0 v = (1 + \chi_0 W)^{-1}. \tag{2.151}$$

2.6.1.1 Constrained random-phase approximation

The form of the RPA formulas allows us to split the polarizability into two parts, $\chi_0 = \chi_0^{\mathrm{M}} + \chi_0^{\mathrm{R}}$, where χ_0^{M} could be the screening to be treated in a model Hamiltonian and χ_0^{R} would be the rest. Thus, the screening of the Coulomb interaction becomes a two-step process,

$$W^{-1} = \underbrace{v^{-1} - \chi_0^{\mathrm{R}}}_{U^{-1}} - \chi_0^{\mathrm{M}}, \tag{2.152}$$

where we have defined the partially screened Coulomb interaction U. The dielectric functions ϵ_{R} and ϵ_{M} of the two steps are related to the full dielectric function via $\epsilon = \epsilon_{\mathrm{M}}\epsilon_{\mathrm{R}}$ and read

$$\epsilon_{\mathrm{M}} = W^{-1}U = 1 - \chi_0^{\mathrm{M}}U = (1 + \chi_0^{\mathrm{M}}W)^{-1}, \tag{2.153}$$

$$\epsilon_{\mathrm{R}} = U^{-1}v \;\; = 1 - \chi_0^{\mathrm{R}}v \;\; = (1 + \chi_0^{\mathrm{R}}U)^{-1}. \tag{2.154}$$

The RPA under the constraint that the model polarizability χ_0^{M} is excluded is known as the cRPA [48, 49] (cf. Sec. 7.2.4). The cRPA Coulomb interaction U excludes screening from within the active subspace and is thus rather insensitive to changes therein. (If all states near the Fermi level are in the active subspace, all processes between the latter and the rest have large energy denominators and contribute little.) Hence, it can also be used in modified models where, e.g., the doping level has been changed or additional environmental screening has been introduced. The latter can be conveniently described combining the cRPA with Wannier-function continuum electrostatics (WFCE) [24, 149]. The WFCE method is particularly interesting for 2D materials, where we have very long-range Coulomb interactions within the isolated monolayer due to lack of environmental screening. The influence of substrates etc. can then be modeled with WFCE.

2.6.2 Hubbard model

The most simple model of an interacting electron system is the Hubbard model [33–35]. It assumes that electrons only feel the repulsive Coulomb interaction when they are located at the same atomic site,

$$\hat{H} = -t \sum_{\langle \boldsymbol{R}, \boldsymbol{R}' \rangle \sigma} \hat{c}^\dagger_{\boldsymbol{R}'\sigma} \hat{c}_{\boldsymbol{R}\sigma} + U \sum_{\boldsymbol{R}} \hat{n}_{\boldsymbol{R}\downarrow} \hat{n}_{\boldsymbol{R}\uparrow}, \tag{2.155}$$

where $\hat{n}_{\boldsymbol{R}\sigma} = \hat{c}^\dagger_{\boldsymbol{R}\sigma} \hat{c}_{\boldsymbol{R}\sigma}$ is the occupation operator, $\langle \boldsymbol{R}, \boldsymbol{R}' \rangle$ are neighboring atomic sites, and σ is the electron spin. Despite the simplicity of its definitions, solving the Hubbard model is a highly nontrivial task and results in a rich phase diagram.

Most prominently, the correlations-driven Mott transition [33–37] to an insulating state where band theory predicts a metal is captured by the model. More precisely, an electronic band of bandwidth W at the Fermi level can split into upper and lower Hubbard bands with an insulating gap in between (cf. Fig. 4 of Ref. 35), if the local Coulomb interaction U is large compared to the bandwidth, $U > W$.[8] (In a half filled system, this can be viewed as electrons being trapped at their respective lattice sites to avoid a temporary double occupancy of a site.) This can be seen from DMFT, a successful method to treat systems with strong correlations.

2.6.3 Dynamical mean-field theory

The idea of DMFT [46, 151] is to map the complex system of interacting particles on a lattice to an effective single-site problem coupled to a noninteracting bath. The latter is known as an Anderson impurity model (AIM) [45]. This approximation is equivalent to assuming that the electronic self energy is *local*, i.e., $\Sigma_{\boldsymbol{k}}(\omega) \approx \Sigma(\omega)$?[9] It is exact in the limit of infinite dimensions, where each site has an infinite number of neighbors [152]. The mapping to the AIM is a self-consistency problem, as outlined below (cf. Eqs. 112 to 114 of Ref. 153).

The (nonlocal) exact Green function of the lattice fulfills a Dyson equation,

$$[G_{\boldsymbol{k}}(\omega)]^{-1} = [G^0_{\boldsymbol{k}}(\omega)]^{-1} - \Sigma_{\boldsymbol{k}}(\omega). \tag{2.156}$$

Similarly, the ($\boldsymbol{k}$-independent, i.e., local) impurity Green function of the AIM fulfills

$$[G(\omega)]^{-1} = \underbrace{[G^0(\omega)]^{-1} - \Delta(\omega)}_{[\mathcal{G}(\omega)]^{-1}} - \Sigma(\omega), \tag{2.157}$$

where $\mathcal{G}(\omega)$ is known as the *dynamical mean field* and $\Delta(\omega)$ is the hybridization function. Demanding that $\Sigma_{\boldsymbol{k}}(\omega) = \Sigma(\omega)$ creates a self-consistency problem whose solution yields a lattice Green function $G_{\boldsymbol{k}}(\omega)$ that is related to the local Green function via [153]

$$G(\omega) = \frac{1}{N} \sum_{\boldsymbol{k}} G_{\boldsymbol{k}}(\omega). \tag{2.158}$$

One part of this iterative processes is to solve the AIM. Here, Monte Carlo techniques are often the method of choice [154, 155]. (Above, all equations have been written using a generic frequency argument ω. Usually, the calculations are carried out on the imaginary axis using Matsubara frequencies $\mathrm{i}\omega_n$.)

The DMFT total energy can of course also be used to calculate phonon frequencies as in Sec. 2.4.1 [156]. The computational cost is significantly enhanced as compared to DFPT.

[8] The Mott transition can depend on the dielectric environment [150] or on the material thickness, since dielectric screening decreases U, while interlayer hopping increases W.

[9] In turn, in the Hartree–Fock approximation, the self-energy is nonlocal but *static*, $\Sigma_{\boldsymbol{k}}(\omega) \approx \Sigma_{\boldsymbol{k}}$.

Chapter 3

Many-body instabilities

The whole is something
besides its parts.

—Aristotle

On the basis of the complete many-body Hamiltonian discussed before, in this chapter, we will present the properties and basic theory of selected many-body instabilities. With *many-body instabilities*, we refer to phases of matter that arise from the interaction of (quasi)particles, usually superseding a higher-temperature state of higher symmetry. Often, the same material is susceptible to different kinds of instabilities at the same time, resulting in a subtle interplay between instabilities, which can compete [18, 21, 59, 157–161], coexist [162–164], but also cooperate [165–169].

We start with an example. A prominent showplace of competing many-body instabilities is the metallic TMDC 2H-$NbSe_2$, which features both superconductivity and CDWs. Already found to be superconducting by Revolinsky *et al.* in 1963 [7], its superconducting transition temperature was predicted to drop from $T_c = 7\,\mathrm{K}$ [170] to 3.8 K upon reduction of the sample thickness from the bulk to the monolayer by Frindt in 1972 [17]. More recent values by Ugeda *et al.* from 2016 are $T_c = 7.2\,\mathrm{K}$ and 1.9 K for the bulk and monolayer, respectively [158]. Additionally, in 1975, Moncton *et al.* found an incommensurate CDW below $T_{CDW} = 33.5\,\mathrm{K}$, followed by a transition to a commensurate CDW at 5 K [96]. Only one year later, Berthier *et al.* evidenced a connection between the observed superconductivity and CDWs [6]. They found a suppression of T_{CDW} under increased pressure, which is accompanied by an enhancement of T_c, but only up to 36 kbar, where $T_{CDW} < T_c$ for the first time. Hence, the presence of a CDW tends to suppress superconductivity. A connection between the findings by Frindt and Berthier *et al.* was established in 2015, when Xi *et al.* reported that the CDW is strongly enhanced upon reduction of the thickness to the monolayer limit [18]. This was substantiated theoretically in 2018 by Lian *et al.*, who explain the suppression of superconductivity in the monolayer limit by a reduced density of states (DOS) at the Fermi level due to the enhanced CDW [21].

This chapter is organized as follows: Motivated by the above example, we will first give a detailed description of CDWs in Sec. 3.1 and then proceed with superconductivity in Sec. 3.2. The format will be such that the basic theory is intertwined with some exemplary results. Guided by the title of this thesis, the ensuing chapter then gives some insights into the field of 2D materials, showplace of many-body instabilities.

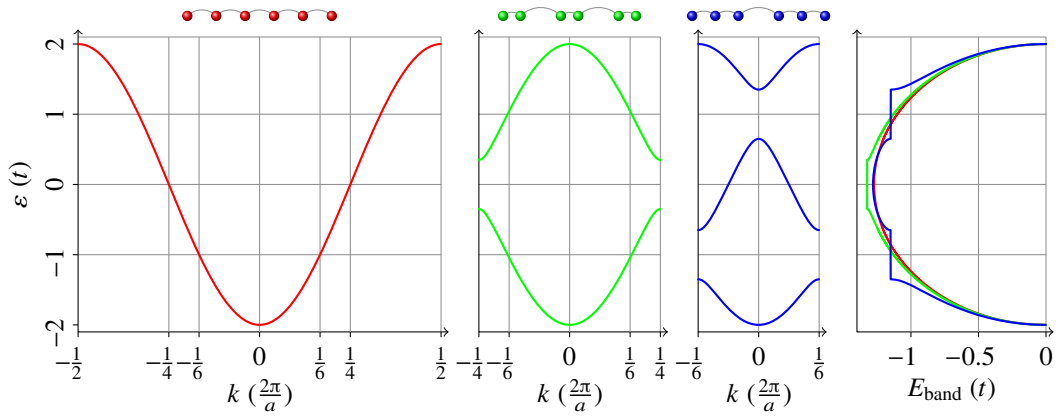

Figure 3.1: Dimerization and trimerization of a 1D monoatomic TB chain with nearest-neighbor hopping t. In the distorted phase, the shorter (longer) bonds are modeled using an increased (decreased) hopping parameter t' (t''). To open band gap(s) of width Δ while preserving the overall bandwidth, we must choose $t' = t + \Delta/4$ and $t'' = t - \Delta/4$ for the dimerization and $t' = \sqrt{t(t + \Delta/2)}$ and $t'' = t - \Delta/2$ for the trimerization. The total energy E_{band} is calculated via the sum of the energies of all occupied electronic states and thus excludes electrostatic contributions from the nuclei.

3.1 Charge-density waves

A CDW is in general a periodic modulation of the electronic charge density of a solid. Since this also involves a change of the effective potential for the nuclei, the effect is always accompanied by a PLD. In fact, the two terms CDW and PLD are often used interchangeably, and we will prefer the former nomenclature throughout this work. The question of whether the CDW causes the PLD or vice versa, is thus an example of the dilemma, *which came first: the chicken or the egg?* [134]. On the theoretical level it is however possible to distinguish CDWs that can also exist for hypothetical clamped nuclei from those that require the atomic displacement. The former can be described by means of purely electronic lattice models and traced back to particularities of the Coulomb interaction. For example, the attractive [171] and the doped repulsive [59] Hubbard model host CDWs.

3.1.1 Peierls instability

The formation of CDWs is usually favored in low dimensions. In his 1955 textbook, Peierls argues that a one-dimensional (1D) monoatomic chain with nearest-neighbor coupling could always be subject to PLD formation such as a dimerization or trimerization as shown in Fig. 3.1 [172].

There is an intuitive explanation for this: In the case of the dimerization, the unit cell length becomes twice, the BZ half as large. The bands fold back and are split due to an avoided crossing, resulting in a gap at the Fermi level [173]. (This requires that the Fermi surface coincides with the edge of the new BZ. For an isolated, half-filled band whose Fermi surface consists of only two points in the original BZ, this is always the case.) The associated downward-shift of the occupied bands makes the PLD energetically favorable, provided that the corresponding kinetic energy gain ΔE_{band} is larger than the increase of potential energy ΔE_{pot}. Peierls states that $\Delta E_{\text{band}} \propto -u \log(u)$ and $\Delta E_{\text{pot}} \propto u^2$, where u is the atomic displacement, thus always favoring the PLD [174]. Similarly, a trimerization or more complicated displacement patterns will open gaps at different energies in the band structure. In consequence, such patters are favored at different doping levels. At arbitrary band filling, the original lattice and the favored CDW are in general incommensurate.

In real one- or two-dimensional materials, CDWs have indeed been observed [8]. However, there are deviations from the idealized picture above. For example, for strongly correlated materials, which are poorly described in a band picture, the above arguments no longer hold. Also, the conditions for nesting Fermi surfaces are seldom if ever perfectly fulfilled and the gaps opened in the distorted phases may only be partial (in some parts of the BZ) or located away from the Fermi level [21, 175–179] (cf. Fig. 3.3). While Peierls's theory suggest that the emergence of CDW gaps might render the existence of 1D metals impossible [172], *ab initio* calculations for perfect monoatomic chains have shown that the predicted dimerization is not always realized [180]. Altogether, Peierls' idealized weak–coupling picture seems to be very fragile with respect to real materials [181].

3.1.2 Chan–Heine criterion

In the previous Sec. 3.1.1, we have essentially seen that a CDW with a wave vector $\boldsymbol{q}$ is favored whenever $\boldsymbol{q}$ maps (parts of) the Fermi surface of a material onto itself. This is usually accompanied by large contributions to the bare electronic susceptibility[1]

$$\chi_{\boldsymbol{q}} = \frac{2}{N} \sum_{\boldsymbol{k}mn} \frac{f(\varepsilon_{\boldsymbol{k}+\boldsymbol{q}m}) - f(\varepsilon_{\boldsymbol{k}n})}{\varepsilon_{\boldsymbol{k}+\boldsymbol{q}m} - \varepsilon_{\boldsymbol{k}n}}. \tag{3.1}$$

Hence, a large bare electronic susceptibility can be a criterion for the presence of a CDW, albeit not a sufficient one. This is because for the electrons to influence the lattice, we also need a finite EPC strength $g_{\boldsymbol{q}}$. Further taking into consideration that a large phonon frequency $\omega_{\boldsymbol{q}}$ is an indicator of dynamical stability (classically this corresponds to hard interatomic springs), and that the accumulation of charge in a CDW is hindered (supported) by the Coulomb (exchange) interaction $U_{\boldsymbol{q}}$ ($V_{\boldsymbol{q}}$), lead Chan and Heine to their condition for the existence of CDWs [162],

$$\frac{4g_{\boldsymbol{q}}^2}{\omega_{\boldsymbol{q}}} - (2U_{\boldsymbol{q}} - V_{\boldsymbol{q}}) \geq \frac{1}{\chi_{\boldsymbol{q}}}. \tag{3.2}$$

The Chan–Heine criterion is based on the fact that the phonon frequencies are lowered by the interaction with the electrons and that the transition to the CDW is marked by the point where a phononic mode finally "freezes" or becomes *soft*. As a consequence, the phonon frequencies in Eq. 3.2 above must be *bare*, i.e., exclude this renormalization. Today, such bare phonons can be obtained from cDFPT. A detailed description of the calculation of screened phonon frequencies (indicating possible instabilities) in this context is given in Chap. 5.

3.1.3 Periodic lattice distortion

As mentioned in the introduction to Sec. 3.1, we can approach the description of CDWs from the viewpoint of either the electrons or the lattice. Now, we will address the latter and give an overview of the theory of lattice instabilities or PLDs.

Again, we use the prominent example of 2H-$NbSe_2$. The symmetric high-temperature and the distorted low-temperature structures of the monolayer are shown in Fig. 3.2 together with the corresponding BZs. In the PLD phase, the niobium atoms move together to form

[1] Actually, the zero-frequency limit of the imaginary part of the bare electronic susceptibility is better suited to measure Fermi-surface nesting. However, for the occurrence of CDWs, the quality of the nesting plays a secondary role in the end. Instead, it is important that the overall energies (and group velocities) are favorable on a larger energy scale, as measured by the real part of the bare electronic susceptibility [182]. We will discuss this in more detail in Chap. 9.

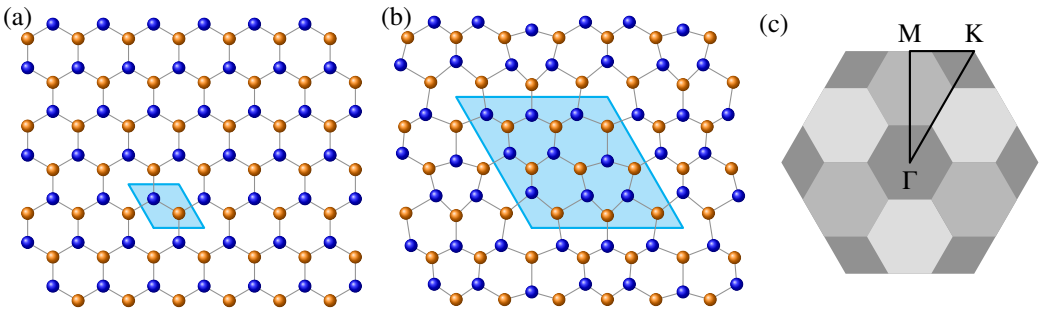

Figure 3.2: (a) Top view of the crystal structure of 1H-$NbSe_2$. A possible unit cell is marked in blue. (b) Exaggerated PLD in the 3×3 CDW phase. The real atomic displacements have been multiplied by a factor of five for better visualization. (c) BZs of original unit cell (large) and the CDW supercell (small). The black line indicates the path connecting the high-symmetry points Γ, M, and K, which encompasses the irreducible wedge, and along which band structures are usually plotted.

two triangles (one with six, the other with three atoms) on a 3×3 supercell. The electronic and phononic dispersions and DOS (cf. App. C.2) for both phases are displayed in Fig. 3.3.

As seen in Fig. 3.3a, the formation of the CDW shows up as a reduction of the electronic DOS close to (especially above) the Fermi level. This is due to a partial gapping in the $\boldsymbol{k}$-space region encircling the K point. The associated downward-shift of spectral weight makes the CDW energetically more favorable.

Figure 3.3b shows that the lattice instability manifests as imaginary frequencies at specific $\boldsymbol{q}$ points in the phonon dispersion of the symmetric structure. Here, the LA mode is affected. The favored PLD on a 3×3 supercell corresponds to $\boldsymbol{q} = 2/3\,\mathrm{M}$ in reciprocal space. This is exactly the wave vector of the leading instability, i.e., the one with the largest imaginary phonon frequency. Upon structural relaxation on the supercell, we obtain the stable CDW structure and the imaginary phonon frequencies disappear.

Here, it is worthwhile to mention that phonon instabilities often appear enhanced within the harmonic approximation (which we apply). In turn, some phonon instabilities may be suppressed by incorporating anharmonic corrections into the calculations [183].

In Fig. 3.3, all bands have been plotted along the same path through the large BZ of the small unit cell of the symmetric structure. This path traverses multiple smaller BZs of the larger cell of the CDW phase. Thus, the corresponding CDW band-structure plots are partially redundant. However, to facilitate the comparison to the symmetric bands, we simulate an *unfolding* of the bands in the *first* BZ of the CDW onto the neighboring BZs by choosing linewidths or weights corresponding to the overlap between CDW and symmetric states. Equivalent procedures are found in Refs. 184–186. The weights are calculated as

$$\begin{aligned} w_{\boldsymbol{k}n} = \sum_m |\langle \psi^{\mathrm{SYM}}_{\boldsymbol{k}m} | \psi^{\mathrm{CDW}}_{\boldsymbol{k}n} \rangle|^2 &= \sum_m \Big| \sum_{\boldsymbol{R}\alpha} \langle \psi^{\mathrm{SYM}}_{\boldsymbol{k}m} | w^{\mathrm{CDW}}_{\boldsymbol{R}\alpha} \rangle \langle w^{\mathrm{CDW}}_{\boldsymbol{R}\alpha} | \psi^{\mathrm{CDW}}_{\boldsymbol{k}n} \rangle \Big|^2 \\ &= \sum_m \Big| \sum_{\boldsymbol{R}\alpha} \langle \psi^{\mathrm{SYM}}_{\boldsymbol{k}m} | w^{\mathrm{SYM}}_{0\alpha} \rangle \mathrm{e}^{\mathrm{i}\boldsymbol{k}(\boldsymbol{\tau}^{\mathrm{CDW}}_{\boldsymbol{R}\alpha} - \boldsymbol{\tau}^{\mathrm{SYM}}_{0\alpha})} \langle w^{\mathrm{CDW}}_{\boldsymbol{R}\alpha} | \psi^{\mathrm{CDW}}_{\boldsymbol{k}n} \rangle \Big|^2 . \end{aligned} \tag{3.3}$$

Here, $|\psi^{\mathrm{SYM}}_{\boldsymbol{k}m}\rangle$ and $|\psi^{\mathrm{CDW}}_{\boldsymbol{k}n}\rangle$ are Bloch states of the symmetric and the CDW phase. Thus, the summation index n runs over 3×3 times as many bands as m. The corresponding Wannier states $|w^{\mathrm{SYM}}_{0\alpha}\rangle$ and $|w^{\mathrm{CDW}}_{\boldsymbol{R}\alpha}\rangle$ (cf. Eq. 2.60) are located at the positions $\boldsymbol{\tau}^{\mathrm{SYM}}_{0\alpha}$ and $\boldsymbol{\tau}^{\mathrm{CDW}}_{\boldsymbol{R}\alpha}$ in the $\boldsymbol{R}$th unit cell of the supercell. Wannier states for the same α may differ only in their position.

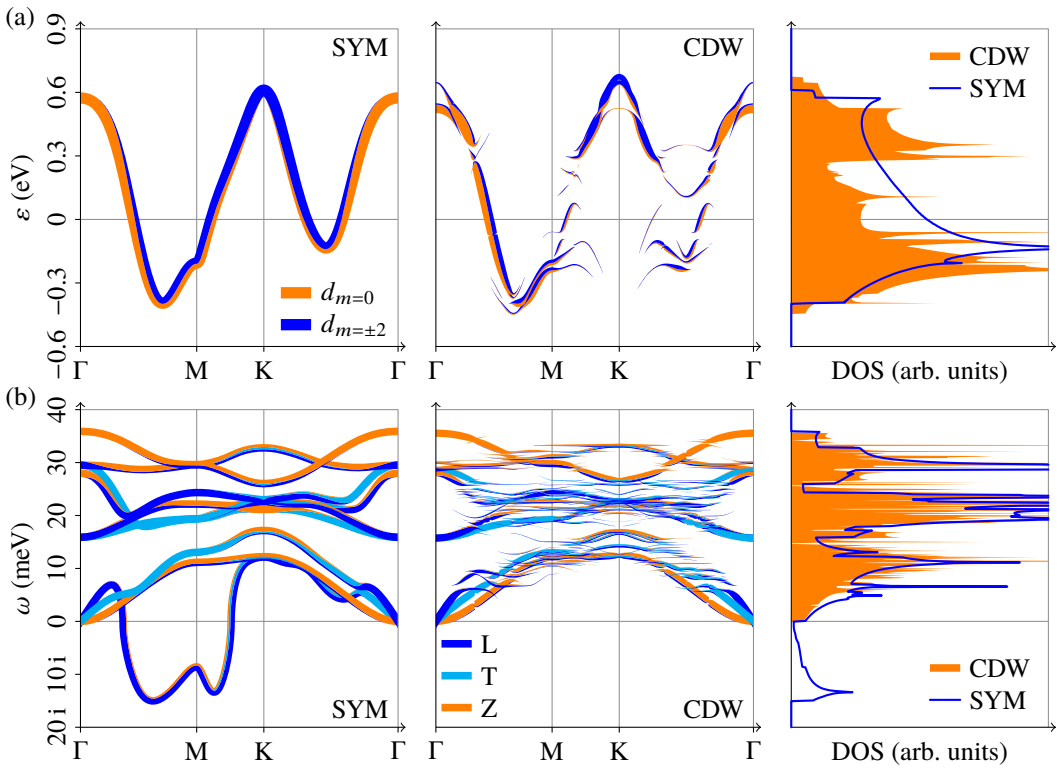

Figure 3.3: (a) Electron and (b) phonon dispersions and DOS of 1H-$NbSe_2$ in the symmetric (SYM) and 3×3 CDW phase. All band structures are shown along a path through the large BZ of the symmetric structure. For this, the band structures of the CDW phase have been unfolded, where the linewidth indicates the overlap with eigenstates of the symmetric phase (cf. Eq. 3.3). The computational parameters are as in Sec. 7.3. For the *ab initio* calculations in the CDW phase, we used only 3×3 $\boldsymbol{q}$ and 6×6 $\boldsymbol{k}$ points. The displayed data has been Fourier-interpolated. See Fig. 4d of Ref. 21 and Fig. 1a of Ref. 164 for equivalents of the central panels above.

Thus defined, the weights at a given $\boldsymbol{k}$ point add up to the number of original bands,

$$\sum_n w_{\boldsymbol{k}n} = \sum_{mn} |\langle \psi^{\mathrm{SYM}}_{\boldsymbol{k}m} | \psi^{\mathrm{CDW}}_{\boldsymbol{k}n} \rangle|^2 = \sum_{mn} \langle \psi^{\mathrm{SYM}}_{\boldsymbol{k}m} | \psi^{\mathrm{CDW}}_{\boldsymbol{k}n} \rangle \langle \psi^{\mathrm{CDW}}_{\boldsymbol{k}n} | \psi^{\mathrm{SYM}}_{\boldsymbol{k}m} \rangle$$
$$= \sum_m \langle \psi^{\mathrm{SYM}}_{\boldsymbol{k}m} | \psi^{\mathrm{SYM}}_{\boldsymbol{k}m} \rangle = \sum_m 1. \quad (3.4)$$

Analogous formulas hold for the unfolding of phonon dispersions. Instead of Bloch states represented in the basis of Wannier states, we then work with phonon eigenvectors in the basis of Cartesian atomic displacements.

An alternative representation of the same data is given in Fig. 3.4. Here, we consistently plot along a path through the smaller BZ of the CDW structure. Then, instead of unfolding the CDW bands onto the larger BZ of the symmetric phase, we have to fold the bands of the symmetric phase back onto the smaller CDW BZ.[2] This process is however straightforward.

The *ab initio* calculation of the phonons of 1H-$NbSe_2$ in the CDW phase has taken about 15 000 processor hours, despite the fact that we only used a small $\boldsymbol{q}$ resolution of 3×3 points (which makes three irreducible $\boldsymbol{q}$ points.) This shows that studies of, e.g., superconductivity in the distorted phase [21] are computationally very challenging and the use of models instead can be worthwhile. Again, the idea is to set up the model in the symmetric phase, where the *ab initio* calculations are cheap, and describe the phase transition in the model framework.

[2]The term "fold" is actually misleading. We rather *shift* bands from neighboring BZs to the first BZ.

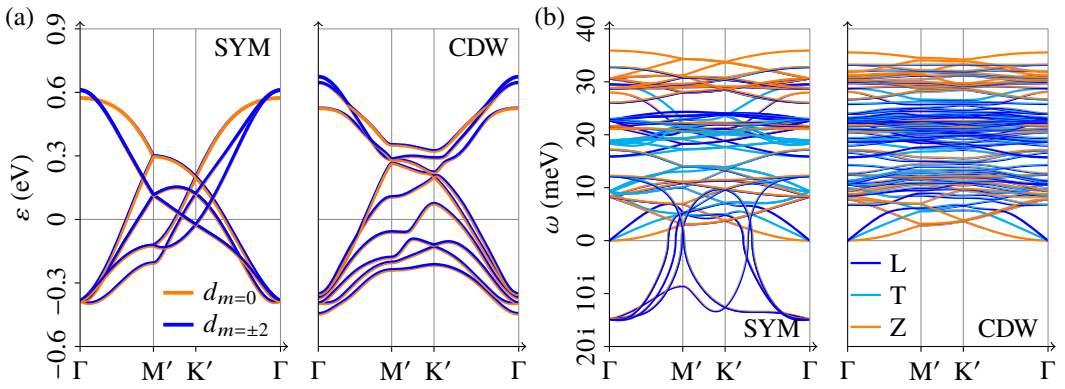

Figure 3.4: (a) Electron and (b) phonon dispersions of 1H-$NbSe_2$ in the symmetric and 3×3 CDW phase. The bands of the symmetric phase have been folded back from the large BZ of the simple unit cell onto the small BZ of the 3×3 supercell. The computational parameters are as in Fig. 3.3.

The displacements of the PLD can be expressed as a linear combination of phononic eigenmodes from all Γ points of the supercell, here denoted as Γ′, which lie inside the BZ of the original unit cell. *[We thank Erik van Loon for pointing this out.]* The transform of the displacement pattern from the Cartesian basis into the basis of eigenmodes is unitary; the expansion coefficients are simple scalar products.

In our example of the 3×3 CDW in 1H-$NbSe_2$, we have nine potentially relevant Γ′ points, namely Γ, both K points, and the six images of $\boldsymbol{q} = 2/3\,\mathrm{M}$ (of the original BZ). Neglecting anharmonic effects, we only have contributions from unstable modes, i.e., from the LA mode at the six images of $\boldsymbol{q} = 2/3\,\mathrm{M}$. Choosing a gauge where the components of the phonon eigenvector belonging to the transition-metal atoms are real, we find (cf. Eq. 2.65)

$$u_{\boldsymbol{R}i} \propto \frac{1}{\sqrt{M_i}} \sum_{\eta=1}^{6} c_\eta e_{\boldsymbol{q}_\eta i\mathrm{LA}} \mathrm{e}^{-\mathrm{i}\boldsymbol{q}_\eta \boldsymbol{R}}, \tag{3.5a}$$

$$\boldsymbol{c} = \mathrm{e}^{\mathrm{i}\pi(2,1,-7,-2,-1,7)/9}, \tag{3.5b}$$

$$\boldsymbol{q} = (\boldsymbol{b}_1, \boldsymbol{b}_2, \boldsymbol{b}_2 - \boldsymbol{b}_1, -\boldsymbol{b}_1, -\boldsymbol{b}_2, \boldsymbol{b}_1 - \boldsymbol{b}_2)/3. \tag{3.5c}$$

Here, we have an angle of 60° between the reciprocal basis vectors $\boldsymbol{b}_1$ and $\boldsymbol{b}_2$. The latter points in the same direction as the vector from the Nb atom to the (in-plane projection of the) Se atoms in the same unit cell. The error from neglecting the remaining $\boldsymbol{q}$ points is small. In some strongly anharmonic materials, it might be necessary to include contributions from phonon modes that are stable in DFPT to satisfactorily reproduce the CDW displacements.

3.2 Superconductivity

Superconductivity was discovered in 1911 by the Dutch low-temperature physicist Kamerlingh Onnes [187], when he discovered that the electric resistivity of mercury drops to zero at a critical temperature $T_\mathrm{c} \approx 4\,\mathrm{K}$. This was not quite unexpected at that time, albeit for the wrong reasons. It was known that the electric current is hindered by scattering with the lattice. As a consequence, freezing the lattice could indeed allow the electrons to move freely (provided that the electrons themselves are not frozen at the same time) [188]. Later, it would turn out that it is precisely the lattice vibrations that drive superconductivity. The misconception became evident at the latest in 1933, when Meißner and Ochsenfeld found superconductors to be perfect diamagnets [189], which expel magnetic fields up to a critical strength under *any* conditions, i.e., not via induction as in ideal normal conductors.

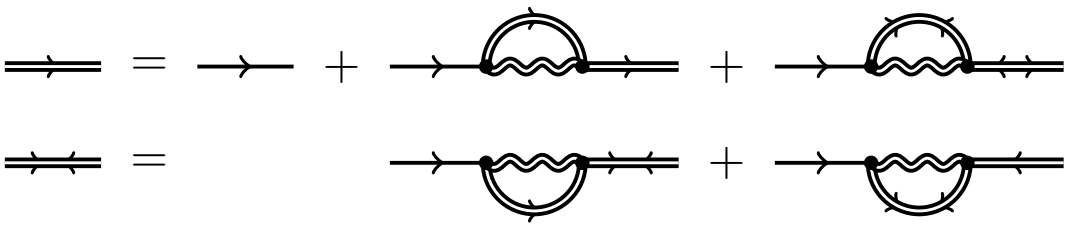

Figure 3.5: Feynman diagrams of Eliashberg theory.

Early theories of superconductivity include the macroscopic theory by London and London from 1935 [190] and the phenomenological theory based on the idea of an *order parameter* by Ginzburg and Landau from 1950 [191]. In the same year, the discovery of the isotope effect [192, 193] finally brought the role of the lattice vibrations into focus and lead Fröhlich to his field-theoretical description of electrons that are object to an effective attraction mediated by lattice vibrations [194, 195]: One electron attracts the surrounding nuclei and the accumulated positive charge attracts another electron in turn. This results in a formation of Cooper pairs [196] of electrons, whose formation is favored for time-reversed partners (opposite momentum and spin). The pairs have bosonic character and collapse into a Bose–Einstein condensate, leaving a gap at the Fermi level. Based on this idea, Bardeen, Cooper, and Schrieffer (BCS) developed their theory of superconductivity in 1957 [95, 197]. A generalization with respect to the *retarded* nature of the phonon-mediated interaction was developed by Eliashberg in 1960 [198].

The pairing mechanism is not restricted to a phonon-mediated interaction. Stimulating the search for ever-higher transition temperatures T_c, which would greatly facilitate the technological application of superconductivity, in 1986, Bednorz and Müller were the first to find $T_c > 30\,\mathrm{K}$ in a member of the family of cuprates [58]. The exact origin of these *unconventional* superconductors is still a matter of debate. More recently, in 2006, another class of unconventional superconductors, the iron-based superconductors, has been discovered by Kamihara *et al.* [199, 200]. By 2019, the highest transition temperature is $T_c \approx -23\,^\circ\mathrm{C}$—almost room temperature—, observed in LaH_{10} under high pressure by Drozdov *et al.* [57]. Hydrides are, again, conventional superconductors.

In this section, we will consider some aspects of the Eliashberg theory of conventional superconductivity [198], with a focus of the role of the electronic bandwidth. For in-depth explanations of the discussed formulas, we refer to the review by Allen and Mitrović [201].

3.2.1 Eliashberg theory

The Eliashberg theory of superconductivity [198] is based on a diagrammatic representation of the dynamic electronic self-energy, and thus explicitly takes the retardation of the phonon-mediated interaction into account. The diagrams of the Dyson equation for the electronic Green function are shown in Fig. 3.5. They are formally similar to the diagram of the GW approximation [202], where the Coulomb interaction is replaced with the phonons and the EPC. Furthermore, besides the normal bare and screened propagators, we have the *anomalous* Gor'kov Green functions (with two in- or outgoing arrows) [203]. They are associated to the creation and annihilation of Cooper pairs. They vanish in the normal state and are related to the gap in the superconducting state, and thus they play the role of an order parameter. As a consequence, there is no perturbative solution to the problem. (Contributions to all finite orders vanish since the noninteracting anomalous propagator is zero.) Instead, the equations (derived as if the perturbation series existed) have to be solved self-consistently.

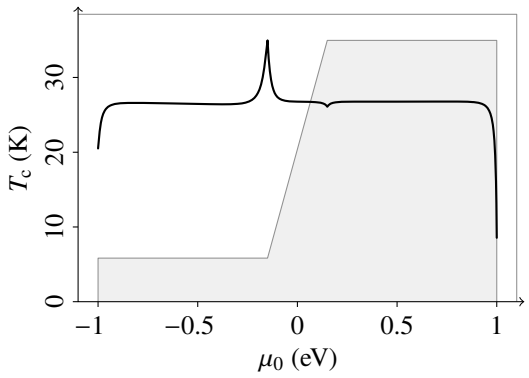

Figure 3.6: Critical temperature T_c from local Eliashberg equations (Eq. 3.6) as a function of the normal-state chemical potential for a steplike DOS (cf. Ref. 204). We used an EPC strength $\lambda = 1$, no Coulomb interaction $\mu = 0$, a phonon frequency $\langle\omega\rangle = 20\,\text{meV}$, and a Matsubara cutoff $\omega_c = 100\,\langle\omega\rangle$. Across a slope that extends over 0.3 eV, the DOS increases sixfold. Calculated with EBMB [205] (cf. App. A.7.1).

3.2.1.1 Local Eliashberg equations

Using the Nambu formalism [127], the electronic self-energy in the Eliashberg theory can be written in terms of Pauli matrices as $\Sigma_n = \mathrm{i}(\omega_n - \widetilde{\omega}_n)\boldsymbol{\sigma}_0 + \varphi_n\boldsymbol{\sigma}_1 + \chi_n\boldsymbol{\sigma}_3$ with the renormalized frequency $\widetilde{\omega}_n$, the order parameter φ_n, and the energy shift χ_n, which all depend on fermionic Matsubara frequencies $\omega_n = (2n+1)\pi T$. The superconducting gap is given by $\Delta_n = \varphi_n\omega_n/\widetilde{\omega}_n$. For simplicity, all $\boldsymbol{k}$ dependencies have been neglected. The Dyson equation yields a set of equations, the local *Eliashberg equations* (cf. Eq. 4.7 of Ref. 206), which have to be solved self-consistently for the components of the electronic self-energy,

$$\widetilde{\omega}_n = \omega_n + T\sum_m \int_{-\infty}^{\infty} \mathrm{d}\varepsilon \frac{N(\varepsilon)}{N(0)} \frac{\widetilde{\omega}_m}{\Theta_m(\varepsilon)} \lambda_{n-m}, \tag{3.6a}$$

$$\varphi_n = T\sum_m \int_{-\infty}^{\infty} \mathrm{d}\varepsilon \frac{N(\varepsilon)}{N(0)} \frac{\varphi_m}{\Theta_m(\varepsilon)} [\lambda_{n-m} - \mu], \tag{3.6b}$$

$$\chi_n = -T\sum_m \int_{-\infty}^{\infty} \mathrm{d}\varepsilon \frac{N(\varepsilon)}{N(0)} \frac{\varepsilon + \chi_m}{\Theta_n(\varepsilon)} \lambda_{n-m}, \tag{3.6c}$$

with the common denominator $\Theta_n(\varepsilon) = \widetilde{\omega}_n^2 + \varphi_n^2 + [\varepsilon + \chi_n]^2$. Here, $\mu = N(0)\langle W\rangle$ is the effective (static) Coulomb interaction opposing superconductivity, λ is the effective EPC strength, and $N(\varepsilon)$ is the DOS per spin and unit cell. Both μ and λ are proportional to the DOS at the Fermi level $N(0)$. While writing Ref. 206, we implemented Eq. 3.6 (generalized to multiple bands) in the program EBMB [205], briefly described in App. A.7.1.

We define the *Eliashberg spectral function* (Eq. 1 of Ref. 207),

$$\alpha^2F(\omega) = N(0)\frac{\sum_{\boldsymbol{q}\nu\boldsymbol{k}mn} |g^2_{\boldsymbol{q}\nu\boldsymbol{k}mn}|\delta(\omega_{\boldsymbol{q}\nu} - \omega)\delta(\varepsilon_{\boldsymbol{k}n})\delta(\varepsilon_{\boldsymbol{k}+\boldsymbol{q}m})}{\sum_{\boldsymbol{q}\boldsymbol{k}mn} \delta(\varepsilon_{\boldsymbol{k}n})\delta(\varepsilon_{\boldsymbol{k}+\boldsymbol{q}m})}, \tag{3.7}$$

which is the phonon DOS ("F") weighted with the double Fermi-surface average of the squared EPC ("α^2"). An example for Sr_2RuO_4 is given in App. D.5. With the bosonic Matsubara frequencies $\nu_n = 2n\pi T$, we can then write (Eq. 10 of Ref. 207)

$$\lambda_n = 2\int_0^{\infty} \mathrm{d}\omega \frac{\omega}{\omega^2 + \nu_n^2} \alpha^2F(\omega) \tag{3.8}$$

and define the scalar EPC strength $\lambda \equiv \lambda_0$. Here, we will work with a single effective phonon frequency $\langle\omega\rangle$ ("Einstein spectrum"). This allows us to write Eq. 3.8 as $\lambda_n = \lambda/(1+\nu_n^2/\langle\omega\rangle^2)$. An established choice for $\langle\omega\rangle$ is the logarithmic average (Eq. 30 of Ref. 207)

$$\langle\omega\rangle = \exp\left[\frac{2}{\lambda}\int_0^{\infty} \frac{\mathrm{d}\omega}{\omega} \alpha^2F(\omega)\log(\omega)\right]. \tag{3.9}$$

Carrying out the ω integration, we can also write

$$\lambda = N(0)\frac{\sum_{\boldsymbol{q}\nu\boldsymbol{k}mn}\frac{|d_{\boldsymbol{q}\nu\boldsymbol{k}mn}|^2}{\omega_{\boldsymbol{q}\nu}^2}\delta(\varepsilon_{\boldsymbol{k}n})\delta(\varepsilon_{\boldsymbol{k}+\boldsymbol{q}m})}{\sum_{\boldsymbol{q}\boldsymbol{k}mn}\delta(\varepsilon_{\boldsymbol{k}n})\delta(\varepsilon_{\boldsymbol{k}+\boldsymbol{q}m})}, \tag{3.10a}$$

$$\log\langle\omega\rangle = \frac{\sum_{\boldsymbol{q}\nu\boldsymbol{k}mn}\log(\omega_{\boldsymbol{q}\nu})\frac{|d_{\boldsymbol{q}\nu\boldsymbol{k}mn}|^2}{\omega_{\boldsymbol{q}\nu}^2}\delta(\varepsilon_{\boldsymbol{k}n})\delta(\varepsilon_{\boldsymbol{k}+\boldsymbol{q}m})}{\sum_{\boldsymbol{q}\nu\boldsymbol{k}mn}\frac{|d_{\boldsymbol{q}\nu\boldsymbol{k}mn}|^2}{\omega_{\boldsymbol{q}\nu}^2}\delta(\varepsilon_{\boldsymbol{k}n})\delta(\varepsilon_{\boldsymbol{k}+\boldsymbol{q}m})}. \tag{3.10b}$$

where the $d^2 = 2\omega g^2$ (cf. Eq. 2.133) does *not* depend on ω and is an energy to the power of three. The expression in Eq. 3.10a is very instructive because it clearly shows why λ is the effective EPC. It is simply the most relevant part of the EPC (on the Fermi surface), rescaled to the energy scales of the electrons ($N(0)$ is inversely proportional to the electronic bandwidth) and phonons (changes in ω^2 are proportional to d^2).

The double Fermi-surface averages are numerically hard to converge. Similar to the tetrahedron method for the calculation of the DOS (cf. App. B.3.1), we can however apply a method, where we just average over the few points (in 2D) where the Fermi surfaces at $\boldsymbol{k}$ and $\boldsymbol{k}+\boldsymbol{q}$ intersect, as visualized in Fig. B.3 of App. B.3.2.

In practical calculations, the summation over Matsubara frequencies ω_n must be restricted to some cutoff frequency ω_c, such that $|\omega_n| < \omega_c$. This requires special care in relation to the constant Coulomb interaction μ, which has to be replaced by a rescaled μ^* to obtain reasonable convergence with ω_c. For sufficiently large cutoffs, we have (Eq. 11 of Ref. 208 and Eq. 4.17 of Ref. 206),

$$\frac{1}{\mu^*} = \frac{1}{\mu} + \frac{1}{\pi}\int_{-\infty}^{\infty}\mathrm{d}\varepsilon\frac{N(\varepsilon)}{N(0)}\frac{1}{\varepsilon}\arctan\frac{\varepsilon}{\omega_c}. \tag{3.11}$$

The Eliashberg equations (Eq. 3.6) can be solved for a fixed temperature T, usually under the constraint that the occupation number

$$n = 1 - 2T\sum_m\int_{-\infty}^{\infty}\mathrm{d}\varepsilon\, N(\varepsilon)\frac{\varepsilon+\chi_m}{\Theta_m(\varepsilon)} \in [0,2] \tag{3.12}$$

is conserved. If the resulting φ_n is nonzero, we are in the superconducting state.

Figure 3.6 shows the thus determined critical temperature T_c for a steplike model DOS. This example emphasizes the relevance of the fact that $N(0)$ is included in the definition of the coupling strengths μ and λ. In energy regions, where the DOS *exactly* at the Fermi level is not representative for the DOS in the immediate surroundings, e.g., at the onset of the step, T_c may differ significantly from what we find in regions of an approximately constant DOS.

3.2.1.2 McMillan's formula

A common approximate expression for the critical temperature of Eliashberg theory is given by McMillan's formula [209, 210],

$$T_c = \frac{\langle\omega\rangle}{1.20}\exp\left[\frac{-1.04(1+\lambda)}{\lambda - 0.62\lambda\mu^* - \mu^*}\right], \tag{3.13}$$

where Morel and Anderson's Coulomb pseudopotential [211] is determined by the ratio of the electronic and phononic energy scales (natural cutoffs in the respective spectra),

$$\frac{1}{\mu^*} = \frac{1}{\mu} + \log\left[\frac{\varepsilon_c}{\omega_c}\right]. \tag{3.14}$$

Interestingly, McMillan derived the constants in his formula via a fit to Eliashberg results for a constant electronic DOS and the special case of the phononic DOS of niobium [209]. Nevertheless, the formula is *universally* used to estimate the T_c of superconductors. This is justified because the approximations involved in the derivation of Eliashberg theory and finally McMillan's formula by far outweigh the influence of the fine tuning of parameters.

3.2.1.3 Linearized finite-bandwidth Eliashberg equations

To investigate the importance of the bandwidth, we now consider a special case of the Eliashberg equations. First, we assume that we are at the critical temperature where $\varphi = 0$ by definition. Next, we assume that the DOS is constant in an interval $[-\varepsilon_c, \varepsilon_c]$ centered at the Fermi level and zero otherwise. By symmetry, this implies that the energy shift χ vanishes.

Using the relation

$$\int_{-\varepsilon_c}^{\varepsilon_c} \mathrm{d}\varepsilon \, \frac{\omega}{\omega^2 + \varepsilon^2} = 2 \arctan\left[\frac{\varepsilon_c}{\omega}\right], \tag{3.15}$$

we find the linearized, bandwidth-dependent Eliashberg equations (cf. Eq. 13 of Ref. 212)

$$\widetilde{\omega}_n = \omega_n + 2T \sum_m \arctan\left[\frac{\varepsilon_c}{\widetilde{\omega}_m}\right] \lambda_{n-m}, \tag{3.16a}$$

$$\varphi_n = 2T \sum_m \frac{\varphi_m}{\widetilde{\omega}_m} \arctan\left[\frac{\varepsilon_c}{\widetilde{\omega}_m}\right] (\lambda_{n-m} - \mu). \tag{3.16b}$$

Since $\widetilde{\omega}_n$ does not depend on φ_n, for any temperature T, we can solve Eq. 3.16a first. Then, the equation for φ can be written as (cf. Eq. 5 of Ref. 208)

$$\varphi_n = \sum_m K_{nm}(T) \varphi_m \quad \text{with} \quad K_{nm}(T) = \frac{2T}{\widetilde{\omega}_m} \arctan\left[\frac{\varepsilon_c}{\widetilde{\omega}_m}\right] (\lambda_{n-m} - \mu), \tag{3.17}$$

which is an eigenvalue equation for the temperature-dependent kernel $K(T)$ for the eigenvalue 1. Thus, the critical temperature T_c is the temperature for which the (largest) eigenvalue of $K(T)$ is unity. The largest eigenvalue of $K(T)$ can be conveniently determined with the power method, which allows to efficiently update the eigenvalue for slightly modified $K(T)$. In turn, for T we can set up a fixed-point equation like $T = T \cdot \kappa^\eta(T)$, where $\kappa(T)$ is the largest eigenvalue of $K(T)$ and η is an exponent chosen such that the fixed-point equation converges. Similar equations can be written down for λ, μ, or $\langle\omega\rangle$ instead of T, if a set of critical parameters for a given T_c is searched for. Thus, the complete algorithm to find a critical value x_c for all other parameters fixed is as follows:

While x changes:

Calculate $K(x)$.

While $\boldsymbol{\varphi}$ changes:

$$\boldsymbol{\varphi} \leftarrow [K(x) + \alpha]\boldsymbol{\varphi}/|\boldsymbol{\varphi}|. \tag{3.18a}$$

$$x \leftarrow x \cdot (|\boldsymbol{\varphi}| - \alpha)^\eta. \tag{3.18b}$$

Here, α shifts the spectrum of K to ensure that there are no negative eigenvalues with an absolute value larger than the largest positive eigenvalue searched for. To avoid an oscillation around the solution, it might also help to multiply η by a factor, say 0.99, after each use. Empirical initial values, which have been shown to yield excellent convergence, are $\eta = 2.3$ for T, -1.3 for λ, 4 for μ, -2.3 for $\langle\omega\rangle$, and -22 for ε_c as the variable.

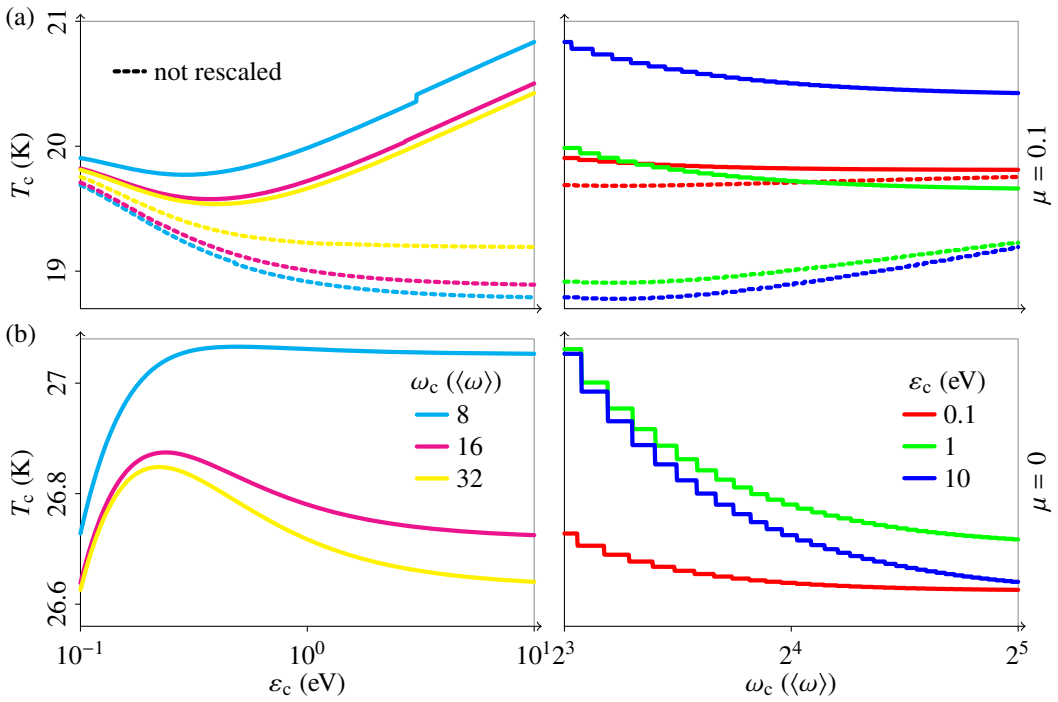

Figure 3.7: Critical temperature T_c from finite-bandwidth Eliashberg equations (Eq. 3.16) as a function of the Matsubara cutoff ω_c and the electronic cutoff ε_c for an effective Coulomb interaction (a) $\mu = 0.1$ and (b) $\mu = 0$. The effective EPC strength $\lambda = 1$ and phonon frequency $\langle\omega\rangle = 20\,\text{meV}$ are kept fixed. The steps arise from the fact that the (integer) number of Matsubara frequencies below ω_c depends on the temperature. Calculated with EBBW [213] (cf. App. A.7.2).

Finally, Eq. 3.11 for the finite-bandwidth case becomes

$$\frac{1}{\mu^*} = \frac{1}{\mu} + \frac{2}{\pi}\int_0^{\frac{\varepsilon_c}{\omega_c}} \frac{\mathrm{d}x}{x}\arctan(x), \tag{3.19}$$

which can be evaluated via a fast-converging[3] series,

$$\int_0^r \frac{\mathrm{d}x}{x}\arctan(x) = \begin{cases} \sum_{n=0}^{\infty}(-1)^n \frac{r^{2n+1}}{(2n+1)^2} & \text{for } r \le 1, \\ \sum_{n=0}^{\infty}(-1)^n \frac{r^{-(2n+1)}}{(2n+1)^2} + \frac{\pi}{2}\log(r) & \text{for } r > 1. \end{cases} \tag{3.20}$$

For large r, only the $\log(r)$ term survives and we reproduce the well-known rescaling formula $1/\mu^* = 1/\mu + \log(\varepsilon_c/\omega_c)$ for the pseudopotential to be used in McMillan's formula (Eq. 3.14).[4]

This formula tells us that the convergence with the Matsubara cutoff ω_c worsens for large bandwidths $2\varepsilon_c$ if we do not care about rescaling of the static Coulomb interaction. Conversely, rescaling becomes particularly important for large bandwidths. In the limit of an infinite bandwidth, there is no convergence without rescaling. In fact, the "standard" formulation of the Eliashberg equations (cf. Eqs. 2.1 and 2.2 of Ref. 215) relies on the assumption of a constant DOS of infinite bandwidth [212].[5] To obtain reasonable results within this approximation, we must either rescale $\mu \to \mu^*$ according to Eq. 3.14 or choose the "natural cutoff" $\omega_c = \varepsilon_c$ for which $\mu^* = \mu$. In other words, we cannot simply plug a given μ^* into our standard Eliashberg equations and expect reasonable results for "large enough" ω_c.

[3] Except for $r = \varepsilon_c/\omega_c \approx 1$, where the convergence is not optimal.

[4] If we go beyond half-filling, the same rescaling formula hold if we replace ε_c by $\sqrt{\varepsilon_+\varepsilon_-}$, where $\varepsilon_\pm$ is the energy difference between the chemical potential and the (upper) lower band edge (Eq. 14 of Ref. 214).

[5] In this case, calculating the kernel in Eq. 3.17 is no longer a self-consistency problem (cf. Eq. 6 of Ref. 208).

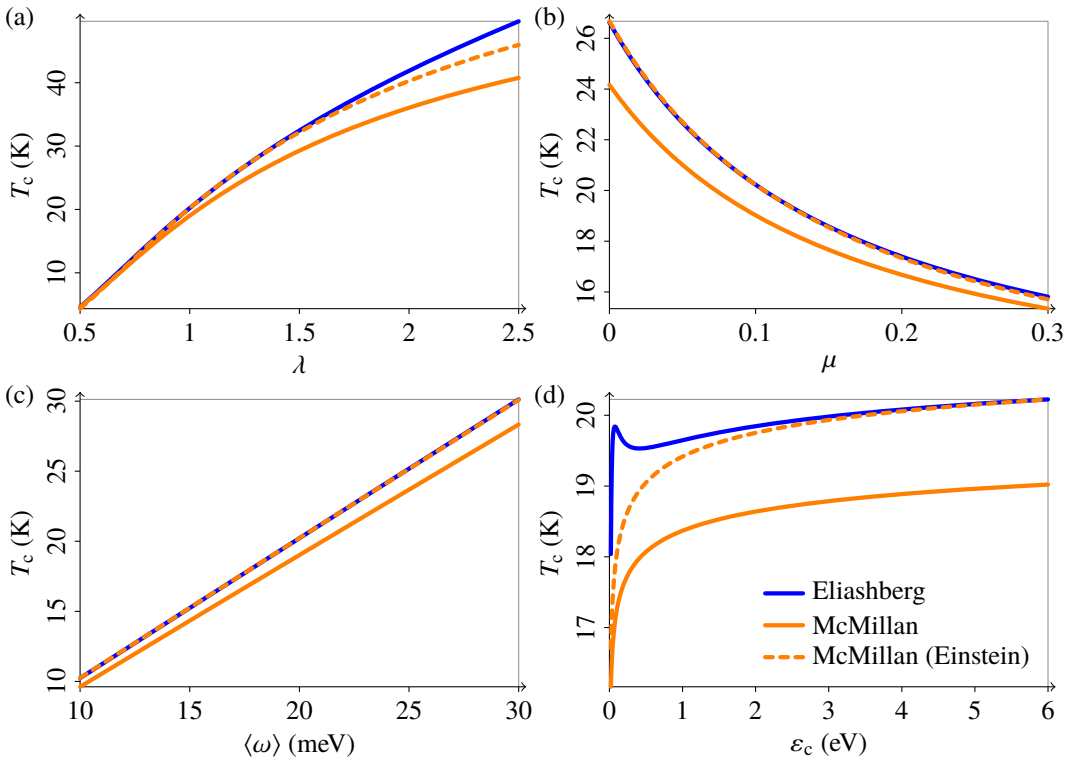

Figure 3.8: Critical temperature T_c from finite-bandwidth Eliashberg equations (Eq. 3.16) and McMillan's formula (Eq. 3.13) as a function of (a) the EPC strength λ, (b) the Coulomb interaction μ, (c) the phonon frequency $\langle\omega\rangle$, and (d) the electronic cutoff ε_c for $\lambda = 1$, $\mu = 0.1$, $\langle\omega\rangle = 20\,\text{meV}$, $\varepsilon_c = 6\,\text{eV}$, and $\omega_c = 100\,\langle\omega\rangle$ if not stated otherwise. Calculated with EBBW [213] (cf. App. A.7.2).

We implemented the finite-bandwidth Eliashberg equations in the PYTHON module EBBW [213], which is documented line by line in App. A.7.2. In the following, we will briefly present some convergence tests and comparisons to results from McMillan's formula.

Figure 3.7 shows results for the critical temperature T_c as a function of the (artificial) Matsubara cutoff ω_c and the (natural) electronic cutoff ε_c. In Fig. 3.7a, we use a nonzero Coulomb interaction μ. If we rescale μ, T_c is an increasing function of ε_c for large values of ε_c—remember that μ is proportional to the DOS $N(0)$ at the Fermi level—and converges well with increasing ω_c. However, if we do not rescale μ, T_c goes to a constant for large ε_c and converges slowly with increasing ω_c, especially for large ε_c. In Fig. 3.7b, we consider the case $\mu = 0$. Here, we do not have to worry about rescaling. We find that there is an intermediate value of ε_c for which T_c is maximal and that we overestimate T_c for small ω_c.

In Fig. 3.8, we compare the results of the Eliashberg equations for a finite bandwidth to the results from McMillan's formula. In the latter case, the bandwidth $2\varepsilon_c$ only enters via the rescaled pseudopotential (Eq. 3.14), where we set $\omega_c = \langle\omega\rangle$. We find that T_c from the Eliashberg equations is always larger than the corresponding value from McMillan's formula, which can however be traced back to the fact that we work with an Einstein spectrum $\delta(\langle\omega\rangle - \omega)$, while McMillan used the phonon DOS of niobium. It has been shown [207] that an Einstein spectrum maximizes T_c (for fixed integrated parameters λ and $\langle\omega\rangle$). Refitting the numerical constants in McMillan's equation to an Einstein spectrum [206] yields the replacements $1.20 \to 0.95$, $1.04 \to 1.11$, and $0.62 \to 0.74$ and an overall improved agreement. Deviations remain for large λ, where McMillan's formula is known to fail [207], and for small ε_c, where, on the one hand, changes in the DOS close to the Fermi become important and, on the other hand, the formula for the rescaled pseudopotential does not hold.

Chapter 4

Two-dimensional materials

Crystals are like people: it is the defects in them which tend to make them interesting!

—Sir Colin Humphreys [216]

The field of 2D materials was established in 2004, when Novoselov *et al.* succeeded to obtain freestanding, strictly 2D crystals via exfoliation from a variety of long-known bulk crystals [5, 219]. Driven by the prospect of unprecedented electronic, optical, and elastic properties—often markedly different from the those of the corresponding bulk systems—the field has been continuously growing ever since.

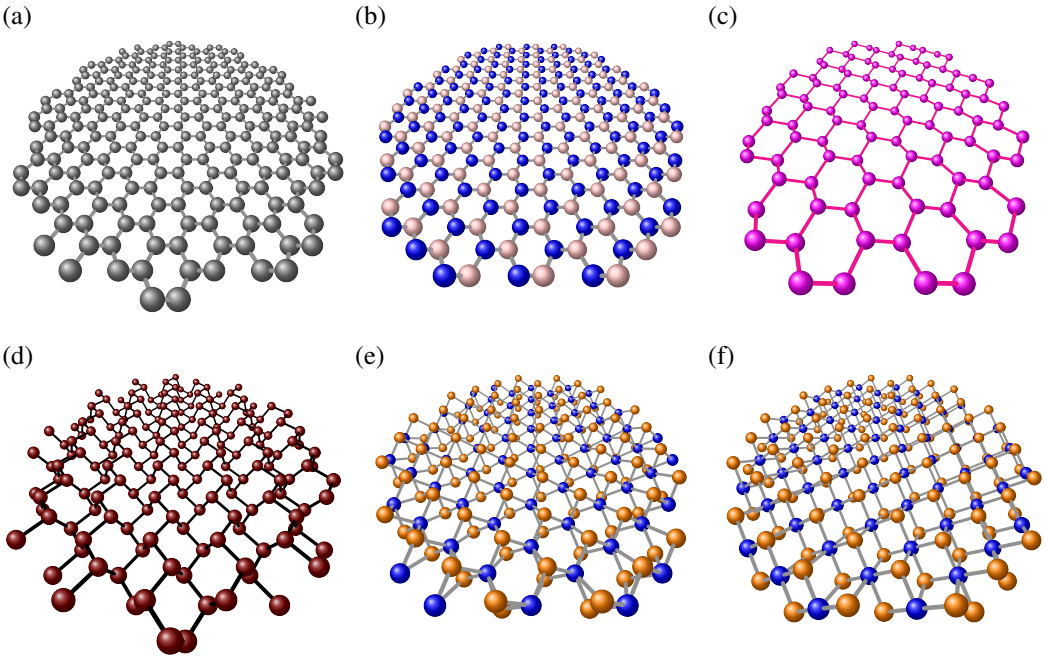

Figure 4.1: Crystal structures of (a) graphene, (b) hexagonal boron nitride, (c) germanene, (d) black phosphorus or phosphorene, (e) TP TMDCs, and (f) octahedral TMDCs. The atomic coordinates stem from the curated data set *2D structures and layered materials* [217] hosted on *Materials Cloud*, except for the data shown in panel (c), which originates from *2DMatPedia* [218].

Today, the family of 2D materials includes CDW materials [8], flat-band systems [28, 29, 53, 220], Mott insulators [28, 29, 221, 222], topological insulators [223], magnets [10, 224], metals [225], piezoelectrics [226], semiconductors [227], Weyl semimetals [228], conventional superconductors [7, 19], Fe-based superconductors [25, 229, 230], and light-induced superconductors [15, 231]. Applications encompass electronics [232], lubrication [233], optics [227], optoelectronics [234], quantum information technology [235, 236], spintronics [237], and valleytronics [237]. Proposed and realized devices are diodes [238], field-effect transistors [239], microprocessors [240], nanopores [241], phototransistors [242], printable electronics [232], single-photon emitters [235], and switches [240, 243, 244].

Many 2D materials are well established today, and they can be commercially obtained from the "Graphene Supermarket." Examples include—most prominently—graphene (Fig. 4.1a), the monolayer of graphite, whose exfoliation in 2004 [219] brought Geim and Novoselov the 2010 Nobel Pize [245]; the semiconductor MoS_2, which has long been known as a dry lubricant [233]; or the chemically inert hexagonal boron nitride (Fig. 4.1b), whose optically active defects may serve as single photon emitters [236]. But the search for new 2D materials continues and further examples range from phosphorene (Fig. 4.1d) via the metallic TMDCs (Figs. 4.1e and 4.1f) to very complex materials such as honeycomb lattices made out of (organic) molecules [246]. In App. D.4, we will discuss the example of the hypothetical 2D material CP_3 [247].

Besides large efforts to find new 2D materials experimentally, much effort is spent on this search on the theoretical side too. Here, one route is via computational exfoliation of well-known bulk materials. This way, the *Materials Cloud* project [217] has generated a database of more than 1000 promising 2D materials from analyzing more than 100 000 materials found in well-maintained databases such as the Inorganic Crystal Structure Database (ICSD) and the Crystallography Open Database (COD). Materials are classified into easily vs. potentially exfoliable structures. Interestingly, many candidates for exfoliation have trigonal symmetry. The probability that the 2D counterpart of a bulk material is stable is enhanced for small binding or exfoliation energies of the bulk and especially if the bulk consists of clearly distinguishable layers. Ideally, parts are only bond via weak van der Waals interactions. Here, it is particularly important that correct relaxed interlayer distances are obtained via adequate functionals and PPs. The state of the art of describing these dispersion interactions is via RPA [248]. Once a preselection is made, the stability can be verified via a DFPT calculation of the vibrational properties. Here, it is advisable to truncate the long-range Coulomb interaction in the vertical direction to avoid a coupling of layer images. Such a 2D version of DFPT [249] is, e.g., implemented in QE [39, 40].

2D materials can not only be obtained via exfoliation of layered bulk materials. Another way is via epitaxy. Depending on factors such as the temperature or the substrate, different phases of a material can be obtained [220, 250].

Whether a novel material is finally established in technological applications is also largely determined by the production cost. E.g., germanium, sole constituent of germanene (Fig. 4.1c), is usually recovered from extractive waste (as found, e.g., in tin mines in Bolivia) [251][1].

As opposed to bulk systems, 2D materials are surface-only and thus completely accessible from the outside. This allows for the easy manipulation of many material properties, either noninvasively through the choice of substrates [23–25] or dielectric environments [12, 149] or via, e.g., the deposition of adatoms [30, 111]. Often, the band gap increases when reducing the thickness to the monolayer [252].

[1] According to Castro Neto's talk at the 2017 Conference "Flatlands beyond Graphene" in Lausanne. Actually, many theoretical and experimental facts brought together in this chapter have been presented at this conference.

Another class of materials closely related to 2D materials are the (quasi) 1D *nanotubes*, hollow cylinders whose surface is basically a rolled up 2D layer. Carbon nanotubes are known for several decades [253]. As an example, (multiwall) WS_2 nanotubes might be useful to reinforce concrete [254], since they have a tensile strength of several GPa. The same material, when electrochemically doped, becomes superconducting below 5.8 K [255]. One step further, the (quasi) zero-dimensional *fullerenes* [256, 257] are hollow spheres whose surface is basically graphene. These 2D and 1D systems can also be seen as a real-world realization of periodic boundary conditions.

4.1 Properties of selected 2D materials

4.1.1 Graphene

Graphene (Fig. 4.1a) is the monolayer of graphite and the first and most prominent 2D material, obtained via exfoliation by Novoselov *et al.* in 2004 [219]. Its electronic and phononic band structures are shown in Fig. 2.9. One remarkable property is the conical, linear dispersion of the electrons at the Fermi level. It implies that the electrons behave like massless Dirac fermions (formally governed by the relativistic Dirac equation) [258].

Because of its vanishing band gap, in microelectronics, functionalized graphene (cf. App. D.1) can be used as a semiconductor in digital devices and as a metal in analogue devices [232]. (Usually, digital applications require larger band gaps than analogue ones.)

In 2018, graphene research enjoyed a revival, when Cao *et al.* discovered that the temperature- and doping-dependent phase diagram of a bilayer of graphene, twisted by a *magic* angle, features superconducting and Mott-insulating phases [28, 29]. More precisely, at a twist angle of about 1.1°, the moiré superstructure formed by the two layers gives rise to a flat hybridization band at the Fermi level. Via the temperature and both electron and hole doping, the system can be tuned into a superconductor, Mott insulator, or metal.

4.1.2 Transition-metal dichalcogenides

Material-wise, this work is largely focused on the TMDCs. Known since more than five decades as layered bulk materials [4], the more recent discovery of freestanding monolayers [5] has brought them back into focus. TMDCs occur in different compositions and geometries, but the most common stoichiometry is MX_2, where M is a transition-metal and X is a chalcogen atom, as highlighted in Fig. 4.2a.

Figures 4.2b and 4.2c show the electronic band structure of TP TMDCs monolayers, consisting of a hexagonal transition-metal layer sandwiched between two hexagonal chalcogen layers whose atoms are facing each other. Together, seen from above, they form a honeycomb lattice (Figs. 2.8 and 4.1e). Depending on whether the transition-metal atoms are from group V or VI of the periodic table, they are metallic or semiconducting.

In the metallic case shown in Fig. 4.2b, there is an isolated low-energy band of M-d character, which later in this work will often serve as our model subspace. The apparent energy minimum between Γ and K is actually a saddle point and leads to the Van Hove singularity (VHS) in the DOS (cf. App. C.2).

In the semiconducting case shown in Fig. 4.2c, the electron dispersion looks very similar, but now there is one additional electron in the unit cell and the former metallic band becomes completely filled. As a consequence, we have a band gap, usually between the maximum of the valence band at the K point and the minimum of the conduction band, which is found either at the K or Σ point, defining whether the band gap is direct or indirect [227].

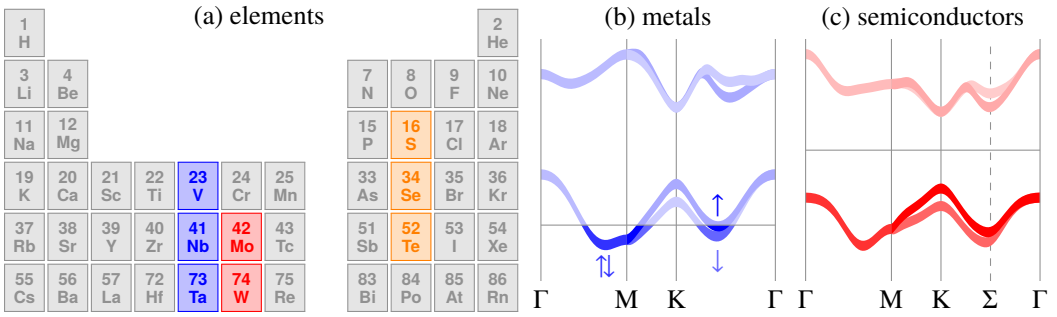

Figure 4.2: (a) Periodic table. Selected group-V and -VI transition metals (blue, red) and chalcogens (orange), which are typical constituents of layered TMDCs, are highlighted. (b, c) Exemplary band structures of (b) metallic group-V and (c) semiconducting group-VI TMDCs.

4.1.2.1 Polytypes

Further basic forms of TMDC monolayers exist, which are stoichiometric (MX_2) but differ in the atomic coordination (cf. Fig. 1 of Ref. 4). Besides the TP layer, the octahedral layer is very common, where one of the outer chalcogen planes is horizontally displaced such that the monolayer becomes inversion-symmetric (Fig. 4.1f). Here, distorted variants exists, which feature a modulation of the vertical chalcogen positions (cf. Figs. 4 and 5 of Ref. 4). Even more complicated coordinates have been predicted. One of them is the Haeckelite structure [259], shown to be dynamically stable in phonon calculations [260].

In multilayer systems, the symmetry is also determined by the *stacking* of the layers. Different stackings of differently coordinated monolayers yield a variety of *polytypes*. A good overview is found in Fig. 3 of the 1969 review by Wilson and Yoffe [4]. The TP polytype is usually stacked such that neighboring layers are rotated by 180° with respect to each other, which restores the inversion symmetry. Hence, in the out-of-plane direction the system is periodic after *two* layers. This polytype is accordingly referred to as 2H. (In this thesis, we use the nonstandard nomenclature 1H for TP *mono*layers.) Another polytype composed of TP building blocks is 3R, which is periodic after three layers. Here, the stacking is such that the inversion symmetry is broken for any number of layers [261]. The octahedral monolayers are usually stacked without any rotation or displacement and thus the unit cell contains a single layer only. This polytype is referred to as 1T—or 1T′ in the distorted case.

The electronic structure of different polytypes can differ significantly. For instance, the classification of group-V and group-VI as metals and insulators holds only for the TP polytypes. A particularly interesting example are 1T′-WTe_2 and 1T′-WSe_2, which have been found to be *topological insulators* [223, 262]. Transitions between polytypes are also possible; a recent example is the photo-induced transition between 1T- and 1T′-$MoTe_2$ [16].

4.1.2.2 Optics

The semiconducting TMDCs, which are not at the heart of this thesis, are interesting for optical applications. For example, the spin-polarized electronic band structure around the K and K′ points [263] (cf. Fig. 4.2c) leads to certain optical selection rules [237, 264]. This allows for spintronics applications and the existence of valley exciton–polaritons [265]. Furthermore, the two degenerate K and K′ valleys possess an exactly opposite Berry curvature, giving rise to the valley Hall effect [266]. First experimental observations of the valley Hall conductivity have been reported in Ref. 261.

Excitons in 2D are more tightly bond due to lack of screening of the Coulomb interaction [267]. However, band-structure calculations with DFT usually fail in the sense that the band gap is not correctly described. Since correct band gaps are essential for the description of excitons and optical properties, more precise theories such as GW are required in this case. Also, to obtain correct optical absorption spectra at finite temperatures, it might be necessary to include the EPC in the calculations [268].

Optical properties depend on the symmetries of the structures and, inversely, light can be used to measure the symmetries of a system. For example, second-harmonic generation, also known as frequency doubling, is only possible if there is no inversion symmetry. It can thus be largely influenced by strain [269, 270]. For the same reason, different polytypes have different optical properties.

4.1.3 Phosphorene

2D black phosphorus (Fig. 4.1d), also known as *phosphorene*, is a semiconductor with a band gap intermediate between graphene (infinitesimal gap) and TMDCs (large gap). The size of the gap can be modified via oxidation [271, 272], strain [226, 243], or the material thickness [273], resulting in highly tunable optical properties [234]. However, phosphorene is also very reactive. It oxidizes very easily because the trilateral bond of each phosphorus atom via sp^3 hybridization leaves one open pair per atom. One way to overcome this is via molecular passivation [273]. Here, a full coverage of the sample is needed and possible. Another way to suppress chemical reactions with the environment is via capping with an inert layer of hexagonal boron nitride [226].

4.2 Heterostructures

Finally, 2D materials of different chemical composition or polytype can be combined with each other in different spatial arrangements, resulting in various kinds of *heterostructures*.

In *lateral heterostructures,* the single layer itself is a "patchwork" of different materials. For example, two semiconducting TMDCs such as WSe_2 and MoS_2 can be grown epitaxially in adjacent regions of the same substrate, resulting in samples with spatially modulated emission spectra [274]. In such cases, we always have a particular band alignment, where valence- and conduction-band edges are shifted with respect to each other [275]. Band-gap modulations can also be induced in a homogeneous layer by manipulating the Coulomb interaction using structured dielectric environments [149]. Yet another type are lattice-matched heterostructures, where different TMDC polytypes (such as 1T, 2H, 3R) coexist in different spatial regions of the same sample [276].

Vertical heterostructures in turn are obtained from stacking different layers. Here, optically interesting samples can be obtained from combining two layers with a small lattice mismatch [235]. The latter leads to a long-wavelength moiré pattern accompanied by a spatial band gap modulation. This can influence, e.g., interlayer excitons, where electrons and holes favor different layers.

Finally, a very different kind of (in a broader sense) heterostructures are so-called *Janus monolayers*, where the upper and lower chalcogen layers of TMDCs are formed by different elements [277]. An exemplary production workflow of such materials is as follows: A pristine monolayer of MoS_2 is turned into MoSH via H_2 plasma stripping. In a second step, thermal selenization yields MoSSe. A variant are randomized monolayers fabricated at higher temperatures, where the different chalcogen elements are mixed disorderly.

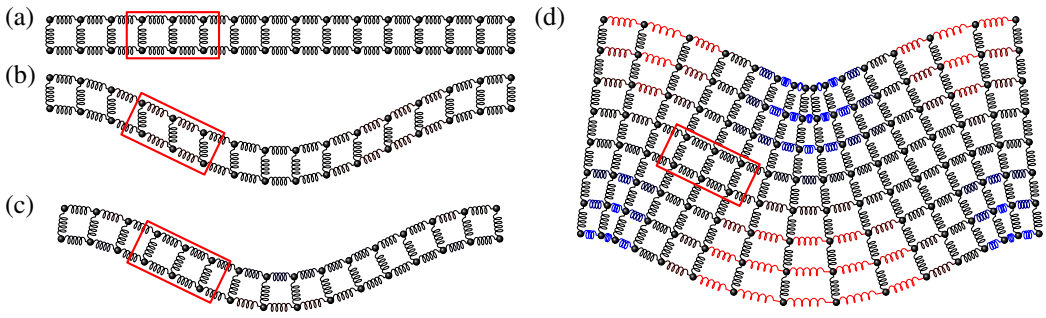

Figure 4.3: Buckling of (quasi) 2D materials. (a) As an example, we consider a monolayer composed of two atomic layers with an idealized short-range interaction in form of a spring coupling nearest neighbors. The red box serves as a reference. (b) An out-of-plane displacement streches the in-plane bonds and changes the bond angles. In the limit of a large wavelength–amplitude ratio, however, the restoring forces vanish. (c) Additional in-plane modes approximately recover the original bonds lengths and angles. For long wavelengths, close-ups suggest that the crystal is only rotated. Hence, since the interaction is short-range, the restoring forces are small even for reduced wavelength-amplitude ratios. (d) Such buckling is not possible in bulk materials, where the enhanced coordination of the atoms will always generate restoring forces.

4.3 Mermin–Wagner theorem

In this chapter, we have presented selected properties of a variety of 2D materials that have, without any doubt, been realized experimentally. However, there is a famous theoretical statement that, at least at the first glance, is in strong contrast to the existence of 2D materials. It is the *Mermin–Wagner theorem* [278–280], often additionally associated to the names Hohenberg [281], Berezinskiĭ [282], and Coleman [283]. It states that there is no long-range order in 2D and 1D systems with sufficiently short-range interactions at nonzero temperatures.

The theorem is tightly linked with the Goldstone theorem (Sec. 2.4.6). Since Goldstone bosons are gapless, a large number of them can be excited at no cost already at the smallest temperatures. In 2D and 1D systems, where stabilizing interactions with the surroundings are missing in one and two directions, respectively, this leads to logarithmically diverging fluctuations eventually destroying long-range order [278]. Even more, in the special cases of 2D and 1D crystalline order, we also have flexural Goldstone (phonon) modes with a quadratic instead of linear dispersion, enhancing the divergence [284].

In reality it turns out, however, that membrane-like (quasi) 2D structures are not completely unstable [245, 285], but rather stabilize in a buckled phase [286]. This results from the anharmonic coupling of bending (out-of-plane) and stretching (in-plane) modes [287]; the symmetry-breaking dislocations are “screened” due to the buckling of the surface [288]. The buckling of (quasi) 2D materials in visualized in Fig. 4.3.

Chapter 5

Phonon renormalization

Darkness born from darkness.
The beginning of all understanding.

—Lao Tse

After the digression on 2D materials, we now come to the crux of this thesis. As explained in Chap. 3, CDWs can be seen as softened phonon modes, i.e., lattice vibrations whose frequency vanishes, resulting in a static PLD of the lattice. Moreover, the cDFPT results in Chap. 2 have shown that reductions of phonon frequencies or "Kohn anomalies" (cf. App. D.2) are due to screening from the low-energy electrons in the case of the metallic TMDCs. Taken together, to understand CDW physics of metallic TMDCs and similar materials, we have to understand how the electrons influence or *renormalize* the phonons.

From the *ab initio* point of view, now that we know how to calculate the fully screened phonons from DFPT and the partially screened ones from cDFPT, we ask for the phonon self-energy that links them. The relevant formulas are presented below.

From the *technical* point of view, many details have to be considered, which might not become obvious from a superficial glance at these formulas. In the course of working on this thesis, we developed the software package ELPHMOD [289], documented in App. A.6, which facilitates the treatment of electron–phonon-coupled systems. In App. A.10, a minimal working example is given.

On the basis of the presented phonon renormalization, we were able to realize two projects on 1H-TaS_2, dealt with in later chapters. First, we calculated the phase diagram of lattice instabilities of this material (Chap. 8, Ref. 111). Second, we introduced the theoretical technique of fluctuation diagnostics [64, 65] to the field of electron–phonon physics, which allowed us to investigate the origin behind the observed CDW phases (Chap. 9, Ref. 86).

5.1 Random-phase approximation

In second-order perturbation theory (cf. App. C.4), the electron-induced change of the phonons can be written using Feynman diagrams as

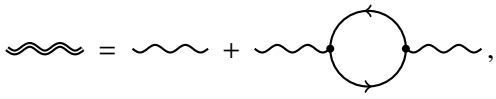

(5.1)

where the single (double) wiggly lines, the arrow lines, and the black dots represent the bare (screened) phonons, the electrons, and the bare EPC. Further similar processes are possible,

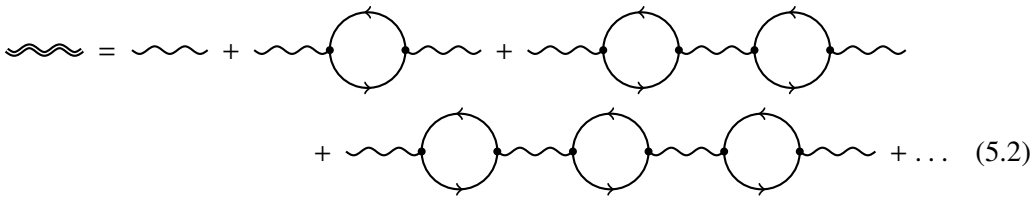

(5.2)

Recognizing a geometric series, this can be rewritten as the self-consistent Dyson equation

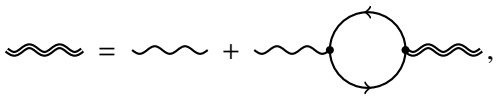

(5.3)

where the electron pair bubble and the attached EPCs act as a *self-energy*.

So far, we only considered the interaction between electrons and phonons. However, the electrons also interact among each other via the Coulomb repulsion. In the simplest case,

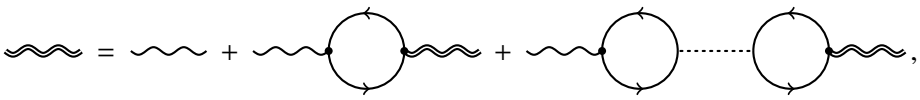

(5.4)

where the dotted line represents the bare Coulomb interaction. But also here, an infinite number of similar higher-order processes is possible,

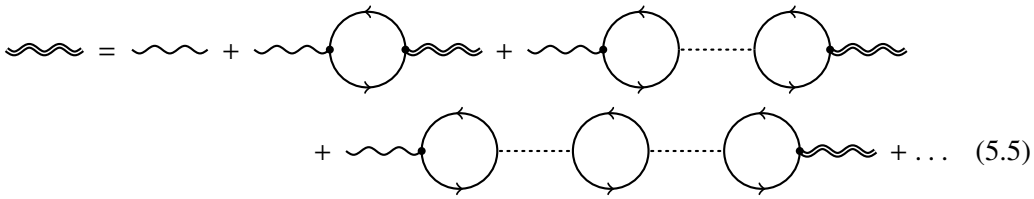

(5.5)

With a second Dyson equation for the Coulomb interaction, this can again be rewritten as

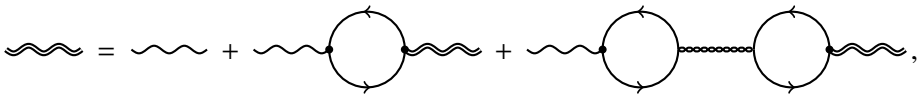

(5.6a)

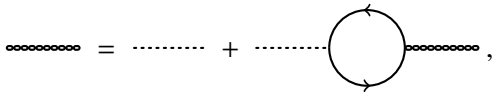

(5.6b)

where the thick dotted line represents the screened Coulomb interaction. Finally, defining the screened EPC, we obtain a set of three coupled equations for the phonon renormalization,

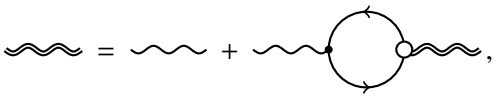

(5.7a)

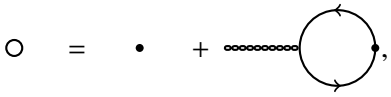

(5.7b)

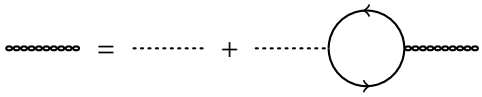

(5.7c)

This covers all possible diagrams where the electrons only appear in pair bubbles—as in the RPA [141–146] (cf. Sec. 2.6.1). It includes the most divergent diagrams of each order [148].

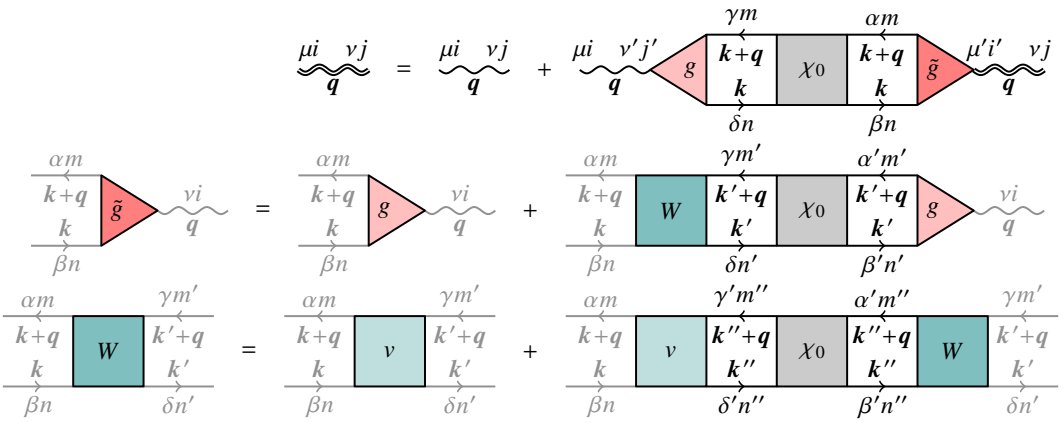

Figure 5.1: Feynman diagrams of the RPA phonon renormalization. Single and double wiggly lines represent bare and screened phonons, straight directed lines (screened) electrons. g ($\widetilde{g}$) and U (W) are the bare (screened) electron–phonon and Coulomb interaction. χ_0 is the bare electronic susceptibility. We represent it as a box (instead of a bubble) to spatially separate in- and outgoing electron lines. Labels like αm and μi are redundant. Here, the former and latter indices refer to localized and eigenbases, respectively, and should be read as alternatives. According to the Feynman rules for evaluating diagrams, all internal degrees of freedom have to be summed over.

So far, all electronic and phononic quantum numbers have been omitted for simplicity. A more detailed representation of Eq. 5.7 is given in Fig. 5.1. Equivalent diagrams can be found, e.g., in Figs. 1 and 2 of Ref. 102 and Fig. 1 of Ref. 101.

In the following, we will translate the above Feynman diagrams to formulas that we can calculate with (cf. App. C.3). Section 5.2 deals with the correct renormalization of phonons once the bare phonons and the bare *and screened* EPCs are known, as defined in Eq. 5.7a. Afterwards, in Sec. 5.3, we will discuss the renormalization of the EPC once the screened Coulomb interaction is known, following Eq. 5.7b. The renormalization of the Coulomb interaction in RPA according to Eq. 5.7c has already been discussed in Secs. 2.6.1 and 2.6.1.1 and will thus not be addressed in this chapter.

5.2 Phononic Dyson equation

In this section, the symbol D will label the phonon *Green function*, departing from its use for the dynamical matrix elsewhere. The dynamical matrix will in turn be denoted (like its eigenvalues) as ω^2. Our derivation is partly guided by the review of Giustino [101].

The Dyson equation for the phonon Green function (Eq. 5.7a) can be written as

$$\widetilde{D}_{\boldsymbol{q}\mu\nu}(\omega) = D_{\boldsymbol{q}\mu\nu}(\omega) + \sum_{\mu'\nu'} D_{\boldsymbol{q}\mu\nu'}(\omega)\Pi_{\boldsymbol{q}\nu'\mu'}(\omega)\widetilde{D}_{\boldsymbol{q}\mu'\nu}(\omega), \tag{5.8a}$$

where the phonon self-energy Π comprises the pair bubble and the EPCs. Inversion yields

$$\widetilde{D}^{-1}_{\boldsymbol{q}\mu\nu}(\omega) = D^{-1}_{\boldsymbol{q}\mu\nu}(\omega) - \Pi_{\boldsymbol{q}\mu\nu}(\omega). \tag{5.8b}$$

Here, μ and ν label bare phonon eigenmodes and ω is the (nonadiabatic) frequency. Since the bare phonon Green function is diagonal in this basis (cf. Eq. 132 of Ref. 101),

$$D_{\boldsymbol{q}\mu\nu}(\omega) = \frac{2\omega_{\boldsymbol{q}\nu}}{\omega^2 - \omega^2_{\boldsymbol{q}\nu}}\delta_{\mu\nu}, \tag{5.9}$$

we can further write (cf. Eq. 136 of Ref. 101)

$$\widetilde{D}^{-1}_{\boldsymbol{q}\mu\nu}(\omega) = \frac{1}{2\omega_{\boldsymbol{q}\nu}}[(\omega^2 - \omega^2_{\boldsymbol{q}\nu})\delta_{\mu\nu} - 2\omega_{\boldsymbol{q}\nu}\Pi_{\boldsymbol{q}\mu\nu}(\omega)] \tag{5.10a}$$

or, more symmetrically,

$$\widetilde{D}^{-1}_{\boldsymbol{q}\mu\nu}(\omega) = \frac{1}{2\sqrt{\omega_{\boldsymbol{q}\mu}\omega_{\boldsymbol{q}\nu}}}[(\omega^2 - \omega^2_{\boldsymbol{q}\nu})\delta_{\mu\nu} - 2\sqrt{\omega_{\boldsymbol{q}\mu}\omega_{\boldsymbol{q}\nu}}\Pi_{\boldsymbol{q}\mu\nu}(\omega)]. \tag{5.10b}$$

Since the screened dispersion follows from the poles of the screened Green function, we can rewrite this as a "Dyson equation" for the dynamical matrix. In the *static* case $\omega = 0$,

$$\widetilde{\omega}^2_{\boldsymbol{q}\mu\nu} = \omega^2_{\boldsymbol{q}\nu}\delta_{\mu\nu} + 2\sqrt{\omega_{\boldsymbol{q}\mu}\omega_{\boldsymbol{q}\nu}}\Pi_{\boldsymbol{q}\mu\nu}. \tag{5.11a}$$

Diagonalization of the screened dynamical matrix yields the screened phonon frequencies and corresponding eigenvectors. (All calculations can also be carried out in the Cartesian basis. This has the advantage that the eigenvectors of the dynamical matrix can be easily interpreted in terms of displacements of individual atoms as opposed to collective displacements.)

From second-order perturbation theory (App. C.4) we know the expression for the leading contribution to the phonon self-energy. Replacing one bare EPC g by the screened $\widetilde{g}$ and performing the spin summation, the static phonon self-energy reads (cf. Eq. 2.131)

$$\Pi_{\boldsymbol{q}\mu\nu} = \frac{2}{N}\sum_{\boldsymbol{k}mn} g^*_{\boldsymbol{q}\mu\boldsymbol{k}mn}\frac{f(\varepsilon_{\boldsymbol{k}+\boldsymbol{q}m}) - f(\varepsilon_{\boldsymbol{k}n})}{\varepsilon_{\boldsymbol{k}+\boldsymbol{q}m} - \varepsilon_{\boldsymbol{k}n}}\widetilde{g}_{\boldsymbol{q}\nu\boldsymbol{k}mn}. \tag{5.11b}$$

Here, the couplings $g_{\boldsymbol{q}\nu}$ and $\widetilde{g}_{\boldsymbol{q}\nu}$ depend on the bare phonon frequencies $\omega_{\boldsymbol{q}\nu}$, as opposed to $d_{\boldsymbol{q}\nu} = \sqrt{2\omega_{\boldsymbol{q}\nu}}g_{\boldsymbol{q}\nu}$ and $\widetilde{d}_{\boldsymbol{q}\nu} = \sqrt{2\omega_{\boldsymbol{q}\nu}}\widetilde{g}_{\boldsymbol{q}\nu}$ (cf. Eq. 2.133). Using the latter, Eq. 5.11 becomes

$$\widetilde{\omega}^2_{\boldsymbol{q}\mu\nu} = \omega^2_{\boldsymbol{q}\nu}\delta_{\mu\nu} + \Pi'_{\boldsymbol{q}\mu\nu}, \tag{5.12a}$$

$$\Pi'_{\boldsymbol{q}\mu\nu} = \frac{2}{N}\sum_{\boldsymbol{k}mn} d^*_{\boldsymbol{q}\mu\boldsymbol{k}mn}\frac{f(\varepsilon_{\boldsymbol{k}+\boldsymbol{q}m}) - f(\varepsilon_{\boldsymbol{k}n})}{\varepsilon_{\boldsymbol{k}+\boldsymbol{q}m} - \varepsilon_{\boldsymbol{k}n}}\widetilde{d}_{\boldsymbol{q}\nu\boldsymbol{k}mn}. \tag{5.12b}$$

This way, the bare and the screened phonon frequencies as well as the phonon self-energy all occur in separate terms of the Dyson equation.

The static phonon self-energy from Eq. 5.11b is formally equivalent to the electronic contribution to the dynamical matrix calculated in DFPT (cf. Eq. 2.131). Because of this, Eq. 5.11 with g from cDFPT and $\widetilde{g}$ from DFPT can be directly used to go from cDFPT to DFPT phonons and vice versa. However, in practical calculations, various points require special attention.

5.2.1 Combination of bare and screened couplings

First, the requirement to combine d with $\widetilde{d}$ (cf. Sec. V.A.3 of Ref. 101) shall be repeated. The bulk of calculations in the literature depend on the screened coupling $\widetilde{d}$ only [101]. One reason for this is certainly that the partially screened couplings d (in the framework of DFT) were inaccessible before the development of cDFPT.

An example that shows the differences between bare and screened EPCs and the result of their incorrect usage is given in Figs. 5.2 and 5.3. In Fig. 5.2, we plot the $\boldsymbol{k}$-dependent LA EPC of 1H-TaS_2 (responsible for the lattice instabilities in this material) for selected $\boldsymbol{q}$ points. In the shown cases, the differences between $|d|^2$ and $|\widetilde{d}|^2$ are evident but not striking. In turn, in the corresponding renormalized phonon dispersions in Fig. 5.3, we find serious errors if we use either of them in Eq. 5.12 in lieu of the correct combination.

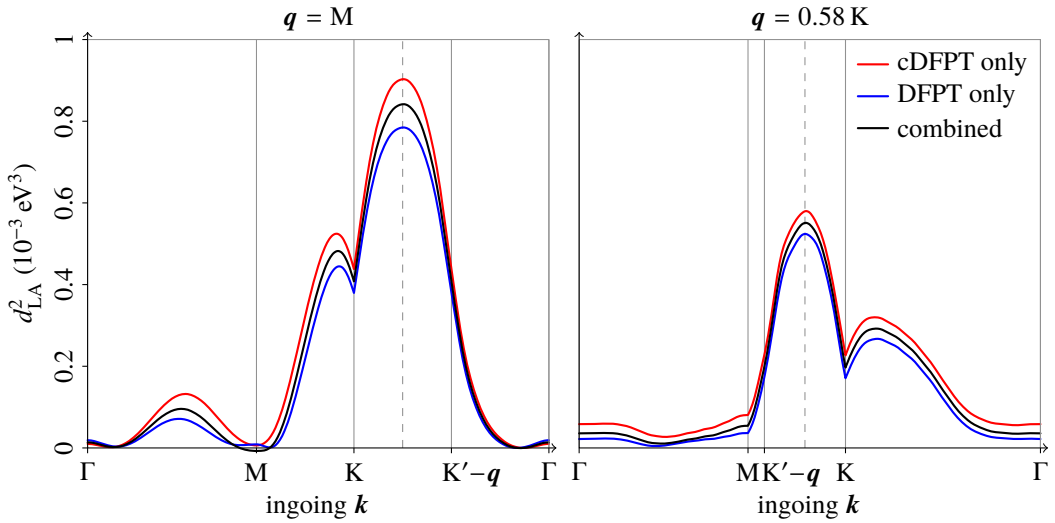

Figure 5.2: Comparison of selected EPCs of 1H-TaS_2 from DFPT and cDFPT and their combination. We show the cDFPT-LA diagonal elements of the symmetrized coupling matrices as defined in Eq. 5.14, where we replaced $\widetilde{d}$ with d ("cDFPT only"), replaced d with $\widetilde{d}$ ("DFPT only"), or used the correct formula ("combined"). Unlike the (c)DFPT-only data, the combined squared coupling must not necessarily be positive. In fact, we find small negative values for $\boldsymbol{k} = \boldsymbol{q} = \mathrm{M}$. According to our current knowledge, however, we cannot rule out numerical errors as the cause of this feature. The computational parameters are as in Sec. 9.8.

5.2.2 Off-diagonal phonon self-energy

Since the character of the phononic eigenmodes changes upon renormalization, it can be important to take the off-diagonal elements of the phonon self-energy (in the space of atomic displacements) into account. This is another point (cf. Secs. V.A.2 and V.A.3 of Ref. 101) that is often disregarded in the literature. The error to be expected from neglecting the off-diagonal phonon self-energy will be quantified in Figs. 9.2c and 9.3 of Chap. 9, again for the example of 1H-TaS_2.

5.2.3 Consistent gauge

If g and $\widetilde{g}$ stem from independent cDFPT and DFPT calculations, care has to be taken that a consistent *gauge* is applied. More precisely, we have a gauge freedom regarding the electronic eigenstates at each $\boldsymbol{k}$ point and of each band index n [138],

$$\hat{H}|\boldsymbol{k}n\rangle = \varepsilon_{\boldsymbol{k}n}|\boldsymbol{k}n\rangle, \tag{5.13a}$$

$$|\boldsymbol{k}n\rangle \to \mathrm{e}^{\mathrm{i}\varphi_{\boldsymbol{k}n}}|\boldsymbol{k}n\rangle. \tag{5.13b}$$

The *a priori* arbitrary complex phase factors $\mathrm{e}^{\mathrm{i}\varphi_{\boldsymbol{k}n}}$ attached to the electronic eigenstates entering g and $\widetilde{g}$ must be the same. This can be accomplished in two ways: First, both phonon calculations, cDFPT and DFPT, have to be fed with identical electronic data. (De facto, this means that temporary data files written and read by the DFT and DFPT codes must be copied hence and forth.) Second and preferably, a detour via a well-defined (or even real) basis is taken. If the EPCs are available in the basis of (real) Wannier functions, we can circumvent the problem of gauge inconsistencies with the additional advantage that Fourier interpolation (cf. App. B.4.2) to arbitrarily dense $\boldsymbol{q}$ and $\boldsymbol{k}$ meshes is possible. (We choose the latter approach throughout this work.) Noncompliance to this point usually leads to random interferences and thus to completely wrong results.

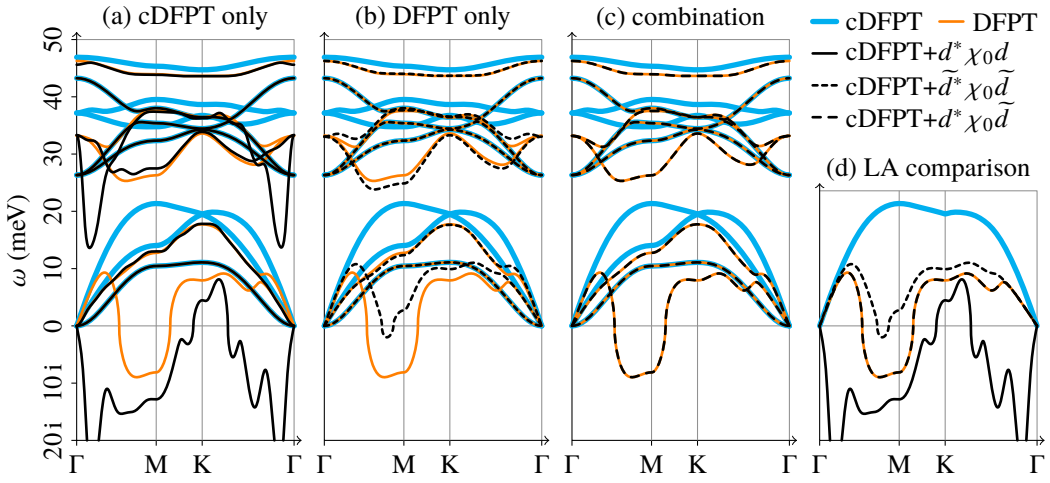

Figure 5.3: Importance of combination of bare and screened EPCs. We show the screened phonon dispersion of 1H-TaS_2 from cDFPT, DFPT, and Eq. 5.12, where we (a) replaced $\widetilde{d}$ with d, (b) replaced d^* with $\widetilde{d}^*$, and (c) used the correct d^* and $\widetilde{d}$. (d) Comparison of LA dispersions only. Even though the EPCs from cDFPT and DFPT can be qualitatively similar for some $\boldsymbol{q}$ points (cf. Fig. 5.2), the overall error is significant. Completely neglecting the metallic screening in the EPCs leads to pronounced additional instabilities, especially for small, nonzero $\boldsymbol{q}$ points. In turn, using only screened EPCs underestimates the softening near the edge of the BZ. The computational parameters are as in Sec. 9.8.

5.2.4 Smearing functions

From statistical physics and perturbation theory (App. C.4), we find that the functions f occurring in Eq. 5.12 must be Fermi functions. In practical DFT and DFPT calculations, however, the electronic occupations are often smeared using different kinds of step functions (cf. App. C.7). If we want to *exactly* reproduce a given DFPT calculation, we have to choose the same step function f as used in the *ab initio* code. In fact, especially imaginary phonon dispersions can depend significantly on the chosen smearing type.

5.2.5 Removable singularities

Both the enumerator and the denominator of the fraction in Eq. 5.12 vanish at Γ in the intraband case $m = n$. Hence, to obtain a reasonable static phonon self-energy at Γ (which is consistent with DFPT), the fraction has to be replaced by the derivative of the Fermi function (or similar step function) in this case (cf. App. C.7). Alternatively, we can add a small regularization $i\eta$ to the denominator of Eq. 5.12 and take the real part. However, we only find perfect agreement with results from QE using the former approach.

5.2.6 Cancellation of anti-Hermitian coupling

Because of the symmetry of the Feynman diagrams in Fig. 5.1, it must not matter, whether we calculate the phonon self-energy in Eq. 5.12 with $d^*_\mu \widetilde{d}_\nu$, $\widetilde{d}^*_\mu d_\nu$, or any weighted averages of these matrices resulting from outer products. Hence, we define the symmetrized EPC matrix

$$d^2_{\boldsymbol{q}\mu\nu\boldsymbol{k}mn} = \frac{d^*_{\boldsymbol{q}\mu\boldsymbol{k}mn} \cdot \widetilde{d}_{\boldsymbol{q}\nu\boldsymbol{k}mn} + \widetilde{d}^*_{\boldsymbol{q}\mu\boldsymbol{k}mn} \cdot d_{\boldsymbol{q}\nu\boldsymbol{k}mn}}{2}. \tag{5.14}$$

The different combinations of $d^*_\mu \widetilde{d}_\nu$ and $\widetilde{d}^*_\mu d_\nu$ on their own are, however, not equal. Only the one defined in Eq. 5.14 is Hermitian and thus has real diagonal elements in arbitrary bases.

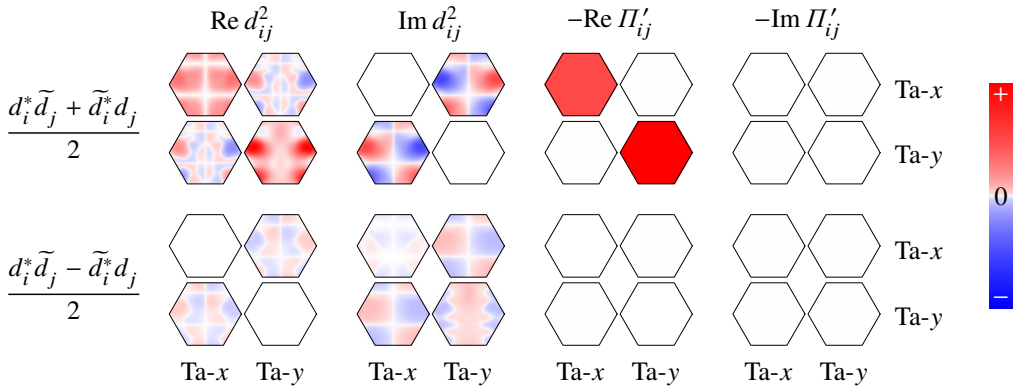

Figure 5.4: Cancellation of anti-Hermitian components of the EPC. On the left, we show the real and imaginary parts of the Hermitian (upper row) and anti-Hermitian components (lower row) of the $\boldsymbol{k}$-dependent combined EPC of 1H-TaS_2 at $\boldsymbol{q} = 2/3\,\mathrm{M}$ for the in-plane Ta displacements. On the right, we show the corresponding phonon self-energy according to Eq. 5.12 (thus after $\boldsymbol{k}$ integration).

In turn, since the static phonon self-energy *is* Hermitian, this means that all anti-Hermitian components must somehow cancel in the calculation of physical observables.

Figure 5.4 shows selected Hermitian and anti-Hermitian components of the $\boldsymbol{k}$-dependent combined EPC of 1H-TaS_2. After $\boldsymbol{k}$ integration (right panels), indeed all anti-Hermitian parts have canceled. For some components this is obvious because the coupling is antisymmetric with respect to a horizontal reflection. For others, e.g., the diagonal components of the imaginary part, this is rather surprising.

5.3 Renormalization of coupling

By using the DFPT coupling, we implicitly take the Coulomb interaction into account, which relates the bare and screened EPCs via the diagram from Eq. 5.7b. Translated to formulas,

$$\widetilde{g}_{\boldsymbol{q}\nu\boldsymbol{k}mn} = g_{\boldsymbol{q}\nu\boldsymbol{k}mn} + \Delta g_{\boldsymbol{q}\nu\boldsymbol{k}mn}, \tag{5.15a}$$

$$\Delta g_{\boldsymbol{q}\nu\boldsymbol{k}mn} = \frac{2}{N} \sum_{\boldsymbol{k}'m'n'} W_{\boldsymbol{q}\boldsymbol{k}mn\boldsymbol{k}'m'n'} \frac{f(\varepsilon_{\boldsymbol{k}'+\boldsymbol{q}m'}) - f(\varepsilon_{\boldsymbol{k}'n'})}{\varepsilon_{\boldsymbol{k}'+\boldsymbol{q}m'} - \varepsilon_{\boldsymbol{k}'n'}} g_{\boldsymbol{q}\nu\boldsymbol{k}'m'n'}. \tag{5.15b}$$

To be precise, the screening of the EPC from DFPT includes processes beyond RPA via the XC kernel $K_{\mathrm{XC}} = \delta V_{\mathrm{XC}}/\delta n$ (cf. Sec. 2.3.1.2). The screening in DFT is formally equivalent to RPA, except that the additional XC effects are included at the level of the bare Coulomb interaction v. Precisely, the screening of the change of the SCF potential reads [50] (cf. Eqs. 2.132 and 2.151)

$$\partial V_{\mathrm{SCF}} = \epsilon^{-1}_{\mathrm{DFT}} \partial V, \tag{5.16a}$$

$$\epsilon_{\mathrm{DFT}} = 1 - \chi_0 \widetilde{v}, \tag{5.16b}$$

$$\widetilde{v} = v + K_{\mathrm{XC}}. \tag{5.16c}$$

In a localized basis, the screened Coulomb interaction is assumed to have a weak $\boldsymbol{k}$ dependence, which can be neglected (cf. Sec. 2.3.3 of Ref. 290). In this case, it is more convenient to also write the change of the coupling Δg in this localized electronic basis (where it is $\boldsymbol{k}$-independent too) and transform the bare electronic susceptibility on the fly,

$$\Delta g_{\boldsymbol{q}i\alpha\beta} = \frac{2}{N} \sum_{\substack{\boldsymbol{k}mn \\ \alpha'\beta'\gamma\delta}} W_{\boldsymbol{q}\alpha\beta\gamma\delta} U_{\boldsymbol{k}+\boldsymbol{q}\gamma m} U^*_{\boldsymbol{k}\delta n} \frac{f(\varepsilon_{\boldsymbol{k}+\boldsymbol{q}m}) - f(\varepsilon_{\boldsymbol{k}n})}{\varepsilon_{\boldsymbol{k}+\boldsymbol{q}m} - \varepsilon_{\boldsymbol{k}n}} U^*_{\boldsymbol{k}+\boldsymbol{q}\alpha' m} U_{\boldsymbol{k}\beta' n} g_{\boldsymbol{q}i\boldsymbol{k}\alpha'\beta'}. \tag{5.17}$$

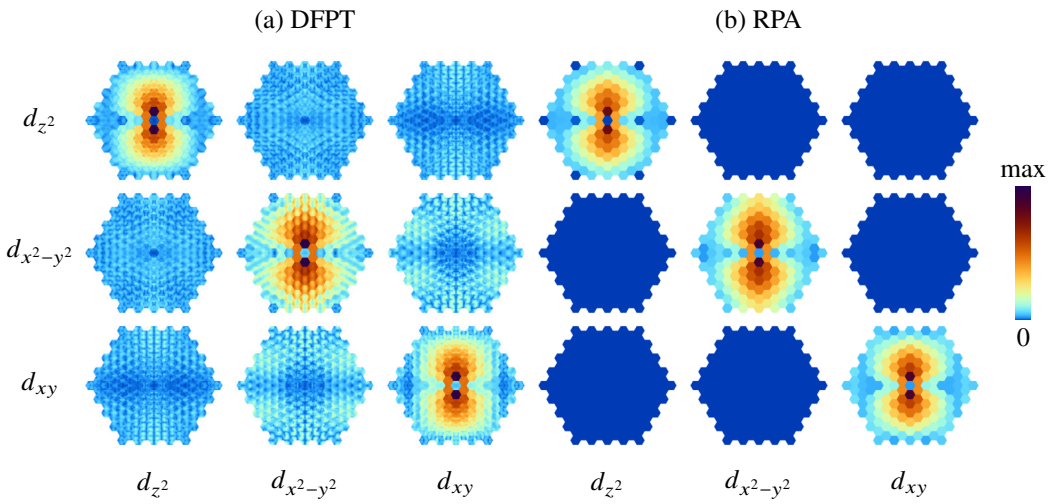

Figure 5.5: $\boldsymbol{q}$-, $\boldsymbol{k}$-, and orbital-dependent change $|\Delta g|$ of the EPC of 1H-TaS_2 for the Ta-y direction (a) as the difference $|\widetilde{g} - g|$ between DFPT and cDFPT data and (b) from Eq. 5.18. We plot the $\boldsymbol{k}$ dependence in mini-BZs located at their respective positions in the $\boldsymbol{q}$-space BZ. This allows us to visualize the complete $\boldsymbol{q}$ and $\boldsymbol{k}$ dependencies of a matrix element in a single image. The computational parameters are as in Sec. 9.8.

We can go even further and consider only density–density terms of a fully local (independent of both $\boldsymbol{k}$ and $\boldsymbol{q}$) Coulomb interaction, $W_{\alpha\alpha\gamma\gamma} \equiv W_{\alpha\gamma}$. Then,

$$\Delta g_{\boldsymbol{q}i\alpha} = \sum_{\gamma} W_{\alpha\gamma} c_{\boldsymbol{q}i\gamma}, \tag{5.18a}$$

$$c_{\boldsymbol{q}i\gamma} = \frac{2}{N} \sum_{\substack{\boldsymbol{k}mn \\ \alpha\beta}} U_{\boldsymbol{k}+\boldsymbol{q}\gamma m} U^*_{\boldsymbol{k}\gamma n} \frac{f(\varepsilon_{\boldsymbol{k}+\boldsymbol{q}m}) - f(\varepsilon_{\boldsymbol{k}n})}{\varepsilon_{\boldsymbol{k}+\boldsymbol{q}m} - \varepsilon_{\boldsymbol{k}n}} U^*_{\boldsymbol{k}+\boldsymbol{q}\alpha m} U_{\boldsymbol{k}\beta n} g_{\boldsymbol{q}i\boldsymbol{k}\alpha\beta}. \tag{5.18b}$$

If $\Delta g_{\boldsymbol{q}i\alpha}$ is known and the number of $\boldsymbol{q}$ points and Cartesian coordinates i is large compared to the number of orbitals γ, we can approximately invert Eq. 5.18a to determine $W_{\alpha\gamma}$. This is what we will do in the following for the case of 1H-TaS_2.

Figure 5.5 shows the $\boldsymbol{q}$-, $\boldsymbol{k}$-, and orbital-dependent change $|\Delta g|$ of the EPC of 1H-TaS_2 for the Ta-y direction. The *ab initio* results are displayed in Fig. 5.5a, the results of Eq. 5.18a for an optimized W in Fig. 5.5b. Please note that the results of Eq. 5.18a are diagonal in the orbital indices and have no $\boldsymbol{k}$ dependence. This is approximately true for the *ab initio* results as well, showing that the assumption of a local density–density interaction is reasonable. (It is expected that fully screened interactions are very short-range, thus almost local.) In the basis of Ta-d_{z^2}, -$d_{x^2-y^2}$, and -d_{xy} orbitals, the optimized Coulomb interaction reads

$$W = \begin{bmatrix} 311 & 330 & 330 \\ 330 & 199 & 542 \\ 330 & 542 & 213 \end{bmatrix} \text{meV}. \tag{5.19}$$

The RPA screening in Eq. 5.18b disobeys the Pauli principle [291, 292], since the bare electronic susceptibility contributes a spin factor of 2 even for intraorbital interactions, which can only take place between opposite spins in the case of a fully local Coulomb interaction. To correct for this, the diagonal of W must be multiplied by 2. In this case, we would find a corresponding Hubbard parameter $\langle W_{\alpha\alpha} \rangle_\alpha \approx 0.5$, similar to the RPA value in Fig. 2.1.

Consistently incorporating the Coulomb interaction into our phonon-renormalization scheme is inevitable if we want to completely prescind from the use of screened quantities such as the EPC from DFPT. We finally aim for a Hamiltonian that contains partially screened quantities only. It is the basis for any proper treatment of the solid-state problem by means of many-body techniques. We still have to perform various sanity checks and benchmark calculations (e.g., regarding the spin prefactor related to the Pauli principle) before we can bonafide work with this extended scheme.

Chapter 6

CDW and Mott physics in 1T-$NbSe_2$

The work presented in this chapter is a paragon of intertwined physics of lattice instabilities and strong correlations. It has been almost verbatim published in J. Phys. Condens. Matter ***30****, 325601 (2018) [293]. It is a collaboration with E. Kamil, G. Schönhoff, M. Rösner, M. Schüler, G. Sangiovanni, and T. O. Wehling. We thank M. Kaltak and G. Kresse for useful discussions. I only contributed all phonon-related results including Figs. 6.1 and 6.4, I helped preparing the manuscript, and I was involved in the estimate of the Coulomb interaction. In App. C.8, I present two alternative estimates. Two similar works [167, 168] were reported during the final stage of the preparation of the manuscript.*

Using *ab initio* calculations, we reveal the nature of the insulating phase recently found experimentally in monolayer 1T-$NbSe_2$. We find soft phonon modes in a large part of the BZ indicating a CDW instability of strong-coupling nature. Structural relaxation on a $\sqrt{13}\times\sqrt{13}$ supercell reveals a SoD reconstruction with an energy gain of 60 meV per primitive unit cell. The band structure of the distorted phase exhibits a half-filled flat band, which is associated with orbitals that are delocalized over several atoms in each SoD. By including many-body corrections through a combined GW, hybrid-functional, and DMFT treatment, we find the flat band to split into narrow Hubbard bands. The lowest-energy excitation across the gap turns out to be between itinerant Se-p states and the upper Hubbard band, which makes the system a charge-transfer (as opposed to a Mott–Hubbard) insulator. Combined hybrid-functional and GW calculations show that long-range interactions shift the Se-p states to lower energies. Thus, a delicate interplay of local and long-range correlations determines the nature of the gap and its size in this distorted phase of monolayer 1T-$NbSe_2$.

6.1 Introduction

2D materials often exhibit properties that are distinct from those of their bulk counterparts. The electronic structure and phase diagrams can strongly depend on the thickness of the material, as evident from findings such as the Dirac cone in graphene [258], a change from indirect to direct semiconductors [227], increasing and decreasing critical temperatures of superconductivity [18, 19, 25], or possibly layer-dependent CDWs [294, 295]. Due to the all-surface nature of 2D materials, the substrates that they are placed on during growth and in experiments can also have a strong influence on the electronic properties.

In layered materials, the interplay between strong electron–electron and electron–phonon interactions can lead to rich series of many-body instabilities including Mott-insulating, CDW, and superconducting phases. 1T-TaS_2 presents a classical example in this respect [53, 60, 175, 296, 297], where a Mott-insulating state emerges within the commensurate $\sqrt{13}\times\sqrt{13}$ CDW

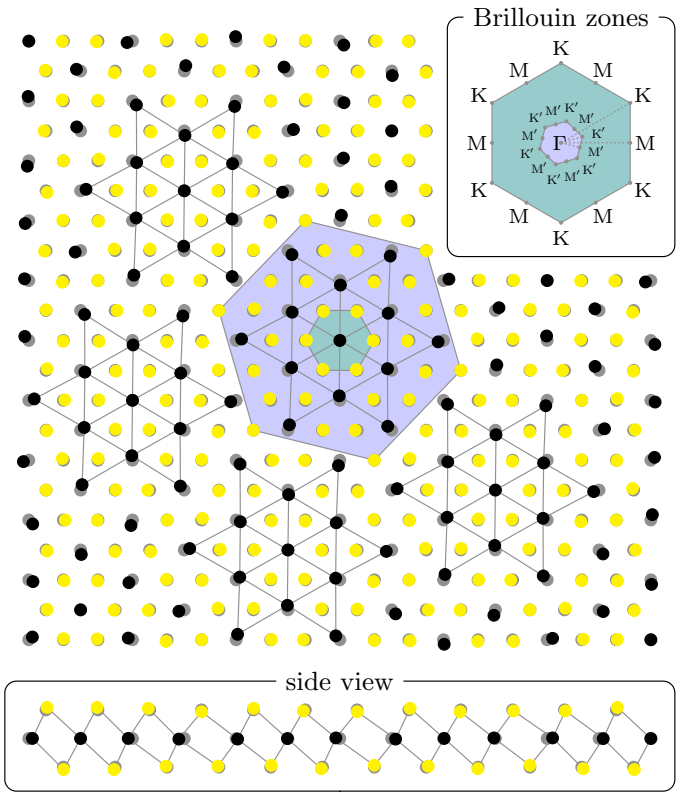

Figure 6.1: Atomic positions in CDW (black and yellow dots for Nb and Se) and symmetric phase (underlying gray dots). Unit cells and associated BZs have the same color.

in the bulk. Whether or not this CDW and Mott states are realized down to the monolayer thickness is currently a matter of debate [221, 295, 298].

1T-TaS_2 is just one representative of the class of TMDCs MX_2 with a transition metal M and a chalcogen X. The TMDCs occur in two common polytypes, namely the 1T and 2H structures that consist of octahedral and TP units, respectively (cf. Sec. 4.1.2). An isoelectronic partner of 1T-TaS_2 is 1T-$NbSe_2$. While this material usually crystallizes in the 2H phase, Nakata *et al.* recently succeeded in synthesizing a monolayer of 1T-$NbSe_2$ via epitaxial growth on bilayer graphene [220]. Their experiments suggest that unlike 2H-$NbSe_2$, which is a metal and hosts a CDW phase with a 3×3 periodicity both in bulk and monolayer form [158], 1T-$NbSe_2$ realizes a CDW with $\sqrt{13} \times \sqrt{13}$ periodicity and SoD-like cluster formation (cf. Fig. 6.1). In this distorted phase, monolayer 1T-$NbSe_2$ turned out to be an insulator with a gap of around 400 meV, phenomenologically similar to 1T-TaS_2.

Here, we provide a first-principles-based account of the electronic structure of monolayer 1T-$NbSe_2$, including Coulomb interaction effects and PLDs. We find that monolayer 1T-$NbSe_2$ can indeed realize an insulating phase once a SoD-like CDW is formed. We show that a delicate interplay of local and long-range electronic interaction effects determines the size and nature of the insulating gap.

This chapter is organized as follows: In Sec. 6.2, we start with a presentation of the methods used. On this basis, in Sec. 6.3, we discuss the electronic structure of the undistorted phase, including the influence of nonlocal exchange through GW and hybrid-functional calculations in Sec. 6.3.1. Next, in Sec. 6.4, we relate the lattice dynamics of the undistorted phase to the SoD reconstruction on the $\sqrt{13} \times \sqrt{13}$ supercell. Finally, the electronic structure of this distorted phase is analyzed in Sec. 6.5, where we also estimate the local Coulomb interaction for the flat band and find an opening of a charge-transfer gap in DMFT.

6.2 Methods

We investigate the electronic structure of monolayer 1T-$NbSe_2$ by means of DFT with semilocal and hybrid functionals as well as many-body perturbation theory by employing the GW approximation. In this section, all technical details of these simulations are given. The lattice dynamics is studied using DFPT as detailed in Sec. 6.2.2. The *ab initio* estimate of the Coulomb interaction is provided in Sec. 6.2.3. Finally, the way we combine first-principles calculations with DMFT to study the effects of local correlations is discussed in Sec. 6.2.4.

6.2.1 Density-functional theory

We use DFT [31, 32] to study the electronic structure of monolayer 1T-$NbSe_2$. The DFT calculations presented here are performed using VASP [299, 300] with the PBE XC functional [75, 76]. For the structural relaxation and self-consistent computation of the electronic density and energy, we use an energy cutoff of 500 eV and a uniform $\boldsymbol{k}$ mesh of 18×18 points. The DOS on the other hand is evaluated using a denser 24×24 mesh. The chosen unit-cell height of 20 Å is large enough to prevent significant interactions between periodic images. We also study the distorted phase on a $\sqrt{13} \times \sqrt{13}$ supercell, which can host the commensurate CDW observed in scanning–tunneling microscopy (STM) [220]. Here, we choose a 6×6 $\boldsymbol{k}$-point mesh in DFT. The positions of the atoms within the unit cell for each structure are relaxed until the residual forces on them are reduced to about 10 meV/Å.

6.2.1.1 Effects of nonlocal exchange

To study the effects of nonlocal exchange we use the GW formalism where the quasiparticle energies—the KS energies—are renormalized by the self-energy, which is evaluated as a product of the single-particle Green function and the screened Coulomb interaction [202]. In particular, we use the G_0W_0 approximation where the single-particle Green function is the noninteracting Green function of the KS system. The screened Coulomb interaction is evaluated within the RPA as in Eq. 2.150.

Fully converged GW calculations for large supercells that account for the SoD clusters have enormous computational requirements of both processor time and memory. For the supercell, we therefore use hybrid functionals that admix a certain amount of Fock exchange to the semi-local (GGA) density functional. In particular, we use the range-separated Heyd–Scuseria–Ernzerhof (HSE06) hybrid functional [301]. The amount of admixing is controlled by a free parameter α that needs to be chosen *a priori*. The calculations for GW and HSE06 were also performed using VASP [302, 303].

6.2.2 Density-functional perturbation theory

The vibrational properties and thus possible structural instabilities of a material can be inferred from its response to atomic displacements, which we calculate within the BO [66] and harmonic [304] approximation, using the PBE functional [75, 76] and DFPT [106] as implemented in QE [39, 40].

In QE, we apply ultrasoft PBE PPs from the PSLIBRARY 1.0.0 [305] at energy cutoffs of 70 Ry and 490 Ry for wave functions and the electron density, respectively. Uniform meshes of 36×36 $\boldsymbol{k}$ and 12×12 $\boldsymbol{q}$ points are combined with a Methfessel–Paxton smearing [306] of 10 mRy (cf. App. C.7.3). Again assuming a fixed unit-cell height of 20 Å, minimizing forces and in-plane pressure to below 1 µRy/Bohr and 0.1 kbar yields lattice parameters in agreement with those obtained from VASP.

6.2.3 Estimate of screened Coulomb interaction

The relevant low-energy subspace of the undistorted phase consists of three bands (cf. Fig. 6.2) with predominantly Nb-d_{z^2}, -$d_{x^2-y^2}$, and -d_{xy} character. We represent it in the Wannier basis using the WANNIER90 [92–94] package. The corresponding screened Coulomb interaction W is also evaluated in this basis, using the RPA implementation of VASP [307]. From it, we estimate the local Hubbard-type interaction for the flat band in the SoD phase as follows:

- We calculate the static RPA Coulomb tensor $W_{\boldsymbol{q}\alpha\beta\gamma\delta}$ and the corresponding bare interaction $v_{\boldsymbol{q}\alpha\beta\gamma\delta}$ for undistorted 1T-$NbSe_2$ on a 18×18 $\boldsymbol{q}$-point mesh.
- We only keep the dominant density–density terms $W_{\boldsymbol{q}\alpha\alpha\beta\beta} \equiv W_{\boldsymbol{q}\alpha\beta}$ and $v_{\boldsymbol{q}\alpha\alpha\beta\beta} \equiv v_{\boldsymbol{q}\alpha\beta}$.
- The eigenvectors $e_{\boldsymbol{q}\alpha r}$ of the bare Coulomb matrix $v_{\boldsymbol{q}\alpha\beta}$ are used to (approximately) diagonalize the corresponding screened Coulomb matrix $W_{\boldsymbol{q}\alpha\beta}$,

$$\lambda_{\boldsymbol{q}r} = \sum_{\alpha\beta} e^*_{\boldsymbol{q}\alpha r} W_{\boldsymbol{q}\alpha\beta} e_{\boldsymbol{q}\beta r}. \tag{6.1}$$

- We consider only the leading "eigenvalue" $W_{\boldsymbol{q}} = \max_r \lambda_{\boldsymbol{q}r}$, which describes the dominant contribution to the effective interaction whenever several unit cells (as in the case of the CDW here) are involved [24]. *[Thus defined, the leading "eigenvalue" depends on the size of the basis set, since for large distances, the bare Coulomb interaction in the orbital basis is proportional to a matrix of ones (whose only nonzero eigenvalue is its dimension) instead of an identity matrix (whose eigenvalues are all ones). In this sense, we should have considered dividing $W_{\boldsymbol{q}}$ by the number of orbitals.]*
- We calculate $W_{\boldsymbol{R}}$ via a discrete Fourier transform of $W_{\boldsymbol{q}}$, where $\boldsymbol{R}$ are lattice vectors of the undistorted structure.
- Finally, we estimate the Hubbard U in the SoD as the average of all (local and nonlocal) interactions $W_{\boldsymbol{R}-\boldsymbol{R}'}$ between the N atoms located at $\boldsymbol{R}$ and $\boldsymbol{R}'$ that are part of the SoD,

$$U = \frac{1}{N^2} \sum_{\boldsymbol{R}\boldsymbol{R}' \in \hexagram} W_{\boldsymbol{R}-\boldsymbol{R}'}. \tag{6.2}$$

  Here, N is 7 or 13, depending on whether the outer ring of the SoD is excluded or not. We put the (conceptually partially screened) U on a level with the fully screened W. We justify this for our rough estimate (lower bound) by the smallness of our active subspace. (The flat band makes up one thirteenth of one band of the undistorted phase.)

6.2.4 Dynamical mean-field theory

To treat correlation effects stemming from local Coulomb interactions adequately, we use the LDA++ approach [308, 309], i.e., we augment a DFT-based TB model with local Coulomb interactions and solve the resulting generalized Hubbard model in DMFT [151]. We solve the impurity problem using the continuous-time quantum Monte Carlo (CT-QMC) algorithm in the hybridization expansion [154, 310]. The worm algorithm [311–313] is used for the global updates in the CT-QMC and five millions measurement sweeps are performed. We estimate the local Coulomb interaction U as outlined in the prior Sec. 6.2.3. Starting from the *ab initio* solution, we perform a unitary transformation from the delocalized KS states to localized states, which we obtain by orthonormalizing optimized projector states [314] available in the projector-augmented wave (PAW) framework [315] implemented in VASP. Note however that by choice of the three-band subspace here, the "localized" effective orbitals resulting from this projection are indeed spread over several atoms in each SoD.

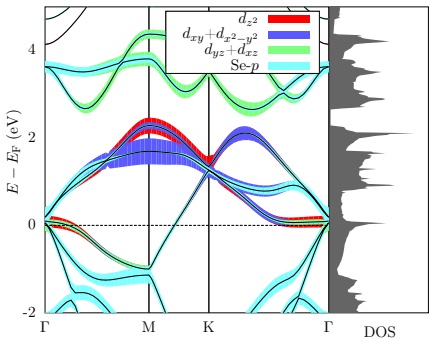

Figure 6.2: Non-spin-polarized band energies and orbital-projected DOS (color-shaded region) along the path Γ–M–K–Γ connecting high-symmetry points in the BZ corresponding to the unit cell of the undistorted monolayer 1T-$NbSe_2$. The right part corresponds to the total DOS.

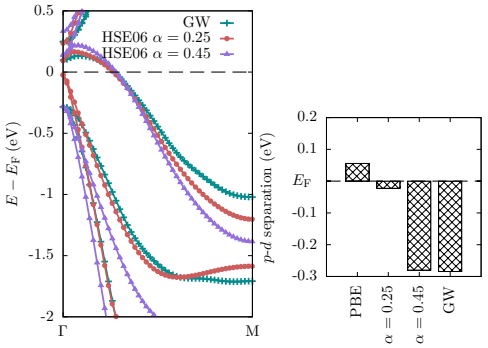

Figure 6.3: Non-spin-polarized GW and HSE06 band energies along the path Γ–M. The bar graph shows the position of Se-p-like bands at the Γ point relative to the Fermi energy, obtained from GGA, GW, and HSE06 functionals.

6.3 Electronic structure of the undistorted phase

We start by discussing the structural and electronic properties of monolayer 1T-$NbSe_2$ in the undistorted phase. To this end, we consider a simple hexagonal unit cell containing one niobium and two selenium atoms. The structural relaxation using a PBE functional leads to a lattice constant $a = 3.49$ Å and a layer height $h = 3.34$ Å (distance between the selenium layers). Next, the electronic properties were calculated for the relaxed lattice parameters. In Fig. 6.2, the band energies and the orbital characters are plotted along the BZ path Γ–M–K–Γ connecting the high-symmetry points. As evident, DFT with the PBE density functional predicts 1T-$NbSe_2$ to be a metal with a high DOS at the Fermi level E_F. The bands in the range from 0 to 2 eV above the Fermi level have mostly Nb-d_{z^2}, -d_{xy}, and -$d_{x^2-y^2}$ character. Bands in the range from −1 to 0 eV below the Fermi level have Se-p orbital character. The Se-p bands are not well separated and hybridize strongly with Nb-d bands around the Γ point near the Fermi level, which distinguishes the electronic structure of 1T-$NbSe_2$ from 1T-TaS_2, where the Se-p bands are well separated from the Fermi level [221]. The high DOS at the Fermi level in the monolayer 1T-$NbSe_2$ indicates possible electronic instabilities.

6.3.1 Effects of nonlocal exchange on Se-p bands.

The hybridization of the downward-dispersing Se-p bands with the Nb-d bands at the Γ point is strongly affected by nonlocal exchange effects. In Fig. 6.3, the band structures obtained from GW and HSE06 approximations for the undistorted structure are plotted along the path Γ–M. Unlike the PBE functional, which leads to Se-p bands starting at about 55 meV above the Fermi level around the Γ point (cf. Fig. 6.2), the nonlocal exchange accounted for in the GW approximation shifts the Se-p bands to about 280 meV below the Fermi level such that they are separated from the Nb-d bands. The GW prediction of the position of downward-dispersing Se-p bands around the Γ point is in agreement with the angle-resolved photoemission spectroscopy (ARPES) results for the SoD phase from Ref. 220.

To be able to study the effect of (screened) nonlocal exchange also in the distorted phase, where GW calculations are numerically too demanding, we turn to hybrid-functional calculations and compare band structures of the undistorted phase obtained with different flavors of HSE06 to those from GW (cf. Fig. 6.3). The traditional admixture of $\alpha = 0.25$

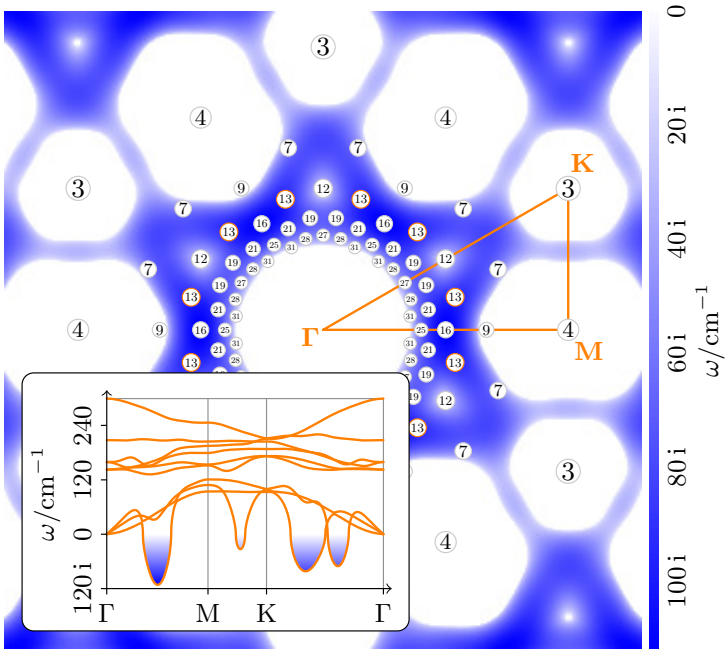

Figure 6.4: Distribution of unstable phonon modes in reciprocal space, as obtained from DFPT for 1T-$NbSe_2$ in the undistorted phase. The magnitude of imaginary frequencies is displayed in shades of blue. $\boldsymbol{q}$ points belonging to potential commensurate $\sqrt{N} \times \sqrt{N}$ CDWs are marked with encircled numbers N. Please note that $N = n^2+nm+m^2$, where n and m are integers, are squared distances between points of a triangular lattice with lattice constant unity. Inset: Full dispersion along Γ–M–K–Γ.

exact Fock exchange reproduces the shape of the GW bands in most parts of the Γ–M path quite well, except for the maximum of the Se-p bands right at Γ, where the top of the Se-p bands is already about 22 meV below the Fermi level. To obtain the same separation within the HSE06 approximation, a large admixing $\alpha = 0.45$ of the exact Fock exchange is required. However, in the case of $\alpha = 0.45$, the Se-p bands are much further below the Nb-d bands in most parts of the Γ–M path. Hence, the match between HSE06 and GW is best for the traditional value of $\alpha = 0.25$, which we will also employ in the following.

6.4 Periodic lattice distortion

The islands of monolayer 1T-$NbSe_2$ in the experiment were reported [220] to host a CDW with $\sqrt{13} \times \sqrt{13}$ periodicity and a formation of SoD clusters as shown in Fig. 6.1.

To detect possible lattice instabilities from first principles, we calculate the phonon dispersion of the undistorted structure via DFPT, which is displayed in the inset of Fig. 6.4. It features imaginary frequencies of in-plane acoustic modes in large parts of reciprocal space—better seen from the color plot in the main panel of the figure—, which indicate structural instability. The wave vectors belonging to a $\sqrt{13} \times \sqrt{13}$ CDW are located deep inside this unstable region. By contrast, there is no indication of the 3×3 CDW found in the 2H polytype of many TMDCs [158].

To account for the SoD-like cluster formation, we consider a supercell (cf. Fig. 6.1) with $\sqrt{13} \times \sqrt{13}$ periodicity and perform a structural relaxation within the GGA approximation for the density functional. As evident from Fig. 6.1, the optimized structure reveals an inward displacement of the niobium atoms within the transition-metal plane toward the central atom of the SoD configuration. The energy gain through a SoD-like reconstruction amounts to about 60 meV per primitive unit cell.

To summarize, the soft phonon modes in a large part of the BZ hint toward a strong-coupling nature of the CDW instability, as opposed to a Fermi-surface-nesting scenario, and the emergence of the commensurate CDW with SoD reconstruction is associated with a sizeable energy gain when compared with the undistorted phase.

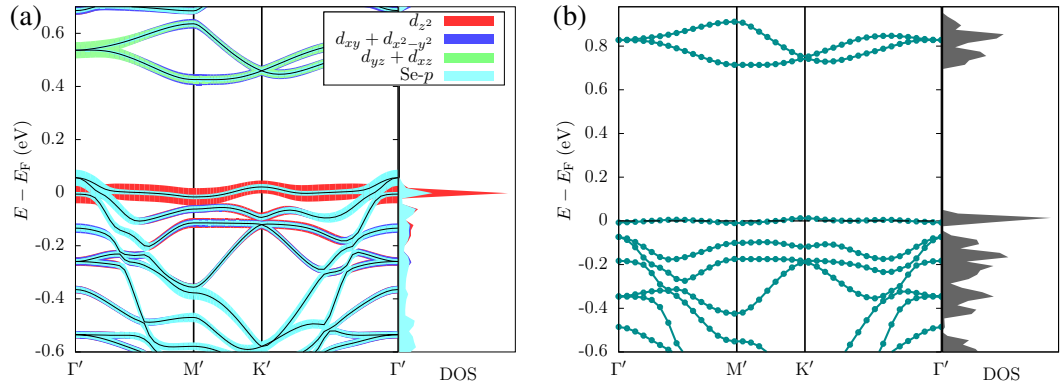

Figure 6.5: The band structure for monolayer 1T-$NbSe_2$ in the distorted CDW phase obtained from non-spin-polarized (a) GGA and (b) HSE06 ($\alpha = 0.25$) calculations, along the path Γ–M′–K′–Γ connecting the high-symmetry points of the BZ corresponding to the SoD supercell.

6.5 Electronic properties of the distorted phase

The theoretical description of the insulating behavior of the distorted phase of the monolayer 1T-$NbSe_2$ requires the inclusion of electronic correlations beyond DFT. Therefore, we now study the electronic properties of the SoD-distorted phase at different levels of approximation.

In Fig. 6.5a, the GGA band structure of the distorted lattice is plotted along the path Γ–M′–K′–Γ connecting the high-symmetry points in the BZ corresponding to the $\sqrt{13} \times \sqrt{13}$ supercell. At the Fermi level, there is a flat band with predominantly Nb-d_{z^2} character, which hybridizes with Se-p bands around the Γ point. The partial charge density corresponding to the flat band is plotted in Fig. 6.7, from which it is evident that the flat band is associated with orbitals that are delocalized over several atoms in each SoD. The maximum contribution arises from niobium atoms in the center and the inner ring of the SoD. This observation will be used in the following subsection to obtain an *ab initio* estimate of the effective Hubbard-type interaction for the flat band.

Next, we study the effects of nonlocal exchange on the hybridization of the flat band with Se-p-like bands around the Γ point. As evident from Fig. 6.5b, the hybridization is strongly suppressed upon the inclusion of nonlocal exchange through the HSE06 functional ($\alpha = 0.25$). The position of the band lying below the flat band is rather sensitive to the exact-exchange admixing parameter α. In the following subsection, when presenting DMFT calculations for the relevant Nb-d and Se-p orbitals, we will show that the position of the Se-p bands indeed affects the size and nature of the insulating gap.

In Fig. 6.6, we have unfolded [316, 317] the distorted GGA band structure to the primitive BZ (cf. Sec. 3.1.3). There is a considerable reduction of spectral weight along the edge M–K and deep inside the BZ. In addition, we observe the opening of a CDW gap at about 400 meV above the Fermi level.

So far we have seen that, though acting in the right direction to explain experiments, neither the CDW order nor the nonlocal exchange makes the system insulating. We therefore improve our treatment of local many-body effects by means of DMFT. The goal of the next subsection is hence to see if this yields a correct description of the insulating nature of monolayer 1T-$NbSe_2$ in the distorted phase.

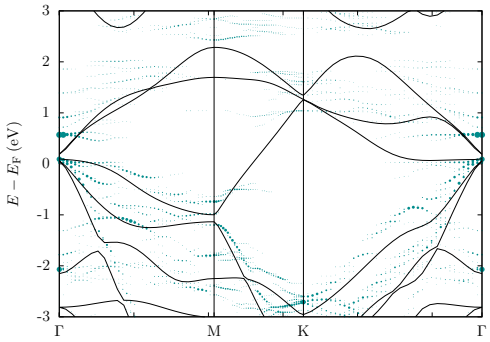

Figure 6.6: Solid dots: The band structure in the CDW phase unfolded to the primitive BZ. The size of the dots corresponds to the spectral weight. Solid lines: The band structure of the undistorted lattice for comparison.

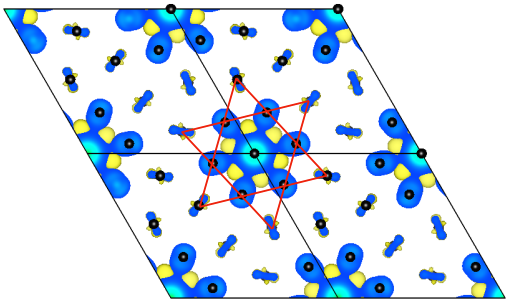

Figure 6.7: Partial charge density associated with the flat band at the Fermi level. The solid black circles correspond to the position of niobium atoms. The predominant part of the charge density is concentrated on the atoms in the center and the inner ring of the SoD (seven atoms).

6.5.1 Possibility of Mott physics

The GGA+DMFT calculations described in the following allow us to quantify the relative importance of two competing effects involving the d_{z^2}-derived flat band close to the Fermi level. The first is the electron–electron correlation on the d_{z^2}-orbital. The second is the single-particle hybridization between this orbital and the rest of the system, in particular Se-p orbitals. On the one hand, it is well known that "d-only" DMFT calculations have a strong tendency to yield Mott-insulating phases close to integer fillings. On the other hand, when "ligand" orbitals are explicitly included in the basis set used for DMFT, this tendency is drastically reduced due to important charge fluctuations between the d and the p manifolds. This is mitigated by introducing double-counting counter terms and nonlocal interaction terms. We will investigate both effects and determine whether or not in the case of 1T-$NbSe_2$ the tendency toward a Mott-insulating solution remains strong, even in the presence of the p–d hybridization derived from first principles. Computational details are described in Sec. 6.2.4.

We start with the estimate of the Hubbard-type interaction for the flat band from first principles. As mentioned in the previous section, the character or the flat band is associated with orbitals delocalized over several atoms in each SoD. Therefore, to obtain an estimate for the Hubbard-type interaction, we evaluate the screened Coulomb interaction for the undistorted phase and perform an average over the SoD. The fact that atoms on the outer ring of the SoD have a minor contribution to the partial charge density of the flat band (cf. Fig. 6.7) motivates us to perform the average once excluding and once including the outer ring. The scheme is described in detail in Sec. 6.2.3 and leads to $U \approx 390\,\text{meV}$ (300 meV) by excluding (including) the outer ring of the SoD in the averaging procedure. This estimate provides a lower bound for the Hubbard-type interaction due to the fact that we use the nonconstrained RPA for the screened Coulomb interaction, which also includes screening effects from the bands within the correlated subspace. In fact, we would need to perform cRPA calculations to exclude any screening from the correlated subspace, which would increase the effective U. To account for this effect, we use the rounded up $U = 400\,\text{meV}$ in the following.

In the next step we obtain a GGA-based TB model where we include the three bands closest to the Fermi energy. We use a projection onto the d_{z^2} orbitals to define a correlated subspace that is augmented with the Hubbard-type interaction of $U = 400\,\text{meV}$. We discuss

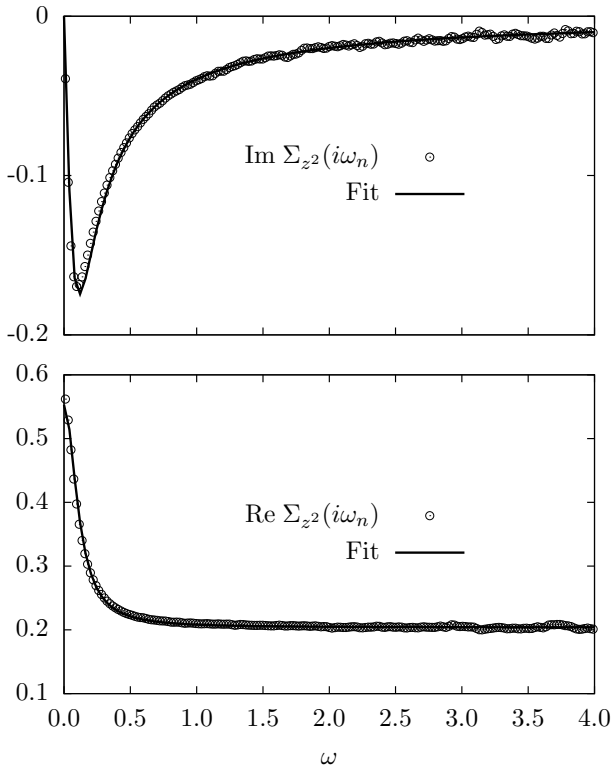

Figure 6.8: Imaginary and real part of the self-energy $\Sigma_{z^2}(\mathrm{i}\omega)$ for the correlated d_{z^2}-like orbital from DMFT. We use $U = 400\,\mathrm{meV}$ at $T = 40\,\mathrm{K}$ and fix the double-counting correction μ_{dc} to the FLL. Solid dots correspond to the CT-QMC data whereas the solid line is the fit function defined in Eq. 6.3. The fit parameters are $\bar{\sigma} = 0.203$ and $\omega_0 = 0.458$.

the outcome of this projection in terms of a comparison of the original partial DOS from GGA and the DOS of the projection, both shown in Figs. 6.9a and 6.9b. In GGA, the states at the Fermi energy are predominantly of d_{z^2} character and the states ranging from -200 to -50 meV are a mixture of d and p states. This is reflected in the projected Hamiltonian, whose spectral weight is distributed among three local orbitals only, namely the Nb-d_{z^2} orbitals and the two "ligand" orbitals made of a mixture of the other Nb-d and Se-p orbitals. This set of three orbitals constitutes therefore the basis for our GGA+DMFT calculations. The estimated value of $U = 400\,\mathrm{meV}$ is applied in the following to the d_{z^2} orbital only. The other two orbitals are treated as uncorrelated but, being included in the low-energy Hamiltonian, they can exchange charge with the d_{z^2}-like orbital by means of hybridization processes.

Treating orbitals with different degrees of correlation in DFT+DMFT requires the inclusion of a double-counting correction, which compensates the DFT contribution. We denote it by μ_{dc} and use the fully localized limit (FLL) [318]. As discussed in Sec. 6.3, long-range interactions shift the Se-p bands to lower energies. Since we do not consider any long-range interactions in DMFT, we mimic this behavior by adjusting the position of the uncorrelated bands with respect to the correlated states by an additional energy shift Δ_p in the projected Hamiltonian.

We solve the DMFT equations self-consistently with a CT-QMC impurity solver using the w2dynamics package [154, 155]. In Fig. 6.8, we show the d_{z^2} self-energy on Matsubara frequencies, with a "pure" FLL double counting ($\Delta_p = 0$). We fit the numerical data with an analytic expression for a (non-particle–hole-symmetric) atomic self-energy,

$$\Sigma_{z^2}^{\mathrm{fit}}(\mathrm{i}\omega_n) = \bar{\sigma} + \frac{U^2}{4\mathrm{i}\omega_n + \omega_0}. \tag{6.3}$$

The excellent agreement shows that the system is deep in the atomic limit.

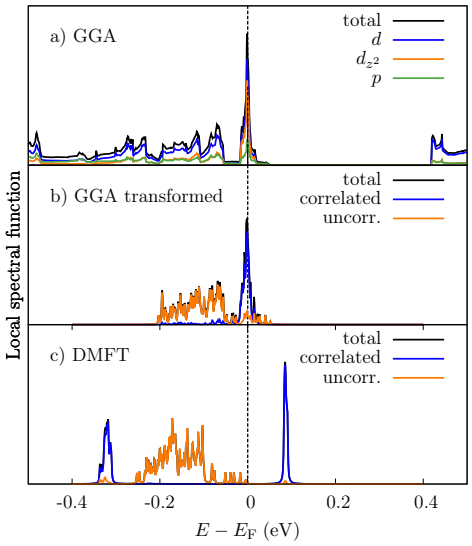

Figure 6.9: Local spectral function in the distorted phase (a) from GGA with partial DOS of d orbitals, only d_{z^2} orbitals, and p orbitals, (b) after the unitary transformation with partial DOS of orbitals considered correlated and uncorrelated, and (c) from DMFT calculations with $U = 400\,\text{meV}$ at $T = 40\,\text{K}$ and the double-counting correction μ_{dc} fixed to the FLL.

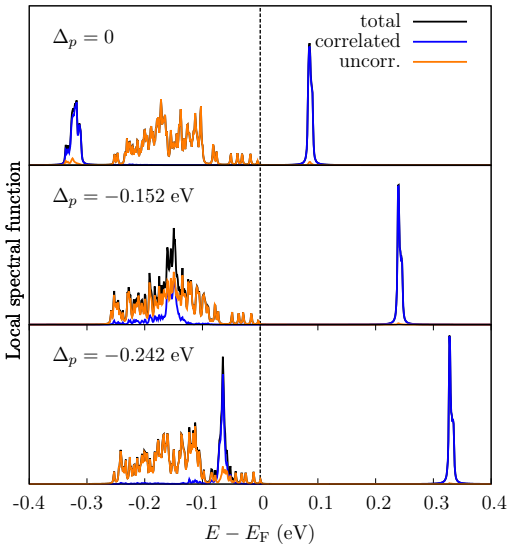

Figure 6.10: Local spectral function in the distorted phase from DMFT calculations with $U = 400\,\text{meV}$ at $T = 40\,\text{K}$ for different values of energy shifts Δ_p for the uncorrelated bands. The double-counting correction μ_{dc} for the correlated band is fixed to the FLL.

The analytic form of the self-energy makes it easily possible to calculate the DMFT spectral function on real frequencies, which we show in Fig. 6.9c. The correlated d_{z^2}-like states are split into sharp upper and lower Hubbard bands, separated approximately by the Coulomb interaction U. We find the system to be insulating with a gap of about 100 meV between p-like and d_{z^2}-like states, i.e., we find a charge-transfer insulator (where the excitations of lowest energy take place between one of the two Hubbard bands and a third, uncorrelated band) [319].

To mimic the influence of the nonlocal exchange effects on the p–d splitting (cf. Figs. 6.3 and 6.5b) in the DMFT simulations, we shift the uncorrelated bands by $\Delta_p = -150\,\text{meV}$ and $\Delta_p = -240\,\text{meV}$, which approximately corresponds to the shifts observed in HSE06 ($\alpha = 0.25$) and GW/HSE06 ($\alpha = 0.45$) calculations, respectively. From the resulting spectral functions presented in Fig. 6.10, we observe that the gap grows with Δ_p. The case of $\Delta_p = -240\,\text{meV}$, which closely mimics the p–d shift from DFT to GW calculations found in Sec. 6.3, together with a local Coulomb interaction of $U = 400\,\text{meV}$, leads to a gap close to the experimentally observed one of 400 meV [220]. Slightly larger shifts Δ_p will push the system from a charge-transfer to a Mott–Hubbard insulator.

In our DFT+DMFT approach we have used a low-energy model for DMFT, derived after including the contribution of nonlocal exchange and the CDW symmetry breaking. This choice of the low-energy model is a generalization of previous (successful) low-energy treatments of distorted 1T-TaS_2 [320, 321], but strictly speaking it is valid only under the assumption that a full DFT+DMFT treatment with the appropriate supercell, nonlocal corrections, and extended basis set would give similar results. Such a prohibitively large calculation goes beyond the purpose of the present work.

6.6 Conclusions

We have investigated monolayer 1T-$NbSe_2$ by combined DFT, GW, DFPT, and DMFT simulations. With DFPT and DFT (GGA) simulations, we have shown that there are unstable phonon modes in large parts of the BZ including those wave vectors corresponding to a commensurate $\sqrt{13}\times\sqrt{13}$ CDW and that the formation of this particular CDW with a SoD-like PLD is energetically stable with respect to the undistorted phase. A very flat band at the Fermi level in the CDW phase renders the system susceptible to a Mott instability in the presence of a local Coulomb interaction. A first-principles estimate of the Hubbard-type interaction for the flat band is provided. Subsequent GGA+DMFT p–d calculations in the distorted phase yield a correlated insulator deep in the atomic limit. The size and nature of the insulating gap is determined by an interplay of local and long-range Coulomb interactions. For strongly screened nonlocal interactions, as assumed in GGA, we arrive at a charge-transfer insulator, while inclusion of nonlocal interactions on a GW level rather suggests free-standing 1T-$NbSe_2$ to be at the verge between a Mott–Hubbard and a charge-transfer insulator. Importantly, substrates can be used to effectively tune nonlocal interactions in 2D materials and to possibly switch 1T-$NbSe_2$ between the clear charge-transfer insulator and an insulator of enhanced Mott–Hubbard character.

Chapter 7

Material systematics of metallic transition-metal dichalcogenides

The results presented in this chapter are the starting point for our studies on the metallic TP TMDCs. They have not been published yet. The work has been realized in collaboration with G. Schönhoff, M. Rösner, E. Kamil, and T. O. Wehling. All PBE/cRPA data and the spin susceptibility have been calculated by E. Kamil and G. Schönhoff using VASP (cf. App. A.4) and PLASMOS (cf. App. A.9). The latter code itself has been implemented by M. Rösner. Table 7.1 is based on an idea by G. Schönhoff. I performed the LDA/cDFPT calculations and created all figures shown.

The 2D TMDCs constitute a prominent showplace for competing many-body instabilities such as superconductivity [17], CDWs [158], and magnetism [224]. In this study, we show that even though the observed phase diagrams are complex, the underlying mechanisms are captured by a compact unifying theoretical framework. We apply the cRPA [48, 49] and cDFPT [50] to the metallic TP monolayers 1H-MX_2, where M stands for V, Nb, or Ta and X for S or Se, and summarize the material specifics with a small number of representative Coulomb and EPC parameters. Both cRPA and cDFPT imply a separation of the electrons into an active subspace, here an isolated metallic band, and the rest. We find that all relevant physics emerges from interactions within this subspace alone. Beyond that, the materials can be well described by very similar TB and mass–spring models.

7.1 Introduction

In this work, we focus on spin and charge order in the sulfides and selenides of the TP group-V transition metals, a topic that has been addressed by several experimental [18, 22, 96, 111, 158, 325, 328, 329, 332] and theoretical [136, 294, 322–324, 326, 327, 330, 331, 333] studies in the past decades. Table 7.1 aims to reflect the findings in a structured way. Generally speaking, the vanadium compounds tend to be magnetic, the tantalum compounds are more susceptible to charge order, and the niobium compounds appear to be on the verge between the two. Both phenomena depend significantly on dimensionality, i.e., the number of layers.[1]

To get a systematic understanding of these phenomena, we study the underlying processes, namely the Coulomb and electron–phonon interaction, from first principles in the framework of DFT [31, 32]. With the help of the established cRPA [49] and the novel cDFPT [50] downfolding methods, we construct model Hamiltonians with fully and partially screened

[1] The same holds for superconductivity [17–20], neither shown in the table nor discussed here.

	S_2	Refs.	Se_2	Refs.
V	**Ferromagnetic** *Bulk:* $\sim 0.85\mu_B$ *ML:* $\sim 1\mu_B$	322–324	**Ferromagnetic** *ML:* $\sim 1\mu_B$	330
Nb	**Unclear** *Bulk:* close to CDW *ML:* SDW (~ 0.4 M), CDW	325–328	**CDW** *Bulk:* $T_{CDW} = 33.5$ K *ML:* T_{CDW} enhanced	18, 22, 96, 136, 158, 294, 331
Ta	**CDW** *Bulk:* $T_{CDW} = 75$ K *ML:* confirmed at low T	111, 328, 329	**CDW** *Bulk:* $T_{CDW} = 122.3$ K *ML:* predicted to persist	96, 332, 333

Table 7.1: *[An early version of this table has been created by Gunnar Schönhoff.]* Overview of the metallic TP TMDCs according to the literature. The background color indicates trends toward spin (blue) and charge order (orange). ML stands for monolayer.

parameters for electrons, phonons, and their interaction and thereby reduce the problem to the relevant physics alone. Based on these models, we then investigate the susceptibility (cf. App. C.5) of the different materials to the many-body instabilities of interest. The results are presented in Sec. 7.2. The relevant computational details are listed in Sec. 7.3.

The idea of the *constrained* methods cRPA and cDFPT is the separation of the electronic problem into an active subspace $\mathcal{S}$, where all relevant physics takes place, and the rest. The methods are explained in detail in Secs. 2.4.2.2 and 2.6.1.1, respectively. In the case of all studied materials, we have an isolated metallic band around the Fermi level, as seen in Fig. 7.1 and earlier in Fig. 2.5a, which we identify as our active subspace $\mathcal{S}$. Since the orbital character of this band is largely given by the d_{z^2}, d_{xy}, and $d_{x^2-y^2}$ orbitals of the transition-metal atoms, we work in the basis of these orbitals. However, the subspace spanned by these three orbitals includes two more bands above the Fermi level (cf. Fig. 2.5a), which have to be considered in the calculation even though they are not part of our active subspace.

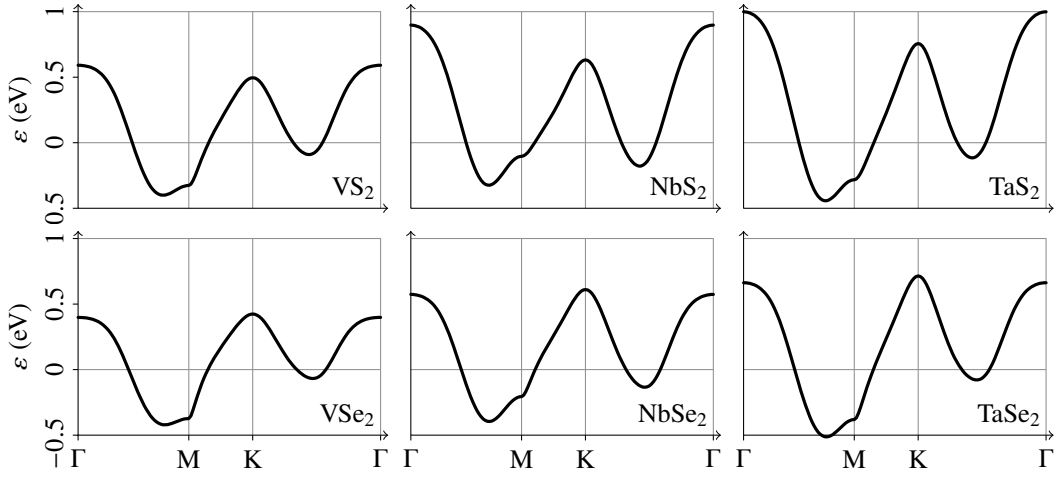

Figure 7.1: Similar dispersions, different bandwidths I: Electrons.

	PBE •		LDA •		exp. (bulk) •		
	a/Å	h/Å	a/Å	h/Å	a/Å	h/Å	Ref.
VS_2	3.166	2.974	3.077	2.923	—	—	—
VSe_2	3.322	3.196	3.227	3.131	—	—	—
NbS_2	3.349	3.127	3.279	3.102	3.31	3.14	334
$NbSe_2$	3.477	3.359	3.395	3.319	3.45	3.36	335
TaS_2	3.335	3.122	3.271	3.094	3.314	3.116	336
$TaSe_2$	3.469	3.349	3.393	3.307	3.436	3.35	337

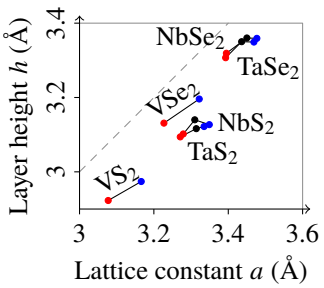

Table 7.2: Lattice parameters of metallic TP TMDCs monolayers as obtained from variable-cell relaxation using PBE and LDA. The experimental reference values belong to the bulk. Except for Ref. 336, the selection has been borrowed from Ref. 4.

7.2 Results

7.2.1 Lattice parameters

All calculations are performed for the undistorted structures, i.e., simple hexagonal unit cells with one transition-metal atom M and two chalcogen atoms X. Variable-cell relaxation using either LDA or PBE functionals leads to the lattice parameters listed in Tab. 7.2. Here, a is the lattice constant (distance between neighboring M atoms) and h is the layer thickness (distance between X planes). As usual, LDA yields smaller interatomic distances as compared to PBE. Experimental reference values (for the corresponding bulk materials) lie in between.

7.2.2 Electrons

The electronic-structure properties were calculated for the relaxed lattice. In Fig. 7.1, the low-energy LDA band structures of all considered materials are plotted next to each other along the path Γ–M–K–Γ connecting high-symmetry points in the BZ. As mentioned above, we find a half-filled isolated band at the Fermi level in all cases. It is evident that the characteristic shape of this band—with maxima at Γ and K, minima for intermediate crystal momenta and a saddle point at M—is shared among all six materials. The main difference is the bandwidth, which is compared in Fig. 7.3c. It increases (decreases) with the period of the transition metal (chalcogen).

7.2.3 Phonons

Starting from the LDA electronic structure, the phonon dispersions according to both DFPT and cDFPT are calculated and displayed in Fig. 7.2. As for the electrons, all materials have similar dispersions but differ in bandwidth. Here, heavier compounds oscillate more slowly and the mass difference of the involved atomic species correlates with the separation between acoustic and optical modes.

All fully screened dispersions feature a softening of the LA mode. The imaginary frequencies are most prominent around $\boldsymbol{q} = 2/3\,\mathrm{M}$, the wave vector belonging to a commensurate 3×3 CDW. Upon exclusion of screening from within the active subspace $\mathcal{S}$, this feature disappears completely, leaving behind a very smooth dispersion of all branches on the entire BZ. In other words, the interaction of LA phonons with the electrons of the metallic band alone is responsible for the charge order observed in the metallic TP TMDCs.

Some phononic branches remain completely unaltered by the constraint. This applies for instance to the ZA mode, recognizable by the quadratic dispersion in the limit of long wavelengths.

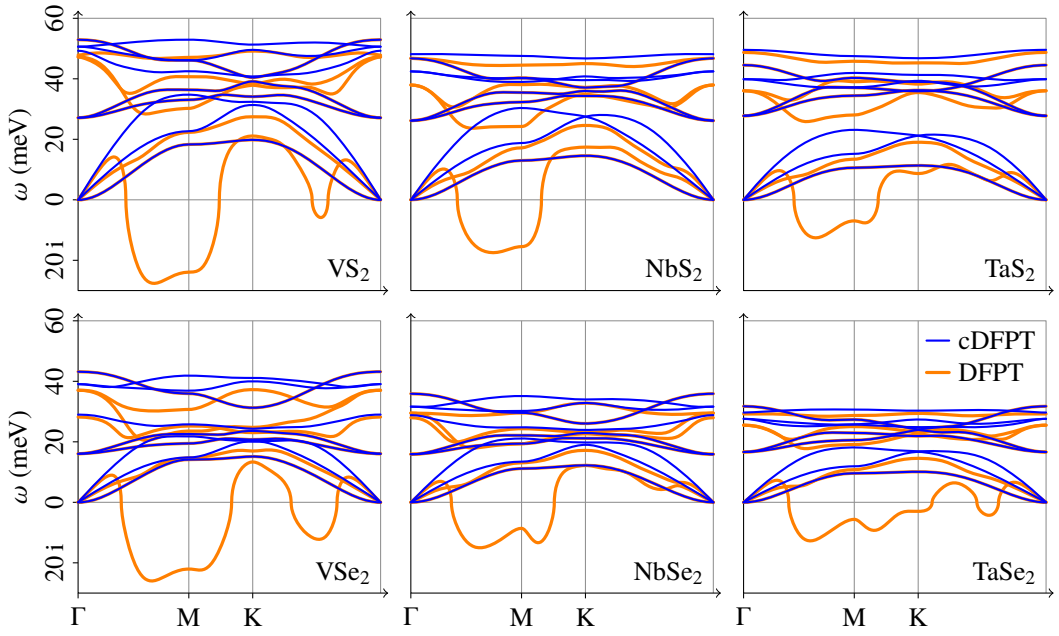

Figure 7.2: Similar dispersions, different bandwidths II: Phonons.

7.2.4 Coulomb interaction

We calculate the partially screened (cRPA) momentum-dependent Coulomb-interaction tensor $U_{\boldsymbol{q}\alpha\beta\gamma\delta}$ according to Eq. 2.152. Here, we neglect the dependencies on the frequency and two electronic momenta $\boldsymbol{k}$ and $\boldsymbol{k}'$. With all dependencies stated explicitly,

$$U_{\boldsymbol{q}\alpha\beta\gamma\delta} = v_{\boldsymbol{q}\alpha\beta\gamma\delta} + \sum_{\alpha'\beta'\gamma'\delta'} v_{\boldsymbol{q}\alpha\beta\gamma'\delta'} \chi^{\mathrm{R}}_{\boldsymbol{q}\gamma'\delta'\alpha'\beta'} U_{\boldsymbol{q}\alpha'\beta'\gamma\delta}, \tag{7.1a}$$

$$\chi^{\mathrm{R}}_{\boldsymbol{q}\gamma\delta\alpha\beta} = \frac{2}{N} \sum_{\substack{\boldsymbol{k}mn \\ \{\boldsymbol{k}n,\boldsymbol{k}+\boldsymbol{q}m\}\notin\mathcal{S}}} U_{\boldsymbol{k}+\boldsymbol{q}\gamma m} U^*_{\boldsymbol{k}\delta n} \frac{f(\varepsilon_{\boldsymbol{k}+\boldsymbol{q}m}) - f(\varepsilon_{\boldsymbol{k}n})}{\varepsilon_{\boldsymbol{k}+\boldsymbol{q}m} - \varepsilon_{\boldsymbol{k}n}} U^*_{\boldsymbol{k}+\boldsymbol{q}\alpha m} U_{\boldsymbol{k}\beta n}. \tag{7.1b}$$

If we are most interested in the local interaction, a suitable way of reducing the Coulomb data in a meaningful way is the Kanamori parametrization [338]. Here we consider only

$$U_{\alpha\beta\gamma\delta} = \frac{1}{N} \sum_{\boldsymbol{q}} U_{\boldsymbol{q}\alpha\beta\gamma\delta}, \tag{7.2}$$

which is nothing but the $\boldsymbol{R} = 0$ component of the Fourier transform, and calculate

$$U = \frac{1}{3} \sum_{\alpha=1}^{3} U_{\alpha\alpha\alpha\alpha}, \tag{7.3a}$$

$$U' = \frac{1}{6} \sum_{\alpha\neq\beta} U_{\alpha\alpha\beta\beta}, \tag{7.3b}$$

$$J = \frac{1}{6} \sum_{\alpha\neq\beta} U_{\alpha\beta\beta\alpha}. \tag{7.3c}$$

U and U' are the local intra- and inter-orbital interaction without electron exchange, whereas J is the local inter-orbital interaction with exchange. The results can be seen in Fig. 7.3. The local Coulomb interaction divided by the electronic bandwidth increases when going to lighter transition-metal atoms (Ta → Nb → V) and heavier chalcogen atoms (S → Se).

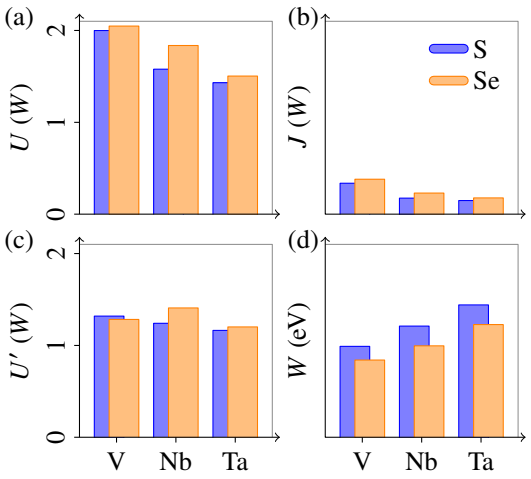

Figure 7.3: Kanamori parametrization of the local Coulomb interaction according to Eq. 7.3a. Please note that the intra-orbital (U) and inter-orbital repulsion with (J) and without exchange (U') are displayed in units of the electronic bandwidth (W).

7.2.5 Spin susceptibility

We calculate the momentum-dependent spin susceptibility (cf. App. C.5) within the GW and T-matrix approximation following the scheme given in Ref. 339 as implemented in PLASMOS (cf. App. A.9). Diagrammatically, it is a series of ladder diagrams,

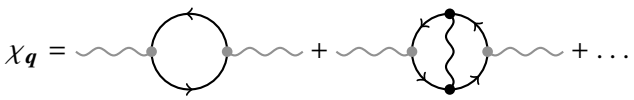

(7.4)

Here, the gray wiggly lines are not part of the diagram but represent its appropriate contacts.

The results are displayed in Fig. 7.4. In Fig. 7.4a, we only consider the first term, which is nothing but the bare electronic susceptibility of the noninteracting KS system (cf. Fig. 2.12). It is similar for all materials. The results for the full series in Fig. 7.4b give a different picture. In accordance with Ref. 327, we find a tendency toward a spin-density wave (SDW) instability with wave vector $\boldsymbol{q} \approx 0.4\,\mathrm{M}$ for the niobium- and tantalum-based compounds. Corresponding to the strength of the Coulomb interaction from Sec. 7.2.4, the compounds with lighter transition metals (Ta → Nb → V) and heavier chalcogens (S → Se) are more susceptible to external magnetic fields.

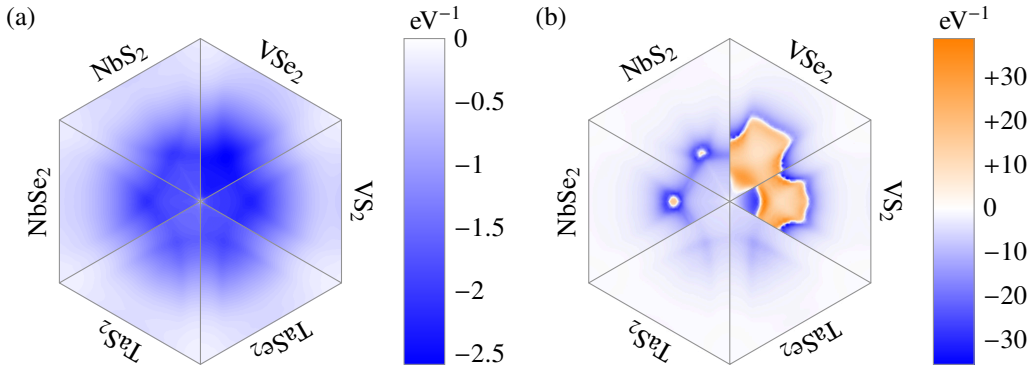

Figure 7.4: Spin susceptibility for different TMDCs for (a) the noninteracting KS system and (b) interactions within T-matrix approximation switched on. Calculated with PLASMOS (cf. App. A.9).

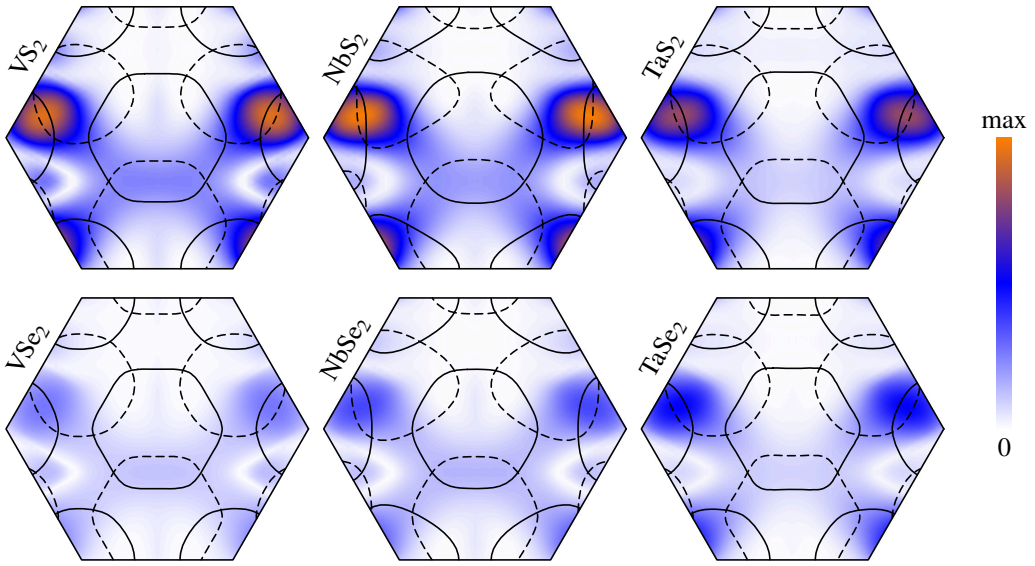

Figure 7.5: Similar dispersions, different bandwidths III: EPC. We show the $\boldsymbol{k}$-dependent squared cDFPT EPC d^2 between the metallic band and the LA phonons for $\boldsymbol{q} = 2/3\,\mathrm{M}$ together with the in- (solid) and outgoing Fermi surface (dashed lines). A detailed analysis for 1H-TaS_2 is found in Chap. 9.

7.2.6 Electron–phonon coupling

The wave vector of the leading lattice instability is $\boldsymbol{q} = 2/3\,\mathrm{M}$. In Fig. 7.5, we show the $\boldsymbol{k}$-dependent EPC between the metallic band and the unstable LA phonon mode for this $\boldsymbol{q}$ point together with the in- and outgoing Fermi surface. In all cases, we find the maximum of the EPC halfway between K and the shifted K′ point. Additionally, in this $\boldsymbol{k}$-space region, the hole pockets around K and the shifted K′ point are approximately touching each other, leading to a large bare electronic susceptibility. This combination of matrix-element and Fermiology effects is the origin of the CDWs in the metallic TMDCs. For a more detailed analysis, we refer to Chap. 9.

We now compare the strengths of the EPC for the different materials. Here, we restrict our analysis to the maximum of the matrix elements shown in Fig. 7.5. The dimensionless quantity $d^2/W\omega^2$ represents the EPC in the natural energy units of the system, analogous to the definition of the effective EPC in the Eliashberg theory (Eq. 3.10a). We find that this coupling increases when going to heavier transition-metal atoms (V → Nb → Ta).

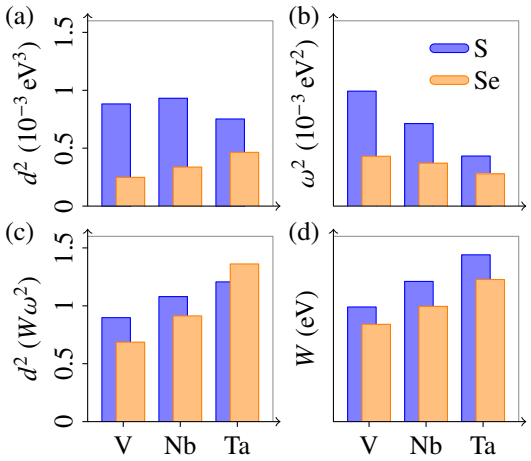

Figure 7.6: Effective EPCs. We consider the largest matrix element of the squared coupling d^2 between the metallic band and the LA phonon mode for $\boldsymbol{q} = 2/3\,\mathrm{M}$. Division by the bandwidth W and the LA phonon frequency squared ω^2 makes this quantity dimensionless.

7.3 Computational parameters

Most calculations are performed with QE [39, 40] using the LDA functional and normconserving Hartwigsen–Goedecker–Hutter (HGH) PPs [340, 341] at a kinetic-energy cutoff of 100 Ry. Electrons and phonons are calculated on uniform 36×36 $\boldsymbol{k}$- and 12×12 $\boldsymbol{q}$-point meshes, in combination with a Methfessel–Paxton smearing [306] of 10 mRy (cf. App. C.7.3). Assuming a fixed unit cell height of $c = 20$ Å, forces and in-plane pressure are reduced to below 1 µRy/Bohr and 0.1 kbar, respectively. For the transformation of electronic quantities into the basis of Wannier functions, we use the WANNIER90 package [92].

In contrast, all calculations related to the Coulomb interaction are performed with VASP [299, 300] and with different DFT parameters. Here, we use the PBE functional [75, 76], an energy cutoff of 500 eV, 18×18 $\boldsymbol{k}$ points, a unit cell height of $c = 30$ Å, and a force threshold of 10 meV/Å. For possible more in-depth analyses in the future, consistent DFT parameters should be chosen. Here, PBE is favored over LDA.

Chapter 8

Phase diagram of lattice instabilities in mono- and bilayer 2H-TaS_2

The results of the previous Chap. 7 stimulated the development of our phonon-renormalization scheme (cf. Chap. 5), which we first applied in this collaboration with the experimental groups of T. Michely and A. Grüneis. Most of the work presented in this chapter has been published in ACS Nano ***13****, 10210 (2019) [111]. Authors of the published article include J. Hall, N. Ehlen, C. van Efferen, C. Murray, J. Li, B. V. Senkovskiy, M. Hell, M. Rolf, T. Heider, M. C. Asensio, J. Avila, and L. Plucinski. However, here I only show the theory part prepared by E. van Loon, M. Rösner, T. Wehling, and myself. I performed all numerical calculations and created the corresponding figures. The* "arctan" *formula describing hybridization (cf. App. C.7.4) has been derived by E. van Loon. For this thesis, I added an introduction as well as Figs. 8.4 and 8.6 and the corresponding discussions. A trimmed version of Fig. 8.4 has already been published together with the Supporting Information of Ref. 111.*

Figure 8.1 shows three STM images of monolayer 1H-TaS_2. Figure 8.1a from Sanders *et al.* in Aarhus [342] does not show any sign of CDWs. The modulation visible in the picture is a moiré pattern due to a lattice mismatch between the probe and the substrate. Figures 8.1b and 8.1c from Hall *et al.* in Cologne [111] however show CDWs, even of different periodicities. In Fig. 8.1b we have a 3×3, in Fig. 8.1c a 2×2 superstructure. Additionally, Hall *et al.* observed a 2×2 CDW for bilayer 2H-TaS_2.

To understand these diverse findings, we have to compare the experimental conditions. The main difference between the experiments is the substrate used and the absence or presence of adatoms. In Fig. 8.1a, the substrate is gold (Au), which is known to strongly hybridize with the probe. In Figs. 8.1b and 8.1c, the substrate is graphene (Gr) on top of iridium (Ir), which is much more decoupled from the sample. We consider the (111) surface of both Au and Ir, where the surface atoms form a close-packed layer. For the results in Fig. 8.1c, the sample was additionally exposed to lithium, which contributes negative charge doping.

Hybridization with the substrate has two fundamental effects. First, the electronic linewidth is broadened. Second, the chemical potential is effectively shifted due to pseudodoping [13, 14], which comes in addition to the effect of real charge doping. If the sample consists of more than one layer, the different layers are affected in a biased way.

From the literature [325, 345] and former DFPT calculations for similar materials, we already have some previous knowledge of the effect of doping and broadening on the phonons. Figure 8.2 shows the DFPT phonon dispersion of monolayer 1H-$NbSe_2$ for different occupations and occupation smearings. In Fig. 8.2a, we see that upon electron doping, the leading instability moves toward the M point and is finally suppressed. Also an increased

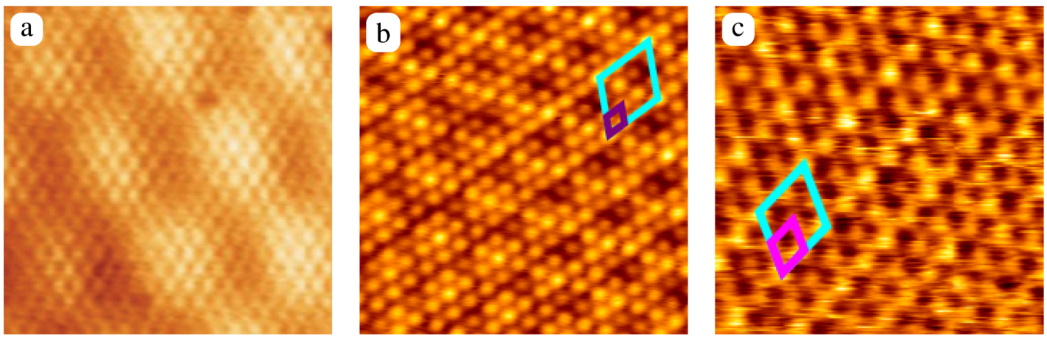

Figure 8.1: STM images of monolayer 1H-TaS_2 on different substrates. (a) No CDW in 1H-TaS_2/Au. *[Image taken from Ref. 342 © 2016 American Physical Society].* (b) 3×3 CDW in 1H-TaS_2/Gr/Ir. *[Image taken from Ref. 111].* (c) 2×2 CDW in Li-doped 1H-TaS_2/Gr/Ir. *[Image taken from Ref. 111].* In STM, the tunneling current I between the sample and the tip of the microscope is measured. Within the approximation by Tersoff and Hamann [343, 344], I as a function of the sample bias V and the tip position $\boldsymbol{r}$ is given by $I_V(\boldsymbol{r}) \propto \sum_{\boldsymbol{kn}}[f(\varepsilon_{\boldsymbol{kn}}) - f(\varepsilon_{\boldsymbol{kn}} - V)]|\psi_{\boldsymbol{kn}}(\boldsymbol{r})|^2$, where ε, f, and ψ are electronic single-particle energies, occupations, and wave functions. Hence, the local DOS ρ (LDOS), measured by scanning–tunneling spectroscopy (STS), is proportional to the derivative $\partial I_V(\boldsymbol{r})/\partial V \propto \sum_{\boldsymbol{kn}} \delta(\varepsilon_{\boldsymbol{kn}} - V)|\psi_{\boldsymbol{kn}}(\boldsymbol{r})|^2 \equiv \rho_V(\boldsymbol{r})$.

smearing suppresses the instability, as seen in Fig. 8.2b, albeit without shifting the wave vector of the instability. In App. D.6, we will find analogous dependencies for bilayer 2H-$MoSe_2$.

Such DFPT calculations are computationally costly. To calculate the phase diagram of lattice instabilities at a high resolution, we take another route: We perform only two *ab initio* simulations—one with DFPT and another with cDFPT—and perform the phonon renormalization on the model level (cf. Chap. 5). This way, each point in phase space can be analyzed within seconds on a single processor instead of several hours on a supercomputer.

After describing the methods used in Sec. 8.1, we will present our results for monolayer 1H- and bilayer 2H-TaS_2 in Sec. 8.2. The computational details are given in Sec. 8.3.

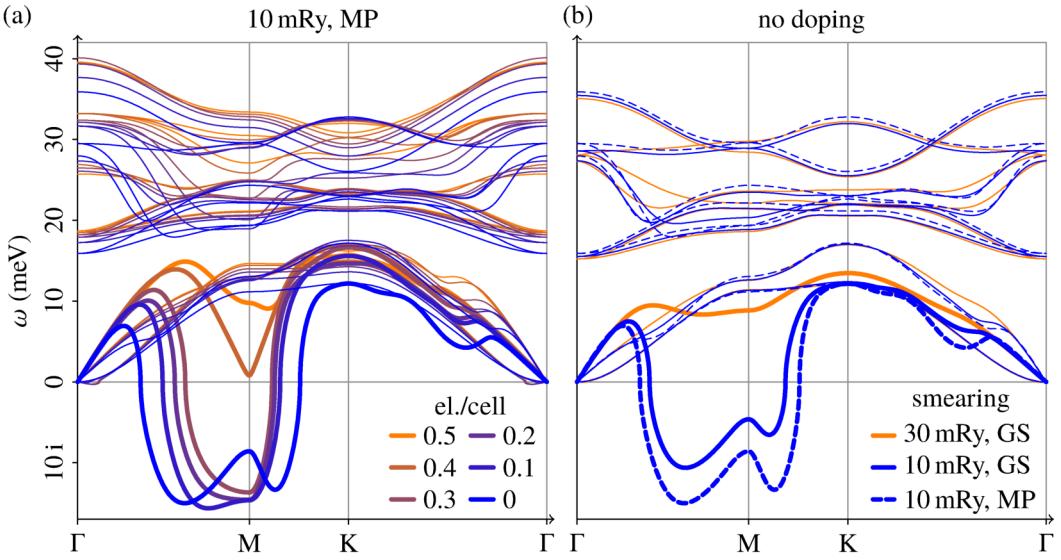

Figure 8.2: *Ab initio* phonon dispersion of the metallic TMDC monolayer 1H-$NbSe_2$ for different (a) doping levels and (b) electronic smearings, where MP stands for Methfessel–Paxton and GS for Gaussian smearing (cf. Apps. C.7.2 and C.7.3).

8.1 Methods

The goal of our theoretical modeling is to understand the influence of different external stimuli such as hybridization with substrates or electron doping on the 1H- and 2H-TaS_2 phonon dispersion, and thereby on the lattice instabilities that emerge from the softening of LA phonons due to metallic screening. To this end, we downfold the electronic structure and lattice dynamics of 1H- and 2H-TaS_2 to a material-realistic low-energy model containing all phonons and the low-energy electrons shown in the lower panels of Fig. 8.4 and the left panels of Fig. 8.6. The phonons entering this model are bare (or, more precisely, partially screened) in the sense that they remain to be renormalized by interactions with the low-energy electrons [50]. The bare phonons and the corresponding dynamical matrices D are obtained from cDFPT [50] (cf. Sec. 2.4.2.2). The final experimentally observable phonon dispersion results from the screened dynamical matrix $\widetilde{D} = D + \Pi'$, which accounts for the coupling of the lattice vibrations and the low-energy electrons through the phonon "self-energy" Π' according to Eq. 5.12. On this basis, we analyze the influence of charge doping, hybridization with substrates, and interlayer bias potentials (bilayer case) on the phonon dispersions and particularly lattice instabilities of 1H- and 2H-TaS_2.

The combined effect of real and pseudodoping is accounted for in a rigid-band model by shifting the band energies ε relative to the Fermi level. This is justified because it is known that doping does hardly influence the shape of the electronic dispersion of the considered material [345].

Broadening from hybridization enters via a modification of the shape of the Fermi functions f in Eq. 5.12. As derived in App. C.7.4, hybridization with the substrate leads to a Lorentzian broadening of the electronic levels and the occupation function at $T = 0$ becomes $f(\varepsilon) = 1/2 - \arctan(\varepsilon/\Gamma)/\pi$, where Γ is the half-width at half-maximum (HWHM) of the broadening. Note that the arctangent decays only polynomially, contrary to the exponential decay of the Fermi–Dirac distribution. This means that states further away from the Fermi level are more relevant for hybridization than for temperature effects.

Our low-energy model is set up in the localized basis of atom-centered Wannier functions and atomic displacements. This allows us to also manipulate the model on the level of hopping parameters and on-site energies, which helps us to study the bilayer. Here, an interlayer bias potential $\Delta\varepsilon_0$ is introduced to the bilayer by adding $\Delta\varepsilon_0/2$ to all on-site energies of one layer, while subtracting the same value from all on-site energies of the other layer.

8.2 Results

8.2.1 Monolayer

In Fig. 8.3a, we show the screened phonon dispersion of monolayer 1H-TaS_2 for selected values of the charge doping and broadening due to hybridization with a substrate. Here, the renormalization has been calculated on the model level as described above.

In the quasi-freestanding case, where we have no doping ($x = 0$) and only a weak hybridization ($\Gamma = 10\,\mathrm{meV}$), the LA phonon branch exhibits a strong Kohn anomaly. Phonon modes with imaginary energy imply that the lattice is unstable with respect to corresponding PLDs and charge ordering. The DFT establishes a local extremum in the Landau energy functional $E(u) = E_0 + \frac{1}{2}\omega_{\boldsymbol{q}}^2 u_{\boldsymbol{q}}^2 + \ldots$ that quantifies the energy cost of moving the atoms out of the DFT equilibrium positions by some distortion $u_{\boldsymbol{q}}$. The square of the phonon frequency $\omega_{\boldsymbol{q}}$ is the coefficient of the quadratic contribution to the energy. Therefore, an imaginary phonon frequency implies an energy *gain*, which means that the equilibrium is unstable toward PLDs with the corresponding wave vector $\boldsymbol{q}$.

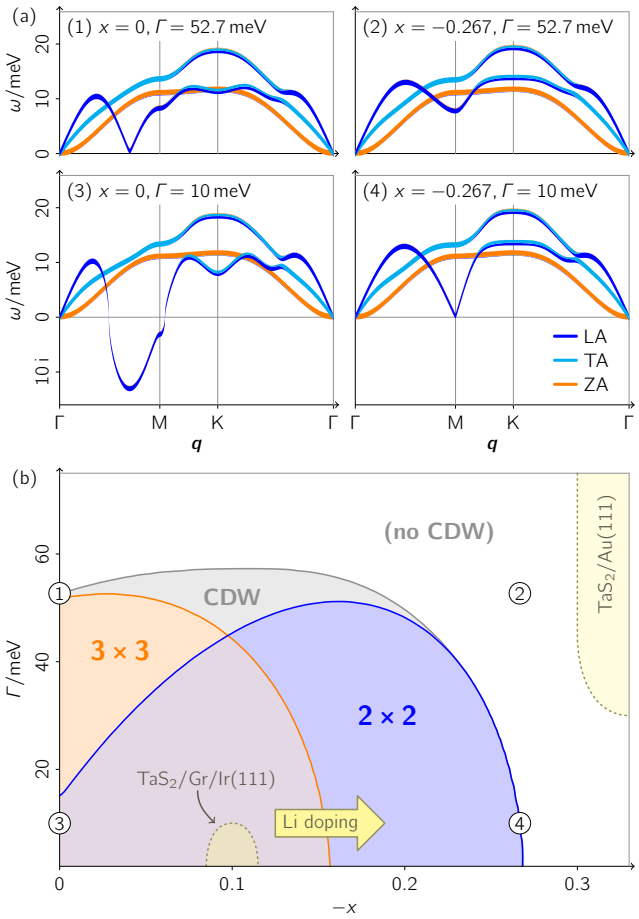

Figure 8.3: Phonon dispersions and lattice instabilities of monolayer 1H-TaS_2 for different levels of the (pseudo) chage doping $-x$ (in units of electrons per Ta atom such that negative x refer to electron addition) and the hybridization broadening Γ (HWHM of the electronic lines) at zero temperature. (a) Acoustic phonon dispersions for selected conditions. The character of the phonon modes (LA, TA, or ZA) is shown with colors. Imaginary phonon frequencies at certain $\boldsymbol{q}$ points indicate that the lattice is unstable toward corresponding PLDs. (b) Complete phase diagram of lattice instabilities. The CDW region is defined by the presence of an imaginary phonon frequency at one or more $\boldsymbol{q}$ points. Subsets are regions with instabilities at $\boldsymbol{q} = 2/3\,\mathrm{M}$ for the 3×3 CDW and at $\boldsymbol{q} = \mathrm{M}$ for the 2×2 CDW. The experimentally realized situations of 1H-TaS_2/Au [14, 342] and pristine and Li-doped 1H-TaS_2/Gr/Ir (this work) are indicated. Points corresponding to the dispersions shown in (a) are marked with encircled numbers 1–4.

This linear-response theory reveals the existence of instabilities, but it does not predict the distorted structure (corresponding to the global minimum of the Landau functional). However, the mode with the largest imaginary frequency, also called leading instability, is a clear indicator of energetically particularly favorable PLDs. In the quasi-freestanding case, the instability region extends over large parts of the BZ including the wave vectors $\boldsymbol{q} = 2/3\,\mathrm{M}$ and M. At $\boldsymbol{q} = 2/3\,\mathrm{M}$, which is associated with the 3×3 CDW, the instability is particularly strong as indicated by a large imaginary phonon frequency.

The doping and hybridization with a substrate can strongly affect the phonon dispersions, as shown in the other panels. In essence, we find that electron doping moves the wave vector of the leading instability, i.e., largest imaginary frequency, from $\boldsymbol{q} \approx 2/3\,\mathrm{M}$ to M such that the CDW shifts in wavelength. At an electron doping exceeding about 0.27 electrons per Ta atom, the lattice becomes dynamically stable, which is in agreement with previous calculations [345]. An increase in hybridization on the other hand leaves the wavelength of the leading CDW instability largely unchanged, but weakens the Kohn anomaly and eventually also stabilizes the lattice. Thus, both charge doping and hybridization trigger a quantum phase transition from CDW to undistorted states of the lattice, but via different critical wave vectors.

The overall relation between lattice instabilities, doping, and hybridization is summarized in the phase diagram shown in Fig. 8.3b. Here, the condition for the 3×3, 2×2, and further CDW phases is the presence of imaginary phonon frequencies at $\boldsymbol{q} = 2/3\,\mathrm{M}$, M, and anywhere in the BZ, respectively.

Applied to the experiments performed by Hall *et al.*, we can state the following: In 1H-TaS_2/Gr/Ir, a doping level of 0.1 excess electrons per unit cell is measured in ARPES, while no signs of hybridization are experimentally observed. We therefore locate 1H-TaS_2/Gr/Ir in the phase diagram of Fig. 8.3b in the region around $x = -0.10$ and $\Gamma \approx 0$, which is in line with the 3×3 CDW observed in STM. Intercalating Li increases the doping and moves the experiment toward the right-hand side of the diagram. This is consistent with the experimental observation of a 2×2 CDW in the Li-doped system.

Previous experiments [342] on 1H-TaS_2/Au did not find any charge order down to 4.7 K. A major difference to the experiments reported here, including those with Li intercalation, is significant hybridization of 1H-TaS_2 with the Au substrate [14]. Our calculations show that hybridization can be very effective at destabilizing charge order. The hybridization affects the phonon dispersions through the phonon self-energy Π, and it is much more effective in quenching Π than thermal broadening (cf. Sec. 8.1). For 1H-TaS_2/Au, the hybridization is energy-dependent [14] and the HWHM of the broadening Γ spans a range between 30 meV and 90 meV! Placing 1H-TaS_2/Au in the phase diagram of Fig. 8.3b, we have to account for both the electron (pseudo)doping [14] in the range between $x = -0.3$ [342] and -0.4 [14] and the hybridization broadening between $\Gamma = 30$ meV and 90 meV. Clearly the interplay of both stabilizes the lattice. Lattice relaxation can further support this stabilization [345, 346].

[1]We base our estimate for the electronic broadening on the results of Ref. 14, which contains DFT results for 1H-TaS_2 with and without Au substrate. A broadening of 30 meV explains the change in spectral weight at the VHS, and a broadening of up to 90 meV is needed to describe the transfer of spectral weight into the gap.

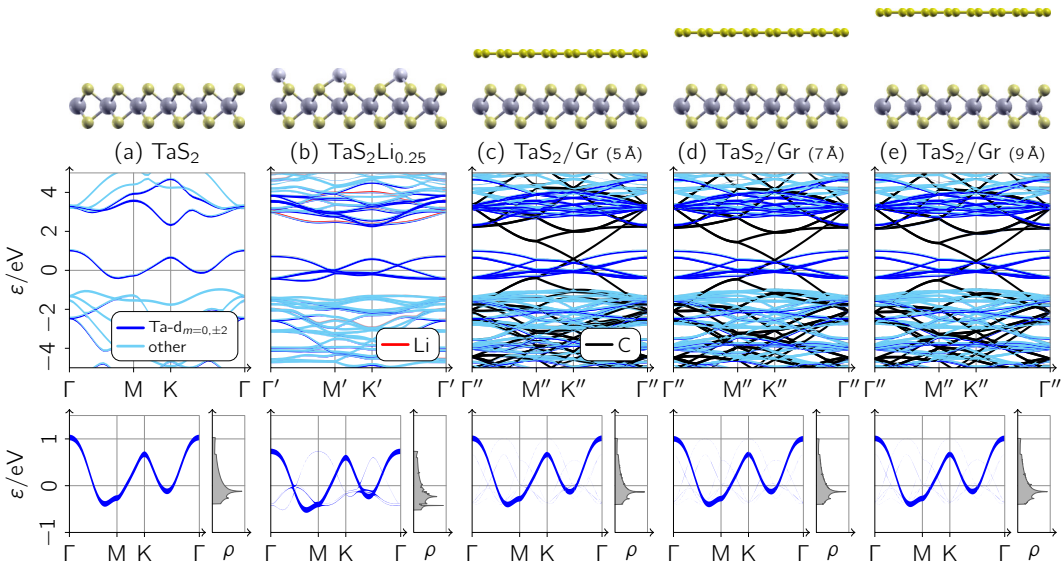

Figure 8.4: Band structure of monolayer 1H-TaS_2 in different environments: (a) freestanding, (b) with one Li adatom per four Ta atoms, and (c–e) on top of graphene with a vertical Ta-C distance of (c) 5 Å (relaxed), (d) 7 Å, and (e) 9 Å. The upper panels show the bands along paths through the respective BZs of the systems. Line widths and colors visualize the projections onto atomic orbitals. The lower panels show the low-energy band of 1H-TaS_2 alone. In (b–e), the data is unfolded to the same $\boldsymbol{k}$ points as in (a), revealing that the band is hardly changed in shape but shifted downward with respect to the Fermi level (on average). The effective doping levels and corresponding average shifts of the chemical potential are (b) $x = -0.240$, $\Delta\mu = 133$ meV, (c) $x = -0.030$, $\Delta\mu = 13$ meV, (d) $x = -0.021$, $\Delta\mu = 10$ meV, and (e) $x = -0.016$, $\Delta\mu = 8$ meV. The Dirac point of graphene is located at (c) 584 meV, (d) 527 meV, and (e) 479 meV above the Fermi level.

To illustrate the effect of the environment on the (pseudo)doping level of 1H-TaS_2 in an approximate way, we perform supercell calculations for 1H-TaS_2 on graphene and for Li-doped 1H-TaS_2 with DFT. The results are summarized in Fig. 8.4. The upper panels show the bands along a path through the BZ corresponding to the supercell. In the lower panels, the bands have been unfolded to the larger BZ of the original unit cell (cf. Sec. 3.1.3).

Li-doped 1H-TaS_2 is modeled assuming that one Li adatom is positioned on top of every fourth Ta atom in a 2×2 supercell. As apparent in Fig. 8.4b, there are now unoccupied Li-derived states above the gap, which donate an additional electron per supercell to the 1H-TaS_2 bands. The resulting doping level is $x = -0.25$, as expected from this stoichiometry.

1H-TaS_2/Gr is modeled combining a 3×3 supercell of 1H-TaS_2 with a 4×4 supercell of graphene. We leave 1H-TaS_2 unstrained, which results in a lattice constant of 2.5 Å for the graphene. In addition to the relaxed layer spacing (Fig. 8.4c), we also consider two increased spacings (Figs. 8.4d and 8.4e). As opposed to the results for the Li-doped system, only a slight pseudodoping of electrons (the charge transfer is one order of magnitude weaker) is induced by the presence of the graphene layer, which is mitigated by the additional layer spacing. This behavior is understandable from the low DOS provided by graphene in the vicinity of the Dirac point.

8.2.2 Bilayer

Calculated phonon dispersions of freestanding undoped bilayer 2H-TaS_2 are shown in Fig. 8.5a. They are, including the instability region, indeed very similar to the corresponding monolayer case (cf. Fig. 8.3a). Thus, it is *a priori* unexpected that bilayer 2H-TaS_2/Gr/Ir features a 2×2 CDW in contrast to the 3×3 CDW in monolayer 1H-TaS_2/Gr/Ir and also in bulk 2H-TaS_2 [329].

What could drive the CDW order in the bilayer toward the 2×2 periodicity? First, as in the monolayer case, charge doping could be responsible. Since a direct interaction of the bilayer with the graphene substrate is limited to the bottom layer, a stronger average charge doping than in the monolayer due to interaction with the graphene substrate is however unlikely. A possible cause of stronger average charge doping could be Ta self-intercalation

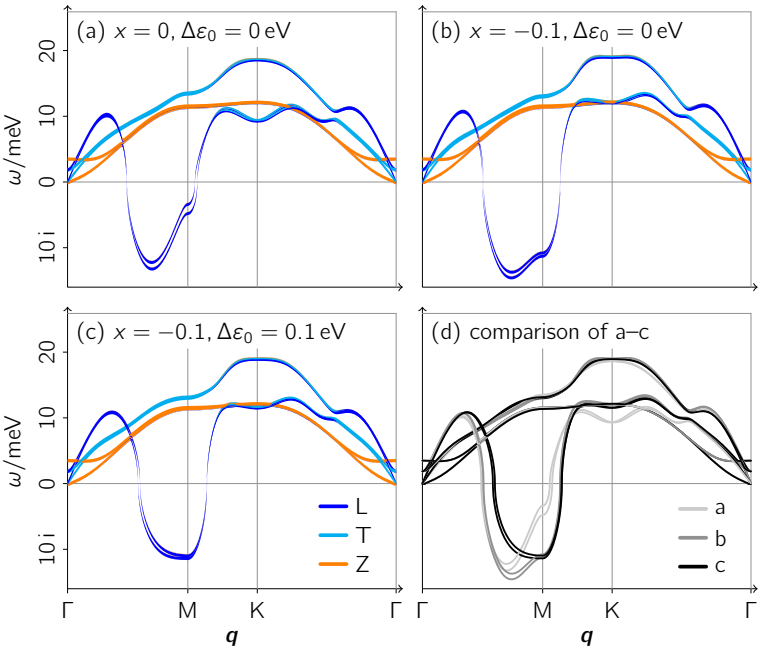

Figure 8.5: (a–c) The three acoustic phonon branches and their layer-shifting optical counterparts of bilayer 2H-TaS_2 for a fixed broadening $\Gamma = 1$ meV, using three different combinations of the (pseudo) charge doping x and the interlayer bias potential $\Delta\varepsilon_0$. (d) Direct comparison of panels (a–c).

between the two layers as observed in bulk 2H-TaS_2 [347, 348]. Second, in the bilayer, the doping from and hybridization with the substrate are naturally different for the bottom and top layer. Also doping due to defects within the layers or by self-intercalation can be different for each layer. Such asymmetries between bottom and top layer might affect the CDW formation.

In our model, this kind of asymmetries are most simply accounted for in terms of an interlayer bias potential $\Delta\varepsilon_0$ (energy gain $-\Delta\varepsilon_0/2$ or penalty $+\Delta\varepsilon_0/2$ for an electron residing in the bottom or the top layer), the effect of which is illustrated in Figs. 8.5b and 8.5c. We find that the interlayer bias can flatten the phonon dispersion in the regions of the instability and eventually also shift the $\boldsymbol{q}$ vector of the leading instability from $\boldsymbol{q} \approx 2/3\,\mathrm{M}$ toward M.

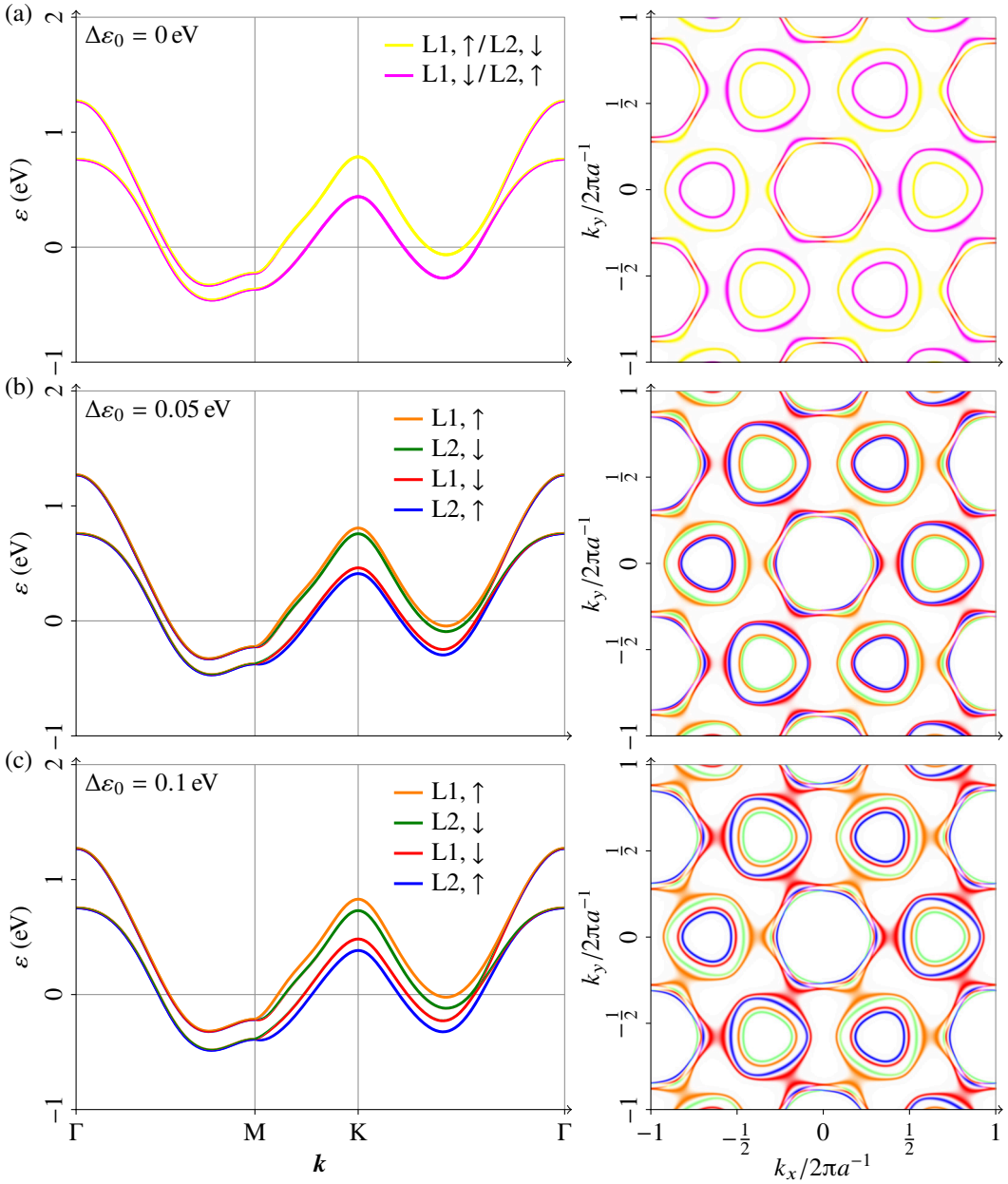

Figure 8.6: Band structure and Fermi surface of bilayer 2H-TaS_2 with SOC for a charge doping $x = -0.1$ and an interlayer bias potential $\Delta\varepsilon_0$ of (a) 0.00 eV, (b) 0.05 eV, and (c) 0.10 eV. The corresponding interlayer charge difference Δx is (a) 0.000, (b) 0.066, and (c) 0.131. (For $\Delta x = 1$, all electrons would reside in the same layer.)

Thus, an effective interlayer bias could also explain the observation of the 2×2 CDW in the bilayer regions. Whether additional doping or interlayer asymmetries are the cause for the switching from the 3×3 to the 2×2 CDW in the bilayer experiments remains speculative.

The immediate effect of the interlayer bias potential on the electrons and thus the mechanism behind the change in the phonons can be seen in Fig. 8.5. The low-energy dispersion and the corresponding Fermi surface is shown for the three different bias potentials considered. In the case without bias potential (Fig. 8.6a), we have a bonding and an antibonding band, both of which are spin-degenerate and layer-degenerate. However, close to the K point and at the minimum between Γ and K, electrons of different spins are in different layers and the spin direction in the same layer is opposite for different bands. When going from K to K′, the spin is flipped. Introducing an interlayer bias potential $\Delta\varepsilon_0 = 0.05\,\mathrm{eV}$ (Fig. 8.6b) lifts the layer degeneracy and, as a consequence thereof, also the spin degeneracy is lifted. The hole pockets belonging to the first and second layer grow and shrink, respectively, which is a clear indication of an electron transfer from the first to the second layer. When the bias potential is further increased to $\Delta\varepsilon_0 = 0.1\,\mathrm{eV}$ (Fig. 8.6c), the minimum of the topmost band between Γ and $\mathrm{K}^{(\prime)}$ gets very close to the Fermi level. This minimum is actually a saddle point that gives rise to a VHS in the DOS of the first layer.

8.3 Computational parameters

All DFT and DFPT calculations have been carried out using QE [39, 40]. The modification that is required for cDFPT is described in detail in Ref. 50. Our implementation is documented in App. A.1. For the transformation of the electronic energies and EPCs to the Wannier basis we used Wannier90 [92–94] and the EPW code [138–140].

We apply the GGA by Perdew, Burke, and Ernzerhof (PBE) [75, 76] and optimized normconserving Vanderbilt PPs [349] from the PseudoDojo table [350] at a plane-wave cutoff of 70 Ry. Uniform meshes (including Γ) of 18×18 $\boldsymbol{k}$ and 6×6 $\boldsymbol{q}$ points are combined with a Gaussian occupation smearing of 10 mRy (cf. App. C.7.2). SOC and van der Waals interactions are taken into account, the latter via the DFT-D3 method by Grimme *et al.* [351].

For the monolayer (bilayer), assuming a fixed unit cell height of 15 Å (25 Å), minimizing the total energy and forces to below 10 µRy/Bohr yields a lattice constant of 3.34 Å (3.33 Å and a distance of 6.10 Å between the two Ta layers).

For the supercell calculations—because of the different types of atoms involved and the partially large height of the systems—we raise the plane-wave cutoff to 90 Ry and use the larger unit-cell height of 25 Å exclusively. In turn, because we do not expect significant effects on the physics of interest here, SOC is disregarded for the sake of computational efficiency. For simplicity, we further assume that the atomic positions of 1H-TaS_2 are not affected by the presence of Li adatoms and a graphene substrate, and we only relax the vertical distances of the latter. Here, the relaxed vertical Ta–Li and Ta–C distances amount to 2.9 Å and 5.0 Å, respectively.

For the calculation of the phonon renormalization using Eq. 5.12, the $\boldsymbol{k}$ resolution is increased to 216×216 points via Fourier interpolation of the electronic dispersions and the EPC matrix elements. This ensures convergence also for small values of the broadening.

Chapter 9

Fluctuation diagnostics of lattice instabilities in monolayer 1H-TaS_2

In Chap. 8, we have seen that doping can influence the CDW periodicity in monolayer 1H-TaS_2. Now, we would like to understand the microscopic mechanism behind this particular observation and the origin of CDWs in this class of materials in general. The work presented in this chapter has been almost verbatim published in Phys. Rev. B ***101****, 155107 (2020) [86]. It is a collaboration with E. G. C. P. van Loon, A. Schobert, M. Rösner, and T. O. Wehling. I performed all numerical calculations and created all figures except for Figs. 9.10b and 9.10c by E. G. C. P. van Loon. I derived the TB model; the Dirac model traces back to T. O. Wehling. Figures 9.3 and 9.12 and the discussion thereof originate from the reply to the referees. For this thesis, I added Fig. 9.8 with discussion. For further details on the calculations, I refer to App. A, in particular App. A.10.*

We present an *ab initio* approach for the calculation of phonon self-energies and their fluctuation diagnostics, which allows us to identify the electronic processes behind phonon anomalies. Application to the TP TMDC monolayer 1H-TaS_2 reveals that coupling between the LA phonons and the electrons from an isolated low-energy metallic band is entirely responsible for phonon anomalies such as the mode softening and associated CDWs observed in this material. Our analysis allows us to distinguish between different mode-softening mechanisms including matrix-element effects, Fermi-surface nesting, and Van Hove scenarios. We find that matrix-element effects originating from a peculiar type of Dirac pseudospin textures control the CDW physics in 1H-TaS_2 and similar TMDCs.

9.1 Introduction

Different states of electronic quantum matter are often tightly linked to lattice degrees of freedom. Examples include superconductivity, PLDs and CDWs, metal–insulator transitions, and nematic, magnetic, "stripe," or excitonic order across vastly different material classes ranging from cuprate [52, 58, 59, 352, 353] and Fe-based high-temperature superconductors [200, 354, 355] to hydride compounds [54, 55, 57]. Disentangling the interplay of lattice and electronic degrees of freedom has remained a formidable challenge in many cases.

Phonon anomalies and mode softening are often an indicator of instabilities of the electronic system. However, the question of whether and which electronic processes are responsible for a given phonon anomaly is the source of many controversies in the literature. Often suggestions for very different mechanisms such as matrix-element effects [356], Fermi-surface nesting [296], or Van Hove scenarios [357] are made for a phonon anomaly in one and

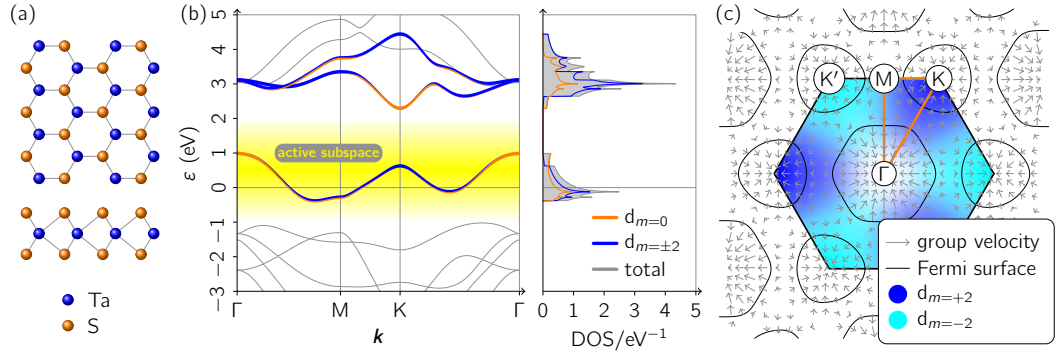

Figure 9.1: Crystal and electronic structure of 1H-TaS_2. (a) Top and side view of the crystal structure. (b) Orbital-resolved band structure and DOS. The active subspace with the isolated low-energy metallic band is highlighted in yellow. (c) Fermi surface, orbital character, and group velocity of the low-energy band.

the same material [134, 358, 359]. Unambiguously distinguishing between such mechanisms is complicated and has typically required the combination of experimental probes of lattice and electron dynamics [360, 361] with theoretical modeling [320].

Here, we present *ab initio* calculations of phonon self-energies, and we introduce the concept of fluctuation diagnostics [64, 65] to the domain of lattice dynamics. This scheme can distinguish between different strong- and weak-coupling effects and combinations thereof in the context of phonon anomalies in a quantitative and material-specific way.

One prototypical class of materials hosting phonon anomalies are the hexagonal polytypes of the layered group-V TMDCs [4]. Bulk and monolayer (Fig. 9.1a) are denoted by 2H- and 1H-MX_2, where M stands for Nb or Ta and X for S or Se. Temperature-dependent phonon-mode softening and CDWs are ubiquitous in these materials, but explanations have remained controversial for several decades, and suggestions include strong-coupling arguments based on matrix elements [18, 135, 158, 176, 182, 294, 356, 362–369] or local chemical bonding [177, 370–374] as well as weak-coupling arguments based on Fermi-surface nesting [8, 225, 296, 375–378] or Van Hove scenarios [165, 357, 379]. Our phonon-self-energy calculations and fluctuation diagnostics for monolayer 1H-TaS_2 reveal that coupling between the LA phonons and the electrons from an isolated low-energy metallic band (Figs. 9.1b and 9.1c) is entirely responsible for the mode softening and associated CDWs observed in this material. A combination of imperfect Fermiology conditions and matrix-element effects resulting from Dirac pseudospin textures is pinpointed as the cause of the CDW phase diagram of 1H-TaS_2 and similar TMDCs.

9.2 Bare and screened phonons

A general Hamiltonian describing systems of interacting electrons and phonons reads

$$\hat{H} = \hat{H}_{\text{el}} + \hat{H}_{\text{el–el}} + \hat{H}_{\text{ph}} + \hat{H}_{\text{el–ph}} \tag{9.1a}$$

and contains one-body electron terms $\hat{H}_{\text{el}}$, the Coulomb interaction $\hat{H}_{\text{el–el}}$, pure phonon terms $\hat{H}_{\text{ph}}$, and the electron–phonon interaction $\hat{H}_{\text{el–ph}}$. The necessity to account simultaneously for the complexity of the single-particle electronic wave functions and the difficulties arising from the interactions present in $\hat{H}$ render realistic descriptions of solid-state systems notoriously complicated. One way to proceed and to gain insights in practice is via material-realistic low-energy Hamiltonians, where the electronic degrees of freedom accounted for in $\hat{H}$

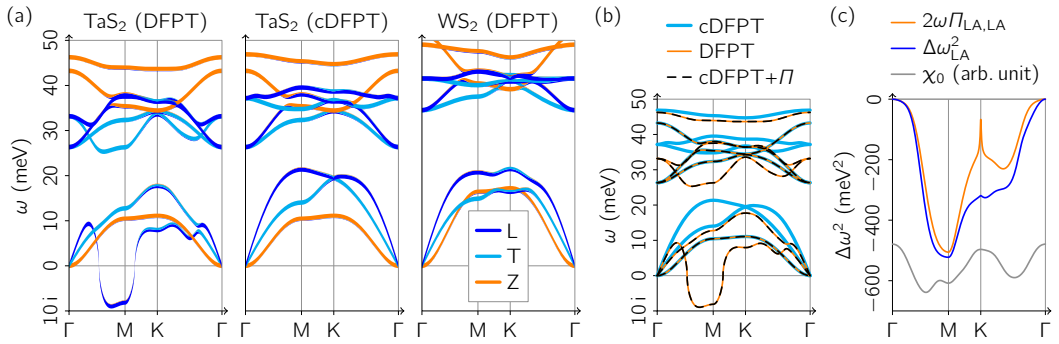

Figure 9.2: (a) Phonon dispersions of 1H-TaS_2 (DFPT, cDFPT) and 1H-WS_2 (DFPT). (b) Bare phonon dispersion of 1H-TaS_2 from cDFPT compared to screened ones from DFPT and according to Eq. 5.11 (cDFPT phonon frequencies renormalized *a posteriori* with the adiabatic phonon self-energy). The two screened dispersions are identical, showing that Eq. 5.11 provides the exact link between cDFPT and DFPT. (c) LA diagonal matrix element of the phonon self-energy, squared-energy change of the (predominantly) LA phonon branch, and bare electronic susceptibility of 1H-TaS_2.

are restricted to some low-energy subspace, often also dubbed correlated subspace, target subspace, or active subspace. We will adopt the latter nomenclature. In the presented case of 1H-TaS_2, we take as a natural choice for the active subspace the electronic states of the low-energy band highlighted in Fig. 9.1b, where SOC is disregarded for simplicity. A discussion of SOC effects is given in Sec. 9.7.1.

Then, all quantities entering $\hat{H}$ have to be partially renormalized to account for the elimination of the higher-energy degrees of freedom [48, 50]. More precisely, the phonon frequencies entering

$$\hat{H}_{\text{ph}} = \sum_{\boldsymbol{q}\nu} \omega_{\boldsymbol{q}\nu} \left[\hat{b}^\dagger_{\boldsymbol{q}\nu} \hat{b}_{\boldsymbol{q}\nu} + \frac{1}{2} \right] \tag{9.1b}$$

and the EPCs in

$$\hat{H}_{\text{el–ph}} = \frac{1}{\sqrt{N}} \sum_{\boldsymbol{q}\nu\boldsymbol{k}mn} g_{\boldsymbol{q}\nu\boldsymbol{k}mn} [\hat{b}^\dagger_{-\boldsymbol{q}\nu} + \hat{b}_{\boldsymbol{q}\nu}] \hat{c}^\dagger_{\boldsymbol{k}+\boldsymbol{q}m} \hat{c}_{\boldsymbol{k}n} \tag{9.1c}$$

are partially renormalized from the viewpoint of a full first-principles Hamiltonian and "bare" from the viewpoint of the model.

Directly experimentally observable are the fully renormalized quantities, which can be obtained by either solving the model Hamiltonian $\hat{H}$ (Eq. 9.1) or by direct treatment of the full system from first principles. For instance, DFPT [106] yields the (in practice approximate) fully renormalized phonon dispersions and EPCs from first principles.

Partially screened phonon dispersions and EPCs can be obtained from cDFPT [50] (cf. Sec. 2.4.2.2). Analogously to the cRPA [48] to partially screened Coulomb interactions (cf. Sec. 2.6.1.1), cDFPT excludes polarization processes taking place inside the active subspace from the screening of phonon dispersions and EPCs. As elsewhere in this thesis, we distinguish fully from partially screened quantities by a tilde (~) on top of symbols for the former. In the following, we refer to them as "screened" and "bare" for brevity.

Selected bare (cDFPT) and screened (DFPT) phonon dispersions are shown in Fig. 9.2a. The bare phonon dispersion of 1H-TaS_2 (middle), which excludes screening intrinsic to the active subspace, is smooth in reciprocal space indicating correspondingly short-range IFCs, and it does not show any Kohn anomalies [380] or dynamical lattice instabilities. In contrast, the screened phonon dispersion of 1H-TaS_2 (left) shows strong Kohn anomalies, softening, and instabilities in the LA phonon branch in extended regions of the BZ. The instability

regions include the wave vector $\boldsymbol{q} = 2/3\,\mathrm{M}$ associated with the 3×3 CDW observed in bulk [176, 329, 379, 381–384] and thin 1H-TaS_2 [111, 328]. The leading instability in the screened dispersion as signaled by the (in absolute value) largest imaginary phonon frequency is indeed close to $\boldsymbol{q} = 2/3\,\mathrm{M}$. As the bare phononic system is dynamically stable and has a smooth LA dispersion in contrast to the screened one, renormalization processes taking place inside the low-energy band must be fully responsible for the mode softening and the CDW physics observed in 1H-TaS_2 (cf. Secs. 2.4.2.2 and 7.2.3).

While the bare phonon dispersion is not directly experimentally observable, screening due to the low-energy band can be suppressed also in experiment, for instance by effective doping. If the low-energy band is completely filled, no intraband screening processes are possible. Such a situation is realized in group-VI TMDCs such as 1H-WS_2, which is isostructural to the undistorted high-temperature phase of 1H-TaS_2 and has one additional electron per primitive cell but otherwise a similar electronic band structure. As seen in Fig. 9.2a, the screened phonon dispersion of 1H-WS_2 (right) is indeed very similar to the bare phonon dispersion of 1H-TaS_2 (middle). Thus, studies of isostructural compounds with different filling of the electronic bands present a route toward experimental estimates of bare phonon dispersions.

9.3 *Ab initio* phonon self-energies

There are two different ways to calculate screened phonon dispersions: first, with DFPT, and second, by approximately solving the model Hamiltonian $\hat{H}$. In the latter case, the experimentally observable lattice dynamics is encoded in the screened phonon Green function. Here, we choose the latter approach as detailed in Sec. 5.2.

Our bare and screened EPCs g and $\widetilde{g}$ are identical to g^{SCF} in Eq. 2.132 as obtained from cDFPT and DFPT calculations, respectively. We note that these EPCs are complex quantities that contain *a priori* arbitrary phase factors from the electronic eigenstates at $\boldsymbol{k}$ and $\boldsymbol{k} + \boldsymbol{q}$. Therefore, care has to be taken that a consistent gauge is applied when obtaining g and $\widetilde{g}$ from independent cDFPT and DFPT calculations (cf. Sec. 5.2.3). We address this problem by fixing the gauge in a localized basis of Wannier functions, which as an additional advantage allows for the Fourier interpolation (cf. App. B.4.2) to arbitrary $\boldsymbol{q}$ and $\boldsymbol{k}$ resolutions [138].

We calculated the phonon self-energy (Eq. 5.11b) for the case of 1H-TaS_2 and renormalized the bare phonon dispersions obtained from cDFPT accordingly (Eq. 5.11a). A comparison of the bare phonon dispersion to the screened ones as obtained from DFPT and from the phonon self-energy is shown in Fig. 9.2b. We see that both screened dispersions are the same throughout the BZ path. Indeed, the approximations involved in the DFPT calculation (adiabaticity and a semilocal XC functional) can be shown to be equivalent to Eq. 5.11 [50]. XC effects beyond RPA only enter through the difference between g and $\widetilde{g}$ (cf. Sec. 5.3).

The phonon self-energy is a matrix in the space of atomic displacement coordinates. The renormalization according to Eq. 5.11 accounts for this full matrix structure. To lowest order, corrections to the bare phonon frequency from low-energy electronic screening are contained in the diagonal components $\Pi_{\boldsymbol{q}\nu\nu}$ of the phonon self-energy. Figure 9.2c shows a comparison of the change $\Delta\omega^2_{\mathrm{LA}} = \widetilde{\omega}^2_{\mathrm{LA}} - \omega^2_{\mathrm{LA}}$ of the (predominantly) LA phonon branch upon low-energy electronic screening to the corresponding diagonal matrix element $2\omega\Pi_{\mathrm{LA,LA}}$ in the eigenbasis of the bare phonons. We see that $\Delta\omega^2_{\mathrm{LA}}$ and $2\omega\Pi_{\mathrm{LA,LA}}$ show a qualitatively similar $\boldsymbol{q}$ dependence, but there are also deviations between the two, particularly close to the K point. This is due to changes in the normal-mode eigenvectors upon renormalization.

Additionally, in Fig. 9.3, we decompose the LA mode from DFPT at $\boldsymbol{q} = 2/3\,\mathrm{M}$ into the modes from cDFPT obtained for the same $\boldsymbol{q}$ point. We find that the eigenvector of the unstable mode is still predominantly of LA type, but gains a small longitudinal–optical (LO)

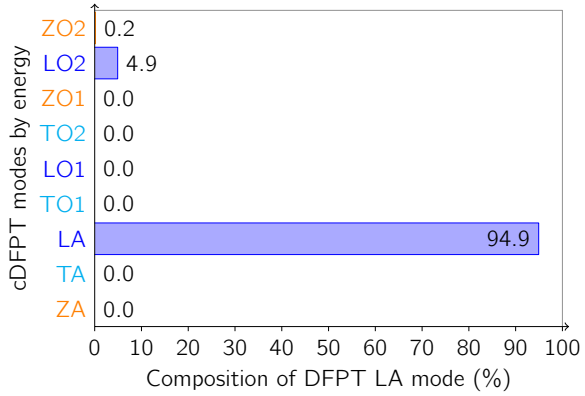

Figure 9.3: LA mode from DFPT decomposed into contributions from all cDFPT modes at the same $\boldsymbol{q} = 2/3\,\mathrm{M}$. The cDFPT modes are sorted by phonon frequency (cf. Fig. 9.2a).

component of about 5 %. Thus, the diagonal part of the phonon self-energy can serve as a qualitative guide for the understanding of phonon-renormalization phenomena, but any quantitative calculation must account for its full matrix structure.

Phonon self-energies, screened, and bare phonon dispersions for 1H-TaS_2 have also been calculated in Ref. 345, albeit with a different procedure. While the screened phonon dispersions in Ref. 345 are similar to those depicted in Fig. 9.2a, the bare phonon dispersions in Ref. 345, which have not been obtained from cDFPT but were estimated from DFPT data, differ from those found here by not being smooth but still displaying a dip at the wave vector associated with the 3×3 CDW. Possible origins of this discrepancy are that the analysis in Ref. 345 has been restricted to the diagonal components of the phonon self-energy and that the calculations involved only screened electron–phonon vertices instead of the required combination of bare and screened vertices as in Eq. 5.11b.

Several works, e.g., Refs. 135, 356, 372, 373, 385, 386, addressed the renormalization of phonons due to chosen subsets of interaction processes, but they had to rely on further, often semiempirical models or assumptions on the shape of the "bare" phonon dispersion. In this context, partially screened phonons and EPCs from cDFPT as considered in this work are very helpful, since cDFPT delivers an unambiguous bare starting point. Additionally, when analyzing nonadiabaticity [129, 387–392], cDFPT can provide a well-defined adiabatic starting point together with the correct coupling for nonadiabatic correction terms.

9.4 Fluctuation diagnostics of phonon self-energies

We seek to understand unambiguously how the electrons renormalize the phonon dispersion. The expression for the phonon self-energy makes this possible: Each summand in Eq. 5.11b quantifies how much specific electronic states contribute to the phonon self-energy and allows us to identify the mechanism responsible for the phonon renormalization. A similar kind of "fluctuation diagnostics" has previously been applied in correlated electron systems to identify antiferromagnetic correlations as the mechanism responsible for the pseudogap in the Hubbard model [64].

The phonon self-energy as approximated by Eq. 5.11b is a BZ, band, and spin sum of electronic fluctuations

$$\chi^0_{\boldsymbol{q}\boldsymbol{k}mn} = \frac{f(\varepsilon_{\boldsymbol{k}+\boldsymbol{q}m}) - f(\varepsilon_{\boldsymbol{k}n})}{\varepsilon_{\boldsymbol{k}+\boldsymbol{q}m} - \varepsilon_{\boldsymbol{k}n}} \tag{9.2a}$$

weighted by the combined EPC matrix elements g^2 from DFPT and cDFPT, for which we adopt the symmetrized, Hermitian representation of Eq. 5.14. By analyzing

$$\Pi_{\boldsymbol{q}\mu\nu\boldsymbol{k}mn} = g^2_{\boldsymbol{q}\mu\nu\boldsymbol{k}mn} \cdot \chi^0_{\boldsymbol{q}\boldsymbol{k}mn} \tag{9.2b}$$

as a function of electronic momenta $\boldsymbol{k}$ and $\boldsymbol{k}+\boldsymbol{q}$, we can perform "fluctuation diagnostics" and identify which fermionic fluctuations contribute most dominantly to the phonon self-energy. Furthermore, by comparison of Π to χ_0 and g^2 we can directly distinguish purely electronic band-structure and "Fermiology" effects from matrix-element effects.

One can similarly quantify the contribution of electronic states from a certain energy range to the phonon renormalization. Considering a single band for brevity, the integral

$$\Pi(\Delta) = \frac{2}{A_{\mathrm{BZ}}} \int \mathrm{d}^2k \, \Pi_{\boldsymbol{k}} \Theta(|\varepsilon_{\boldsymbol{k}}| - \Delta)\Theta(|\varepsilon_{\boldsymbol{k}+\boldsymbol{q}}| - \Delta) \tag{9.3a}$$

with the reciprocal BZ area A_{BZ} accounts only for fermionic modes with energies outside of an energy window $[-\Delta, +\Delta]$ around the Fermi level. In the renormalization-group spirit, this corresponds to integrating out all electrons outside of the energy window. The full result of the calculation is recovered by letting $\Delta \to 0$. The derivative

$$\partial_\Delta \Pi(\Delta) = -\frac{2}{A_{\mathrm{BZ}}} \int \mathrm{d}^2k \, \Pi_{\boldsymbol{k}} [\delta(|\varepsilon_{\boldsymbol{k}}| - \Delta)\Theta(|\varepsilon_{\boldsymbol{k}+\boldsymbol{q}}| - \Delta) + \Theta(|\varepsilon_{\boldsymbol{k}}| - \Delta)\delta(|\varepsilon_{\boldsymbol{k}+\boldsymbol{q}}| - \Delta)] \tag{9.3b}$$

then quantifies the contribution of states with energies from the shell $|\varepsilon_{\boldsymbol{k}}| = \Delta$ to Π![1]

Matrix-element effects, Fermi-surface nesting, and Van Hove scenarios as possible causes of phonon-mode softening manifest markedly differently in the fluctuation diagnostics. For a generic d-dimensional system, in the absence of any Fermi-surface anomalies like nesting, $\Pi(\Delta)$ remains finite as $\Delta \to 0$. On the other hand, Fermi-surface nesting, as realized in 1D systems for $q_{\mathrm{c}} = 2k_{\mathrm{F}}$ [172] or also in higher-dimensional systems for parallel sheets of the Fermi surface linked by some nesting vector $\boldsymbol{q}_{\mathrm{c}}$, leads to diverging $\Pi_{\boldsymbol{q}_{\mathrm{c}}}(\Delta) \propto \log|\Delta|$ and $\partial_\Delta \Pi_{\boldsymbol{q}_{\mathrm{c}}}(\Delta) \propto 1/\Delta$ [393]. We expect the same kind of divergences in so-called Van Hove scenarios, where the Fermi level is at the energy of VHS in the electronic DOS, e.g., for wave vectors $\boldsymbol{q}_{\mathrm{c}} = \boldsymbol{q}_{\mathrm{VHS}}$ connecting two saddle points [357] as found in 1H-TaS_2. In turn, nesting and Van Hove scenarios can be clearly distinguished in $\boldsymbol{k}$-space fluctuation diagnostics by dominant contributions to Π originating from line segments in the case of nesting and being centered around the Van Hove points in the latter case. The role of the matrix elements is seen by comparing χ_0 to Π.

9.5 Fluctuation diagnostics of CDW formation in 1H-TaS_2

The CDW physics of 1H-TaS_2 is associated with softening of LA phonon modes in the undistorted phase toward dynamical lattice instabilities. As shown in Sec. 9.2, this softening is entirely due to coupling of the phonons to the electrons from the active subspace in Fig. 9.1b. In the following, we identify which processes inside this active subspace contribute most dominantly to the phonon-mode softening for pristine (Sec. 9.5.1) and doped 1H-TaS_2 (Sec. 9.5.2). Only the LA diagonal elements of $2\omega g^2$ and $2\omega\Pi$ in the eigenbasis of the bare phonons are shown. The prefactor of 2ω cancels with the prefactor in Eq. 2.132. Most subscripts are omitted for brevity. All computational parameters are listed in Sec. 9.8.

9.5.1 Pristine 1H-TaS_2

The wave vector associated with the 3×3 CDW in pristine 1H-TaS_2, i.e., at the chemical potential $\mu = 0$, is $\boldsymbol{q} = 2/3\,\mathrm{M}$. The fluctuation diagnostics of the corresponding phonon self-energy $2\omega\Pi$ (Fig. 9.4a) reveals that the dominant contributions to $2\omega\Pi$ are peaked in distinct regions of $\boldsymbol{k}$ space: The Fermi surface (contour) of undoped 1H-TaS_2 consists of

[1] The information contained in $\partial_\Delta \Pi(\Delta)$ is similar to the information contained in $\mathrm{Im}\,\Pi(\omega + \mathrm{i}0^+)$.

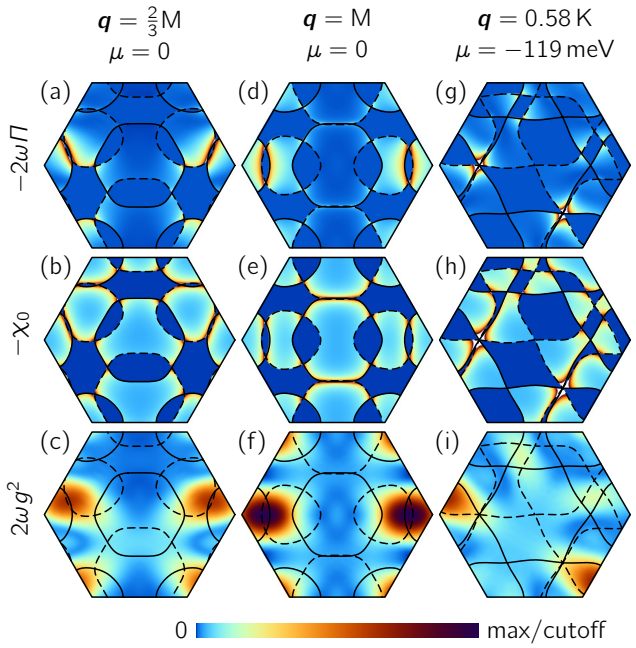

Figure 9.4: $\boldsymbol{k}$-resolved fluctuation diagnostics of the softening of the LA phonon mode at $\boldsymbol{q} = 2/3\,\mathrm{M}$ (left) and $\boldsymbol{q} = \mathrm{M}$ (middle) for undoped 1H-TaS_2 and at $\boldsymbol{q} = 0.58\,\mathrm{K}$ (right) at Van Hove filling (chemical potential $\mu = -119\,\mathrm{meV}$). The $\boldsymbol{k}$-dependent contributions to the phonon self-energy $2\omega\Pi$, the bare electronic susceptibility χ_0, and the coupling matrix elements $2\omega g^2$ are shown color-coded. Solid (dashed) lines indicate the Fermi surface (shifted by the respective $\boldsymbol{q}$ vectors).

three hole pockets encircling Γ, K, and K′, respectively. The strongest contributions to $2\omega\Pi$ originate from regions where the original pocket around K approximately touches the pocket around K′, shifted by $-\boldsymbol{q}$, and vice versa. There are two such regions of touching K and K′ pockets (intervalley processes) and two regions of touching K and shifted K pockets or touching K′ and shifted K′ pockets (intravalley processes) in the BZ. While all four of these regions contribute to the bare electronic susceptibility χ_0 (Fig. 9.4b), only the two regions associated with the intervalley coupling contribute significantly to the phonon self-energy $2\omega\Pi$ (Fig. 9.4a). The coupling matrix elements $2\omega g^2$ (Fig. 9.4c) filter out these two of the four regions of (approximately) touching hole pockets.

One might be tempted to explain the contributions to $2\omega\Pi$ from the two remaining regions with touching K and K′ pockets in terms of nesting. However, our results rule out such a nesting scenario: As a first indication already seen in Fig. 9.2c, $\boldsymbol{q}$ dependencies in χ_0 are much less pronounced than those in $2\omega\Pi$, which is opposite to the expectation of a logarithmically divergent χ_0 in a nesting scenario. $2\omega\Pi$ shows a pronounced extremum for $\boldsymbol{q} = \mathrm{M}$, while χ_0 shows significantly smaller and opposite variations. The $\boldsymbol{k}$-resolved fluctuation diagnostics of $2\omega\Pi$ at $\boldsymbol{q} = \mathrm{M}$ (Fig. 9.4d) shows that dominant contributions come again from K and K′ pockets, which are now slightly overlapping rather than approximately touching and clearly not nested at $\boldsymbol{q} = \mathrm{M}$. Indeed, there is nesting for the hole pocket around Γ, which contributes to χ_0 (Fig. 9.4e). However, the resultant approximate divergence is logarithmic, thus already weak on the level of χ_0, and fully masked by matrix-element effects in the phonon self-energy. Consequently, matrix-element effects clearly dominate here.

A basic and widely used model [130, 135] of the interaction between electrons and LA phonons assumes that $g_{\boldsymbol{q}\boldsymbol{k}} \propto \boldsymbol{q}(\boldsymbol{v}_{\boldsymbol{k}} - \boldsymbol{v}_{\boldsymbol{k}+\boldsymbol{q}})$, which suggests that the EPC is most effective if the group velocities $\boldsymbol{v}_{\boldsymbol{k}} = \boldsymbol{\nabla}_{\boldsymbol{k}}\varepsilon_{\boldsymbol{k}}$ and $\boldsymbol{v}_{\boldsymbol{k}+\boldsymbol{q}}$ of the coupled electronic states are opposed to each other and parallel to $\boldsymbol{q}$. Interestingly, those regions with strong (suppressed) EPC identified by our analysis (Figs. 9.4c, 9.4f, and 9.4i) are characterized by group velocities mainly orthogonal (parallel) to $\boldsymbol{q}$, which is exactly opposite to the expectation from the model. The reason for this deviation is the massive-Dirac-fermion nature of the low-energy-band states and associated pseudospin textures, as will be explained in Sec. 9.6.2.

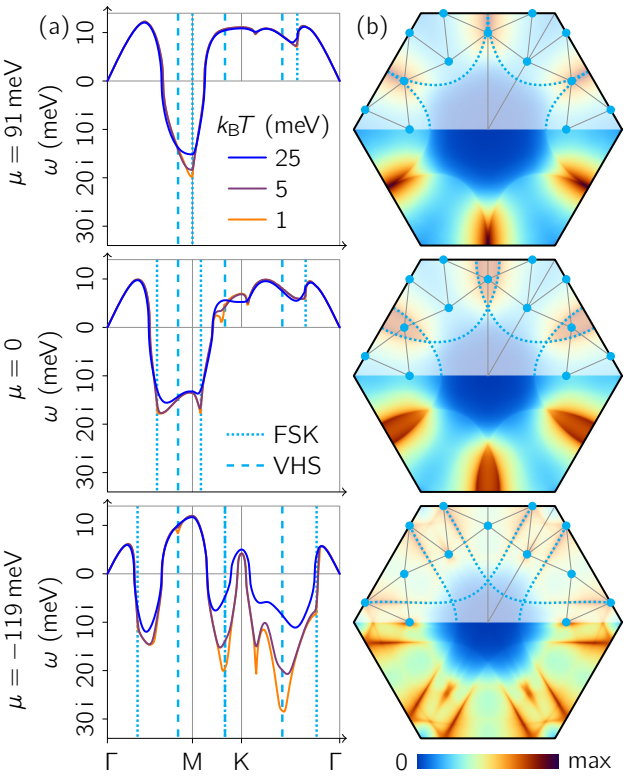

Figure 9.5: $\boldsymbol{q}$-resolved fluctuation diagnostics. (a) LA phonon dispersion and (b) $\boldsymbol{q}$-dependent LA phonon self-energy ($-2\omega\Pi$) at different chemical potentials μ. At $\mu = -119$ meV, the VHS is at the Fermi level; $\mu = 0$ is the undoped case; at $\mu = 91$ meV, we have touching K and K′ pockets for $\boldsymbol{q} = \mathrm{M}$. The dispersion is shown for different broadenings T, the phonon self-energy only for $T = 1$ meV. Special $\boldsymbol{q}$ points are marked in cyan, where FSK and VHS stands for touching K and K′ pockets and superimposed saddle points, respectively.

9.5.2 Doping dependence

Charge doping is known to affect CDW instabilities by shifting the ordering wave vectors and suppressing or supporting CDW order in many materials from high-T_c superconductors [59] to TMDCs [8, 295, 394–396] and 1H-TaS_2 in particular [14, 111, 342, 345]. We studied the dependence of the LA phonon mode on charge doping in the phonon-self-energy formalism (Eq. 5.11) by changing the electronic chemical potential μ in the model Hamiltonian H. In doing so, we disregard changes in the screened coupling $\widetilde{g}$. This approximation is justified by the small relative difference between g and $\widetilde{g}$ in the undoped case. A comparison of phonon self-energies and resulting screened phonon dispersions for hole doping ($\mu = -119$ meV), the charge-neutral system ($\mu = 0$), and electron doping ($\mu = 91$ meV) is given in Fig. 9.5.

In line with former theoretical results [345] and experiments [111], we find that electron doping pushes the wave vector of the leading lattice instability toward the M point (cf. Chap. 8). Hole doping of $\mu = -119$ meV, on the other hand, shifts the instabilities further away from M and also lets additional "fragile" instabilities between Γ and K emerge, which depend very sensitively on the thermal broadening T of the electronic Fermi distribution. At smallest temperatures $T \approx 1$ meV, the leading instabilities occurring in the phonon dispersions (Fig. 9.5a) coincide with the extrema of the corresponding phonon self-energies (Fig. 9.5b). The latter are fully determined by the Fermiology conditions of touching K and K′ pockets and (approximately) superimposed Van Hove points over the whole range of doping levels. However, these extrema are by no means isolated points of enhanced/divergent phonon self-energies but embedded in extended $\boldsymbol{q}$-space regions with appreciable mode softening.

Fluctuation diagnostics (Fig. 9.6) reveals the mechanisms behind the doping dependencies found in Fig. 9.5: While the filter determined by the EPC remains the same regardless of the doping level (blue-shaded regions in Fig. 9.6a), electron doping shrinks the hole pockets around K, K′, and Γ. Correspondingly, touching or partially overlapping K and K′ pockets are realized for CDW wave vectors larger than $\boldsymbol{q} = 2/3\,\mathrm{M}$. For $\mu = 91$ meV, $\boldsymbol{q} = \mathrm{M}$ leads to

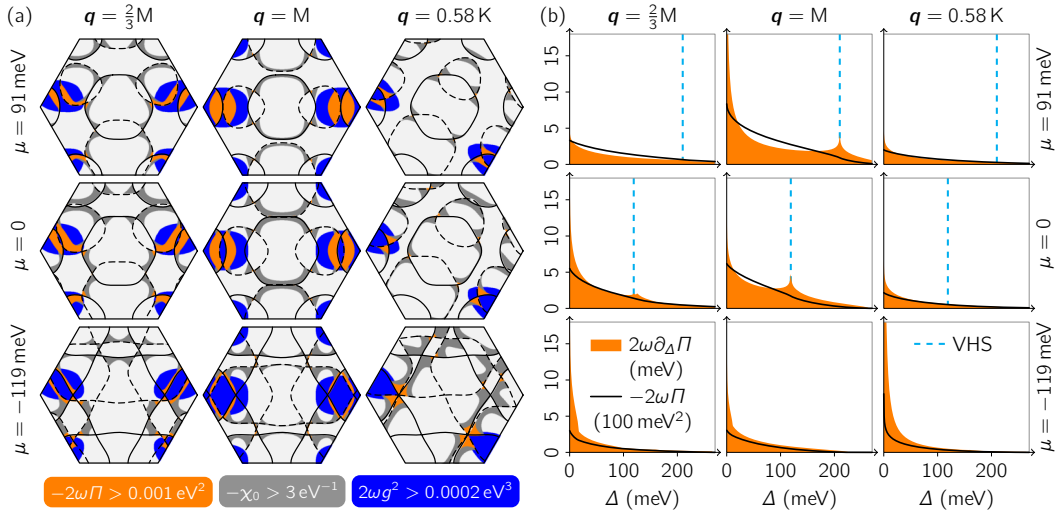

Figure 9.6: (a) $\boldsymbol{k}$- and (b) energy-resolved fluctuation diagnostics of LA-phonon-mode softening in 1H-TaS_2 as a function of charge doping (chemical potential μ) at $\boldsymbol{q} = 2/3\,\mathrm{M}$, M, and K. The blue-, gray-, and orange-shaded regions in panel (a) indicate $\boldsymbol{k}$ points with significant contributions to the phonon self-energy, the bare electronic susceptibility, and the EPC as defined in Eq. 9.2.

touching K and K′ pockets. Therefore, contributions to $2\omega\Pi$ are correspondingly enhanced at M, while the mode softening at $\boldsymbol{q} = 2/3\,\mathrm{M}$ is weaker in this electron-doped case. Hence, nearly overlapping hole pockets and corresponding contributions to χ_0 are necessary for effective mode softening.

If the instability at M in this case was a pure nesting effect, one should find a logarithmic divergence in the energy-resolved fluctuation diagnostics in $\Pi(\Delta)$ and a corresponding $1/\Delta$ divergence in $\partial_\Delta\Pi(\Delta)$ for small energy-window sizes Δ. As one can see from Fig. 9.6b, we do not find such divergences for the electron-doped case at $\boldsymbol{q} = \mathrm{M}$ nor for the undoped case at $\boldsymbol{q} = 2/3\,\mathrm{M}$. (While from Fig. 9.6b the exact type of divergence does not become evident, the representation of the data shown Fig. 9.7 is more suitable for this purpose.) Thus, sufficiently large matrix elements of the EPC and sufficiently large albeit finite bare electronic susceptibilities are of central importance in both cases. This finding is in line with Refs. 181, 333, 397, 398.

9.5.3 Van Hove scenarios

For an electronic chemical potential of $\mu = -119\,\mathrm{meV}$ one realizes "Van Hove doping," i.e., hole doping such that the electronic VHS at $\boldsymbol{k} = 0.58\,\mathrm{K}$ and symmetry-equivalent $\boldsymbol{k}$ points are directly at the Fermi level. In this situation, it is possible to realize phonon-mode softening as put forward in the so-called Van Hove scenario [357], where low-energy electronic fluctuations from the vicinity of VHS yield diverging contributions to the bare electronic susceptibility and possibly to the phonon self-energy. However, the situation in 1H-TaS_2 at Van Hove doping is intricate: There are dynamical lattice instabilities in large parts of the BZ, particularly between Γ and K. For most unstable parts of the Γ–K section, one has imperfect nesting. The notable exception is $\boldsymbol{q}_{\mathrm{VHS}} = 0.58\,\mathrm{K}$, which realizes a Van Hove scenario on top of imperfect nesting. For this $\boldsymbol{q}$ vector there are sizable contributions to χ_0 from the vicinity of the VHS (Fig. 9.4h). Also the electron–phonon matrix elements are nonzero in the vicinity of the matched VHS (Fig. 9.4i). Thus, at sufficiently small energies, the VHS-induced logarithmic divergence in χ_0 manifests also in $2\omega\Pi$ (Fig. 9.4g). That becomes more obvious in the energy-resolved fluctuation diagnostics (Figs. 9.6b and 9.7).

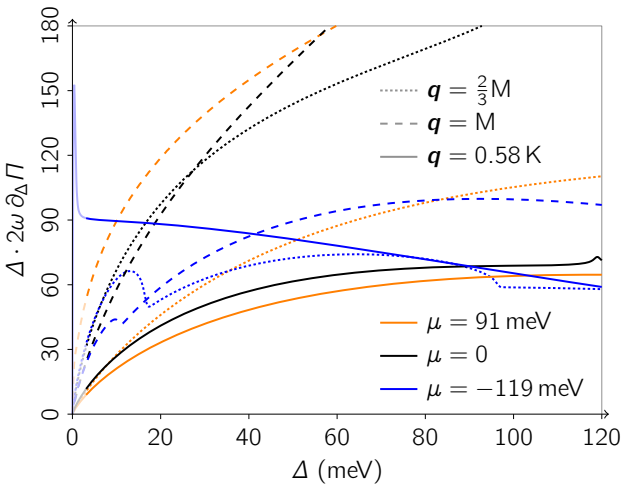

Figure 9.7: Product of energy-window size Δ and derivative of phonon self-energy $\partial_\Delta \Pi$ for all situations shown in Fig. 9.6b. Different line styles refer to different $\boldsymbol{q}$ points while different line colors refer to different chemical potentials. For a diverging $\partial_\Delta \Pi \propto 1/\Delta$, the displayed quantity is a nonzero constant in the limit of small Δ. As expected, this is only the case in the Van Hove scenario (solid, blue line). The artefacts in the grayed-out region where $\Delta < 3$ meV stem from smearing-related inaccuracies.

There, we find divergences $\partial_\Delta \Pi \propto 1/\Delta$ and $\Pi \propto \log \Delta$ as expected in the Van Hove scenario. However, in absolute numbers, very small energy scales have to be reached for the Van Hove contribution to dominate over more conventional effects (e.g., imperfect nesting and matrix-element effects). That can be seen from the dependence of the screened phonon dispersions on electronic broadening in the VHS-doped case (Fig. 9.5a). $\boldsymbol{q}_{\mathrm{VHS}}$ clearly defines the leading instability only for electronic temperatures below $T \approx 1$ meV, while instabilities in large parts of the BZ exist already at $T = 25$ meV.

Apart from $\boldsymbol{q}_{\mathrm{VHS}} = 0.58$ K, there are two additional nonequivalent $\boldsymbol{q}$ points in the BZ that superimpose VHS. In units of reciprocal basis vectors $\boldsymbol{b}_1$ and $\boldsymbol{b}_2$ (with an angle of $2\pi/3$ between them), the three different $\boldsymbol{q}_{\mathrm{VHS}}$ read

$$\boldsymbol{q}_1 = k(\boldsymbol{b}_1 + \boldsymbol{b}_2) \approx 0.58\,\mathrm{K}, \tag{9.4a}$$
$$\boldsymbol{q}_2 = (1 - 3k)\boldsymbol{b}_2 \approx 0.83\,\mathrm{M}, \tag{9.4b}$$
$$\boldsymbol{q}_3 = (1 - 4k)\boldsymbol{b}_1 + 2k\boldsymbol{b}_2 \approx 0.34\,\mathrm{M} + 0.66\,\mathrm{K}, \tag{9.4c}$$

where $k \approx 0.19$. Interestingly, they are the vertices of an equilateral triangle that perfectly fits into the irreducible wedge (cf. Fig. 9.5b). Analogous to Figs. 9.4c, 9.4f, and 9.4i, the Fermi surface and EPC for these three $\boldsymbol{q}$ points is shown in Fig. 9.8. The first point $\boldsymbol{q}_1$ (Fig. 9.8a) has already been discussed.

The second point $\boldsymbol{q}_2$ is close to the leading instability at $\boldsymbol{q} = 2/3$ M in the undoped case. This lead Rice and Scott to assume that this Van Hove scenario is at the origin of the CDW in 1H-TaS_2 [357]. However, as seen in Fig. 9.8a, in the $\boldsymbol{k}$-space regions where the VHS are superimposed, the EPC approximately vanishes. Thus, the VHS *cannot* be responsible for the phonon softening in this case.

The third point $\boldsymbol{q}_3$ seems to be very relevant from a first glance at Fig. 9.8c. The VHS are superimposed exactly at the maximum of the EPC. This is because this Van Hove scenario is the limiting case of touching K and K′ pockets; the VHS are located halfway between K and K′. However, the saddle points are aligned such that occupied regions are mapped onto occupied ones and unoccupied regions are mapped onto unoccupied ones, thus strongly suppressing the electronic susceptibility. In the first and second case, we always had some overlap of occupied and unoccupied regions and vice versa. Moreover, for $\boldsymbol{q}_3$ the superposition of VHS occurs only once in the BZ, whereas for $\boldsymbol{q}_1$ and $\boldsymbol{q}_2$ this happens twice.

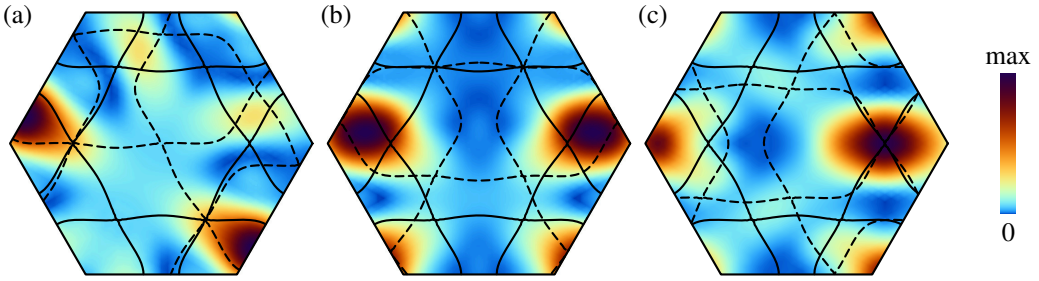

Figure 9.8: Van Hove scenarios (a) $\boldsymbol{q} = 0.58\,\mathrm{K}$, (b) $\boldsymbol{q} = 0.83\,\mathrm{M}$, and (c) $\boldsymbol{q} = 0.34\,\mathrm{M} + 0.66\,\mathrm{K}$. The LA EPC $2\omega g^2$ is plotted together with the in- (solid lines) and outgoing (dashed lines) Fermi surface.

9.6 Model electron–phonon couplings of 1H-TaS_2

Taken together, our fluctuation diagnostics confirmed that Fermiology alone is insufficient to understand the phonon renormalization. The matrix-element filter provided by the EPC in its interplay with the Fermiology determines the phonon self-energies and mode softening in 1H-TaS_2. To obtain a microscopic understanding of these matrix-element effects, we calculate the EPC for a nearest-neighbor TB model, following two widely used approaches by Varma *et al.* [130, 135], and we compare it to the *ab initio* results. We find that the momentum dependence of the EPC results from the multiorbital nature of the active subspace and can be understood in terms of pseudospin textures of massive Dirac fermions.

9.6.1 Tight binding

We make use of the nearest-neighbor TB model introduced in Sec. 2.3.2.3. However, here we will explicitly consider the reflection S_y along the y axis. The Hamiltonian then reads

$$H_{\boldsymbol{k}} = \varepsilon + \sum_{n=1}^{6} t_n \mathrm{e}^{\mathrm{i}\boldsymbol{a}_n \boldsymbol{k}}, \tag{9.5a}$$

$$t_n = \left(\frac{r_n}{a}\right)^{\beta} R_{\varphi_n} \cdot S_y^n \cdot t_0 \cdot S_y^n \cdot R_{-\varphi_n}, \tag{9.5b}$$

with bond vectors $\boldsymbol{a}_n = r_n(\cos\varphi_n, \sin\varphi_n)$ defined by lengths $r_n = a$ and angles $\varphi_n = n\pi/3$. $\beta = -5$ quantifies the distance dependence of d–d bonds [134, 399] (cf. Eq. 2.142).

Moreover, we will work in the basis of complex harmonics d_m with $m \in \{-2, 0, 2\}$ instead of real harmonics d_{z^2}, $d_{x^2-y^2}$, and d_{xy}. The transform that links both representations reads

$$d_{m=0} = d_{z^2}, \tag{9.6a}$$

$$d_{m=\pm 2} = \frac{1}{\sqrt{2}}(d_{x^2-y^2} \pm \mathrm{i} d_{xy}), \tag{9.6b}$$

$$\left.\begin{matrix} d_{x^2-y^2} \\ \mathrm{i} d_{xy} \end{matrix}\right\} = \frac{1}{\sqrt{2}}(d_{m=+2} \pm d_{m=-2}). \tag{9.6c}$$

In this basis, the reflection along the y axis reads $S_y = \mathrm{diag}(1, \sigma_x)$ with the Pauli matrix σ_x and the rotation about the z axis reads $R_\varphi = \mathrm{diag}(1, \mathrm{e}^{2\mathrm{i}\varphi}, \mathrm{e}^{-2\mathrm{i}\varphi})$. The on-site energy is invariant under the basis transform. In turn, the hopping in x direction becomes

$$t_0 = \begin{bmatrix} -139 & 339 - 271\,\mathrm{i} & 339 + 271\,\mathrm{i} \\ 339 - 271\,\mathrm{i} & 35 + 311\,\mathrm{i} & -290 \\ 339 + 271\,\mathrm{i} & -290 & 35 - 311\,\mathrm{i} \end{bmatrix} \mathrm{meV}. \tag{9.7}$$

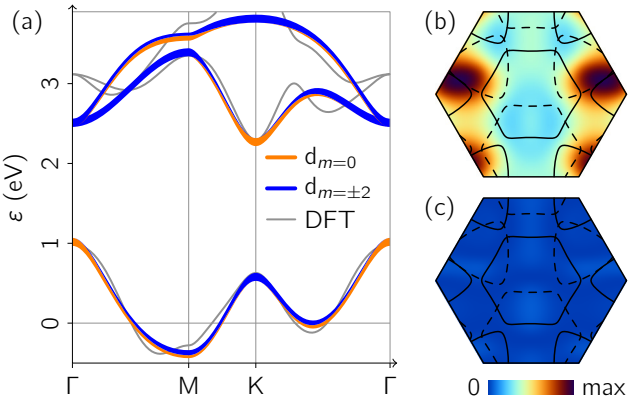

Figure 9.9: (a) Electronic band structure of 1H-TaS_2 from the TB model (Eq. 9.5) compared to DFT, (b) the resulting $\boldsymbol{k}$-resolved EPC $2\omega g^2$ of LA phonons with the low-energy band for $\boldsymbol{q} = 2/3\,\mathrm{M}$ from Eq. 9.8, and (c) the corresponding simplified EPC from Eq. 9.9.

The resulting band structure is—again—plotted in Fig. 9.9a (cf. Fig. 2.3a). At least the low-energy band fits the reference from DFT quite well.

To analyze the EPC, we rescale the hopping matrix elements in the distorted structures according to Eq. 9.5b (cf. Eq. 2.143). Here, we neglect the angular dependence, i.e., we work with the EPC as defined in Eq. 2.148,

$$g_{\boldsymbol{q}\nu\boldsymbol{k}mn} \propto \boldsymbol{e}_{\boldsymbol{q}\nu} \sum_l (A_{\boldsymbol{q}\boldsymbol{k}ml} \boldsymbol{v}_{\boldsymbol{k}ln} - \boldsymbol{v}_{\boldsymbol{k}+\boldsymbol{q}ml} A_{\boldsymbol{q}\boldsymbol{k}ln}), \tag{9.8}$$

As mentioned in Sec. 2.5.2, another widely used approximation (cf. A.12 of Ref. 130 and Eq. 2 of Ref. 135) neglects the off-diagonal matrix elements of the velocity operator in the band basis and thus only accounts for the standard electronic group velocities $\boldsymbol{v}_{\boldsymbol{k}nn} = \boldsymbol{\nabla}_{\boldsymbol{k}} \varepsilon_{\boldsymbol{k}n}$,

$$g_{\boldsymbol{q}\nu\boldsymbol{k}mn} \propto \boldsymbol{e}_{\boldsymbol{q}\nu} (\boldsymbol{v}_{\boldsymbol{k}nn} - \boldsymbol{v}_{\boldsymbol{k}+\boldsymbol{q}mm}) A_{\boldsymbol{q}\boldsymbol{k}mn}. \tag{9.9}$$

In Figs. 9.9b and 9.9c, we show the $\boldsymbol{k}$-dependent coupling of the LA phonons with the low-energy band for $\boldsymbol{q} = 2/3\,\mathrm{M}$ within the approximations of Eqs. 9.8 and 9.9. According to (c)DFPT (Fig. 9.4c), there are only two spots in the vicinity of K and K′ where the coupling is large. Equation 9.8 reproduces the structure of the coupling found in (c)DFPT qualitatively (Fig. 9.9b). However, the simplified Eq. 9.9 does not capture the relevant physics, as the resulting coupling is much weaker and has its maximum in the hole pocket around Γ (Fig. 9.9c). Therefore, intraband variation of orbital characters and the full matrix structure of the velocity operator must be decisive in determining the LA EPC.

9.6.2 Massive Dirac fermions

Both the TB model and the first-principles calculations (Sec. 9.5.1) suggest that the coupling between electrons and LA phonons is strong when the group velocities of the electronic states are (largely) orthogonal to the phonon momentum $\boldsymbol{q}$. This is exactly opposite to the expectation from Eq. 9.9. To understand the origin of this behavior, we resort to an even simpler model and describe the low-energy band of 1H-TaS_2 around K and K′ in terms of massive Dirac fermions [237]. The corresponding Hamiltonian reads

$$H_\mathrm{D} = v_0(\tau p_x \sigma_x + p_y \sigma_y) + \frac{\Delta}{2}\sigma_z. \tag{9.10}$$

Here, $\tau = \pm 1$ is the valley index, which selects between regions around K and K′ (Fig. 9.1c), v_0 is an effective velocity playing the role of the speed of light in the relativistic Dirac equation, and Δ is the band gap. The Pauli matrices σ_i with $i \in \{x, y, z\}$ act on pseudospinors $\chi_{\tau\boldsymbol{p}}$ from a space of two Ta-d orbitals: The upper (lower) component of $\chi_{\tau\boldsymbol{p}}$ describes the

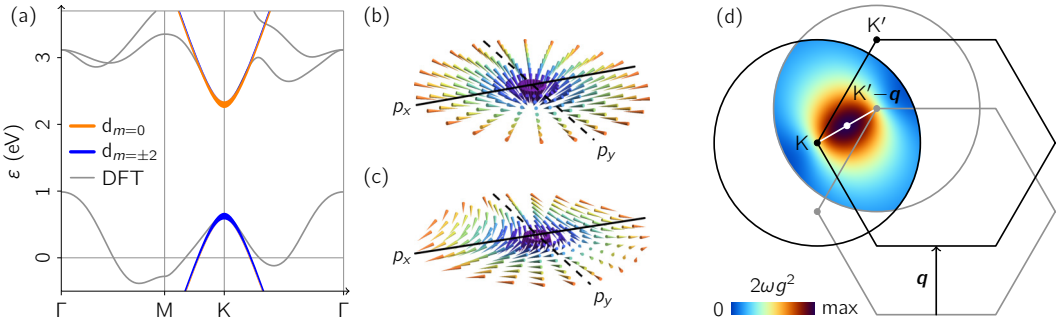

Figure 9.10: (a) Electronic band structure from a model of massive Dirac fermions compared to DFT. (b, c) *[Figures by Erik van Loon.]* Dirac pseudospin texture of the lower band around (b) K and (c) K′. (d) The resulting intervalley EPC strength $2\omega g^2$ for $\boldsymbol{q} = 2/3\,\mathrm{M}$ exhibits a clear maximum halfway between K and K′ − $\boldsymbol{q}$.

d orbitals with orbital angular momentum $m = 0$ ($m = 2\tau$). As shown in Fig. 9.10a, the eigenvalues of H_D at momentum $\boldsymbol{p}$ relative to K or K′ are

$$\varepsilon_{\boldsymbol{p}} = \pm\sqrt{\frac{\Delta^2}{4} + v_0^2 p^2}. \tag{9.11}$$

The velocity operator resulting from the Dirac Hamiltonian (Eq. 9.10) is

$$\boldsymbol{v}_\mathrm{D} = \boldsymbol{\nabla}_{\boldsymbol{p}} H_\mathrm{D} = v_0(\tau \boldsymbol{e}_x \sigma_x + \boldsymbol{e}_y \sigma_y). \tag{9.12}$$

This operator describes the change in both eigenvalues *and* the change in eigenvectors of H_D. As in relativistic quantum theory, the Dirac velocity operator is independent of $\boldsymbol{k} = \mathrm{K}^{(\prime)} + \boldsymbol{p}$ inside either valley. Therefore, the intravalley EPC according to Eq. 9.8 vanishes. Thus, the massive-Dirac-fermion nature of the quasiparticles and the resultant pseudospin–momentum coupling causes the smallness of the matrix elements of the EPC associated with intravalley scattering, as seen in Figs. 9.4c and 9.9b.

Regarding the intervalley coupling, we first note that the operator $\boldsymbol{v}_\mathrm{D}$ has contributions perpendicular and parallel to the equal-energy contours of H_D,[2] resulting from the pseudospin–momentum coupling intrinsic to the Dirac equation (Eq. 9.10). As a consequence, the Dirac velocity operator $\boldsymbol{v}_\mathrm{D}$ is very different from the naïve expectation for the group velocity $\boldsymbol{v}_{\boldsymbol{k}} = \boldsymbol{\nabla}_{\boldsymbol{k}} \varepsilon_{\boldsymbol{k}} = v_0^2 \boldsymbol{k}/\varepsilon_{\boldsymbol{k}}$, which only describes the change in energy eigenvalues and always points perpendicular to the equal-energy contours.

The rotation of pseudospins in the lower band around K and K′ indeed gives rise to a velocity component *parallel* to the equal-energy contours. This allows, generically, for intervalley coupling between electrons and LA phonons at arbitrary angles between equal-energy contours and phonon momentum $\boldsymbol{q}$, in contrast to the simplified model of Eq. 9.9. For the specific analysis of intervalley scattering in TMDCs, one has to be careful since in the model of Eq. 9.10 the orbital character associated with one of the pseudospin components changes from $m = +2$ to -2 when going from K to K′.

Let χ_K and $\chi_{\mathrm{K}'}$ be pseudospinors belonging to lower-band states at $\boldsymbol{k} = \mathrm{K} + \boldsymbol{p}$ and $\boldsymbol{k} + \boldsymbol{q} = \mathrm{K}' + \boldsymbol{p}'$ located in the K and K′ valleys, respectively. That is, χ_K ($\chi_{\mathrm{K}'}$) is the

[2] It is instructive to rewrite the valley Hamiltonians and velocity operators in polar coordinates. We find $H_{p\varphi} = v_0 p \boldsymbol{e}_p \boldsymbol{\sigma}_\tau + \Delta/2\,\sigma_z$ and $\boldsymbol{v}_{p\varphi} = v_0[(\boldsymbol{e}_p \boldsymbol{\sigma}_\tau)\boldsymbol{e}_p + (\boldsymbol{e}_\varphi \boldsymbol{\sigma}_\tau)\boldsymbol{e}_\varphi]$ with $\boldsymbol{\sigma}_\tau = (\tau\sigma_x, \sigma_y)$, the radial (angular) momentum coordinate p (φ), and the corresponding unit vectors in the radial (angular) direction $\boldsymbol{e}_p$ ($\boldsymbol{e}_\varphi$). The equal-energy contours are circles with constant p. We see that $\boldsymbol{v}_{p\varphi}$ has contributions perpendicular ($\boldsymbol{e}_p$ direction) and parallel ($\boldsymbol{e}_\varphi$ direction) to the equal-energy contours.

negative-eigenvalue eigenvector of H_D for $\tau = +1$ (-1) and for momentum $\boldsymbol{p}$ $(\boldsymbol{p}')$. Then, the EPC from Eq. 9.8 can be expressed using projection operators P_0 on the $m = 0$ orbitals,

$$g_{\boldsymbol{q}\boldsymbol{k}} \propto \boldsymbol{e}_{\boldsymbol{q}\nu} \chi^{\dagger}_{\mathrm{K}'} (\boldsymbol{v}_{\mathrm{K}} P_0 - P_0 \boldsymbol{v}_{\mathrm{K}'}) \chi_{\mathrm{K}}. \tag{9.13}$$

In the same matrix representation as used in Eq. 9.10, we have $P_0 = (1 + \sigma_z)/2$, where 1 is the 2×2 identity matrix. With Eq. 9.12 we then find

$$g_{\boldsymbol{q}\boldsymbol{k}} \propto \boldsymbol{e}_{\boldsymbol{q}\nu} (\boldsymbol{e}_x + \mathrm{i}\boldsymbol{e}_y) \chi^{\dagger}_{\mathrm{K}'} \sigma_x \chi_{\mathrm{K}}. \tag{9.14}$$

The direction of the phonon eigenvector $\boldsymbol{e}_{\boldsymbol{q}\nu}$ enters merely as a phase factor. For the absolute value of the LA coupling, the angle between the equal-energy contours and $\boldsymbol{q}$ is not decisive. Instead, the coupling strength is determined by $\chi^{\dagger}_{\mathrm{K}'} \sigma_x \chi_{\mathrm{K}}$ and thus results from the pseudospin textures of the lower-band states around K and K′ shown in Figs. 9.10b and 9.10c alone. Contributions to g according to Eq. 9.14 arise from opposite-sign pseudospin projections $\chi^{\dagger} \sigma_i \chi$ of χ_{K} and $\chi_{\mathrm{K}'}$ in the y or z direction and equal-sign pseudospin projection in the x direction. The z projection of all lower-band pseudospins is "down," which does not lead to contributions to g. The winding of the in-plane pseudospin component is opposite in the K and K′ valleys (Figs. 9.10b and 9.10c). The condition of maximum coupling $|g|$ is fulfilled if χ_{K} and $\chi_{\mathrm{K}'}$ belong to time-reversed crystal momenta, $\boldsymbol{p} = -\boldsymbol{p}'$, preferably with large absolute value. This is realized for $\boldsymbol{k}$ being halfway between K and the shifted K′ point (Fig. 9.10d), i.e., exactly in the region where we find enhanced EPC in (c)DFPT (Fig. 9.4c) and also in the TB model (Fig. 9.9b). Hence, the momentum-space selection rule for the EPC, which we identified using fluctuation diagnostics, originates from the massive-Dirac-fermion nature of the low-energy-band states in 1H-TaS_2.

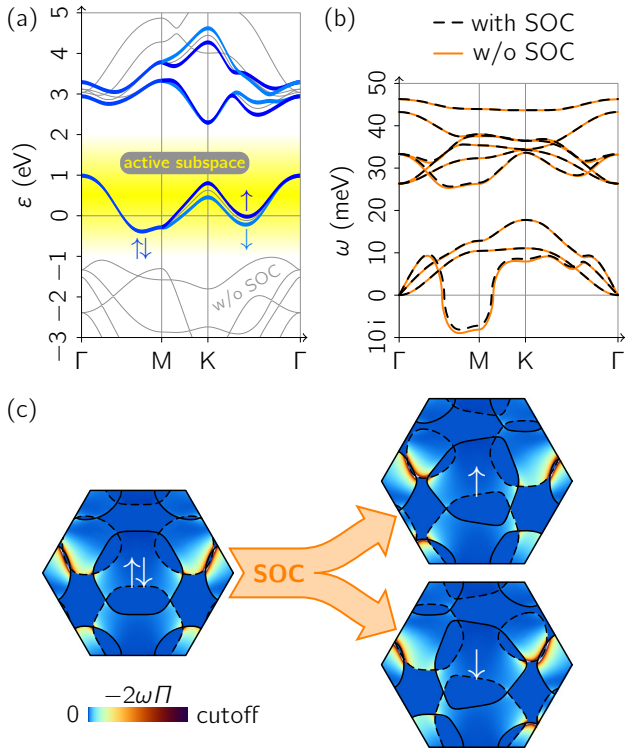

Figure 9.11: Effect of SOC on dispersions and fluctuations. (a) Spin-resolved electronic band structure. (b) Screened phonon dispersion with and without SOC. (c) Spin- and $\boldsymbol{k}$-resolved LA phonon self-energy for $\boldsymbol{q} = 2/3\,\mathrm{M}$ in the undoped case with (right panels) and without SOC (left panel). Solid (dashed) lines indicate the Fermi surface (shifted by $\boldsymbol{q}$) for the respective spin direction(s). To match color scales, the data on the right are multiplied by a factor of 2.

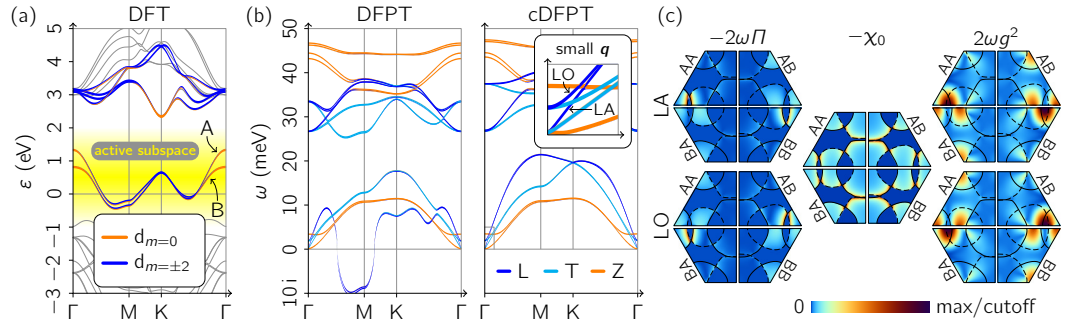

Figure 9.12: Selected results for bilayer 2H-TaS_2. (a) Orbital-resolved electronic band structure. (b) Phonon dispersions from DFPT and cDFPT. Inset: Close-up of the low-energy, long-wavelength dispersion. (c) $\boldsymbol{k}$-, band-, and mode-resolved fluctuation diagnostics for $\boldsymbol{q}$ = M in the undoped case. Each BZ panel is split into four parts, each showing the contribution for a different combination of in- and outgoing bands. The bare electronic susceptibility is shown only once because it does not depend on the phonon mode.

9.7 Generalizations of the method

9.7.1 Effect of spin–orbit coupling

We have so far disregarded the spin splitting of the electronic bands due to SOC. In the following, we will briefly outline how SOC affects our findings.

We include SOC by modifying the electronic Hamiltonian, where each spin direction is treated separately [400]. In the basis of real harmonics d_{z^2}, $d_{x^2-y^2}$, and d_{xy},

$$H_{\mathrm{el}}^{\uparrow,\downarrow} \to H_{\mathrm{el}}^{\uparrow,\downarrow} \pm \begin{bmatrix} 0 & 0 & 0 \\ 0 & 0 & -\mathrm{i} \\ 0 & \mathrm{i} & 0 \end{bmatrix} \lambda. \tag{9.15}$$

We choose a SOC strength $\lambda = 174\,\mathrm{meV}$ to reproduce the splitting of the experimental and theoretical bands in Ref. 342.

Figure 9.11a shows the resulting modified electron dispersion (cf. Fig. 9.1b). Along Γ–M, the d bands remain spin-degenerate. Beyond this line, the bands split with a maximum splitting of 2λ of the low-energy band at K.

The screened phonon dispersions with and without SOC according to Eq. 5.11 are compared in Fig. 9.11b (cf. Fig. 9.2b). We note that there is no prefactor of 2 in Eq. 5.11b when the spin is explicitly included in the band summations. As expected, SOC does not cause qualitative changes in the phonon dispersion.

This can be explained by the $\boldsymbol{k}$-space fluctuation diagnostics. In Fig. 9.11c, the LA phonon self-energy for $\boldsymbol{q} = 2/3\,\mathrm{M}$ in the undoped case is displayed together with the Fermi surface, both with and without SOC (cf. Fig. 9.4a). The argument of touching K and K′ pockets is hardly affected by SOC: For each spin direction, one pocket shrinks while the other expands, leaving their overlap region and thus the resulting phonon self-energy essentially unchanged.

9.7.2 Multiple bands and dimensions

The presented method is applicable to multiband as well as bulk systems, since Eq. 5.11 holds generally. Of course, the visualization of the results becomes more complicated. In more detail, the number of relevant $\boldsymbol{k}$-resolved plots (cf. Figs. 9.4 and 9.6a) grows quadratically

(linearly) with the number of low-energy electron bands (unstable phonon modes). The number of relevant energy-resolved plots (cf. Fig. 9.6b) does not depend on the number of bands though, and might be more practical for investigating multiband systems. Alternatively, it is possible to perform partial summations over band indices, but in that case the self-energy is no longer a mere element-wise product of bare electronic susceptibility and the EPC. For bulk systems with a significant out-of-plane dispersion, it might additionally be necessary to analyze various cross sections of the Fermi surface.

As an example, we will here apply the method to the bilayer 2H-TaS_2, a very simple multiband system. Figure 9.12a shows the electronic band structure. It is energetically similar to the monolayer case (cf. Fig. 9.1b), but the low-energy band is split into a bonding (B) and an anti-bonding band (A). Similarly, the bare and screened phonons displayed in Fig. 9.12b (cf. Fig. 9.2a) are split into in-phase and anti-phase modes (with respect to the different layers). That way, the former LA mode splits into an in-phase LA and an anti-phase LO mode, better seen in the inset, which both inherit the known instability.

For these two modes, we perform $\boldsymbol{k}$- and band-resolved fluctuation diagnostics for $\boldsymbol{q} = \mathrm{M}$ in the undoped case. The results are shown in Fig. 9.12c. Despite the reshaping of the Fermi surface, the mechanisms are similar to the monolayer case: The dominant contributions to the phonon self-energy arise from large bare electronic susceptibilities due to approximately touching K and K′ pockets in combination with strong EPC halfway between K and $\mathrm{K}' - \boldsymbol{q}$. Interestingly, the LA and LO instabilities are mainly driven by intraband (AA, BB) and interband processes (AB, BA), respectively.

9.8 Computational parameters

All DFT and DFPT calculations are carried out using QE [39, 40]. The modification that is required for cDFPT is described in detail in Ref. 50. Our implementation is documented in App. A.1. For the transformation of the electron energies and EPCs to the Wannier basis, we use Wannier90 [92–94] and the EPW code [138–140].

We apply the GGA by Perdew, Burke, and Ernzerhof (PBE) [75, 76] and use normconserving HGH PPs [340, 341] at a plane-wave cutoff of 100 Ry. For the monolayer, uniform meshes (including Γ) of 12×12 $\boldsymbol{q}$ and 36×36 $\boldsymbol{k}$ points are combined with a Fermi–Dirac smearing of 5 mRy (cf. App. C.7.1). For a fixed cell height of 15 Å, minimizing forces and in-plane pressure to below 1 µRy/Bohr and 0.1 kbar yields a lattice constant of 3.39 Å. For the bilayer, we only use 6×6 $\boldsymbol{q}$ and 18×18 $\boldsymbol{k}$ points together with a Gaussian smearing of 10 mRy. Considering van der Waals interactions via Grimme's DFT-D3 method [351], structural relaxation at a fixed cell height of 25 Å yields a lattice constant of 3.37 Å and a Ta–Ta layer distance of 6.14 Å.

On the model level, for the DFPT comparison shown in Figs. 9.2b and 9.2c, we use the same meshes and smearings as stated above. For the fluctuation diagnostics for selected $\boldsymbol{q}$ points shown in Figs. 9.4, 9.6, 9.7, and 9.11, we use 5040×5040 $\boldsymbol{k}$ points together with a Fermi–Dirac smearing of 0.07 meV and a Gaussian smearing of 0.7 meV for the step and delta functions in Eq. 9.3 (cf. App. C.7.2). For the $\boldsymbol{q}$-dependent results shown in Fig. 9.5, we use 360×360 $\boldsymbol{q}$ and $\boldsymbol{k}$ points together with a Fermi–Dirac smearing of 1 meV, if not stated otherwise. For the multiband results shown in Fig. 9.12, we use 1680×1680 $\boldsymbol{k}$ points together with a Fermi–Dirac smearing of 0.07 meV. The Fermi level is not recalculated for each mesh and smearing but kept fixed at the *ab initio* value throughout this work.

9.9 Conclusions

We have presented an *ab initio*–based scheme for the calculation of phonon self-energies from material-realistic low-energy models. This approach allows us to generalize the idea of fluctuation diagnostics [64] to electron–phonon-coupled systems and to identify the contributions of the different electronic fluctuation channels to the renormalization of phonons in complex materials.

Application of this scheme to the model CDW compound of 1H-TaS_2 showed that polarization processes taking place in an isolated low-energy metallic band are entirely responsible for the mode softening and CDW physics in this material. While Fermi-surface effects originating from this band can affect the CDW ordering wave vector, we give direct proof that lattice instabilities in 1H-TaS_2 are largely controlled by electron–phonon-coupling matrix-element effects. The origin of these matrix-element effects is shown to be the massive-Dirac-fermion nature, the resultant pseudospin textures, and associated anomalous intervalley velocity matrix elements of electronic quasiparticles in the low-energy band of 1H-TaS_2. Thus, the fluctuation diagnostics provides a purely *ab initio* way to settle the long-standing debate on the nature of CDW physics in group-V TMDCs and to reveal its physical origin.

The scheme for the calculation of phonon self-energies and for performing fluctuation diagnostics outlined here should be generally insightful to disentangle the interplay of electronic and lattice degrees of freedom in complex materials. Promising areas of future application range from materials like $TiSe_2$, where excitonic physics intertwines with lattice instabilities [401–408], to strongly correlated electron systems with coupled lattice, spin, and superconducting phenomena as take place in Fe-based superconductors [200, 354, 355] or in proximity to stripe phases in cuprate high-temperature superconductors [52, 58, 59, 352, 353]. Finally, generalizations beyond the adiabatic limit should be conveniently possible and allow, e.g., for the description of phonons in flat-band systems such as twisted bilayer graphene.

Chapter 10

Conclusions

It is good that you're still having resources.

—Fortune Cookie

In the first chapters of this thesis, we meticulously portrayed the Hamiltonian of the solid state and its individual constituents, namely the electrons, phonons, and their interactions. We reviewed how the different quantities are customary calculated from *first principles* and how the problem can be *downfolded* onto effective minimal models, which allow us to study more complex aspects with more involved methods. Here, our motivation was always to better understand many-body instabilities such as CDWs and superconductivity in 2D materials.

In the end, this thesis was very much focused on CDWs and thus on lattice vibrations. We adopted the downfolding method cDFPT to obtain partially renormalized phonons and EPCs (analogous to partially screened Coulomb interactions from cRPA) and finally arrived at a consistent and efficient *ab initio*–based phonon-renormalization scheme. In a sense, the presented theoretical background was not only the basis for the different studies presented afterwards. To the contrary, relevant parts of the theory only became clear to us while working on the different projects and can thus be seen as results on their own. Here, the general ideas are by no means *new*; the novelty is rather found in their technical realization.

Our first project was a study of monolayer 1T-$NbSe_2$, with the objective to theoretically verify experiments that found a CDW phase with Mott-insulating behavior. Our phonon calculations with DFPT and supercell calculations with DFT could confirm that the system is unstable with respect to a PLD, where the atoms form clusters resembling a "Star of David." In the distorted phase, we have found a flat band at the Fermi level that, according to our estimates for the local Coulomb interaction, will split into lower and upper Hubbard bands. However, the resulting system is likely to be a charge-transfer insulator.

We have also studied and compared the different members of the family of the metallic TP TMDC monolayers. Our *ab initio* calculations of electron and phonon dispersions from DFT and DFPT and of partially screened EPCs and Coulomb interactions from cDFPT and cRPA have shown that these materials are qualitatively very similar but quantitatively differ in bandwidths and interaction strengths. These differences suggest, in line with the literature, that the materials become more susceptible to charge order but less susceptible to magnetic order with increasing period of the transition metals. Furthermore, our cDFPT calculations have shown that lattice instabilities in these materials are exclusively driven by interactions of the lattice with the electrons from a single, isolated low-energy band.

This allowed us to theoretically explain contradictory experimental findings for the TP monolayer 1H-TaS_2. STM measurements of 1H-TaS_2 on different substrates and in presence or absence of adatoms have found either no charge order or CDWs with 3×3 or 2×2 periodicities. We set up a material-realistic model with phonons and EPCs from cDFPT and only a single electronic band (found to be responsible for the CDW). On this basis, we could model the relevant experimental parameters—which we identified as (pseudo)charge doping and broadening due to hybridization—and calculate the complete phase diagram of lattice instabilities at a negligible computational cost. We found that both electron doping and broadening can suppress the CDW and that the former shifts its periodicity from 3×3 to 2×2, in qualitative agreement with experiment. However, the exact microscopic mechanisms behind these effects still remained unclear.

To answer this question and to resolve the longstanding controversy about the origin of these CDWs in general, we introduced the method of "fluctuation diagnostics" to the field of electron–phonon physics. Being able to calculate the phonon self-energy, which is nothing but the reduction of phonon frequencies finally leading to the instability, we could also decompose it into its different contributions and thus identify the relevant electronic fluctuations. We found that the observed CDW arises from interactions between specific Fermi pockets (around K and K′) that are not filtered out by the heavily momentum-dependent EPC. Since doping changes the size of these pockets and thus the phonon momenta connecting them, this explained the observed phase diagram of lattice instabilities. Furthermore, we showed that the contributing electronic energy window extends well beyond the Fermi level, and we could rule out purely electronic CDW mechanisms such as Van Hove scenarios, except under very special circumstances. Finally, we explained the momentum dependence of the EPC by the relevant electrons being massive Dirac fermions.

Beyond this study, electron–phonon fluctuation diagnostics promises to be a method that can be universally applied to disentangle the interplay between electrons and phonons in real materials. With its help, we aim to understand the origin of CDWs also in other systems (the octahedral TMDC being to the most obvious example). Here, an interesting question is whether the formation of CDWs in the out-of-plane direction can be accurately described or whether this is impeded by anharmonic effects. In the latter case, it might be necessary to generalize our scheme beyond the harmonic approximation.

Another most interesting field, where anharmonic effects play an important role, are calculations in the distorted phases. These are inevitable in, e.g., Eliashberg and DMFT studies of superconductivity and Mott physics in CDW systems (such as 2H- and 1T-$NbSe_2$), respectively. Fully *ab initio* calculations on appropriate supercells quickly become unfeasible. In turn, a model-based approach (starting from the undistorted phase) is very efficient. As long as possible anharmonicities are driven by the low-energy electrons *in* the model—the presence of a slightly distorted ground state and an anharmonic potential-energy landscape are irremediably related—, this constitutes a promising alternative.

As of yet, a shortcoming of our scheme is that we still rely on EPCs from DFPT, which *implicitly* take account of relevant Coulomb and correlation effects. It would be more desirable to completely exclude fully screened quantities from the models and instead consider the appropriate interaction terms *explicitly*. (An immediate obstacles on this route is the fact that we currently apply different codes for the cDFPT and cRPA calculations, which makes it hard to be consistent.) A *complete* model Hamiltonian is the basis for any diagrammatic treatment. Particularly, it would allow us to study the interrelation between the screening of the different model constituents, and possibly environmental screening. Furthermore, it would facilitate generalizations beyond the static approximation, which would introduce frequency arguments into our formulas and thus provide nonadiabatic corrections.

Appendix A

Software

When I first started using the term "software engineering," it was considered to be quite amusing. [. . .] *Software eventually and necessarily gained the same respect as any other discipline.*

—Margaret Hamilton

In this appendix, we present different software related to this thesis. Some are popular applications with a broad user group worldwide (including ourselves). These comprise the *ab initio* codes QE (App. A.1), WANNIER90 (App. A.2), EPW (App. A.3), VASP (App. A.4), and the methods toolbox TRIQS (App. A.5). Others have been developed in our and related working groups and have a much more limited number of users. These are the electron–phonon modules ELPHMOD (App. A.6), the Eliashberg solvers EBMB and EBBW (App. A.7), the plotting class STORYLINES (App. A.8), and the RPA code PLASMOS (App. A.9). Additionally, in App. A.10, we provide a minimal working example of how to calculate and renormalize cDFPT phonons with QE and ELPHMOD.

A.1 QUANTUM ESPRESSO

QE is an open-source project that integrates various codes for *ab initio* simulations based on DFT [39, 40]. Calculations are performed in a plane-wave basis in combination with PPs. QE has been particularly useful during the work on this thesis, since it natively supports the calculation of phonons via DFPT.

In this section, we will present some modifications of the source code of QE's phonon program `ph.x` that allow us to perform cDFPT calculations. They are based on and fully equivalent to the modifications originally proposed by Nomura and Arita [50]. They have been thoroughly tested for the version QE 6.3 (backports), more specifically the commit `9931d1e` of the Git repository [409].

To avoid having to recompile QE for each considered problem, we do not hardcode any parameters. Instead we introduce two new variables to control the calculation: The logical variable `cdfpt` switches the cDFPT modification on or off; the integer array `cdfpt_subspace` defines the active subspace via band indices for the individual $\boldsymbol{k}$ points. We declare them in the file `LR_Modules/lrcom.f90` of the QE distribution, which contains the control parameters for linear-response calculations.

```
38 MODULE control_lr
39   !
40   USE kinds,      ONLY : DP
41   !
42   ! ... The variables controlling the run of linear response codes
43   !
44   SAVE
45   !
46   INTEGER, ALLOCATABLE :: nbnd_occ(:)  ! occupied bands in metals
47   REAL(DP) :: alpha_pv       ! the alpha value for shifting the bands
48   LOGICAL  :: lgamma         ! if .TRUE. this is a q=0 computation
49   LOGICAL  :: lrpa           ! if .TRUE. uses the Random Phace Approximation
+    LOGICAL  :: cdfpt          ! if .TRUE. applies cDFPT
+    INTEGER, ALLOCATABLE :: cdfpt_subspace(:, :, :, :)
50   !
51 END MODULE control_lr
```

The actual cDFPT modification takes place in `LR_Modules/orthogonalize.f90`, which contains the routine to orthogonalize the change of the potential $\partial\hat{V}_{\mathrm{SCF}}$ to the valence states (cf. Eq. 2.98). Here, we need access to the current $\boldsymbol{k}$ point in Cartesian coordinates `xk`, the dimensions of the `nk1` × `nk2` × `nk3` mesh it belongs to, and the Bravais lattice vectors `at`.

```
31   USE kinds,            ONLY : DP
32   USE klist,            ONLY : lgauss, degauss, ngauss, ltetra, wk, xk
+    USE start_k,          ONLY : nk1, nk2, nk3
+    USE cell_base,        ONLY : at
33   USE noncollin_module, ONLY : noncolin, npol
```

Of course, we also need our new variables `cdfpt` and `cdfpt_subspace`.

```
42   USE gvect,            ONLY : gstart
43   USE control_lr,       ONLY : alpha_pv, nbnd_occ, cdfpt, cdfpt_subspace
44   USE dfpt_tetra_mod,   ONLY : dfpt_tetra_beta
```

With that, we can calculate the mesh-point indices `kk1` $\in \{1, 2, \ldots, \texttt{nk1}\}$ etc. of $\boldsymbol{k}$ and $\boldsymbol{k} + \boldsymbol{q}$, where `kk1` = `kk2` = `kk3` = 1 is the Γ point. (Fortran indices are 1-based by default.)

```
54   COMPLEX(DP), ALLOCATABLE :: ps(:,:)
55   REAL(DP), ALLOCATABLE    :: ps_r(:,:)
56   INTEGER :: ibnd, jbnd, nbnd_eff, n_start, n_end, kk1, kk2, kk3, kq1, kq2, kq3
57   REAL(DP) :: wg1, w0g, wgp, wwg, deltae, theta
58   REAL(DP), EXTERNAL :: w0gauss, wgauss
59   ! functions computing the delta and theta function
+    !
+    kk1 = modulo(nint(nk1 * dot_product(at(:, 1), xk(:, ikk))), nk1) + 1
+    kk2 = modulo(nint(nk2 * dot_product(at(:, 2), xk(:, ikk))), nk2) + 1
+    kk3 = modulo(nint(nk3 * dot_product(at(:, 3), xk(:, ikk))), nk3) + 1
+    !
+    kq1 = modulo(nint(nk1 * dot_product(at(:, 1), xk(:, ikq))), nk1) + 1
+    kq2 = modulo(nint(nk2 * dot_product(at(:, 2), xk(:, ikq))), nk2) + 1
+    kq3 = modulo(nint(nk3 * dot_product(at(:, 3), xk(:, ikq))), nk3) + 1
```

Now we are ready to implement the central Eq. 2.99. We eliminate the response of the electronic density whenever both the initial state $|\boldsymbol{k}n\rangle \equiv |$`kk1 kk2 kk2 ibnd`$\rangle$ and the final state $|\boldsymbol{k}+\boldsymbol{q}m\rangle \equiv |$`kq1 kq2 kq2 jbnd`$\rangle$ are in the active subspace `cdfpt_subspace`.

```
86      DO ibnd = 1, nbnd_occ (ikk)
87         !
88         IF ( lgauss ) THEN
89            !
90            wg1 = wgauss ((ef-et(ibnd,ikk)) / degauss, ngauss)
91            w0g = w0gauss((ef-et(ibnd,ikk)) / degauss, ngauss) / degauss
92            DO jbnd = 1, nbnd
+                IF (cdfpt) THEN
+                   IF (any(cdfpt_subspace(:, kk1, kk2, kk3) == ibnd) .AND. &
+                       any(cdfpt_subspace(:, kq1, kq2, kq3) == jbnd)) THEN
+                      ps(jbnd, ibnd) = wg1 * ps(jbnd, ibnd)
+                      CYCLE
+                   ENDIF
+                ENDIF
+                !
93              wgp = wgauss ( (ef - et (jbnd, ikq) ) / degauss, ngauss)
94              deltae = et (jbnd, ikq) - et (ibnd, ikk)
95              theta = wgauss (deltae / degauss, 0)
96              wwg = wg1 * (1.d0 - theta) + wgp * theta
```

The only step missing is to read the parameters `cdfpt` and `cdfpt_subspace` from the input file for `ph.x`. This happens in `PHonon/PH/phq_readin.f90`.

```
73    USE qpoint,         ONLY : nksq, xq
74    USE control_lr,     ONLY : lgamma, lrpa, cdfpt, cdfpt_subspace
```

We choose to read the (sometimes lengthy) definition of the active subspace from an additional input file rather than the main input file for `ph.x`. The name of the former, `subspace`, must be given in the latter. Thus, the main input file can contain two new parameters: the logical `cdfpt` and the string `subspace`.

```
+     CHARACTER(LEN=256) :: subspace
+     !
111   NAMELIST / INPUTPH / tr2_ph, amass, alpha_mix, niter_ph, nmix_ph,  &
112                          nat_todo, verbosity, iverbosity, outdir, epsil,  &
113                          trans,  zue, zeu, max_seconds, reduce_io, &
114                          modenum, prefix, fildyn, fildvscf, fildrho, &
115                          ldisp, nq1, nq2, nq3, &
116                          eth_rps, eth_ns, lraman, elop, dek, recover,  &
117                          fpol, asr, lrpa, lnoloc, start_irr, last_irr, &
118                          start_q, last_q, nogg, ldiag, search_sym, lqdir, &
119                          nk1, nk2, nk3, k1, k2, k3, &
120                          drho_star, dvscf_star, only_init, only_wfc, &
121                          elph_nbnd_min, elph_nbnd_max, el_ph_ngauss, &
122                          el_ph_nsigma, el_ph_sigma,  electron_phonon, &
123                          q_in_band_form, q2d, qplot, low_directory_check, &
124                          lshift_q, cdfpt, subspace
```

Their default values are `cdfpt = .false.` and `cdfpt_subspace = 'subspace.dat'`.

```
301   lshift_q = .false.
302   !
+     cdfpt = .false.
+     subspace = 'subspace.dat'
+     !
303   ! ...  reading the namelist inputph
304   !
305   IF (meta_ionode) THEN
306      READ( 5, INPUTPH, ERR=30, IOSTAT = ios )
```

At this point, in a parallel calculation, only the processor on which the input has been read knows about the chosen values. It is thus important to broadcast the information to all processors. Otherwise, only one processor would impose the cDFPT constraint at the $\boldsymbol{k}$ points assigned to it. Reading and broadcasting of the active subspace takes place in a separate subroutine `setup_subspace`.

```
335   CALL bcast_ph_input ( )
336   CALL mp_bcast(nogg, meta_ionode_id, world_comm  )
337   CALL mp_bcast(q2d, meta_ionode_id, world_comm  )
338   CALL mp_bcast(q_in_band_form, meta_ionode_id, world_comm  )
+     !
+     CALL mp_bcast(cdfpt, meta_ionode_id, world_comm)
+     IF (cdfpt) CALL setup_subspace(cdfpt_subspace, subspace)
```

This subroutine is defined at the end of the file. The subspace file must start with a line with five integers, separated by spaces and/or commas: the $\boldsymbol{k}$-mesh dimensions `nk1`, `nk2`, and `nk3`, the number of bands in the active subspace, and the band-index offset. Afterwards, the indices of the bands as used in QE must be defined for all `nk1` × `nk2` × `nk3` $\boldsymbol{k}$ points. As customary in Fortran, the first index, in this case `nk1`, varies fastest. Band indices in QE are 1-based. The defined offset is added to all values. This can be used to avoid large numbers in the input file. Line breaks can be placed at will but are expected after each complete definition of an individual band.

```
843   RETURN
844   !
+  CONTAINS
+     !
+     SUBROUTINE setup_subspace(subspace, filename)
+        INTEGER, ALLOCATABLE, INTENT(OUT) :: subspace(:, :, :, :)
+        CHARACTER(LEN=256), INTENT(IN) :: filename
+        !
+        INTEGER, EXTERNAL :: find_free_unit
+        INTEGER :: id, nk(3), bands, band, offset
+        !
+        id = find_free_unit()
+        !
+        IF (meta_ionode) THEN
+           OPEN (id, file=filename, action='read', status='old')
+           READ (id, *) nk, bands, offset
```

```
+       ENDIF
+       !
+       CALL mp_bcast(nk, meta_ionode_id, world_comm)
+       CALL mp_bcast(bands, meta_ionode_id, world_comm)
+       !
+       ALLOCATE(subspace(bands, nk(1), nk(2), nk(3)))
+       !
+       IF (meta_ionode) THEN
+          DO band = 1, bands
+             READ (id, *) subspace(band, :, :, :)
+          ENDDO
+          CLOSE (id)
+          subspace(:, :, :, :) = subspace + offset
+       ENDIF
+       !
+       CALL bcast_integer(subspace, size(subspace), meta_ionode_id, world_comm)
+    END SUBROUTINE
845 END SUBROUTINE phq_readin
```

One way to obtain the subspace definition for a particular system is to have QE output all band energies for a uniform mesh and compare the values to those obtained for a subset of bands from WANNIER90 for the very same $\boldsymbol{k}$ points. A difficulty of this approach that cannot be easily circumvented is that we are unable to distinguish between degenerate energy levels.

A.2 WANNIER90

The program WANNIER90 [92–94] represents electronic structure from *ab initio* data in the basis of Wannier functions. Crucial steps in this process are the disentanglement of the subset of bands to be represented [91] and the calculation of "maximally-localized Wannier functions" [89, 90] to make the resulting TB models short-range. WANNIER90 is interfaced to various *ab initio* codes, including QE and VASP.

In this thesis, WANNIER90 is extensively used, not only for electronic data but also for the EPC. In the latter case, WANNIER90 is operated behind the scenes by EPW. It should be mentioned that throughout this work, we omit the step of maximal localization and instead work with Wannier functions that resemble atomic orbitals and thus have a clear interpretation.

A.3 EPW

The EPW code [138–140] is distributed as a part of QE. It is crucial for the work presented in this thesis, since it provides the gauge-free representation $g_{\boldsymbol{R}i\boldsymbol{R}'\alpha\beta}$ of the EPC in the Wannier basis from which we can obtain the EPC for arbitrary $\boldsymbol{q}$ and $\boldsymbol{k}$ points via Eq. 2.149.

By default, the elements of $g_{\boldsymbol{R}i\boldsymbol{R}'\alpha\beta}$ are written (consecutively, as double-precision floating-point numbers) to the file `<outdir>/<prefix>.epmatwp1`, where the output directory `<outdir>` and the job prefix `<prefix>` are QE input parameters. However, to correctly interpret them, we also need the corresponding lattice vectors $\boldsymbol{R}$ and $\boldsymbol{R}'$ within the WS supercell, which are not output by default. Thus, we add some lines to `EPW/src/ephwann_shuffle.f90` to save them to disk, also in binary representation.

```
355   ! Determine the size of the respective WS sets based on the length of the matrices
356   nrr_k = SIZE(irvec_k(1,:))
357   nrr_q = SIZE(irvec_q(1,:))
358   nrr_g = SIZE(irvec_g(1,:))
+     !
+     IF (ionode) THEN
+       OPEN (13, file='wigner.dat', action='write', status='replace', access='stream')
+       WRITE (13) nrr_k, irvec_k, ndegen_k, wslen_k
+       WRITE (13) nrr_q, irvec_q, ndegen_q, wslen_q
+       WRITE (13) nrr_g, irvec_g, ndegen_g, wslen_g
+       CLOSE (13)
+     ENDIF
```

Here, `nrr_`x is the number of lattice vectors `irvec_`x of lengths `wslen_`x. The corresponding elements of the EPC must be weighted with the inverse of `ndegen_`x to avoid a double counting on the edge of the WS supercell. x = `k`, `q`, and `g` labels WS supercells shifted by zero, $\boldsymbol{\tau}_l - \boldsymbol{\tau}_k$, and $\boldsymbol{\tau}_k$ (where $\boldsymbol{\tau}_k$ are atomic positions within the unit cell) as used for electrons, phonons, and the EPC (cf. App. B.4.2). For the transformation of the EPC, we only need `irvec_k` and `irvec_g`; the other quantities are stored for completeness.

A.4 VASP

VASP [299, 300] is a very popular proprietary program for DFT (and beyond). Like QE, it is based on plane waves and PPs, with emphasis on the PAW method [315]. In this thesis, we used VASP to calculate the RPA and cRPA Coulomb interactions and the electronic structure in Sec. 7.2.4 and Chap. 6.

A.5 TRIQS

The Toolbox for Research on Interacting Quantum Systems (TRIQS) [410] is a collection of C++ and Python libraries currently maintained by the Center for Computational Quantum Physics at the Flatiron Institute in New York. It is free software and promotes the field of strongly correlated physics by systematically providing a variety of useful tools to a broad audience[1]. In the future, we plan to make the functionality of our elphmod codes, presented in the following section, compatible with TRIQS.

A.6 elphmod

The Python package elphmod [289] is a collection of Python modules to handle *ab initio*–based electron–phonon models. It was developed in the course of the work behind this thesis. It is meant to be used in the context of scripting, but since it is parallelized using the Message Passing Interface (MPI) via MPI for Python [411] and heavily relies on the efficient NumPy library [412], it can also be used for computationally demanding calculations on a supercomputer. The core functionality is not limited to particular systems, whereas several specialized functions are focused on (especially hexagonal) 2D materials. The different modules of elphmod accomplish the following tasks:

[1] Especially compared to the usual outreach of many scientific software, which is unfortunately often limited to an institute's corridor.

el reads TB models from WANNIER90 (Eq. 2.35); sets up Hamiltonians (Eq. 2.36); reads (projected) electronic band structures from QE.

ph reads mass–spring models from QE (Eq. 2.100); sets up dynamical matrices (Eq. 2.63); maps IFCs to WS supercells (App. B.4.2); reads (and writes) dynamical matrices from QE; applies the ASR (Eq. 2.114); classifies phonon modes as longitudinal, transverse, or out-of-plane (Sec. 2.4.4); symmetry-transforms and Fourier-interpolates dynamical matrices (Eq. B.2).

elph reads EPCs from EPW (App. A.3) (or directly from QE); transforms EPCs from localized to electronic and phononic eigenbases (Eq. 2.149).

elel reads local and $\boldsymbol{q}$-dependent Coulomb tensors from VASP (Sec. 7.2.4); transforms the Coulomb interaction between orbital and band basis.

MPI distributes work among processors; splits processors into subcommunicators; creates arrays in shared memory; prints on a single processor.

bravais provides Bravais basis vectors (App. C.1); calculates reciprocal basis vectors (Eq. C.3); finds sets of equivalent points; generates sets of irreducible points (Fig. C.1); finds symmetries; completes symmetry-reduced data (App. B.2); relates points on periodic axis (App. B.4.1.1); interpolates linearly (App. B.4.1); Fourier-interpolates (App. B.4.2); resizes data arrays via interpolation; calculates distances on skew lattices; maps lattice vectors to (different types of) WS supercells; samples high-symmetry paths (App. C.1.1); reads structures from QE input; reads VASP's `POSCAR` files.

dispersion calculates eigenvalues and -vectors for selected points or the full BZ (using symmetries); sorts entangled bands by character (App. B.1).

dos calculates DOS (App. B.3.1), weighted DOS ("α^2F") (App. B.3.2), and double-delta integrals (App. B.3.3) via 2D tetrahedron methods (App. B.3).

diagrams calculates bare electronic susceptibility (Eqs. 3.1 and C.42) and polarizability (Eq. 7.1b); calculates phonon self-energy; renormalizes EPCs (work in progress) (Sec. 5.3); averages over Fermi-surface (Eqs. 3.7 and 3.10).

occupations provides Fermi–Dirac (App. C.7.1), Gaussian (App. C.7.2), Methfessel–Paxton (App. C.7.3), and Lorentzian (App. C.7.4) step and delta functions.

eliashberg calculates parameters of McMillan's formula (Eq. 3.13) for the superconducting T_c.

plot maps mesh data onto Cartesian axes via linear interpolation (App. B.4.1); creates (double) BZ plots (Figs. 5.5 and D.6); mixes colors from different color models; handles colormaps; arranges bitmaps; creates "fatbands."

misc shows status bars; groups points by neighborhood.

A.7 Eliashberg solvers

A.7.1 EBMB

The package EBMB [205] solves the multiband Eliashberg equations (Eq. 3.6) with additional band or orbital dependence. It is applied and discussed in detail in Ref. 206. It provides three FORTRAN programs and a PYTHON interface:

ebmb itself solves the multiband Eliashberg equations on a cut-off imaginary axis and optionally continues the results to the real axis via Padé approximants. A material is defined by nothing but an effective phonon frequency $\langle\omega\rangle$, intra- and interband EPCs $\lambda_{\alpha\beta}$ and Coulomb pseudo-potentials $\mu^*_{\alpha\beta}$, and, if desired, the electronic DOS $N(\varepsilon)$, otherwise assumed to be constant.

tc finds the critical temperature T_c for each band separately via the bisection method. Superconductivity is defined by the order parameter exceeding a certain threshold.

critical finds the critical point via the bisection method varying a parameter of choice. Superconductivity is defined by the kernel of the linearized gap equation having an eigenvalue greater than or equal to unity. The DOS is assumed to be constant.

ebmb.py is a Python wrapper around the above Fortran programs. It allows to pass input parameters and retrieve output data via intermediate text or binary files.

A.7.2 EBBW

The compact Python module `ebbw` [213] can be used to solve the linearized Eliashberg equations for finite bandwidths (Eq. 3.16). Below, we will describe its content step by step.

The only dependency is NumPy. We load it and define Boltzmann's constant and a convergence threshold.

```
1  #!/usr/bin/env python3
2
3  import numpy as np
4
5  kB = 8.61733e-5
6  epsilon = 1e-10
```

As a reference, we define McMillan's formula for the critical temperature T_c (Eq. 3.13).

```
8  def Tc(l, u, w, E, A=1.20, B=1.04, C=0.62, **ignore):
9      u /= 1 + u * np.log(E / w)
10     return w / (kB * A) * np.exp(-B * (1 + l) / (l - C * l * u - u))
```

The largest eigenvalue of the kernel K of the gap equation (Eq. 3.17) is determined via the power method. To avoid that a negative eigenvalue is the one largest in magnitude, we temporarily shift the spectrum of the kernel by a constant. To speed up consecutive calculations (with slightly different parameters), the current eigenvector $\boldsymbol{\varphi}$ is preserved during different function calls. Only on the first call, it is initialized with random numbers.

```
12 def eigenvalue(matrix):
13    N = len(matrix)
14
15    absolute = abs(matrix)
16    shift = min(absolute.sum(axis=0).max(), absolute.sum(axis=1).max())
17
18    matrix.flat[::N + 1] += shift
19
20    i = eigenvalue
21
22    if not hasattr(i, 'vector') or len(i.vector) != N:
```

```
23        i.vector = np.random.rand(N)
24
25    x0 = np.nan
26
27    while True:
28        i.vector = matrix.dot(i.vector)
29        x = np.sqrt(i.vector.dot(i.vector))
30        i.vector /= x
31
32        if abs(x - x0) < epsilon:
33            return x - shift
34
35        x0 = x
```

We also have to rescale the Coulomb interaction μ. The addend in Eq. 3.19 is evaluated via a series expansion around $\varepsilon_c/\omega_c = 0$ for $\varepsilon_c \leq \omega_c$ and around $\varepsilon_c/\omega_c = \infty$ for $\varepsilon_c > \omega_c$.

```
37 def residue(x):
38     base, series = (1 / x, np.log(x)) if x > 1 else (x, 0)
39
40     n = 1
41     pre = 2 / np.pi
42
43     while True:
44         term = base ** n / n ** 2
45         series += pre * term
46
47         if term < epsilon:
48             return series
49
50         n += 2
51         pre *= -1
```

The kernel K in Eq. 3.17 itself is found by repeatedly renormalizing the frequencies $\widetilde{\omega}_n$ until convergence. This is done in the following routine, which returns the eigenvalue of the kernel for the current parameters. In the same way the eigenvector $\boldsymbol{\varphi}$ of the kernel is remembered between function calls, here we remember the renormalized frequencies $\widetilde{\omega}_n$.

```
53 def Eliashberg(T, l, u, w, E, W, rescale=True, N=1e4, **ignore):
54     T *= kB
55
56     w /= 2 * np.pi * T
57
58     N = int(min(N, np.ceil(W * w - 0.5)))
59
60     l /= 1 + (np.arange(2 * N) / w) ** 2
61
62     if u and rescale:
63         u /= 1 + u * residue(E / ((2 * N + 1) * np.pi * T))
64
65     I = np.empty((N, N))
```

```
66    J = np.empty((N, N))
67
68    l *= 2 * T
69    u *= 4 * T
70    for n in range(N):
71       I[n:, n] = I[n, n:] = l[:N - n] - l[2 * n + 1:N + n + 1]
72       J[n:, n] = J[n, n:] = l[:N - n] + l[2 * n + 1:N + n + 1] - u
73
74    w = (2 * np.arange(N) + 1) * np.pi * T
75
76    i = Eliashberg
77
78    if not hasattr(i, 'w') or len(i.w) != N:
79       i.w = w
80
81    while True:
82       w0 = i.w
83       i.w = w + np.arctan2(E, i.w).dot(I)
84
85       if np.all(abs(i.w - w0) < epsilon):
86          break
87
88    return eigenvalue(np.arctan2(E, i.w) / i.w * J)
```

Please note that above we make use of the symmetry of the self-energy with respect to the sign of the frequency and thus reduce the dimension of the problem by half.

Now, we can vary any of the parameters—the temperature T, the effective EPC strength λ, the effective Coulomb interaction μ, the effective phonon frequency $\langle\omega\rangle$, or the electronic cutoff ε_c—to find its critical value. Here we formulate the problem as a fixed-point equation that, again, is solved iteratively. The choice of the initial exponents is not unique. They have been chosen such that the iteration converges, and fast.

```
90 def critical(variable='T', epsilon=1e-3, exponent=None, **parameters):
91    if exponent is None:
92       exponent = dict(T=2.3, l=-1.3, u=4.0, w=-2.3, E=-22.0)[variable]
93
94    while True:
95       x = parameters[variable] * Eliashberg(**parameters) ** exponent
96       exponent *= 0.99
97
98       if abs(x - parameters[variable]) < epsilon:
99          return x
100
101      parameters[variable] = x
```

By default, the critical temperature is calculated.

```
103 if __name__ == '__main__':
104    print(critical(T=10.0, l=1.0, u=0.1, w=0.02, E=1.0, W=15.0))
```

A.8 StoryLines

The Python module StoryLines [413] creates line plots with Ti*k*Z [414]. Is has been used to create the majority of the figures in this thesis, and it has been continuously refined in the process. Its main feature are listed below:

`Irrelevant points` of a line can be identified and omitted. This way, the file size can be drastically reduced without noticeable losses when plotting densely sampled data.

`Composite fatbands` to visualize, e.g., electronic and phononic band characters can be drawn using perpendicular (rotating) or fixed nib angles.

`Protruding objects` can be automatically cut at the plot edges.

`Self-intersecting outlines` of filled areas can be simplified by removing closed loops.

`Arbitrary TikZ code` can be inserted at arbitrary positions (in paper or data coordinates).

A.9 PlasMoS

PlasMoS ("Plasmons in MoS_2 monolayers") is a multiorbital RPA code (and beyond) maintained and largely developed by Malte Rösner. It is programmed in Python 3 and Fortran, and it is parallelized with MPI. It can be used to calculate, e.g., GW and GdW band structures, spin and charge susceptibilities, EELS spectra, conventional and plasmonic superconductivity with density-functional theory for superconductors (SCDFT), and dielectric screening of 2D materials via WFCE.

In this thesis, we used PlasMoS to calculate the spin susceptibilities presented in Sec. 7.2.5. Some parts of elphmod have also been inspired by this software.

A.10 Phonon renormalization with QE and elphmod

In the following, we will present a minimal working example that shows how to use QE and elphmod to perform a cDFPT calculation, work with electrons, phonons, and their coupling in localized bases, and consistently renormalize phonon dispersions, i.e., go from cDFPT to DFPT. Material-wise, we will consider a monolayer 1H-TaS_2—an old acquaintance in this thesis (cf. Chaps. 8 and 9). The example is also provided in the elphmod repository [289]. To run the example, we need a modified version of QE as described in detail in App. A.1. Please note that the results obtained in this example are very far from converged. In return, the *ab initio* part takes less than a minute on a laptop with only two cores.

We start with the workflow of the example, as defined in the `bash` script `run.sh` given below. Once we have downloaded the PP files from the QE homepage, we conduct the same sequence of steps for the DFPT and cDFPT calculations: First, we perform a self-consistent DFT calculation with the program `pw.x`. On this basis, we calculate the dynamical matrices from either DFPT or cDFPT using `ph.x`. These are Fourier-transformed with `q2r.x` to obtain the IFCs. Before we can proceed with the EPW calculation, we have to collect the necessary input files from the output of `ph.x` using the script `ph2epw.sh` and perform a non-self-consistent DFT calculation on a uniform $\boldsymbol{k}$-point mesh. Finally, we make copies of the relevant output files with the IFCs and the EPC in the localized basis. At this point, we collected all necessary data to proceed with the postprocessing using elphmod. Here, the script `renormalize.py` demonstrates the renormalization of cDFPT phonons as well as the visualization of electronic and phononic band structures.

```
#!/bin/bash

for pp in S.pbe-hgh.UPF Ta.pbe-hgh.UPF
do
    test -e $pp || wget https://www.quantum-espresso.org/upf_files/$pp
done

nk=2

for method in dfpt cdfpt
do
    mpirun pw.x -nk $nk < scf.in | tee scf.out
    mpirun ph.x -nk $nk < $method.in | tee $method.out

    mpirun q2r.x < q2r.in | tee q2r.out
    ./ph2epw.sh

    mpirun pw.x -nk $nk < nscf.in | tee nscf.out
    mpirun -n 1 epw.x -nk 1 < epw.in | tee epw.out

    cp ifc $method.ifc
    cp work/TaS2.epmatwp1 $method.epmatwp1
done

mpirun python3 renormalize.py
```

Below, we show the input file `scf.in` for the self-consistent DFT calculation with `pw.x`. As mentioned above, the parameters are chosen in favor of a fast calculation and will not yield physically sound results. For example, the unit-cell height `c` is too small to decouple the periodic images of the layer, the energy cutoff `ecutwfc` for the plane-wave basis is one order of magnitude too low, and also a $\boldsymbol{k}$ mesh of 4×4 points is much to coarse.

```
&CONTROL
     prefix = 'TaS2'
     outdir = 'work'
 pseudo_dir = '.'

calculation = 'scf'
/
&SYSTEM
      ibrav = 4
       ntyp = 2
        nat = 3

          a = 3.37
          c = 10.0

    ecutwfc = 10.0

occupations = 'smearing'
    smearing = 'fermi-dirac'
     degauss = 0.005
/
&ELECTRONS
    conv_thr = 1e-12
/

ATOMIC_SPECIES
Ta 180.95 Ta.pbe-hgh.UPF
S   32.06  S.pbe-hgh.UPF

ATOMIC_POSITIONS crystal
S   0.333333333  0.666666667  0.160998168
Ta  0.000000000  0.000000000  0.000000000
S   0.333333333  0.666666667 -0.160998168

K_POINTS automatic
4 4 1 0 0 0
```

The input file for the DFPT calculation with `ph.x` is more compact. The relevant output files are `fildyn` with the dynamical matrices and `dvscf` with the change of the SCF potential needed by EPW to calculate the EPC. The input parameters `cdfpt` and `subspace` are only allowed in our modified version of QE.

```
TaS2
&INPUTPH
  prefix = 'TaS2'
  outdir = 'work'

  fildyn = 'dyn'
fildvscf = 'dvscf'

   ldisp = .true.
      nq1 = 2
      nq2 = 2
      nq3 = 1

    cdfpt = .false.
subspace = 'subspace.in'

   tr2_ph = 1e-12
/
```

For the Fourier transform from the dynamical matrices to the IFCs with `q2r.x`, we only have to specify the names of the corresponding input and output files in `q2r.in`.

```
&INPUT
fildyn = 'dyn'
 flfrc = 'ifc'
/
```

EPW will need the dynamical matrices, the change of the SCF potential, and some metadata of the DFPT calculations. Hence, we copy all of this to a separate directory using the Python script `ph2epw.py`.

```
#!/bin/bash
# adapted from Samuel Ponce's pp.py

prefix=TaS2
points=2

mkdir -p save

cp -r work/_ph0/$prefix.phsave save

for n in `seq 1 $points`
do
    cp dyn$n save/$prefix.dyn_q$n

    path=work/_ph0

    test $n -gt 1 && path=$path/$prefix.q_$n

    cp $path/$prefix.dvscf1 save/$prefix.dvscf_q$n
done
```

The self-consistent DFT calculation has been performed on a set of irreducible $\boldsymbol{k}$ points only. However, to calculate the EPC, we need the KS states for a complete uniform mesh of $\boldsymbol{k}$ points. Thus, we now perform a *non*-self-consistent DFT calculation for these $\boldsymbol{k}$ points—

again with `pw.x`—on the basis of the converged SCF potential and density. The corresponding input file `nscf.in` differs only slightly from `scf.in`. First, we choose the correct algorithm.

```
6  calculation = 'nscf'
```

Next, we reduce the desired convergence threshold for the total energy.

```
23    conv_thr = 1e-10
```

Finally, we explicitly define the $\boldsymbol{k}$ points of the uniform 4×4 mesh.

```
35 K_POINTS crystal
36 16
37 0.00 0.00 0.00 0.0625
38 0.00 0.25 0.00 0.0625
39 0.00 0.50 0.00 0.0625
40 0.00 0.75 0.00 0.0625
41 0.25 0.00 0.00 0.0625
42 0.25 0.25 0.00 0.0625
43 0.25 0.50 0.00 0.0625
44 0.25 0.75 0.00 0.0625
45 0.50 0.00 0.00 0.0625
46 0.50 0.25 0.00 0.0625
47 0.50 0.50 0.00 0.0625
48 0.50 0.75 0.00 0.0625
49 0.75 0.00 0.00 0.0625
50 0.75 0.25 0.00 0.0625
51 0.75 0.50 0.00 0.0625
52 0.75 0.75 0.00 0.0625
```

Now, we come to the input file `epw.in` for `epw.x`, which also contains some parameters that are simply redirected to WANNIER90. We ask EPW to calculate the Wannier Hamiltonian and the EPC and to write the EPC in the localized basis to disk. We choose the three Ta-d_{z^2}, -$d_{x^2-y^2}$, and -d_{xy} orbitals, which span the relevant low-energy bands, as initial projections and disable the maximal localization of Wannier functions by setting `num_iter` to zero. Since we want to do the back-transform to arbitrary $\boldsymbol{k}$ and $\boldsymbol{q}$ points with ELPHMOD, we simply choose "fine" meshes identical to the original coarse meshes and ignore the interpolated results.

```
1  TaS2
2  &INPUTEPW
3        prefix = 'TaS2'
4        outdir = 'work/'
5     dvscf_dir = 'save'
6
7    wannierize = .true.
8          elph = .true.
9      epwwrite = .true.
10
11       nbndsub = 3
12      nbndskip = 8
13
14       proj(1) = 'Ta: dz2; dx2-y2; dxy'
15
16  dis_win_min = 1.0
17  dis_win_max = 8.0
18  dis_froz_min = 2.0
19  dis_froz_max = 4.0
20
21      num_iter = 0
22      wdata(1) = 'dis_num_iter 10000'
23      wdata(2) = 'write_hr true'
24
25  nk1 = 4, nk2 = 4, nk3 = 1
26  nq1 = 2, nq2 = 2, nq3 = 1
27
28  nkf1 = 4, nkf2 = 4, nkf3 = 1
29  nqf1 = 2, nqf2 = 2, nqf3 = 1
30  /
31
32  2 cartesian
33  0.0  0.000000000 0.0
34  0.0 -0.577350269 0.0
```

All steps can now be repeated for the cDFPT case. The input file `cdfpt.in` differs from `dfpt.in` in only one line.

```
14    cdfpt = .true.
```

This makes `ph.x` read the text file `subspace.in` with the definition of the active subspace. In the first line, we define a $6 \times 6 \times 1$ $\boldsymbol{k}$ point mesh, a single band, and no band-index offset.

In the second line, we pick the ninth band, which we previously identified as the band at the Fermi level, for all 36 $\boldsymbol{k}$ points of the mesh.

```
6 6 1 1 0
36*9
```

Now the *ab initio* part of the calculation is finished and we can proceed with the postprocessing part using the script `renormalize.py`.

First, we import the necessary modules, introduce the abbreviations `comm` for the MPI communicator and `info` for a "parallel print" function, and define constants and parameters such as the smearing temperature `kT` (cf. App. C.7), the mesh dimensions `nk` and `nq`, and the numbers of electronic and phononic bands `nel` and `nph`.

```
#!/usr/bin/env python3

import copy
import elphmod
import matplotlib.pyplot as plt
import numpy as np

comm = elphmod.MPI.comm
info = elphmod.MPI.info

Ry2eV = 13.605693009

kT = 0.005 * Ry2eV

nk = 4
nq = 2

nel = 1
nph = 9
```

Then we set up the list of irreducible $\boldsymbol{q}$ points and the high-symmetry path Γ–M–K–Γ.

```
q = sorted(elphmod.bravais.irreducibles(nq))
q = 2 * np.pi * np.array(q, dtype=float) / nq

k, x, GMKG = elphmod.bravais.GMKG(100, corner_indices=True)
```

We load the TB model from Wannier90 and the Fermi level from QE and diagonalize the Hamiltonian on the uniform mesh (without using the symmetries of the eigenvalues since we are interested in the complex phase of the eigenvectors, which have lower symmetry).

```
el = elphmod.el.Model('TaS2_hr.dat')
mu = elphmod.el.read_Fermi_level('scf.out')

e, U = elphmod.dispersion.dispersion_full_nosym(el.H, nk, vectors=True)

e = e[..., :nel] - mu
U = U[..., :nel]
```

We also load the cDFPT and DFPT mass–spring models from QE.

```
ph = dict()

for method in 'cdfpt', 'dfpt':
    ph[method] = elphmod.ph.Model('%s.ifc' % method, apply_asr=True)
```

As the last ingredient, we load the corresponding EPCs from EPW, Fourier-transform them to the chosen $\boldsymbol{q}$ and $\boldsymbol{k}$ points, and transform them into the electronic band basis. Then we combine the EPCs from cDFPT and DFPT into a matrix in the basis of Cartesian displacements and symmetrize it to obtain a Hermitian matrix (cf. Sec. 5.2.6).

```
g = dict()

for method in sorted(ph):
    elph = elphmod.elph.Model('%s.epmatwp1' % method, 'wigner.dat',
        el, ph['cdfpt'])

    g[method] = elph.sample(q=q, nk=nk, U=U, u=None, broadcast=False)

if comm.rank == 0:
    g2 = np.einsum('qiklnm,qjklnm->qijklnm', g['cdfpt'].conj(), g['dfpt'])
    g2 *= Ry2eV ** 3

    g2 += np.einsum('qijklnm->qjiklnm', g2.conj())
    g2 /= 2

else:
    g2 = np.empty((len(q), nph, nph, nk, nk, nel, nel), dtype=complex)

comm.Bcast(g2)
```

Now, we are ready to calculate the "phonon self-energy" or, more precisely, the change of the dynamical matrix for all irreducible $\boldsymbol{q}$ points.

```
Pi = elphmod.diagrams.phonon_self_energy(q, e, g2, kT=kT,
    occupations=elphmod.occupations.fermi_dirac)

Pi = np.reshape(Pi, (len(q), nph, nph))
Pi /= Ry2eV ** 2
```

We also need the bare dynamical matrices from cDFPT, which we want to renormalize. Here, the parallelization is not hidden in function calls.

```
sizes, bounds = elphmod.MPI.distribute(len(q), bounds=True)

D    = np.empty((len(q),           nph, nph), dtype=complex)
my_D = np.empty((sizes[comm.rank], nph, nph), dtype=complex)

for my_iq, iq in enumerate(range(*bounds[comm.rank:comm.rank + 2])):
    my_D[my_iq] = ph['cdfpt'].D(*q[iq])

comm.Allgatherv(my_D, (D, sizes * nph * nph))
```

The renormalization itself consists of simply adding the "self-energy" to the bare dynamical matrices. At this point, however, we know the renormalized phonons only for the irreducible $\boldsymbol{q}$ points. To be able to plot these phonons for arbitrary $\boldsymbol{q}$ points, we have to set up the corresponding mass–spring model first. This is done by completing the full uniform $\boldsymbol{q}$ mesh via the symmetry operations of the lattice (cf. App. B.2), applying a discrete Fourier transform, and mapping the resulting IFCs to the WS supercell.

```
ph['pp'] = copy.copy(ph['cdfpt'])

elphmod.ph.q2r(ph['pp'], D + Pi, q, nq, apply_asr=True)
```

Finally, we calculate and plot all relevant dispersions along Γ-M-K-Γ. Here, we use the band-disentanglement procedure outlined in App. B.1. We start with the orbital-resolved electrons. The shown plot should look qualitatively similar to, e.g., Fig. 9.1b.

```
e, U, order = elphmod.dispersion.dispersion(el.H, k, vectors=True, order=True)
e -= mu

if comm.rank == 0:
    proj = 0.1 * abs(U) ** 2

    for n in range(el.size):
        fatbands = elphmod.plot.compline(x, e[:, n], proj[:, :, n])

        for fatband, color in zip(fatbands, 'rgb'):
            plt.fill(*fatband, color=color, linewidth=0.0)

    plt.ylabel(r'$\epsilon$ (eV)')
    plt.xlabel(r'$k$')
    plt.xticks(x[GMKG], 'GMKG')
    plt.show()
```

Completely analogous, we obtain the cDFPT, DFPT, and "manually" renormalized phonons. The modes are classified according to Sec. 2.4.4. The results should roughly resemble Fig. 9.2a. Most importantly, the DFPT and postprocessed phonons should look identical. As expected, we exactly reproduce DFPT when choosing identical parameters in the *ab initio* calculations and in the postprocessing. However, because of the extremely coarse meshes and low accuracy chosen, the results might strongly vary with the mesh dimensions `nk` and `nq`. A reasonable interpolation of the EPC can only be expected for better inputs.

```
for method in sorted(ph):
    w2, u, order = elphmod.dispersion.dispersion(ph[method].D, k,
        vectors=True, order=True)

    w = elphmod.ph.sgnsqrt(w2) * Ry2eV * 1e3

    if comm.rank == 0:
        proj = elphmod.ph.polarization(u, k)

        for nu in range(ph[method].size):
            fatbands = elphmod.plot.compline(x, w[:, nu], proj[:, nu])

            for fatband, color in zip(fatbands, 'ymk'):
                plt.fill(*fatband, color=color, linewidth=0.0)

        plt.ylabel(r'$\omega$ (meV)')
        plt.xlabel(r'$q$')
        plt.xticks(x[GMKG], 'GMKG')
        plt.show()
```

Appendix B

Algorithms

Science is what we understand well
enough to explain to a computer.
Art is everything else we do.

—Donald Knuth

This appendix is a collection of numerical algorithms, which have been used in but whose applicability is not limited to this thesis. First, we will explain how bands can be sorted by their character (App. B.1). Next, we will show how to complete irreducible data using symmetries (App. B.2). Afterwards, we will present some tetrahedron methods for the efficient evaluation of 2D BZ integrals (App. B.3). We will conclude with algorithms for linear and Fourier interpolation (App. B.4).

B.1 Band disentanglement

Since most eigenvalue solvers return the eigenvalues (and corresponding eigenvectors) in ascending order, the band structures resulting from most *ab initio* codes or TB models are likewise sorted by energy. As a consequence, a band that is *smooth* in $\boldsymbol{k}$ space, in the sense

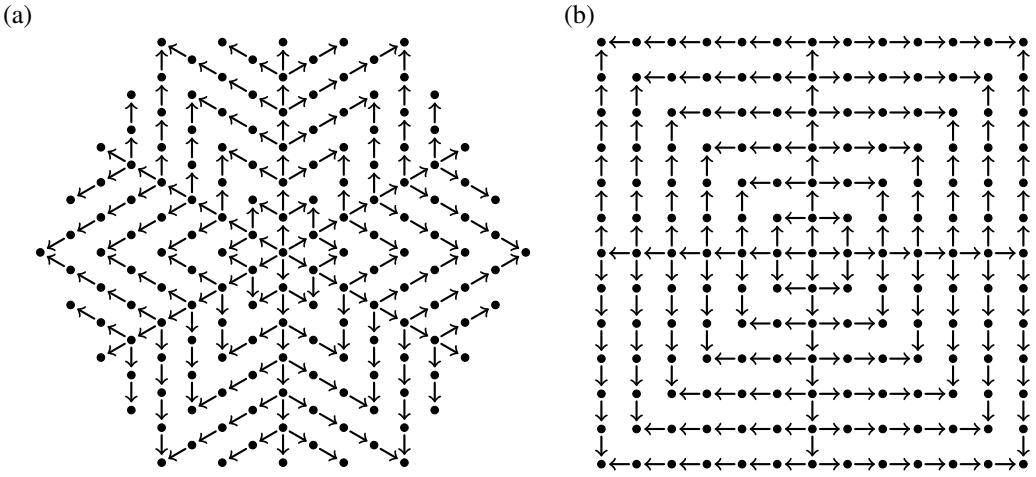

Figure B.1: Sorting paths through the BZs of (a) hexagonal and (b) square lattices.

that there is no kink in the eigenvalue while the eigenvector changes continuously (except for an arbitrary phase factor), does not necessarily have the same band index n for all $\boldsymbol{k}$ points. At each band crossing, two bands swap their band index. Whenever the band structure is topologically simple, it is however possible to disentangle the bands such that each band index corresponds to a smooth band. This is beneficial for, e.g., plotting and interpolation.

The sorting is performed locally in $\boldsymbol{k}$ space. We choose the order of the band indices n of the states $|\boldsymbol{k}n\rangle$ such that $|\langle\boldsymbol{k}_0 n|\boldsymbol{k}n\rangle|$ is maximized. Here, $\boldsymbol{k}_0$ is the "previous" $\boldsymbol{k}$ point, which implies that we have to sort along a selected path. Often, we plot band structures for paths connecting high-symmetry points. In this case, the sorting path is already well defined. But if we want to sort the bands on the whole BZ, we have to define an appropriate sorting path first. In Fig. B.1, two tried and tested dendritic paths for hexagonal and square lattices are shown. In practice, the sorting has to be performed for the irreducible wedge only and can be mapped to the rest of the BZ (cf. App. B.2).

Importantly, the eigenvectors belonging to degenerate eigenvalues can be arbitrarily mixed. Therefore, states with negligible energy differences (i.e., precisely at the relevant band crossings) should not be used as "previous" $\langle\boldsymbol{k}_0 n|$. Hence, if a very crossing point is met by our $\boldsymbol{k}$-point sampling, we have to compare states just before and after the crossing.

B.2 Completion of irreducible data

Often, we save resources by performing calculations for an irreducible set of points only (e.g., a wedge of the BZ). In the end, we can recover the data for all points (e.g., the full BZ) via application of all symmetries of the system. For real, scalar objects such as band energies, this procedure is straightforward. However, for complex vectorial or matrix objects, such as Hamiltonians, dynamical matrices, or matrices of eigenvectors, more care has to be taken.

First, we consider a scalar quantity defined on a uniform $L \times L$ mesh such that each lattice point is associated with an index tuple (k_1, k_2), where $k_i \in \{0, 1, \ldots, L-1\}$. The angle between the axes of 2D meshes can be either 60°, 90° or 120°. The data on such meshes is often invariant with respect to rotations by 60°, 90°, and 60°, respectively, and multiples thereof. These *generating* rotations transform the mesh indices as follows:

$$(k_1', k_2') = \begin{cases} (-k_2, k_1 + k_2) & \mod L \quad \text{for a } 60° \text{ rotation on a } 60° \text{ mesh,} \\ (-k_2, k_1) & \mod L \quad \ldots\ 90° \ldots \quad \ldots\ 90° \ldots \\ (k_1 - k_2, k_1) & \mod L \quad \ldots\ 60° \ldots \quad \ldots\ 120° \ldots \end{cases} \tag{B.1}$$

Additionally, a reflection across the angle bisector reads $(k_1', k_2') = (k_2, k_1)$. Via these simple mappings, which do not involve any floating-point arithmetics, the data of the full mesh can be straightforwardly completed if it is defined on a set of irreducible points only.

Next, we will discuss the example of the dynamical matrix. This is especially useful for calculating renormalized IFCs. Since the renormalization is usually performed for the irreducible $\boldsymbol{q}$ points, we have the renormalized dynamical matrices for these points only. For the Fourier transform to real-space IFCs however, we need the dynamical matrices on the complete mesh. The mapping of the mesh-point indices is exactly as above. But now we also have to transform the object itself. Let S be a symmetry transform of the lattice. Then,

$$D_{S\boldsymbol{q}kl} = S \cdot D_{\boldsymbol{q}kl} \cdot S^{-1} \mathrm{e}^{\mathrm{i}(1-S)\boldsymbol{q}(\boldsymbol{\tau}_k - \boldsymbol{\tau}_l)}, \tag{B.2}$$

where $\boldsymbol{\tau}_k$ is the position of the kth atom in the unit cell. Thus, we do not only have to transform the Cartesian axes of the dynamical matrix, but we also have to correct the phase factors associated with the atomic positions in respect of the transformed $\boldsymbol{q}$ point.

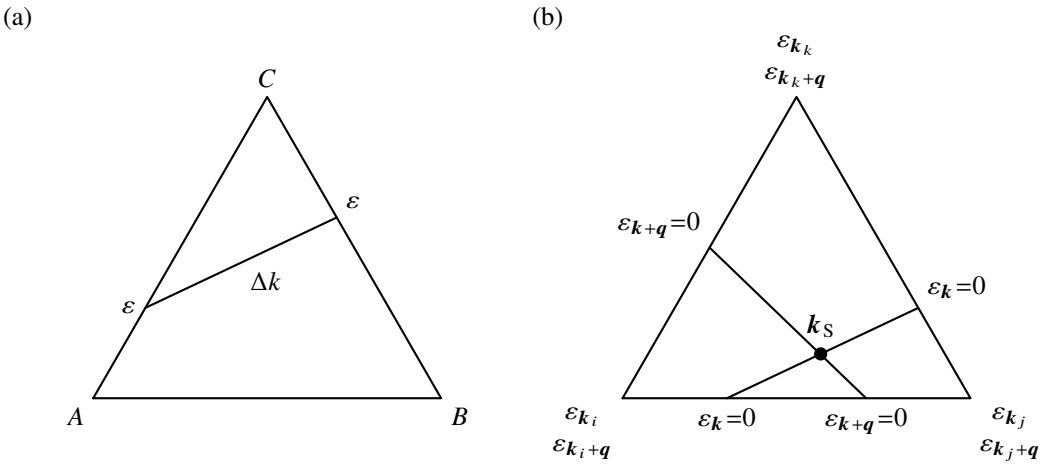

Figure B.2: 2D tetrahedron methods. (a) Calculation of DOS. (b) Double-delta approximation.

B.3 2D tetrahedron methods

There are two widespread ways to calculate integrals over the BZ. First, we can representatively sample the BZ via a set of special points (usually a uniform mesh) and simply sum over the contributions from the individual points [415, 416]. If the integral contains delta functions as appear in the definition of the DOS, these have to be broadened because otherwise all summands would be either zero or infinity. Second, we can use the tetrahedron method [417]. Here, the reciprocal space is divided into tetrahedra (or triangles in the 2D case) within which the integrand is assumed to be linear, i.e., we linearly interpolate (cf. App. B.4.1) the integrand between the vertices of the tetrahedra (which may coincide with the special points of the first method). Then, the interpolated integrand can be integrated analytically. The latter method usually requires much less sample points for satisfactorily converged results. Improved versions of the tetrahedron method exist [418] but will not be discussed here. Instead, we only consider the special case of a 2D BZ that is divided into equilateral triangles. For the case of a hexagonal Bravais lattice, this division is the most natural one. For the square lattice, the application is more involved albeit possible.

B.3.1 Density of states

We want to calculate the DOS starting from the expression in Eq. C.10. Here, we consider a 2D reciprocal unit cell that can be divided into $2N$ equilateral triangles of reciprocal side length b, on each of which the energy is interpolated linearly (cf. Fig. B.2a).

On the ith triangle with the energies $A \leq B \leq C$ at its corners, the absolute gradient of the energy plane is

$$|\nabla \varepsilon_{\boldsymbol{k}}|_i = \frac{2}{\sqrt{3}b}\sqrt{A^2 + B^2 + C^2 - AB - AC - BC}. \tag{B.3}$$

In the special case $A < B < \varepsilon < C$, the reciprocal length of the ε isoline within the triangle is

$$\Delta k_i = b\sqrt{A^2 + B^2 + C^2 - AB - AC - BC}\,\frac{C - \varepsilon}{(C - A)(C - B)}. \tag{B.4}$$

With the BZ area $A_{\mathrm{BZ}} = N\frac{\sqrt{3}}{2}b^2$, we find the contribution of this triangle to the DOS,

$$c_i = \frac{1}{A_{\mathrm{BZ}}}\frac{\Delta k_i}{|\nabla \varepsilon_{\boldsymbol{k}}|_i} = \frac{1}{N}\frac{C - \varepsilon}{(C - A)(C - B)}. \tag{B.5}$$

Equivalently, for $A < \varepsilon < B < C$ we find

$$\Delta k_i = b\sqrt{A^2 + B^2 + C^2 - AB - AC - BC}\,\frac{\varepsilon - A}{(B-A)(C-A)} \tag{B.6}$$

and thus

$$c_i = \frac{1}{A_{\mathrm{BZ}}}\frac{\Delta k_i}{|\boldsymbol{\nabla}\varepsilon_{\boldsymbol{k}}|_i} = \frac{1}{N}\frac{\varepsilon - A}{(B-A)(C-A)}. \tag{B.7}$$

If $A = \varepsilon < B < C$, $A < B = \varepsilon < C$, or $A < B < C = \varepsilon$, the ε isoline touches the triangle at one of the vertices only. In this case, the length Δk_i of the ε isoline within the triangle and thus the contribution vanishes. In turn, if $A = \varepsilon = B < C$ or $A < B = \varepsilon = C$, the ε isoline coincides with one of the edges of the triangle. In this case, we can use the limits of the above formulas, but to avoid a double counting, we must only count half the contribution because each edge is shared among two triangles. Finally, if $A = B = C = \varepsilon$, we are at a VHS and the contribution is infinite. In all other cases, the ε isoline does not have any overlap with the triangle, and the contribution is zero.

Adding all contributions, we find the DOS (cf. Eqs. C.9 and C.10)

$$N(\varepsilon) = \frac{1}{N}\sum_{\boldsymbol{k}}\delta(\varepsilon_{\boldsymbol{k}} - \varepsilon) = \frac{1}{A_{\mathrm{BZ}}}\int_{\varepsilon_{\boldsymbol{k}}=\varepsilon}\frac{\mathrm{d}k}{|\boldsymbol{\nabla}\varepsilon_{\boldsymbol{k}}|} \approx \frac{1}{A_{\mathrm{BZ}}}\sum_i \frac{\Delta k_i}{|\boldsymbol{\nabla}\varepsilon_{\boldsymbol{k}}|_i} = \sum_i c_i. \tag{B.8}$$

Integration over all energies yields unity.

B.3.2 Weighted density of states

Examples of weighted DOS are orbital-resolved DOS or the Eliashberg spectral function α^2F (Eq. 3.7). With a $\boldsymbol{k}$-dependent weight $w_{\boldsymbol{k}}$, they can be written as

$$A(\varepsilon) = \frac{1}{N}\sum_{\boldsymbol{k}}\delta(\varepsilon - \varepsilon_{\boldsymbol{k}})w_{\boldsymbol{k}} = \frac{1}{A_{\mathrm{BZ}}}\int_{\varepsilon_{\boldsymbol{k}}=\varepsilon}\frac{\mathrm{d}k}{|\boldsymbol{\nabla}\varepsilon_{\boldsymbol{k}}|}w_{\boldsymbol{k}}. \tag{B.9}$$

If we interpolate the weights $w_{\boldsymbol{k}}$ in the same way as we interpolate the energies $\varepsilon_{\boldsymbol{k}}$, we can evaluate such expressions with a modified version of the above 2D tetrahedron method.

Let A, B, and C (a, b, and c) denote the energies $\varepsilon_{\boldsymbol{k}}$ (weights $w_{\boldsymbol{k}}$) at the vertices of the ith triangle. Then, for the case $A < B < \varepsilon < C$, we find the contribution,

$$c_i = \frac{1}{A_{\mathrm{BZ}}}\frac{\Delta k_i}{|\boldsymbol{\nabla}\varepsilon_{\boldsymbol{k}}|_i}\langle w_{\boldsymbol{k}}\rangle_i \tag{B.10a}$$

$$= \frac{1}{N}\frac{C-\varepsilon}{(C-A)(C-B)} \times \frac{1}{2}\left[\frac{(C-\varepsilon)a + (\varepsilon - A)c}{C-A} + \frac{(C-\varepsilon)b + (\varepsilon - B)c}{C-B}\right]. \tag{B.10b}$$

Here, the first factor is the same as in the case of the plain DOS, whereas the second factor is the average weight $\langle w_{\boldsymbol{k}}\rangle_i$ along the ε isoline within the triangle.

Equivalently, for $A < \varepsilon < B < C$ we find

$$c_i = \frac{1}{A_{\mathrm{BZ}}}\frac{\Delta k_i}{|\boldsymbol{\nabla}\varepsilon_{\boldsymbol{k}}|_i}\langle w_{\boldsymbol{k}}\rangle_i \tag{B.11a}$$

$$= \frac{1}{N}\frac{\varepsilon - A}{(B-A)(C-A)} \times \frac{1}{2}\left[\frac{(\varepsilon - A)b + (B-\varepsilon)a}{B-A} + \frac{(\varepsilon - A)c + (C-\varepsilon)a}{C-A}\right]. \tag{B.11b}$$

All other arguments hold as above.

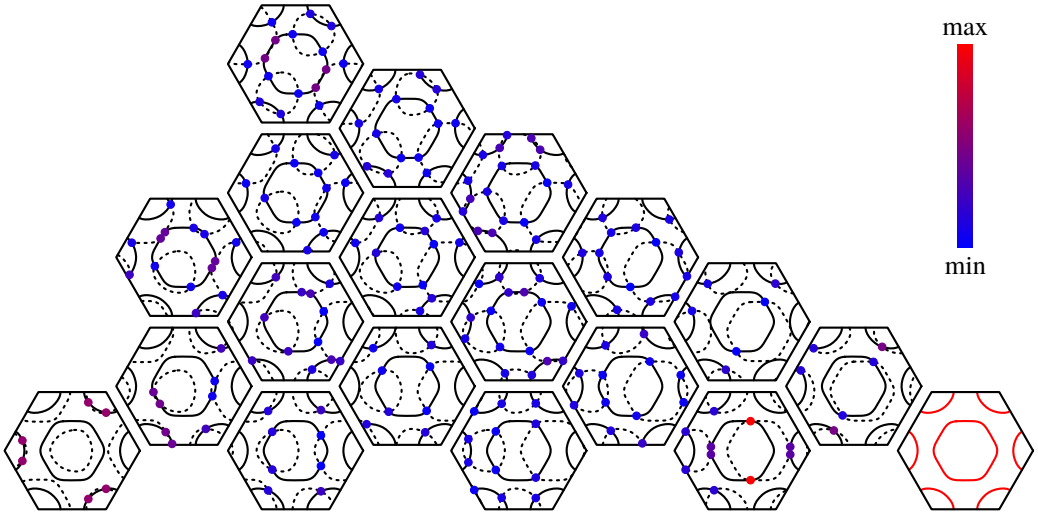

Figure B.3: Double-delta approximation for the example of 1H-TaS_2. For each $\boldsymbol{q}$ point of an irreducible wedge of a 12×12 mesh, the original and the shifted Fermi surface are shown. The intersection points, which are relevant for the double Fermi-surface average, are marked with colored dots, where blue corresponds to a small contribution (orthogonal intersection) and red corresponds to a large contribution (almost-parallel intersection). The electronic data is the same as in Chap. 9.

B.3.3 Double-delta approximation

Sometimes (cf. Eqs. 3.7 and 3.10) we want to calculate 2D integrals of the form

$$I = \int \mathrm{d}^2k \, \delta(\varepsilon_{\boldsymbol{k}}) \delta(\varepsilon_{\boldsymbol{k}+\boldsymbol{q}}) f(\boldsymbol{k}). \tag{B.12}$$

The two delta functions restrict the integral to neighborhoods of the intersection points $\boldsymbol{k}_\mathrm{S}$ where $\varepsilon_{\boldsymbol{k}_\mathrm{S}} = \varepsilon_{\boldsymbol{k}_\mathrm{S}+\boldsymbol{q}} = 0$. In these neighborhoods, $\varepsilon_{\boldsymbol{k}}$ and $\varepsilon_{\boldsymbol{k}+\boldsymbol{q}}$ can be linearized in $\boldsymbol{k}$,

$$I = \sum_{\boldsymbol{k}_\mathrm{S}} \int_{\boldsymbol{k} \approx \boldsymbol{k}_\mathrm{S}} \mathrm{d}^2k \, \delta\Big(\frac{\partial \varepsilon_{\boldsymbol{k}}}{\partial \boldsymbol{k}}\Big|_{\boldsymbol{k}_\mathrm{S}} \cdot \boldsymbol{k}\Big) \delta\Big(\frac{\partial \varepsilon_{\boldsymbol{k}+\boldsymbol{q}}}{\partial \boldsymbol{k}}\Big|_{\boldsymbol{k}_\mathrm{S}} \cdot \boldsymbol{k}\Big) f(\boldsymbol{k}). \tag{B.13}$$

A change to coordinates $k_1 = \partial \varepsilon_{\boldsymbol{k}} / \partial \boldsymbol{k}|_{\boldsymbol{k}_\mathrm{S}} \cdot \boldsymbol{k}$ and $k_2 = \partial \varepsilon_{\boldsymbol{k}+\boldsymbol{q}} / \partial \boldsymbol{k}|_{\boldsymbol{k}_\mathrm{S}} \cdot \boldsymbol{k}$ can be performed if the gradients $\partial \varepsilon_{\boldsymbol{k}} / \partial \boldsymbol{k}$ and $\partial \varepsilon_{\boldsymbol{k}+\boldsymbol{q}} / \partial \boldsymbol{k}$ are not parallel to each other at $\boldsymbol{k}_\mathrm{S}$. Then, the integration can be trivially carried out and yields

$$I = \sum_{\boldsymbol{k}_\mathrm{S}} \int_{\boldsymbol{k} \approx \boldsymbol{k}_\mathrm{S}} \mathrm{d}k_1 \, \mathrm{d}k_2 \, \frac{\delta(k_1) \delta(k_2) f(\boldsymbol{k})}{\left| \det \frac{\partial(k_1, k_2)}{\partial(k_x, k_y)} \right|} = \sum_{\boldsymbol{k}_\mathrm{S}} \frac{f(\boldsymbol{k}_\mathrm{S})}{\left| \frac{\partial \varepsilon_{\boldsymbol{k}}}{\partial k_x} \frac{\partial \varepsilon_{\boldsymbol{k}+\boldsymbol{q}}}{\partial k_y} - \frac{\partial \varepsilon_{\boldsymbol{k}+\boldsymbol{q}}}{\partial k_x} \frac{\partial \varepsilon_{\boldsymbol{k}}}{\partial k_y} \right|_{\boldsymbol{k}_\mathrm{S}}}. \tag{B.14}$$

This expression is conveniently evaluated using the 2D tetrahedron method. Let $\varepsilon_{\boldsymbol{k}}$ and $\varepsilon_{\boldsymbol{k}+\boldsymbol{q}}$ be defined on a triangular mesh and interpolated linearly in between. We consider the contribution to I from a single triangle with the vertices $\boldsymbol{k}_n$ with $n \in \{1, 2, 3\}$ (cf. Fig. B.2b). Excluding (including) the edge of the triangle, it contains an intersection point

$$\boldsymbol{k}_\mathrm{S} = \sum_n a_n \boldsymbol{k}_n \quad \text{with} \quad a_n = \frac{c_n}{\sum_m c_m} \quad \text{and} \quad c_n = \sum_{ij} \epsilon_{ijn} \varepsilon_{\boldsymbol{k}_i} \varepsilon_{\boldsymbol{k}_j+\boldsymbol{q}} \tag{B.15}$$

if $0 < a_n < 1$ ($0 \leq a_n \leq 1$) for all n. Here, ϵ_{ijn} is the Levi–Civita symbol. If the triangle is equilateral, the denominator in Eq. B.14 is given by $|\sum_n c_n|$. Since on each triangle $f(\boldsymbol{k})$ is assumed to depend linearly on $\boldsymbol{k}$, the enumerator is given by $f(\boldsymbol{k}_\mathrm{S}) = \sum_n a_n f(\boldsymbol{k}_n)$.

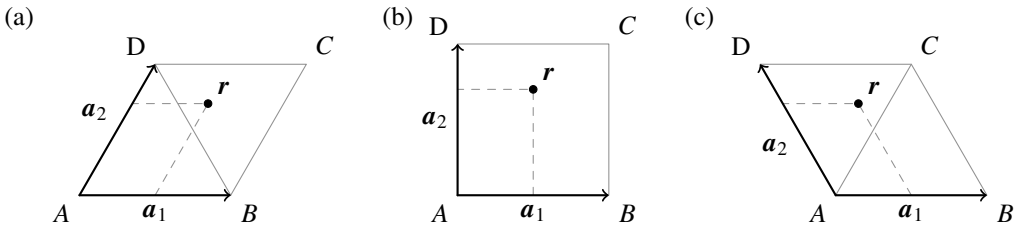

Figure B.4: Linear interpolation on 2D lattices with angles of (a) 60°, (b) 90°, and (c) 120°.

B.4 Interpolation

In numerical calculations, we always have to restrict ourselves to a discrete set of data points. However, especially when plotting results, it becomes necessary to reasonably interpolate between these points. The most simple way to do this is via linear interpolation. This is also a very stable procedure since, e.g., it guarantees that the value of each segment of the interpolant is bound by the values of its endpoints, i.e., no overshooting is possible. Alternatively, for the interpolation of periodic data, the most natural choice is via Fourier interpolation. As opposed to the linear case, the interpolant is smooth everywhere, but its choice is not unique anymore and the calculation computationally more expensive. In this section, we will present both linear (App. B.4.1) and Fourier interpolation (App. B.4.2) for the special case of data on a 2D lattice.

B.4.1 Linear interpolation

We consider a uniform mesh that is spanned by the basis vectors $\boldsymbol{a}_1$ and $\boldsymbol{a}_2$,

$$\boldsymbol{R} = n_1\boldsymbol{a}_1 + n_2\boldsymbol{a}_2 \quad \text{with} \quad n_1, n_2 \in \mathbb{Z}. \tag{B.16}$$

For all $\boldsymbol{R}$, $f(\boldsymbol{R})$ is known. We want to obtain the interpolated data $f(\boldsymbol{r})$ for arbitrary points

$$\boldsymbol{r} = r_1\boldsymbol{a}_1 + r_2\boldsymbol{a}_2 \quad \text{with} \quad r_1, r_2 \in \mathbb{R}. \tag{B.17}$$

By calculating $d_i = r_i \bmod 1$ and $n_i = r_i - d_i$, we can identify the cell anchored at $\boldsymbol{R} = n_1\boldsymbol{a}_1 + n_2\boldsymbol{a}_2$ to which an arbitrary point $\boldsymbol{r}$ belongs. Let the values of f at its corners be $A = f(\boldsymbol{R})$, $B = f(\boldsymbol{R} + \boldsymbol{a}_1)$, $C = f(\boldsymbol{R} + \boldsymbol{a}_1 + \boldsymbol{a}_2)$, and $D = f(\boldsymbol{R} + \boldsymbol{a}_2)$, as shown in Fig. B.4.

First, we consider the case where the angle between $\boldsymbol{a}_1$ and $\boldsymbol{a}_2$ amounts to 60° (Fig. B.4a). Here, the cell consists of two equilateral triangles. Depending on whether $d_1 + d_2 < 1$, the point $\boldsymbol{r}$ is located in one or the other triangle. The linear interpolation yields

$$f(\boldsymbol{r}) = \begin{cases} d_1 B + d_2 D + (1 - d_1 - d_2)A & \text{if } d_1 + d_2 < 1, \\ (1 - d_1)D + (1 - d_2)B + (d_1 + d_2 - 1)C & \text{otherwise.} \end{cases} \tag{B.18}$$

For an angle of 90° (Fig. B.4b), we do not have to differentiate between cases and find

$$f(\boldsymbol{r}) = (1 - d_1)(1 - d_2)A + d_1(1 - d_2)B + d_1 d_2 C + (1 - d_1)d_2 D. \tag{B.19}$$

Finally, for an angle of 120° (Fig. B.4c), we again have two triangles. Here, the criterion for $\boldsymbol{r}$ being in one or the other is $d_1 < d_2$. Hence,

$$f(\boldsymbol{r}) = \begin{cases} d_1 C + (1 - d_2)A + (d_2 - d_1)D & \text{if } d_1 < d_2, \\ (1 - d_1)A + d_2 C + (d_1 - d_2)B & \text{otherwise.} \end{cases} \tag{B.20}$$

In any case, if we interpolate periodic data on an $L \times L$ mesh, n_1 and n_2 have to be considered modulo L.

B.4.1.1 Interpolation of angles

A further complication arises if $f(\boldsymbol{r})$ is not only periodic in $\boldsymbol{r}$, i.e., $f(\boldsymbol{r} + L\boldsymbol{a}_i) = f(\boldsymbol{r})$, but if we instead want to interpolate a function $g(f(\boldsymbol{r})) = g(f(\boldsymbol{r} + L\boldsymbol{a}_i) + P)$. In other words, the value of $f(\boldsymbol{r})$ is only meaningful modulo a period P, e.g., $f(\boldsymbol{r})$ could be an angle and $P = 2\pi$. In this case, we must ensure that the values of f between which we interpolate (namely A, B, C, and possibly D) are as close together as possible. This can be achieved as follows:

We consider a general sequence of N points $g_1 = (A, B, C, \ldots)$, where we assume that $A \leq B \leq C \leq \ldots$ and $A, B, C, \ldots \in [0, P)$. If this is not initially given, it can be easily obtained by adding and subtracting multiples of P and subsequent sorting. We recursively define $N - 1$ additional sequences $g_{n+1} = (g_{n2}, g_{n3}, \ldots, g_{nN}, g_{n1} + P)$ by shifting the lowest point up by one period in each case. Then we can simply choose the group g_n that minimizes the spread $\langle (g_n - \langle g_n \rangle)^2 \rangle$.

B.4.2 Fourier interpolation

The Fourier interpolation is based on the discrete Fourier transform,

$$f_{\boldsymbol{k}} = \sum_{\boldsymbol{R}} f_{\boldsymbol{R}} \mathrm{e}^{\mathrm{i}\boldsymbol{k}\boldsymbol{R}}, \tag{B.21a}$$

$$f_{\boldsymbol{R}} = \frac{1}{N} \sum_{\boldsymbol{k}} f_{\boldsymbol{k}} \mathrm{e}^{-\mathrm{i}\boldsymbol{k}\boldsymbol{R}}, \tag{B.21b}$$

where $\boldsymbol{R}$ could label the N unit cells of a supercell and $\boldsymbol{k}$ would label the corresponding N discrete points in the reciprocal unit cell. The idea of Fourier interpolation is that if our $f_{\boldsymbol{R}}$ are known, we can generalize Eq. B.21a with respect to continuous $\boldsymbol{k}$. Here, it is guaranteed that the original $f_{\boldsymbol{k}}$ for discrete $\boldsymbol{k}$ are reproduced and that $f_{\boldsymbol{k}}$ is continuous in between. However, the interpolant is not necessarily smooth in the sense that there are no unnecessary wiggles.

Because of the periodicity of $f_{\boldsymbol{R}}$, for the original $f_{\boldsymbol{k}}$ it does not matter over which set of $\boldsymbol{R}$ points we sum, provided that this set is *complete*. In other words, with arbitrary vectors $\boldsymbol{S}$ that translate one supercell onto another one, we have

$$\sum_{\boldsymbol{R}} f_{\boldsymbol{R}} \mathrm{e}^{\mathrm{i}\boldsymbol{k}\boldsymbol{R}} = \sum_{\boldsymbol{R}} f_{\boldsymbol{R}+\boldsymbol{S}_{\boldsymbol{R}}} \mathrm{e}^{\mathrm{i}\boldsymbol{k}(\boldsymbol{R}+\boldsymbol{S}_{\boldsymbol{R}})}, \tag{B.22}$$

where the subscript $\boldsymbol{R}$ signifies that we can choose a different supercell vector for each unit-cell vector. As if that were not enough, we can even choose linear combinations of different supercell translations. With appropriately chosen weights $w_{\boldsymbol{R}}$,

$$\sum_{\boldsymbol{R}} f_{\boldsymbol{R}} \mathrm{e}^{\mathrm{i}\boldsymbol{k}\boldsymbol{R}} = \sum_{\boldsymbol{R}} \frac{1}{n_{\boldsymbol{R}}} \sum_{i=1}^{n_{\boldsymbol{R}}} f_{\boldsymbol{R}+\boldsymbol{S}_{\boldsymbol{R}i}} \mathrm{e}^{\mathrm{i}\boldsymbol{k}(\boldsymbol{R}+\boldsymbol{S}_{\boldsymbol{R}i})} \equiv \sum_{\boldsymbol{R}\boldsymbol{S}} w_{\boldsymbol{R}+\boldsymbol{S}} f_{\boldsymbol{R}+\boldsymbol{S}} \mathrm{e}^{\mathrm{i}\boldsymbol{k}(\boldsymbol{R}+\boldsymbol{S})}. \tag{B.23}$$

The choice of the $w_{\boldsymbol{R}}$ becomes important as soon as we allow for continuous $\boldsymbol{k}$. Since, notwithstanding that the interpolant $f_{\boldsymbol{k}}$ is always guaranteed to reproduce the original points, its exact shape depends on the choice of $\boldsymbol{R}$ we sum over. If we want the interpolant to be as smooth as possible, the wavelengths of $\mathrm{e}^{\mathrm{i}\boldsymbol{k}\boldsymbol{R}}$ must be as long as possible; in turn, the $\boldsymbol{R}$ must be as close to the origin as possible. This is ensured by taking $\boldsymbol{R}$ from the WS supercell. Here, to ensure a symmetric set of $\boldsymbol{R}$, we include *all* vertices and edges of the WS supercell and in turn reduce the weight of these lattice vectors.

The simplest choice for a WS supercell is the one centered at $\boldsymbol{R} = 0$. However, depending on the context, it can be advisable to shift the WS supercell to ensure that, e.g., hoppings and IFCs are associated with the shortest-possible distance between periodic images of the same atom or orbital. This way, physically sound TB and mass–spring models can be obtained.

Appendix C

Concepts and derivations

Grau, teurer Freund, ist alle Theorie,
Und grün des Lebens goldner Baum.

—Mephisto

In this appendix, we will reproduce some theoretical concepts, definitions, and derivations that should not go unmentioned but did not find their place in the main part of this thesis. In App. C.1, we start with the concept of Bravais and reciprocal lattices. Next, in App. C.2, we will define the DOS and related terminology. For overall consistency, in App. C.3, we choose our conventions for indexing and basis transforms. Because of its relevance in this thesis, in App. C.4, we will derive the expression for the phonon self-energy from perturbation theory. In App. C.5, we will shortly go into spin and charge susceptibilities. Since phonon physics is largely about forces acting on atoms, App. C.6 will be about the latter. Various functions used for occupation smearing are defined in App. C.7. Finally, in App. C.8, we will present two ways to estimate effective Coulomb interactions.

C.1 Lattices

A crystal that extends periodically in all spatial directions can be described by a lattice, the *Bravais lattice*, and a configuration of atoms, the *basis*, attached to each lattice point. The lattice points are

$$\boldsymbol{R} = n_1\boldsymbol{a}_1 + n_2\boldsymbol{a}_2 + n_3\boldsymbol{a}_3, \tag{C.1}$$

where n_1, n_2, and n_3 are integers and $\boldsymbol{a}_1$, $\boldsymbol{a}_2$, and $\boldsymbol{a}_3$ are the basis vectors of the Bravais lattice. The whole space is divided into identical unit cells, each of them attached to a lattice point. One possible division into unit cells is to assign each point $\boldsymbol{r}$ in space to the lattice point $\boldsymbol{R}$ closest to it (in terms of the Euclidean distance). Then, the unit cells are the *Voronoi cells* of the lattice and the unit cell centered at the origin is also called the *WS cell*.

Satisfying duality, we also define the *reciprocal lattice* as the set of points

$$\boldsymbol{G} = m_1\boldsymbol{b}_1 + m_2\boldsymbol{b}_2 + m_3\boldsymbol{b}_3, \tag{C.2}$$

where m_1, m_2, and m_3 are again integers and $\boldsymbol{b}_1$, $\boldsymbol{b}_2$, and $\boldsymbol{b}_3$ the reciprocal basis vectors. The assignment of points $\boldsymbol{k}$ in reciprocal space to reciprocal unit cells is analogous to the case of the Bravais lattice. The WS cell of the reciprocal lattice is known as the *first BZ*.

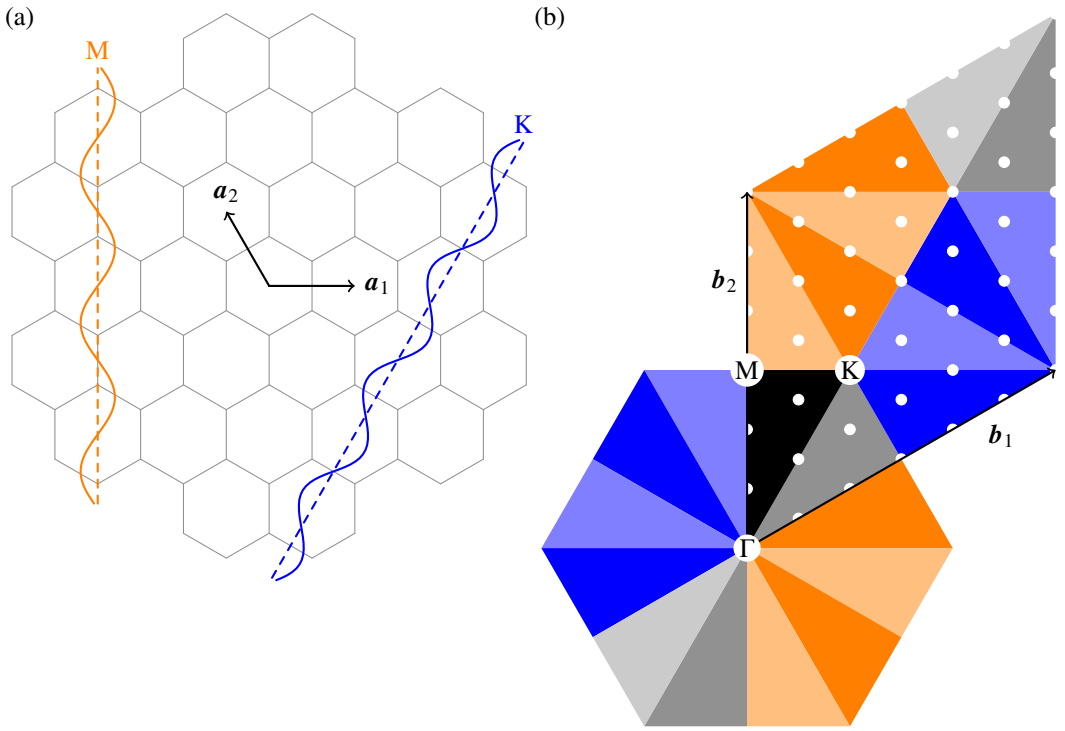

Figure C.1: Hexagonal (a) Bravais and (b) reciprocal lattice. The hexagon centered at the origin of the Bravais (reciprocal) lattice is the WS cell (first BZ). The high-symmetry points M and K in reciprocal space can be visualized as plane waves in real space. The $\boldsymbol{k}$ points of an exemplary uniform 6×6 mesh in reciprocal space are marked with white dots. Here, the irreducible wedge, shown in black, contains only seven $\boldsymbol{k}$ points.

The basis vectors of the Bravais and reciprocal lattice are related via (cf. Eq. 1.1 of Ref. 67)

$$\boldsymbol{b}_i = 2\pi \frac{\boldsymbol{a}_j \times \boldsymbol{a}_k}{\boldsymbol{a}_i \cdot (\boldsymbol{a}_j \times \boldsymbol{a}_k)} \quad \text{for} \quad \epsilon_{ijk} = 1 \tag{C.3}$$

such that

$$\boldsymbol{a}_i \cdot \boldsymbol{b}_j = 2\pi\delta_{ij} \quad \text{and} \quad \boldsymbol{R} \cdot \boldsymbol{G} = 0 \mod 2\pi. \tag{C.4}$$

The transformation that relates the Bravais to the reciprocal lattice is the Fourier transform. In practice, the lattice vectors are restricted to a supercell consisting of N unit cells with periodic boundary conditions. (Analogous to the case of a simple unit cell, we can also define a *WS supercell*.) Then, we can use a discrete Fourier transform. Here, an important property is (cf. Eq. 1.18 of Ref. 67)

$$\sum_{\boldsymbol{R}} \mathrm{e}^{\mathrm{i}\boldsymbol{k}\boldsymbol{R}} = N \sum_{\boldsymbol{G}} \delta_{\boldsymbol{k}\boldsymbol{G}}. \tag{C.5}$$

C.1.1 Hexagonal lattice

The majority of materials that are dealt with in this thesis have hexagonal 2D Bravais lattices. We use the convention that

$$\boldsymbol{a}_1 = \begin{pmatrix} a \\ 0 \end{pmatrix}, \quad \boldsymbol{a}_2 = \frac{a}{2}\begin{pmatrix} -1 \\ \sqrt{3} \end{pmatrix}, \quad \boldsymbol{b}_1 = \frac{2\pi}{a}\frac{1}{\sqrt{3}}\begin{pmatrix} \sqrt{3} \\ 1 \end{pmatrix}, \quad \boldsymbol{b}_2 = \frac{2\pi}{a}\frac{2}{\sqrt{3}}\begin{pmatrix} 0 \\ 1 \end{pmatrix}, \tag{C.6}$$

so that we have an angle of 120° (60°) degrees between the first and second Bravais (reciprocal) basis vectors (cf. Fig. C.1). As long as time-reversal symmetry holds, the BZ can be divided

into twelve equivalent wedges, whose corners are the *high-symmetry points* Γ, M, and K. Computationally, it is advantageous to perform calculations on a single wedge only rather than on the whole BZ. In this case, we always choose the wedge defined by

$$\Gamma = 0, \quad \mathrm{M} = \frac{\boldsymbol{b}_2}{2}, \quad \mathrm{K} = \frac{\boldsymbol{b}_1 + \boldsymbol{b}_2}{3}. \tag{C.7}$$

Dispersion relations are usually plotted along the path Γ–M–K–Γ. Here, to avoid a kink at K, we continue straight to $\Gamma = \boldsymbol{b}_1$ of the neighboring BZ (or, equivalently, jump to $\mathrm{K} = (\boldsymbol{b}_2 - 2\boldsymbol{b}_1)/3$ and return to the original $\Gamma = 0$).

Many quantities in solid-state physics are BZ integrals. To evaluate these numerically, we need a representative sample of $\boldsymbol{k}$ points [415, 416]. Here, instead of restricting all points to the first BZ, it is convenient to define a uniform $L \times L$ mesh as

$$\boldsymbol{k} = k_1\boldsymbol{b}_1 + k_2\boldsymbol{b}_2 \quad \text{with} \quad k_1, k_2 \in \left\{0, \tfrac{1}{L}, \tfrac{2}{L}, \ldots, \tfrac{L-1}{L}\right\}. \tag{C.8}$$

If we want all high-symmetry points to be included in this set of points, L must be divisible by two and three, i.e., we need a $6n \times 6n$ mesh with n an integer. In this case, the number of inequivalent or *irreducible* $\boldsymbol{k}$ points can be calculated as follows: Each of the twelve symmetry-equivalent wedges △ΓMK effectively contains $(6n)^2/12 = 3n^2$ points. To obtain this number, only half of the $3n - 1$, $n - 1$ and $2n - 1$ points on the open line segments Γ–M, M–K, and K–Γ are counted, and only one twelfth, forth, and sixth of the corner points Γ, M, and K. This makes $6n$ points with an effective weight of $3n - 1$ points only. This results in $3n^2 + 3n + 1$ inequivalent $\boldsymbol{k}$ points. If we additionally assume a discrete translation symmetry in the out-of-plane direction, this number has to be multiplied by $m/2 + 1$ ($m/2 + 1/2$), where m is the even (odd) number of $\boldsymbol{k}$ points in this direction.

C.2 Density of states

Multivalued functions of $\boldsymbol{k}$ or $\boldsymbol{q}$ in the BZ (such as energies of electrons and phonons) are known as *band structures* or *dispersions*. In the following, we consider the electronic single-band case, where we have a single electronic energy $\varepsilon_{\boldsymbol{k}}$ for each $\boldsymbol{k}$.

Often, we are not interested in the $\boldsymbol{k}$ dependence but rather in the distribution of states on the energy axis. Then, the relevant quantity is the DOS (cf. Eqs. 3.91 and 4.135 of Ref. 67)

$$N(\varepsilon) = \frac{1}{N}\sum_{\boldsymbol{k}} \delta(\varepsilon_{\boldsymbol{k}} - \varepsilon), \tag{C.9}$$

where the sum is over all N $\boldsymbol{k}$ points of the BZ. In the 2D case, this can also be expressed as (cf. Eqs. 3.102 and 4.138 of Ref. 67)

$$N(\varepsilon) = \frac{1}{A_{\mathrm{BZ}}}\int_{\varepsilon_{\boldsymbol{k}}=\varepsilon} \frac{\mathrm{d}k}{|\boldsymbol{\nabla}\varepsilon_{\boldsymbol{k}}|}, \tag{C.10}$$

where A_{BZ} is the BZ area and the integral is over equal-energy contours in $\boldsymbol{k}$ space. (Equivalent formulas hold for surfaces or points in the other dimensions.) While Eq. C.9 can be evaluated using a finite number of $\boldsymbol{k}$ points in combination with a smeared-out delta function (cf. App. C.7), Eq. C.10 is efficiently calculated using the tetrahedron method (cf. App. B.3.1).

As can be seen in Eq. C.10, the integrand of the DOS diverges for a vanishing gradient of the dispersion, i.e., at local extrema or saddle points. These singularities are known as VHS. A saddle point in a 2D dispersion leads to a logarithmic divergence in the DOS [419].

The equal-energy surface at the Fermi level, $\varepsilon_{\boldsymbol{k}} = \mu$, is of particular importance, since it contains the electrons that are most susceptible to excitations (because of the availability of both occupied and unoccupied states within very small energy intervals). It is referred to as the *Fermi surface*.

C.3 Representations and basis transforms

This section gives an overview of the transformations between the relevant quantum numbers as used in this thesis. As many quantities that we have to deal with are high-dimensional and can be transformed independently along different dimensions, care has to be taken that index orders, complex phases, and alike are consistent.

First, we have to clearly define the order of indices. We do this with reference to Feynman diagrams as shown in Fig. 5.1. Assuming that bosonic momenta $\boldsymbol{q}$ are transferred from right to left and that electron lines are directed anticlockwise, we sort the involved quantum numbers by particle type (with highest precedence), from left to right (with intermediate precedence), and from top to bottom (with lowest precedence). For example, we translate the diagrams for the screened EPC and Coulomb interaction (left-hand sides in Fig. 5.1) as $g_{\boldsymbol{q}i\boldsymbol{k}\alpha\beta}$ and $W_{\boldsymbol{q}\boldsymbol{k}\alpha\beta\boldsymbol{k}'\gamma\delta}$. This ensures that summed-away indices and index pairs can be written in direct adjacency in dot products.

Different conventions for the discrete Fourier transform exist. They differ with respect to a prefactor p and a sign s in the exponent. Additionally, we have to deal with transforms between orbital and band bases. Using the example of the electronic Hamiltonian, we make a consistent choice by demanding that

$$\begin{aligned}
\varepsilon_{\boldsymbol{k}n} = \langle \boldsymbol{k}n|\hat{H}|\boldsymbol{k}n\rangle &= \sum_{\boldsymbol{R}\boldsymbol{R}'\alpha\beta} \overbrace{\langle \boldsymbol{k}n|\boldsymbol{R}\alpha\rangle}^{pU^*_{\boldsymbol{k}\alpha n}\mathrm{e}^{s\mathrm{i}\boldsymbol{k}\boldsymbol{R}}} \underbrace{\langle \boldsymbol{R}\alpha|\hat{H}|\boldsymbol{R}'\beta\rangle}_{t_{\boldsymbol{R}-\boldsymbol{R}'\alpha\beta}} \overbrace{\langle \boldsymbol{R}'\beta|\boldsymbol{k}n\rangle}^{pU_{\boldsymbol{k}\beta n}\mathrm{e}^{-s\mathrm{i}\boldsymbol{k}\boldsymbol{R}'}} && \text{(C.11a)}\\
&= p^2 \sum_{\boldsymbol{R}\boldsymbol{R}'\alpha\beta} U^*_{\boldsymbol{k}\alpha n} t_{\boldsymbol{R}-\boldsymbol{R}'\alpha\beta} U_{\boldsymbol{k}\beta n} \mathrm{e}^{s\mathrm{i}\boldsymbol{k}(\boldsymbol{R}-\boldsymbol{R}')} && \text{(C.11b)}\\
&= p^2 N \sum_{\boldsymbol{R}\alpha\beta} U^*_{\boldsymbol{k}\alpha n} t_{\boldsymbol{R}\alpha\beta} U_{\boldsymbol{k}\beta n} \mathrm{e}^{s\mathrm{i}\boldsymbol{k}\boldsymbol{R}} && \text{(C.11c)}\\
&\overset{!}{=} \sum_{\boldsymbol{R}\alpha\beta} U^*_{\boldsymbol{k}\alpha n} t_{\boldsymbol{R}\alpha\beta} U_{\boldsymbol{k}\beta n} \mathrm{e}^{\mathrm{i}\boldsymbol{k}\boldsymbol{R}}. && \text{(C.11d)}
\end{aligned}$$

Hence, if we want to avoid the number of unit cells N and a minus sign in the definition of the $\boldsymbol{k}$-dependent Hamiltonian in terms of hopping parameters, we have to choose a prefactor $p = 1/\sqrt{N}$ and a sign $s = 1$. Thus, the relevant electronic transformation coefficient reads

$$\langle \boldsymbol{R}\alpha|\boldsymbol{k}n\rangle = \frac{1}{\sqrt{N}} U_{\boldsymbol{k}\alpha n} \mathrm{e}^{-\mathrm{i}\boldsymbol{k}\boldsymbol{R}}, \tag{C.12}$$

where U is the matrix of right eigenvectors of the Hamiltonian. (In the literature on Wannier functions [89–92, 94, 138, 139], the band-mixing matrix U usually corresponds to the *left* eigenvectors of the Hamiltonian.) Thus, the transform from Wannier to Bloch states reads

$$|\boldsymbol{k}n\rangle = \sum_{\boldsymbol{R}\alpha} |\boldsymbol{R}\alpha\rangle\langle \boldsymbol{R}\alpha|\boldsymbol{k}n\rangle = \frac{1}{\sqrt{N}} \sum_{\boldsymbol{R}\alpha} |\boldsymbol{R}\alpha\rangle U_{\boldsymbol{k}\alpha n} \mathrm{e}^{-\mathrm{i}\boldsymbol{k}\boldsymbol{R}}. \tag{C.13}$$

It might be easily overlooked that the annihilation operator $\hat{c}_{\boldsymbol{k}n}$ transforms like $\langle \boldsymbol{k}n|$,

$$\hat{c}_{\boldsymbol{k}n} = \frac{1}{\sqrt{N}} \sum_{\boldsymbol{R}\alpha} U^*_{\boldsymbol{k}\alpha n} \hat{c}_{\boldsymbol{R}\alpha} \mathrm{e}^{\mathrm{i}\boldsymbol{k}\boldsymbol{R}}. \tag{C.14}$$

This follows from the definition of $\hat{c}^\dagger\hat{c}$ in terms of the single-particle states, where i enumerates the particles (Eq. 5.24 of Ref. 67),

$$\hat{c}^\dagger_{\boldsymbol{k}m}\hat{c}_{\boldsymbol{k}'n} = \sum_i |\boldsymbol{k}m\rangle_i\langle\boldsymbol{k}'n|_i = \sum_i \sum_{\boldsymbol{R}\boldsymbol{R}'\alpha\beta} |\boldsymbol{R}\alpha\rangle_i\langle\boldsymbol{R}\alpha|\boldsymbol{k}m\rangle_i\langle\boldsymbol{k}'n|\boldsymbol{R}'\beta\rangle_i\langle\boldsymbol{R}'\beta|_i \tag{C.15a}$$

$$= \sum_i \sum_{\boldsymbol{R}\boldsymbol{R}'\alpha\beta} |\boldsymbol{R}\alpha\rangle_i U_{\boldsymbol{k}\alpha m} \mathrm{e}^{-\mathrm{i}\boldsymbol{k}\boldsymbol{R}} U^*_{\boldsymbol{k}'\beta n} \mathrm{e}^{\mathrm{i}\boldsymbol{k}'\boldsymbol{R}'} \langle\boldsymbol{R}'\beta|_i \tag{C.15b}$$

$$= \sum_{\boldsymbol{R}\alpha} \hat{c}^\dagger_{\boldsymbol{R}\alpha} U_{\boldsymbol{k}\alpha m} \mathrm{e}^{-\mathrm{i}\boldsymbol{k}\boldsymbol{R}} \sum_{\boldsymbol{R}'\beta} U^*_{\boldsymbol{k}'\beta n} \hat{c}_{\boldsymbol{R}'\beta} \mathrm{e}^{\mathrm{i}\boldsymbol{k}'\boldsymbol{R}'}. \tag{C.15c}$$

Finally, within the chosen conventions, the Bloch theorem [420] reads

$$\begin{aligned}\langle\boldsymbol{r}-\boldsymbol{R}|\boldsymbol{k}n\rangle &= \sum_{\boldsymbol{R}'\alpha}\langle\boldsymbol{r}-\boldsymbol{R}|\boldsymbol{R}'\alpha\rangle\langle\boldsymbol{R}'\alpha|\boldsymbol{k}n\rangle = \sum_{\boldsymbol{R}'\alpha}\langle\boldsymbol{r}|\boldsymbol{R}'+\boldsymbol{R}\alpha\rangle\langle\boldsymbol{R}'\alpha|\boldsymbol{k}n\rangle \\ &= \sum_{\boldsymbol{R}'\alpha}\langle\boldsymbol{r}|\boldsymbol{R}'\alpha\rangle\langle\boldsymbol{R}'-\boldsymbol{R}\alpha|\boldsymbol{k}n\rangle = \sum_{\boldsymbol{R}'\alpha}\langle\boldsymbol{r}|\boldsymbol{R}'\alpha\rangle\langle\boldsymbol{R}'\alpha|\boldsymbol{k}n\rangle\mathrm{e}^{\mathrm{i}\boldsymbol{k}\boldsymbol{R}} = \langle\boldsymbol{r}|\boldsymbol{k}n\rangle\mathrm{e}^{\mathrm{i}\boldsymbol{k}\boldsymbol{R}}.\end{aligned} \tag{C.16}$$

For the transform of an electronic object from the orbital to the band basis, coefficients of the form $\langle\boldsymbol{R}\alpha|\boldsymbol{k}n\rangle$ and its complex conjugate $\langle\boldsymbol{k}n|\boldsymbol{R}\alpha\rangle$ must be used for ingoing and outgoing electrons, respectively. For the transform from the band to the orbital basis, vice versa.

Equivalent relations hold for the phonons, if we consider the dynamical matrix D instead of the Hamiltonian H, its right eigenvectors e instead of U, and the wave number $\boldsymbol{q}$ instead of $\boldsymbol{k}$. We use the same prefactor (p) and sign (s) conventions for electrons and phonons.

C.4 Perturbation theory

Since a large part of this thesis deals with the phonon self-energy, in this section we will briefly outline how to calculate its analytical expression from Feynman–Dyson perturbation theory [421, 422]. For this, we need some preliminary definitions, which will, however, not be explained in-depth. For this, we refer to the known literature, e.g., Mahan's textbook [423].

The quantities we consider are the bare (labeled with a superscript zero) and screened Green functions of the electrons (G) and phonons (D). Leaving spin and possible band indices understood for brevity,

$$G^0_{\boldsymbol{k}}(\tau) = -\langle\hat{T}\hat{c}_{\boldsymbol{k}}[\tau]\hat{c}^\dagger_{\boldsymbol{k}}[0]\rangle_0, \tag{C.17a}$$

$$D^0_{\boldsymbol{q}}(\tau) = -\langle\hat{T}\hat{\varphi}_{\boldsymbol{q}}[\tau]\hat{\varphi}^\dagger_{\boldsymbol{q}}[0]\rangle_0, \tag{C.17b}$$

$$G_{\boldsymbol{k}}(\tau) = -\langle\hat{T}\hat{c}_{\boldsymbol{k}}(\tau)\hat{c}^\dagger_{\boldsymbol{k}}(0)\rangle = -\langle\hat{T}\hat{c}_{\boldsymbol{k}}[\tau]\hat{S}(1/T)\hat{c}^\dagger_{\boldsymbol{k}}[0]\rangle^{\mathrm{c}}_0, \tag{C.17c}$$

$$D_{\boldsymbol{q}}(\tau) = -\langle\hat{T}\hat{\varphi}_{\boldsymbol{q}}(\tau)\hat{\varphi}^\dagger_{\boldsymbol{q}}(0)\rangle = -\langle\hat{T}\hat{\varphi}_{\boldsymbol{q}}[\tau]\hat{S}(1/T)\hat{\varphi}^\dagger_{\boldsymbol{q}}[0]\rangle^{\mathrm{c}}_0. \tag{C.17d}$$

Here, $\hat{\varphi}_{\boldsymbol{q}} = \hat{b}^\dagger_{-\boldsymbol{q}} + \hat{b}_{\boldsymbol{q}}$, and $\hat{T}$ is the time-ordering operator. $\langle\ldots\rangle_{(0)}$ are expectation values with respect to the (noninteracting) Hamiltonian $\hat{H}_{(0)}$, where $\hat{H} = \hat{H}_0 + \hat{V}$. The superscript "c" indicates that later on, when they are interpreted as Feynman diagrams, only *connected* diagrams are counted, all parts of which are (indirectly) linked to the in- and outgoing lines. Round and square brackets indicate time dependencies in the Heisenberg and Dirac picture,

$$\hat{X}(\tau) = \mathrm{e}^{\hat{H}\tau}\hat{X}\mathrm{e}^{-\hat{H}\tau} \quad \text{and} \quad \hat{X}[\tau] = \mathrm{e}^{\hat{H}_0\tau}\hat{X}\mathrm{e}^{-\hat{H}_0\tau} \tag{C.18}$$

with the imaginary time $\tau = \mathrm{i}t$. Finally, the time-evolution operator reads [424]

$$\hat{S}(\tau) = \sum_{n=0}^{\infty} \frac{(-1)^n}{n!} \int_0^\tau \mathrm{d}\tau_1\,\mathrm{d}\tau_2\ldots\mathrm{d}\tau_n\,\hat{T}\hat{V}[\tau_1]\hat{V}[\tau_2]\ldots\hat{V}[\tau_n] \tag{C.19}$$

with the interaction Hamiltonian $\hat{V}$. Here, we consider a simplified EPC (cf. Eq. 2.127),

$$\hat{V} = \frac{1}{\sqrt{N}} \sum_{\boldsymbol{q}\boldsymbol{k}} g_{\boldsymbol{q}\boldsymbol{k}} \hat{\varphi}_{\boldsymbol{q}} \hat{c}^\dagger_{\boldsymbol{k}+\boldsymbol{q}} \hat{c}_{\boldsymbol{k}}, \tag{C.20}$$

where the prefactor $1/\sqrt{N}$ ensures that the phonon self-energy, which we will find in the end, is an intensive quantity.

Inserting the time-evolution operator of Eq. C.19 into Eq. C.17d, we can express the screened Green function of the phonons as

$$D_{\boldsymbol{q}}(\tau) = -\sum_{n=0}^{\infty} \frac{(-1)^n}{n!} \int_0^{1/T} \mathrm{d}\tau_1 \, \mathrm{d}\tau_2 \ldots \mathrm{d}\tau_n \, \langle \hat{T} \hat{\varphi}_{\boldsymbol{q}}[\tau] \hat{V}[\tau_1] \hat{V}[\tau_2] \ldots \hat{V}[\tau_n] \hat{\varphi}^\dagger_{\boldsymbol{q}}[0] \rangle^{\mathrm{c}}_0. \tag{C.21}$$

To second order, we find

$$D^{\mathrm{2nd}}_{\boldsymbol{q}}(\tau) = -\frac{1}{2} \int_0^{1/T} \mathrm{d}\tau' \, \mathrm{d}\tau'' \, \langle \hat{T} \hat{\varphi}_{\boldsymbol{q}}[\tau] \hat{V}[\tau'] \hat{V}[\tau''] \hat{\varphi}^\dagger_{\boldsymbol{q}}[0] \rangle^{\mathrm{c}}_0 \tag{C.22a}$$

$$= -\frac{1}{2N} \sum_{\boldsymbol{k}\boldsymbol{k}'\boldsymbol{q}'\boldsymbol{q}''} g_{\boldsymbol{q}'\boldsymbol{k}} g_{\boldsymbol{q}''\boldsymbol{k}'} \int_0^{1/T} \mathrm{d}\tau' \, \mathrm{d}\tau'' \, \langle \ldots \rangle^{\mathrm{c}}_0, \tag{C.22b}$$

where the expectation value can be evaluated using Wick's theorem [422, 425–427],

$$\begin{aligned}
\langle \ldots \rangle^{\mathrm{c}}_0 &= \langle \hat{T} \hat{\varphi}_{\boldsymbol{q}}[\tau] \hat{\varphi}_{\boldsymbol{q}'}[\tau'] \hat{c}^\dagger_{\boldsymbol{k}+\boldsymbol{q}'}[\tau'] \hat{c}_{\boldsymbol{k}}[\tau'] \hat{\varphi}_{\boldsymbol{q}''}[\tau''] \hat{c}^\dagger_{\boldsymbol{k}'+\boldsymbol{q}''}[\tau''] \hat{c}_{\boldsymbol{k}'}[\tau''] \hat{\varphi}^\dagger_{\boldsymbol{q}}[0] \rangle^{\mathrm{c}}_0 \\
&= \langle \hat{T} \hat{\varphi}_{\boldsymbol{q}}[\tau] \hat{\varphi}_{\boldsymbol{q}'}[\tau'] \rangle_0 \; \langle \hat{T} \hat{c}_{\boldsymbol{k}}[\tau'] \hat{c}^\dagger_{\boldsymbol{k}+\boldsymbol{q}'}[\tau'] \rangle_0 \quad \langle \hat{T} \hat{c}_{\boldsymbol{k}'}[\tau''] \hat{c}^\dagger_{\boldsymbol{k}'+\boldsymbol{q}''}[\tau''] \rangle_0 \, \langle \hat{T} \hat{\varphi}_{\boldsymbol{q}''}[\tau''] \hat{\varphi}^\dagger_{\boldsymbol{q}}[0] \rangle_0 \\
&+ \langle \hat{T} \hat{\varphi}_{\boldsymbol{q}}[\tau] \hat{\varphi}_{\boldsymbol{q}''}[\tau''] \rangle_0 \, \langle \hat{T} \hat{c}_{\boldsymbol{k}}[\tau'] \hat{c}^\dagger_{\boldsymbol{k}+\boldsymbol{q}'}[\tau'] \rangle_0 \quad \langle \hat{T} \hat{c}_{\boldsymbol{k}'}[\tau''] \hat{c}^\dagger_{\boldsymbol{k}'+\boldsymbol{q}''}[\tau''] \rangle_0 \, \langle \hat{T} \hat{\varphi}_{\boldsymbol{q}'}[\tau'] \hat{\varphi}^\dagger_{\boldsymbol{q}}[0] \rangle_0 \\
&- \langle \hat{T} \hat{\varphi}_{\boldsymbol{q}}[\tau] \hat{\varphi}_{\boldsymbol{q}'}[\tau'] \rangle_0 \; \langle \hat{T} \hat{c}_{\boldsymbol{k}}[\tau'] \hat{c}^\dagger_{\boldsymbol{k}'+\boldsymbol{q}''}[\tau''] \rangle_0 \, \langle \hat{T} \hat{c}_{\boldsymbol{k}'}[\tau''] \hat{c}^\dagger_{\boldsymbol{k}+\boldsymbol{q}'}[\tau'] \rangle_0 \quad \langle \hat{T} \hat{\varphi}_{\boldsymbol{q}''}[\tau''] \hat{\varphi}^\dagger_{\boldsymbol{q}}[0] \rangle_0 \\
&- \langle \hat{T} \hat{\varphi}_{\boldsymbol{q}}[\tau] \hat{\varphi}_{\boldsymbol{q}''}[\tau''] \rangle_0 \, \langle \hat{T} \hat{c}_{\boldsymbol{k}}[\tau'] \hat{c}^\dagger_{\boldsymbol{k}'+\boldsymbol{q}''}[\tau''] \rangle_0 \, \langle \hat{T} \hat{c}_{\boldsymbol{k}'}[\tau''] \hat{c}^\dagger_{\boldsymbol{k}+\boldsymbol{q}'}[\tau'] \rangle_0 \quad \langle \hat{T} \hat{\varphi}_{\boldsymbol{q}'}[\tau'] \hat{\varphi}^\dagger_{\boldsymbol{q}}[0] \rangle_0.
\end{aligned} \tag{C.23}$$

The quantum numbers of the bracketed terms much be conserved. This yields delta relations,

$$\begin{aligned}
&\sum_{\boldsymbol{k}\boldsymbol{k}'\boldsymbol{q}'\boldsymbol{q}''} g_{\boldsymbol{q}'\boldsymbol{k}} g_{\boldsymbol{q}''\boldsymbol{k}'} \quad \langle \ldots \rangle^{\mathrm{c}}_0 \\
&= \sum_{\boldsymbol{k}\boldsymbol{k}'} \delta_{\boldsymbol{q}0} g_{\boldsymbol{q}\boldsymbol{k}} g_{\boldsymbol{q}\boldsymbol{k}'} \quad D^0_0(\tau - \tau') \quad G^0_{\boldsymbol{k}}(0) \quad G^0_{\boldsymbol{k}'}(0) \quad D^0_0(\tau'') && \text{(C.24a)} \\
&+ \sum_{\boldsymbol{k}\boldsymbol{k}'} \delta_{\boldsymbol{q}0} g_{\boldsymbol{q}\boldsymbol{k}} g_{\boldsymbol{q}\boldsymbol{k}'} \quad D^0_0(\tau - \tau'') \quad G^0_{\boldsymbol{k}}(0) \quad G^0_{\boldsymbol{k}'}(0) \quad D^0_0(\tau') && \text{(C.24b)} \\
&- \sum_{\boldsymbol{k}} \quad |g_{-\boldsymbol{q}\boldsymbol{k}}|^2 \quad D^0_{\boldsymbol{q}}(\tau - \tau') \quad G^0_{\boldsymbol{k}}(\tau' - \tau'') \quad G^0_{\boldsymbol{k}-\boldsymbol{q}}(\tau'' - \tau') \quad D^0_{\boldsymbol{q}}(\tau'') && \text{(C.24c)} \\
&- \sum_{\boldsymbol{k}} \quad |g_{\boldsymbol{q}\boldsymbol{k}}|^2 \quad D^0_{\boldsymbol{q}}(\tau - \tau'') \quad G^0_{\boldsymbol{k}}(\tau' - \tau'') \quad G^0_{\boldsymbol{k}+\boldsymbol{q}}(\tau'' - \tau') \quad D^0_{\boldsymbol{q}}(\tau'). && \text{(C.24d)}
\end{aligned}$$

The first two terms are a special case for $\boldsymbol{q} = 0$, where in- and outgoing phonon lines are disconnected and end in electron bubbles. We stick to the last two terms and find

$$D^{\mathrm{2nd}}_{\boldsymbol{q}}(\tau) = \frac{1}{N} \sum_{\boldsymbol{k}} |g_{\boldsymbol{q}\boldsymbol{k}}|^2 \int_0^{1/T} \mathrm{d}\tau' \, \mathrm{d}\tau'' \, D^0_{\boldsymbol{q}}(\tau - \tau'') G^0_{\boldsymbol{k}}(\tau' - \tau'') G^0_{\boldsymbol{k}+\boldsymbol{q}}(\tau'' - \tau') D^0_{\boldsymbol{q}}(\tau'). \tag{C.25}$$

A transform to fermionic and bosonic Matsubara frequencies $\omega_n = (2n+1)\pi T$ and $\nu_n = 2n\pi T$,

$$G(\tau) = T\sum_{n\in\mathbb{Z}} G(\mathrm{i}\omega_n)\mathrm{e}^{-\mathrm{i}\omega_n\tau} \quad \text{and} \quad G(\mathrm{i}\omega_n) = \int_0^{1/T} \mathrm{d}\tau\, G(\tau)\mathrm{e}^{\mathrm{i}\omega_n\tau}, \tag{C.26}$$

and defining the leading contribution Π to the phonon self-energy yields

$$D_{\boldsymbol{q}}^{\mathrm{2nd}}(\mathrm{i}\nu_n) = D_{\boldsymbol{q}}^0(\mathrm{i}\nu_n)\Pi_{\boldsymbol{q}}(\mathrm{i}\nu_n)D_{\boldsymbol{q}}^0(\mathrm{i}\nu_n), \tag{C.27a}$$

$$\Pi_{\boldsymbol{q}}(\mathrm{i}\nu_n) = \frac{T}{N}\sum_{\boldsymbol{k}m} |g_{\boldsymbol{q}\boldsymbol{k}}|^2 G_{\boldsymbol{k}}^0(\mathrm{i}\omega_m)G_{\boldsymbol{k}+\boldsymbol{q}}^0(\mathrm{i}\omega_m + \mathrm{i}\nu_n), \tag{C.27b}$$

where the bare Green functions simply read

$$G_{\boldsymbol{k}}^0(\mathrm{i}\omega_n) = \frac{1}{\mathrm{i}\omega_n - \varepsilon_{\boldsymbol{k}}} \quad \text{and} \quad D_{\boldsymbol{q}}^0(\mathrm{i}\nu_n) = -\frac{2\omega_{\boldsymbol{q}}}{\nu_n^2 + \omega_{\boldsymbol{q}}^2}. \tag{C.28}$$

The (irreducible) approximate self-energy Π generates an infinite number of (reducible) diagrams via the Dyson series,

$$\begin{aligned} D_{\boldsymbol{q}}(\mathrm{i}\nu_n) &= D_{\boldsymbol{q}}^0(\mathrm{i}\nu_n) + D_{\boldsymbol{q}}^0(\mathrm{i}\nu_n)\Pi_{\boldsymbol{q}}(\mathrm{i}\nu_n)D_{\boldsymbol{q}}(\mathrm{i}\nu_n) \\ &= \frac{1}{[D_{\boldsymbol{q}}^0(\mathrm{i}\nu_n)]^{-1} - \Pi_{\boldsymbol{q}}(\mathrm{i}\nu_n)} = -\frac{2\omega_{\boldsymbol{q}}}{\nu_n^2 + \omega_{\boldsymbol{q}}^2 + 2\omega_{\boldsymbol{q}}\Pi_{\boldsymbol{q}}(\mathrm{i}\nu_n)}. \end{aligned} \tag{C.29}$$

Performing the frequency summation (cf. Chap. 3.5 of Ref. 423), Eq. C.27b finally becomes

$$\Pi_{\boldsymbol{q}}(\mathrm{i}\nu_n) = \frac{T}{N}\sum_{\boldsymbol{k}m} |g_{\boldsymbol{q}\boldsymbol{k}}|^2 \frac{1}{\mathrm{i}\omega_m - \varepsilon_{\boldsymbol{k}}} \frac{1}{\mathrm{i}\omega_m + \mathrm{i}\nu_n - \varepsilon_{\boldsymbol{k}+\boldsymbol{q}}} \tag{C.30a}$$

$$= \frac{1}{N}\sum_{\boldsymbol{k}} |g_{\boldsymbol{q}\boldsymbol{k}}|^2 \frac{f(\varepsilon_{\boldsymbol{k}}) - f(\varepsilon_{\boldsymbol{k}+\boldsymbol{q}})}{\mathrm{i}\nu_n + \varepsilon_{\boldsymbol{k}} - \varepsilon_{\boldsymbol{k}+\boldsymbol{q}}}. \tag{C.30b}$$

C.5 Charge and spin susceptibility

Let $n = n_\uparrow + n_\downarrow$ be the electron density, where $n_\sigma = \frac{1}{N}\sum_{\boldsymbol{k}}\langle c_{\boldsymbol{k}\sigma}^\dagger c_{\boldsymbol{k}\sigma}\rangle = \frac{1}{2} + \frac{T}{N}\sum_{\boldsymbol{k}n} G_{\boldsymbol{k}\sigma}(\mathrm{i}\omega_n)$ is an ensemble average of the electron number. We can analogously define the magnetization $m = n_\uparrow - n_\downarrow$. To lift the spin degeneracy, we introduce a spin-dependent chemical potential $\mu_\sigma = \mu + \sigma h$, where $\sigma = \pm 1$ and h is an infinitesimal magnetic field. We can then define the uniform charge and spin susceptibilities as [428]

$$\chi_{\mathrm{c}} = \frac{\partial n}{\partial \mu} = \sum_\sigma \frac{\partial n_\sigma}{\partial \mu} = \sum_{\sigma\sigma'} \frac{\partial n_\sigma}{\partial \mu_{\sigma'}}\frac{\partial \mu_{\sigma'}}{\partial \mu} = \sum_{\sigma\sigma'} \frac{\partial n_\sigma}{\partial \mu_{\sigma'}}, \tag{C.31}$$

$$\chi_{\mathrm{s}} = \frac{\partial m}{\partial h} = \sum_\sigma \sigma\frac{\partial n_\sigma}{\partial h} = \sum_{\sigma\sigma'} \sigma\frac{\partial n_\sigma}{\partial \mu_{\sigma'}}\frac{\partial \mu_{\sigma'}}{\partial h} = \sum_{\sigma\sigma'} \sigma\sigma'\frac{\partial n_\sigma}{\partial \mu_{\sigma'}}. \tag{C.32}$$

χ_{c} is also known as the compressibility. In the noninteracting case, the Matsubara Green function reads $G_{\boldsymbol{k}\sigma}(\mathrm{i}\omega_n) = (\mathrm{i}\omega_n - \varepsilon_{\boldsymbol{k}\sigma} + \mu_\sigma)^{-1}$ and thus [429]

$$\chi_{\mathrm{c}} = \chi_{\mathrm{s}} = \sum_\sigma \frac{\partial}{\partial \mu_\sigma}\left[\frac{1}{2} + \frac{T}{N}\sum_{\boldsymbol{k}n} G_{\boldsymbol{k}\sigma}(\mathrm{i}\omega_n)\right] = -\frac{T}{N}\sum_{\boldsymbol{k}\sigma n} G_{\boldsymbol{k}\sigma}^2(\mathrm{i}\omega_n). \tag{C.33}$$

This is nothing but the pair bubble at $\boldsymbol{q} = 0$.

C.6 Hellmann–Feynman theorem

For an arbitrary real operator $\hat{H}$ (usually the Hamiltonian) with eigenstate $|\psi\rangle$ and corresponding eigenvalue E, which depends on a parameter λ, we have

$$\frac{\partial E}{\partial \lambda} = \frac{\partial \langle\psi|\hat{H}|\psi\rangle}{\partial \lambda} \tag{C.34a}$$

$$= \frac{\partial \langle\psi|}{\partial \lambda}\hat{H}|\psi\rangle + \langle\psi|\frac{\partial \hat{H}}{\partial \lambda}|\psi\rangle + \langle\psi|\hat{H}\frac{\partial|\psi\rangle}{\partial \lambda} \tag{C.34b}$$

$$= E\frac{\partial \langle\psi|}{\partial \lambda}|\psi\rangle + \langle\psi|\frac{\partial \hat{H}}{\partial \lambda}|\psi\rangle + E\langle\psi|\frac{\partial|\psi\rangle}{\partial \lambda} \tag{C.34c}$$

$$= E\frac{\partial \langle\psi|\psi\rangle}{\partial \lambda} + \langle\psi|\frac{\partial \hat{H}}{\partial \lambda}|\psi\rangle = \langle\psi|\frac{\partial \hat{H}}{\partial \lambda}|\psi\rangle. \tag{C.34d}$$

This is known as the *Hellmann–Feynman theorem* [430, 431] and follows equivalently from first-order perturbation theory. It is the basis for the calculation of forces in *ab initio* methods such as DFT and thus allows us to, e.g, perform simulations of molecular dynamics at a reasonable cost.

Please note that the absence of forces is not an indicator that a system is fully relaxed. This is because there are no effective forces for stress resulting from uniform strain. Thus, for calculations like variable-cell relaxations, we additionally have to consider the *pressure* of the system [432]. Once both forces and pressure are minimized, the total energy is minimized.

C.7 Occupation smearing

Even though DFT is a ground-state, i.e., zero-temperature theory, in practical calculations we often have to assume something very similar to an electronic temperature: a smearing of the occupation of the low-energy states [306, 433, 434]. For systems without a band gap, the assumption of fully occupied (empty) states below (above) the Fermi level leads to convergence problems. This is because during the SCF loop, the low-energy states would frequently jump across the Fermi level between iterations, leading to a discontinuous evolution of the total energy. Consequently, the more states ($\boldsymbol{k}$ points) are considered in the calculation, the lower is the required smearing temperature. It is important that results obtained from first principles are carefully validated with respect to the influence of smearing. In extreme cases, a careless use of smearing can lead to wrong predictions, as demonstrated in Ref. 435 (cf. Fig. 6), where a previously reported polyhydride superconductor is traced back to excessive smearing.

The most natural choice for the smearing function f is the Fermi function. However, also because the smearing temperature can anyway *not* be identified with the real temperature of the system,[1] we are not restricted to this choice. To the contrary, it is common to use alternative steplike functions that often yield better convergence for fewer $\boldsymbol{k}$ points.

In this section, we will present the most popular smearing functions used in *ab initio* calculations (and one more). We will always specify both the steplike function (corresponding to the Fermi function) and its negative derivative (approximating Dirac's [436] delta function). For brevity, we consider the dimensionless function argument $x = \varepsilon/T$. The functions are visually compared in Fig. C.2.

[1] In fact, commonly used smearings for reasonably coarse $\boldsymbol{k}$-point meshes correspond to temperatures many times higher than room temperature.

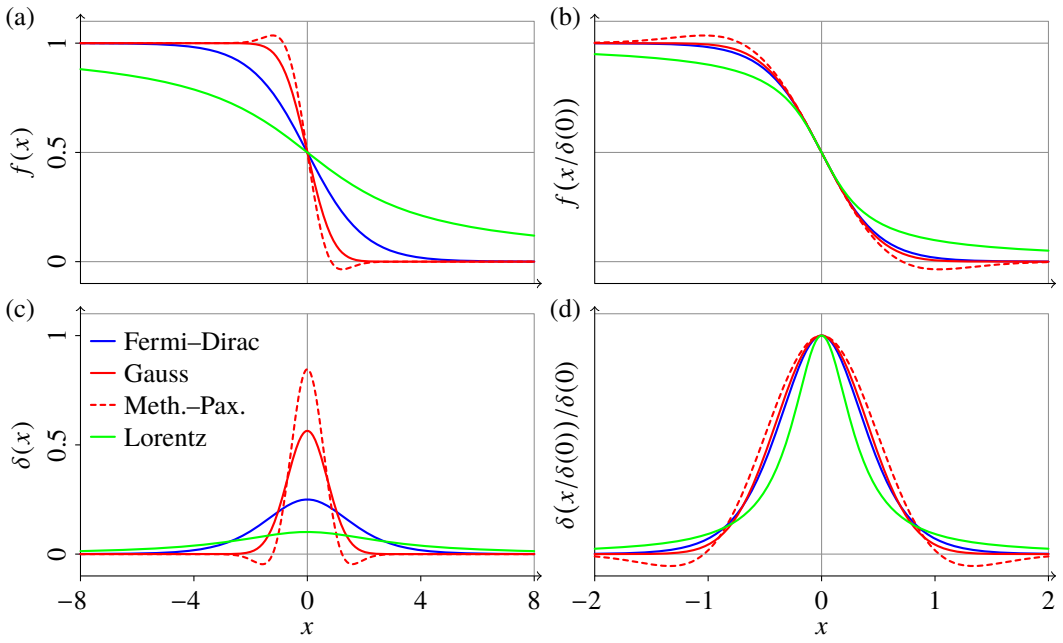

Figure C.2: Different (a, b) step and (c, d) delta functions for occupation smearing. On the left (a, c), the functions are shown exactly as defined in the text. On the right (b, d), they are rescaled such that their values and slopes at $x = 0$ coincide, revealing differences in the HWHM of the delta functions.

C.7.1 Fermi–Dirac smearing

The Fermi–Dirac function and its negative derivative read

$$f_{\mathrm{FD}}(x) = \frac{1}{\mathrm{e}^x + 1}, \tag{C.35a}$$

$$\delta_{\mathrm{FD}}(x) = \frac{1}{2\cosh(x) + 2}. \tag{C.35b}$$

Using this functions to smear out electronic occupations is easily motivated by the fact that $f_{\mathrm{FD}}(\varepsilon_{\boldsymbol{k}n}) = \langle \hat{c}^\dagger_{\boldsymbol{k}n} \hat{c}_{\boldsymbol{k}n} \rangle_0$ is nothing but the thermal occupation of free fermions [437, 438].

C.7.2 Gaussian smearing

A more common approximation to the delta function is a Gaussian. It is quite similar to the Fermi–Dirac function but decays slightly faster. Integration yields the error function,

$$f_{\mathrm{G}}(x) = \frac{1 - \mathrm{erf}(x)}{2}, \tag{C.36a}$$

$$\delta_{\mathrm{G}}(x) = \frac{1}{\sqrt{\pi}} \mathrm{e}^{-x^2}. \tag{C.36b}$$

C.7.3 Methfessel–Paxton smearing

Using Fermi–Dirac or Gaussian occupations, the chemical potential will depend on the smearing temperature unless the DOS is constant close to the Fermi level. Albeit physically reasonable for real temperatures, we would like to avoid this effect in the case of occupation smearing as a mere trick to enhance convergence and instead stick as close to the chemical potential from $T = 0$ as possible.

As shown by Methfessel and Paxton [306], the effect can be mitigated by adding certain correction terms to the Gaussian,

$$f_{\mathrm{MP}}^{N}(x) = f_{\mathrm{G}}(x) + \sum_{n=1}^{N} A_n H_{2n-1}(x)\mathrm{e}^{-x^2}, \tag{C.37a}$$

$$\delta_{\mathrm{MP}}^{N}(x) = \sum_{n=0}^{N} A_n H_{2n}(x)\mathrm{e}^{-x^2}. \tag{C.37b}$$

Here, the expansion coefficients A_n are given by

$$A_n = \frac{(-1)^n}{4^n\sqrt{\pi}n!} \tag{C.38}$$

and the Hermite polynomials H_n can be defined recursively,

$$H_0(x) = 1, \tag{C.39a}$$

$$H_1(x) = 2x, \tag{C.39b}$$

$$H_{n+1}(x) = 2xH_n(x) - 2nH_{n-1}(x). \tag{C.39c}$$

As seen in Fig. C.2, where we only plot functions up to first order ($N = 1$), a disadvantage of this approach is that the values of the step function are no longer strictly limited to the interval $(0, 1)$. Both f_{MP} and δ_{MP} can become negative for intermediate values of x.

C.7.4 Lorentzian smearing

[*The derivation of Lorentzian smearing in the context of hybridization is originally by Erik van Loon. Is has been used in the publication [111] presented in Chap. 8.*]

The use of Lorentzian functions,

$$f_{\mathrm{L}}(x) = \frac{1}{2} - \frac{1}{\pi}\arctan\left[\frac{x}{\pi}\right], \tag{C.40a}$$

$$\delta_{\mathrm{L}}(x) = \frac{1}{x^2 + \pi^2}, \tag{C.40b}$$

is appropriate to model a smearing that is not due to thermal fluctuations but due to hybridization (e.g., with a substrate) at zero temperature.

This can be derived as follows: We introduce a constant (i.e., energy- and $\boldsymbol{k}$-independent) hybridization $\Delta = -\mathrm{i}\pi h$ on the level of the electronic Green function,

$$G_{\boldsymbol{k}}(\mathrm{i}\omega_m) = \frac{1}{\mathrm{i}\omega_m - \varepsilon_{\boldsymbol{k}} - \Delta}. \tag{C.41}$$

Now we consider the static bare electronic susceptibility (cf. Eq. C.27b),

$$\chi_0(\mathrm{i}\nu_n) = \frac{T}{N}\sum_{\boldsymbol{k}m} G_{\boldsymbol{k}}(\mathrm{i}\omega_m)G_{\boldsymbol{k}+\boldsymbol{q}}(\mathrm{i}\omega_m) = \frac{1}{N}\sum_{\boldsymbol{k}} \frac{\widetilde{f}(\varepsilon_{\boldsymbol{k}+\boldsymbol{q}}) - \widetilde{f}(\varepsilon_{\boldsymbol{k}})}{\varepsilon_{\boldsymbol{k}+\boldsymbol{q}} - \varepsilon_{\boldsymbol{k}}}. \tag{C.42}$$

We obtain the well-known expression, where f is replaced by the "modified Fermi function"

$$\widetilde{f}(\varepsilon_{\boldsymbol{k}}) = T\sum_{m} G_{\boldsymbol{k}}(\mathrm{i}\omega_m) \overset{T\to 0}{=} \frac{1}{2} - \frac{1}{\pi}\arctan\left[\frac{\varepsilon_{\boldsymbol{k}}}{\pi h}\right] \equiv f_{\mathrm{L}}\left[\frac{\varepsilon_{\boldsymbol{k}}}{h}\right]. \tag{C.43}$$

Thus, in the limit of zero temperature, hybridization can be modeled by replacing the Fermi function by an integrated Lorentzian (at least in contexts where the bare electronic susceptibility is a useful concept).

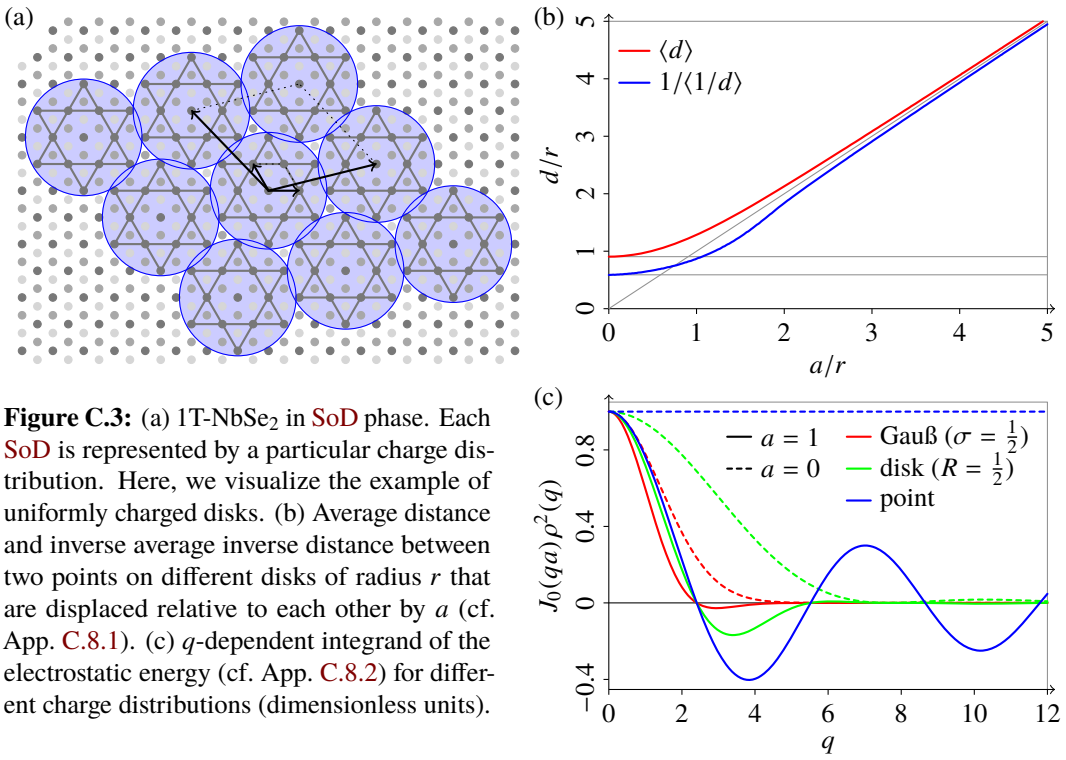

Figure C.3: (a) 1T-$NbSe_2$ in SoD phase. Each SoD is represented by a particular charge distribution. Here, we visualize the example of uniformly charged disks. (b) Average distance and inverse average inverse distance between two points on different disks of radius r that are displaced relative to each other by a (cf. App. C.8.1). (c) q-dependent integrand of the electrostatic energy (cf. App. C.8.2) for different charge distributions (dimensionless units).

C.8 Estimates of the Coulomb interaction

Here, we will present two ways to estimate the Coulomb interaction from classical electrostatics as alternatives to the approach shown in Sec. 6.2.3. We consider the electrostatic energy of a charge distribution of the form $P(\boldsymbol{r}) = \rho(\boldsymbol{r}) + \rho(\boldsymbol{r} - \boldsymbol{a})$, where $\rho(\boldsymbol{r})$ could be the charge distribution of a SoD (cf. Fig. C.3a) and $\boldsymbol{a}$ could be zero or the vector connecting two neighboring SoD, depending on whether we want to calculate the local or nonlocal Coulomb interaction U or V, respectively.

The electrostatic energy reads

$$U(\boldsymbol{a}) = \frac{1}{2}\int \mathrm{d}^3r\,\mathrm{d}^3r'\,\frac{P(\boldsymbol{r})P(\boldsymbol{r}')}{|\boldsymbol{r}-\boldsymbol{r}'|} \tag{C.44a}$$

$$= \int \mathrm{d}^3r\,\mathrm{d}^3r'\,\frac{\rho(\boldsymbol{r})\rho(\boldsymbol{r}')}{|\boldsymbol{r}-\boldsymbol{r}'|} + \int \mathrm{d}^3r\,\mathrm{d}^3r'\,\frac{\rho(\boldsymbol{r})\rho(\boldsymbol{r}'-\boldsymbol{a})}{|\boldsymbol{r}-\boldsymbol{r}'|}, \tag{C.44b}$$

where the first term on the right-hand side is the electrostatic self-energy.

For the special case of two equal point charges, $\rho(\boldsymbol{r}) = Q\delta(\boldsymbol{r})$, we find a divergent electrostatic self-energy and the well-known $1/r$ law,

$$U(\boldsymbol{a}) = \underbrace{\int \mathrm{d}^3r\,\mathrm{d}^3r'\,\frac{Q^2\delta(\boldsymbol{r})\delta(\boldsymbol{r}')}{|\boldsymbol{r}-\boldsymbol{r}'|}}_{\infty} + \underbrace{\int \mathrm{d}^3r\,\mathrm{d}^3r'\,\frac{Q^2\delta(\boldsymbol{r})\delta(\boldsymbol{r}'-\boldsymbol{a})}{|\boldsymbol{r}-\boldsymbol{r}'|}}_{Q^2/|\boldsymbol{a}|}. \tag{C.45}$$

C.8.1 Homogeneous disks

We now calculate the electrostatic energy of a pair of disks with radius R and charge Q in a plane, which are displaced relative to each other by $\boldsymbol{a}$. Assuming a homogeneous charge distribution, $\rho(\boldsymbol{r}) = \frac{Q}{\pi R^2}\Theta(x^2+y^2-R^2)\delta(z)$. Excluding the self-energies of the disks,

$$U(\boldsymbol{a}) = \int \mathrm{d}^3r\,\mathrm{d}^3r'\,\frac{\rho(\boldsymbol{r})\rho(\boldsymbol{r}'-\boldsymbol{a})}{|\boldsymbol{r}-\boldsymbol{r}'|} = \left(\frac{Q}{\pi R^2}\right)^2 \int_{①} \mathrm{d}^2r \int_{②} \mathrm{d}^2r'\,\frac{1}{|\boldsymbol{r}-\boldsymbol{r}'|} \equiv \frac{Q^2}{d_{\mathrm{eff}}}, \tag{C.46}$$

where ⓘ labels the points on the ith disk. Thus, we get the $1/r$ law with an effective distance

$$d_{\mathrm{eff}}^{(1)} = 1\Big/\left\langle \frac{1}{|\boldsymbol{r}-\boldsymbol{r}'|}\right\rangle_{\boldsymbol{r}\in①,\,\boldsymbol{r}'\in②}. \tag{C.47}$$

Alternatively, we can consider the interaction of point charges at random positions on the disks and average over all possible configurations. In this case, we simply have

$$d_{\mathrm{eff}}^{(2)} = \langle|\boldsymbol{r}-\boldsymbol{r}'|\rangle_{\boldsymbol{r}\in①,\,\boldsymbol{r}'\in②}. \tag{C.48}$$

For $\boldsymbol{a} = 0$, the "inverse average inverse distance" and the average distance between two points on the different disks read (cf. p. 36 of Ref. 439)

$$d_{\mathrm{eff}}^{(1)} = \frac{3\pi R}{16}, \tag{C.49a}$$

$$d_{\mathrm{eff}}^{(2)} = \frac{128R}{45\pi}. \tag{C.49b}$$

For arbitrary $\boldsymbol{a} \neq 0$, we do not have an analytical expression for the effective distances. But in any case, we can calculate them via Monte Carlo integration. More precisely, we take the average for large sets of random pairs of points on the disks. The resulting effective distances are shown in Fig. C.3b.

Above, we calculated the *bare* electrostatic energy. For realistic estimates, we have to divide the result by the effective dielectric constant ϵ. E.g., in the experiments by Nakata *et al.* [220], the sample is grown on bilayer graphene on top of silicon carbide (6H-SiC). The static dielectric constants of these substrates are 3 to 16 [440] and 10 [441], respectively.

C.8.2 Radially inhomogeneous disks

Finally, we derive a formula for the electrostatic energy $U(a)$ of two identical planar and radially symmetric charge distributions $\rho(r)$ displaced relative to each other by a distance a. This formula can be evaluated for arbitrary q-dependent dielectric functions $\epsilon(q)$.

Here, we use the nonsymmetric convention for the 2D Fourier transform,

$$f(\boldsymbol{q}) = \int \mathrm{d}^2r\, f(\boldsymbol{r})\mathrm{e}^{\mathrm{i}\boldsymbol{q}\boldsymbol{r}}, \tag{C.50a}$$

$$f(\boldsymbol{r}) = \frac{1}{(2\pi)^2}\int \mathrm{d}^2q\, f(\boldsymbol{q})\mathrm{e}^{-\mathrm{i}\boldsymbol{q}\boldsymbol{r}}. \tag{C.50b}$$

The Fourier transform of the bare Coulomb potential $v(r) = 1/r$ reads

$$\begin{aligned} v(q) &= \int \mathrm{d}^2r\,\frac{\mathrm{e}^{\mathrm{i}\boldsymbol{q}\boldsymbol{r}}}{r} = \int_0^\infty \mathrm{d}r \int_0^{2\pi} \mathrm{d}\varphi\,\mathrm{e}^{\mathrm{i}qr[\cos(\varphi_q)\cos(\varphi)+\sin(\varphi_q)\sin(\varphi)]} \\ &= \int_0^\infty \mathrm{d}r \int_0^{2\pi} \mathrm{d}\varphi\,\mathrm{e}^{\mathrm{i}qr\cos(\varphi-\varphi_q)} = 2\pi\int_0^\infty \mathrm{d}r\, J_0(qr) = \frac{2\pi}{q} \equiv \epsilon(q)W(q). \end{aligned} \tag{C.51}$$

Here, we have used the zeroth Bessel function of the first kind,

$$J_n(x) = \frac{1}{2\pi}\int_0^{2\pi} \mathrm{d}\varphi\, \mathrm{e}^{\mathrm{i}(x\sin(\varphi)-n\varphi)}. \tag{C.52}$$

We can write the screened electrostatic energy as

$$\begin{aligned}
U(a) &= \int \mathrm{d}^2r\,\mathrm{d}^2r'\,\rho(\boldsymbol{r})\rho(\boldsymbol{r}'-\boldsymbol{a})W(\boldsymbol{r}-\boldsymbol{r}') && \text{(C.53a)}\\
&= \frac{1}{(2\pi)^6}\int \mathrm{d}^2r\,\mathrm{d}^2r'\,\mathrm{d}^2k\,\mathrm{d}^2k'\,\mathrm{d}^2q\,\rho(\boldsymbol{k})\rho(\boldsymbol{k}')W(\boldsymbol{q})\mathrm{e}^{-\mathrm{i}\boldsymbol{k}\boldsymbol{r}}\mathrm{e}^{-\mathrm{i}\boldsymbol{k}'(\boldsymbol{r}'-\boldsymbol{a})}\mathrm{e}^{-\mathrm{i}\boldsymbol{q}(\boldsymbol{r}-\boldsymbol{r}')} && \text{(C.53b)}\\
&= \frac{1}{(2\pi)^6}\int \mathrm{d}^2r\,\mathrm{d}^2r'\,\mathrm{d}^2k\,\mathrm{d}^2k'\,\mathrm{d}^2q\,\rho(\boldsymbol{k})\rho(\boldsymbol{k}')W(\boldsymbol{q})\mathrm{e}^{-\mathrm{i}(\boldsymbol{k}+\boldsymbol{q})\boldsymbol{r}}\mathrm{e}^{-\mathrm{i}(\boldsymbol{k}'-\boldsymbol{q})\boldsymbol{r}'}\mathrm{e}^{\mathrm{i}\boldsymbol{k}'\boldsymbol{a}} && \text{(C.53c)}\\
&= \frac{1}{(2\pi)^2}\int \mathrm{d}^2k\,\mathrm{d}^2k'\,\mathrm{d}^2q\,\rho(\boldsymbol{k})\rho(\boldsymbol{k}')W(\boldsymbol{q})\delta(\boldsymbol{k}+\boldsymbol{q})\delta(\boldsymbol{k}'-\boldsymbol{q})\mathrm{e}^{\mathrm{i}\boldsymbol{k}'\boldsymbol{a}} && \text{(C.53d)}\\
&= \frac{1}{(2\pi)^2}\int \mathrm{d}^2q\,\rho(-\boldsymbol{q})\rho(\boldsymbol{q})W(\boldsymbol{q})\mathrm{e}^{\mathrm{i}\boldsymbol{q}\boldsymbol{a}} && \text{(C.53e)}\\
&= \frac{1}{(2\pi)^2}\int_0^\infty \mathrm{d}q\int_0^{2\pi}\mathrm{d}\varphi\, q\rho^2(q)W(q)\mathrm{e}^{\mathrm{i}qa\cos(\varphi)} && \text{(C.53f)}\\
&= \frac{1}{2\pi}\int_0^\infty \mathrm{d}q\, qJ_0(qa)\rho^2(q)W(q) && \text{(C.53g)}
\end{aligned}$$

Inserting the expression for the screened Coulomb interaction from Eq. C.51, we find

$$U(a) = \int_0^\infty \mathrm{d}q\, J_0(qa)\rho^2(q)\epsilon^{-1}(q). \tag{C.54}$$

To conclude, we will evaluate the above formula for exemplary charge distributions. The corresponding integrands are plotted in Fig. C.3c. For simplicity, we set the charge $Q = 1$.

The Fourier transform of a point charge distribution $\rho(r) = \delta(r)$ is simply

$$\rho(q) = \int \mathrm{d}^2r\,\delta(r)\mathrm{e}^{\mathrm{i}\boldsymbol{q}\boldsymbol{r}} = 1. \tag{C.55a}$$

This generates the $1/r$ law for the electrostatic energy of two unscreened point charges,

$$U(a) = \int_0^\infty \mathrm{d}q\, J_0(qa) = \frac{1}{a}. \tag{C.55b}$$

Next, for a Gaussian charge distribution $\rho_\sigma(r) = \frac{1}{2\pi\sigma^2}\mathrm{e}^{-\frac{1}{2}(\frac{r}{\sigma})^2}$, we have

$$\rho_\sigma(q) = \mathrm{e}^{-\frac{(q\sigma)^2}{2}}. \tag{C.56a}$$

Hence, the electrostatic energy of two unscreened Gaussians reads

$$U(a) = \int_0^\infty \mathrm{d}q\, J_0(qa)\mathrm{e}^{-(q\sigma)^2} = \frac{\sqrt{\pi}}{2\sigma}J_0\left[\frac{\mathrm{i}}{8}\left(\frac{a}{\sigma}\right)^2\right]\mathrm{e}^{-\frac{1}{8}(\frac{a}{\sigma})^2}. \tag{C.56b}$$

Finally, for a homogeneously charged disk $\rho_R(\boldsymbol{r}) = \frac{1}{\pi R^2}\Theta(R-r)$,

$$\rho_R(q) = \frac{1}{\pi R^2}\int_0^R \mathrm{d}r\int_0^{2\pi}\mathrm{d}\varphi\, r\mathrm{e}^{\mathrm{i}qr\cos(\varphi)} = \frac{2}{R^2}\int_0^R \mathrm{d}r\, rJ_0(qr) = \frac{2J_1(qR)}{qR}. \tag{C.57}$$

Here, we do not find a simple analytical expression for the electrostatic energy.

Appendix D

Miscellaneous projects

Do not quench the Spirit.
Do not treat prophecies with contempt
but test them all; hold on to what is good

—1 Thessalonians 5:19–21

In this appendix, we will present miscellaneous projects, which have not lead to a publication yet. Some of them were important for the understanding of a particular problem; others might be further developed in the future. Each project is about a specific material, namely, in order of presentation, graphone (App. D.1), monolayer beryllium (App. D.2), nitrogen and benzene molecules (App. D.3), the hypothetical 2D material CP_3 (App. D.4), the perovskite superconductor Sr_2RuO_4 (App. D.5), and finally bilayer 2H-$MoSe_2$ (App. D.6).

D.1 Graphone

In search for a dynamically stable 2D metal with a simple dispersion and hexagonal symmetry, ideal for debugging and testing, we calculated the electrons, phonons, and EPC of hydrogenated graphene, also referred to as "graphone." For a general overview on this material, we refer to Refs. 442–444.

The crystal structure is shown in Fig. D.1a. On every second carbon atom, i.e., on one of the sublattices of graphene, a hydrogen adatom is adsorbed. The vertical position of the hydrogenated sublattice is slightly lifted with respect to the pristine sublattice.

The electronic low-energy dispersion is shown in Fig. D.1b. In a non-spin-polarized calculation, we find a single isolated metallic band of predominantly hydrogen character at the Fermi level![1] Allowing for spin polarization, however, this band is rather uniformly split, opening a gap at the Fermi level. One spin direction is completely occupied, the other completely unoccupied. In the following, we will only consider the non-spin-polarized case.

The corresponding phonon dispersion from DFPT is displayed in Fig. D.1c. As opposed to what we hoped for, the system is *not* dynamically stable, but features imaginary phonon modes of ZA character in most parts of the BZ. Increasing the Gaussian electronic smearing (cf. App. C.7) from 10 mRy to 40 mRy (not shown) makes these instabilities disappear. This suggests that the softening is due to low-energy metallic screening. Indeed, removing the screening from within the isolated metallic band via cDFPT stabilizes the lattice.

[1] In fact, the DFT calculation was motivated by a simple TB calculation for this system, which suggested the presence of a single flat band at the Fermi level (cf. Fig. 3.3 of Ref. 445).

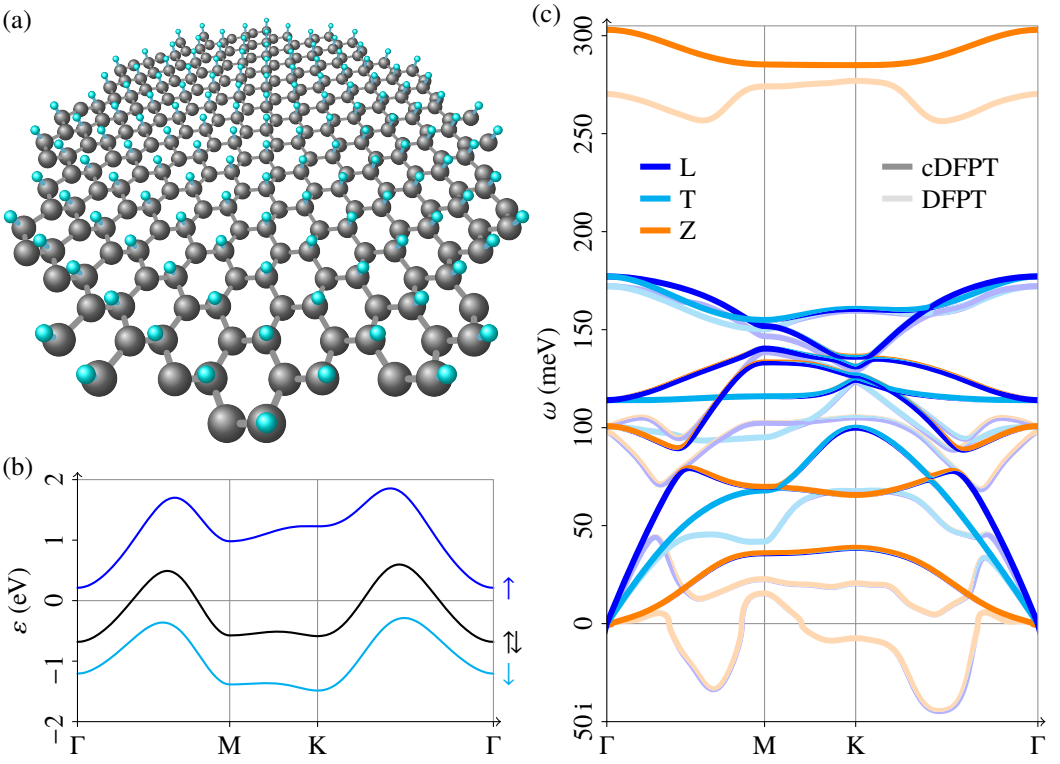

Figure D.1: Hydrogenated graphene or "graphone." (a) Crystal structure. (b) Non-spin-polarized and spin-polarized electronic band structure from DFT. (c) Phonon dispersion from DFPT and cDFPT. Computational parameters: PBE functional; ultrasoft PPs from the PSLIBRARY 1.0.0 [305]; energy cutoffs of 70 Ry and 700 Ry for wave functions and charge density; 36×36 $\boldsymbol{k}$ points; 12×12 $\boldsymbol{q}$ points; Gaussian smearing of 10 mRy; unit-cell height $c = 15$ Å; relaxed lattice constant $a = 2.53$ Å.

The phonon softening is most pronounced halfway between Γ and K. To investigate its origin, in Fig. D.2, we inspect the Fermi surface and the EPC between the metallic band and the soft phonon mode. The Fermi surface features a circular electron pocket around Γ, surrounded by a broad annular hole pocket (Fig. D.2a). For $\boldsymbol{q} = 1/2\,\mathrm{K}$, the Fermi surface is approximately nested in several regions, some of which additionally show significant EPC (Fig. D.2b). The global maximum of the EPC is halfway between the original and the shifted Γ point, but there are also maxima halfway between K and the shifted K′ point.

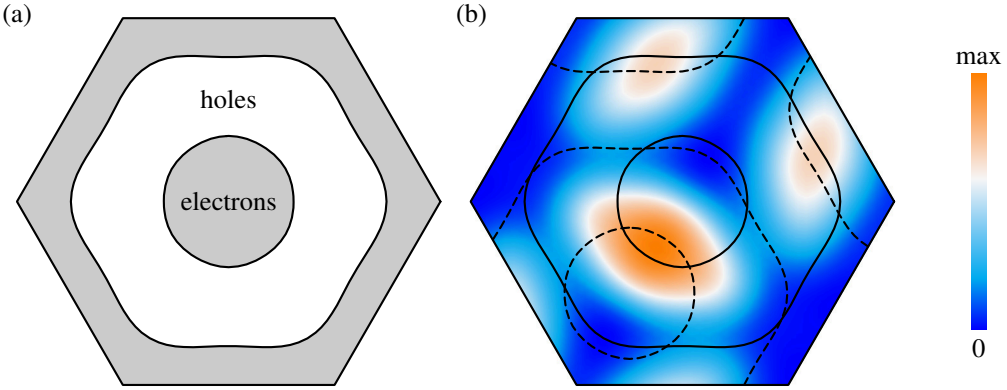

Figure D.2: (d) Fermi surface of non-spin-polarized graphone. (e) Original and shifted Fermi surface together with EPC between metallic band and lowest phonon mode for $\boldsymbol{q} = 1/2\,\mathrm{K}$.

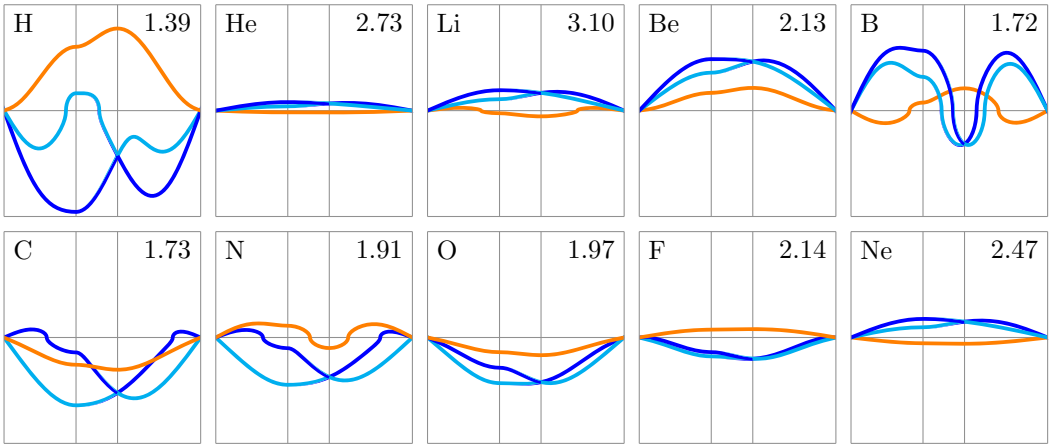

Figure D.3: Stability of monoatomic triangular lattices. The relaxed lattice constants (Å) are indicated in the top–right corners of the panels. Computational parameters: PBE functional; ultrasoft PPs from the PSLIBRARY 1.0.0 [305]; minimum energy cutoffs as recommended in PP files; 12×12 $\boldsymbol{k}$ points; 3×3 $\boldsymbol{q}$ points; Gaussian smearing of 20 mRy; unit-cell height $c = 10$ Å.

D.2 Monolayer beryllium

The study of graphone revealed some interesting physics, but it did not solve the problem of finding a simple hexagonal 2D metal. Hence, we have to approach this problem more systematically. Since the most simple crystal structure is monoatomic, we consider only monoatomic triangular lattices. In search for potential stable candidates, we perform structural relaxations followed by DFPT calculations for several elements, starting with hydrogen and proceeding along the periodic table. The results are shown in Fig. D.3. The only element from hydrogen to neon for which we find a phonon dispersion without imaginary frequencies is beryllium. The fact that a triangular lattice of beryllium atoms is stable in DFPT (which does not necessarily imply stability in real environments) might be related to the fact that this element crystallizes in a hexagonal close-packed structure in the bulk [446].

D.2.1 *Ab initio*

We first perform more precise *ab initio* calculations. The resulting electrons and phonons shown in Fig. D.4 are in line with Ref. 446 and Ref. 447, respectively.

The electrons in Fig. D.4a feature a graphene-like dispersion formed by $2s$ and in-plane $2p_x$ and $2p_y$ states. In the following, we will refer to the lowest of these bands as the σ band. Compared to graphene, the Dirac cone is however shifted upward, away from the Fermi level. This is because some electrons at the Fermi level also go into a $2p_z$ band that is completely decoupled from the rest. This band is labeled as the π band.

The phonons in Fig. D.4b feature a Kohn anomaly between M and K in the TA mode, which we will analyze in more detail below. The Kohn anomaly disappears upon exclusion of screening from within the σ band (below the Dirac point) via cDFPT. The ZA mode has the quadratic dispersion for long wavelengths as expected for 2D materials. For this mode, the standard Fourier interpolation (cf. App. B.4.2) of the dynamical matrix turned out to be very wiggly. To mitigate these unphysical wiggles, we made an exception and directly Fourier-interpolated $\omega_{\boldsymbol{q}}$ instead of $\omega_{\boldsymbol{q}}^2$ in this case. Since the ZA mode behaves as $|\boldsymbol{q}|^2$ instead of $|\boldsymbol{q}|$ for small $\boldsymbol{q}$, this is straightforwardly possible.

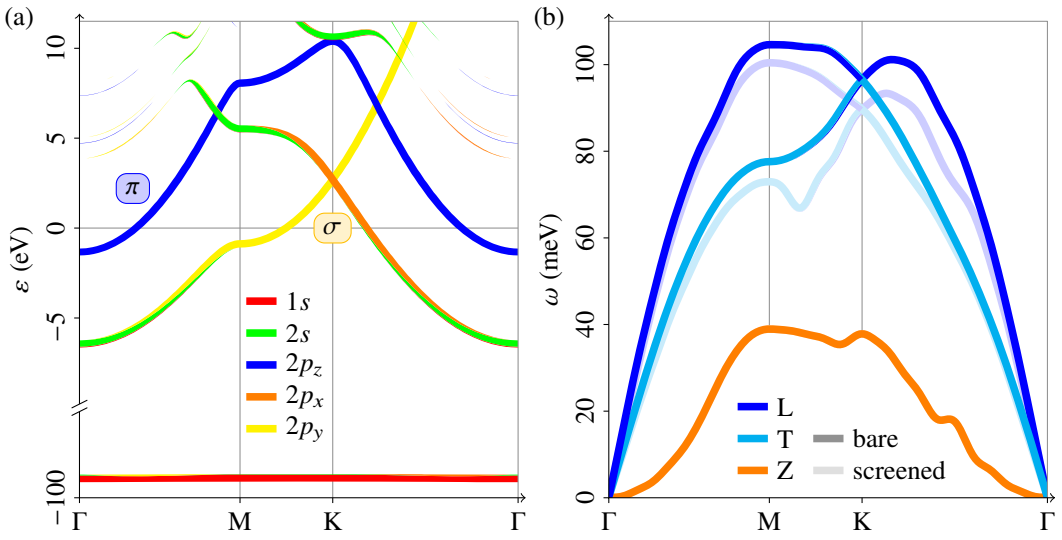

Figure D.4: *Ab initio* dispersions of monolayer beryllium. The path segments Γ–M and M–K–Γ are oriented in the y and x direction, respectively. (a) Electrons. Computational parameters: PBE functional; ultrasoft PPs from the PSLIBRARY 1.0.0 [305]; energy cutoffs of 100 Ry and 1000 Ry for wave functions and charge density; 36×36 $\boldsymbol{k}$ points; Gaussian smearing of 10 mRy; unit-cell height $c = 15$ Å; relaxed lattice constant $a = 2.13$ Å. (b) Phonons. The bare phonons result from exclusion of screening from within the σ band. Computational parameters: LDA functional; normconserving HGH PPs [340, 341]; energy cutoff of 300 Ry for wave functions; 36×36 $\boldsymbol{k}$ points; 18×18 $\boldsymbol{q}$ points; Gaussian smearing of 10 mRy; unit-cell height $c = 10$ Å; relaxed lattice constant $a = 2.07$ Å.

D.2.2 Model

The dispersions shown in Fig. D.4 are very similar to the examples for TB and mass–spring model in Figs. 2.2 and 2.7. Indeed, the models introduced in Secs. 2.3.2.1 and 2.4.3.1 are almost directly applicable to the present system, except that here also the $2s$ orbitals play an important role as they hybridize with the in-plane $2p_x$ and $2p_y$ orbitals.

In the basis of $2s$, $2p_x$, $2p_y$, and $2p_z$ orbitals, the on-site energies and the nearest-neighbor hoppings in x direction fitted to the DFT data read

$$\varepsilon = \begin{bmatrix} 3.0 & 0 & 0 & 0 \\ 0 & 8.1 & 0 & 0 \\ 0 & 0 & 8.1 & 0 \\ 0 & 0 & 0 & 2.7 \end{bmatrix} \text{eV}, \qquad t_0 = \begin{bmatrix} -1.6 & 2.2 & 0 & 0 \\ -2.2 & 3.1 & 0 & 0 \\ 0 & 0 & 0.4 & 0 \\ 0 & 0 & 0 & -0.7 \end{bmatrix} \text{eV}. \tag{D.1}$$

Considering the fact that s orbitals are invariant under all point-symmetry transformations, the rotation about the z axis in this basis simply reads $\text{diag}(1, R_\varphi)$, where 1 accounts for the $2s$ orbital and the rotation matrix R_φ in the Cartesian basis for the remaining $2p$ orbitals.

The resulting electron dispersion is shown in Fig. D.5a. Close to the Fermi level, the DFT data from Fig. D.4 is exactly reproduced. Only for higher energies there are some deviations.

Fitting the parameters of the mass–spring model from Sec. 2.4.3.1 to the cDFPT data, we find $C_x = -15.9\,\text{eV}/a^2$, $C_y = -3.5\,\text{eV}/a^2$, and $C_z = -1.1\,\text{eV}/a^2$ with the lattice constant $a = 2.1$ Å. The resulting phonon dispersion is shown in Fig. D.5b. The LA and TA modes are well reproduced, the ZA mode however does not exhibit the quadratic dispersion since this is impossible within the constraints of a nearest-neighbor mass–spring model (with only a single parameter for the ZA mode).

In the framework of the TB model, we can also calculate the EPC as described in detail in Sec. 2.5.2. As our reference, Fig. D.6a shows the $\boldsymbol{q}$- and $\boldsymbol{k}$-dependent EPC between the

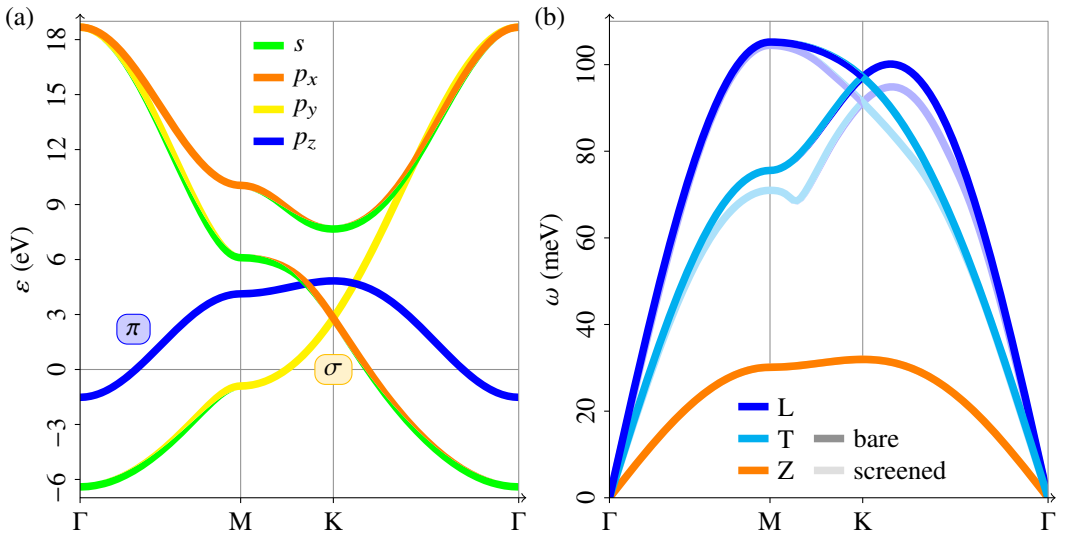

Figure D.5: (a) TB electrons and (b) mass–spring phonons of monolayer beryllium (cf. Fig. D.4). The screened phonon dispersion has been calculated with Eq. 5.11, replacing the bare EPC g by the screened $\widetilde{g}$. The computational parameters of the reference data are as in Fig. D.4b.

lower σ band and the TA phonons as results from DFPT. We find that the $\boldsymbol{k}$ dependence stems mainly from the angular dependence of the hopping. Choosing a very small radial scaling factor $\beta = 0.5$, we can very well reproduce the reference data, as seen in Fig. D.6b.

To model not only the cDFPT but also the DFPT dispersion, we calculate the screened dynamical matrix according to Eq. 5.11. However, since we do not have straightforward access to partially screened EPCs from our TB model, we do not combine different screening levels as in Eq. 5.11b and instead simply replace g by $\widetilde{g}$. The resulting screened phonon dispersion is also shown in Fig. D.5b. Indeed, it is very similar to the DFPT result. The Kohn anomaly of the beryllium layer can be reproduced using nearest-neighbor TB and mass–spring models and the corresponding EPC alone.

Finally, we also wish to understand the mechanism behind the Kohn anomaly. To that end, in Fig. D.6, we plot the relevant TB EPC for the wave vector of the Kohn anomaly, which is $\boldsymbol{q} = 1.62\,\mathrm{K}'$ folded back to the first BZ, together with the original and shifted Fermi surface. We have both maximum EPC and approximately nesting Fermi surfaces where the K and shifted K′ pockets meet, which explains the phonon softening at this $\boldsymbol{q}$ point.

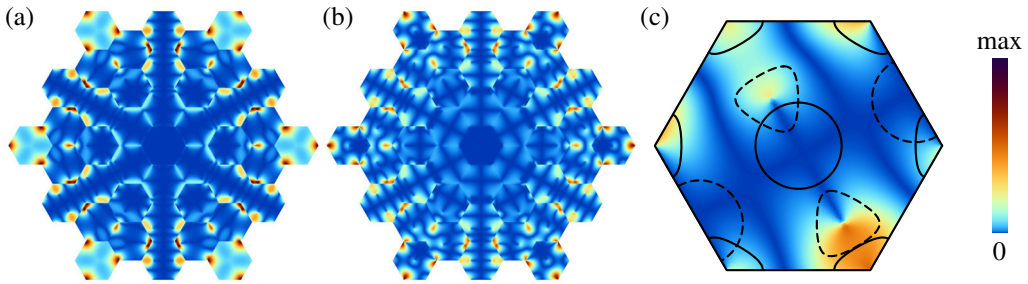

Figure D.6: $\boldsymbol{q}$- and $\boldsymbol{k}$-dependent EPC between TA mode and lower σ band of monolayer beryllium (a) from DFPT and (b) from TB model. The representation is as in Fig. 5.5 with mini-BZs showing the $\boldsymbol{k}$ dependence for fixed $\boldsymbol{q}$. (c) Origin of Kohn anomaly. We show the TB EPC for $\boldsymbol{q} = 1.62\,\mathrm{K}'$ (mapped to the first BZ), together with the in- (solid lines) and outgoing (dashed lines) Fermi surface.

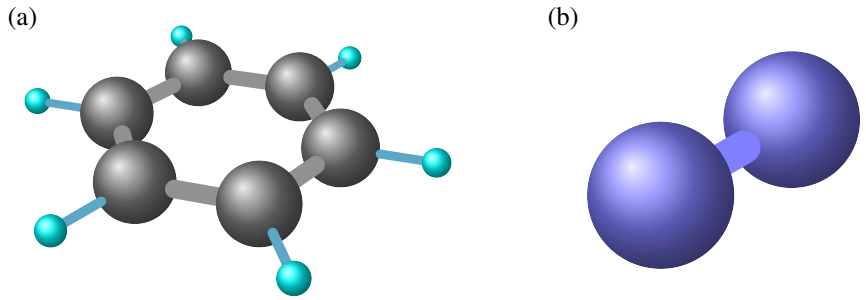

Figure D.7: Ball–stick models of (a) benzene and (b) nitrogen molecules.

D.3 Molecules

The idea to investigate molecules arose from a collaboration with Filippo Balzaretti and Susan Köppen from the Hybrid Materials Interfaces Group and the Computational Materials Science Group at the University of Bremen. Among other things, Filippo Balzaretti works on the understanding of photo-catalytic activity such as the photo-degradation of pollutants at TiO_2 surfaces. On the large scale, this can be favorably studied with the help of force fields. Our collaboration is based on the idea that we can possibly apply our phonon-renormalization scheme (Chap. 5) also to derive exited-state force fields from ground-state force fields and therewith conveniently study the photo-catalytic activity. We are, however, still far away from this. Nevertheless, preliminary calculations for example systems have already lead to interesting results that we will present here.

We perform DFT, DFPT, and cDFPT calculations for nitrogen and benzene molecules, N_2 and C_6H_6, as visualized in Fig. D.7. The resulting electronic and vibrational energy levels are shown in Figs. D.8 and D.9. Here, for the electrons we also show the eigenvalues of a TB model generated with WANNIER90 [92–94]. Please consider that, since DFT is a ground-state theory and KS eigenvalues are not guaranteed to be physically meaningful, especially the electronic energy levels must be appreciated with reservations.

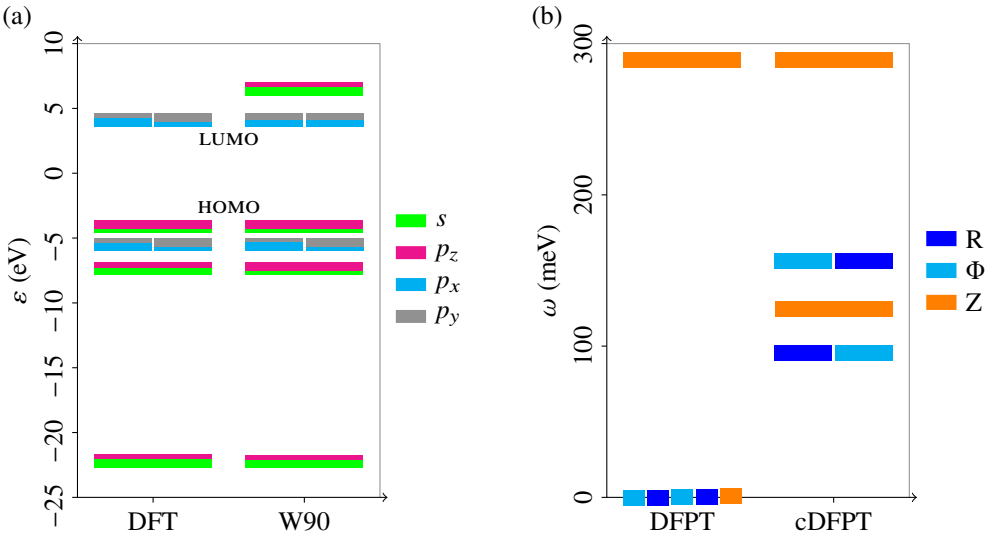

Figure D.8: (a) Electrons and (b) phonons of nitrogen. Computational parameters: PBE functional; normconserving PPs from the PSEUDODOJO table [350]; energy cutoff of 100 Ry; Gaussian smearing of 0.1 Ry; cubic unit cell with side length of 10 Å; relaxed bond length of 1.10 Å.

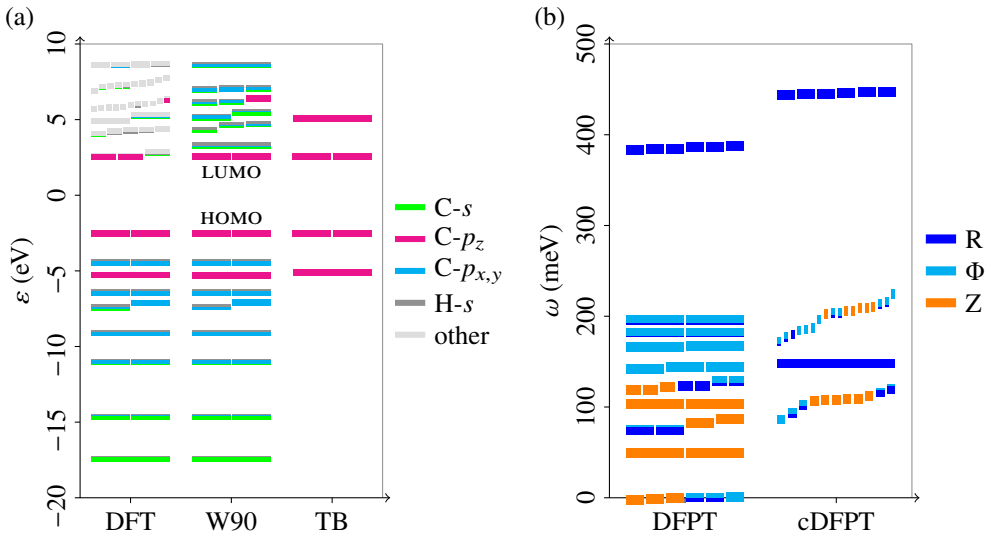

Figure D.9: (a) Electrons and (b) phonons of benzene. The computational parameters are as in Fig. D.8 expect for a slightly reduced energy cutoff of 90 Ry. We find relaxed C–C and C–H bond lengths of 1.40 Å and 1.09 Å, respectively.

The cDFPT calculations have been performed with *all* electronic states considered in the DFT calculations inside the active subspace. But still, the resulting phonons are not *fully* bare, since high-energy electrons not explicitly calculated in DFT contribute screening in the Sternheimer approach (cf. Sec. 2.4.2.2). The renormalization scheme presented in Chap. 5 allows us to switch back and forth between the cDFPT and DFPT data. Here, we do not even have to take special care of complex phase factors since we have no translational invariance.

The electrons of nitrogen are shown in Fig. D.8a. The highest occupied molecular orbital (HOMO) and the lowest unoccupied molecular orbital (LUMO) have s/p_z and p_x/p_y character, respectively, and are separated by about 8.2 eV. Here, it is relevant that in our calculations the bond points in the z direction. The corresponding phonons are shown in Fig. D.8b. In DFPT, we have five gapless modes (cf. Sec. 2.4.6) associated with displacements that do not produce a restoring force and whose oscillation frequency thus vanishes. These gapless modes can be classified into three translations (which transform as $x_1 + x_2$, $y_1 + y_2$, and $z_1 + z_2$, where the indices enumerate the atoms) and two rotations (which transform as $x_1 - x_2$ and $y_1 - y_2$). In DFPT, all modes have a nonzero frequency. Hence, DFPT breaks the translational and rotational invariance and thus the sum rules for the IFCs (cf. Sec. 2.4.5). The only physically relevant bond-stretching mode (which transforms as $z_1 - z_2$) does not change from DFPT to cDFPT.

The electrons of benzene are shown in Fig. D.9a. Here, both the HOMO and LUMO states are degenerate, have C-p_z character, and are separated by about 5.1 eV. The molecule lies in the x–y plane to which the C-p_z orbitals are orthogonally oriented. The low-energy electrons are well described by a simple TB model, namely a six-site chain with nearest-neighbor hopping t, whose eigenvalues are $\pm t$ and $\pm 2t$ (the former of which are doubly degenerate). For the phonons shown in Fig. D.9b, a new classification of the eigenmodes into radial (R), angular (Φ) and out-of-plane (Z) displacements is helpful. In DFPT, we have six gapless modes, more precisely three translations of R/Φ ($\times 2$) and Z character and three rotations of Φ and Z ($\times 2$) character. Again, the corresponding sum rules are broken in cDFPT and the modes obtain nonzero frequencies. The modes with the by far highest frequencies are six almost-degenerate modes, where mainly the hydrogen atoms oscillate in the radial direction.

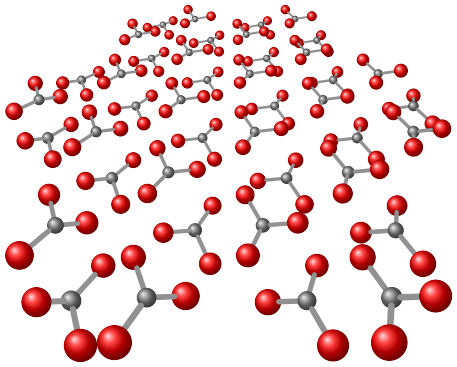

Figure D.10: Crystal structure of the hypothetical 2D material CP_3. It consists of a hexagonal lattice of carbon atoms, just like graphene, where each carbon atom is surrounded by a triangle of phosphor atoms. These triangles are alternately shifted upward and downward relative to the carbon layer.

D.4 CP_3

Motivated by studies on GeP_3 [448], our collaborators Ramzan et al. investigated the electronic and vibrational properties of a new possible family of 2D materials, XP_3 [247]. Since CP_3 has remarkably high phonon frequencies and an electronic structure that is similar to the outstanding conventional superconductor MgB_2 [449, 450], we decided to investigate possible conventional superconductivity in the former in collaboration with Ramzan et al.

The crystal structure, electrons, and phonons of CP_3 are shown in Figs. D.10 and D.11. There are no imaginary phonon frequencies, which suggests that CP_3 is another example of a 2D metal that is stable without CDW formation, in contrast to, e.g., the metallic TMDCs. Our preliminary estimates of the critical temperature T_c via McMillan's formula (Sec. 3.2.1.2) do not suggest that CP_3 is a conventional superconductor at considerable temperatures.

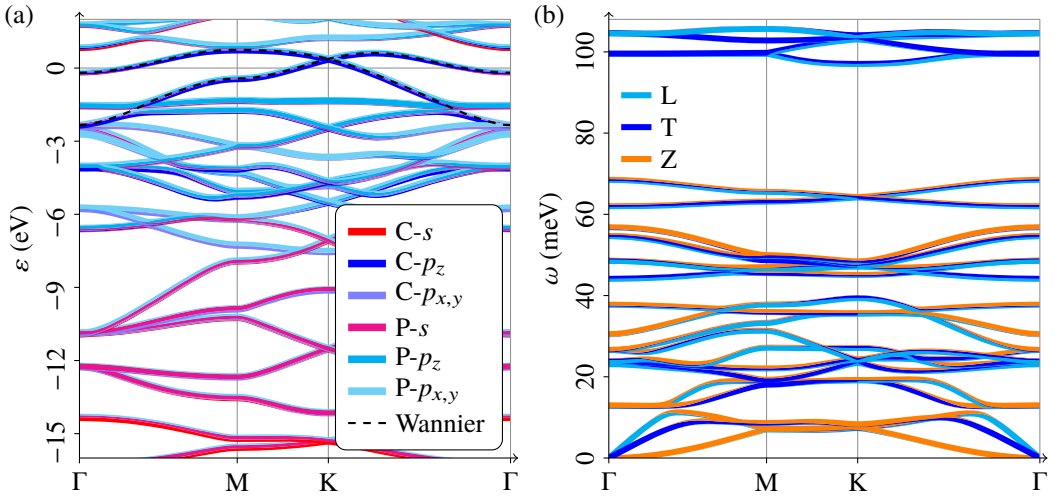

Figure D.11: Electrons and phonons of CP_3. (a) Electronic band structure. The dispersion of the low-energy electrons faintly resembles the dispersion of graphene, but it is heavily reconstructed. The Dirac cone is shifted away from the Fermi level and we have an electron pocket around Γ. The orbital character is still predominantly C-p_z, but there are also significant contributions of P-p_z orbitals. The Wannier bands have been calculated in the basis of the C-p_z orbitals only. (b) Phonon dispersion. It consists of two blocks of lower and higher frequency, separated by a gap of about 30 meV. There are no indications of dynamical instability. Computational parameters: PBE functional; normconserving PPs from the PseudoDojo table [350]; energy cutoff of 90 Ry; 12×12 $\boldsymbol{k}$ points; 6×6 $\boldsymbol{q}$ points; Gaussian smearing of 10 mRy; unit-cell height $c = 20$ Å; relaxed lattice constant $a = 6.24$ Å.

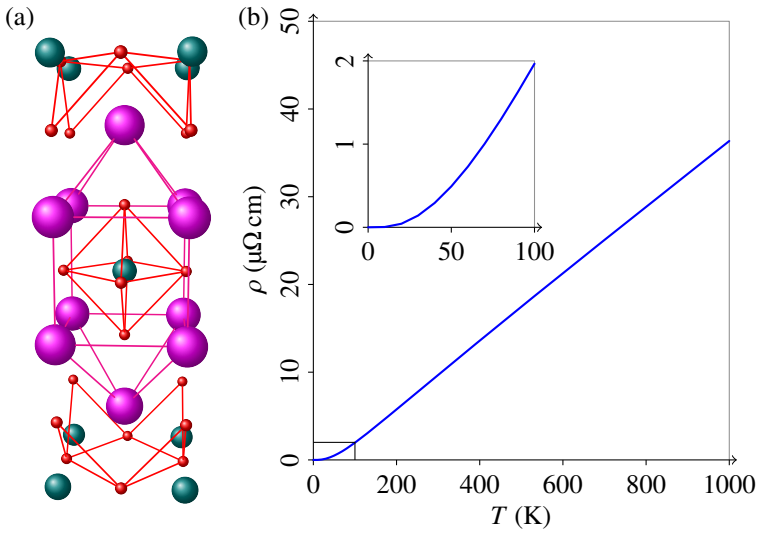

Figure D.12: (a) Crystal structure and (b) resistivity (Eq. D.3) of Sr_2RuO_4.

D.5 Sr_2RuO_4

The project on Sr_2RuO_4 is a collaboration with Manuel Zingl from the Center for Computational Quantum Physics at the Flatiron Institute in New York. Sr_2RuO_4 is known for being the first perovskite superconductor beyond the cuprates [451], but here we will focus on the normal electrical resistivity. The electrical in-plane resistivity of Sr_2RuO_4 is correctly described by DFT+DMFT calculations for low temperatures [452]. However, for higher temperatures, a saturation rather than the experimentally observed linear behavior [453] is obtained. Since theoretical results for the Hall coefficient by Zingl et al. [454] also deviate from experiment for high temperatures, Zingl et al. consider that both inconsistencies could be due to neglected phonon scattering.

We investigate the effect of the EPC on the electrical resistivity of Sr_2RuO_4 from first principles. Here, we use normconserving PPs from the PseudoDojo table [350], an energy cutoff of 100 Ry, $8 \times 8 \times 4$ $\boldsymbol{k}$ and $4 \times 4 \times 2$ $\boldsymbol{q}$ points, and a Fermi–Dirac smearing of 5 mRy. We take the crystal structure from Ref. 455 and perform a structural relaxation. The in- and out-of-plane lattice constants are however kept fixed at their experimental values $a = 3.86$ Å and $c = 12.72$ Å. The crystal is visualized in Fig. D.12a. Except for bond lengths and atomic species, it is identical to the cuprate superconductor LASCO (cf. Fig. 1.1b).

Figure D.13 shows the electrons and phonons from DFT and DFPT. The low-energy electrons have Ru-t_{2g} orbital character. (t_{2g} combines the d_{xy}, d_{xz}, and d_{yz} orbitals as opposed to e_g, which combines d_{z^2} and $d_{x^2-y^2}$.) The dispersion is similar to the results of Ref. 456. Phonon dispersions of Sr_2RuO_4 have also been calculated in Refs. 457, 458.

We also compute the normal and transport EPCs and Eliashberg spectral functions using the EPW code [138–140]. Here, the transport properties are implemented by weighting the $\boldsymbol{q}$- and $\boldsymbol{k}$-dependent squared EPC by a function of the group velocity (cf. Eq. 56 of Ref. 140),

$$g^2_{\boldsymbol{q}\boldsymbol{k},\mathrm{tr}} = g^2_{\boldsymbol{q}\boldsymbol{k}} \left[1 - \frac{v_{\boldsymbol{k}n} v_{\boldsymbol{k}+\boldsymbol{q}m}}{|v_{\boldsymbol{k}n}|^2} \right]. \tag{D.2}$$

We can then evaluate the Eliashberg spectral functions α^2F and α^2F_{tr} (Eq. 3.7) and the corresponding effective EPC strengths λ and λ_{tr} (Eq. 3.10a) as usual. The Fermi-surface averages occurring in Eqs. 3.7 and 3.10a are not evaluated using the tetrahedron method

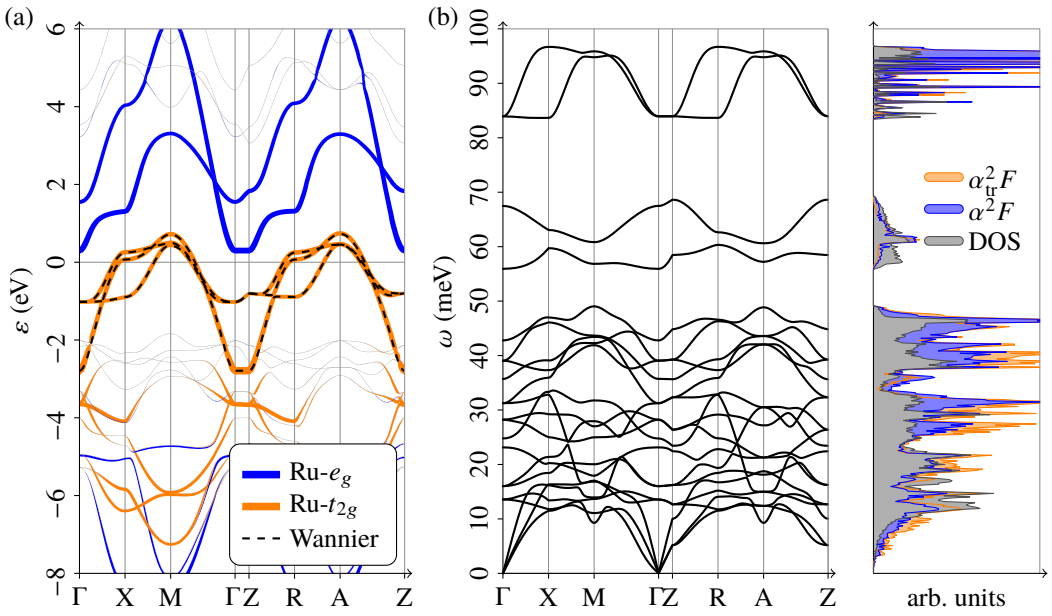

Figure D.13: Electrons, phonons, and EPC of Sr_2RuO_4. (a) Electronic band structure. (b) Phonon dispersion, phonon DOS, and (transport) Eliashberg spectral function.

(App. B.3) in this case. Instead, we use a summation over smeared-out delta functions as implemented in EPW. Here, we apply $64 \times 64 \times 32$ $\boldsymbol{k}$ points and $32 \times 32 \times 16$ $\boldsymbol{q}$ points in combination with smearings $\sigma_{\boldsymbol{k}} = 30\,\text{meV}$ and $\sigma_{\boldsymbol{q}} = 60\,\text{meV}$, respectively. We find the spectral functions shown in Fig. D.13b and comparably small [459] $\lambda = 0.21$ and $\lambda_{\text{tr}} = 0.27$.

Additionally, we calculate the resistivity using the Ziman formula as implemented in EPW (cf. Eq. 54 of Ref. 140),

$$\rho(T) \propto \int_0^\infty \mathrm{d}\omega\, \omega \alpha^2_{\text{tr}} F(\omega) n(\omega)[1 + n(\omega)], \tag{D.3}$$

where the temperature enters via the Bose–Einstein distribution function $n(\omega)$. The result is displayed in Fig. D.12b. At a temperature of 100 K, we find a resistivity of $2\,\mu\Omega\,\text{cm}$. On the other hand, the experimental in-plane resistivity at this temperature is roughly $25\,\mu\Omega\,\text{cm}$ [453]. Thus, within the approximations made, the EPC only contributes about 8 % of the resistivity, which is much less than the discrepancy between experiment and DFT+DMFT. Thus, phonons can probably not explain the disagreement. This finding is qualitatively in line with Ref. 452, whose authors state that the EPC effects account for less then 5 % of the total resistivity (cf. Supplemental Material of Ref. 452).

	relaxed			fixed		fixed, less smearing		
x (charge per cell)	0.0	−0.1	−0.2	−0.1	−0.2	0.0	−0.1	−0.2
a (Å)	3.323	3.344	3.376	3.323	3.323	3.324	3.324	3.324
$d_{\text{Mo–Se, inner}}$ (Å)	1.672	1.667	1.652	1.672	1.672	1.675	1.675	1.675
$d_{\text{Mo–Se, outer}}$ (Å)	1.676	1.666	1.652	1.676	1.676	1.672	1.672	1.672
$\varepsilon^{\text{c}}_{\text{K}} - \varepsilon^{\text{c}}_{\Sigma}$ (eV)	0.039	−0.044	−0.189	0.057	0.076	0.035	0.052	0.071
$\varepsilon^{\text{v}}_{\Gamma} - \varepsilon^{\text{v}}_{\text{K}}$ (eV)	0.082	0.129	0.216	0.074	0.065	0.084	0.077	0.068

Table D.1: Lattice parameters and band-edge energy differences of doped bilayer 2H-$MoSe_2$.

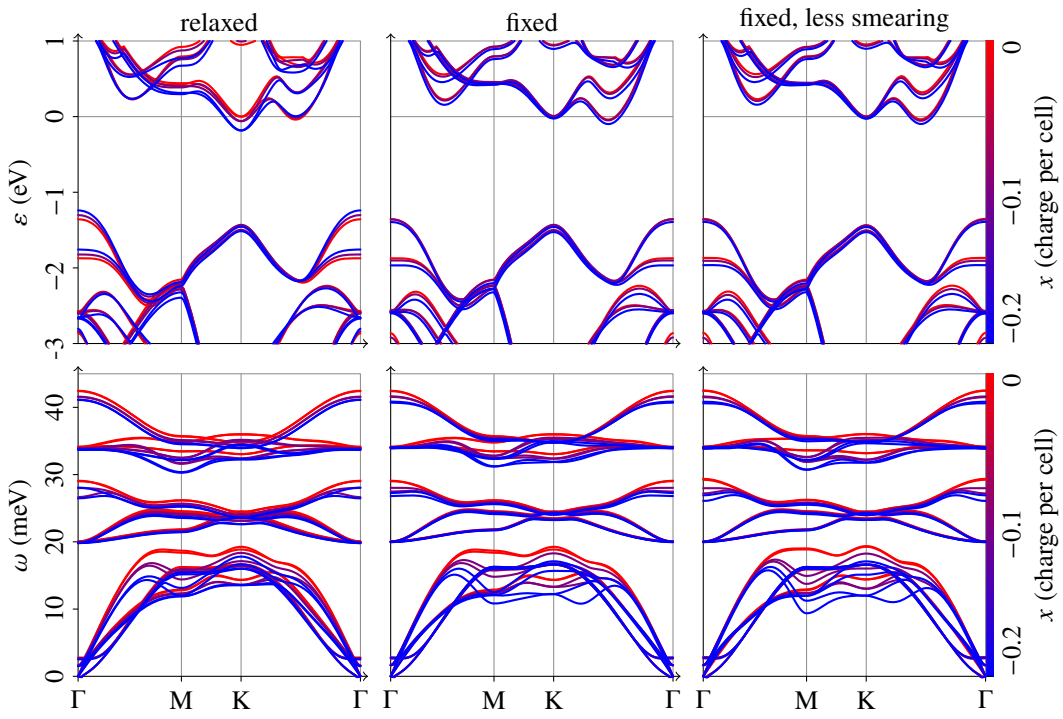

Figure D.14: Electrons and phonons of doped bilayer 2H-$MoSe_2$.

D.6 Doped bilayer 2H-$MoSe_2$

Finally, we calculate the electronic and phononic band structures of a bilayer of 2H-$MoSe_2$ for different doping levels $-x$, namely 0.0, 0.1, and 0.2 additional electrons per (bilayer) unit cell. The two layers are rotated by 180° with respect to each other and stacked such that the in-plane positions of Mo and Se are exchanged in one layer with respect to the other (cf. Sec. 4.1.2). Throughout the calculations, the interlayer Mo–Mo distance is kept fixed at 6.7 Å, as experimentally observed for thin films [460]. A unit-cell height of 25 Å ensures that periodic images of the bilayer are well separated. The lattice constants a and the inner and outer vertical Mo–Se distances are shown in Tab. D.1. For electrons and phonons, 24×24 $\boldsymbol{k}$-point and 6×6 $\boldsymbol{q}$-point meshes are used, respectively. A kinetic energy cutoff of 60 Ry in combination with normconserving, nonrelativistic Martins–Troullier [79] PBE [75, 76] PPs and a Methfessel–Paxton smearing [306] of 10 mRy and 5 mRy are chosen (cf. App. C.7.3).

The band structures are shown in Fig. D.14. The electronic energies are measured relative to the respective Fermi levels, which have been moved to the LUMO if they are found inside the gap. Σ denotes the point between K and Γ, where the lowest conduction band has a local or global minimum. The relevant energy differences in the lowest conduction band and in the highest valence band are shown in Tab. D.1. If we allow the crystal structure to relax upon doping, most of the additional charge occupies the K valley. However, if we keep the structure fixed, the Σ valley is preferred. The acoustic phonon frequencies of the doped system turn out to be slightly reduced with respect to the undoped case, in some branches especially in the vicinity of the M point. This effect is enhanced for the reduced smearing and can be traced back to the onset of metallic screening (cf. Fig. 8.2).

Acknowledgments

This thesis would not have been realized without the longstanding or occasional support by many people whom I would like to thank in the following. I also thank the people I forgot to mention for helping me anyway.

First, I would like to thank my supervisor Tim Wehling for supporting me since my bachelor's thesis already many years ago. His ideas were the source of many interesting projects that I very much enjoyed being a part of.

I am also very grateful to Ludger Wirtz for agreeing to read my thesis as the second examiner. I hope this task turned out to be sufficiently enjoyable in the end.

Likewise, I thank Gerd Czycholl, Jürgen Gutowski, Edin Kapetanović, and Monty Drechsler for completing the examination committee.

I am much obliged to my colleagues at the institute and thank, in alphabetical order, Alexander, Arne, Bin, Christian, Christina, Christopher, Daniel C., Daniel E., Daniel M., Ebad, Edin, Elham, Erik, Frederik, Gunnar, Chema, Malte H., Malte R., Malte S., Matthias, Michael, Niklas, Patrick, Philip, Simon, Stefan, and Tobias for great company, inspiring discussions, useful feedback, coffee and juice, and enjoyable journeys.

I would also like to thank Klaus Bowe, Andreas Beuthner, and Christof Köhler for technical and Sarah-Jane Farley, Sandra Smit, Ann-Kathrin Risken, and Ania Mohammadi for organizational support.

I was lucky to be part of Research Training Group 2247 "Quantum-Mechanical Materials Modelling" (RTG QM^3). I am particularly grateful for the collaborations with Filippo Balzaretti, Susan Köppen, Muhammad Sufyan Ramzan, and Vladimir Bačić. Furthermore, the support from the *Deutsche Forschungsgemeinschaft* (DFG) allowed me to travel to international workshops and conferences, which were great experiences and opportunities.

I am particularly grateful for our experimental collaboration with Joshua Hall, Camiel van Efferen, Thomas Michely, Alexander Grüneis, and coworkers from the University of Cologne.

Furthermore, I owe many thanks to the developers of free software such as QE [39, 40], EPW [138–140], Wannier90 [92–94], Python, MPI for Python [411], NumPy [412], SciPy [461], SymPy [462], Matplotlib [463], LaTeX, Ti*k*Z, and Git (after some initial doubts, I finally counted more than 8000 commits). I am also grateful to people who post in forums. My special thanks goes to Ryotaro Arita and Yusuke Nomura for sharing their cDFPT code with us.

My work would also not have been possible without access to the supercomputers of the North-German Supercomputing Alliance (HLRN) and the cluster of the RTG QM^3.

I am very grateful to Miriam Nüß for her encouragement and proofreading.

Finally, I thank my parents Brigitte Berges and Ulrich Seevers for continuously supporting me, that's for sure.

Erklärung

Hiermit versichere ich, dass ich

1. die Arbeit ohne unerlaubte fremde Hilfe angefertigt habe,
2. keine anderen als die von mir angegeben Quellen und Hilfsmittel benutzt habe,
3. die den benutzten Werken wörtlich oder inhaltlich entnommenen Stellen als solche kenntlich gemacht habe.

Bremen, 25. Juli 2020

Jan Berges

Publications and presentations

Publications

[86] **J. Berges**, E. G. C. P. van Loon, A. Schobert, M. Rösner, and T. O. Wehling, *Ab initio phonon self-energies and fluctuation diagnostics of phonon anomalies: Lattice instabilities from Dirac pseudospin physics in transition metal dichalcogenides,* Phys. Rev. B **101**, 155107 (2020)

[111] J. Hall, N. Ehlen, **J. Berges**, E. van Loon, C. van Efferen, C. Murray, M. Rösner, J. Li, B. V. Senkovskiy, M. Hell, M. Rolf, T. Heider, M. C. Asensio, J. Avila, L. Plucinski, T. Wehling, A. Grüneis, and T. Michely, *Environmental control of charge density wave order in monolayer 2H-TaS_2,* ACS Nano **13**, 10210 (2019)

[293] E. Kamil, **J. Berges**, G. Schönhoff, M. Rösner, M. Schüler, G. Sangiovanni, and T. O. Wehling, *Electronic structure of single layer 1T-$NbSe_2$: Interplay of lattice distortions, nonlocal exchange, and Mott–Hubbard correlations,* J. Phys. Condens. Matter **30**, 325601 (2018)

[464] M. Rösner, R. E. Groenewald, G. Schönhoff, **J. Berges**, S. Haas, and T. O. Wehling, *Plasmonic superconductivity in layered materials,* arXiv:1803.04576 (2018)

Talks

8. **J. Berges**, E. van Loon, A. Schobert, M. Rösner, and T. Wehling, *Many-body instabilities in 2D materials*, RTG QM^3 Mid-term Workshop, Etelsen, Germany (28–30 October 2019)

7. **J. Berges**, M. Rösner, E. van Loon, and T. Wehling, *Phonon renormalization in ab-initio-based lattice models,* DPG Spring Meeting, Regensburg, Germany (31 March–5 April 2019)

6. **J. Berges**, M. Rösner, E. Kamil, G. Schönhoff, M. Schüler, and T. Wehling, *Many-body instabilities in 2D materials,* RTG QM^3 Mid-term Workshop, Etelsen, Germany (26–28 September 2018)

5. G. Schönhoff, M. Rösner, E. Kamil, **J. Berges**, and T. Wehling, *Realistic description of competing interactions in metallic TMDCs,* DPG Spring Meeting, Berlin, Germany (11–16 March 2018)

4. G. Schönhoff, M. Rösner, E. Kamil, **J. Berges**, and T. Wehling, *Realistic description of competing interactions in metallic TMDCs,* APS March Meeting, Los Angeles, USA (5–9 March 2018)

3. E. Kamil, **J. Berges**, M. Schüler, G. Schönhoff, and T. Wehling, *Theory of Mott physics in 1T-$NbSe_2$,* APS March Meeting, Los Angeles, USA (5–9 March 2018)

2. **J. Berges**, G. Schönhoff, M. Rösner, C. Steinke, E. Kamil, R. Groenewald, and T. Wehling, *Electron–phonon interaction in transition-metal dichalcogenides,* RTG QM^3 Half-day Workshop, Bremen, Germany (21 August 2017)

1. **J. Berges**, *Phonons in 2D TMDCs,* RTG QM^3 Students Corner, Bremen, Germany (19 June 2017)

Posters

10. **J. Berges**, M. Rösner, E. van Loon, A. Schobert, and T. Wehling, *Phonon renormalization in ab-initio-based lattice models* (SPECS Best Poster Award, third place), International Workshop on Strong Correlations and Angle-Resolved Photoemission Spectroscopy CORPES19, Oxford, United Kingdom (15–19 July 2019)

9. **J. Berges**, M. Rösner, E. van Loon, and T. Wehling, *Phonon renormalization in ab-initio-based lattice models,* MAPEX Symposium, Bremen, Germany (17–18 June 2019)

8. **J. Berges**, M. Rösner, E. van Loon, and T. Wehling, *Phonon renormalization in ab-initio-based lattice models,* International CECAM Workshop "Correlated electron physics beyond the Hubbard model," Bremen, Germany (4–8 February 2019)

7. G. Schönhoff, M. Rösner, E. Kamil, **J. Berges**, and T. Wehling, *Competing interactions in metallic TMDCs,* International Conference SPSTM-7 & LTSPM-1, Nijmegen, The Netherlands (28–30 July 2018)

6. G. Schönhoff, M. Rösner, E. Kamil, **J. Berges**, and T. Wehling, *Competing interactions in metallic TMDCs,* Summer School "Bandstructure meets quantum field theory," Vienna, Austria (2–6 July 2018)

5. G. Schönhoff, M. Rösner, E. Kamil, **J. Berges**, and T. Wehling, *Competing interactions in metallic TMDCs,* ICTP School on Electron-Phonon Physics from First Principles, Trieste, Italy (19–23 March 2018)

4. **J. Berges**, G. Schönhoff, M. Rösner, and T. Wehling, *Electron–phonon interaction in TMDCs,* Autumn School on Correlated Electrons, Jülich, Germany (25–29 September 2017)

3. **J. Berges**, G. Schönhoff, M. Rösner, and T. Wehling, *Electron–phonon interaction in TMDCs,* Workshop "Dynamical mean-field approach for strongly correlated materials," Dresden, Germany (19–22 September 2017)

2. **J. Berges**, G. Schönhoff, M. Rösner, and T. Wehling, *Electron–phonon interaction in TMDCs,* Conference "Flatlands beyond Graphene," Lausanne, Switzerland (29 August–1 September 2017)

1. **J. Berges**, T. Wehling, G. Schönhoff, M. Rösner, C. Steinke, and E. Kamil, *Many-body instabilities in 2D materials,* RTG QM^3 Kick-Off Workshop, Bremen, Germany (28 February–2 March 2017)

Participations

6. International CECAM Workshop "Thinking outside of the box: Beyond machine learning for quantum chemistry," Bremen, Germany (8–11 October 2019)

5. TRIQS meeting, Paris, France (11–14 June 2019)

4. International CECAM Workshop "Reliable and quantitative prediction of defect properties in Ga-based semiconductors," Bremen, Germany (8–12 October 2018)

3. International CECAM Workshop "Charge carrier dynamics in nanostructures," Bremen, Germany (9–13 October 2017)

2. International CECAM Workshop "Tackling complexity of the nano/bio interface," Bremen, Germany (12–16 June 2017)

1. BremHLR Workshop "Parallel programming with MPI and OpenMP," Bremen, Germany (9–13 January 2017)

Tutorials

2. **J. Berges**, J. Pizarro, T. Wehling, and C. Köhler, *Hands on density-functional theory with VASP,* RTG QM^3 Hands-on Tutorial, Bremen, Germany (5 March 2020)

1. **J. Berges**, T. Wehling, and C. Köhler, *Phonons and electron–phonon interaction (of 2H-TaS_2) from Quantum ESPRESSO,* RTG QM^3 Hands-on Tutorial, Bremen, Germany (10 January 2019)

Bibliography

I declare after all there is no enjoyment like reading!

—Jane Austen

[1] C. Emmeche, S. Køppe, and F. Stjernfelt, *Explaining emergence: Towards an ontology of levels*, J. Gen. Philos. Sci. **28**, 83 (1997). Cited on page 1.

[2] S. B. Cooper, *What makes a computation unconventional?*, in *Computing Nature: Turing Centenary Perspective*, edited by G. Dodig-Crnkovic and R. Giovagnoli (Springer, Berlin, Heidelberg, 2013) arXiv:1303.2507. Cited on page 1.

[3] R. K. Sawyer, *Emergence in sociology: Contemporary philosophy of mind and some implications for sociological theory*, Am. J. Sociol. **107**, 551 (2001). Cited on page 1.

[4] J. Wilson and A. Yoffe, *The transition metal dichalcogenides: Discussion and interpretation of the observed optical, electrical and structural properties*, Adv. Phys. **18**, 193 (1969). Cited on pages 1, 58, 59, 84, and 98.

[5] K. S. Novoselov, D. Jiang, F. Schedin, T. J. Booth, V. V. Khotkevich, S. V. Morozov, and A. K. Geim, *Two-dimensional atomic crystals*, Proc. Natl. Acad. Sci. USA **102**, 10451 (2005), arXiv:cond-mat/0503533. Cited on pages 1, 56, and 58.

[6] C. Berthier, P. Molinié, and D. Jérome, *Evidence for a connection between charge density waves and the pressure enhancement of superconductivity in 2H-$NbSe_2$*, Solid State Commun. **18**, 1393 (1976). Cited on pages 1 and 44.

[7] E. Revolinsky, E. P. Lautenschlager, and C. H. Armitage, *Layer structure superconductor*, Solid State Commun. **1**, 59 (1963). Cited on pages 1, 44, and 57.

[8] J. A. Wilson, F. J. Di Salvo, and S. Mahajan, *Charge-density waves in metallic, layered, transition-metal dichalcogenides*, Phys. Rev. Lett. **32**, 882 (1974). Cited on pages 1, 46, 57, 98, and 104.

[9] J. A. Wilson, *Concerning the semimetallic characters of TiS_2 and $TiSe_2$*, Solid State Commun. **22**, 551 (1977). Cited on page 1.

[10] M. Bonilla, S. Kolekar, Y. Ma, H. C. Diaz, V. Kalappattil, R. Das, T. Eggers, H. R. Gutierrez, M.-H. Phan, and M. Batzill, *Strong room-temperature ferromagnetism in VSe_2 monolayers on van der Waals substrates*, Nat. Nanotechnol. **13**, 289 (2018). Cited on pages 1 and 57.

[11] G. Schönhoff, M. Rösner, R. E. Groenewald, S. Haas, and T. O. Wehling, *Interplay of screening and superconductivity in low-dimensional materials*, Phys. Rev. B **94**, 134504 (2016), arXiv:1605.07489. Cited on page 1.

[12] A. Raja, A. Chaves, J. Yu, G. Arefe, H. M. Hill, A. F. Rigosi, T. C. Berkelbach, P. Nagler, C. Schüller, T. Korn, C. Nuckolls, J. Hone, L. E. Brus, T. F. Heinz, D. R. Reichman, and A. Chernikov, *Coulomb engineering of the bandgap and excitons in two-dimensional materials*, Nat. Commun. **8**, 1 (2017). Cited on pages 1 and 57.

[13] T. O. Wehling, *Pseudodoping of metallic two-dimensional materials*, arXiv:1609.00220 (2016). Cited on pages 1 and 89.

[14] B. Shao, A. Eich, C. Sanders, A. S. Ngankeu, M. Bianchi, P. Hofmann, A. A. Khajetoorians, and T. O. Wehling, *Pseudodoping of a metallic two-dimensional material by the supporting substrate*, Nat. Commun. **10**, 1 (2019), arXiv:1807.00756. Cited on pages 1, 89, 92, 93, and 104.

[15] O. Cotleţ, S. Zeytinoğlu, M. Sigrist, E. Demler, and A. Imamoğlu, *Superconductivity and other collective phenomena in a hybrid Bose-Fermi mixture formed by a polariton condensate and an electron system in two dimensions*, Phys. Rev. B **93**, 054510 (2016), arXiv:1510.02001. Cited on pages 1 and 57.

[16] B. Peng, H. Zhang, W. Chen, B. Hou, Z.-J. Qiu, H. Shao, H. Zhu, B. Monserrat, D. Fu, H. Weng, and C. M. Soukoulis, *Sub-picosecond photo-induced displacive phase transition in two-dimensional $MoTe_2$*, npj 2D Mater. Appl. **4**, 1 (2020), arXiv:1903.09757. Cited on pages 1 and 59.

[17] R. F. Frindt, *Superconductivity in ultrathin $NbSe_2$ layers*, Phys. Rev. Lett. **28**, 299 (1972). Cited on pages 1, 44, and 82.

[18] X. Xi, L. Zhao, Z. Wang, H. Berger, L. Forró, J. Shan, and K. F. Mak, *Strongly enhanced charge-density-wave order in monolayer $NbSe_2$*, Nat. Nanotechnol. **10**, 765 (2015), arXiv:1507.05595. Cited on pages 1, 44, 71, 82, 83, and 98.

[19] D. Costanzo, S. Jo, H. Berger, and A. F. Morpurgo, *Gate-induced superconductivity in atomically thin MoS_2 crystals*, Nat. Nanotechnol. **11**, 339 (2016), arXiv:1512.03222. Cited on pages 1, 57, 71, and 82.

[20] E. Khestanova, J. Birkbeck, M. Zhu, Y. Cao, G. L. Yu, D. Ghazaryan, J. Yin, H. Berger, L. Forró, T. Taniguchi, K. Watanabe, R. V. Gorbachev, A. Mishchenko, A. K. Geim, and I. V. Grigorieva, *Unusual suppression of the superconducting energy gap and critical temperature in atomically thin $NbSe_2$*, Nano Lett. **18**, 2623 (2018), arXiv:1803.04920. Cited on pages 1 and 82.

[21] C.-S. Lian, C. Si, and W. Duan, *Unveiling charge-density wave, superconductivity, and their competitive nature in two-dimensional $NbSe_2$*, Nano Lett. **18**, 2924 (2018). Cited on pages 1, 44, 46, and 48.

[22] D. Lin, S. Li, J. Wen, H. Berger, L. Forró, H. Zhou, S. Jia, T. Taniguchi, K. Watanabe, X. Xi, and M. S. Bahramy, *Patterns and driving forces of dimensionality-dependent charge density waves in 2H-type transition metal dichalcogenides*, Nat. Commun. **11**, 2406 (2020), arXiv:2002.03386. Cited on pages 1, 82, and 83.

[23] A. Allard and L. Wirtz, *Graphene on metallic substrates: Suppression of the Kohn anomalies in the phonon dispersion*, Nano Lett. **10**, 4335 (2010). Cited on pages 1 and 57.

[24] M. Rösner, E. Şaşıoğlu, C. Friedrich, S. Blügel, and T. O. Wehling, *Wannier function approach to realistic Coulomb interactions in layered materials and heterostructures*, Phys. Rev. B **92**, 085102 (2015), arXiv:1504.05230. Cited on pages 1, 42, 57, and 74.

[25] J.-F. Ge, Z.-L. Liu, C. Liu, C.-L. Gao, D. Qian, Q.-K. Xue, Y. Liu, and J.-F. Jia, *Superconductivity above 100 K in single-layer FeSe films on doped $SrTiO_3$*, Nat. Mater. **14**, 285 (2015), arXiv:1406.3435. Cited on pages 1, 57, and 71.

[26] A. K. Geim and I. V. Grigorieva, *Van der Waals heterostructures*, Nature **499**, 419 (2013), arXiv:1307.6718. Cited on page 1.

[27] L. Waldecker, A. Raja, M. Rösner, C. Steinke, A. Bostwick, R. J. Koch, C. Jozwiak, T. Taniguchi, K. Watanabe, E. Rotenberg, T. O. Wehling, and T. F. Heinz, *Rigid band shifts in two-dimensional semiconductors through external dielectric screening*, Phys. Rev. Lett. **123**, 206403 (2019), arXiv:1907.05535. Cited on page 1.

[28] Y. Cao, V. Fatemi, S. Fang, K. Watanabe, T. Taniguchi, E. Kaxiras, and P. Jarillo-Herrero, *Unconventional superconductivity in magic-angle graphene superlattices*, Nature **556**, 43 (2018), arXiv:1803.02342. Cited on pages 1, 57, and 58.

[29] Y. Cao, V. Fatemi, A. Demir, S. Fang, S. L. Tomarken, J. Y. Luo, J. D. Sanchez-Yamagishi, K. Watanabe, T. Taniguchi, E. Kaxiras, R. C. Ashoori, and P. Jarillo-Herrero, *Correlated insulator behaviour at half-filling in magic-angle graphene superlattices*, Nature **556**, 80 (2018), arXiv:1802.00553. Cited on pages 1, 57, and 58.

[30] T. O. Wehling, B. Grundkötter-Stock, B. Aradi, T. Frauenheim, and T. Niehaus, *Charge-doping-induced phase transitions in hydrogenated and fluorinated graphene*, Phys. Rev. B **90**, 085422 (2014), arXiv:1312.2276. Cited on pages 1, 31, and 57.

[31] P. Hohenberg and W. Kohn, *Inhomogeneous electron gas*, Phys. Rev. **136**, B864 (1964). Cited on pages 2, 8, 73, and 82.

[32] W. Kohn and L. J. Sham, *Self-consistent equations including exchange and correlation effects*, Phys. Rev. **140**, A1133 (1965). Cited on pages 2, 8, 9, 10, 11, 73, and 82.

[33] J. Hubbard and B. H. Flowers, *Electron correlations in narrow energy bands*, Proc. R. Soc. Lond. A **276**, 238 (1963). Cited on pages 2 and 43.

[34] J. Hubbard and B. H. Flowers, *Electron correlations in narrow energy bands. II. The degenerate band case*, Proc. R. Soc. Lond. A **277**, 237 (1964). Cited on pages 2 and 43.

[35] J. Hubbard and B. H. Flowers, *Electron correlations in narrow energy bands III. An improved solution*, Proc. R. Soc. Lond. A **281**, 401 (1964). Cited on pages 2 and 43.

[36] N. F. Mott, *Metal–insulator transition*, Rev. Mod. Phys. **40**, 677 (1968). Cited on pages 2 and 43.

[37] M. Imada, A. Fujimori, and Y. Tokura, *Metal-insulator transitions*, Rev. Mod. Phys. **70**, 1039 (1998). Cited on pages 2 and 43.

[38] A. Marini, C. Hogan, M. Grüning, and D. Varsano, *yambo: An ab initio tool for excited state calculations*, Comput. Phys. Commun. **180**, 1392 (2009), arXiv:0810.3118. Cited on page 2.

[39] P. Giannozzi, S. Baroni, N. Bonini, M. Calandra, R. Car, C. Cavazzoni, D. Ceresoli, G. L. Chiarotti, M. Cococcioni, I. Dabo, A. D. Corso, S. d. Gironcoli, S. Fabris, G. Fratesi, R. Gebauer, U. Gerstmann, C. Gougoussis, A. Kokalj, M. Lazzeri, L. Martin-Samos, N. Marzari, F. Mauri, R. Mazzarello, S. Paolini, A. Pasquarello, L. Paulatto, C. Sbraccia, S. Scandolo, G. Sclauzero, A. P. Seitsonen, A. Smogunov, P. Umari, and R. M. Wentzcovitch, *Quantum ESPRESSO: A modular and open-source software project for quantum simulations of materials*, J. Phys. Condens. Matter **21**, 395502 (2009), arXiv:0906.2569. Cited on pages 2, 57, 73, 88, 96, 112, 116, and 164.

[40] P. Giannozzi, O. Andreussi, T. Brumme, O. Bunau, M. B. Nardelli, M. Calandra, R. Car, C. Cavazzoni, D. Ceresoli, M. Cococcioni, N. Colonna, I. Carnimeo, A. D. Corso, S. d. Gironcoli, P. Delugas, R. A. DiStasio, A. Ferretti, A. Floris, G. Fratesi, G. Fugallo, R. Gebauer, U. Gerstmann, F. Giustino, T. Gorni, J. Jia, M. Kawamura, H.-Y. Ko, A. Kokalj, E. Küçükbenli, M. Lazzeri, M. Marsili, N. Marzari, F. Mauri, N. L. Nguyen, H.-V. Nguyen, A. Otero-de-la-Roza, L. Paulatto, S. Poncé, D. Rocca, R. Sabatini, B. Santra, M. Schlipf, A. P. Seitsonen, A. Smogunov, I. Timrov, T. Thonhauser, P. Umari, N. Vast, X. Wu, and S. Baroni, *Advanced capabilities for materials modelling with Quantum ESPRESSO*, J. Phys. Condens. Matter **29**, 465901 (2017), arXiv:1709.10010. Cited on pages 2, 57, 73, 88, 96, 112, 116, and 164.

[41] X. Gonze, B. Amadon, G. Antonius, F. Arnardi, L. Baguet, J.-M. Beuken, J. Bieder, F. Bottin, J. Bouchet, E. Bousquet, N. Brouwer, F. Bruneval, G. Brunin, T. Cavignac, J.-B. Charraud, W. Chen, M. Côté, S. Cottenier, J. Denier, G. Geneste, P. Ghosez, M. Giantomassi, Y. Gillet, O. Gingras, D. R. Hamann, G. Hautier, X. He, N. Helbig, N. Holzwarth, Y. Jia, F. Jollet, W. Lafargue-Dit-Hauret, K. Lejaeghere, M. A. L. Marques, A. Martin, C. Martins, H. P. C. Miranda, F. Naccarato, K. Persson, G. Petretto, V. Planes, Y. Pouillon, S. Prokhorenko, F. Ricci, G.-M. Rignanese, A. H. Romero, M. M. Schmitt, M. Torrent, M. J. van Setten, B. Van Troeye, M. J. Verstraete, G. Zérah, and J. W. Zwanziger, *The Abinit project: Impact, environment and recent developments*, Comput. Phys. Commun. **248**, 107042 (2020). Cited on page 2.

[42] E. Ising, *Beitrag zur Theorie des Ferromagnetismus*, Z. Physik **31**, 253 (1925). Cited on page 2.

[43] W. Heisenberg, *Zur Theorie des Ferromagnetismus*, Z. Physik **49**, 619 (1928). Cited on page 2.

[44] T. Holstein, *Studies of polaron motion: Part I. The molecular-crystal model*, Ann. Phys. (N. Y.) **8**, 325 (1959). Cited on pages 2 and 41.

[45] P. W. Anderson, *Localized magnetic states in metals*, Phys. Rev. **124**, 41 (1961). Cited on pages 2 and 43.

[46] G. Kotliar, S. Y. Savrasov, K. Haule, V. S. Oudovenko, O. Parcollet, and C. A. Marianetti, *Electronic structure calculations with dynamical mean-field theory*, Rev. Mod. Phys. **78**, 865 (2006), arXiv:cond-mat/0511085. Cited on pages 2 and 43.

[47] M. Imada and T. Miyake, *Electronic structure calculation by first principles for strongly correlated electron systems*, J. Phys. Soc. Jpn. **79**, 112001 (2010), arXiv:1009.3851. Cited on page 2.

[48] F. Aryasetiawan, M. Imada, A. Georges, G. Kotliar, S. Biermann, and A. I. Lichtenstein, *Frequency-dependent local interactions and low-energy effective models from electronic structure calculations*, Phys. Rev. B **70**, 195104 (2004), arXiv:cond-mat/0401620. Cited on pages 2, 7, 42, 82, and 99.

[49] F. Aryasetiawan, K. Karlsson, O. Jepsen, and U. Schönberger, *Calculations of Hubbard U from first-principles*, Phys. Rev. B **74**, 125106 (2006), arXiv:cond-mat/0603138. Cited on pages 2, 7, 42, and 82.

[50] Y. Nomura and R. Arita, *Ab initio downfolding for electron-phonon-coupled systems: Constrained density-functional perturbation theory*, Phys. Rev. B **92**, 245108 (2015), arXiv:1509.01138. Cited on pages 2, 3, 7, 21, 26, 68, 82, 91, 96, 99, 100, 112, and 116.

[51] H. Wang, J. S. Tse, K. Tanaka, T. Iitaka, and Y. Ma, *Superconductive sodalite-like clathrate calcium hydride at high pressures*, Proc. Natl. Acad. Sci. USA **109**, 6463 (2012), arXiv:1203.0263. Cited on page 2.

[52] A. Cavalleri, *Photo-induced superconductivity*, Contemp. Phys. **59**, 31 (2018). Cited on pages 2, 97, and 113.

[53] P. Fazekas and E. Tosatti, *Electrical, structural and magnetic properties of pure and doped 1T-TaS_2*, Philos. Mag. B **39**, 229 (1979). Cited on pages 2, 57, and 71.

[54] L. P. Gor'kov and V. Z. Kresin, *Colloquium: High pressure and road to room temperature superconductivity*, Rev. Mod. Phys. **90**, 011001 (2018), arXiv:1802.02296. Cited on pages 3 and 97.

[55] N. W. Ashcroft, *Metallic hydrogen: A high-temperature superconductor?*, Phys. Rev. Lett. **21**, 1748 (1968). Cited on pages 3 and 97.

[56] A. P. Drozdov, M. I. Eremets, I. A. Troyan, V. Ksenofontov, and S. I. Shylin, *Conventional superconductivity at 203 kelvin at high pressures in the sulfur hydride system*, Nature **525**, 73 (2015), arXiv:1506.08190. Cited on page 3.

[57] A. P. Drozdov, P. P. Kong, V. S. Minkov, S. P. Besedin, M. A. Kuzovnikov, S. Mozaffari, L. Balicas, F. F. Balakirev, D. E. Graf, V. B. Prakapenka, E. Greenberg, D. A. Knyazev, M. Tkacz, and M. I. Eremets, *Superconductivity at 250 K in lanthanum hydride under high pressures*, Nature **569**, 528 (2019), arXiv:1812.01561. Cited on pages 3, 50, and 97.

[58] J. G. Bednorz and K. A. Müller, *Possible high-T_c superconductivity in the Ba–La–Cu–O system*, Z. Phys. B **64**, 189 (1986). Cited on pages 3, 50, 97, and 113.

[59] E. Fradkin, S. A. Kivelson, and J. M. Tranquada, *Colloquium: Theory of intertwined orders in high temperature superconductors*, Rev. Mod. Phys. **87**, 457 (2015), arXiv:1407.4480. Cited on pages 3, 44, 45, 97, 104, and 113.

[60] P. Fazekas and E. Tosatti, *Charge carrier localization in pure and doped 1T-TaS_2*, Physica B+C **99**, 183 (1980). Cited on pages 3 and 71.

[61] Y. Nomura, S. Sakai, M. Capone, and R. Arita, *Exotics-wave superconductivity in alkali-doped fullerides*, J. Phys. Condens. Matter **28**, 153001 (2016), arXiv:1512.05755. Cited on pages 3 and 26.

[62] Y. Nomura, *Ab Initio Studies on Superconductivity in Alkali-Doped Fullerides* (Springer Singapore, 2016). Cited on pages 3 and 26.

[63] R. Arita, T. Koretsune, S. Sakai, R. Akashi, Y. Nomura, and W. Sano, *Nonempirical calculation of superconducting transition temperatures in light-element superconductors*, Adv. Mater. **29**, 1602421 (2017). Cited on pages 3 and 26.

[64] O. Gunnarsson, T. Schäfer, J. P. F. LeBlanc, E. Gull, J. Merino, G. Sangiovanni, G. Rohringer, and A. Toschi, *Fluctuation diagnostics of the electron self-energy: Origin of the pseudogap physics*, Phys. Rev. Lett. **114**, 236402 (2015), arXiv:1411.6947. Cited on pages 3, 62, 98, 101, and 113.

[65] O. Gunnarsson, T. Schäfer, J. P. F. LeBlanc, J. Merino, G. Sangiovanni, G. Rohringer, and A. Toschi, *Parquet decomposition calculations of the electronic self-energy*, Phys. Rev. B **93**, 245102 (2016), arXiv:1604.01614. Cited on pages 3, 62, and 98.

[66] M. Born and R. Oppenheimer, *Zur Quantentheorie der Molekeln*, Ann. Phys. **389**, 457 (1927). Cited on pages 6 and 73.

[67] G. Czycholl, *Theoretische Festkörperphysik: Von den klassischen Modellen zu modernen Forschungsthemen*, 3rd ed. (Springer, Berlin, Heidelberg, 2008). Cited on pages 6, 8, 19, 141, 142, and 144.

[68] R. O. Jones, *Density functional theory: Its origins, rise to prominence, and future*, Rev. Mod. Phys. **87**, 897 (2015). Cited on pages 8 and 9.

[69] E. Runge and E. K. U. Gross, *Density-functional theory for time-dependent systems*, Phys. Rev. Lett. **52**, 997 (1984). Cited on page 8.

[70] L. H. Thomas, *The calculation of atomic fields*, Math. Proc. Camb. Philos. Soc. **23**, 542 (1927). Cited on page 9.

[71] E. Fermi, *Un metodo statistico per la determinazione di alcune proprietà dell'atomo*, Rend. Lincei **6**, 602 (1927). Cited on page 9.

[72] J. F. Janak, *Proof that $\partial E/\partial n_i = \varepsilon_i$ in density-functional theory*, Phys. Rev. B **18**, 7165 (1978). Cited on page 10.

[73] T. Koopmans, *Über die Zuordnung von Wellenfunktionen und Eigenwerten zu den einzelnen Elektronen eines Atoms*, Physica **1**, 104 (1934). Cited on page 10.

[74] J. P. Perdew and A. Zunger, *Self-interaction correction to density-functional approximations for many-electron systems*, Phys. Rev. B **23**, 5048 (1981). Cited on page 11.

[75] J. P. Perdew, K. Burke, and M. Ernzerhof, *Generalized gradient approximation made simple*, Phys. Rev. Lett. **77**, 3865 (1996). Cited on pages 11, 73, 88, 96, 112, and 163.

[76] J. P. Perdew, K. Burke, and M. Ernzerhof, *Generalized gradient approximation made simple [Phys. Rev. Lett. 77, 3865 (1996)]*, Phys. Rev. Lett. **78**, 1396 (1997). Cited on pages 11, 73, 88, 96, 112, and 163.

[77] C. Herring, *A new method for calculating wave functions in crystals*, Phys. Rev. **57**, 1169 (1940). Cited on page 11.

[78] J. C. Phillips and L. Kleinman, *New method for calculating wave functions in crystals and molecules*, Phys. Rev. **116**, 287 (1959). Cited on page 11.

[79] N. Troullier and J. L. Martins, *Efficient pseudopotentials for plane-wave calculations*, Phys. Rev. B **43**, 1993 (1991). Cited on pages 12 and 163.

[80] D. R. Hamann, M. Schlüter, and C. Chiang, *Norm-conserving pseudopotentials*, Phys. Rev. Lett. **43**, 1494 (1979). Cited on page 12.

[81] L. Kleinman and D. M. Bylander, *Efficacious form for model pseudopotentials*, Phys. Rev. Lett. **48**, 1425 (1982). Cited on page 12.

[82] Y. S. Lee, W. C. Ermler, and K. S. Pitzer, *Ab initio effective core potentials including relativistic effects. I. Formalism and applications to the Xe and Au atoms*, J. Chem. Phys. **67**, 5861 (1977). Cited on page 12.

[83] L. Kleinman, *Relativistic norm-conserving pseudopotential*, Phys. Rev. B **21**, 2630 (1980). Cited on page 12.

[84] J. C. Slater and G. F. Koster, *Simplified LCAO method for the periodic potential problem*, Phys. Rev. **94**, 1498 (1954). Cited on page 13.

[85] W. A. Harrison, *Elementary Electronic Structure*, rev. ed. (World Scientific, Singapore, 2004). Cited on pages 13 and 40.

[86] J. Berges, E. G. C. P. van Loon, A. Schobert, M. Rösner, and T. O. Wehling, *Ab initio phonon self-energies and fluctuation diagnostics of phonon anomalies: Lattice instabilities from Dirac pseudospin physics in transition metal dichalcogenides*, Phys. Rev. B **101**, 155107 (2020), arXiv:1911.02450. Cited on pages 17, 26, 40, 62, 97, and 166.

[87] G. H. Wannier, *The structure of electronic excitation levels in insulating crystals*, Phys. Rev. **52**, 191 (1937). Cited on page 18.

[88] P.-O. Löwdin, *On the non-orthogonality problem connected with the use of atomic wave functions in the theory of molecules and crystals*, J. Chem. Phys. **18**, 365 (1950). Cited on page 18.

[89] N. Marzari and D. Vanderbilt, *Maximally localized generalized Wannier functions for composite energy bands*, Phys. Rev. B **56**, 12847 (1997), arXiv:cond-mat/9707145. Cited on pages 18, 120, and 143.

[90] N. Marzari, A. A. Mostofi, J. R. Yates, I. Souza, and D. Vanderbilt, *Maximally localized Wannier functions: Theory and applications*, Rev. Mod. Phys. **84**, 1419 (2012), arXiv:1112.5411. Cited on pages 18, 120, and 143.

[91] I. Souza, N. Marzari, and D. Vanderbilt, *Maximally localized Wannier functions for entangled energy bands*, Phys. Rev. B **65**, 035109 (2001), arXiv:cond-mat/0108084. Cited on pages 18, 120, and 143.

[92] A. A. Mostofi, J. R. Yates, Y.-S. Lee, I. Souza, D. Vanderbilt, and N. Marzari, *wannier90: A tool for obtaining maximally-localised Wannier functions*, Comput. Phys. Commun. **178**, 685 (2008), arXiv:0708.0650. Cited on pages 18, 74, 88, 96, 112, 120, 143, 158, and 164.

[93] A. A. Mostofi, J. R. Yates, G. Pizzi, Y.-S. Lee, I. Souza, D. Vanderbilt, and N. Marzari, *An updated version of wannier90: A tool for obtaining maximally-localised Wannier functions*, Comput. Phys. Commun. **185**, 2309 (2014). Cited on pages 18, 74, 96, 112, 120, 158, and 164.

[94] G. Pizzi, V. Vitale, R. Arita, S. Blügel, F. Freimuth, G. Géranton, M. Gibertini, D. Gresch, C. Johnson, T. Koretsune, J. Ibañez Azpiroz, H. Lee, J.-M. Lihm, D. Marchand, A. Marrazzo, Y. Mokrousov, J. I. Mustafa, Y. Nohara, Y. Nomura, L. Paulatto, S. Poncé, T. Ponweiser, J. Qiao, F. Thöle, S. S. Tsirkin, M. Wierzbowska, N. Marzari, D. Vanderbilt, I. Souza, A. A. Mostofi, and J. R. Yates, *Wannier90 as a community code: New features and applications*, J. Phys. Condens. Matter **32**, 165902 (2020). Cited on pages 18, 74, 96, 112, 120, 143, 158, and 164.

[95] J. Bardeen, L. N. Cooper, and J. R. Schrieffer, *Microscopic theory of superconductivity*, Phys. Rev. **106**, 162 (1957). Cited on pages 19 and 50.

[96] D. E. Moncton, J. D. Axe, and F. J. DiSalvo, *Study of superlattice formation in 2H-$NbSe_2$ and 2H-$TaSe_2$ by neutron scattering*, Phys. Rev. Lett. **34**, 734 (1975). Cited on pages 19, 44, 82, and 83.

[97] J.-H. Lee, Y.-C. Hsue, and A. J. Freeman, *Magnetically induced variations in phonon frequencies*, Phys. Rev. B **73**, 172405 (2006). Cited on page 19.

[98] J. M. Skelton, L. A. Burton, S. C. Parker, A. Walsh, C.-E. Kim, A. Soon, J. Buckeridge, A. A. Sokol, C. R. A. Catlow, A. Togo, and I. Tanaka, *Anharmonicity in the high-temperature Cmcm phase of SnSe: Soft modes and three-phonon interactions*, Phys. Rev. Lett. **117**, 075502 (2016), arXiv:1602.03762. Cited on page 19.

[99] V. J. Gokhale and M. Rais-Zadeh, *Phonon-electron interactions in piezoelectric semiconductor bulk acoustic wave resonators*, Sci. Rep. **4**, 1 (2014). Cited on page 19.

[100] A. A. Maradudin and S. H. Vosko, *Symmetry properties of the normal vibrations of a crystal*, Rev. Mod. Phys. **40**, 1 (1968). Cited on page 19.

[101] F. Giustino, *Electron-phonon interactions from first principles*, Rev. Mod. Phys. **89**, 015003 (2017), arXiv:1603.06965. Cited on pages 20, 38, 64, 65, and 66.

[102] R. Heid, *Density functional perturbation theory and electron phonon coupling*, in *Emergent Phenomena in Correlated Matter*, edited by E. Pavarini, E. Koch, and U. Schollwöck (Forschungszentrum Jülich, Jülich, 2013). Cited on pages 21 and 64.

[103] X. Gonze and J.-P. Vigneron, *Density-functional approach to nonlinear-response coefficients of solids*, Phys. Rev. B **39**, 13120 (1989). Cited on page 21.

[104] N. E. Zein, *Density functional calculations of elastic moduli and phonon spectra of crystals*, Sov. Phys. Solid State **26**, 1825 (1984). Cited on page 21.

[105] S. Baroni, P. Giannozzi, and A. Testa, *Green's-function approach to linear response in solids*, Phys. Rev. Lett. **58**, 1861 (1987). Cited on pages 21 and 24.

[106] S. Baroni, S. de Gironcoli, A. Dal Corso, and P. Giannozzi, *Phonons and related crystal properties from density-functional perturbation theory*, Rev. Mod. Phys. **73**, 515 (2001), arXiv:cond-mat/0012092. Cited on pages 21, 26, 73, and 99.

[107] I. Timrov, N. Marzari, and M. Cococcioni, *Hubbard parameters from density-functional perturbation theory*, Phys. Rev. B **98**, 085127 (2018), arXiv:1805.01805. Cited on page 21.

[108] R. M. Sternheimer, *Electronic polarizabilities of ions from the Hartree-Fock wave functions*, Phys. Rev. **96**, 951 (1954). Cited on pages 22 and 25.

[109] S. de Gironcoli, *Lattice dynamics of metals from density-functional perturbation theory*, Phys. Rev. B **51**, 6773 (1995). Cited on page 24.

[110] F. Giustino, M. L. Cohen, and S. G. Louie, *GW method with the self-consistent Sternheimer equation*, Phys. Rev. B **81**, 115105 (2010), arXiv:0912.3087. Cited on page 25.

[111] J. Hall, N. Ehlen, J. Berges, E. van Loon, C. van Efferen, C. Murray, M. Rösner, J. Li, B. V. Senkovskiy, M. Hell, M. Rolf, T. Heider, M. C. Asensio, J. Avila, L. Plucinski, T. Wehling, A. Grüneis, and T. Michely, *Environmental control of charge density wave order in monolayer 2H-TaS_2*, ACS Nano **13**, 10210 (2019). Cited on pages 26, 57, 62, 82, 83, 89, 90, 93, 100, 104, 149, and 166.

[112] S.-F. Wang, H.-L. Zhang, and X.-Z. Wu, *A new rotation sum rule for the atomic force constants*, J. Phys. Condens. Matter **19**, 386233 (2007). Cited on pages 30, 31, and 33.

[113] R. A. Jishi, L. Venkataraman, M. S. Dresselhaus, and G. Dresselhaus, *Phonon modes in carbon nanotubules*, Chem. Phys. Lett. **209**, 77 (1993). Cited on page 31.

[114] R. Sahoo and R. R. Mishra, *Phonon dispersion of graphene revisited*, J. Exp. Theor. Phys. **114**, 805 (2012). Cited on page 31.

[115] L. Wirtz and A. Rubio, *The phonon dispersion of graphite revisited*, Solid State Commun. **131**, 141 (2004), arXiv:cond-mat/0404637. Cited on page 31.

[116] A. Molina-Sánchez and L. Wirtz, *Phonons in single-layer and few-layer MoS_2 and WS_2*, Phys. Rev. B **84**, 155413 (2011), arXiv:1109.5499. Cited on page 32.

[117] R. S. Mulliken, *Report on notation for the spectra of polyatomic molecules*, J. Chem. Phys. **23**, 1997 (1955). Cited on page 32.

[118] K. C. Molloy, *Group Theory for Chemists: Fundamental Theory and Applications*, 2nd ed. (Woodhead Publishing, Cambridge, 2013). Cited on page 32.

[119] M. Born and K. Huang, *Dynamical Theory of Crystal Lattices* (Clarendon, Oxford, 1954). Cited on page 33.

[120] D. C. Gazis and R. F. Wallis, *Conditions for rotational invariance of a harmonic lattice*, Phys. Rev. **151**, 578 (1966). Cited on page 33.

[121] L. Elcoro and J. Etxebarria, *Common misconceptions about the dynamical theory of crystal lattices: Cauchy relations, lattice potentials and infinite crystals*, Eur. J. Phys. **32**, 25 (2011). Cited on page 33.

[122] J.-W. Jiang, B.-S. Wang, J.-S. Wang, and H. S. Park, *A review on the flexural mode of graphene: Lattice dynamics, thermal conduction, thermal expansion, elasticity and nanomechanical resonance*, J. Phys. Condens. Matter **27**, 083001 (2015), arXiv:1408.1450. Cited on page 33.

[123] S. K. Sarkar and S. Sengupta, *On Born-Huang invariance conditions*, Phys. Status Solidi B **83**, 263 (1977). Cited on page 33.

[124] E. Schmidt, *Zur Theorie der linearen und nichtlinearen Integralgleichungen*, Math. Ann. **63**, 433 (1907). Cited on page 34.

[125] J. Carrete, W. Li, L. Lindsay, D. A. Broido, L. J. Gallego, and N. Mingo, *Physically founded phonon dispersions of few-layer materials and the case of borophene*, Mater. Res. Lett. **4**, 204 (2016), arXiv:1601.02884. Cited on page 34.

[126] J. Goldstone, *Field theories with «superconductor» solutions*, Nuovo Cim. **19**, 154 (1961). Cited on page 34.

[127] Y. Nambu, *Quasi-particles and gauge invariance in the theory of superconductivity*, Phys. Rev. **117**, 648 (1960). Cited on pages 34 and 51.

[128] H. Georgi, *The Physics of Waves* (Prentice Hall, New Jersey, 1993). Cited on page 34.

[129] M. Calandra, G. Profeta, and F. Mauri, *Adiabatic and nonadiabatic phonon dispersion in a Wannier function approach*, Phys. Rev. B **82**, 165111 (2010), arXiv:1007.2098. Cited on pages 35 and 101.

[130] C. M. Varma, E. I. Blount, P. Vashishta, and W. Weber, *Electron-phonon interactions in transition metals*, Phys. Rev. B **19**, 6130 (1979). Cited on pages 38, 39, 40, 103, 107, and 108.

[131] N. Vukmirović and L.-W. Wang, *Quantum dots: Theory*, in *Comprehensive Nanoscience and Technology* (Academic Press, Amsterdam, 2011). Cited on page 39.

[132] F. Guinea, M. I. Katsnelson, and A. K. Geim, *Energy gaps and a zero-field quantum Hall effect in graphene by strain engineering*, Nat. Phys. **6**, 30 (2010), arXiv:0909.1787. Cited on page 40.

[133] S. Froyen and W. A. Harrison, *Elementary prediction of linear combination of atomic orbitals matrix elements*, Phys. Rev. B **20**, 2420 (1979). Cited on page 40.

[134] K. Rossnagel, *On the origin of charge-density waves in select layered transition-metal dichalcogenides*, J. Phys. Condens. Matter **23**, 213001 (2011). Cited on pages 40, 45, 98, and 107.

[135] F. Flicker and J. van Wezel, *Charge order from orbital-dependent coupling evidenced by $NbSe_2$*, Nat. Commun. **6**, 7034 (2015), arXiv:1502.06816. Cited on pages 40, 98, 101, 103, 107, and 108.

[136] F. Flicker and J. van Wezel, *Charge order in $NbSe_2$*, Phys. Rev. B **94**, 235135 (2016), arXiv:1609.03521. Cited on pages 40, 82, and 83.

[137] H. Fröhlich, *Electrons in lattice fields*, Adv. Phys. **3**, 325 (1954). Cited on page 41.

[138] F. Giustino, M. L. Cohen, and S. G. Louie, *Electron-phonon interaction using Wannier functions*, Phys. Rev. B **76**, 165108 (2007). Cited on pages 41, 66, 96, 100, 112, 120, 143, 161, and 164.

[139] J. Noffsinger, F. Giustino, B. D. Malone, C.-H. Park, S. G. Louie, and M. L. Cohen, *EPW: A program for calculating the electron–phonon coupling using maximally localized Wannier functions*, Comput. Phys. Commun. **181**, 2140 (2010), arXiv:1005.4418. Cited on pages 41, 96, 112, 120, 143, 161, and 164.

[140] S. Poncé, E. Margine, C. Verdi, and F. Giustino, *EPW: Electron–phonon coupling, transport and superconducting properties using maximally localized Wannier functions*, Comput. Phys. Commun. **209**, 116 (2016), arXiv:1604.03525. Cited on pages 41, 96, 112, 120, 161, 162, and 164.

[141] D. Bohm and D. Pines, *A collective description of electron interactions. I. Magnetic interactions*, Phys. Rev. **82**, 625 (1951). Cited on pages 42 and 63.

[142] D. Pines and D. Bohm, *A collective description of electron interactions: II. Collective vs individual particle aspects of the interactions*, Phys. Rev. **85**, 338 (1952). Cited on pages 42 and 63.

[143] D. Bohm and D. Pines, *A collective description of electron interactions: III. Coulomb interactions in a degenerate electron gas*, Phys. Rev. **92**, 609 (1953). Cited on pages 42 and 63.

[144] D. Pines, *A collective description of electron interactions: IV. Electron interaction in metals*, Phys. Rev. **92**, 626 (1953). Cited on pages 42 and 63.

[145] M. Gell-Mann and K. A. Brueckner, *Correlation energy of an electron gas at high density*, Phys. Rev. **106**, 364 (1957). Cited on pages 42 and 63.

[146] X. Ren, P. Rinke, C. Joas, and M. Scheffler, *Random-phase approximation and its applications in computational chemistry and materials science*, J. Mater. Sci. **47**, 7447 (2012), arXiv:1203.5536. Cited on pages 42 and 63.

[147] J. Lindhard, *On the properties of a gas of charged particles*, Dan. Mat. Fys. Medd. **28**, 8 (1954). Cited on page 42.

[148] H. Bruus and K. Flensberg, *Many-Body Quantum Theory in Condensed Matter Physics: An Introduction* (Oxford University Press, New York, 2004). Cited on pages 42 and 63.

[149] M. Rösner, C. Steinke, M. Lorke, C. Gies, F. Jahnke, and T. O. Wehling, *Two-dimensional heterojunctions from nonlocal manipulations of the interactions*, Nano Lett. **16**, 2322 (2016). Cited on pages 42, 57, and 60.

[150] E. G. C. P. van Loon, M. Schüler, D. Springer, G. Sangiovanni, J. M. Tomczak, and T. O. Wehling, *Coulomb engineering of two-dimensional Mott materials*, arXiv:2001.01735 (2020). Cited on page 43.

[151] A. Georges, G. Kotliar, W. Krauth, and M. J. Rozenberg, *Dynamical mean-field theory of strongly correlated fermion systems and the limit of infinite dimensions*, Rev. Mod. Phys. **68**, 13 (1996). Cited on pages 43 and 74.

[152] W. Metzner and D. Vollhardt, *Correlated lattice fermions in $d = \infty$ dimensions*, Phys. Rev. Lett. **62**, 324 (1989). Cited on page 43.

[153] D. Vollhardt, *Dynamical mean-field theory of electronic correlations in models and materials*, AIP Conf. Proc. **1297**, 339 (2010), arXiv:1004.5069. Cited on page 43.

[154] N. Parragh, A. Toschi, K. Held, and G. Sangiovanni, *Conserved quantities of SU(2)-invariant interactions for correlated fermions and the advantages for quantum Monte Carlo simulations*, Phys. Rev. B **86**, 155158 (2012), arXiv:1209.0915. Cited on pages 43, 74, and 79.

[155] M. Wallerberger, A. Hausoel, P. Gunacker, A. Kowalski, N. Parragh, F. Goth, K. Held, and G. Sangiovanni, *w2dynamics: Local one- and two-particle quantities from dynamical mean field theory*, Comput. Phys. Commun. **235**, 388 (2019), arXiv:1801.10209. Cited on pages 43 and 79.

[156] W. H. Appelt, A. Östlin, I. Di Marco, I. Leonov, M. Sekania, D. Vollhardt, and L. Chioncel, *Lattice dynamics of palladium in the presence of electronic correlations*, Phys. Rev. B **101**, 075120 (2020), arXiv:1711.01493. Cited on page 43.

[157] A. M. Gabovich, A. I. Voitenko, and M. Ausloos, *Charge- and spin-density waves in existing superconductors: Competition between Cooper pairing and Peierls or excitonic instabilities*, Phys. Rep. **367**, 583 (2002). Cited on page 44.

[158] M. M. Ugeda, A. J. Bradley, Y. Zhang, S. Onishi, Y. Chen, W. Ruan, C. Ojeda-Aristizabal, H. Ryu, M. T. Edmonds, H.-Z. Tsai, A. Riss, S.-K. Mo, D. Lee, A. Zettl, Z. Hussain, Z.-X. Shen, and M. F. Crommie, *Characterization of collective ground states in single-layer $NbSe_2$*, Nat. Phys. **12**, 92 (2016), arXiv:1506.08460. Cited on pages 44, 72, 76, 82, 83, and 98.

[159] I. Esterlis, B. Nosarzewski, E. W. Huang, B. Moritz, T. P. Devereaux, D. J. Scalapino, and S. A. Kivelson, *Breakdown of the Migdal-Eliashberg theory: A determinant quantum Monte Carlo study*, Phys. Rev. B **97**, 140501 (2018), arXiv:1711.01493. Cited on page 44.

[160] P. M. Coelho, K. Nguyen Cong, M. Bonilla, S. Kolekar, M.-H. Phan, J. Avila, M. C. Asensio, I. I. Oleynik, and M. Batzill, *Charge density wave state suppresses ferromagnetic ordering in VSe_2 monolayers*, J. Phys. Chem. C **123**, 14089 (2019). Cited on page 44.

[161] A. O. Fumega, M. Gobbi, P. Dreher, W. Wan, C. González-Orellana, M. Peña Díaz, C. Rogero, J. Herrero-Martín, P. Gargiani, M. Ilyn, M. M. Ugeda, V. Pardo, and S. Blanco-Canosa, *Absence of ferromagnetism in VSe_2 caused by its charge density wave phase*, J. Phys. Chem. C **123**, 27802 (2019), arXiv:1907.02034. Cited on page 44.

[162] S. K. Chan and V. Heine, *Spin density wave and soft phonon mode from nesting Fermi surfaces*, J. Phys. F: Met. Phys. **3**, 795 (1973). Cited on pages 44 and 46.

[163] B. Sipos, A. F. Kusmartseva, A. Akrap, H. Berger, L. Forró, and E. Tutiš, *From Mott state to superconductivity in 1T-TaS_2*, Nat. Mater. **7**, 960 (2008). Cited on page 44.

[164] F. Zheng and J. Feng, *Electron-phonon coupling and the coexistence of superconductivity and charge-density wave in monolayer $NbSe_2$*, Phys. Rev. B **99**, 161119 (2019), arXiv:1904.03672. Cited on pages 44 and 48.

[165] T. Kiss, T. Yokoya, A. Chainani, S. Shin, T. Hanaguri, M. Nohara, and H. Takagi, *Charge-order-maximized momentum-dependent superconductivity*, Nat. Phys. **3**, 720 (2007). Cited on pages 44 and 98.

[166] Q. Zhang, L.-Y. Gan, Y. Cheng, and U. Schwingenschlögl, *Spin polarization driven by a charge-density wave in monolayer 1T-TaS_2*, Phys. Rev. B **90**, 081103 (2014). Cited on page 44.

[167] M. Calandra, *Phonon-assisted magnetic Mott-insulating state in the charge density wave phase of single-layer 1T-$NbSe_2$*, Phys. Rev. Lett. **121**, 026401 (2018), arXiv:1803.08361. Cited on pages 44 and 71.

[168] D. Pasquier and O. V. Yazyev, *Charge density wave phase, Mottness, and ferromagnetism in monolayer 1T-$NbSe_2$*, Phys. Rev. B **98**, 045114 (2018), arXiv:1803.10727. Cited on pages 44 and 71.

[169] D. Bansal, J. L. Niedziela, S. Calder, T. Lanigan-Atkins, R. Rawl, A. H. Said, D. L. Abernathy, A. I. Kolesnikov, H. Zhou, and O. Delaire, *Magnetically driven phonon instability enables the metal–insulator transition in h-FeS*, Nat. Phys. , 1 (2020). Cited on page 44.

[170] E. Revolinsky, G. A. Spiering, and D. J. Beerntsen, *Superconductivity in the niobium-selenium system*, J. Phys. Chem. Solids **26**, 1029 (1965). Cited on page 44.

[171] R. Micnas, J. Ranninger, and S. Robaszkiewicz, *Superconductivity in narrow-band systems with local nonretarded attractive interactions*, Rev. Mod. Phys. **62**, 113 (1990). Cited on page 45.

[172] R. E. Peierls, *Quantum Theory of Solids* (Oxford University Press, London, 1955). Cited on pages 45, 46, and 102.

[173] G. Grüner, *The dynamics of charge-density waves*, Rev. Mod. Phys. **60**, 1129 (1988). Cited on page 45.

[174] R. Peierls, *More Surprises in Theoretical Physics* (Princeton University Press, New Jersey, 1991). Cited on pages 45 and 46.

[175] N. V. Smith, S. D. Kevan, and F. J. DiSalvo, *Band structures of the layer compounds 1T-TaS_2 and 2H-$TaSe_2$ in the presence of commensurate charge-density waves*, J. Phys. C: Solid State Phys. **18**, 3175 (1985). Cited on pages 46 and 71.

[176] C. Wang, B. Giambattista, C. G. Slough, R. V. Coleman, and M. A. Subramanian, *Energy gaps measured by scanning tunneling microscopy*, Phys. Rev. B **42**, 8890 (1990). Cited on pages 46, 98, and 100.

[177] J. A. Silva-Guillén, P. Ordejón, F. Guinea, and E. Canadell, *Electronic structure of 2H-$NbSe_2$ single-layers in the CDW state*, 2D Mater. **3**, 035028 (2016), arXiv:1603.09072. Cited on pages 46 and 98.

[178] P. Chen, W. W. Pai, Y.-H. Chan, V. Madhavan, M. Y. Chou, S.-K. Mo, A.-V. Fedorov, and T.-C. Chiang, *Unique gap structure and symmetry of the charge density wave in single-layer VSe_2*, Phys. Rev. Lett. **121**, 196402 (2018), arXiv:1811.05690. Cited on page 46.

[179] J. Feng, D. Biswas, A. Rajan, M. D. Watson, F. Mazzola, O. J. Clark, K. Underwood, I. Marković, M. McLaren, A. Hunter, D. M. Burn, L. B. Duffy, S. Barua, G. Balakrishnan, F. Bertran, P. Le Fèvre, T. K. Kim, G. van der Laan, T. Hesjedal, P. Wahl, and P. D. C. King, *Electronic structure and enhanced charge-density wave order of monolayer VSe_2*, Nano Lett. **18**, 4493 (2018). Cited on page 46.

[180] D. Kartoon, U. Argaman, and G. Makov, *Driving forces behind the distortion of one-dimensional monatomic chains: Peierls theorem revisited*, Phys. Rev. B **98**, 165429 (2018). Cited on page 46.

[181] M. D. Johannes and I. I. Mazin, *Fermi surface nesting and the origin of charge density waves in metals*, Phys. Rev. B **77**, 165135 (2008), arXiv:0708.1744. Cited on pages 46 and 105.

[182] M. D. Johannes, I. I. Mazin, and C. A. Howells, *Fermi-surface nesting and the origin of the charge-density wave in $NbSe_2$*, Phys. Rev. B **73**, 205102 (2006), arXiv:cond-mat/0510390. Cited on pages 46 and 98.

[183] M. Leroux, I. Errea, M. Le Tacon, S.-M. Souliou, G. Garbarino, L. Cario, A. Bosak, F. Mauri, M. Calandra, and P. Rodière, *Strong anharmonicity induces quantum melting of charge density wave in 2H-$NbSe_2$ under pressure*, Phys. Rev. B **92**, 140303 (2015), arXiv:1508.06463. Cited on page 47.

[184] P. B. Allen, T. Berlijn, D. A. Casavant, and J. M. Soler, *Recovering hidden bloch character: Unfolding electrons, phonons, and slabs*, Phys. Rev. B **87**, 085322 (2013), arXiv:1212.5702. Cited on page 47.

[185] M. Tomić, H. O. Jeschke, and R. Valentí, *Unfolding of electronic structure through induced representations of space groups: Application to Fe-based superconductors*, Phys. Rev. B **90**, 195121 (2014), arXiv:1408.2258. Cited on page 47.

[186] F. Zheng and P. Zhang, *Phonon unfolding: A program for unfolding phonon dispersions of materials*, Comput. Phys. Commun. **210**, 139 (2017), arXiv:1602.07030. Cited on page 47.

[187] H. Kamerlingh Onnes, *Further experiments with liquid helium. D. On the change of electrical resistance of pure metals at very low temperatures, etc. V. The disappearance of the resistance of mercury*, Proc. Kon. Ned. Akad. Wetensch. **14**, 113 (1911). Cited on page 49.

[188] D. van Delft and P. Kes, *The discovery of superconductivity*, Phys. Today **63**, 38 (2010). Cited on page 49.

[189] W. Meißner and R. Ochsenfeld, *Ein neuer Effekt bei Eintritt der Supraleitfähigkeit*, Sci. Nat. **21**, 787 (1933). Cited on page 49.

[190] F. London and H. London, *The electromagnetic equations of the supraconductor*, Proc. R. Soc. Lond. A **149**, 71 (1935). Cited on page 50.

[191] V. L. Ginzburg and L. D. Landau, *On the theory of superconductivity*, Zh. Eksp. Teor. Fiz. **20**, 1064 (1950). Cited on page 50.

[192] E. Maxwell, *Isotope effect in the superconductivity of mercury*, Phys. Rev. **78**, 477 (1950). Cited on page 50.

[193] C. A. Reynolds, B. Serin, W. H. Wright, and L. B. Nesbitt, *Superconductivity of isotopes of mercury*, Phys. Rev. **78**, 487 (1950). Cited on page 50.

[194] H. Fröhlich, *Theory of the superconducting state. I. The ground state at the absolute zero of temperature*, Phys. Rev. **79**, 845 (1950). Cited on page 50.

[195] H. Fröhlich, *Interaction of electrons with lattice vibrations*, Proc. R. Soc. Lond. A **215**, 291 (1952). Cited on page 50.

[196] L. N. Cooper, *Bound electron pairs in a degenerate Fermi gas*, Phys. Rev. **104**, 1189 (1956). Cited on page 50.

[197] J. Bardeen, L. N. Cooper, and J. R. Schrieffer, *Theory of superconductivity*, Phys. Rev. **108**, 1175 (1957). Cited on page 50.

[198] G. M. Eliashberg, *Interactions between electrons and lattice vibrations in a superconductor*, Sov. Phys. JETP **11**, 697 (1960). Cited on page 50.

[199] Y. Kamihara, H. Hiramatsu, M. Hirano, R. Kawamura, H. Yanagi, T. Kamiya, and H. Hosono, *Iron-based layered superconductor: LaOFeP*, J. Am. Chem. Soc. **128**, 10012 (2006). Cited on page 50.

[200] Y. Kamihara, T. Watanabe, M. Hirano, and H. Hosono, *Iron-based layered superconductor La[$O_{1-x}F_x$]FeAs ($x = 0.05$–0.12) with $T_c = 26$ K*, J. Am. Chem. Soc. **130**, 3296 (2008). Cited on pages 50, 97, and 113.

[201] P. B. Allen and B. Mitrović, *Theory of superconducting T_c*, in *Solid State Physics: Advances in Research and Applications*, edited by H. Ehrenreich, F. Seitz, and D. Turnbull (Academic Press, New York, London, 1982). Cited on page 50.

[202] L. Hedin, *New method for calculating the one-particle Green's function with application to the electron-gas problem*, Phys. Rev. **139**, A796 (1965). Cited on pages 50 and 73.

[203] L. P. Gor'kov, *On the energy spectrum of superconductors*, Sov. Phys. JETP **34**, 735 (1958). Cited on page 50.

[204] R. Akashi and R. Arita, *Density functional theory for superconductors with particle-hole asymmetric electronic structure*, Phys. Rev. B **88**, 014514 (2013), arXiv:1305.0390. Cited on page 51.

[205] J. Berges, *ebmb: Solve multiband Eliashberg equations*, bitbucket.org/berges/ebmb (2017). Cited on pages 51 and 122.

[206] J. Berges, *On the scope of McMillan's formula*, Master's thesis, Universität Bremen (2016). Cited on pages 51, 52, 55, and 122.

[207] P. B. Allen and R. C. Dynes, *Transition temperature of strong-coupled superconductors reanalyzed*, Phys. Rev. B **12**, 905 (1975). Cited on pages 51 and 55.

[208] C. S. Owen and D. J. Scalapino, *S-state instabilities for retarded interactions*, Physica **55**, 691 (1971). Cited on pages 52, 53, and 54.

[209] W. L. McMillan, *Transition temperature of strong-coupled superconductors*, Phys. Rev. **167**, 331 (1968). Cited on pages 52 and 53.

[210] R. C. Dynes, *McMillan's equation and the T_c of superconductors*, Solid State Commun. **10**, 615 (1972). Cited on page 52.

[211] P. Morel and P. W. Anderson, *Calculation of the superconducting state parameters with retarded electron-phonon interaction*, Phys. Rev. **125**, 1263 (1962). Cited on page 52.

[212] F. Marsiglio, *Eliashberg theory of the critical temperature and isotope effect. Dependence on bandwidth, band-filling, and direct Coulomb repulsion*, J. Low Temp. Phys. **87**, 659 (1992). Cited on pages 53 and 54.

[213] J. Berges, *ebbw: Solve Eliashberg equations for finite bandwidths*, bitbucket.org/berges/ebbw (2016). Cited on pages 54, 55, and 123.

[214] F. Marsiglio, *Eliashberg theory of superconductivity with repulsive Coulomb enhancement*, Physica C **160**, 305 (1989). Cited on page 54.

[215] J. P. Carbotte, *Properties of boson-exchange superconductors*, Rev. Mod. Phys. **62**, 1027 (1990). Cited on page 54.

[216] C. J. Humphreys, *Stem imaging of crystals and defects*, in *Introduction to Analytical Electron Microscopy*, edited by J. J. Hren, J. I. Goldstein, and D. C. Joy (Springer US, Boston, MA, 1979). Cited on page 56.

[217] N. Mounet, M. Gibertini, P. Schwaller, D. Campi, A. Merkys, A. Marrazzo, T. Sohier, I. E. Castelli, A. Cepellotti, G. Pizzi, and N. Marzari, *Two-dimensional materials from high-throughput computational exfoliation of experimentally known compounds*, Nat. Nanotechnol. **13**, 246 (2018), arXiv:1611.05234. Cited on pages 56 and 57.

[218] J. Zhou, L. Shen, M. D. Costa, K. A. Persson, S. P. Ong, P. Huck, Y. Lu, X. Ma, Y. Chen, H. Tang, and Y. P. Feng, *2DMatPedia, an open computational database of two-dimensional materials from top-down and bottom-up approaches*, Sci. Data **6**, 1 (2019). Cited on page 56.

[219] K. S. Novoselov, A. K. Geim, S. V. Morozov, D. Jiang, Y. Zhang, S. V. Dubonos, I. V. Grigorieva, and A. A. Firsov, *Electric field effect in atomically thin carbon films*, Science **306**, 666 (2004), arXiv:cond-mat/0410550. Cited on pages 56, 57, and 58.

[220] Y. Nakata, K. Sugawara, R. Shimizu, Y. Okada, P. Han, T. Hitosugi, K. Ueno, T. Sato, and T. Takahashi, *Monolayer 1T-$NbSe_2$ as a Mott insulator*, NPG Asia Mater. **8**, e321 (2016). Cited on pages 57, 72, 73, 75, 76, 80, and 151.

[221] P. Darancet, A. J. Millis, and C. A. Marianetti, *Three-dimensional metallic and two-dimensional insulating behavior in octahedral tantalum dichalcogenides*, Phys. Rev. B **90**, 045134 (2014), arXiv:1401.0246. Cited on pages 57, 72, and 75.

[222] S. Qiao, X. Li, N. Wang, W. Ruan, C. Ye, P. Cai, Z. Hao, H. Yao, X. Chen, J. Wu, Y. Wang, and Z. Liu, *Mottness collapse in 1T-$TaS_{2-x}Se_x$ transition-metal dichalcogenide: An interplay between localized and itinerant orbitals*, Phys. Rev. X **7**, 041054 (2017), arXiv:1611.08957. Cited on page 57.

[223] L. Wang, I. Gutiérrez-Lezama, C. Barreteau, N. Ubrig, E. Giannini, and A. F. Morpurgo, *Tuning magnetotransport in a compensated semimetal at the atomic scale*, Nat. Commun. **6**, 1 (2015), arXiv:1510.04827. Cited on pages 57 and 59.

[224] Y. Ma, Y. Dai, M. Guo, C. Niu, Y. Zhu, and B. Huang, *Evidence of the existence of magnetism in pristine VX_2 monolayers ($X = S, Se$) and their strain-induced tunable magnetic properties*, ACS Nano **6**, 1695 (2012). Cited on pages 57 and 82.

[225] G. Wexler and A. M. Woolley, *Fermi surfaces and band structures of the 2H metallic transition-metal dichalcogenides*, J. Phys. C: Solid State Phys. **9**, 1185 (1976). Cited on pages 57 and 98.

[226] Z. Zhang, L. Li, J. Horng, N. Z. Wang, F. Yang, Y. Yu, Y. Zhang, G. Chen, K. Watanabe, T. Taniguchi, X. H. Chen, F. Wang, and Y. Zhang, *Strain-modulated bandgap and piezo-resistive effect in black phosphorus field-effect transistors*, Nano Lett. **17**, 6097 (2017), arXiv:1701.08041. Cited on pages 57 and 60.

[227] K. F. Mak, C. Lee, J. Hone, J. Shan, and T. F. Heinz, *Atomically thin MoS_2: A new direct-gap semiconductor*, Phys. Rev. Lett. **105**, 136805 (2010), arXiv:1004.0546. Cited on pages 57, 58, and 71.

[228] A. Crepaldi, G. Autès, G. Gatti, S. Roth, A. Sterzi, G. Manzoni, M. Zacchigna, C. Cacho, R. T. Chapman, E. Springate, E. A. Seddon, P. Bugnon, A. Magrez, H. Berger, I. Vobornik, M. Kalläne, A. Quer, K. Rossnagel, F. Parmigiani, O. V. Yazyev, and M. Grioni, *Enhanced ultrafast relaxation rate in the Weyl semimetal phase of $MoTe_2$ measured by time- and angle-resolved photoelectron spectroscopy*, Phys. Rev. B **96**, 241408 (2017), arXiv:1709.09854. Cited on page 57.

[229] Q.-Y. Wang, Z. Li, W.-H. Zhang, Z.-C. Zhang, J.-S. Zhang, W. Li, H. Ding, Y.-B. Ou, P. Deng, K. Chang, J. Wen, C.-L. Song, K. He, J.-F. Jia, S.-H. Ji, Y.-Y. Wang, L.-L. Wang, X. Chen, X.-C. Ma, and Q.-K. Xue, *Interface-induced high-temperature superconductivity in single unit-cell FeSe films on $SrTiO_3$*, Chin. Phys. Lett. **29**, 037402 (2012), arXiv:1201.5694. Cited on page 57.

[230] S. Tan, Y. Zhang, M. Xia, Z. Ye, F. Chen, X. Xie, R. Peng, D. Xu, Q. Fan, H. Xu, J. Jiang, T. Zhang, X. Lai, T. Xiang, J. Hu, B. Xie, and D. Feng, *Interface-induced superconductivity and strain-dependent spin density waves in FeSe/$SrTiO_3$ thin films*, Nat. Mater. **12**, 634 (2013), arXiv:1301.2748. Cited on page 57.

[231] A. Kavokin and P. Lagoudakis, *Exciton-mediated superconductivity*, Nat. Mater. **15**, 599 (2016). Cited on page 57.

[232] G. Fiori, F. Bonaccorso, G. Iannaccone, T. Palacios, D. Neumaier, A. Seabaugh, S. K. Banerjee, and L. Colombo, *Electronics based on two-dimensional materials*, Nat. Nanotechnol. **9**, 768 (2014). Cited on pages 57 and 58.

[233] V. Buck, *Morphological properties of sputtered MoS_2 films*, Wear **91**, 281 (1983). Cited on page 57.

[234] T. Low, A. S. Rodin, A. Carvalho, Y. Jiang, H. Wang, F. Xia, and A. H. Castro Neto, *Tunable optical properties of multilayer black phosphorus thin films*, Phys. Rev. B **90**, 075434 (2014), arXiv:1404.4030. Cited on pages 57 and 60.

[235] H. Yu, G.-B. Liu, J. Tang, X. Xu, and W. Yao, *Moiré excitons: From programmable quantum emitter arrays to spin-orbit–coupled artificial lattices*, Sci. Adv. **3**, e1701696 (2017), arXiv:1710.07015. Cited on pages 57 and 60.

[236] J. Feng, H. Deschout, S. Caneva, S. Hofmann, I. Lončarić, P. Lazić, and A. Radenovic, *Imaging of optically active defects with nanometer resolution*, Nano Lett. **18**, 1739 (2018), arXiv:1706.06313. Cited on page 57.

[237] D. Xiao, G.-B. Liu, W. Feng, X. Xu, and W. Yao, *Coupled spin and valley physics in monolayers of MoS_2 and other group-VI dichalcogenides*, Phys. Rev. Lett. **108**, 196802 (2012), arXiv:1112.3144. Cited on pages 57, 59, and 108.

[238] H. Jeong, H. M. Oh, S. Bang, H. J. Jeong, S.-J. An, G. H. Han, H. Kim, S. J. Yun, K. K. Kim, J. C. Park, Y. H. Lee, G. Lerondel, and M. S. Jeong, *Metal–insulator–semiconductor diode consisting of two-dimensional nanomaterials*, Nano Lett. **16**, 1858 (2016). Cited on page 57.

[239] A. Allain, J. Kang, K. Banerjee, and A. Kis, *Electrical contacts to two-dimensional semiconductors*, Nat. Mater. **14**, 1195 (2015). Cited on page 57.

[240] S. Wachter, D. K. Polyushkin, O. Bethge, and T. Mueller, *A microprocessor based on a two-dimensional semiconductor*, Nat. Commun. **8**, 1 (2017), arXiv:1612.00965. Cited on page 57.

[241] J. Feng, M. Graf, K. Liu, D. Ovchinnikov, D. Dumcenco, M. Heiranian, V. Nandigana, N. R. Aluru, A. Kis, and A. Radenovic, *Single-layer MoS_2 nanopores as nanopower generators*, Nature **536**, 197 (2016). Cited on page 57.

[242] J. Han, J. Wang, M. Yang, X. Kong, X. Chen, Z. Huang, H. Guo, J. Gou, S. Tao, Z. Liu, Z. Wu, Y. Jiang, and X. Wang, *Graphene/organic semiconductor heterojunction phototransistors with broadband and bi-directional photoresponse*, Adv. Mater. **30**, 1804020 (2018). Cited on page 57.

[243] L. Li, Y. Yu, G. J. Ye, Q. Ge, X. Ou, H. Wu, D. Feng, X. H. Chen, and Y. Zhang, *Black phosphorus field-effect transistors*, Nat. Nanotechnol. **9**, 372 (2014), arXiv:1401.4117. Cited on pages 57 and 60.

[244] X. Qian, J. Liu, L. Fu, and J. Li, *Quantum spin Hall effect in two-dimensional transition metal dichalcogenides*, Science **346**, 1344 (2014), arXiv:1406.2749. Cited on page 57.

[245] K. S. Novoselov, *Nobel lecture: Graphene: Materials in the flatland*, Rev. Mod. Phys. **83**, 837 (2011). Cited on pages 57 and 61.

[246] N. A. A. Zwaneveld, R. Pawlak, M. Abel, D. Catalin, D. Gigmes, D. Bertin, and L. Porte, *Organized formation of 2D extended covalent organic frameworks at surfaces*, J. Am. Chem. Soc. **130**, 6678 (2008). Cited on page 57.

[247] M. S. Ramzan, V. Bačić, Y. Jing, and A. Kuc, *Electronic properties of a new family of layered materials from groups 14 and 15: First-principles simulations*, J. Phys. Chem. C **123**, 25470 (2019). Cited on pages 57 and 160.

[248] T. Björkman, A. Gulans, A. V. Krasheninnikov, and R. M. Nieminen, *van der Waals bonding in layered compounds from advanced density-functional first-principles calculations*, Phys. Rev. Lett. **108**, 235502 (2012), arXiv:1204.3753. Cited on page 57.

[249] T. Sohier, M. Calandra, and F. Mauri, *Density functional perturbation theory for gated two-dimensional heterostructures: Theoretical developments and application to flexural phonons in graphene*, Phys. Rev. B **96**, 075448 (2017), arXiv:1705.04973. Cited on page 57.

[250] N. Balakrishnan, E. D. Steer, E. F. Smith, Z. R. Kudrynskyi, Z. D. Kovalyuk, L. Eaves, A. Patanè, and P. H. Beton, *Epitaxial growth of γ-InSe and α, β, and γ-In_2Se_3 on ϵ-GaSe*, 2D Mater. **5**, 035026 (2018). Cited on page 57.

[251] R. Höll, M. Kling, and E. Schroll, *Metallogenesis of germanium—a review*, Ore Geol. Rev. **30**, 145 (2007). Cited on page 57.

[252] A. Kuc, N. Zibouche, and T. Heine, *Influence of quantum confinement on the electronic structure of the transition metal sulfide TS_2*, Phys. Rev. B **83**, 245213 (2011), arXiv:1104.3670. Cited on page 57.

[253] S. Iijima, *Helical microtubules of graphitic carbon*, Nature **354**, 56 (1991). Cited on page 58.

[254] R. Nadiv, M. Shtein, A. Peled, and O. Regev, *WS_2 nanotube – reinforced cement: Dispersion matters*, Constr. Build. Mater. **98**, 112 (2015). Cited on page 58.

[255] F. Qin, W. Shi, T. Ideue, M. Yoshida, A. Zak, R. Tenne, T. Kikitsu, D. Inoue, D. Hashizume, and Y. Iwasa, *Superconductivity in a chiral nanotube*, Nat. Commun. **8**, 14465 (2017). Cited on page 58.

[256] E. Osawa, *Superaromaticity*, Kagaku **25**, 854 (1970). Cited on page 58.

[257] H. W. Kroto, J. R. Heath, S. C. O'Brien, R. F. Curl, and R. E. Smalley, *C_{60}: Buckminsterfullerene*, Nature **318**, 162 (1985). Cited on page 58.

[258] K. S. Novoselov, A. K. Geim, S. V. Morozov, D. Jiang, M. I. Katsnelson, I. V. Grigorieva, S. V. Dubonos, and A. A. Firsov, *Two-dimensional gas of massless Dirac fermions in graphene*, Nature **438**, 197 (2005), arXiv:cond-mat/0509330. Cited on pages 58 and 71.

[259] Y. Ma, A. Kuc, Y. Jing, P. Philipsen, and T. Heine, *Two-dimensional Haeckelite NbS_2: A diamagnetic high-mobility semiconductor with Nb^{4+} ions*, Angew. Chem. Int. Ed. **56**, 10214 (2017). Cited on page 59.

[260] H. Terrones and M. Terrones, *Electronic and vibrational properties of defective transition metal dichalcogenide Haeckelites: New 2D semi-metallic systems*, 2D Mater. **1**, 011003 (2014). Cited on page 59.

[261] N. Ubrig, S. Jo, M. Philippi, D. Costanzo, H. Berger, A. B. Kuzmenko, and A. F. Morpurgo, *Microscopic origin of the valley Hall effect in transition metal dichalcogenides revealed by wavelength-dependent mapping*, Nano Lett. **17**, 5719 (2017), arXiv:1708.06914. Cited on page 59.

[262] S. Tang, C. Zhang, D. Wong, Z. Pedramrazi, H.-Z. Tsai, C. Jia, B. Moritz, M. Claassen, H. Ryu, S. Kahn, J. Jiang, H. Yan, M. Hashimoto, D. Lu, R. G. Moore, C.-C. Hwang, C. Hwang, Z. Hussain, Y. Chen, M. M. Ugeda, Z. Liu, X. Xie, T. P. Devereaux, M. F. Crommie, S.-K. Mo, and Z.-X. Shen, *Quantum spin Hall state in monolayer $1T'$-WTe_2*, Nat. Phys. **13**, 683 (2017), arXiv:1703.03151. Cited on page 59.

[263] Z. Wang, L. Zhao, K. F. Mak, and J. Shan, *Probing the spin-polarized electronic band structure in monolayer transition metal dichalcogenides by optical spectroscopy*, Nano Lett. **17**, 740 (2017), arXiv:1702.05647. Cited on page 59.

[264] G. Wang, C. Robert, M. M. Glazov, F. Cadiz, E. Courtade, T. Amand, D. Lagarde, T. Taniguchi, K. Watanabe, B. Urbaszek, and X. Marie, *In-plane propagation of light in transition metal dichalcogenide monolayers: Optical selection rules*, Phys. Rev. Lett. **119**, 047401 (2017), arXiv:1704.05341. Cited on page 59.

[265] N. Lundt, S. Stoll, P. Nagler, A. Nalitov, S. Klembt, S. Betzold, J. Goddard, E. Frieling, A. V. Kavokin, C. Schüller, T. Korn, S. Höfling, and C. Schneider, *Observation of*

macroscopic valley-polarized monolayer exciton-polaritons at room temperature, Phys. Rev. B **96**, 241403 (2017), arXiv:1708.00313. Cited on page 59.

[266] A. Kormányos, V. Zólyomi, V. I. Fal'ko, and G. Burkard, *Tunable berry curvature and valley and spin Hall effect in bilayer MoS_2*, Phys. Rev. B **98**, 035408 (2018), arXiv:1804.06830. Cited on page 59.

[267] A. Steinhoff, M. Rösner, F. Jahnke, T. O. Wehling, and C. Gies, *Influence of excited carriers on the optical and electronic properties of MoS_2*, Nano Lett. **14**, 3743 (2014). Cited on page 60.

[268] A. Molina-Sánchez, D. Sangalli, L. Wirtz, and A. Marini, *Ab initio calculations of ultrashort carrier dynamics in two-dimensional materials: Valley depolarization in single-layer WSe_2*, Nano Lett. **17**, 4549 (2017), arXiv:1708.06568. Cited on page 60.

[269] I. L. Lyubchanskii, N. N. Dadoenkova, M. I. Lyubchanskii, T. Rasing, J.-W. Jeong, and S.-C. Shin, *Second-harmonic generation from realistic film–substrate interfaces: The effects of strain*, Appl. Phys. Lett. **76**, 1848 (2000). Cited on page 60.

[270] L. Mennel, M. Paur, and T. Mueller, *Second harmonic generation in strained transition metal dichalcogenide monolayers: MoS_2, $MoSe_2$, WS_2, and WSe_2*, APL Photonics **4**, 034404 (2018). Cited on page 60.

[271] A. Ziletti, A. Carvalho, P. E. Trevisanutto, D. K. Campbell, D. F. Coker, and A. H. Castro Neto, *Phosphorene oxides: Bandgap engineering of phosphorene by oxidation*, Phys. Rev. B **91**, 085407 (2015), arXiv:1410.3906. Cited on page 60.

[272] A. Ziletti, A. Carvalho, D. K. Campbell, D. F. Coker, and A. H. Castro Neto, *Oxygen defects in phosphorene*, Phys. Rev. Lett. **114**, 046801 (2015), arXiv:1407.5880. Cited on page 60.

[273] V. Artel, Q. Guo, H. Cohen, R. Gasper, A. Ramasubramaniam, F. Xia, and D. Naveh, *Protective molecular passivation of black phosphorus*, npj 2D Mater. Appl. **1**, 1 (2017). Cited on page 60.

[274] X. Duan, C. Wang, J. C. Shaw, R. Cheng, Y. Chen, H. Li, X. Wu, Y. Tang, Q. Zhang, A. Pan, J. Jiang, R. Yu, Y. Huang, and X. Duan, *Lateral epitaxial growth of two-dimensional layered semiconductor heterojunctions*, Nat. Nanotechnol. **9**, 1024 (2014). Cited on page 60.

[275] A. Pant, Z. Mutlu, D. Wickramaratne, H. Cai, R. K. Lake, C. Ozkan, and S. Tongay, *Fundamentals of lateral and vertical heterojunctions of atomically thin materials*, Nanoscale **8**, 3870 (2016). Cited on page 60.

[276] G. Eda, T. Fujita, H. Yamaguchi, D. Voiry, M. Chen, and M. Chhowalla, *Coherent atomic and electronic heterostructures of single-layer MoS_2*, ACS Nano **6**, 7311 (2012). Cited on page 60.

[277] A.-Y. Lu, H. Zhu, J. Xiao, C.-P. Chuu, Y. Han, M.-H. Chiu, C.-C. Cheng, C.-W. Yang, K.-H. Wei, Y. Yang, Y. Wang, D. Sokaras, D. Nordlund, P. Yang, D. A. Muller, M.-Y. Chou, X. Zhang, and L.-J. Li, *Janus monolayers of transition metal dichalcogenides*, Nat. Nanotechnol. **12**, 744 (2017). Cited on page 60.

[278] N. D. Mermin, *Crystalline order in two dimensions*, Phys. Rev. **176**, 250 (1968). Cited on page 61.

[279] H. Wagner, *Long-wavelength excitations and the Goldstone theorem in many-particle systems with "broken symmetries"*, Z. Physik **195**, 273 (1966). Cited on page 61.

[280] N. D. Mermin and H. Wagner, *Absence of ferromagnetism or antiferromagnetism in one- or two-dimensional isotropic Heisenberg models*, Phys. Rev. Lett. **17**, 1133 (1966). Cited on page 61.

[281] P. C. Hohenberg, *Existence of long-range order in one and two dimensions*, Phys. Rev. **158**, 383 (1967). Cited on page 61.

[282] V. L. Berezinskiĭ, *Destruction of long-range order in one-dimensional and two-dimensional systems having a continuous symmetry group I. Classical systems*, Sov. Phys. JETP **32**, 493 (1971). Cited on page 61.

[283] S. Coleman, *There are no Goldstone bosons in two dimensions*, Commun. Math. Phys. **31**, 259 (1973). Cited on page 61.

[284] M. V. Fischetti and W. G. Vandenberghe, *Mermin-Wagner theorem, flexural modes, and degraded carrier mobility in two-dimensional crystals with broken horizontal mirror symmetry*, Phys. Rev. B **93**, 155413 (2016), arXiv:1511.06796. Cited on page 61.

[285] A. K. Geim and K. S. Novoselov, *The rise of graphene*, Nat. Mater. **6**, 183 (2007). Cited on page 61.

[286] A. Fasolino, J. H. Los, and M. I. Katsnelson, *Intrinsic ripples in graphene*, Nat. Mater. **6**, 858 (2007), arXiv:0704.1793. Cited on page 61.

[287] M. I. Katsnelson, *Graphene: Carbon in two dimensions*, Mater. Today **10**, 20 (2007). Cited on page 61.

[288] D. R. Nelson and L. Peliti, *Fluctuations in membranes with crystalline and hexatic order*, J. Phys. France **48**, 1085 (1987). Cited on page 61.

[289] J. Berges, *elphmod: Python modules for electron–phonon models*, bitbucket.org/berges/elphmod (2017). Cited on pages 62, 121, and 126.

[290] M. Rösner, *Electronic Structure of Novel Two-dimensional Materials and Graphene Heterostructures*, Ph.D. thesis, Universität Bremen (2016). Cited on page 68.

[291] H. Shinaoka, M. Troyer, and P. Werner, *Accuracy of downfolding based on the constrained random-phase approximation*, Phys. Rev. B **91**, 245156 (2015), arXiv:1410.1276. Cited on page 69.

[292] C. Honerkamp, H. Shinaoka, F. F. Assaad, and P. Werner, *Limitations of constrained random phase approximation downfolding*, Phys. Rev. B **98**, 235151 (2018), arXiv:1809.03742. Cited on page 69.

[293] E. Kamil, J. Berges, G. Schönhoff, M. Rösner, M. Schüler, G. Sangiovanni, and T. O. Wehling, *Electronic structure of single layer 1T-$NbSe_2$: Interplay of lattice distortions, non-local exchange, and Mott–Hubbard correlations*, J. Phys. Condens. Matter **30**, 325601 (2018), arXiv:1804.03898. Cited on pages 71 and 166.

[294] M. Calandra, I. I. Mazin, and F. Mauri, *Effect of dimensionality on the charge-density wave in few-layer 2H-$NbSe_2$*, Phys. Rev. B **80**, 241108(R) (2009), arXiv:0910.0956. Cited on pages 71, 82, 83, and 98.

[295] Y. Yu, F. Yang, X. F. Lu, Y. J. Yan, Y.-H. Cho, L. Ma, X. Niu, S. Kim, Y.-W. Son, D. Feng, S. Li, S.-W. Cheong, X. H. Chen, and Y. Zhang, *Gate-tunable phase transitions in thin flakes of 1T-TaS_2*, Nat. Nanotechnol. **10**, 270 (2015), arXiv:1407.3480. Cited on pages 71, 72, and 104.

[296] J. Wilson, F. Di Salvo, and S. Mahajan, *Charge-density waves and superlattices in the metallic layered transition metal dichalcogenides*, Adv. Phys. **24**, 117 (1975). Cited on pages 71, 97, and 98.

[297] S. Yi, Z. Zhang, and J.-H. Cho, *Coupling of charge, lattice, orbital, and spin degrees of freedom in charge density waves in 1T-TaS_2*, Phys. Rev. B **97**, 041413 (2018), arXiv:1708.00213. Cited on page 71.

[298] O. R. Albertini, R. Zhao, R. L. McCann, S. Feng, M. Terrones, J. K. Freericks, J. A. Robinson, and A. Y. Liu, *Zone-center phonons of bulk, few-layer, and monolayer 1T-TaS_2: Detection of commensurate charge density wave phase through Raman scattering*, Phys. Rev. B **93**, 214109 (2016), arXiv:1511.04462. Cited on page 72.

[299] G. Kresse and J. Hafner, *Norm-conserving and ultrasoft pseudopotentials for first-row and transition elements*, J. Phys. Condens. Matter **6**, 8245 (1994). Cited on pages 73, 88, and 121.

[300] G. Kresse and D. Joubert, *From ultrasoft pseudopotentials to the projector augmented-wave method*, Phys. Rev. B **59**, 1758 (1999). Cited on pages 73, 88, and 121.

[301] A. V. Krukau, O. A. Vydrov, A. F. Izmaylov, and G. E. Scuseria, *Influence of the exchange screening parameter on the performance of screened hybrid functionals*, J. Chem. Phys. **125**, 224106 (2006). Cited on page 73.

[302] M. Shishkin and G. Kresse, *Implementation and performance of the frequency-dependent GW method within the PAW framework*, Phys. Rev. B **74**, 035101 (2006). Cited on page 73.

[303] J. Paier, R. Hirschl, M. Marsman, and G. Kresse, *The Perdew–Burke–Ernzerhof exchange-correlation functional applied to the G2-1 test set using a plane-wave basis set*, J. Chem. Phys. **122**, 234102 (2005). Cited on page 73.

[304] T. von Kármán and M. Born, *Über Schwingungen in Raumgittern*, Physik. Zeitschr. **13**, 297 (1912). Cited on page 73.

[305] A. Dal Corso, *Pseudopotentials periodic table: From H to Pu*, Comput. Mater. Sci. **95**, 337 (2014). Cited on pages 73, 154, 155, and 156.

[306] M. Methfessel and A. T. Paxton, *High-precision sampling for Brillouin-zone integration in metals*, Phys. Rev. B **40**, 3616 (1989). Cited on pages 73, 88, 147, 149, and 163.

[307] M. Kaltak, *Merging GW with DMFT*, Ph.D. thesis, Universität Wien (2015). Cited on page 74.

[308] V. I. Anisimov, A. I. Poteryaev, M. A. Korotin, A. O. Anokhin, and G. Kotliar, *First-principles calculations of the electronic structure and spectra of strongly correlated systems: Dynamical mean-field theory*, J. Phys. Condens. Matter **9**, 7359 (1997), arXiv:cond-mat/9704231. Cited on page 74.

[309] A. I. Lichtenstein and M. I. Katsnelson, *Ab initio calculations of quasiparticle band structure in correlated systems: LDA++ approach*, Phys. Rev. B **57**, 6884 (1998), arXiv:cond-mat/9707127. Cited on page 74.

[310] E. Gull, A. J. Millis, A. I. Lichtenstein, A. N. Rubtsov, M. Troyer, and P. Werner, *Continuous-time Monte Carlo methods for quantum impurity models*, Rev. Mod. Phys. **83**, 349 (2011), arXiv:1012.4474. Cited on page 74.

[311] N. V. Prokof'ev, B. V. Svistunov, and I. S. Tupitsyn, *Exact, complete, and universal continuous-time worldline Monte Carlo approach to the statistics of discrete quantum systems*, J. Exp. Theor. Phys. **87**, 310 (1998), arXiv:cond-mat/9703200. Cited on page 74.

[312] P. Gunacker, M. Wallerberger, E. Gull, A. Hausoel, G. Sangiovanni, and K. Held, *Continuous-time quantum Monte Carlo using worm sampling*, Phys. Rev. B **92**, 155102 (2015), arXiv:1506.01905. Cited on page 74.

[313] P. Gunacker, M. Wallerberger, T. Ribic, A. Hausoel, G. Sangiovanni, and K. Held, *Worm-improved estimators in continuous-time quantum Monte Carlo*, Phys. Rev. B **94**, 125153 (2016), arXiv:1607.01211. Cited on page 74.

[314] M. Schüler, O. E. Peil, G. J. Kraberger, R. Pordzik, M. Marsman, G. Kresse, T. O. Wehling, and M. Aichhorn, *Charge self-consistent many-body corrections using optimized projected localized orbitals*, J. Phys. Condens. Matter **30**, 475901 (2018), arXiv:1804.02055. Cited on page 74.

[315] P. E. Blöchl, *Projector augmented-wave method*, Phys. Rev. B **50**, 17953 (1994). Cited on pages 74 and 121.

[316] P. V. C. Medeiros, S. Stafström, and J. Björk, *Effects of extrinsic and intrinsic perturbations on the electronic structure of graphene: Retaining an effective primitive cell band structure by band unfolding*, Phys. Rev. B **89**, 041407 (2014). Cited on page 77.

[317] P. V. C. Medeiros, S. S. Tsirkin, S. Stafström, and J. Björk, *Unfolding spinor wave functions and expectation values of general operators: Introducing the unfolding-density operator*, Phys. Rev. B **91**, 041116 (2015), arXiv:1409.5343. Cited on page 77.

[318] M. T. Czyżyk and G. A. Sawatzky, *Local-density functional and on-site correlations: The electronic structure of La_2CuO_4 and $LaCuO_3$*, Phys. Rev. B **49**, 14211 (1994). Cited on page 79.

[319] J. Zaanen, G. A. Sawatzky, and J. W. Allen, *Band gaps and electronic structure of transition-metal compounds*, Phys. Rev. Lett. **55**, 418 (1985). Cited on page 80.

[320] L. Perfetti, P. A. Loukakos, M. Lisowski, U. Bovensiepen, H. Berger, S. Biermann, P. S. Cornaglia, A. Georges, and M. Wolf, *Time evolution of the electronic structure of 1T-TaS_2 through the insulator-metal transition*, Phys. Rev. Lett. **97**, 067402 (2006). Cited on pages 80 and 98.

[321] J. K. Freericks, H. R. Krishnamurthy, Y. Ge, A. Y. Liu, and T. Pruschke, *Theoretical description of time-resolved pump/probe photoemission in TaS_2: A single-band DFT+DMFT(NRG) study within the quasiequilibrium approximation*, Phys. Status Solidi B **246**, 948 (2009), arXiv:0809.2347. Cited on page 80.

[322] H. Zhang, L.-M. Liu, and W.-M. Lau, *Dimension-dependent phase transition and magnetic properties of VS_2*, J. Mater. Chem. A **1**, 10821 (2013). Cited on pages 82 and 83.

[323] H. L. Zhuang and R. G. Hennig, *Stability and magnetism of strongly correlated single-layer VS_2*, Phys. Rev. B **93**, 054429 (2016). Cited on pages 82 and 83.

[324] E. B. Isaacs and C. A. Marianetti, *Electronic correlations in monolayer VS_2*, Phys. Rev. B **94**, 035120 (2016), arXiv:1602.08483. Cited on pages 82 and 83.

[325] M. Leroux, M. Le Tacon, M. Calandra, L. Cario, M.-A. Méasson, P. Diener, E. Borrissenko, A. Bosak, and P. Rodière, *Anharmonic suppression of charge density waves in 2H-NbS_2*, Phys. Rev. B **86**, 155125 (2012), arXiv:1210.2327. Cited on pages 82, 83, and 89.

[326] Y. Xu, X. Liu, and W. Guo, *Tensile strain induced switching of magnetic states in $NbSe_2$ and NbS_2 single layers*, Nanoscale **6**, 12929 (2014). Cited on pages 82 and 83.

[327] F. Güller, V. L. Vildosola, and A. M. Llois, *Spin density wave instabilities in the NbS_2 monolayer*, Phys. Rev. B **93**, 094434 (2016), arXiv:1510.06477. Cited on pages 82, 83, and 86.

[328] H. Lin, W. Huang, K. Zhao, C. Lian, W. Duan, X. Chen, and S.-H. Ji, *Growth of atomically thick transition metal sulfide films on graphene/6H-SiC(0001) by molecular beam epitaxy*, Nano Res. **11**, 4722 (2018). Cited on pages 82, 83, and 100.

[329] J. P. Tidman, O. Singh, A. E. Curzon, and R. F. Frindt, *The phase transition in 2H-TaS_2 at 75 K*, Philos. Mag. **30**, 1191 (1974). Cited on pages 82, 83, 94, and 100.

[330] F. Li, K. Tu, and Z. Chen, *Versatile electronic properties of VSe_2 bulk, few-layers, monolayer, nanoribbons, and nanotubes: A computational exploration*, J. Phys. Chem. C **118**, 21264 (2014). Cited on pages 82 and 83.

[331] R. Bianco, L. Monacelli, M. Calandra, F. Mauri, and I. Errea, *Weak dimensionality dependence and dominant role of ionic fluctuations in the charge-density-wave transition of $NbSe_2$*, Phys. Rev. Lett. **125**, 106101 (2020), arXiv:2004.08147. Cited on pages 82 and 83.

[332] C. W. Chu, L. R. Testardi, F. J. Di Salvo, and D. E. Moncton, *Pressure effects on the charge-density-wave phases in 2H-$TaSe_2$*, Phys. Rev. B **14**, 464 (1976). Cited on pages 82 and 83.

[333] Y. Ge and A. Y. Liu, *Effect of dimensionality and spin-orbit coupling on charge-density-wave transition in 2H-$TaSe_2$*, Phys. Rev. B **86**, 104101 (2012). Cited on pages 82, 83, and 105.

[334] F. Jellinek, G. Brauer, and H. Müller, *Molybdenum and niobium sulphides*, Nature **185**, 376 (1960). Cited on page 84.

[335] B. E. Brown and D. J. Beerntsen, *Layer structure polytypism among niobium and tantalum selenides*, Acta Cryst. **18**, 31 (1965). Cited on page 84.

[336] A. Meetsma, G. A. Wiegers, R. J. Haange, and J. L. de Boer, *Structure of 2H-TaS_2*, Acta Cryst. C **46**, 1598 (1990). Cited on page 84.

[337] E. Bjerkelund and A. Kjekshus, *On the structural properties of the $Ta_{1+x}Se_2$ phase*, Acta Chem. Scand. **21**, 513 (1967). Cited on page 84.

[338] J. Kanamori, *Electron correlation and ferromagnetism of transition metals*, Prog. Theor. Phys. **30**, 275 (1963). Cited on page 85.

[339] E. Şaşıoğlu, A. Schindlmayr, C. Friedrich, F. Freimuth, and S. Blügel, *Wannier-function approach to spin excitations in solids*, Phys. Rev. B **81**, 054434 (2010), arXiv:1002.4897. Cited on page 86.

[340] S. Goedecker, M. Teter, and J. Hutter, *Separable dual-space Gaussian pseudopotentials*, Phys. Rev. B **54**, 1703 (1996), arXiv:mtrl-th/9512004. Cited on pages 88, 112, and 156.

[341] C. Hartwigsen, S. Goedecker, and J. Hutter, *Relativistic separable dual-space Gaussian pseudopotentials from H to Rn*, Phys. Rev. B **58**, 3641 (1998), arXiv:cond-mat/9803286. Cited on pages 88, 112, and 156.

[342] C. E. Sanders, M. Dendzik, A. S. Ngankeu, A. Eich, A. Bruix, M. Bianchi, J. A. Miwa, B. Hammer, A. A. Khajetoorians, and P. Hofmann, *Crystalline and electronic structure of single-layer TaS_2*, Phys. Rev. B **94**, 081404(R) (2016), arXiv:1606.05856. Cited on pages 89, 90, 92, 93, 104, and 111.

[343] J. Tersoff and D. R. Hamann, *Theory of the scanning tunneling microscope*, Phys. Rev. B **31**, 805 (1985). Cited on page 90.

[344] A. Palczewski, *Angle-resolved photoemission spectroscopy (ARPES) studies of cuprate superconductors*, Graduate Theses and Dissertations **11641** (2010). Cited on page 90.

[345] O. R. Albertini, A. Y. Liu, and M. Calandra, *Effect of electron doping on lattice instabilities in single-layer 1H-TaS_2*, Phys. Rev. B **95**, 235121 (2017), arXiv:1702.08588. Cited on pages 89, 91, 92, 93, 101, and 104.

[346] H. M. Lefcochilos-Fogelquist, O. R. Albertini, and A. Y. Liu, *Substrate-induced suppression of charge density wave phase in monolayer 1H-TaS_2 on Au(111)*, Phys. Rev. B **99**, 174113 (2019), arXiv:1903.05177. Cited on page 93.

[347] F. Jellinek, *The system tantalum-sulfur*, J. Alloys Compd. **4**, 9 (1962). Cited on page 95.

[348] K. Sakamaki, A. Funshima, and Y. Onuki, *Definitive structure of a stacking boundary of charge density waves in 1T-TaS_2 using a scanning tunneling microscope*, J. Phys. Chem. Solids **52**, 409 (1991). Cited on page 95.

[349] D. R. Hamann, *Optimized norm-conserving Vanderbilt pseudopotentials*, Phys. Rev. B **88**, 085117 (2013), arXiv:1306.4707. Cited on page 96.

[350] M. J. van Setten, M. Giantomassi, E. Bousquet, M. J. Verstraete, D. R. Hamann, X. Gonze, and G. M. Rignanese, *The PseudoDojo: Training and grading a 85 element optimized norm-conserving pseudopotential table*, Comput. Phys. Commun. **226**, 39 (2018), arXiv:1710.10138. Cited on pages 96, 158, 160, and 161.

[351] S. Grimme, J. Antony, S. Ehrlich, and H. Krieg, *A consistent and accurate ab initio parametrization of density functional dispersion correction (DFT-D) for the 94 elements H–Pu*, J. Chem. Phys. **132**, 154104 (2010). Cited on pages 96 and 112.

[352] Z.-X. Shen, A. Lanzara, S. Ishihara, and N. Nagaosa, *Role of the electron-phonon interaction in the strongly correlated cuprate superconductors*, Philos. Mag. B **82**, 1349 (2002). Cited on pages 97 and 113.

[353] O. Gunnarsson and O. Rösch, *Interplay between electron–phonon and Coulomb interactions in cuprates*, J. Phys. Condens. Matter **20**, 043201 (2008), arXiv:0708.1407. Cited on pages 97 and 113.

[354] G. R. Stewart, *Superconductivity in iron compounds*, Rev. Mod. Phys. **83**, 1589 (2011), arXiv:1106.1618. Cited on pages 97 and 113.

[355] D. Huang and J. E. Hoffman, *Monolayer FeSe on $SrTiO_3$*, Annu. Rev. Condens. Matter Phys. **8**, 311 (2017), arXiv:1703.09306. Cited on pages 97 and 113.

[356] C. M. Varma and A. L. Simons, *Strong-coupling theory of charge-density-wave transitions*, Phys. Rev. Lett. **51**, 138 (1983). Cited on pages 97, 98, and 101.

[357] T. M. Rice and G. K. Scott, *New mechanism for a charge-density-wave instability*, Phys. Rev. Lett. **35**, 120 (1975). Cited on pages 97, 98, 102, 105, and 106.

[358] R. L. Withers and J. A. Wilson, *An examination of the formation and characteristics of charge-density waves in inorganic materials with special reference to the two- and one-dimensional transition-metal chalcogenides*, J. Phys. C: Solid State Phys. **19**, 4809 (1986). Cited on page 98.

[359] D. Pasquier and O. V. Yazyev, *Unified picture of lattice instabilities in metallic transition metal dichalcogenides*, Phys. Rev. B **100**, 201103(R) (2019), arXiv:1901.10588. Cited on page 98.

[360] A. Cavalleri, T. Dekorsy, H. H. W. Chong, J. C. Kieffer, and R. W. Schoenlein, *Evidence for a structurally-driven insulator-to-metal transition in VO_2: A view from the ultrafast timescale*, Phys. Rev. B **70**, 161102(R) (2004), arXiv:cond-mat/0403214. Cited on page 98.

[361] S. Hellmann, T. Rohwer, M. Kalläne, K. Hanff, C. Sohrt, A. Stange, A. Carr, M. M. Murnane, H. C. Kapteyn, L. Kipp, M. Bauer, and K. Rossnagel, *Time-domain classification of charge-density-wave insulators*, Nat. Commun. **3**, 1 (2012). Cited on page 98.

[362] K. Rossnagel, O. Seifarth, L. Kipp, M. Skibowski, D. Voß, P. Krüger, A. Mazur, and J. Pollmann, *Fermi surface of 2H-$NbSe_2$ and its implications on the charge-density-wave mechanism*, Phys. Rev. B **64**, 235119 (2001). Cited on page 98.

[363] T. Valla, A. V. Fedorov, P. D. Johnson, P.-A. Glans, C. McGuinness, K. E. Smith, E. Y. Andrei, and H. Berger, *Quasiparticle spectra, charge-density waves, superconductivity, and electron-phonon coupling in 2H-$NbSe_2$*, Phys. Rev. Lett. **92**, 086401 (2004), arXiv:cond-mat/0308278. Cited on page 98.

[364] F. Weber, S. Rosenkranz, J.-P. Castellan, R. Osborn, R. Hott, R. Heid, K.-P. Bohnen, T. Egami, A. H. Said, and D. Reznik, *Extended phonon collapse and the origin of the charge-density wave in 2H-$NbSe_2$*, Phys. Rev. Lett. **107**, 107403 (2011), arXiv:1103.5755. Cited on page 98.

[365] A. Soumyanarayanan, M. M. Yee, Y. He, J. van Wezel, D. J. Rahn, K. Rossnagel, E. W. Hudson, M. R. Norman, and J. E. Hoffman, *Quantum phase transition from triangular to stripe charge order in $NbSe_2$*, Proc. Natl. Acad. Sci. USA **110**, 1623 (2013), arXiv:1212.4087. Cited on page 98.

[366] C. J. Arguello, S. P. Chockalingam, E. P. Rosenthal, L. Zhao, C. Gutiérrez, J. H. Kang, W. C. Chung, R. M. Fernandes, S. Jia, A. J. Millis, R. J. Cava, and A. N. Pasupathy, *Visualizing the charge density wave transition in 2H-$NbSe_2$ in real space*, Phys. Rev. B **89**, 235115 (2014). Cited on page 98.

[367] C. J. Arguello, E. P. Rosenthal, E. F. Andrade, W. Jin, P. C. Yeh, N. Zaki, S. Jia, R. J. Cava, R. M. Fernandes, A. J. Millis, T. Valla, R. M. Osgood, and A. N. Pasupathy, *Quasiparticle interference, quasiparticle interactions, and the origin of the charge density wave in 2H-$NbSe_2$*, Phys. Rev. Lett. **114**, 037001 (2015), arXiv:1408.4432. Cited on page 98.

[368] X. Zhu, Y. Cao, J. Zhang, E. W. Plummer, and J. Guo, *Classification of charge density waves based on their nature*, Proc. Natl. Acad. Sci. USA **112**, 2367 (2015), arXiv:1503.01858. Cited on page 98.

[369] Y. Nakata, K. Sugawara, S. Ichinokura, Y. Okada, T. Hitosugi, T. Koretsune, K. Ueno, S. Hasegawa, T. Takahashi, and T. Sato, *Anisotropic band splitting in monolayer $NbSe_2$: Implications for superconductivity and charge density wave*, npj 2D Mater. Appl. **2**, 12 (2018). Cited on page 98.

[370] W. L. McMillan, *Microscopic model of charge-density waves in 2H-$TaSe_2$*, Phys. Rev. B **16**, 643 (1977). Cited on page 98.

[371] C. Haas, *Chemical bond model of lattice distortions in hexagonal layers*, Solid State Commun. **26**, 709 (1978). Cited on page 98.

[372] J. E. Inglesfield, *Bonding and phase transitions in transition metal dichalcogenide layer compounds*, J. Phys. C: Solid State Phys. **13**, 17 (1980). Cited on pages 98 and 101.

[373] J. E. Inglesfield, *Bonding and charge density wave phase transitions*, Physica B+C **99**, 238 (1980). Cited on pages 98 and 101.

[374] M. H. Whangbo and E. Canadell, *Analogies between the concepts of molecular chemistry and solid-state physics concerning structural instabilities. Electronic origin of the structural modulations in layered transition metal dichalcogenides*, J. Am. Chem. Soc. **114**, 9587 (1992). Cited on page 98.

[375] J. A. Wilson, *Charge-density waves in the 2H-$TaSe_2$ family: Action on the Fermi surface*, Phys. Rev. B **15**, 5748 (1977). Cited on page 98.

[376] T. Straub, T. Finteis, R. Claessen, P. Steiner, S. Hüfner, P. Blaha, C. S. Oglesby, and E. Bucher, *Charge-density-wave mechanism in 2H-$NbSe_2$: Photoemission results*, Phys. Rev. Lett. **82**, 4504 (1999). Cited on page 98.

[377] D. W. Shen, Y. Zhang, L. X. Yang, J. Wei, H. W. Ou, J. K. Dong, B. P. Xie, C. He, J. F. Zhao, B. Zhou, M. Arita, K. Shimada, H. Namatame, M. Taniguchi, J. Shi, and D. L. Feng, *Primary role of the barely occupied states in the charge density wave formation of $NbSe_2$*, Phys. Rev. Lett. **101**, 226406 (2008), arXiv:0806.1344. Cited on page 98.

[378] S. V. Borisenko, A. A. Kordyuk, V. B. Zabolotnyy, D. S. Inosov, D. Evtushinsky, B. Büchner, A. N. Yaresko, A. Varykhalov, R. Follath, W. Eberhardt, L. Patthey, and H. Berger, *Two energy gaps and Fermi-surface "arcs" in $NbSe_2$*, Phys. Rev. Lett. **102**, 166402 (2009), arXiv:0904.3277. Cited on page 98.

[379] W. C. Tonjes, V. A. Greanya, R. Liu, C. G. Olson, and P. Molinié, *Charge-density-wave mechanism in the 2H-$NbSe_2$ family: Angle-resolved photoemission studies*, Phys. Rev. B **63**, 235101 (2001). Cited on pages 98 and 100.

[380] W. Kohn, *Image of the Fermi surface in the vibration spectrum of a metal*, Phys. Rev. Lett. **2**, 393 (1959). Cited on page 99.

[381] G. A. Scholz, O. Singh, R. F. Frindt, and A. E. Curzon, *Charge density wave commensurability in 2H-TaS_2 and Ag_xTaS_2*, Solid State Commun. **44**, 1455 (1982). Cited on page 100.

[382] R. V. Coleman, B. Giambattista, P. K. Hansma, A. Johnson, W. W. McNairy, and C. G. Slough, *Scanning tunnelling microscopy of charge-density waves in transition metal chalcogenides*, Adv. Phys. **37**, 559 (1988). Cited on page 100.

[383] C. Wang, C. G. Slough, and R. V. Coleman, *Spectroscopy of dichalcogenides and trichalcogenides using scanning tunneling microscopy*, J. Vac. Sci. Technol. B: Microelectron. Process. Phenom. **9**, 1048 (1991). Cited on page 100.

[384] S. Nagata, T. Aochi, T. Abe, S. Ebisu, T. Hagino, Y. Seki, and K. Tsutsumi, *Superconductivity in the layered compound 2H-TaS_2*, J. Phys. Chem. Solids **53**, 1259 (1992). Cited on page 100.

[385] C. M. Varma and W. Weber, *Phonon dispersion in transition metals*, Phys. Rev. Lett. **39**, 1094 (1977). Cited on page 101.

[386] F. Weber, R. Hott, R. Heid, K.-P. Bohnen, S. Rosenkranz, J.-P. Castellan, R. Osborn, A. H. Said, B. M. Leu, and D. Reznik, *Optical phonons and the soft mode in 2H-$NbSe_2$*, Phys. Rev. B **87**, 245111 (2013), arXiv:1303.6503. Cited on page 101.

[387] E. G. Maksimov and S. V. Shulga, *Nonadiabatic effects in optical phonon self-energy*, Solid State Commun. **97**, 553 (1996). Cited on page 101.

[388] M. Lazzeri and F. Mauri, *Nonadiabatic Kohn anomaly in a doped graphene monolayer*, Phys. Rev. Lett. **97**, 266407 (2006), arXiv:cond-mat/0611708. Cited on page 101.

[389] N. Caudal, A. M. Saitta, M. Lazzeri, and F. Mauri, *Kohn anomalies and nonadiabaticity in doped carbon nanotubes*, Phys. Rev. B **75**, 115423 (2007). Cited on page 101.

[390] S. Pisana, M. Lazzeri, C. Casiraghi, K. S. Novoselov, A. K. Geim, A. C. Ferrari, and F. Mauri, *Breakdown of the adiabatic Born–Oppenheimer approximation in graphene*, Nat. Mater. **6**, 198 (2007), arXiv:cond-mat/0611714. Cited on page 101.

[391] S. Piscanec, M. Lazzeri, J. Robertson, A. C. Ferrari, and F. Mauri, *Optical phonons in carbon nanotubes: Kohn anomalies, Peierls distortions, and dynamic effects*, Phys. Rev. B **75**, 035427 (2007), arXiv:cond-mat/0611693. Cited on page 101.

[392] A. M. Saitta, M. Lazzeri, M. Calandra, and F. Mauri, *Giant nonadiabatic effects in layer metals: Raman spectra of intercalated graphite explained*, Phys. Rev. Lett. **100**, 226401 (2008), arXiv:0802.4426. Cited on page 101.

[393] L. M. Roth, H. J. Zeiger, and T. A. Kaplan, *Generalization of the Ruderman-Kittel-Kasuya-Yosida interaction for nonspherical Fermi surfaces*, Phys. Rev. **149**, 519 (1966). Cited on page 102.

[394] F. J. Di Salvo, J. A. Wilson, B. G. Bagley, and J. V. Waszczak, *Effects of doping on charge-density waves in layer compounds*, Phys. Rev. B **12**, 2220 (1975). Cited on page 104.

[395] X. M. Chen, A. J. Miller, C. Nugroho, G. A. de la Peña, Y. I. Joe, A. Kogar, J. D. Brock, J. Geck, G. J. MacDougall, S. L. Cooper, E. Fradkin, D. J. Van Harlingen, and P. Abbamonte, *Influence of Ti doping on the incommensurate charge density wave in 1T-TaS_2*, Phys. Rev. B **91**, 245113 (2015). Cited on page 104.

[396] D. F. Shao, R. C. Xiao, W. J. Lu, H. Y. Lv, J. Y. Li, X. B. Zhu, and Y. P. Sun, *Manipulating charge density waves in 1T-TaS_2 by charge-carrier doping: A first-principles investigation*, Phys. Rev. B **94**, 125126 (2016), arXiv:1512.06553. Cited on page 104.

[397] N. J. Doran, *A calculation of the electronic response function in 2H-$NbSe_2$ including electron-phonon matrix element effects*, J. Phys. C: Solid State Phys. **11**, L959 (1978). Cited on page 105.

[398] A. H. Castro Neto, *Charge density wave, superconductivity, and anomalous metallic behavior in 2D transition metal dichalcogenides*, Phys. Rev. Lett. **86**, 4382 (2001), arXiv:cond-mat/0012147. Cited on page 105.

[399] W. A. Harrison and S. Froyen, *Universal linear-combination-of-atomic-orbitals parameters for d-state solids*, Phys. Rev. B **21**, 3214 (1980). Cited on page 107.

[400] G.-B. Liu, W.-Y. Shan, Y. Yao, W. Yao, and D. Xiao, *Three-band tight-binding model for monolayers of group-VIB transition metal dichalcogenides*, Phys. Rev. B **88**, 085433 (2013), arXiv:1305.6089. Cited on page 111.

[401] J. A. Wilson, *Modelling the contrasting semimetallic characters of TiS_2 and $TiSe_2$*, Phys. Status Solidi B **86**, 11 (1978). Cited on page 113.

[402] K. Rossnagel, L. Kipp, and M. Skibowski, *Charge-density-wave phase transition in 1T-$TiSe_2$: Excitonic insulator versus band-type Jahn-Teller mechanism*, Phys. Rev. B **65**, 235101 (2002). Cited on page 113.

[403] H. Cercellier, C. Monney, F. Clerc, C. Battaglia, L. Despont, M. G. Garnier, H. Beck, P. Aebi, L. Patthey, H. Berger, and L. Forró, *Evidence for an excitonic insulator phase in 1T-$TiSe_2$*, Phys. Rev. Lett. **99**, 146403 (2007), arXiv:0704.0159. Cited on page 113.

[404] J. van Wezel, P. Nahai-Williamson, and S. S. Saxena, *Exciton-phonon-driven charge density wave in $TiSe_2$*, Phys. Rev. B **81**, 165109 (2010). Cited on page 113.

[405] C. Monney, C. Battaglia, H. Cercellier, P. Aebi, and H. Beck, *Exciton condensation driving the periodic lattice distortion of 1T-$TiSe_2$*, Phys. Rev. Lett. **106**, 106404 (2011), arXiv:1012.1119. Cited on page 113.

[406] C. Chen, B. Singh, H. Lin, and V. M. Pereira, *Reproduction of the charge density wave phase diagram in 1T-$TiSe_2$ exposes its excitonic character*, Phys. Rev. Lett. **121**, 226602 (2018), arXiv:1712.04967. Cited on page 113.

[407] T. Kaneko, Y. Ohta, and S. Yunoki, *Exciton-phonon cooperative mechanism of the triple-q charge-density-wave and antiferroelectric electron polarization in $TiSe_2$*, Phys. Rev. B **97**, 155131 (2018), arXiv:1711.08547. Cited on page 113.

[408] D. Pasquier and O. V. Yazyev, *Excitonic effects in two-dimensional $TiSe_2$ from hybrid density functional theory*, Phys. Rev. B **98**, 235106 (2018), arXiv:1805.11560. Cited on page 113.

[409] Quantum ESPRESSO Foundation, *Quantum ESPRESSO*, gitlab.com/QEF/q-e (2020). Cited on page 116.

[410] O. Parcollet, M. Ferrero, T. Ayral, H. Hafermann, I. Krivenko, L. Messio, and P. Seth, *TRIQS: A toolbox for research on interacting quantum systems*, Comput. Phys. Commun. **196**, 398 (2015), arXiv:1504.01952. Cited on page 121.

[411] L. Dalcín, R. Paz, and M. Storti, *MPI for Python*, J. Parallel Distr. Com. **65**, 1108 (2005). Cited on pages 121 and 164.

[412] T. E. Oliphant, *Python for scientific computing*, Comput. Sci. Eng. **9**, 10 (2007). Cited on pages 121 and 164.

[413] J. Berges, *StoryLines: Line plots with Python and TikZ*, bitbucket.org/berges/storylines (2016). Cited on page 126.

[414] T. Tantau, *TikZ & PGF*, github.com/pgf-tikz (2007). Cited on page 126.

[415] D. J. Chadi and M. L. Cohen, *Special points in the Brillouin zone*, Phys. Rev. B **8**, 5747 (1973). Cited on pages 135 and 142.

[416] H. J. Monkhorst and J. D. Pack, *Special points for Brillouin-zone integrations*, Phys. Rev. B **13**, 5188 (1976). Cited on pages 135 and 142.

[417] O. Jepsen and O. K. Andersen, *The electronic structure of h.c.p. ytterbium*, Solid State Commun. **9**, 1763 (1971). Cited on page 135.

[418] P. E. Blöchl, O. Jepsen, and O. K. Andersen, *Improved tetrahedron method for Brillouin-zone integrations*, Phys. Rev. B **49**, 16223 (1994). Cited on page 135.

[419] L. Van Hove, *The occurrence of singularities in the elastic frequency distribution of a crystal*, Phys. Rev. **89**, 1189 (1953). Cited on page 142.

[420] F. Bloch, *Über die Quantenmechanik der Elektronen in Kristallgittern*, Z. Physik **52**, 555 (1929). Cited on page 144.

[421] F. J. Dyson, *The radiation theories of Tomonaga, Schwinger, and Feynman*, Phys. Rev. **75**, 486 (1949). Cited on page 144.

[422] T. Matsubara, *A new approach to quantum-statistical mechanics*, Prog. Theor. Phys. **14**, 351 (1955). Cited on pages 144 and 145.

[423] G. D. Mahan, *Many-Particle Physics*, 3rd ed. (Kluwer Academic/Plenum Publishers, New York, 2000). Cited on pages 144 and 146.

[424] F. J. Dyson, *The S matrix in quantum electrodynamics*, Phys. Rev. **75**, 1736 (1949). Cited on page 144.

[425] G. C. Wick, *The evaluation of the collision matrix*, Phys. Rev. **80**, 268 (1950). Cited on page 145.

[426] D. J. Thouless, *Use of field theory techniques in quantum statistical mechanics*, Phys. Rev. **107**, 1162 (1957). Cited on page 145.

[427] M. Gaudin, *Une démonstration simplifiée du théorème de Wick en mécanique statistique*, Nucl. Phys. **15**, 89 (1960). Cited on page 145.

[428] K. Yoshimi, T. Kato, and H. Maebashi, *Enhanced spin susceptibility toward the charge-ordering transition in a two-dimensional extended Hubbard model*, J. Phys. Soc. Jpn. **78**, 104002 (2009), arXiv:0904.4302. Cited on page 146.

[429] B. S. Shastry, *Magnetic susceptibility of an electron gas in the random-phase approximation*, Phys. Rev. B **17**, 385 (1978). Cited on page 146.

[430] H. Hellmann, *Einführung in die Quantenchemie* (Franz Deuticke, Leipzig, Wien, 1937). Cited on page 147.

[431] R. P. Feynman, *Forces in molecules*, Phys. Rev. **56**, 340 (1939). Cited on page 147.

[432] L. J. Bartolotti and R. G. Parr, *The concept of pressure in density functional theory*, J. Chem. Phys. **72**, 1593 (1980). Cited on page 147.

[433] K. M. Ho, C. L. Fu, B. N. Harmon, W. Weber, and D. R. Hamann, *Vibrational frequencies and structural properties of transition metals via total-energy calculations*, Phys. Rev. Lett. **49**, 673 (1982). Cited on page 147.

[434] C. L. Fu and K. M. Ho, *First-principles calculation of the equilibrium ground-state properties of transition metals: Applications to Nb and Mo*, Phys. Rev. B **28**, 5480 (1983). Cited on page 147.

[435] C. Heil, G. B. Bachelet, and L. Boeri, *Absence of superconductivity in iron polyhydrides at high pressures*, Phys. Rev. B **97**, 214510 (2018), arXiv:1804.03572. Cited on page 147.

[436] P. A. M. Dirac, *The Principles of Quantum Mechanics*, 4th ed. (Clarendon Press, Oxford, 1958). Cited on page 147.

[437] E. Fermi, *Zur Quantelung des idealen einatomigen Gases*, Z. Physik **36**, 902 (1926). Cited on page 148.

[438] P. A. M. Dirac and R. H. Fowler, *On the theory of quantum mechanics*, Proc. R. Soc. Lond. A **112**, 661 (1926). Cited on page 148.

[439] H. Solomon, *Geometric Probability* (Society for Industrial and Applied Mathematics, Philadelphia, 1978). Cited on page 151.

[440] E. J. G. Santos and E. Kaxiras, *Electric-field dependence of the effective dielectric constant in graphene*, Nano Lett. **13**, 898 (2013). Cited on page 151.

[441] L. Patrick and W. J. Choyke, *Static dielectric constant of SiC*, Phys. Rev. B **2**, 2255 (1970). Cited on page 151.

[442] J. Zhou, Q. Wang, Q. Sun, X. S. Chen, Y. Kawazoe, and P. Jena, *Ferromagnetism in semihydrogenated graphene sheet*, Nano Lett. **9**, 3867 (2009). Cited on page 153.

[443] L. Feng and W. X. Zhang, *The structure and magnetism of graphone*, AIP Adv. **2**, 042138 (2012), arXiv:1206.6166. Cited on page 153.

[444] X. Zhou, Y. Huang, X. Chen, and W. Lu, *Density functional theory study of the vibrational properties of hydrogenated graphene*, Solid State Commun. **157**, 24 (2013). Cited on page 153.

[445] J. Berges, *Phasen ladungsabhängiger Adsorbatstrukturen auf Graphen*, Bachelor's thesis, Universität Bremen (2014). Cited on page 153.

[446] J. W. Mintmire, J. R. Sabin, and S. B. Trickey, *Local-density-functional methods in two-dimensionally periodic systems. Hydrogen and beryllium monolayers*, Phys. Rev. B **26**, 1743 (1982). Cited on page 155.

[447] A. Leonardo, I. Y. Sklyadneva, P. M. Echenique, and E. V. Chulkov, *Electron–phonon interaction in a free standing beryllium monolayer*, Surf. Sci. **600**, 3715 (2006). Cited on page 155.

[448] Y. Jing, Y. Ma, Y. Li, and T. Heine, *GeP_3: A small indirect band gap 2D crystal with high carrier mobility and strong interlayer quantum confinement*, Nano Lett. **17**, 1833 (2017), arXiv:1612.04081. Cited on page 160.

[449] J. Nagamatsu, N. Nakagawa, T. Muranaka, Y. Zenitani, and J. Akimitsu, *Superconductivity at 39 K in magnesium diboride*, Nature **410**, 63 (2001). Cited on page 160.

[450] N. I. Medvedeva, J. E. Medvedeva, A. L. Ivanovskii, V. G. Zubkov, and A. J. Freeman, *Band structure of the superconducting MgB_2 compound and modeling of related ternary systems*, JETP Lett. **73**, 336 (2001). Cited on page 160.

[451] Y. Maeno, H. Hashimoto, K. Yoshida, S. Nishizaki, T. Fujita, J. G. Bednorz, and F. Lichtenberg, *Superconductivity in a layered perovskite without copper*, Nature **372**, 532 (1994). Cited on page 161.

[452] X. Deng, K. Haule, and G. Kotliar, *Transport properties of metallic ruthenates: A DFT+DMFT investigation*, Phys. Rev. Lett. **116**, 256401 (2016), arXiv:1504.00292. Cited on pages 161 and 162.

[453] A. W. Tyler, A. P. Mackenzie, S. NishiZaki, and Y. Maeno, *High-temperature resistivity of Sr_2RuO_4: Bad metallic transport in a good metal*, Phys. Rev. B **58**, R10107 (1998). Cited on pages 161 and 162.

[454] M. Zingl, J. Mravlje, M. Aichhorn, O. Parcollet, and A. Georges, *Hall coefficient signals orbital differentiation in the Hund's metal Sr_2RuO_4*, npj Quantum Mater. **4**, 1 (2019), arXiv:1902.05503. Cited on page 161.

[455] T. Vogt and D. J. Buttrey, *Low-temperature structural behavior of Sr_2RuO_4*, Phys. Rev. B **52**, R9843 (1995). Cited on page 161.

[456] A. Tamai, M. Zingl, E. Rozbicki, E. Cappelli, S. Riccò, A. de la Torre, S. McKeown Walker, F. Y. Bruno, P. D. C. King, W. Meevasana, M. Shi, M. Radović, N. C. Plumb, A. S. Gibbs, A. P. Mackenzie, C. Berthod, H. U. R. Strand, M. Kim, A. Georges, and F. Baumberger, *High-resolution photoemission on Sr_2RuO_4 reveals correlation-enhanced effective spin-orbit coupling and dominantly local self-energies*, Phys. Rev. X **9**, 021048 (2019), arXiv:1812.06531. Cited on page 161.

[457] M. Braden, W. Reichardt, Y. Sidis, Z. Mao, and Y. Maeno, *Lattice dynamics and electron-phonon coupling in Sr_2RuO_4: Inelastic neutron scattering and shell-model calculations*, Phys. Rev. B **76**, 014505 (2007), arXiv:cond-mat/0702293. Cited on page 161.

[458] T. Bauer and C. Falter, *The phonon dynamics of Sr_2RuO_2: Microscopic calculation and comparison with that of La_2CuO_4*, J. Phys. Condens. Matter **21**, 395701 (2009), arXiv:0906.0692. Cited on page 161.

[459] P. B. Allen, *The electron–phonon coupling constant λ*, in *Handbook of Superconductivity*, edited by C. P. Poole (Academic Press, New York, 1999). Cited on page 162.

[460] A. Roy, H. C. P. Movva, B. Satpati, K. Kim, R. Dey, A. Rai, T. Pramanik, S. Guchhait, E. Tutuc, and S. K. Banerjee, *Structural and electrical properties of $MoTe_2$ and $MoSe_2$ grown by molecular beam epitaxy*, ACS Appl. Mater. Interfaces **8**, 7396 (2016), arXiv:1603.02656. Cited on page 163.

[461] P. Virtanen, R. Gommers, T. E. Oliphant, M. Haberland, T. Reddy, D. Cournapeau, E. Burovski, P. Peterson, W. Weckesser, J. Bright, S. J. van der Walt, M. Brett, J. Wilson, K. J. Millman, N. Mayorov, A. R. J. Nelson, E. Jones, R. Kern, E. Larson, C. J. Carey, I. Polat, Y. Feng, E. W. Moore, J. VanderPlas, D. Laxalde, J. Perktold, R. Cimrman, I. Henriksen, E. A. Quintero, C. R. Harris, A. M. Archibald, A. H. Ribeiro, F. Pedregosa, and P. van Mulbregt, *SciPy 1.0: Fundamental algorithms for scientific computing in Python*, Nat. Methods **17**, 261 (2020), arXiv:1907.10121. Cited on page 164.

[462] A. Meurer, C. P. Smith, M. Paprocki, O. Čertík, S. B. Kirpichev, M. Rocklin, A. Kumar, S. Ivanov, J. K. Moore, S. Singh, T. Rathnayake, S. Vig, B. E. Granger, R. P. Muller, F. Bonazzi, H. Gupta, S. Vats, F. Johansson, F. Pedregosa, M. J. Curry, A. R. Terrel, v. Roučka, A. Saboo, I. Fernando, S. Kulal, R. Cimrman, and A. Scopatz, *SymPy: Symbolic computing in Python*, PeerJ Comput. Sci. **3**, e103 (2017). Cited on page 164.

[463] J. D. Hunter, *Matplotlib: A 2D graphics environment*, Comput. Sci. Eng. **9**, 90 (2007). Cited on page 164.

[464] M. Rösner, R. E. Groenewald, G. Schönhoff, J. Berges, S. Haas, and T. O. Wehling, *Plasmonic superconductivity in layered materials*, arXiv:1803.04576 (2018). Cited on page 166.